JOURNAL OF BIOLOGICAL REGULATORS & HOMEOSTATIC AGENTS
Volume 35, No. 1, January - February, 2021

CONTENTS

Editorials

P. Conti, Al. Caraffa, C.E. Gallenga, S.K. Kritas, I. Frydas, A. Younes, P. Di Emidio, G. Tetè, F. Pregliasco and G. Ronconi. The British variant of the new coronavirus-19 (Sars-Cov-2) should not create a vaccine problem 1

T.C. Theoharides, S. Christodoulou and A. Athanasiou. Spontaneous miscarriages in patients with bladder pain syndrome/interstitial cystitis - effect of stress on inflammation? 5

Original articles

M. Leitzke, S. Schimpf, M. Altrock, P. Schönknecht, S. Bischoff, H. Schubert, D. Hoyer, R. Bauer and S. Olbrich. Afferent vagal stimulation via gastric electrical stimulation alters sympathetic-vagal balance in domestic pigs – a pilot trial 11

Y. Feng, S.-J. Gao, R.-D. Wei, T. Liu, X.-P. Fan, Y.-D. Han and N. Zhu. Effects of probiotics on intestinal flora, inflammation and degree of liver cirrhosis in rats with liver cirrhosis by regulating Wnt/β-catenin signaling pathway 25

LH. Qin, XJ. Zhu, LY. Zhang, JQ. Chen, GY. Jin and LJ. Xiang. Identification of hub genes and pathways in the development of gastric cancer by gene coexpression network analysis 35

YL. Ge, FL. Jin and DH. Zhang. Radio-sensitizing effects of microRNA-27a elevation in lung cancer cells by inhibiting ZEB1 expression and activating DNA damage repair pathway 45

X. Zhang, WW. Qin, FG. Ma, LX. Sun and W. Han. Leptin reduces ventilator-induced lung injury in rats by regulating NLRP3, NLRC4 and NLRC3 59

H. Yin, MH. Liu, F. Gao and HM. Shang. Pro-inflammatory and pro-fibrotic role of long non-coding RNA RMRP in pediatric asthma through targeting microRNA-206/CCL2 axis 71

C-J. Wei, F. Hua, Y-H. Chen, Z-W. Zhang and Z-Y. Shen. Muscone alleviates myocardial ischemia-reperfusion injury via inhibition of oxidative stress and enhancement of SIRT3 85

Y. Zhou, P. Chai, J. Wang, L. Li and MH. Chen. Wingless/int-1induced secreted protein-1: a new biomarker for renal fibrosis 97

L. Zhou, SY. Chen, HJ. Han and JQ. Sun. Lactate augments intramuscular triglyceride accumulation and mitochondrial biogenesis in rats 105

LN. Wei, M. Luo, XP. Wang, T. Liang, CJ. Huang and H. Chen. PADI4, negatively regulated by miR-335-5p, participates in regulating the proliferation, migration, invasion and radiosensitivity of nasopharyngeal carcinoma cells 117

YX. He, G. Li, Y. Liu, H. Tang, ZY. Chong, XJ. Wu, X. Jin, SY. Zhang and M. Wang. Endovascular treatment of visceral aneurysms and pseudoaneurysms 131

S. Li, Z. Guo and Z.-Y. Zhang. Protective effects of NLRP3 inhibitor MCC950 on sepsis-induced myocardial dysfunction 141

XT. Feng, C. Wang, FJ. Zhang and XQ. Wu and Z. Zhang. MicroRNA-1274a serves as a prognostic biomarker in patients with osteosarcoma and is involved in tumor progression via targeting ADAM9 151

G. Varvara, B. Sinjari, S. Bernardi, I. Turkyilmaz, V. Malvezzi, M. Piattelli and S. Caputi. Comparative surface detail reproduction for elastomeric impression materials: Study on reproducibility performance 161

G.M. Balzanelli, P. Distratis, O. Catucci, F. Amatulli, A. Cefalo, R. Lazzaro, K.S. Aityan, G. Dalagni, A. Nico, A. De Michele, E. Mazza, M. Tampoia, P. D'Errico, G. Pricolo, A. Prudenzano, E. D'Ettorre, C. Di Stasi, L.F.P. Morrone, HV. Pham, F. Inchingolo, D. Tomassone, KCD. Nguyen and C. Gargiulo Isacco. Clinical and diagnostic findings in COVID-19 patients: an original research from SG Moscati Hospital in Taranto Italy 171

Letters to the Editor

XL. Wu, JH. Cao, CJ. Shan, B. Peng, RD. Zhang, JL. Cao and FC. Zhang. Effects of fast-tracking anesthesia on the surgical efficacy and cerebral oxygen saturation of children with congenital heart disease 185

XY. Sun and Z. Liang. Effect of drug therapy on pregnancy rate, sex hormone levels and adverse reactions after laparoscopic surgery in patients with endometriosis and infertility 191

YJ. Zhang, LL. Zheng, Y. Zhu, L. Zeng, Y. Xun and SR. Deng. Differential expression and functional mechanism of TIMD4 gene in orbital adipose tissues of patients with thyroid-associated ophthalmopathy 197

Y. Chen, YT. Lv, JR. Chen and HY. Zhang. Correlation between the invasion mechanism of papillary thyroid carcinoma and expressions of NF-κB and the epithelial-mesenchymal transition-associated factors 203

B. Liu, T. Gao, H-Y. Wu and M. Wan. Erb-B2 receptor tyrosine kinase 2 knockdown inhibits retinoblastoma progression via Wnt/β-catenin signaling pathway *in vitro* 209

FJ. Qi, Z. Dong, XM. Zhang, RK.Yi, LY. Xie, HJ. Teng, JH. Lin and C. Jia. Role and mechanism of mirna-214-5p in myocardial injury in hypertensive rats 215

BH. Feng, CB. Huang and ZF. Yuan. Expression of Disrupted-in-schizophrenia 1 protein and related inflammatory factors in refractory temporal lobe epilepsy in children 221

K-L. Gao, M. Li, K-P. Zhang. Imperatorin inhibits the invasion and migration of breast cancer cells by regulating HMGB2 227

JP. Hu, HS. Jin, ZF. Lang, L. Yan, J. Liang, KR. Cai, ZS. Jin and BZ. An. Expression of HSP60 in gastric lymphoma treated by a combination of trichosanthin and radiotherapy and its mechanism 231

XZ. Meng, WW. Jiang, HW. Guo, M. Li, MM. Zhao, FJ. Yu and ZT. Gu. lncRNA NEAT1 regulates cerebral ischemia/reperfusion injury through miR-1306-5p 239

Y-M. Lv, J. Fan, M-B. Li, Y. Ma, T-T. Li, G-R. Sun. Comparison of the therapeutic effects of metformin and glibenclamide on patients with gestational diabetes 245

CL. Hu, M. Xin, K. Zhang and LC. Zhang. Double-target longitudinal puncture by freehand on elderly patients with hypertensive cerebral hemorrhage 251

ZY. Li, WZ. Liu, H. Guang, WC. Chen and YH. Yang. Silencing of long noncoding RNA H19 inhibited invasion and migration of papillary thyroid cancer cells via microRNA-138-dependent regulating of LRRK2 253

C. Qiu, JB. Zhao, HC. Lu and J. Ma. Endovascular electrocoagulation via microguidewire for treating intracranial aneurysms 259

H-M. Han, X-Z. Song, M-H. Cui, X. You and X-X. Piao. Vitamin D_3 supplementation in controlling metabolic changes associated with non-alcoholic steatohepatitis 263

L-P. Wang, G-L. Luo, J. Liu, J-X. Xu, K. Liu, F-T. Sun and Q-L. Zhou. Changes and significance of serum sMICA levels in patients with recurrent miscarriage before and after lymphocyte infusion therapy 267

P. Gonzalez Isaza and D.L. Velez Rizo. Vaginal bipolar radiofrequency as non-surgical treatment of stress urinary incontinence: Case series study 271

J. Li, ZX. Zou, CJ. Hao, YX. Shi and YB. Sui. Comparison between diagnostic value of SPECT whole-body bone imaging and magnetic resonance imaging in bone metastasis of prostate cancer 275

HB. Luo, Y. Cao, MC. Tao, XH. Yang and J. Chen. Long non-coding RNA GAS5 inhibits the proliferation and induces the apoptosis of hypertrophic scar fibroblasts by sponging miR-21 283

L. Wang, HL. Dai, X. Tang, YJ. Yang, KY. Sun and L. Yu. Predictive value of $ABCD^3$ score combined with vascular stenosis in the progression of TIA to cerebral infarction 289

W-W. Jin, D-L. Song, X. Gao, H-Y. Zhang, Q-X. Ren and Y. Chen. Analysis of risk factors affecting the prognosis of septic shock and clinical intervention 295

ZY. Ding, G. Dong, G. Yin, LL. Yu, WX. Li and B. Ding. Knockdown of Metadherin suppressed the progression of oral squamous cell carcinoma via PI3K/AKT signaling pathway 303

Y. Zhang, XX. Sun, YC. Liu and YD. Wang. Association of SREBF-2 gene polymorphisms with the risk of developing type 2 diabetes mellitus 311

YB. Zhao, XY. Zhao, J. Jia, J. Liu, JL. Xu and N. Li. Up-regulation of miR-934 serves as an independent prognostic factor for lung cancer and promotes proliferation, migration and invasion of non-small cell lung cancer cells 315

L-Z. Sun, Y-Z. Jiang, S-X. Luan, Y-L. Shi and Q. Wang. Long non-coding RNA FGD5-AS1 promotes cell viability and metastasis in osteosarcoma by regulating miR-520c-3p 323

Q.Q. Shao, T. Zhao, J.H. Ren, B. Wang and H.J. Sun. Color doppler flow imaging evaluates the influence on subclavian artery steal caused by vertebral artery hypoplasia 331

L. Zhang, Z-P. Feng, F-Q. Liu, R. Yan, L-Y. Yin, H. Shen and X-H. Liang. ASCL1 can bind to miR-135a-2 promoter elements to promote miR-135a-2 transcription and stem phenotypes in Huh7 cells 337

MA. Iqbal, Z. Naseem, S. Ahmad and N. Roohi. Endocrine relation of cardiovascular dysfunction with inflammation in hyperthyroidism 343

M. Valenzise, U. Cucinotta, T. Aversa, M.F. Messina, M. Wasniewska and G.B. Pajno. Transient hyperthyroidism in a 6-year-old girl with Epstein-Barr virus infection: a link between infectious mononucleosis and autoimmune thyroid disease 349

A. Pantalone, D. Bruni, P. Pantalone and R. Buda. Interleukin-6 as unfavorable prognostic factor in patients affected by Covid-19 and hip fracture 353

M.T. Colangelo, P. Govoni, S. Belletti, F. Squadrito, S. Guizzardi and C. Galli. Polynucleotide biogel enhances tissue repair, matrix deposition and organization 355

L. Maiolino, I. La Mantia, C. Grillo, Ct. Grillo and G. Ciprandi. Functional recovery in subjects undergoing nasal surgery: a new therapeutic strategy 363

T. Paolucci, F. Agostini, M. Mangone, A. Bernetti, B. Cordiani, R.G. Bellomo, R. Saggini and C. Villani. Sagittal spine alignment and postural balance in pre-puberty age: a multidisciplinary and multi-professional rehabilitative point of view 367

P. Amori, G. Vitiello, A. Cancelli, R. Sadoughifar, M. Tirant, N. Van Thuong, K.M. Lomonosov and T. Lotti. A new concept radiofrequency device for the treatment of cellulite 373

C E. Gallenga, C. Contini, M. Tana, D. D'Eliseo, A.L. Giuliani, F. Di Virgilio and S. Paglia. How to classify the covid-19 phenotype: a response from "the first soldier in the first trench" in Lombardy, north-western Italy 379

A. Notarnicola, G. Maccagnano, G. Farì, F.P. Bianchi, I. Covelli, G. Solarino and B. Moretti. Role of blood cell counts in the treatment of plantar fasciitis with shockwave therapy 385

N. Setaro, S. Amico and A. Gigante. Peripheral longitudinal acute meniscal lesion: conservative treatment based on medium molecular weight hyaluronic acid 391

A. de Sire, M. Ferrillo, A. Gennari, C. Cisari, S. Pasqua, P.L. Foglio Bonda, M. Invernizzi and M. Migliario. Bone health, vitamin D status and oral hygiene screening in breast cancer women before starting osteoporosis treatment: a cross-sectional study 397

L. Giannini, G. Galbiati, P. Cressoni and L. Esposito. Bad oral habits: a review of the literature 403

F. Esposito, M. Boccuzzi, A. Riad, C. Preda, A. Chiesa, G. Oldoini and A.M. Genovesi. Airborne contamination during a full-mouth disinfection session: Pilot study before COVID-19 pandemic 407

ERRATA CORRIGE

AH. Li, YH. Gao, YM. Liu, YQ. Hu, H. Wei and SQ. Lv. Montelukast sodium combined with budesonide for cough variant asthma in children 413

EDITORIAL

The British variant of the new coronavirus-19 (Sars-Cov-2) should not create a vaccine problem

P. Conti[1], Al. Caraffa[2], C.E. Gallenga[3], S.K. Kritas[4], I. Frydas[5], A. Younes[6], P. Di Emidio[7], G. Tetè[8], F. Pregliasco[9] and G. Ronconi[10]

[1]Postgraduate Medical School, University of Chieti, Chieti, Italy; [2]School of Pharmacy, University of Camerino, Camerino, Italy; [3]Molecular Medicine, Department of Morphology, Surgery, Experimental Medicine, University of Ferrara, Ferrara, Italy; [4]Department of Microbiology, University of Thessaloniki, Thessaloniki, Greece; [5]School of Veterinary Medicine, University of Thessaloniki, Thessaloniki, Greece; [6]Centro Medico "Mai più Dolore", Pescara, Italy; [7]Maxillofacial Surgery "G. Mazzini" Hospital, Teramo, Italy; [8]Specialization School in Oral Surgery, Vita-Salute San Raffaele University, Milan, Italy; [9]Medical School, University of Milan, Milan, Italy; [10]Fondazione Policlinico Universitario A. Gemelli IRCCS, Università Cattolica del Sacro Cuore, Roma, Italy

Severe acute respiratory syndrome coronavirus-2 (SARS-CoV-2) is a highly contagious virus that infects humans and a number of animal species causing coronavirus disease-19 (COVID-19), a respiratory distress syndrome which has provoked a global pandemic and a serious health crisis in most countries across our planet. COVID-19 inflammation is mediated by interleukin (IL)-1 and is a disease that can cause symptoms such as fever, cough, lung inflammation, thrombosis, stroke, renal failure and headache, to name a few. Strategies that inhibit IL-1 are certainly helpful in COVID-19 and can represent one of the therapeutic options. However, to date, COVID-19 therapy has been scarce and, in many cases, ineffective, since there are no specific drugs other than vaccine that can solve this serious health problem. Messenger RNA (mRNA) vaccines, which are the newest approach, are already available and will certainly meet the many expectations of the population. mRNA vaccines, coated with protected soft fatty lipids, use genetic mRNA (plus various inactive excipients) to make a piece of the coronavirus spike protein, which will instruct the immune system to produce specific antibodies. The soft fatty lipids allow the entry of mRNA into cells where it is absorbed into the cytoplasm and initiates the synthesis of the spike protein. In addition, vaccination also activates T cells that help the immune system respond to further exposure to the coronavirus. mRNA induces the synthesis of antigens of SARS-CoV-2 virus which stimulates the antibody response of the vaccinated person with the production of neutralizing antibodies. The new variant of the coronavirus-19 has been detected in the UK where, at present, the government has imposed a lockdown with restrictions on international movements. The virus variant had already infected 1/4 of the total cases and in December 2020, it reached 2/3 of those infected in the UK. It has been noted that the spreading rate of the British variant could be greater than 70% of cases compared to the normal SARS-CoV-2 virus, with an R index growth of 0.4. Recent studies suggest

Key words: British; COVID-19; Immunity; RNA; SARS-CoV-2; coronavirus; inflammation; side effect; vaccine; variant; virus

Corresponding Author:
Dr. Pio Conti
Professor of Immunology, Post Graduate School of Medicine
University of Chieti-Pescara, University Zone
Viale Unità d'Italia, 73 - 66013 Chieti, Italy
Tel./Fax +39-0871-574136
e-mail: pioconti editor@biolifesas.org
info@biolifesas.org - www.biolifesas.org
Affiliated Professor
Molecular Immunopharmacology and Drug Discovery Laboratory
Tufts University, Boston, MA 02111, USA

0393-974X (2021)
Copyright © by BIOLIFE, s.a.s.
This publication and/or article is for individual use only and may not be further reproduced without written permission from the copyright holder.
Unauthorized reproduction may result in financial and other penalties
DISCLOSURE: ALL AUTHORS REPORT NO CONFLICTS OF INTEREST RELEVANT TO THIS ARTICLE.

that coronavirus-19 variation occurs at the N501Y level of the spike protein and involves 23 separate mutations on the spike, 17 of which are linked to the virus proteins, thus giving specific characteristics to the virus. In general, coronaviruses undergo many mutations that are often not decisive for their biological behavior and do not significantly alter the structure and the components of the virus. This phenomenon also occurs in SARS-CoV-2. It is highly probable that the variants recently described in the UK will not hinder vaccine-induced immunity. In fact, the variant will not neutralise the vaccine, although it may possibly make it a little less effective. It is therefore pertinent to think that the vaccine will work also against the SARS-CoV-2 variant. In today's pandemic, the D614G mutation of the amino acid of corronavirus-19, which emerged in Europe in February 2020, is the most frequent form and causes high viral growth. The previously infrequent D614G mutation is now globally dominant. This variant, which is being tested in many international laboratories, is rapidly spreading across the continents and a series of vaccinated subjects are being tested to see whether their antibodies can neutralize the new variant of SARS-CoV-2. This variant has a very high viral growth and is less detectable with the RT-PCR technique in the laboratory. It has been reported that the British variant that increases viral load does not cause more severe effects in the respiratory tract and lung disease, therefore, it is certain that the variant is growing rapidly and must be kept under control; for this reason, laboratory data is awaited impatiently. The study on the many variants that coronavirus-19 presents is very interesting and complete and clearer data on this topic will be available in the near future. In addition, it is still unclear whether the different variants discovered in many countries, including Africa, share the same spike protein mutation and therefore, this is another study to elaborate on. In order to be certain and to not have unexpected surprises, we need to reduce the spread and the transmission speed of viral variants that could appear around the world, creating new pandemics. For this reason, the scientific community is on the alert since laboratory tests on serum antibodies from COVID-19 survivors have been reported to be less effective in attacking the variant. In light of the above, the scientific community must be on the alert as larger variants of the spike protein could escape vaccine-induced antibodies, which for now are of great help to the community and can save millions of lives. In depth study of spike protein mutations will help to better understand how to combat coronavirus-19 and its variants.

In December 2019, severe acute respiratory syndrome coronavirus 2 (SARS-CoV-2) emerged for the first time and spread globally, causing an unprecedented severe viral pandemic (1). SARS-CoV-2 is a highly infectious virus that remains active even at temperatures below 0°C, as has been seen recently. The global infection has affected over 40 million people and over a million have died. SARS-CoV-2 can have several effects ranging from asymptomatic respiratory tract infection to mild flu-like illness, or to severe lung disease. It is an RNA virus with a viral envelope coated with the Spike protein, capable of binding to the angiotensin converting enzyme 2 (ACE2) to create infection. Coronavirus-19, in addition to causing a dysregulation of the immune system, also provokes severe lung inflammation and fever, mediated by interleukin (IL)-1 (2). IL-1 shares the same receptor as TLR and is associated primarily with innate immunity, but also intervenes in acquired immunity. IL-1 is used by living organisms for their own immune defense, but when the levels of this cytokine rise outside the physiological state, it becomes highly inflammatory and can be extremely harmful to the body. Infectious microorganisms react with innate immune cells and stimulate the production of IL-1. Both IL-1 and microorganisms can activate TLR receptors, triggering inflammation. Serious infections that induce high levels of IL-1 can lead to death in individuals. Because IL-1 induces other inflammatory cytokines, it can trigger the cytokine storm that also occurs in COVID-19. Infections are characterized by a rapid increase of SAA, the major acute phase reactant in humans and

many other species. IL-1 and IL-6 in combination can act synergistically in inducing serum amyloid A (SAA) (3). IL-1 cytokine causes severe damage to lung tissue and mediates the formation of micro-thrombi. Therefore, IL-1 suppression could be a valid therapeutic strategy to use. The harmful effects due to SARS-CoV-2 have led many laboratories to try to generate a vaccine in order to avoid SARS-CoV-2-induced COVID-19 respiratory disease (4). One of the vaccines made in the short term (less than a year) is that with mRNA that encodes (S-2P antigen) for the spike protein. Vaccination with mRNA is carried out in two doses 21-28 days apart, the first being injected at a higher dose that usually causes an insufficient and unsatisfactory antibody response (Table I) (5). After the second administration, there is a high production of neutralizing serum containing IgG antibodies against the spike protein. Usually these antibody responses to the SARS-CoV-2 virus are equal to or greater than the convalescent serum values. Hence, the mRNA vaccine induces anti-SARS-CoV-2 immune responses, demonstrating its efficacy, and for this has been approved by the Food and Drug Administration (FDA) (6). The vaccine also acts on the stimulation of $CD4^+$ T cells and throughout the TH1 cytokine network and, to a lesser extent, TH2 (IL-4 and IL-13) (7). The mRNA vaccine, supplied with a capsule composed of 4 lipids, has the S-2P antigen which stimulates the IgG antibody. All this together is placed in a sterile saline solution ready to be injected, with the aim of inducing immunity. In general, the mRNA vaccine does not cause serious adverse events, although, in sporadic cases, after the second vaccination, pain at the injection site, transient urticaria, headache, local and systemic allergy, transient fever, fatigue, nausea, swelling, chills, and muscle aches can occur. In these cases, taking analgesics or antipyretics before or after vaccination, could be helpful. After the second vaccination there is an evident and satisfactory increase in the title of the IgG antibodies bound to the S-2P antigen, without any serious toxicity. The mRNA vaccine is already in use globally and has not produced any relevant side effects so far (8). The real question is whether the mRNA vaccines in use today work against the mutated virus.

Table I. *Comparison of two RNA vaccines*

Pfizer-BionTech
Already authorized by FDA
95% efficacy
Two doses: 21 days apart
Storage -80°C to -60°C
Administration at age 16 years and over
Moderna
Already authorized by FDA
94.5% efficacy
Two doses: 28 days apart
Storage -25°C to -15°C
Administration at age 16 years and over

English variant

After SARS-CoV-2 infection, it is difficult to predict the degree of protective immunity, and it is not yet known whether individuals have a chance to become infected again. It is possible that if the patient has a first infection with SARS-CoV-2 virus, with generation of specific antibodies, and subsequently reinfection with a genetically different virus (high variant), the patient may be unprotected. Therefore, individuals already infected the first time should adopt the usual precautions to avoid reinfection. The English variant was found in the USA and carries the same mutation, but in addition to this, other mutations of which little is known have been discovered and are being studied. The gene sequence of the SARS-Cov-2 virus allows to monitor the evolution of the virus (9). The mutations on the surface of the virus can be different, even if they do not belong to the English variant, and appear in different points of our planet. However, these all seem to have the characteristics of making the virus faster in transmission and more contagious. It is important to continue to monitor the evolution and transmission of SARS-CoV-2 in order to control its impact on health and on the therapy to be implemented.

In light of the new English variant of the coronavirus-19, some doubts have arisen about the effectiveness of the vaccine. In fact, there is no data to believe that these mutations will impact the efficacy of vaccines already approved by the FDA. To date, based on current knowledge, it can be said that the English variant (D614G gene mutation of the amino acid) does not harm the vaccine although it could potentially make it a little less effective (10). However, there is no doubt that the benefit obtained from the anti-SARS-CoV-2 vaccination is enormously greater than the risks and provides a new therapeutic weapon against the deadly COVID-19 disease that now afflicts the populations of our planet. Coronavirus variants are nothing new at all, this is what happens every year with seasonal influenza. For example, it has been noted that the spread of cases of the English variant could be 70% higher than the Sars-Cov-2 virus we know, with an R index growth of 0.4. What we know today is that the viral variant is more transmissible, but it is not yet known whether it is more pathogenic, for this reason new laboratory data are awaited. Fortunately, today vaccines also work for the English variant and induce the formation of specific antibodies that fight the virus. However, if the variants are excessive, current vaccines may not work. In this case the vaccine would need to be updated, as occurs with seasonal influenza. It should be noted that the mutation occurs at the level of the N501Y genome of the spike protein, an alteration of the important part of the virus, that is, the one that binds to the receptor of the host cell. However, as already mentioned, there is currently no evidence that this variant is more dangerous than Sars-Cov-2. What can be said is that any increase in transmission and speed of the viral variant could pose a problem for the health system which is already suffering. The lack of other information on the English variant suggests that this is a subject still under study. Therefore, more in-depth work is needed to investigate the exact role of the English variant and other SARS-CoV-2 variants that are sure to appear in the near future, in order to radically combat this terrible, frightening and deadly disease called COVID-19.

REFERENCES

1. Beigel JH, Tomashek KM, Dodd LE, et al. Remdesivir for the treatment of Covid-19 - Final report. N Engl J Med; 383(19):1813826.
2. Conti P, Ronconi G, Caraffa A, Gallenga CE, Ross R, Frydas I, Kritas SK. Induction of pro-inflammatory cytokines (IL-1 and IL-6) and lung inflammation by Coronavirus-19 (COVI-19 or SARS-CoV-2): anti-inflammatory strategies. J Biol Regul Homeost Agents 2020; 34(2):327-31.
3. Conti P, Bartle L, Barbacane RC, Reale M, Placido FC, Sipe J. Synergistic activation of serum amyloid A (SAA) by IL-6 and IL-1 in combination on human Hep 3B hepatoma cell line. Role of PGE2 and IL-1 receptor antagonist. Immunol Invest 1995; 24(3):523-35.
4. Mascola JR, Fauci AS. Novel vaccine technologies for the 21st century. Nat Rev Immunol 2020; 20(2):87-88.
5. Corey L, Mascola JR, Fauci AS, Collins FS. A strategic approach to COVID-19 vaccine R&D. Science.2020; 368(6494):948-50.
6. Gordon DE, Jang GM, Bouhaddou M, et al. A SARS-CoV-2 protein interaction map reveals targets for drug repurposing. Nature. 2020 Jul;583(7816):459-68.
7. Anderson EJ, Rouphael NG, Widge AT, et al. Safety and Immunogenicity of SARS-CoV-2 mRNA-1273 Vaccine in Older Adults. N Engl J Med 2020; 383(25):2427-38.
8. Jackson LA, Anderson EJ, Rouphael NG, et al. An mRNA Vaccine against SARS-CoV-2 — preliminary report. N Engl J Med 2020; NEJMoa2022483. Published online 2020; 14.
9. Daniloski Z, Jordan TX, Wessels HH, et al. Identification of required host factors for SARS-CoV-2 Infection in Human Cells. Cell 2021; 184(1):92-105.e16.
10. Volz E, Hill V, McCrone JT, Price A, et al. Evaluating the effects of SARS-CoV-2 spike mutation D614G on transmissibility and pathogenicity. Cell 2021; 184(1):64-75.e11.

EDITORIAL

Spontaneous miscarriages in patients with bladder pain syndrome/interstitial cystitis - effect of stress on inflammation?

T.C. Theoharides[1,2,3], S. Christodoulou[2,4] and A. Athanasiou[5]

[1]*Laboratory of Molecular Immunopharmacology and Drug Discovery, Department of Immunology, Tufts University School of Medicine, Boston, MA, USA;* [2]*Department of Internal Medicine, Tufts University School of Medicine and Tufts Medical Center, Boston, MA, USA;* [3]*Department of Psychiatry, Tufts University School of Medicine and Tufts Medical Center, Boston, MA, USA;* [4]*Present address: Department of Surgery, Hygeia Hospital, Athens, Greece;* [5]*Department of Obstetrics and Gynecology, South Shore Hospital, South Weymouth, MA, USA*

Received August 28, 2020 – Accepted December 15, 2020

Interstitial cystitis/painful bladder syndrome (IC/PBS) affects mostly women and is characterized by pelvic pain or pressure and frequency of voiding in the absence of urinary tract infection. Acute stress worsens IC/PBS symptoms and bladder inflammation associated with increased number of activated mast cells. We investigated retroactively the incidence of spontaneous miscarriages and any related stress in IC/PBS patients. A questionnaire was posted on an IC/PBS website and patients visiting the site were invited to complete and file it electronically. Limitations include the lack of defined diagnosis those responding, and of a validated stress questionnaire. There were 193 respondents (mean age = 37.3 years) over two weeks. Of those responding, 87% (mean age = 33.2 years) had received a diagnosis of IC/PBS. Of those respondents with IC/PBS, 76% reported having had miscarriages: (a) 55% had one miscarriage, (b) 26% had two, and (c) 23% had three or more. These rates are much higher than those of in the general population: 10-20% with one and 1-2% with habitual spontaneous miscarriages. The majority of patients (78%) reported experiencing significant stress. IC/PBS patients appear to have a much high incidence of spontaneous miscarriages compared to the general population. Most patients reported experiencing stress that has been associated with miscarriages. This finding may be explained via stress stimulating bladder and uterine immune cells, especially mast cells, inhibition of which by the natural flavonoid quercetin may be beneficial.

Interstitial cystitis/painful bladder syndrome (IC/PBS) is a disorder of the urinary bladder affecting mostly women and characterized by chronic pelvic pain, frequency and nocturia (1, 2). As IC/PBS has become better known and the diagnostic criteria do not necessarily include cystoscopy under spinal or general anesthesia, the prevalence has increased to about 1% of female patients (1). IC/PBS pathogenesis appears to be multifactorial (3, 4) and has been considered a neuro-immuno-endocrine disorder (5) associated with variable degrees of bladder inflammation (6) and bladder mastocytosis (7).

Acute stress was shown to worsen chronic pelvic pain and also worsened bladder-related symptoms in humans (8). Psychological stress has also been associated with infertility (9). The effect of stress

Key words: miscarriage; corticotropin-releasing hormone; inflammation; mast cells; stress

Corresponding Author:
T.C. Theoharides, MS, MPhil, PhD, MD
Department of Immunology,
Tufts University School of Medicine
136 Harrison Avenue, Boston, MA 02111, USA
Tel.: +1 617 636 6866 - Fax: +1 617 636 2456
e-mail: theoharis.theoharides@tufts.edu

0393-974X (2021)
Copyright © by BIOLIFE, s.a.s.
This publication and/or article is for individual use only and may not be further reproduced without written permission from the copyright holder.
Unauthorized reproduction may result in financial and other penalties
DISCLOSURE: ALL AUTHORS REPORT NO CONFLICTS OF INTEREST RELEVANT TO THIS ARTICLE.

on miscarriages in IC/PBS has not been investigated and could be higher than in the general population given the evidence of inflammation in the pelvic area. A number of studies have reported increased risk of pregnancy loss associated with psychological stress (10, 11).

Mast cells were increased by more than 10-fold in deciduas in miscarriages (12). Mast cells are essential for allergies (13), but also inflammation (14) by releasing histamine, tryptase, proteoglycans, prostaglandin D_2, leukotriene C_4 and several pro-inflammatory cytokines and chemokines (15, 16). The decidua of women with high levels of stress were reported to have a significantly high number of mast cells positive for their unique proteolytic enzyme, tryptase (10).

Here, we report preliminary findings indicating that spontaneous miscarriages are more frequent in IC/PBS patients than in the general population, and may be associated with antecedent stress.

MATERIALS AND METHODS

A 25-item questionnaire (Table I), which included questions on demographics, medical diagnosis, spontaneous miscarriages and stress, was made available on a website visited by IC/PBS patients (IC-network.com). The survey was posted for three months on http://www.keysurvey.com/. This was an information gathering questionnaire and was not designed to diagnose any disease or quantitate symptoms. No personal information was collected and no HIRB approval was required.

The results are presented as percentage of IC/PBS patients who answered a particular question. Each question is presented in the results. No statistics were applied.

Findings

A total of 193 surveys were returned. The mean age of the responders was 37.3 years, with a mean age of IC/PBS diagnosis being 33.2 years. Of all the respondents, 87% were diagnosed with IC/PBS (Fig. 1A) and 76.7% of them reported having had miscarriages (Fig. 1B). The actual breakdown was as follows: (a) 79 patients (55%) had one miscarriage, (b) 38 patients (26%) had two miscarriages, and (c) 33 patients (18%) had three or more miscarriages (Fig. 1C).

At the time of miscarriage, 8.1% of subjects were 19 years old or younger, 65% were 20-29 years old, 25.7% were

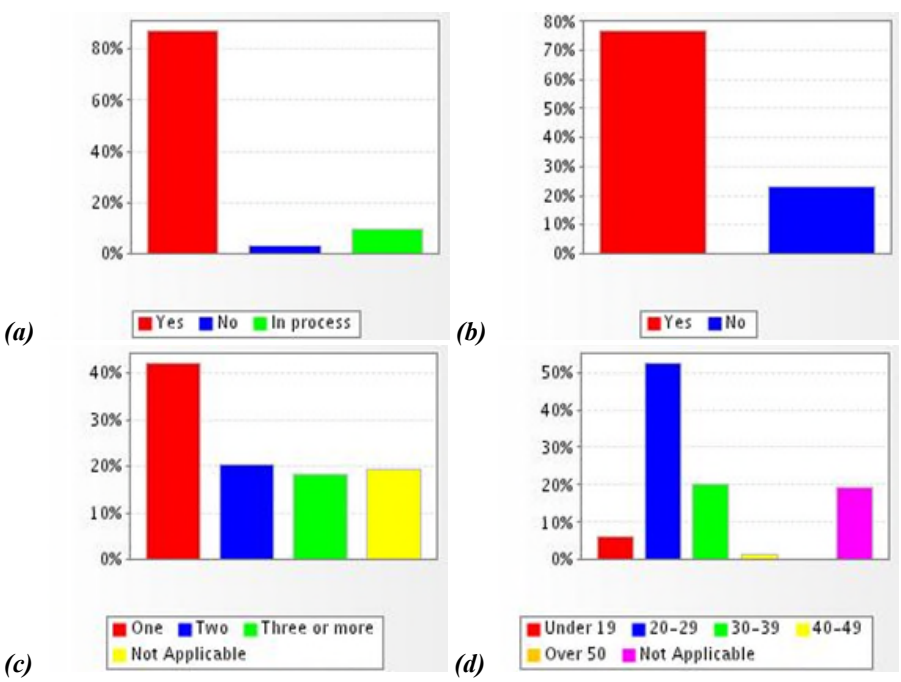

Fig. 1. *The number of BPS/IC patients who reported any miscarriage.* ***a)*** *Have you been diagnosed with IC?* ***b)*** *Have you experienced a miscarriage?* ***c)*** *How many miscarriages have you had?* ***d)*** *How old were you when the miscarriage(s) occurred?*

30-39 years old, and 2% were 40-49 years old (Fig. 1D).

Most responders (57.1%) reported that they had experienced the miscarriage after they developed bladder symptoms (Fig. 2A) and 18.5% after they were diagnosed with IC/PBS (Fig. 2B). The miscarriage was attributed to a genetic or medical condition in less than 10% responders (Fig. 2C). About 42% of responders indicated that they succeeded in having a child eventually (Fig. 2D).

There were four different questions relating to stress. In the first, 25.9% of responders indicated that their miscarriage was associated with an event or period of stress (Fig. 3A). However, almost 80% replied that they had been upset during the last month because of something that had happened unexpectedly (Fig. 3B) and 37.8% indicated they were upset about 50% of the time; 31.1% indicated they were fairly anxious often and 10% very often. Over 71% indicated that during the last month they had felt unable to control the important things in their lives (Fig. 3C). Finally, over 85% reported that they had felt nervous or stressed during the last month, with 57.2% indicating they did so very often (Fig. 3D).

DISCUSSION

The present findings suggest that IC/PBS patients may have a higher incidence of spontaneous miscarriages than the general population. The incidence of one spontaneous miscarriage in IC patients (mean age 33.2 years) was 76.7%, compared to 13.5% in the general population and 8.9% in the age group of 20-24 years (17). The incidence of habitual spontaneous miscarriages (3 or more) was about 23% in IC/PBS patients, compared to 1-2% in the general population (18). A miscarriage after bladder symptom flare-up occurred in 57.1% responders and 18.5% had a miscarriage after IC/PBS diagnosis.

Many IC/PBS patients also experience anxieties (19) and panic disorder (20). The symptoms of IC/PBS are exacerbated by physical or emotional stress (14, 21). A common link between IC/PBS, stress and spontaneous miscarriages may be the mast cells, which are increased and activated in the bladder of

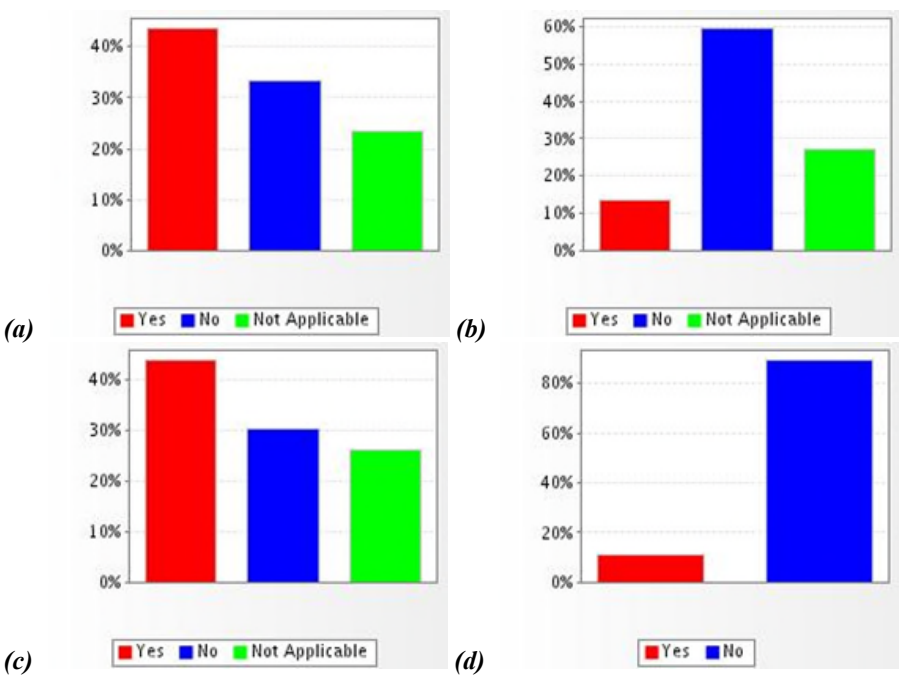

Fig. 2. *Factors that may have contributed to the miscarriages.* ***a****) Did your miscarriage occur after you developed bladder symptoms?* ***b****) Did your miscarriage occur after you were diagnosed with BPS/IC?* ***c****) Have you successfully had a child after miscarriage?* ***d****) Was your miscarriage associated with or attributed to any genetic or medical condition?*

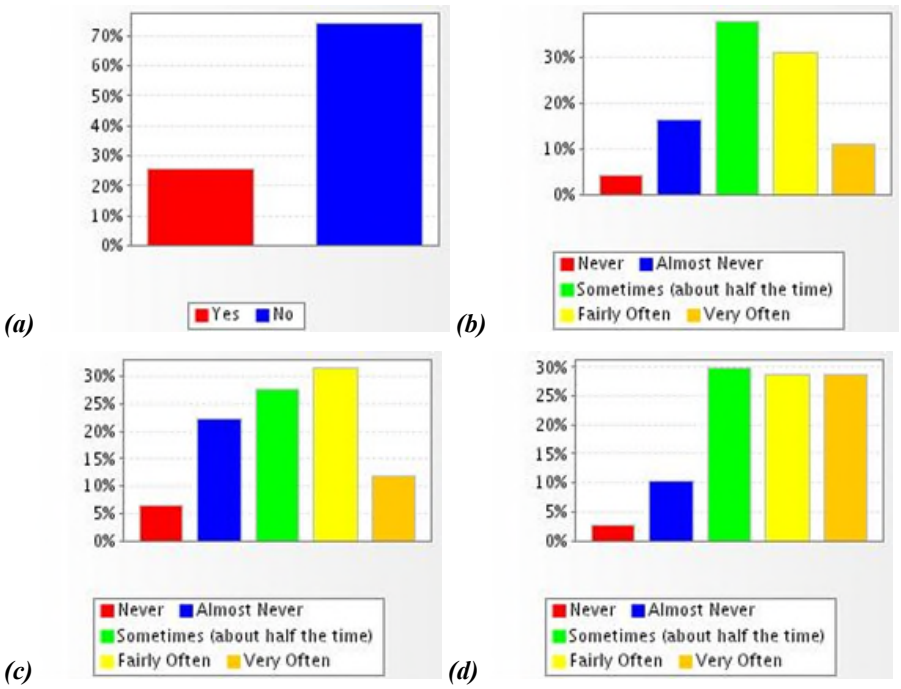

Fig. 3. *Association of miscarriages with stress.* ***a)*** *Was your miscarriage associated with any event or period of stress?* ***b)*** *In the last month, how often had you been upset because of something that happened unexpectedly?* ***c)*** *In the last month, how often had you felt that you were unable to control the important things in your life?* ***d)*** *In the last month, how often had you felt nervous or "stressed"?*

IC/PBS patients (7, 22), and could be triggered by acute stress (23, 24). Systemic or pelvic stressful conditions may increase the incidence of spontaneous miscarriages in IC/PBS patients by inducing the local release of corticotropin-releasing hormone (CRH) or other neuropeptides, such as substance P (SP), which then activate bladder and/or endometrial mast cells. For instance, bladder mast cells are closely associated with SP-positive neurons (25) and respond to SP with release of histamine, cytokines and chemokines (14). We reported high CXCL8 level in subjects with habitual spontaneous miscarriages (26) and CXCL8 was significantly increased in the plasma of women with second trimester miscarriage (27).

Most subjects reported being chronically stressed with 25% indicating the presence of a stressful period associated with the miscarriage. Psychological stress has been associated with preterm delivery and spontaneous miscarriages (10, 28), including recurrent miscarriages (29). In one study, spontaneous miscarriages at about 11 weeks of gestation were strongly associated with more stressful episodes than other gestational periods (30). Another study reported more than two-fold increase in the rise of spontaneous miscarriages in the presence of psychological stress. (28) A systematic review and meta-analysis concluded that the risk of miscarriages was significantly higher in women with a history of psychological stress (31).

Maternal stress due to environmental and/or socioeconomic factors was also linked to preterm delivery and was associated with high levels of CRH secreted under stress (32). In addition to its release from the hypothalamus, CRH is also released in local tissues, where it induces pro-inflammatory effects through mast cell activation (14). Moreover, human mast cells (33) and endometrium (34) can produce CRH, which can stimulate prostaglandin production in uterine tissues, leading to parturition (32). We reported high levels of CRH and tryptase in products of conception from women with habitual spontaneous miscarriages (26).

This study has a number of limitations. The response rate may bias the outcome and overestimate

the percent of patients who had miscarriages because those who did not would be less motivated to take the survey. The questions about whether miscarriage was associated with an event or period of stress are subjective and may be influenced by recall bias. The wording of the question concerning the association of stress and miscarriage may had been misleading.

Implications

The present preliminary findings raise the issue that psychological stress may contribute to spontaneous miscarriages due to stimulation of bladder and uterine mast cells in patients with IC/PBS. Inhibition of mast cells by the natural flavonoid quercetin, especially in a liposomal formulation to increase oral absorption, could provide some degree of protection (35).

ACKNOWLEDGEMENTS

We thank Jill Osborne (IC Network, Santa Rosa, CA, USA) for posting the questionnaire and Ms. Jessica Christian for her word processing skills. This research was supported by Theta Biomedical Consulting and Development Co., Inc. (Brookline, MA, USA).

DISCLOSURES: TCT is the President of Theta, Inc. that developed CystoProtek® marketed by Alaven, Inc. TCT has also been awarded the following patents: US 5,994,357 issued 11/30/99, "Method of treatment of interstitial cystitis" and US 6,635,625 issued 10/21/03, "Proteoglycan compositions for treating prostate and bladder inflammatory conditions." The other authors report no conflict.

REFERENCES

1. Sant GR, Hanno PM. Interstitial cystitis: current issues and controversies in diagnosis. Urology 2001; 57:82-8.
2. Whitmore KE, Theoharides TC. When to suspect interstitial cystitis. J Fam Pract 2011; 60(6):340-8.
3. Peeker R, Aldenborg F, Dahlstrom A, et al. Immunologic and neurobiologic characteristics support that interstitial cystitis is a heterogeneous syndrome. Urology 2001; 57:130.
4. Birder LA. Pathophysiology of interstitial cystitis. Int J Urol 2019; 26 Suppl 1:12-5.
5. Duh K, Funaro MG, DeGouveia W, et al. Crosstalk between the immune system and neural pathways in interstitial cystitis/bladder pain syndrome. Discov Med 2018; 25(139):243-50.
6. Erickson DR, Belchis DA, Dabbs DJ. Inflammatory cell types and clinical features of interstitial cystitis. Urology 1997; 158:790-3.
7. Theoharides TC, Kempuraj D, Sant GR. Mast cell involvement in interstitial cystitis: a review of human and experimental evidence. Urology 2001; 57(Suppl 6A):47-55.
8. Rothrock NE, Lutgendorf SK, Kreder KJ, Ratliff T, Zimmerman B. Stress and symptoms in patients with interstitial cystitis: A life stress model. Urology 2001; 57:422-7.
9. Rooney KL, Domar AD. The relationship between stress and infertility. Dialogues Clin Neurosci 2018; 20(1):41-7.
10. Arck PC, Rose M, Hertwig K, Hagen E, Hildebrandt M, Klapp BF. Stress and immune mediators in miscarriage. Hum Reprod 2001; 16:1505-11.
11. Frazier T, Hogue CJR, Bonney EA, Yount KM, Pearce BD. Weathering the storm; a review of pre-pregnancy stress and risk of spontaneous abortion. Psychoneuroendocrinology 2018; 92:142-54.
12. Marx L, Arck P, Kieslich C, Mitterlechner S, Kapp M, Dietl J. Decidual mast cells might be involved in the onset of human first-trimester abortion. Am J Reprod Immunol 1999; 41:34-40.
13. Theoharides TC, Valent P, Akin C. Mast Cells, Mastocytosis, and Related Disorders. N Engl J Med 2015; 373(2):163-72.
14. Theoharides TC, Cochrane DE. Critical role of mast cells in inflammatory diseases and the effect of acute stress. J Neuroimmunol 2004; 146((1-2)):1-12.
15. Mukai K, Tsai M, Saito H, Galli SJ. Mast cells as sources of cytokines, chemokines, and growth factors. Immunol Rev 2018; 282(1):121-50.
16. Gallenga CE, Pandolfi F, Caraffa A, et al. Interleukin-1 family cytokines and mast cells: activation and inhibition. J Biol Regul Homeost Agents 2019; 33(1):1-6.
17. Nybo Andersen AM, Wohlfahrt J, Christens P, Olsen J, Melbye M. Maternal age and fetal loss: population based register linkage study. BMJ 2000;

320(7251):1708-12.
18. Cohain JS, Buxbaum RE, Mankuta D. Spontaneous first trimester miscarriage rates per woman among parous women with 1 or more pregnancies of 24 weeks or more. BMC Pregnancy Childbirth 2017; 17(1):437.
19. Clemens JQ, Brown SO, Calhoun EA. Mental health diagnoses in patients with interstitial cystitis/painful bladder syndrome and chronic prostatitis/chronic pelvic pain syndrome: A case/control study. J Urol 2008; 180(4):1378-82.
20. Weissman MM, Gross R, Fyer A, et al. Interstitial cystitis and panic disorder: a potential genetic syndrome. Arch gen Psychiatry 2004; 61:273-9.
21. Rothrock NE, Lutgendorf SK, Kreder KJ, Ratliff TL, Zimmerman B. Daily stress and symptom exacerbation in interstitial cystitis patients. Urology 2001; 57(Suppl 6):122.
22. Theoharides TC, Sant GR, El-Mansoury M, Letourneau RJ, Ucci AA, Jr., Meares EM, Jr. Activation of bladder mast cells in interstitial cystitis: a light and electron microscopic study. J Urol 1995; 153:629-36.
23. Ercan F, San T, Cavdar S. The effects of cold-restraint stress on urinary bladder wall compared with interstitial cystitis morphology. Urol Res 1999; 27:454-61.
24. Spanos C, Pang X, Ligris K, et al. Stress-induced bladder mast cell activation: implications for interstitial cystitis. J Urol 1997; 157:669-72.
25. Pang X, Marchand J, Sant GR, Kream RM, Theoharides TC. Increased number of substance P positive nerve fibers in interstitial cystitis. Br J Urol 1995; 75:744-50.
26. Madhappan B, Kempuraj D, Christodoulou S, et al. High levels of intrauterine corticotropin-releasing hormone, urocortin, tryptase and IL-8 in spontaneous abortions. Endocrinology 2003; 144:2285-90.
27. Galazios G, Tsoulou S, Zografou C, et al. The role of cytokines IL-6 and IL-8 in the pathogenesis of spontaneous abortions. J Matern Fetal Neonatal Med 2011; 24(10):1283-5.
28. Bashour H, Abdul Salam A. Psychological stress and spontaneous abortion. Int J Gynaecol Obstet 2001; 73:179-81.
29. Li W, Newell-Price J, Jones GL, Ledger WL, Li TC. Relationship between psychological stress and recurrent miscarriage. Reprod Biomed Online 2012; 25(2):180-9.
30. Boyles SH, Ness RB, Grisso JA, Markovic N, Bromberger J, CiFelli D. Life event stress and the association with spontaneous abortion in gravid women at an urban emergency department. Health Psychol 2000; 19:510-4.
31. Qu F, Wu Y, Zhu YH, et al. The association between psychological stress and miscarriage: A systematic review and meta-analysis. Sci Rep 2017; 7(1):1731.
32. Lockwood CJ. Stress-associated preterm delivery: the role of corticotropin-releasing hormone. Am J Obstet Gynecol 1999; 180:S264-6.
33. Kempuraj D, Papadopoulou NG, Lytinas M, et al. Corticotropin-releasing hormone and its structurally related urocortin are synthesized and secreted by human mast cells. Endocrinology 2004; 145:43-8.
34. Hillhouse EW, Grammatopoulos DK. Role of stress peptides during human pregnancy and labour. Reproduction 2002; 124:323-9.
35. Theoharides TC, Kempuraj D, Vakali S, Sant GR. Treatment of refractory interstitial cystitis/painful bladder syndrome with CystoProtek - an oral multi-agent natural supplement. Canadian Urol 2008; 15:4410-4.

Afferent vagal stimulation via gastric electrical stimulation alters sympathetic-vagal balance in domestic pigs – a pilot trial

M. Leitzke[1], S. Schimpf[2], M. Altrock[3], P. Schönknecht[4], S. Bischoff[5], H. Schubert[5], D. Hoyer[6], R. Bauer[7] and S. Olbrich[8]

[1]Helios Clinics, Department of Anaesthesiology, Leisnig, Germany; [2]Dräger Medical GmbH, Lübeck, Germany; [3]MTU Reman Technologies GmbH, Magdeburg, Germany; [4]Leipzig University, Medical faculty, Saxon hospital, Arnsdorf, Germany; [5]University of Jena, Institute for animal testing, experimentation and animal welfare, Jena, Germany; [6]University of Jena, Hans Berger Department of Neurology, Jena, Germany; [7]University of Jena, Institute for molecular cell biology, Jena, Germany; [8]University of Zurich, Department of Psychiatry, Zürich, Switzerland

Received August 28, 2020 – Accepted December 16, 2020

The disturbance of the sympathetic-vagal balance with increasing sympathetic activity and consecutive increase in cytokine release is a major threat in numerous hyperinflammatory syndromes. Therapeutic interventions that modulate the activity in the sympathetic-vagal system are suggested as an effective treatment in these incidences. The purpose of this pilot study was to investigate the effect of electrical stimulation of the gastric wall on sympathetic-vagal balance. German domestic pigs (n=5) were prepared with a modified gastric tube (mGT) for repetitive gastric electrical stimulation (GES). Electrocardiogram was recorded continuously and heart rate variability (HRV) as measure of sympathetic-vagal activity was calculated for three-minute epochs at baseline condition before GES and during GES condition. In comparison to baseline, activity of the autonomic nervous system (ANS) shifted significantly toward increased dominance of vagal activity during GES with a decrease of normalized low frequency (nLF from 58.00 to 25.52) as marker of sympathetic dominance and parallel increase of normalized high frequency (nHF from 41.48 to 74.16) as marker of vagal dominance. During GES, compared to baseline, no difference in heart rate was found. These results indicate that electrical stimulation of the gastric wall may result in shifting the sympathetic-vagal balance toward a parasympathetic predominance.

The autonomic nervous system (ANS) plays an important role in the regulation of respective immune responses to pathological impact (1). The liberation of pro-inflammatory cytokines underlies a very sensitive regulation by ANS afferent sensing and efferent execution (2). Thus, the balance between the sympathetic and the vagal branch of the ANS is indispensable for an appropriately executed immune response (3). Balance disorders of the ANS can be caused by pathological conditions or even may be pathogenic factors themselves (4). Huang et al. (5), for example, found a sympathetic over excitation to be responsible for the autonomic imbalance following endotoxemia (5). Furthermore, Stauss (6, 7) stated an impaired autonomic regulation characterized by low heart rate variability (HRV) to be a marker for negative outcome after myocardial infarction (6) and described its prognostic power

Key words: sympathetic-vagal balance; vagal nerve stimulation; gastric electrical stimulation; heart rate variability; modified gastric tube; hyperinflammatory syndrome

Corresponding Author:
Dr. Marco Leitzke,
Helios Klinik Leisnig, Department of Anaesthesiology,
Colditzer Straße 48, 04703 Leisnig, Germany
Tel.: +49 15771426004/3432182705
Fax: +49 034321 8-133
e-mail: marco.leitzke@gmx.de

0393-974X (2021)
Copyright © by BIOLIFE, s.a.s.
This publication and/or article is for individual use only and may not be further reproduced without written permission from the copyright holder.
Unauthorized reproduction may result in financial and other penalties

in various different cardiovascular diseases (7). Annane et al. (8) described septic patients with high levels of sympathetic activation and concomitant central autonomic regulatory impairment to be a reasonable explanation for the discrepancy between high sympathetic drive and low HRV (8). In a review, Pavlov et al. (2) pointed out that type 2 diabetes mellitus and the following adverse conditions are also associated with impairment of vagal function (2). Tracey (9) demonstrated the limitation of cytokine release through vagal innervation via the inflammatory reflex (IR) (9). Following pathogen detection in the periphery (10) a vagus-driven afferent signal leads, via central modulation, to an efferent vagal excitation with acetylcholine (Ach) liberation at the spot of impairment. Ach attaches to α7 subunit-characterized nicotinic Ach receptors (α7nAchR) at the surface of cytokine-producing cells, leading to an interruption of cytokine synthesis and release (3). Sepsis and a range of different diseases,, including epilepsy (11–15), depression (12, 13, 16), anxiety (17), Alzheimer's disease (13, 18), dementia (13) vegetative state conditions (19), rheumatoid arthritis (4), inflammatory bowel diseases (20) and potentially chronic heart failure (21), are associated with decreased parasympathetic output and elevated pro-inflammatory serum cytokine levels. The autonomic imbalance therefore catalyzes the pathogenesis of respective disease patterns (22). Elevation of the parasympathetic tone is considered a possible approach (20, 23–26) in the therapeutic management of the aforementioned conditions. Vagal nerve stimulation (VNS) reduces the elevated serum cytokine levels (27), which reveals the enormous therapeutic potential of VNS. Likewise, obesity with its associated comorbidities and metabolic disorders is obviously alleviated by vagal stimulation (28). Recently, Bonaz et al. (29) described the expected high potential of VNS to prevent or ameliorate severe courses of the current pandemic COVID-19 (29), and Staats et al. (30) reported distinct relief of symptoms (fatigue, low appetite, and coughing bouts such as dyspnea and chest pressure/tightness) in two SARS-CoV-2 positive tested patients under the usage of noninvasive vagal nerve stimulation (nVNS) (30).

Numerous investigations presupposed this knowledge to rebalance the ANS via cervical VNS in respective disease patterns and to place an additional tool at the disposal of their treatment (4, 22, 31). In other investigations, the effects of transcutaneous stimulation at the region of the cervical vagus nerve (30, 32) or the auricular branch (33) of the vagus nerve were explored. The results of these trials are promising (34), but to date no investigation (35) has incorporated the IR consisting of an afferent vagal signaling from the spot of impairment, the viscerotopic (36) central sensing and modulation, such as an efferent vagal signal, to deliver Ach for cytokine release control (1). As the cervical vagus nerve contains 20% efferent and 80% afferent fibers (37), cervical VNS causes afferent stimulation of central vagal structures as well as efferent stimulation of vagal innervated organs leading to opposite metabolic effects (38). Furthermore vagal structures are closely connected to sympathetic nerve fibers within the cervical vagus nerve (39) making pure cervical VNS problematic. Thus, cervical VNS in former investigations led to a parallel sympathetic stimulation. This was demonstrated by an enhancement of the low frequency (LF) HRV power (31) and increased firing of stellate ganglion during cervical VNS (40). An anatomic explanation for this effect is given by Seki et al. (39), who found cervical vagal nerves containing sympathetic fibers in every individual (39).

Vagal afferent fibers carry a large amount of information from the gastric wall to the brainstem (41), i.e. the nucleus tractus solitarii (NTS) (41), where this information is transmitted via glutamate related excitation (41) to N-methyl-D-aspartate (NMDA) and non-NMDA neurons of the dorsal vagal motor complex (DVC) to be ultimately converted into accelerated efferent vagal output (41).

Starting from this point, our investigational trial was designed to analyze a stimulation approach, which involves these central structures. In light of the associations mentioned above, the goal of the present pilot study was to investigate whether inductive, i.e. wireless, electrical stimulation of the gastric wall with a modified gastric tube (mGT) can be used for afferent vagal stimulation. We hypothesized that it is possible to enhance the efferent vagal output and suppress

the sympathetic activity, i.e. to shift the sympathetic-vagal balance at the level of HRV towards increased parasympathetic and reduced sympathetic activity via electrical stimulation of the gastric wall without intramural positioning of electrodes.

MATERIALS AND METHODS

Animals

The present study was performed according to the Protection of Animals Act of the Federal Republic of Germany ("Tierschutzgesetz der Bundesrepublik Deutschland") and was approved by the Thuringian State Office for Consumer Protection ("Thüringer Landesamt für Verbraucherschutz, TLV, Reg. No. 02-032/10"). The animals were treated in accordance with the declaration of Helsinki and its guiding principles, with regard to the care and use of animals. Five female German domestic pigs (mean weight: 29.0 kg±1.3 kg) were housed at room temperature before trial preparation. They had access to standard food solution and tap water ad libitum.

Surgical instrumentation

The pigs were sedated by an intramuscular injection with a mixture of ketamine (mean: 0,344 mg/kg ±0.041 mg/kg bodyweight (bw)) and midazolam (mean: 0.067 mg/kg ±0.003 mg/kg bw). An intravenous access (18 Gauge, inner diameter 0.6 mm) was attached to a left-sided ear vein and anesthesia was induced by intravenous administration of fentanyl (mean: 0.003 mg/kg ±0.002 mg/kg bw) and propofol (mean. 0.693 mg/kg ±0.100 mg/kg bw). After positioning and fixation in supine position the animals received orotracheal intubation (spiral tube 5.5 to 6.0 mm inner diameter) and were artificially ventilated to warrant normoxemia and normocapnia. Anesthesia was maintained by sevoflurane (mean alveolar concentration 1.0 to 1.3) in O_2/N_2O (30:70). Proper ventilation was monitored throughout the whole procedure by measurement of arterial oxygen saturation and carbon dioxide concentration in the arterial blood samples. A central venous catheter (PU, 1.4 mm OD) was inserted through a branch of the left external jugular vein to infuse hydroxyethyl starch (HES; 6%; 30ml/h). In addition, an arterial catheter was placed into the left external carotid artery for continuous arterial blood pressure recording and arterial blood sample withdrawal. Electrocardiogram recordings were made from standard limb leads using stainless steel needle electrodes. Catheters and electrode leads were subcutaneously tunneled and led out at the dorsal neck region.

The modified gastric tube (mGT)

We developed a gastric tube based on a percutaneous endoscopic gastrostomy (PEG) tube, providing continuously stable stimulation conditions without mGT impairment from gastric acid. The mucosa adjacent side of

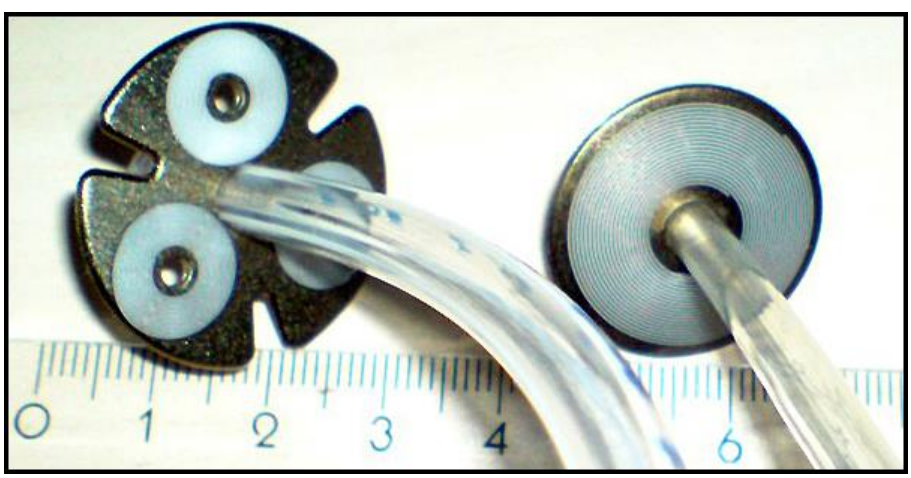

Fig. 1. *Two specimens of the mGT: the mucosa adjacent side of the percutaneous endoscopic gastrostomy (PEG) tube basic plate is metallized with a platinum layer, which is structured by etching to leave a two-dimensional coil. The size of this coil meets with 2 cm diameter the size of the PEG basic plate. In the other specimen three individual coils of 7 mm size have been etched into the platinum layer. For the pilot experiments we used exclusively the greater coils.*

the mGT basic plate was metallized with a two-dimensional platinum coil (Fig. 1) to evoke a signal resulting from an extra corporally placed electromagnet via inductive coupling.

Placement of the mGT

After surgical closure and bandage of the neck incisions, a laparotomy was performed (Fig. 2A). The mGT was placed at the greater curvature in the region of the border between gastric fundus and corpus (Fig. 2B,C) (42) to guarantee optimal stimulation conditions since the density of gastric afferent autonomic neurons is known to be the highest in that region (42). The stomach was sealed by purse-string suture (Fig. 2C). The mGT was driven out through the abdominal wall left beside the incision (Fig. 2D). Surgical closure and sterile bandaging of the abdominal wall were performed. The anesthesia was terminated after the intravenous application of 8 mg phenylbutazone for postoperative analgetic treatment. Extubation was carried out under sufficient spontaneous breathing. After instrumentation, a stabilization period of one hour was given. Subsequently, continuous sedation was established immediately after extubation by α-chloralose infusion (mean 0.14 mg/kg ±0.03 mg/kg bw/min).

Throughout the experiment cardiorespiratory monitoring was performed by regular blood gas check and continuous registration of arterial blood pressure (ABP), respiration movement (RM) and electrocardiogram (ECG). ABP, RM, ECG and body temperature were stored continuously on an external hard drive for off-line data analysis (acquisition software: AtisaPro, Data acquisition & analysis software, GJB Datentechnik GmbH, Langewiesen, Germany; sampling rate 2 kHz).

Pilot experiments

Before starting the original trial, an *ex-vivo* testing of the mGT was performed. Voltage was induced on the mGT through approximately 2.5 cm of porcine muscle tissue. We used a square-wave signal with an amplitude adjusted to 4.5 V as excitation signal. The induction of nerve stimulating voltages through porcine abdominal tissue proved to be feasible and excitation with 4.5 V resulted in induced signal levels with 7 mV amplitudes in the muscular layer.

After a pre-gastric electrical stimulation (pre-GES) condition of at least 15 min, for gastric electrical stimulation (GES) via the mGT a digimess arbitrary wave generator AFG 100 (Grundig electronics) was used. Stimulation (pulse with 330 µs, 30 sec on, 120 sec off) was performed for a stimulation period of at least 10 min. Three animals were stimulated with rectangular and two animals with saw tooth impulses in order to explore whether the waveform of the inductive impulse had an impact on the stimulation effect. Stimulation interval in each animal was carried out with identical intensity parameters (5V; 40Hz). Since vagal afferents originating in the stomach are predominantly unmyelinated C-fibers (41) with a fairly high stimulation threshold responding to short pulse stimulation (43) with a pulse width of 300

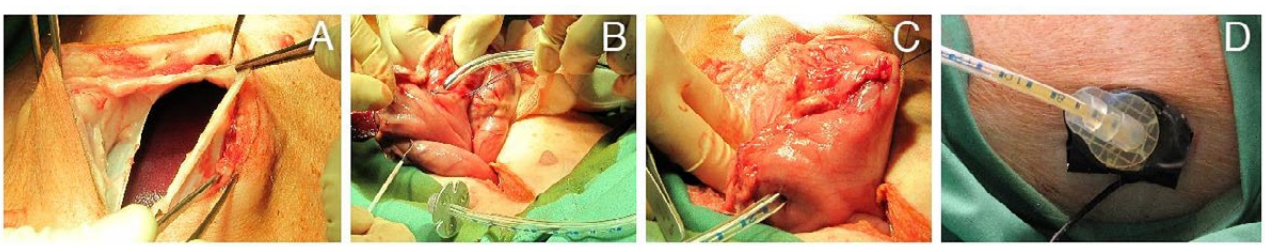

Fig. 2. *Placement of the mGT.* ***A****) laparotomy;* ***B****) placement of the mGT at the greater curvature between gastric fundus and corpus;* ***C****) closure of the stomach by purse string suture;* ***D****) the attached electrical magnet. The electrical magnet envelops the gastric on top of the cutaneous layer of the abdominal wall. An impulse generator is connected to the electrical magnet. This magnet sends a signal (saw tooth or square wave) to the inner coil. This creates inductive impulses in the coil at the basic plate of the mGT. The signal transmission to the inner coil is wireless. The electrical magnet and its alternating field on the abdominal wall induce an electrical voltage on the coil inside the stomach. This voltage excites the structures of the gastric wall outgoing from the mucosal layer.*

μs (44), and with reference to Qin et al. (45) showing neurons in the nucleus tractus solitarii (NTS) are better to stimulate using high amplitude and/or increased pulse width (45), we chose to stimulate with the aforementioned stimulation parameters.

Assessment of cardiac ANS function by HRV analysis

Data from the five pigs was used for statistical analysis, time series included epochs from resting periods (pre-GES) and stimulation periods (GES). After down sampling of ECG raw data from 2000 Hz to 400Hz, done in MATLAB (MATLAB and Statistics Toolbox Release 2012b, The MathWorks, Inc., Natick, Massachusetts, United States.), R-peaks of the ECG- time series were detected automatically using Kubios HRV 2.2 software (http://kubios.uef.fi/). The results were visually inspected for artefacts, epochs with artefacts were excluded. Corrections for erroneous automatic R-peak detections were made if necessary. Electrocardiogram raw data from pre-GES and GES periods were segmented into several artefact-free epochs (ranging from 1-3 epochs for each condition per pig GES or pre-GES), each of 3-minute duration. The first epochs for both conditions and for all pigs were taken from the first three artefact free minutes of recording, consecutive epochs were taken from following artefact free three-minute blocks. Mean duration of pre-GES condition was 45.8 min with SD 25.6 min, GES condition had a mean duration of 20.6 min with SD 22.7 min. A visualization of the timeline from preparation to data assessment can be found in Fig. 3.

Time domain and frequency domain results were computed for each artefact-free three-minute epoch for each pig for the pre-GES and the GES periods. Since for one pig only one epoch of artefact-free data was available, it was discarded from analysis of changes over time. For the 4 other pigs, more than one epoch was available for each of the pre-GES and GES periods. Hence, data was included in the analysis of the impact of time on the time and frequency domain data.

Time domain results included heart rate (HR), root mean square of successive differences (RSSDM) and the proportion of pairs of successive beat-to-beat intervals that differ by more than 50ms (pNN50).

Frequency domain results included total power and

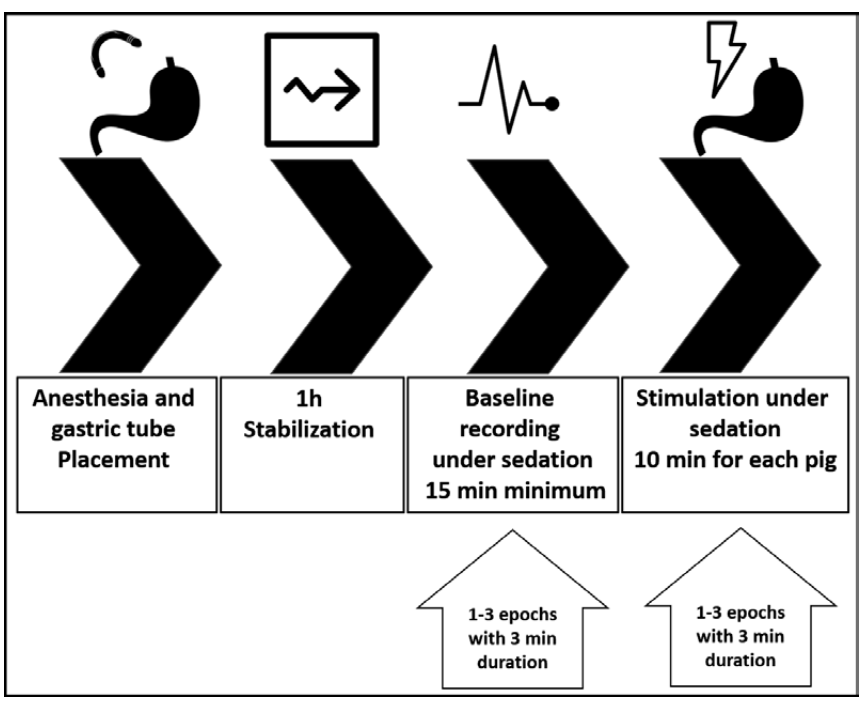

Fig. 3. *Visualisation of the timeline of the study. Visualization of the timeline of preparation and data assessment. Instrumentation was performed under anesthesia, whereas a recovery period from one-hour, such as stimulation and data assessment, was performed under sedation. Since the stimulation period was only 10 minutes, a maximum of 3 three-minute epochs could be included (artefact free).*

the power values of low frequency (LF 0.01-0.13 Hz) and the high frequency (HF 0.13-0.6 Hz), normalized LF (nLF) and the normalized HF (nHF), obtained by fast Fourier transform (FFT), as performed previously (5). Normalized values were computed according to the following formulas (with very low frequency – VLF range from 0-0.01):

$nLF = LF[ms^2]/(\text{total power } [ms^2] - VLF\ [ms^2])$

$nHF = HF[ms^2]/(\text{total power } [ms^2] - VLF\ [ms^2])$

Additionally, we calculated the Poincaré plots with the main parameters of SD 1 (comparable to the parasympathetic driven HF) and SD 2 (comparable to the sympathetic driven LF) for the first epoch of the pre-GES and the GES condition (46).

For the choice of HRV parameters we mainly followed the recommendations of the Task Force of the European Society of Cardiology and the North American Society of Pacing and Electrophysiology (1996) (47). We restricted the time domain measures besides HR to RMSSD and pNN50 since time domain measures are highly intercorrelated. Since the available epochs were restricted to only three-minute segments, RMSSD was especially taken into account since it reflects short-term components of HRV.

For frequency domain analysis, we used a normalized measure to visualize the interaction of both systems. "The representation of LF and HF in normalized units emphasizes the controlled and balanced behavior of the two branches of the autonomic nervous system […and] tends to minimize the effect of the changes in total power on the values of LF and HF components" the (Task Force of the European Society of Cardiology and the North American Society of Pacing and Electrophysiology 1996) (47). However, for reasons of interpretability it is recommended to always also report on the absolute values of HRV power. Furthermore, we decided not to calculate non-linear measures for the presented pilot study due to heterogeneous findings and a lack of clear interpretability.

Statistical analysis

SPSS 20 (IBM Corp. Released 2011. IBM SPSS Statistics, Version 20.0. Armonk, NY: IBM Corp.) was used for statistical analysis. All comparisons between pre-GES and GES condition were made using paired two-sided *T*-tests for the analysis of the first epochs that have been available for all pigs and one-sided for pooling of all epochs of all pigs to test the hypothesis of the direction of change. A p-value < 0.05 was considered significant. For assessment of the effects of time, a repeated measures ANOVA was carried out using the associated HRV parameters of three consecutive time blocks (each of three-minute duration) as repeated measurements. Effect sizes are given in Cohen`s d. A correction for multiple comparison (Bonferroni-correction) was applied to the analysis for test sets from the time domain and frequency

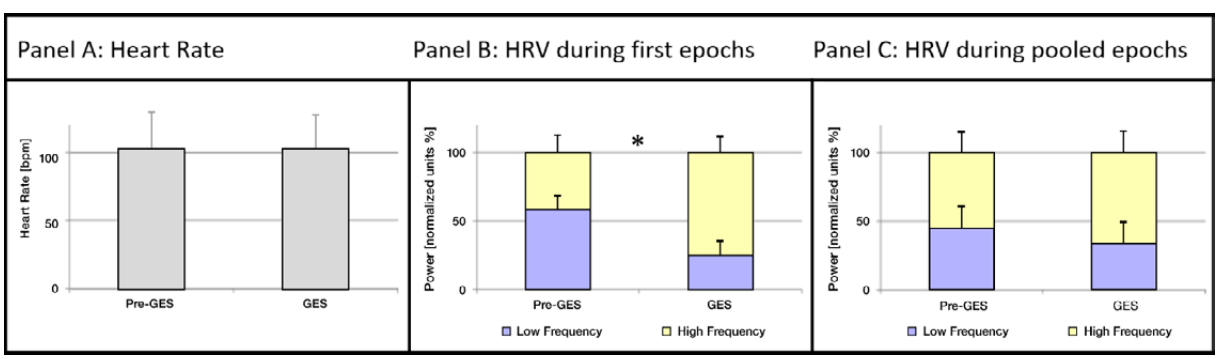

Fig. 4. *HRV parameters: pre-GES vs GES condition. Effect of GES on heart rate (Panel **A**) and HRV (Panel **B**) measures for comparison of the first artefact-free epochs from pre-GES and GES period. While no changes of heart rate occured (Panel A), the data yielded a significant reduction of normalized low-frequency HRV (nLF) and the mathematically corresponding increase of normalized high-frequency power of HRV (nHF) during GES in comparison to pre-GES baseline conditions imediately before stimulation (Panel B). The same pattern can be found for pooling of all epochs, although without statistical significance (Panel **C**), (* - for $p < 0.05$, Bonferroni-corrected for test-sets time domain and frequency domain, whiskers show standard deviation).*

domain. Due to the high inter-correlation, no correction was applied for the number of variables from the test sets (i.e. time domain and frequency domain).

RESULTS

Comparison pre-GES vs GES

Analysis of the first artefact-free three-minute epochs of HRV data during the baseline condition (pre-GES) in comparison to the first artefact-free three-minute epochs during stimulation (GES) revealed no relevant impact on averaged total power or LF/HF ratio (from 1.41 to 0.37, p=0.18 with Cohen`s d=1.52) and a significantly decreased nLF due to stimulation (p=0.04 with Cohen`s d=2.89) with a corresponding increased nHF during stimulation (p=0.04 with Cohen`s d=2.89, Fig. 4, Panel B). No difference was found for the HR (pre-GES 103 b/min, GES 102 b/min; see Fig. 4, Panel A). Likewise no differences were detectable concerning the waveform of the stimulation impulse.

When all available artefact-free epochs of HRV data from the pre-GES and GES periods were pooled (with different amount of epochs from different pigs), again no effect was visible on total power or LF/HF ratio (1.20 to 0.65, not significant with p=0.20, one sided T-test with Cohen`s d=0.84). Again, no differences were found for the HR between pre-GES and GES periods. Also, nLF and nHF showed no-significant differences during GES in comparison to baseline (p=0.16, one sided T-test with Cohen`s d=0.61). Although missing statistical significance in

Table I. *Absolute and normalized time domain and frequency domain values from pre-GES and GES conditions*

	pre-GES (First Epoch)		**GES (First Epoch)**		
	Average	SD	Average	SD	p-Value (t-test two-sided)
HR [bpm]	102.94	26.27	102.60	25.31	1.00
RMSSD [ms]	34.71	17.18	37.16	16.83	1.00
pNN50 [%]	17.65	14.94	16.53	10.84	1.00
Total Power [ms^2]	476.22	500.47	503.60	646.77	1.0
LF [ms^2]	175.95	205.84	93.56	135.01	1.00
HF [ms^2]	138.71	114.51	286.08	316.07	0.64
LF/HF	1.42	0.95	0.37	0.22	0.18
nLF [nu]*	**58.00**	10.57	**25.52**	11.87	**0.04**
nHF [nu]*	**41.48**	10.51	**74.16**	12.08	**0.04**
	pre-GES (All Epochs)		**GES (All Epochs)**		
	Average	SD	Average	SD	p-Value (t-test one-sided)
HR [bpm]	95.94	26.91	97.40	28.29	0.88
RMSSD [ms]	32.15	15.59	34.42	12.05	0.66
pNN50 [%]	16.96	13.03	14.35	8.54	0.56
Total Power [ms^2]	332.09	367.54	411.52	427.72	0.64
LF [ms^2]	106.43	149.80	100.05	92.05	0.90
HF [ms^2]	142.24	136.57	235.49	221.80	0.22
LF/HF	1.12	1.31	0.65	0.66	0.20
nLF [nu]	45.45	21.68	33.69	16.50	0.14
nHF [nu]	54.13	21.66	66.05	16.51	0.14

Table of HRV parameters for pre-GES and GES condition for the first segment of three minutes (top) and all available segments (bottom). (denote p<0.05; Bonferroni-corrected)*

this small group, the direction of change resamples the same reaction found in the analysis for the first available epochs (Fig. 4, Panel C).

Calculating the Poincaré plots revealed that 80% of the pigs showed a decreased SD2/SD1 ratio from pre-GES condition to GES condition (1.1 to 0.6; 1.2 to 1.9; 1.9 to 1.2; 1.2 to 1.0; 1.8 to 1.2) (Fig. 5). This is in line with a decreased sympathetic tone and an increased parasympathetic tone after stimulation.

Repeated measures ANOVA and the impact of time on parameters

To clarify the differences for the "first epoch comparison" of pre-GES *vs* GES periods and "all available epoch" comparisons, a repeated measures ANOVA was carried out with condition (pre-GES vs GES) as group variable and HRV-values of consecutive epochs as time factor (data available for 3 pigs). Heart rate stayed relatively stable during consecutive epochs during pre-GES periods and during GES periods (Fig. 6, Panel A, no group x time interaction). Although LF/HF ratio was higher during pre-GES in comparison to GES epochs, a different picture was seen when analysing nLF and nHF. There was a significant group x time interaction (F=14.03; p=0.03) with a marked decrease of nHF (and consecutive raise of nLF) during GES and the opposite change during baseline condition within the

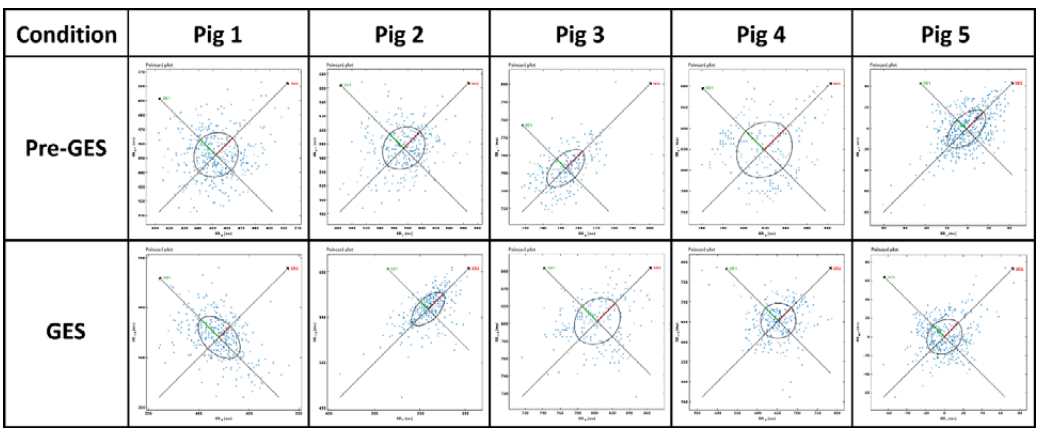

Fig. 5. *Poincaré plots of the pigs for the pre-GES and GES condition. 80% of the pigs (n=5) showed a decreased ratio of the standard deviation 2 (SD2)/standard deviation 1 (SD1) of the plots in line with a shift toward the activity of the parasympathetic branch.*

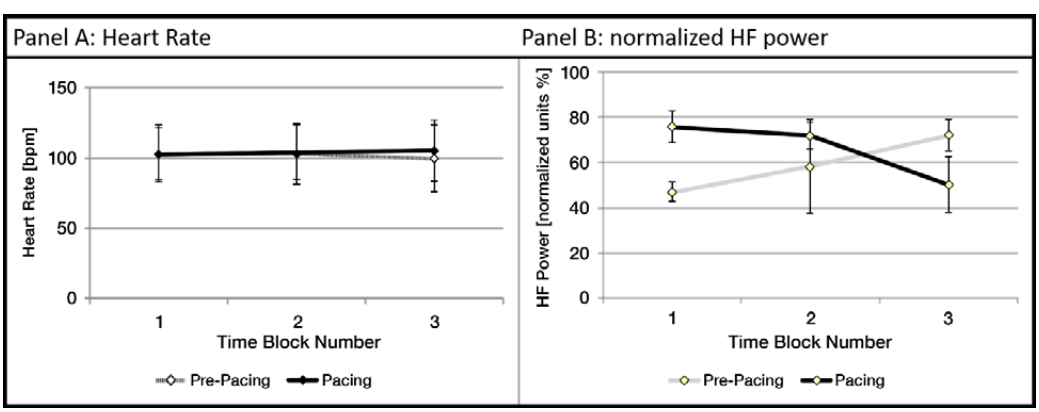

Fig. 6. *Time course of heart rate (Panel **A**) without relevant alterations during consecutive epochs within the pre-GES and GES condition. In contrast, nHF showed a decline during the third epoch of the GES period while during pre-GES epochs an increase occured (Panel **B**). (Whiskers show standard error). The time block numbers are the numbers of the three analyzed consecutive heart rate time series and the corresponding nHF Power values.*

third epoch (Fig. 6, Panel B). Due to the exploratory character of this repeated measures analysis, we did not apply a Bonferroni-correction.

To get a more visual impression of the impact of the stimulation on the HRV parameters and the heart rate itself, we depict a ECG time series before and during GES (Fig. 7). It is clearly visible that while the heart rate did not change, the pattern of RR-interval fluctuations changed dramatically. In the HRV power spectrum a peak within the high frequency reflects this stabilization of RR-interval fluctuations within the stimulation condition in comparison to the baseline.

DISCUSSION

The results of the presented pilot study show that the sympathetic-vagal balance can be shifted toward accelerated activity of the parasympathetic branch of ANS function in pigs by inductive electrical stimulation of the gastric wall. This was found by means of increased normalized high- and respectively decreased normalized low frequency HRV power during stimulation in comparison to baseline condition.

In contrast to former studies for cervical electrical VNS to enhance vagal tone (31, 37, 48, 49), we shifted sympathetic-vagal balance in favor of parasympathetic activity with afferent vagal stimulation via the gastric wall. This stimulation led to relative excitation of central vagal structures resulting in efferent vagal signaling. In comparison to former trials investigating cervical vagal stimulation, the relative enhancement of vagal activity, assessed by analysis of nHF in the current investigation was larger. While in a comparable manner the impairment of relative central sympathetic activity by means of nLF was found to be larger as well (37, 48). In several cervical VNS trials the decrease of sympathetic activity was accompanied by decreasing vagal activity (50) or cervical VNS led to parallel stimulation of the sympathetic ANS branch beside

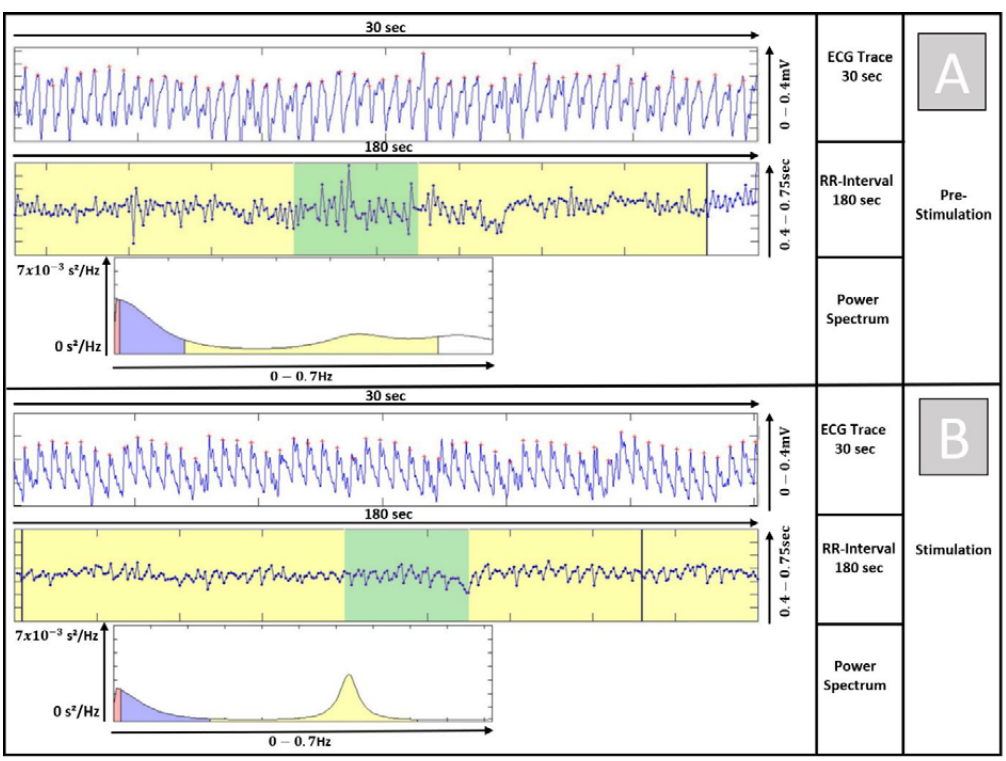

Fig. 7. *Example of ECG traces (30 sec) before (Panel **A**) and during GES (Panel **B**). While the heart rate stayed the same (104bpm in each 3 example), the inter-beat intervals changed as can be visually be assessed within the RR-interval panel for each recording (3 min each). The rhythm stabilized within the high frequency, which also can be seen at the HRV power spectrum where a peak occured within the high frequency range during GES (Panel B) in comparison to pre-GES condition (Panel A).*

increased vagal signaling (31). The current study shows a shift of ANS activity in favor of vagal tone following inductive electrical stimulation of the gastric wall.

The described effects have been identified by evaluation of respective HRV parameters. Since the main difference between former trials and the presented work is that in the current study, using an afferent stimulation approach, we conclude, that these differences in impact on the ANS balance might be attributable to pure afferent stimulation of central vagal structures. It might be hypothesized that this afferent signal is modulated in the NTS (51), representing the principal relay for integrational processing of afferent vagal signaling (52) and converted there, activating dorsal vagal complex (DVC) neurons (51), into efferent vagal pulsation. This central effect could have been evaluated with recording of potentials within the DVC. The impossibility of this measurement due to the study design which focuses on a minimal autonomic interference for evaluating HRV parameters is a clear limitation of our study.

With exclusive afferent stimulation, a stronger efferent autonomic signal promising minor adverse effects seems to be attainable. We think that under clinical conditions the central, and thus integrative part of the IR, is critical for the functionality of the described regulatory loop. Without regarding the current autonomic state, electrical stimulation of the vagal ANS branch results in new autonomic imbalances, which in turn lead to adverse symptoms such as bradycardia (53) up to asystolia (54), bronchoconstriction (38), shortness of breath (12, 14), hoarseness (12, 14, 15), throat pain/dysphagia (12), coughing (12, 14, 15), sleep-related stridor (55) and dizziness (56) or insomnia (12, 56).

However, no significant differences of heart rate (HR), root mean square of successive differences (RSSDM), the proportion of pairs of successive beat-to-beat intervals that differ by more than 50ms (pNN50), absolute HRV power, LF Power or HF power were found in the presented pilot study. Differences were only significant for normalized LF and HF power values, describing a shift of sympathetic-vagal balance rather than changes to one of the ANS branches. Missing significance in non-normalized units might be explained by the quite low number of pigs that increases the variance in the data. The normalization procedure to some degrees counteracts this effect. However, because of missing differences of HR between conditions, an increase of parasympathetic activity at the cost of a decrease of sympathetic power might have led to the differences found in normalized units. Due to the relative low number of pigs in our pilot trial, these effects possibly failed to be significant in the non-normalized absolute values. Although the changes, even of absolute numbers, pointed in this direction, they still fell short of being significant. Trials with more pigs could possibly clarify this issue.

In prior studies (57, 58), heart rate changes were described following efferent VNS, however, they were not observed in the presented study. This initially remarkable fact is attributable to the central rearrangement of viscerotopic (36) afferent vagal signaling (59), which may lead to enhancement of efferent vagal activity without influencing peripheral sympathetic activity.

In the presented study, the effect of vagal stimulation was shown with high significance along the first epoch of the GES interval after pre-GES conditions. Prolonged stimulations (GES) led to a drop of this effect during consecutive epochs, raising the question if the effect was independent of stimulation and would normalize over time by itself. On the other hand-side, it might be explained by the chosen stimulation pattern. Earlier studies detected the stimulation frequency to be the most critical point regarding the stimulation parameters (60–62). Chen et al. (61) pointed out that a presynaptic mechanism contributes to depression of autonomic signal transmission in NTS in frequencies above 0.1 Hz (61). Likewise, Lehrer et Gevirtz (62) showed the resonance frequency of the vagal system to be 0.1 Hz indicated by the HF power of HRV (62), thus, the chosen stimulation frequency was most likely much too high and perhaps could have caused the signal transmitting depression in NTS mentioned above as well as exhaustion of the peripheral signal transmitting structures as defined by a local cholinergic deficit, which limits the excitability of

the stimulated circuit. Nevertheless, the number of included animals within our pilot trial was too small to draw general conclusions and further studies with larger N should be used to replicate this finding. A larger study is underway.

The number of indicators for evaluation of autonomic balance is very low. Some authors investigated the skin conductivity level (SCL) (63) describing solely the sympathetic activity of the ANS (63), which was never used for the measurement of ANS balance in animals. Rocchetti et al. (64) compared the concentration of autonomic agonists (Ach) in sinoatrial myocytes with the baroreflex sensitivity (BRS) and time domain HRV parameters (64) and did find no linear correlation. Zaza and Lombardi (65) referring to the results of Rochetti et al. (64) pointed out that normalized frequency domain indexes of HRV for their HR-independency appear to be appropriate indexes for analyzing sympathetic-vagal balance (65). Furthermore they doubt the validity of the BRS describing ANS balance for its lack of concomitant changes in LF/HF ratio and the high affectability by mean heart rate (65). Chang et al. (66) could show that functional magnetic resonance imaging (fMRI) changes in several brain areas correlate with changes in frequency domain HRV parameters (66). Taking into consideration the issues mentioned above, we performed our observation of the ANS balance analyzing the given HRV parameters.

The evaluation of the ANS tone under sedation remains debatable, but due to animal safety and welfare sedation for GES was unavoidable. The drug α-chloralose is widely used as an anesthetic in studies of the cerebral vascular system because of its presumed minimal depression of autonomic function (67). Different authors pointed out that α-chloralose only minimally affects cardiorespiratory function and preserves autonomic reflex stability remarkably well (68, 69).

We conclude that inductive GES via a mGT appears to be a promising approach to alter sympathetic-vagal balance by enlarging vagal and depressing sympathetic activity relatively in order to prevent consecutive pathologies due to a compromised vagal system. Further investigations of afferent vagal stimulation must explore the optimal stimulation pattern, highlighting the stimulation frequency such as energy and wavelength to maximize the effects on ANS function and balance. Likewise, effects of a longer period of vagal stimulation via the gastric wall must be examined in following trials to appraise the potential of afferent vagal stimulation for a clinical setting.

ACKNOWLEDGEMENTS

We thank the employees at the Institute for Animal Testing, Experimentation and Animal Welfare of Jena University for their careful handling and treatment of the animals and for analyzing the blood samples. We thank Creed Weiler and Ivan Milencovic for critically reading the manuscript. ML thanks his principal consultant Jan Jacob Meyer for providing time to write the manuscript. Not least, thanks to Frank Jabin for his creative work on the figures.

DISCLOSURES: Marco Leitzke, Stefan Schimpf and Martin Altrock are inventors on one patent application (DE 10 2010 055 792.7 Number) related to gastric electrical stimulation, but do not receive any proceeds related to this patent, so that no financial or non-financial compenting interests are given. Harald Schubert, Sabine Bischoff, Dirk Hoyer, Peter Schönknecht and Sebastian Olbrich report no financial and no non-financial conflict of interest. No funding was obtained.

REFERENCES

1. Tracey KJ. Physiology and immunology of the cholinergic antiinflammatory pathway. J Clin Invest 2007; 117(2):289–96.
2. Pavlov VA, Tracey KJ. The vagus nerve and the inflammatory reflex—linking immunity and metabolism. Nat Rev Endocrinol 2012; 8(12):743–54.
3. Wang H, Yu M, Ochani M, et al. Nicotinic acetylcholine receptor alpha7 subunit is an essential regulator of inflammation. Nature. 2003; 421(6921):384–8.
4. Koopman FA, Tang MW, Vermeij J, et al. Autonomic dysfunction precedes development of rheumatoid arthritis: a prospective cohort study. EBioMedicine

2016; 6:231–7.
5. Huang J, Wang Y, Jiang D, Zhou J, Huang X. The sympathetic-vagal balance against endotoxemia. J Neural Transm 2010; 117(6):729–35.
6. Stauss HM. Heart rate variability. Am J Physiol - Regul Integr Comp Physiol 2003; 285(5):R927–31.
7. Stauss HM. Heart rate variability: just a surrogate for mean heart rate? Hypertension 2014; 64(6):1184–6.
8. Annane D, Trabold F, Sharshar T, Jarrin I, Blanc AS, Raphael JC, Gajdos P. Inappropriate sympathetic activation at onset of septic shock: a spectral analysis approach. Am J Respir Crit Care Med 1999; 160(2):458–65.
9. Tracey KJ. The inflammatory reflex. Nature 2002; 420(6917):853–9.
10. Andersson J. The inflammatory reflex--introduction. J Intern Med 2005; 257(2):122–5.
11. Romigi A, Albanese M, Placidi F, et al. Heart rate variability in untreated newly diagnosed temporal lobe epilepsy: Evidence for ictal sympathetic dysregulation. Epilepsia. 2016; 57(3):418–26.
12. Ohemeng KK, Parham K. Vagal nerve stimulation: indications, implantation, and outcomes. Otolaryngol Clin North Am 2020; 53(1):127–43.
13. Broncel A, Bocian R, Kłos-Wojtczak P, Kulbat-Warycha K, Konopacki J. Vagal nerve stimulation as a promising tool in the improvement of cognitive disorders. Brain Res Bull 2020; 155:37–47.
14. Ellrich J. Transcutaneous auricular vagus nerve stimulation. J Clin Neurophysiol Off Publ Am Electroencephalogr Soc 2019; 36(6):437–42.
15. González HFJ, Yengo-Kahn A, Englot DJ. Vagus nerve stimulation for the treatment of epilepsy. Neurosurg Clin N Am 2019; 30(2):219–30.
16. Akar SA, Kara S, Bilgiç V. Investigation of heart rate variability in major depression patients using wavelet packet transform. Psychiatry Res 2016; 238:326–32.
17. Alvares GA, Quintana DS, Hickie IB, Guastella AJ. Autonomic nervous system dysfunction in psychiatric disorders and the impact of psychotropic medications: a systematic review and meta-analysis. J Psychiatry Neurosci 2016; 41(2):89–104.
18. Struhal W, Mahringer C, Lahrmann H, Mörtl C, Buhl P, Huemer M, Ransmayr G. Heart rate spectra confirm the presence of autonomic dysfunction in dementia patients. J Alzheimers Dis JAD. 2016; 54(2):657-67
19. Corazzol M, Lio G, Lefevre A, et al. Restoring consciousness with vagus nerve stimulation. Curr Biol. 2017; 27(18):R994–6.
20. Bonaz B, Sinniger V, Hoffmann D, et al. Chronic vagus nerve stimulation in Crohn's disease: a 6-month follow-up pilot study. Neurogastroenterol 2016; 28(6):948–53.
21. Gold MR, Van Veldhuisen DJ, Hauptman PJ, et al. Vagus nerve stimulation for the treatment of heart failure. J Am Coll Cardiol 2016; 68(2):149–58.
22. Coruzzi P, Castiglioni P, Parati G, et al. Autonomic cardiovascular regulation in quiescent ulcerative colitis and Crohn's disease. Eur J Clin Invest 2007; 37(12):964–70.
23. Tsai J-D, Chang Y-C, Lin L-C, Hung K-L. The neuropsychological outcome of pediatric patients with refractory epilepsy treated with VNS — A 24-month follow-up in Taiwan. Epilepsy Behav 2016; 56:95–8.
24. Milev RV, Giacobbe P, Kennedy SH, et al. Canadian network for mood and anxiety treatments (CANMAT) 2016 clinical guidelines for the management of adults with major depressive disorder: section 4. neurostimulation treatments. Can J Psychiatry 2016; 61(9):561–75.
25. Merrill CA, Jonsson MAG, Minthon L, et al. Vagus nerve stimulation in patients with Alzheimer's disease: Additional follow-up results of a pilot study through 1 year. J Clin Psychiatry 2006; 67(8):1171–8.
26. Nishizaki A, Sakamoto K, Saku K, et al. Optimal titration is important to maximize the beneficial effects of vagal nerve stimulation in chronic heart failure. J Card Fail 2016; 22(8):631–8.
27. Borovikova LV, Ivanova S, Zhang M, et al. Vagus nerve stimulation attenuates the systemic inflammatory response to endotoxin Nature. 2000; 405(6785):458–62.
28. Samniang B, Shinlapawittayatorn K, Chunchai T, et al. Vagus nerve stimulation improves cardiac function by preventing mitochondrial dysfunction in obese-insulin resistant rats. Sci Rep 2016; 6:19749.
29. Bonaz B, Sinniger V, Pellissier S. Targeting the cholinergic anti-inflammatory pathway with vagus nerve stimulation in patients with Covid-19? Bioelectron Med 2020; 6(1):1-7.

30. Staats P, Giannakopoulos G, Blake J, Liebler E, Levy RM. The use of non-invasive vagus nerve stimulation to treat respiratory symptoms associated with COVID-19: a theoretical hypothesis and early clinical experience. Neuromodulation Technol Neural Interface 2020; 23:784-8.
31. Martlé V, Bavegems V, Van Ham L, et al. Evaluation of heart rate variability in dogs during standard and microburst vagus nerve stimulation: a pilot study. Vet J 2014; 202(3):651–3.
32. Xu F, Tan Y, Huang Z, Zhang N, Xu Y, Yin J. Ameliorating effect of transcutaneous electroacupuncture on impaired gastric accommodation in patients with postprandial distress syndrome-predominant functional dyspepsia: a pilot study. Evid Based Complement Alternat Med 2015; 2015:1–7.
33. Van Leusden JWR, Sellaro R, Colzato LS. Transcutaneous Vagal Nerve Stimulation (tVNS): a new neuromodulation tool in healthy humans? Front Psychol 2015 Feb; 6:102.
34. Levine YA, Koopman FA, Faltys M, et al. Neurostimulation of the cholinergic anti-inflammatory pathway ameliorates disease in rat collagen-induced arthritis. PLoS ONE. 2014; 9(8):e104530.
35. Guiraud D, Andreu D, Bonnet S, et al. Vagus nerve stimulation: state of the art of stimulation and recording strategies to address autonomic function neuromodulation. J Neural Eng 2016; 13(4):041002.
36. McDougall SJ, Peters JH, Andresen MC. Convergence of cranial visceral afferents within the solitary tract nucleus. J Neurosci 2009; 29(41):12886–95.
37. Jansen K, Vandeput S, Milosevic M, et al. Autonomic effects of refractory epilepsy on heart rate variability in children: influence of intermittent vagus nerve stimulation. Dev Med Child Neurol 2011; 53(12):1143–9.
38. Meyers EE, Kronemberger A, Lira V, Rahmouni K, Stauss HM. Contrasting effects of afferent and efferent vagal nerve stimulation on insulin secretion and blood glucose regulation. Physiol Rep 2016; 4(4):e12718.
39. Seki A, Green HR, Lee TD, et al. Sympathetic nerve fibers in human cervical and thoracic vagus nerves. Heart Rhythm Off J Heart Rhythm Soc 2014; 11(8):1411–7.
40. Rhee K-S, Hsueh C-H, Hellyer JA, et al. Cervical vagal nerve stimulation activates the stellate ganglion in ambulatory dogs. Korean Circ J 2015; 45(2):149-157.
41. Kentish SJ, Page AJ. Plasticity of gastro-intestinal vagal afferent endings. Physiol Behav 2014; 136:170–8.
42. Komuro T. Structure and organization of interstitial cells of Cajal in the gastrointestinal tract. J Physiol 2006; 576(3):653–8.
43. Liu J, Qiao X, Chen JDZ. Vagal afferent is involved in short-pulse gastric electrical stimulation in rats. Dig Dis Sci 2004; 49(5):729–37.
44. Castoro MA, Yoo PB, Hincapie JG, Hamann JJ, Ruble SB, Wolf PD, Grill WM. Excitation properties of the right cervical vagus nerve in adult dogs. Exp Neurol 2011; 227(1):62–8.
45. Qin C, Sun Y, Chen JDZ, Foreman RD. Gastric electrical stimulation modulates neuronal activity in nucleus tractus solitarii in rats. Auton Neurosci 2005; 119(1):1–8.
46. Hsu C-H, Tsai M-Y, Huang G-S, et al. Poincaré plot indexes of heart rate variability detect dynamic autonomic modulation during general anesthesia induction. Acta Anaesthesiol Taiwan 2012; 50(1):12–8.
47. Task Force of the European Society of Cardiology and the North American Society of Pacing and Electrophysiology. Heart rate variability. Standards of measurement, physiological interpretation, and clinical use. Eur Heart J 1996;17(3):354–81.
48. Zhang Y, Popovic ZB, Bibevski S, Fakhry I, Sica DA, Van Wagoner DR, Mazgalev TN. Chronic vagus nerve stimulation improves autonomic control and attenuates systemic inflammation and heart failure progression in a canine high-rate pacing model. Circ Heart Fail 2009; 2(6):692–9.
49. Verrier RL, Nearing BD, Olin B, Boon P, Schachter SC. Baseline elevation and reduction in cardiac electrical instability assessed by quantitative T-wave alternans in patients with drug-resistant epilepsy treated with vagus nerve stimulation in the AspireSR E-36 trial. Epilepsy Behav 2016; 62:85–9.
50. Schomer AC, Nearing BD, Schachter SC, Verrier RL. Vagus nerve stimulation reduces cardiac electrical instability assessed by quantitative T-wave alternans analysis in patients with drug-resistant focal epilepsy. Epilepsia 2014; 55(12):1996–2002.
51. Travagli RA, Hermann GE, Browning KN, Rogers

RC. Brainstem circuits regulating gastric function. Annu Rev Physiol. 2006 Jan;68(1):279–305.
52. Smith DV, Uteshev VV. Heterogeneity of nicotinic acetylcholine receptor expression in the caudal nucleus of the solitary tract. Neuropharmacology. 2008 Feb;54(2):445–53.
53. Asconapé JJ, Moore DD, Zipes DP, Hartman LM, Duffell WH. Bradycardia and asystole with the use of vagus nerve stimulation for the treatment of epilepsy: a rare complication of intraoperative device testing. Epilepsia 1999; 40(10):1452–4.
54. Tatum WOT, Moore DB, Stecker MM, et al. Ventricular asystole during vagus nerve stimulation for epilepsy in humans. Neurology 1999; 52(6):1267–1267.
55. Louis EKS, Faber K. Reversible sleep-related stridor during vagus nerve stimulation. Epileptic Disord 2010; 12(1):76–80.
56. Sackeim H. Vagus Nerve Stimulation (VNS™) for Treatment-resistant depression efficacy, side effects, and predictors of outcome. Neuropsychopharmacology. 2001; 25(5):713–28.
57. Agarwal R, Mokelke E, Ruble SB, Stolen CM. Vagal nerve stimulation evoked heart rate changes and protection from cardiac remodeling. J Cardiovasc Transl Res. 2016; 9(1):67–76.
58. Yamakawa K, So EL, Rajendran PS, et al. Electrophysiological effects of right and left vagal nerve stimulation on the ventricular myocardium. AJP Heart Circ Physiol 2014; 307(5):H722–31.
59. Niijima A. The afferent discharges from sensors for interleukin 1 beta in the hepatoportal system in the anesthetized rat. J Auton Nerv Syst 1996 Dec; 61(3):287–91.
60. Le Blanc-Louvry I, Guerre F, Songné B, Ducrotté P. Gastric stimulation: influence of electrical parameters on gastric emptying in control and diabetic rats. BMC Surg 2002; 2(1):5.
61. Chen C-Y, Horowitz JM, Bonham AC. A presynaptic mechanism contributes to depression of autonomic signal transmission in NTS. Am J Physiol-Heart Circ Physiol 1999; 277(4):H1350–60.
62. Lehrer PM, Gevirtz R. Heart rate variability biofeedback: how and why does it work? Front Psychol 2014; 5:756
63. Counotte J, Pot-Kolder R, van Roon AM, Hoskam O, van der Gaag M, Veling W. High psychosis liability is associated with altered autonomic balance during exposure to Virtual Reality social stressors. Schizophr Res 2017; 184:14–20.
64. Rocchetti M, Malfatto G, Lombardi F, Zaza A. Role of the input/output relation of sinoatrial myocytes in cholinergic modulation of heart rate variability. J Cardiovasc Electrophysiol 2000; 11(5):522–30.
65. Zaza A, Lombardi F. Autonomic indexes based on the analysis of heart rate variability: a view from the sinus node. Cardiovasc Res 2001; 50(3):434–42.
66. Chang C, Metzger CD, Glover GH, Duyn JH, Heinze H-J, Walter M. Association between heart rate variability and fluctuations in resting-state functional connectivity. NeuroImage 2013; 68:93–104.
67. Luckl J, Keating J, Greenberg JH. Alpha-chloralose is a suitable anesthetic for chronic focal cerebral ischemia studies in the rat: A comparative study. Brain Res 2008; 1191:157–67.
68. Arfors K-E, Arturson G, Malmberg P. Effect of prolonged chloralose anesthesia on acid-base balance and cardiovascular functions in dogs. Acta Physiol Scand 1971; 81(1):47–53.
69. Lindauer U, Villringer A, Dirnagl U. Characterization of CBF response to somatosensory stimulation: model and influence of anesthetics. Am J Physiol. 1993; 264(4 Pt 2):H1223-1228.

Effects of probiotics on intestinal flora, inflammation and degree of liver cirrhosis in rats with liver cirrhosis by regulating Wnt/β-catenin signaling pathway

Y. Feng*, S.-J. Gao*, R.-D. Wei, T. Liu, X.-P. Fan, Y.-D. Han and N. Zhu

Department of Hepatology, Qingdao No.6 People's Hospital, Qingdao, Shandong, China

Received April 24, 2020 – Accepted July 14, 2020

*These Authors contributed equally to this work

We aimed to explore the effects of probiotics on intestinal flora, inflammation and degree of liver cirrhosis in rats with liver cirrhosis, and to verify the Wnt/β-catenin signaling pathway that regulates this process. A total of 30 SD rats were randomly divided into 3 groups, namely, control group (n=10), model group (n=10) and probiotic group (n=10). Rats in the model group were used to construct liver cirrhosis models using carbon tetrachloride (CCL_4) method, and those in the probiotic group were administered with probiotic preparations by gavage for 8 weeks. Then the feces of rats in each group were taken to detect the composition of intestinal flora, and changes in the content of inflammatory cytokines, such as tumor necrosis factor-alpha (TNF-α), interleukin-6 (IL-6), monocyte chemotactic protein 1 (MCP-1) and interferon-gamma (IFN-γ), in peripheral blood collected were examined by enzyme-linked immunosorbent assay (ELISA). Next, changes in the degree of liver cirrhosis were analyzed by hematoxylin and eosin (H&E) staining, and the expression levels of the Wnt/β-catenin signaling pathway-related molecules, including β-catenin, glycogen synthase kinase (GSK)-3β and Frizzled-2, in liver tissues in each group were detected *via* polymerase chain reaction (PCR) and Western blotting (WB). Compared with rats in the control group, those in the model group had a disordered structure of hepatic lobule and hyperplasia of a large number of fibrous tissues. In contrast to those in the model group, the liver lobule structure was greatly improved, the edema cells were obviously reduced, and the hyperplasia of collagen fibers was remarkably alleviated in the probiotic group. Moreover, the degree of liver cirrhosis in the probiotic group was significantly reduced compared with that in the model group. Moreover, the rats in the model group exhibited a higher Bifidobacterium level in the intestinal tract, while those in the probiotic group displayed higher levels of microorganisms in the intestinal tract, such as Lachnospiraceae, Ruminococcaceae, Actinbacteria, Slackia and Pasteurellaceae. In comparison with that in the control group, the level of salt-tolerant Lactobacillus in the intestinal tract of rats in the model group was significantly decreased, while that in the probiotic group was partially increased (P=0.023). Meanwhile, some intestinal flora of rats in the control group, model group and probiotic group were closely correlated. Specifically, highly positive correlations were found between Bacteroidetes and Paraeggerthella (*r*=0.423, P=0.034) and between Firmicutes and Lactobacillus (*r*=0.318, P=0.027), but strongly negative associations were detected between Firmicutes and Paraeggerthella (*r*=-0.691, p=0.004) and between Paraeggerthella and Lactobacillus (*r*=-0.384, P=0.047). In addition, the levels of inflammatory cytokines TNF-α IL-6, MCP-1 and IFN-γ in the plasma of rats in the model group were markedly higher than those in the control group (P<0.05), whereas such levels in the probiotic group were

Corresponding Author:
Nan Zhu, MM
Department of Hepatology, Qingdao No.6 People's Hospital,
9 Fushun Road,
Qingdao 266033, Shandong, China
Tel./Fax: +86 053281636680
e-mail: zhunan19830219@163.com

0393-974X (2021)
Copyright © by BIOLIFE, s.a.s.
This publication and/or article is for individual use only and may not be further reproduced without written permission from the copyright holder.
Unauthorized reproduction may result in financial and other penalties
DISCLOSURE: ALL AUTHORS REPORT NO CONFLICTS OF INTEREST RELEVANT TO THIS ARTICLE.

decreased compared with those in the model group (P<0.05). PCR results revealed that the expression levels of β-catenin and Frizzled-2 in the model group were higher than those in the control group, whereas they were lower in the probiotic group than those in the model group (P<0.05). Furthermore, the model group had a decreased level of GSK-3β in comparison with the control group, but the probiotic group had a higher level of GSK-3β than the model group (P<0.05). WB results were consistent with PCR results. Probiotics can affect intestinal flora, inflammation and degree of liver cirrhosis in rats with liver cirrhosis, and its mechanism may be related to the Wnt/β-catenin signaling pathway.

Key words: probiotics; Wnt/β-catenin signaling pathway; liver cirrhosis; intestinal flora

Liver cirrhosis is a common disease that leads to liver function reduction or even loss, and it is also a vital factor causing liver cancer (1, 2). In most cases, it is triggered by hepatitis B in China, one of the countries with the highest incidence rate of hepatitis B (3). After hepatitis B virus infection, liver cells will be damaged by the virus, thus leading to hepatitis, and a long-term virus carrier state continuously activates the immune system of the body. Moreover, the ceaseless damage of virus-infected liver cells by the monocyte-macrophage system and the constant repair effect lead to the occurrence and development of liver cirrhosis (4) which reduces the digestive function of patients, and its complications, such as portal hypertension, are life-threatening (5). Therefore, researching and improving the therapeutic methods for liver cirrhosis is crucial to increase the survival rate and enhance the quality of life of liver cirrhosis patients.

Intestinal microorganisms consist of diverse flora, and the balance of various kinds of flora is of critical significance to the maintenance of intestinal microenvironment homeostasis (6, 7). Probiotics refer to microorganisms, including Bifidobacterium, probiotic Bacillus, Saccharomycetes and Lactobacillus, that colonize in the body and are beneficial to the host (8), mainly through modulating the balance of various intestinal flora and mucosal immune functions (9, 10). It has been proved that probiotics have notable therapeutic effects on many diseases, but the effects and mechanism on liver cirrhosis have not been reported.

In this study, therefore, the changes in intestinal flora and inflammatory cytokines, such as tumor necrosis factor-alpha (TNF-α), interleukin-6 (IL-6), monocyte chemotactic protein 1 (MCP-1) and interferon-gamma (IFN-γ), in rats were detected by establishing the rat model of liver cirrhosis and applying probiotic preparations for the intervention treatment. Meanwhile, the changes in the degree of liver cirrhosis in each group were determined *via* observing the morphology by hematoxylin and eosin (H&E) staining, and the specific regulatory effect of the Wnt/β-catenin signaling pathway in this process was analyzed.

MATERIALS AND METHODS

Establishment of a rat model

A total of 30 adult female rats (240-260 g) were randomly divided into 3 groups, namely, control group (n=10), model group (n=10) and probiotic group (n=10). Rats in the control group received no treatment. In the model group, a rat model of liver cirrhosis was established using carbon tetrachloride (CCL_4) method (11). CCL_4 oil solution was subcutaneously injected into the rats in the model group every 3 days, with 0.1mL/100g body weight, and the rats were fed with a high-fat, low-protein diet. About 6-7 weeks later, early liver cirrhosis formed. Rats with early liver cirrhosis were administered with probiotic preparations containing Bifidobacterium, Lactobacillus acidophilus and Enterococcus trifecta (Wecare Biotechnology) by gavage, with 1×10^7 CFU per day. After the experiment, the rats were sacrificed to collect serum and liver tissues, and the liver tissues were stained with H&E to detect the changes in degree of liver cirrhosis in each group of rats. This study was approved by the Animal Ethics Committee of Qingdao No.6 People's Hospital Animal Center.

Detection of intestinal microorganisms in rats

The feces of rats in each group were collected and

frozen in a liquid nitrogen container, and the intestinal microorganisms of rats were detected after sample collection. Then the collected samples were sent to Shanghai Vita Balance Co., Ltd. (Shanghai, China) for the analysis of intestinal microorganisms. Following the extraction, amplification, database building and labeling of microbial genomic DNA, Illumina MiSeq and Ion PGM were applied for high-throughput sequencing to detect the species and relative abundance of microorganisms in the feces samples of rats in each group. Thereafter, relevant bioinformatics analysis was performed, and the composition of intestinal flora was finally obtained.

Examination of inflammatory cytokine level

The changes in the content of inflammatory cytokines, TNF-α, IL-6, MCP-1 and IFN-γ, in each group of rats were detected using enzyme-linked immunosorbent assay (ELISA). After that, the content of each cytokine in the serum was analyzed using the ELISA kit (Thermo Fisher Scientific, Waltham, MA, USA) in strict accordance with the instructions. Thereafter, the peripheral blood of rats was centrifuged at 3000 rpm/min for 5 min, and the upper serum was taken for detection. Three replicate wells were set in each group. Finally, the absorbance at 480 nm was read on a microplate reader (Bio-Rad, Hercules, CA, USA) and converted into the actual concentration of TNF-α, IL-6, MCP-1 and IFN-γ based on the standard curve. The average sensitivity of the test was less than 0.38 pg/mL and the inter-assay coefficient of variation was 5.6%.

Fluorescence real-time quantitative polymerase chain reaction (RT-qPCR)

RT-qPCR was adopted to detect the expression changes of the Wnt/β-catenin signaling pathway-related molecules in the liver tissues of rats in each group, including β-catenin, glycogen synthase kinase (GSK)-3β and Frizzled-2. Total ribonucleic acid (RNA) in the liver tissues of rats in the control group, model group and probiotic group was extracted by TRIzol method (Invitrogen, Carlsbad, CA, USA). Primers were as follows: β-catenin: forward: (5'→3') 'CTGGCTTCTACTCCCTGACCT' and reverse: (5'→3') 'ACCAGAACCTAGCATCAAGGA', GSK-3β: forward: (5'→3')' TTGATGCTAGGTTCTGGTGTACC' and reverse: (5'→3') 'CCTTGGACTCTGCTTGTGTC', Frizzled-2: forward: (5'→3') 'TGCACATGCAGCTATACCCAG' and reverse: (5'→3') 'TGGTGGATTCTTGGTGCTTTTC', and glyceraldheyde 3-phosphate dehydrogenase (GAPDH): forward: (5'→3') 'CCACTCTACGAACATTTCAGCA' and reverse: (5'→3') 'ACTGGGCCAGCTCACAGTA'.

Western blotting

The expression levels of the Wnt/β-catenin signaling pathway-related molecules, β-catenin, GSK-3β and Frizzled-2, were examined by Western blot. Firstly, the total protein was extracted from rat liver tissues using radioimmunoprecipitation assay (RIPA) and protease inhibitors in the control group, model group and probiotic group. Following electrophoresis, transfer onto a polyvinylidene fluoride (PVDF) membrane and blocking with bovine serum albumin (BSA) (Roche, Basel, Switzerland), the proteins were incubated overnight with β-catenin, GSK-3β, Frizzled-2 and GAPDH antibodies (Thermo Fisher Scientific, Waltham, MA, USA) diluted appropriately according to the instructions. After 1 h of incubation with secondary antibodies, the proteins were photographed and statistical results were obtained.

Statistical analysis

Statistical Product and Service Solutions (SPSS) 23.0 (IBM, Armonk, NY, USA) was adopted for statistical processing. The comparison of measurement data among multiple groups was detected *via* analysis of variance (ANOVA), and that between two groups was examined *via t*-test. Moreover, Pearson method was utilized for correlation analysis, and linear discriminant analysis effect size (LEfSe) analysis method was employed to analyze intestinal flora. $P<0.05$ suggested that the difference was statistically significant.

RESULTS

Changes in liver cirrhosis degree of rats between groups

Changes in liver cirrhosis degree of rats in the control group, model group and probiotic group were analyzed by H&E staining (Fig. 1). The results manifested that compared with rats in the control group, those in the model group had a disordered structure of hepatic lobule and hyperplasia of a large number of fibrous tissues. In contrast to those in the model group, the liver lobule structure was greatly improved, edema cells were

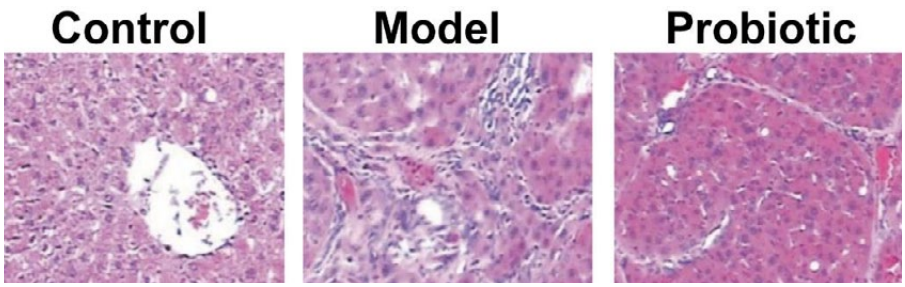

Fig. 1. *H&E staining for changes in liver cirrhosis degree of rats in the control group, model group and probiotic group. (magnification: 400×)*

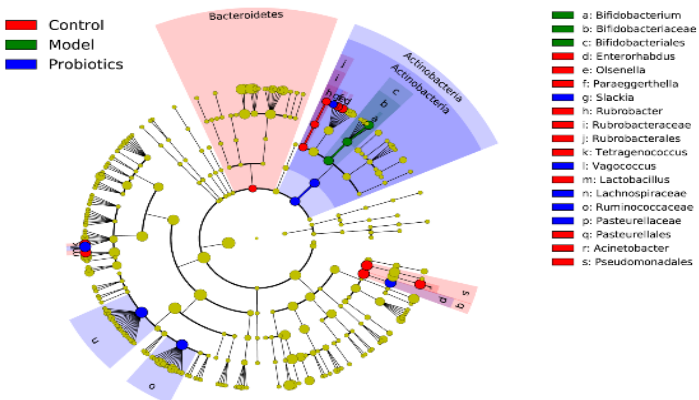

Fig. 2. *LEfSe analysis of the intestinal flora of rats in the control group, model group and probiotic group*

obviously reduced, and the hyperplasia of collagen fibers was remarkably alleviated in the probiotic group. Moreover, the degree of liver cirrhosis in the probiotic group was significantly reduced compared with that in the model group.

Analysis of the intestinal flora of rats between groups

The intestinal flora of rats in the control group, model group and probiotic group were analyzed (Fig. 2-3), and the results showed that the rats in the model group exhibited a higher Bifidobacterium level in the intestinal tract, while those in the probiotic group displayed higher levels of microorganisms in the intestinal tract, such as Lachnospiraceae, Ruminococcaceae, Actinbacteria, Slackia and Pasteurellaceae. The level of salt-tolerant Lactobacillus in the intestinal tract of rats in the control group, model group and probiotic group is shown in Fig. 4. It was found that in comparison with that in the control group, the level of salt-tolerant Lactobacillus in the intestinal tract of rats in the model group was significantly decreased, while that in the probiotic group was partially increased (P=0.023).

Correlation analysis of the intestinal flora of rats between groups

The correlation of the intestinal flora of rats in the control group, model group and probiotic group was assessed (Fig. 5). It was found that some intestinal flora of rats in all three groups were closely correlated. Specifically, highly positive correlations were observed between Bacteroidetes and Paraeggerthella (r=0.423, P=0.034) and between Firmicutes and Lactobacillus (r=0.318, P=0.027), but strongly negative associations were found between Firmicutes and Paraeggerthella (r=-0.691, P=0.004) and between Paraeggerthella and Lactobacillus (r=-0.384, P=0.047).

Table I. *Changes in inflammatory cytokine levels in the control group, model group and probiotic group*

Group	IL-6 (mg/L)	TNF-α (fmol/mL)	MCP-1 (mg/L)	IFN-γ (mg/L)
Control group	23.14±2.36	5.28±0.98	35.17±3.15	13.47±1.75
Model group	73.15±4.84*	12.84±1.12*	67.28±4.12*	22.84±2.41*
Probiotic group	45.15±5.12#	8.96±1.64#	66.52±5.12	15.36±1.25#

*Note: TNF-α, IL-6, MCP-1 and IFN-γ levels were markedly increased in model group but relatively decreased in probiotic group. *P<0.05 vs control group, and #P<0.05 vs model group.*

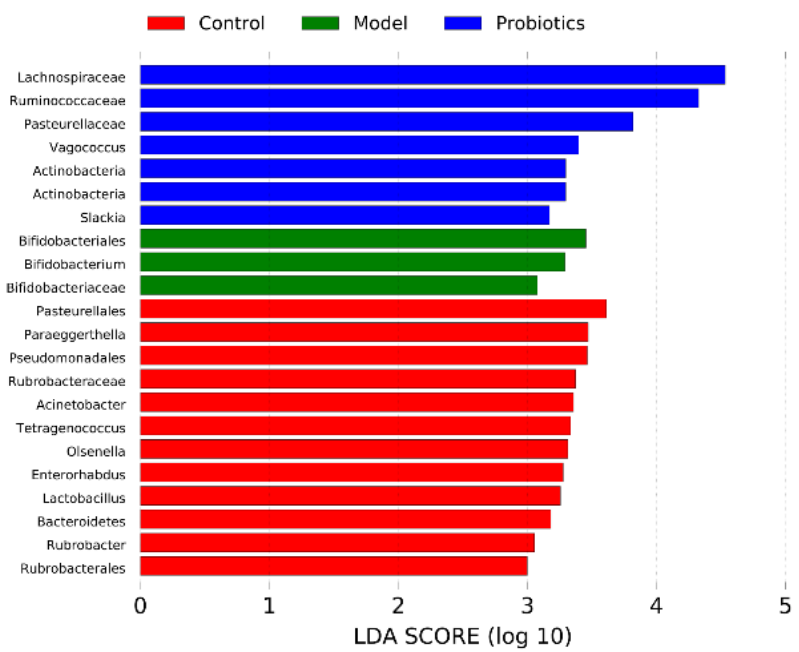

Fig. 3. *LDA score of the intestinal flora of rats in the control group, model group and probiotic group*

Changes in inflammatory cytokine levels between groups

The changes in levels of inflammatory cytokines (TNF-α, IL-6, MCP-1 and IFN-γ) in all three groups are shown in Table I. The levels of inflammatory cytokines in the plasma of rats in the model group were markedly higher than those in the control group (P<0.05), while such levels in the probiotic group were decreased compared with those in the model group (P<0.05).

Expressions of the Wnt/β-catenin signaling pathway-related molecules

The messenger RNA (mRNA) expression levels of the Wnt/β-catenin signaling pathway-related molecules, β-catenin, GSK-3β and Frizzled-2, in all three groups are shown in Fig. 6, and their protein expression levels are given in Fig. 7. PCR results illustrated that the expression levels of β-catenin and Frizzled-2 in the model group were higher than

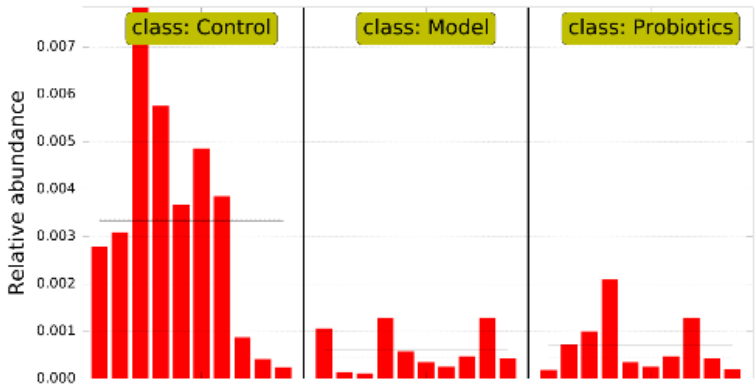

Fig. 4. *Levels of salt-tolerant Lactobacillus in the intestinal tract of rats in the control group, model group and probiotic group.*

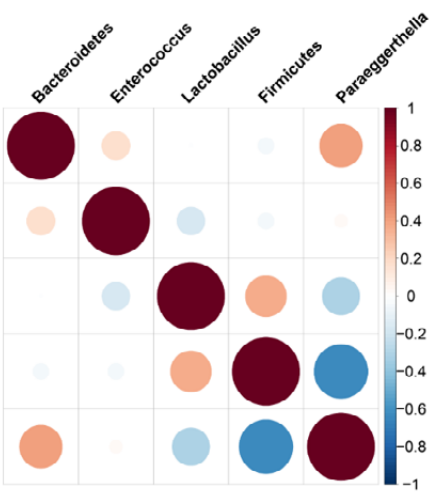

Fig. 5. *Correlation analysis of the intestinal flora of rats in the control group, model group and probiotic group.*

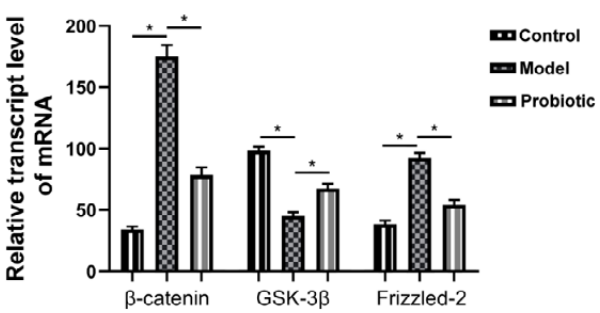

Fig. 6. *MRNA expression levels of the Wnt/β-catenin signaling pathway-related molecules in the control group, model group and probiotic group (*P<0.05).*

those in the control group, whereas they were lower in the probiotic group than those in the model group (P<0.05). Furthermore, the model group had a decreased level of GSK-3β in comparison with the control group, but the probiotic group had a higher level of GSK-3β than the model group (P<0.05). WB results were in consistency with PCR results.

DISCUSSION

As one of the most common diseases of the digestive system, liver cirrhosis has been confirmed to be a vital factor promoting the occurrence of liver cancer. Its incidence rate remains high and the death toll is increasing yearly (12, 13). The disease is mainly a result of the continuous damage of liver cells triggered by diverse factors and the repair of the body itself, leading to a sharp increase in the number of false lobules and nodules in non-functional liver tissues as well as fibrous connective tissues, which makes the liver tissues constantly harden and gradually lose its function (14). Moreover, primary treatment methods for liver cirrhosis include antiviral therapy and symptomatic and supportive treatment, and complications such as portal hypertension should be actively coped with (15). Liver transplantation is regarded as the unique treatment method that is able to cure liver cirrhosis, but it is greatly limited due to the difficulty in finding donors, high costs and

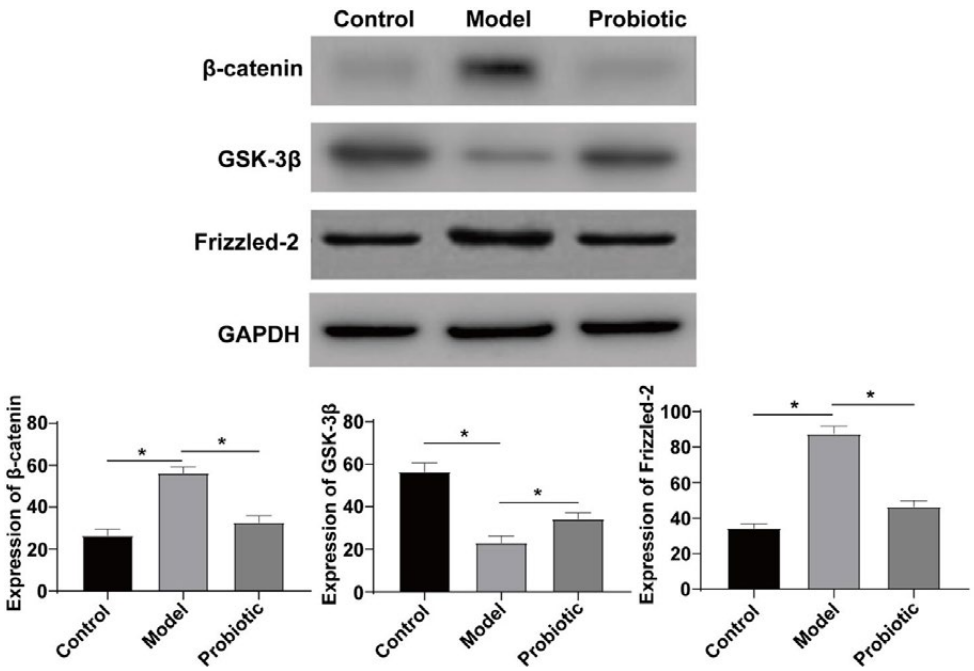

Fig. 7. *Protein expression levels of the Wnt/β-catenin signaling pathway-related molecules in the control group, model group and probiotic group (*P<0.05).*

postoperative immunological rejection (16). Hence, finding a new approach for treatment is of vital significance for the recovery of liver function and the prevention of complications.

It has been proved that probiotics composed of Bifidobacterium, probiotic Bacillus, Saccharomycetes and Lactobacillus influence the functions of different organs in the digestive system, including the colon, liver and stomach (17, 18). They can also affect the functions of diverse organs by their impact on the composition and functions of other microorganisms in intestinal tissues, protecting intestinal mucosal barrier, facilitating the absorption of nutrients by intestinal tissues, enhancing local and systemic immune responses and improving the body's antioxidant capacity (19). In addition, probiotics have been proved to ameliorate the symptoms of numerous diseases, including autism spectrum disorders (20) and Hirschsprung's disease-associated enterocolitis (21). The results of this study demonstrated that, compared with those in the control group, a disordered structure of hepatic lobule and hyperplasia of massive fibrous tissues were observed in the model group. In contrast to those in the model group, the liver lobule structure was greatly improved, edema cells were obviously reduced, and the hyperplasia of collagen fibers was remarkably alleviated in the probiotic group. Moreover, the degree of liver cirrhosis in the probiotic group was significantly reduced compared with that in the model group. The above results not only represent the successful establishment of the rat model of liver cirrhosis using CCL_4 method, but also confirm the impact of probiotic preparations on the process of liver pathological changes through a certain mechanism, and probiotic preparations prominently reduce the degree of liver cirrhosis. It can also be concluded that probiotic preparations have great potential as a treatment method for liver cirrhosis patients, with almost no side effects and easy administration.

Analysis of the composition of intestinal flora of rats in each group illustrated that the rats in the model

group exhibited a higher Bifidobacterium level in the intestinal tract, while those in the probiotic group displayed higher levels of such microorganisms in the intestinal tract, such as Lachnospiraceae, Ruminococcaceae, Actinbacteria, Slackia and Pasteurellaceae. In comparison with that in the model group, the level of salt-tolerant Lactobacillus in the intestinal tract of rats in the model group was significantly decreased, while that in the probiotic group was partially increased (P=0.023). Meanwhile, close correlations were detected among some intestinal flora of rats in the control group, model group and probiotic group. In other words, Bacteroidetes were highly positively associated with Paraeggerthella (r=0.423, P=0.034), and Firmicutes was distinctly related to Lactobacillus (r=0.318, P=0.027). However, Paraeggerthella was strongly negatively correlated with Firmicutes (r=-0.691, P=0.004) and Lactobacillus (r=-0.384, P=0.047). The above results fully demonstrate that probiotics can suppress liver cirrhosis by affecting the composition of intestinal flora, such as *Lachnospiraceae*, *Ruminococcaceae*, Actinbacteria, Slackia and *Pasteurellaceae*.

Furthermore, it was discovered that the levels of TNF-α, IL-6, MCP-1 and IFN-γ in the plasma of rats in the model group were markedly higher than those in the control group (P<0.05), whereas the levels of those inflammatory cytokines in the probiotic group were decreased compared with those in the model group (P<0.05), indicating that probiotics also may influence the occurrence of liver cirrhosis by remarkably inhibiting the inflammation level *in vivo*.

Ultimately, the mechanism of probiotics in affecting the process of liver cirrhosis was investigated. PCR results displayed that the expression levels of β-catenin and Frizzled-2 in the model group were higher than those in the control group, whereas those in the probiotic group were lower than those in the model group (P<0.05). Furthermore, the model group had a decreased level of GSK-3β in comparison with the control and probiotic groups (P<0.05). The same WB results as PCR results were obtained. All the above results denote that probiotics can regulate the Wnt/β-catenin signaling pathway to affect intestinal flora, inflammation and liver cirrhosis degree in rats with liver cirrhosis.

In conclusion, probiotics can improve intestinal flora, inflammation and degree of liver cirrhosis in rats with liver cirrhosis, and its mechanism of action may be related to the Wnt/β-catenin signaling pathway.

REFERENCES

1. Chung W, Jo C, Chung WJ, Kim DJ. Liver cirrhosis and cancer: comparison of mortality. Hepatol Int 2018; 12:269-76.
2. Ascha M, Hanouneh M, S Ascha M, Zein NN, Sands M, Lopez R, Hanouneh IA. Transjugular intrahepatic porto-systemic shunt in patients with liver cirrhosis and model for end-stage liver disease. Dig Dis Sci 2017; 62:534-42.
3. Lai CY, Cheng SB, Lee TY, Liu HT, Huang SC, Huang YC. Possible synergistic effects of glutathione and c-reactive protein in the progression of liver cirrhosis. Nutrients 2018; 10(6):678.
4. Glargaard S, Boysen T, Pilely K, Garred P, Ytting H. Prognostic value of lectin pathway molecules and complement proteins in ascitic fluid and blood in patients with liver cirrhosis. Scand J Gastroenterol 2018; 53:64-69.
5. Lipinski M, Saborowski M, Heidrich B, et al. Clinical characteristics of patients with liver cirrhosis and spontaneous portosystemic shunts detected by ultrasound in a tertiary care and transplantation centre. Scand J Gastroenterol 2018; 53:1107-13.
6. Liu J, Pang JJ, Tu ZC, Wang H, Sha XM, Shao YH, Liu GX. The accumulation, histopathology, and intestinal microorganism effects of waterborne cadmium on Carassius auratus gibelio. Fish Physiol Biochem 2019; 45:231-43.
7. Zuo ZH, Shang BJ, Shao YC, Li WY, Sun JS. Screening of intestinal probiotics and the effects of feeding probiotics on the growth, immune, digestive enzyme activity and intestinal flora of Litopenaeus vannamei. Fish Shellfish Immunol 2019; 86:160-68.
8. Irwin C, Khalesi S, Cox AJ, Grant G, Davey AK, Bulmer AC, Desbrow B. Effect of 8-weeks prebiotics/probiotics supplementation on alcohol metabolism and blood biomarkers of healthy adults: a pilot study. Eur J Nutr 2018; 57:1523-34.
9. Okada Y, Tsuzuki Y, Takeshi T, et al. Novel probiotics isolated from a Japanese traditional fermented

food, Funazushi, attenuates DSS-induced colitis by increasing the induction of high integrin alphav/beta8-expressing dendritic cells. J Gastroenterol 2018; 53:407-18.

10. Khalesi S, Johnson DW, Campbell K, Williams S, Fenning A, Saluja S, Irwin C. Effect of probiotics and synbiotics consumption on serum concentrations of liver function test enzymes: a systematic review and meta-analysis. Eur J Nutr 2018; 57:2037-53.
11. Chang HC, Chiu YW, Lin YM, et al. Herbal supplement attenuation of cardiac fibrosis in rats with CCl(4)-induced liver cirrhosis. Chin J Physiol 2014; 57:41-47.
12. Ponziani FR, Zocco MA, Cerrito L, Gasbarrini A, Pompili M. Bacterial translocation in patients with liver cirrhosis: physiology, clinical consequences, and practical implications. Expert Rev Gastroenterol Hepatol 2018; 12:641-56.
13. Makol A, Kanthaje S, Dhiman RK, Kalra N, Chawla YK, Chakraborti A. Association of liver cirrhosis severity with type 2 diabetes mellitus in hepatocellular carcinoma. Exp Biol Med (Maywood) 2018; 243:323-26.
14. Asti E, Sozzi M, Bonitta G, Bernardi D, Bonavina L. Esophagectomy in patients with liver cirrhosis: a systematic review and Bayesian meta-analysis. J Visc Surg 2018; 155:453-64.
15. Terai S, Tsuchiya A. Status of and candidates for cell therapy in liver cirrhosis: overcoming the “point of no return” in advanced liver cirrhosis. J Gastroenterol 2017; 52:129-40.
16. Jeong JY, Lim S, Sohn JH, Lee JG, Jun DW, Kim Y. Presence of sarcopenia and its rate of change are independently associated with long-term mortality in patients with liver cirrhosis. J Korean Med Sci 2018; 33:e299.
17. Ibrahim NS, Ooi FK, Chen CK, Muhamad AS. Effects of probiotics supplementation and circuit training on immune responses among sedentary young males. J Sports Med Phys Fitness 2018; 58:1102-9.
18. Nikbakht E, Khalesi S, Singh I, Williams LT, West NP, Colson N. Effect of probiotics and synbiotics on blood glucose: a systematic review and meta-analysis of controlled trials. Eur J Nutr 2018; 57:95-106.
19. Principi N, Cozzali R, Farinelli E, Brusaferro A, Esposito S. Gut dysbiosis and irritable bowel syndrome: The potential role of probiotics. J Infect 2018; 76:111-20.
20. Shaaban SY, El GY, Mehanna NS, El-Senousy WM, El-Feki H, Saad K, El-Asheer OM. The role of probiotics in children with autism spectrum disorder: A prospective, open-label study. Nutr Neurosci 2018; 21:676-81.
21. Nakamura H, Lim T, Puri P. Probiotics for the prevention of Hirschsprung-associated enterocolitis: a systematic review and meta-analysis. Pediatr Surg Int 2018; 34:189-93.

Identification of hub genes and pathways in the development of gastric cancer by gene co-expression network analysis

LH. Qin, XJ. Zhu, LY. Zhang, JQ. Chen, GY. Jin and LJ. Xiang

Department of gastroenterology, Shangyu People's Hospital, Shaoxing, Zhejiang, China

Received July 29, 2020 – Accepted December 9, 2020

There are many risk factors for gastric cancer (GC), including chronic atrophic gastritis, which involves multiple genes and signaling pathways. Weighted gene co-expression network analysis (WGCNA) was performed on GSE111762 to construct free-scale gene co-expression network and identified four significant modules that consisted of blue, dark orange, dark red and dark violet. In each module, genes with the most connectivity were selected as hub genes, including G antigen 12J (GAGE12J) in blue, proline, histidine and glycine rich 1 (PHGR1) in dark orange, DNA polymerase gamma 2, accessory subunit (POLG2) in dark red and collagen type XXI alpha 1 chain (COL21A1) in dark violet. The transcription COL21A1 and GAGE12J was up-regulated in atrophic gastritis *vs* normal gastric mucosa, but down-regulated in GC *vs* atrophic gastritis. PHGR1 was consistently down-regulated from normal gastric mucosa to GC, while POLG2 was up-regulated. Gene set enrichment analysis (GSEA) was then conducted to study the biological functions of hub genes in the development of GC. It showed that multiple tumorigenesis-related pathways were enriched, including peroxisome, DNA repair and KRAS signaling pathway in COL21A1, IL6-JAK-STAT3, epithelial mesenchymal transition (EMT) and TNFα-NF-κB signaling pathway in PHGR1, MYC targets, E2F targets and angiogenesis in POLG2 and peroxisome, Notch signaling pathway and androgen response in GAGE12J. The identified four genes, especially for COL21A1, PHGR1 and POLG2, were important in GC tumorigenesis and affected many cancer-related pathways.

Gastric cancer (GC) is the fifth most frequently diagnosed cancer and the third leading cause of cancer-related death worldwide. In 2018, nearly 1.03 million new cases were diagnosed and 0.78 million people died from GC (1). Atrophic gastritis, the persistent inflammation of the gastric mucosa, is a generally accepted cause of GC (2). Persisting *H. pylori* infection and carcinogenic intake are critical risk factors of inflammation-associated gastric oncogenesis (3, 4). Because of the lack of specific early symptoms, the patients are often diagnosed in advanced stages, and even if diagnosed in an early stage, the cancer tends to recur in distant organs after removing the primary tumor. Recently, treatment for GC, such as surgery, chemotherapy and radiotherapy, has been markedly improved, but the 5-year overall survival rate still remains low (5). Hence, it is urgent to identify more effective candidate genes that regulate tumorigenesis-associated inflammation and serve as new biomarkers for prediction and diagnosis.

In recent years, with the rapid advance of microarray and high-throughput sequence technology, many novel biomarkers associated with the initiation and progression of GC have been identified (6-8) .

Key words: gastritis; gastric cancer; WGCNA; GSEA

Corresponding Author:
Dr LJ Xiang,
Department of Gastroenterology,
Shangyu People's Hospital,
Shaoxing, Zhejiang 312300, China
Tel.: +057582185413
e-mail: xianglj_sxsy@sina.com

0393-974X (2021)
Copyright © by BIOLIFE, s.a.s.
This publication and/or article is for individual use only and may not be further reproduced without written permission from the copyright holder.
Unauthorized reproduction may result in financial and other penalties
DISCLOSURE: ALL AUTHORS REPORT NO CONFLICTS OF INTEREST RELEVANT TO THIS ARTICLE.

However, most studies mainly focused on differentially expressed genes (DEGs) between normal and tumor tissues according to a defined threshold, but ignored the interconnection among genes as well as the continuous progression of the pathology. The weighted gene co-expression network analysis (WGCNA) is a robust method to screen out potentially important genes by constructing free-scale gene co-expression networks, which takes the transition process from normal gastric mucosa, chronic gastritis (CG) to GC into account at the same time. Therefore, in the present study, we applied this algorithm to identify key genes correlated with the development of GC.

MATERIALS AND METHODS

Co-expression network construction

The GSE111762 expression profile was obtained from the Gene Expression Omnibus (GEO) database (http://www.ncbi.nlm.nih.gov/geo/). There were 3 normal gastric mucosae, 6 atrophic gastritis and 6 GC tissues within the dataset. We utilized "WGCNA" package to make quality control and calculated Pearson's correlation matrices. Then, an adjacency matrix a_{ij} for each pair of genes was constructed as follows:

$$s_{ij} = |cor(x_i, x_j)| a_{ij} = S_{ij}{}^{\beta}$$

where x_i and x_j were vectors of expression values of gene i and j, S_{ij} was the Pearson's correlation coefficient, and a_{ij} represented the network connection strength. β was a soft thresholding parameter that could strengthen high correlations between genes and weaken low correlations. In this study, β=19 (R^2= 0.90) was applied to ensure a scale-free network. In the co-expression network, the WGCNA method took not only direct correlations between 2 genes into account but the indirect correlations.

In this way, multiple function modules were identified through hierarchical clustering of the weighting coefficient matrix. Furthermore, the topological overlap measure (TOM) of shared neighbors was calculated as follows:

$$TOM_{i,j} = \frac{\Sigma_{K=1}^{N} A_{i,k} \cdot A_{k,j} + A_{i,j}}{min(K_i, K_j) + 1 - A_{i,j}}$$

where A was the weighted adjacency matrix calculated by $A_{i,j} = |cor(x_i, x_j)|^{\beta}$, and β=19 was the soft thresholding parameter. Each module contained a minimum size of 30 genes. Modules would be merged if the similarity values between modules were beyond 75%. Each module was marked with different colors. In this study, the process variable represented a pathological process, including normal gastric mucosa, atrophic gastritis and GC.

Identification of clinically significant modules

Module eigengenes (MEs) were the first principal component that could also be deemed as a representative of all genes within the module. Then we calculated the correlation between MEs and pathological processes. The log10 transformation of P value in the linear regression analysis between gene expression and processes served as gene significance (GS). The average GS for all the genes in the module was defined as Module significance (MS). Modules with $P < 0.05$ were identified and shown in the form of a heatmap. Moreover, we calculated the average expression of all genes in each important module, which could help visualize the expression changes of genes during the pathological process.

Identification and validation of hub genes

Members in each module made up the networks shown using cytoscape software (9). Genes with the highest connectivity in networks were considered as hub genes. Then, we compared expression of hub genes among normal gastric mucosa, atrophic gastritis and GC by *t*-test. Additionally, to validate the expression of hub genes, GSE79973 expression profile was analyzed, and it contained 10 GC tissues and 10 paired normal gastric mucosae.

Analysis of hub genes

Functions of hub genes in overall survival (OS) and stages were analyzed based on GC cohorts from TCGA (https://portal.gdc.cancer.gov/). To further investigate the biological function of hub genes in the development of GC, we rearranged the expression matrix of GSE111762 according to the expression of hub genes. Pathway enrichment analysis was performed by gene set enrichment analysis (GSEA) (http://software.broadinstitute.org/gsea/index.jsp) (10). |Normalized enrichment score (NES)|>1 as well as $P < 0.05$ were statistically significant.

RESULTS

Weighted co-expression network construction and identification of important modules

All samples in GSE111762 passed quality control, and they were clustered via the average linkage hierarchical clustering method and Pearson's correlation (Fig. 1a). The co-expression analysis was performed to construct the co-expression network. In the present study, the power of β=19 (R^2= 0.90) was selected to ensure a scale-free network (Fig. 1b). Under the circumstances, 38 modules were identified (Fig. 2a). Among them, four modules, including blue (cor = -0.57, P = 0.03), dark orange (cor = -0.7, P = 0.004), dark red (cor = 0.64, P = 0.01) and dark violet (cor = -0.588, P = 0.02), were thought significantly correlated with pathological processes and used for subsequent analyses (Fig. 2 b, c). The expression of genes in the four selected modules obviously varied among stages (Fig. 3a). Dark red and blue modules showed continually increased or decreased expression trends from normal gastric mucosa to GC, while dark orange and dark violet modules rose slightly from normal gastric mucosa to atrophic gastritis and then dropped rapidly from atrophic gastritis to GC (Fig. 3b).

Identification and validation of the hub genes

In the four modules, gene pairs with correlation > 0.1 were displayed (Fig. 4 a-d). The shade of color and size of the node were determined by the connectivity. Darker red and bigger size meant more important nodes. Eventually, four hub genes were identified, including POLG2 in the dark red module, GAGE12J in the blue module, COL21A1 in the dark violet module and PHGR1 in the dark orange module (Fig. 5 a-d). After comparing the expression of the four hub genes, we found COL21A1 and GAGE12J were up-regulated in atrophic gastritis *vs* normal gastric mucosa, but down-regulated in GC *vs* atrophic gastritis. PHGR1 was down-regulated in GC *vs* atrophic gastritis and GC *vs* normal gastric mucosa, while POLG2 was up-regulated, indicating functions of genes might be changed or even opposite among different stages of GC. In validation cohort, compared to normal mucosae, PHGR1 was significantly down-regulated in GC tissues (GSE79973 P=0.028; GSE111762 P=0.005; Fig. 6a), while POLG2 had a trend of up-regulation (GSE79973 P=0.16; GSE111762 P=0.067; Fig. 6b) and COL21A1 did not reach statistic difference (GSE79973 P=0.25; GSE111762 P=0.36; Fig. 6c). However, information of GAGE12J was not available in the dataset.

Functions of hub genes in prognosis and stages

Prognosis analysis showed GC patients with high expression of GAGE12J meant a shorter OS than low expression (P=0.04), while COL21A1, PHGR1 and POLG2 were not significantly associated with OS

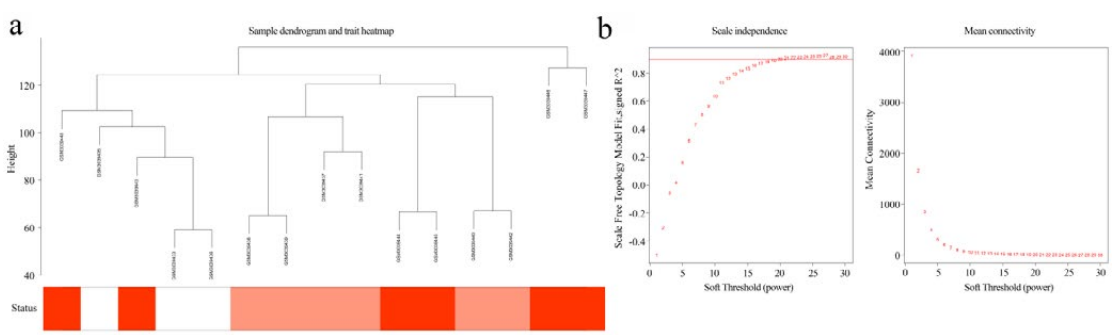

Fig. 1. *Clustering of samples as well as disease status, and determination of soft-thresholding power.* ***a****) The clustering is based on the expression data of all genes in 3 normal mucosae, 6 atrophic gastritis and 6 GC tissues. The color intensity reflects different disease status.* ***b****) Scale-free fit and mean connectivity for a series of soft threshold powers. Checking the scale free topology when β=19.*

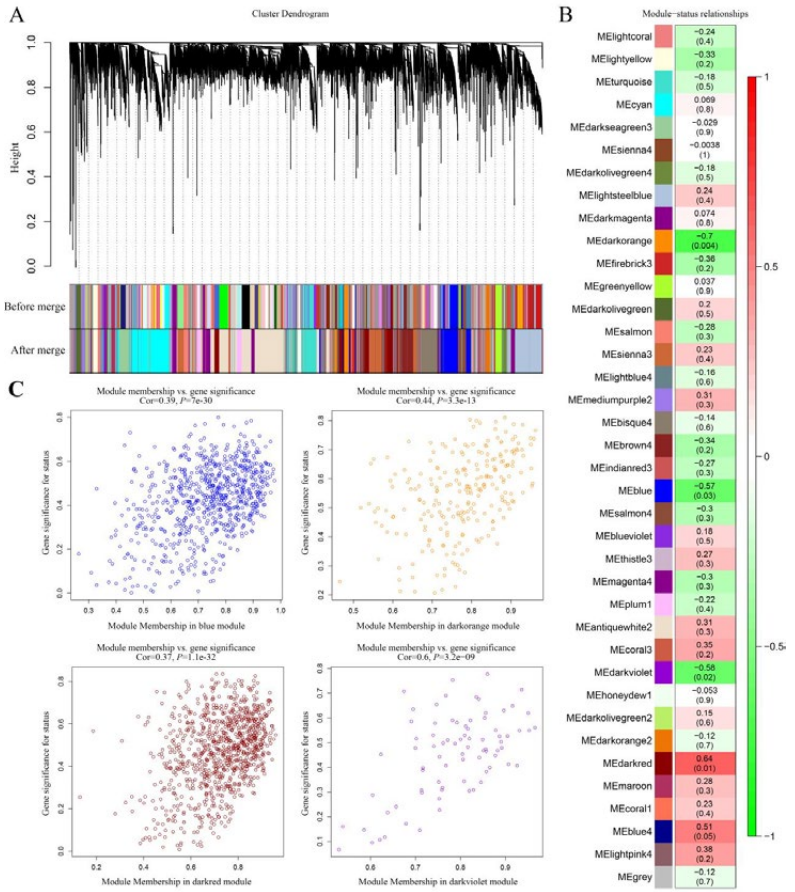

Fig. 2. *Identification of modules associated with disease status.* ***a****) The cluster dendrogram of all genes. Each dropping branch represents one gene, and colors represent different co-expression modules.* ***b****) Heatmap of the association between module eigengenes and status of GC. Dark orange, dark red, dark violet and blue modules significantly correlate with status.* ***c****) Scatter plot of module eigengenes in the four modules.*

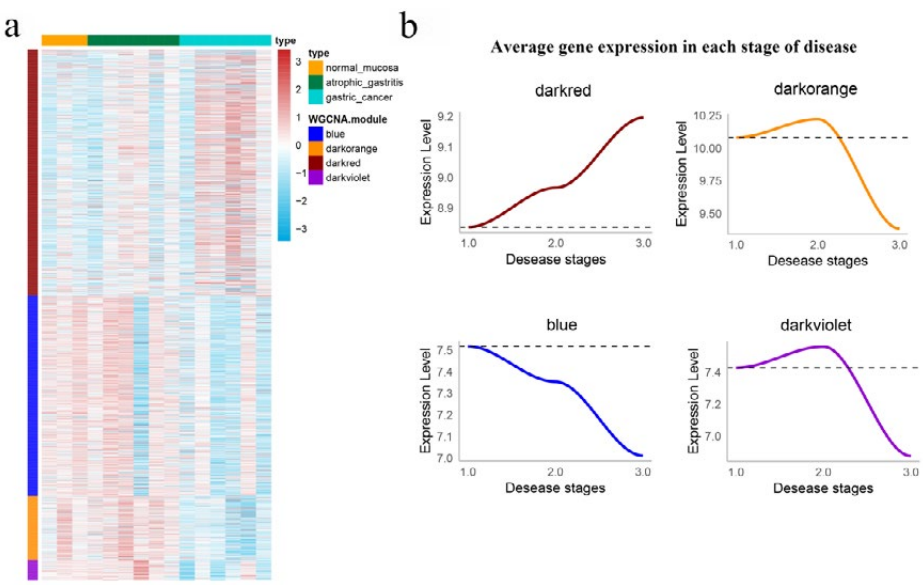

Fig. 3. *Gene expression changes in hub modules.* ***a****) Heatmap of gene expression in the four selected modules.* ***b****) The average expression of genes in corresponding modules from normal mucosa, atrophic gastritis to GC.*

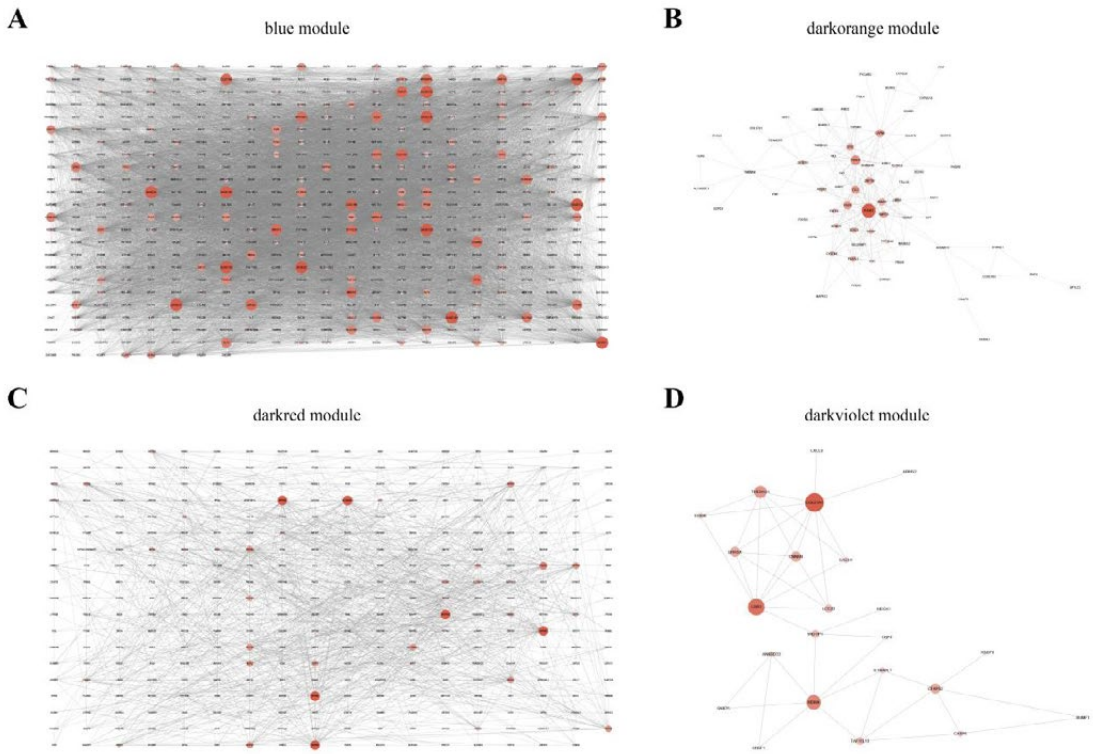

Fig. 4. *Interaction network among genes within modules. The color depth and size are proportional to the importance of the node. POLG2 in dark red module, GAGE12J in blue module, COL21A1 in dark violet module and PHGR1 in dark orange module are screened as hub genes.*

(Fig. 7 a-7d). Furthermore, no significant difference was found between hub genes and stages (Fig. 7 e-h), indicating these genes were mainly involved in the development of GC but not in the advance.

Enrichment analysis for hub genes

Aberrant expression of these hub genes could affect many important pathways. For example, COL21A1 in peroxisome, DNA repair and KRAS signaling pathway (Fig. 8a), POLG2 in MYC targets, E2F targets and angiogenesis (Fig. 8b), PHGR1 in IL6-JAK-STAT3, epithelial mesenchymal transition (EMT) and TNFα-NF-κB signaling pathway (Fig. 8c) and GAGE12J in peroxisome, Notch signaling pathway and androgen response (Fig. 8d).

DISCUSSION

In the present study, WGCNA, as a robust method for screening hub genes, was performed to identify significant co-expression modules associated with the development and progression from normal mucosa, atrophic gastritis to GC. After a series of bioinformatic analyses, a total of four gene modules and four hub genes with the highest connectivity were selected, including POLG2 in the dark red module, GAGE12J in the blue module, COL21A1 in the dark violet module and PHGR1 in the dark orange module. GSEA enrichment analysis showed these four hub genes were all tumorigenesis-related.

COL21A1 was a member of the collagen gene and could induce chemoresistance in ovarian cancer (11). Corresponding research in GC was rare. We found the expression of COL21A1 increased in atrophic gastritis vs normal mucosa but decreased in GC vs atrophic gastritis, indicating it might play different roles in the process of tumorigenesis. High expression of COL21A1 was predicted to activate the DNA repair

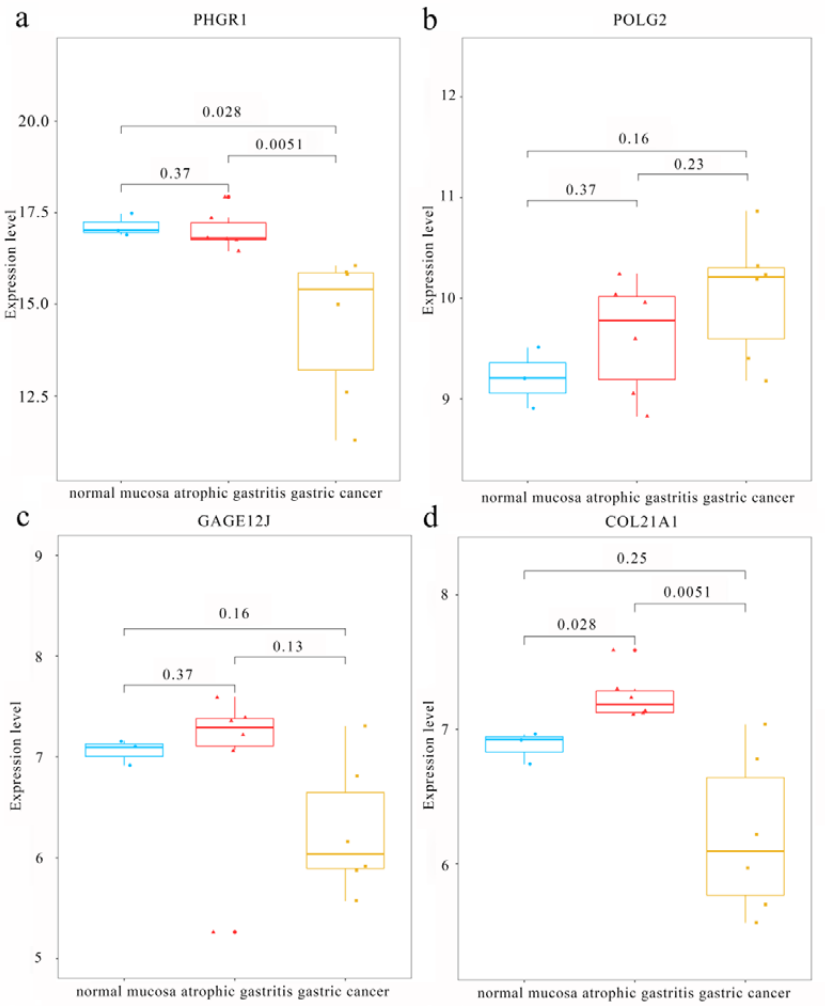

Fig. 5. *Comparative analyses among normal mucosa, atrophic gastritis and gastric cancer. Expression changes of* ***(a)*** *PHGR1,* ***(b)*** *POLG2,* ***(c)*** *GAGE12J, and* ***(d)*** *COL21A1. P < 0.05 is statistically significant.*

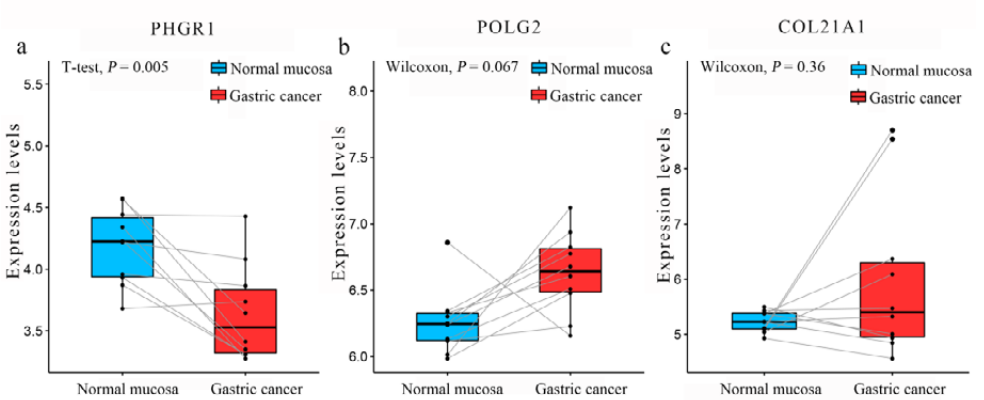

Fig. 6. *Validation of hub genes. Expression changes of* ***(a)*** *PHGR1,* ***(b)*** *POLG2, and* ***(c)*** *COL21A1 between normal mucosa and gastric cancer. P < 0.05 is statistically significant.*

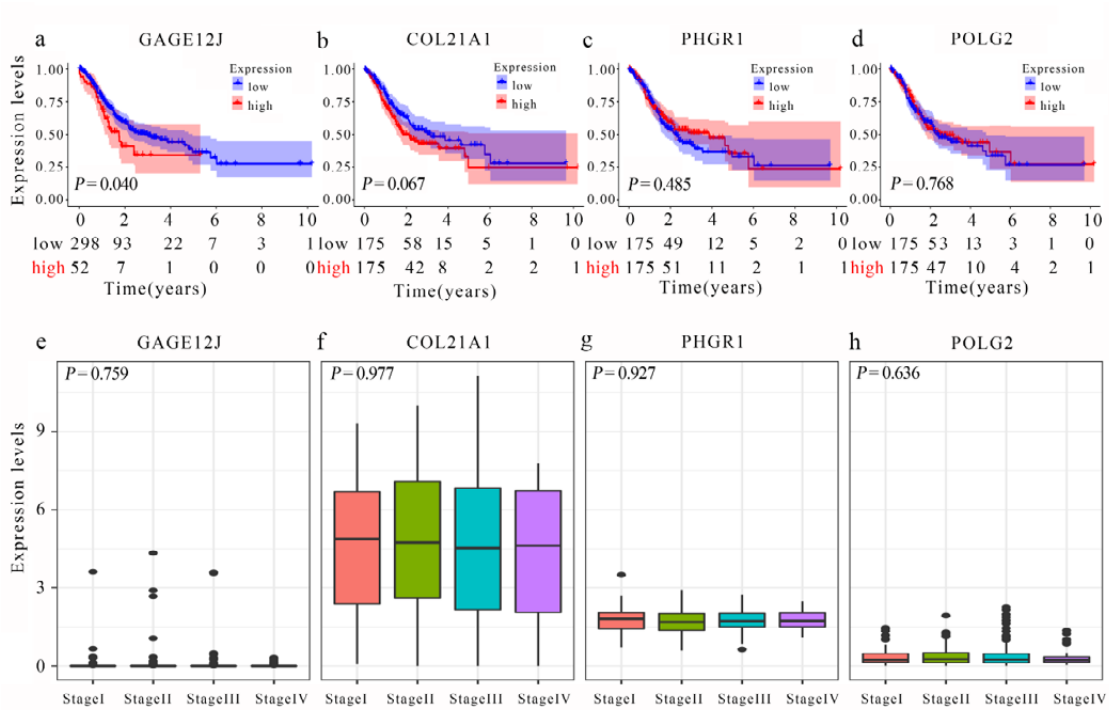

Fig. 7. *Analyses of hub genes in prognosis and stages. Overall survival analysis of (**a**) GAGE12J, (**b**) COL21A1, (**c**) PHGR1, (**d**) POLG2 in gastric cancer patients. Expression changes of (**e**) GAGE12J, (**f**) COL21A1, (**g**) PHGR1, (**h**) POLG2 in different stages. P < 0.05 is statistically significant.*

pathway, and increased DNA damage was already demonstrated to accelerate GC development (12, 13), which might be caused by down-regulated COL21A1 in our study. Moreover, COL21A1 was found to activate the KRAS signaling pathway, which could rapidly result in the initiation of stomach precancerous lesions, including gastric hyperplasia and metaplasia (14). Chung WC. et al. reported that KRAS signaling pathway could drive gastric tumorigenesis by inhibiting Notch signaling and Mist1 expression (15). The mechanisms of COL21A1 involving in GC development and its relationships with these signaling pathways merit further research.

For PHGR1, previous studies demonstrated its active role in tumorigenesis and lymph node metastasis in colorectal cancer (16, 17). In this study, PHGR1 was down-regulated in GC. According to GSEA analysis, it could activate many cancer-related pathways, such as MYC targets, E2F targets, IL6-JAK-STAT3 signaling pathway, epithelial mesenchymal transition (EMT) and TNFα-NF-κB signaling pathway, all of which have been proved to play an important role in the development, proliferation and invasion of GC or other cancers (18-20). Zhou Q. et al. reported EMT mediated by TNFα-NF-κB signaling pathway could significantly enhance migration and invasion ability of GC cells (21). PHGR1 may therefore play an important role in GC initiation.

POLG2 was important to encode the mitochondrial DNA (mtDNA) polymerase (22). More mtDNA induced by overexpressed POLG2 may accelerate a variety of cancers, such as oral, bladder and lung (23-25). It was consistent with an increased expression trend of POLG2 in our data. Moreover, we found POLG2 promoted the initiation of GC via MYC targets, E2F targets, EMT and angiogenesis. Obviously, all of these were highly related to the development of cancers, including GC.

Expression changes of GAGE12J during the process of GC tumorigenesis were similar to that of COL21A1, rising first and then falling. In atrophic gastritis, we found GAGE12J was up-regulated,

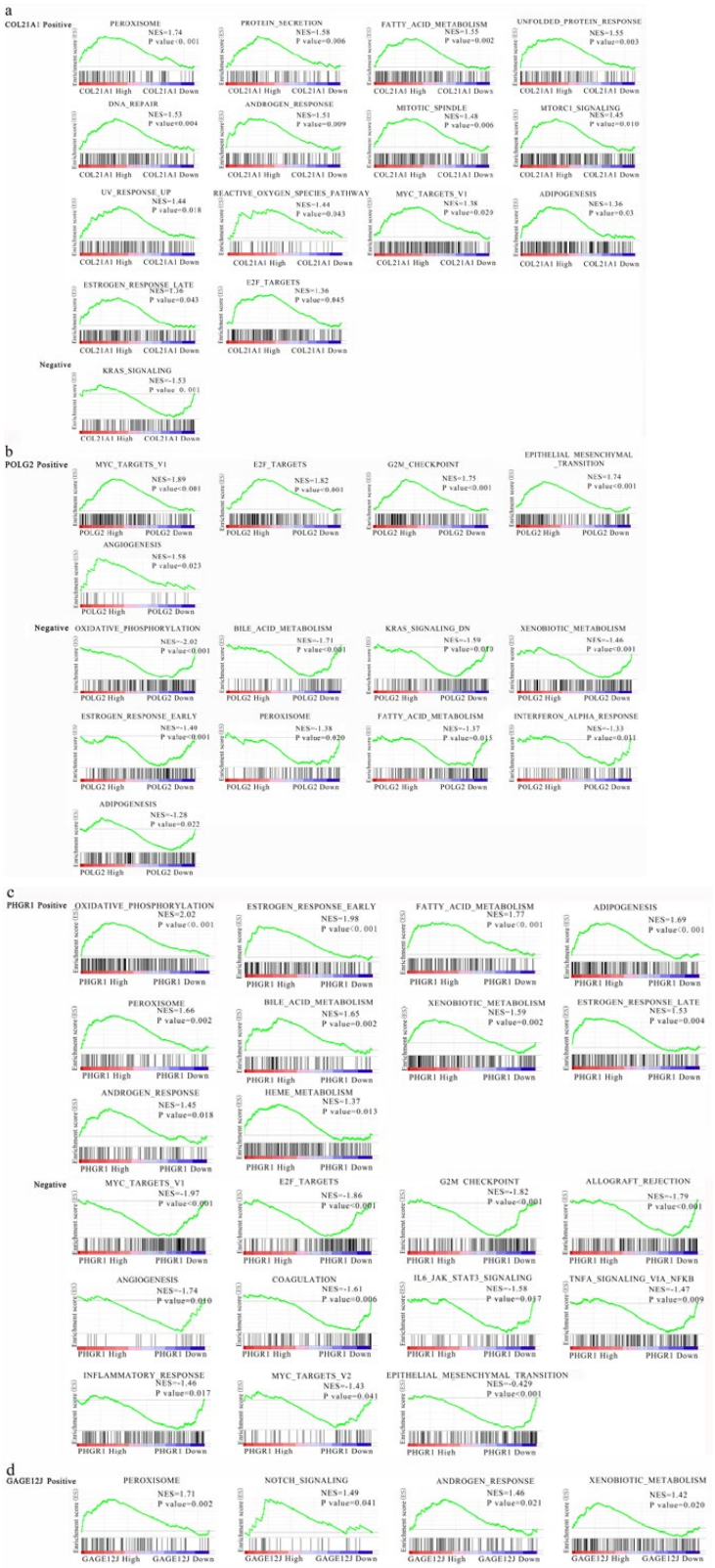

Fig. 8. *Pathway enrichment results associated with the four hub genes in the development of GC.* ***a****) COL21A1,* ***(b****) POLG2,* ***(c****) PHGR1, and* ***(d****) GAGE12J. NES, normalized enrichment score. Positive and negative NES indicate activated and suppressed pathway. |NES|>1 as well as P < 0.05 are statistically significant.*

indicating an increasing activity of peroxisome and Notch signaling pathway. Zuo Xiangsheng et al. demonstrated peroxisome, involving in inflammation, proliferation and metastasis, could promote spontaneous and invasive gastric adenocarcinoma with severe chronic inflammation (26, 27). In this way, we predicted GAGE12J was vital in the development of atrophic gastritis, which provided potential molecular bases for GC.

In summary, we identified 4 hub genes that could affect many classic signaling pathways of tumorigenesis, especially for COL21A1, PHGR1 and POLG2. These genes have great potential to be biomarkers in early diagnosis and treatment of GC.

REFERENCES

1. Bray F, Ferlay J, Soerjomataram I, Siegel RL, Torre LA, Jemal A. Global cancer statistics 2018: GLOBOCAN estimates of incidence and mortality worldwide for 36 cancers in 185 countries. CA Cancer J Clin 2018; 68(6):394-424.
2. Zhang Y, Liu Y, Song R, et al. Validating traditional Chinese syndrome features in varied stages of chronic gastritis malignant transformation: study protocol for a cross-sectional study. BMJ Open 2018; 8(8):e020939.
3. Bornschein J, Selgrad M, Warnecke M, Kuester D, Wex T, Malfertheiner P. H. pylori infection is a key risk factor for proximal gastric cancer. Dig Dis Sci 2010; 55(11):3124-31.
4. Labib S, Guo CH, Williams A, Yauk CL, White PA, Halappanavar S. Toxicogenomic outcomes predictive of forestomach carcinogenesis following exposure to benzo(a)pyrene: relevance to human cancer risk. Toxicol Appl Pharmacol 2013; 273(2):269-80.
5. Allemani C, Weir HK, Carreira H, et al. Global surveillance of cancer survival 1995-2009: analysis of individual data for 25,676,887 patients from 279 population-based registries in 67 countries (CONCORD-2). Lancet 2015; 385(9972):977-1010.
6. Wang X, Xu M, Yan Y, et al. Identification of eight small nucleolar RNAs as survival biomarkers and their clinical significance in gastric cancer. Front Oncol 2019; 9:788.
7. Zhu H, Dai W, Li J, et al. HOXD9 promotes the growth, invasion and metastasis of gastric cancer cells by transcriptional activation of RUFY3. J Exp Clin Cancer Res 2019; 38(1):412.
8. Wang S, Chen Z, Zhu S, et al. PRDX2 protects against oxidative stress induced by H. pylori and promotes resistance to cisplatin in gastric cancer. Redox Biol 2020; 28:101319.
9. Shannon P, Markiel A, Ozier O, et al. Cytoscape: a software environment for integrated models of biomolecular interaction networks. Genome Res 2003; 13(11):2498-504.
10. Subramanian A, Tamayo P, Mootha VK, et al. Gene set enrichment analysis: a knowledge-based approach for interpreting genome-wide expression profiles Proc Natl Acad Sci U S A. 2005; 102(43):15545-50.
11. Januchowski R, Swierczewska M, Sterzynska K, Wojtowicz K, Nowicki M, Zabel M. Increased expression of several collagen genes is associated with drug resistance in ovarian cancer cell lines. J Cancer 2016; 7(10):1295-310.
12. Zhao S, Thakur M, Klattenhoff AW, Kidane D. Aberrant DNA polymerase beta enhances H. pylori infection induced genomic instability and gastric carcinogenesis in mice. Cancers (Basel) 2019; 11(6).
13. Sierra JC, Suarez G, Piazuelo MB, et al. alpha-Difluoromethylornithine reduces gastric carcinogenesis by causing mutations in Helicobacter pylori cagY. Proc Natl Acad Sci U S A 2019; 116(11):5077-85.
14. Matkar SS, Durham A, Brice A, Wang TC, Rustgi AK, Hua X. Systemic activation of K-ras rapidly induces gastric hyperplasia and metaplasia in mice. Am J Cancer Res 2011; 1(4):432-45.
15. Chung WC, Zhou Y, Atfi A, Xu K. Downregulation of notch signaling in Kras-induced gastric metaplasia. Neoplasia 2019; 21(8):810-21.
16. Zhang GL, Pan LL, Huang T, Wang JH. The transcriptome difference between colorectal tumor and normal tissues revealed by single-cell sequencing. J Cancer 2019; 10(23):5883-90.
17. Oltedal S, Korner H, Aasprong OG, et al. The prognostic relevance of sentinel lymph node metastases assessed by PHGR1 mRNA quantification in Stage I to III colon cancer. Transl Oncol 2018; 11(2):436-43.
18. Bell CM, Raffeiner P, Hart JR, Vogt PK. PIK3CA cooperates with KRAS to promote MYC activity and

tumorigenesis via the bromodomain protein BRD9. Cancers (Basel) 2019; 11(11).
19. Dong X, Hu X, Chen J, Hu D, Chen LF. BRD4 regulates cellular senescence in gastric cancer cells via E2F/miR-106b/p21 axis. Cell Death Dis 2018; 9(2):203.
20. Jacobsson H, Harrison H, Hughes E, et al. Hypoxia-induced secretion stimulates breast cancer stem cell regulatory signalling pathways. Mol Oncol 2019; 13(8):1693-705.
21. Zhou Q, Wu X, Wang X, et al. The reciprocal interaction between tumor cells and activated fibroblasts mediated by TNF-alpha/IL-33/ST2L signaling promotes gastric cancer metastasis. Oncogene 2020; 39(7):1414-28.
22. Gorvin CM, Ahmad BN, Stechman MJ, et al. An N-Ethyl-N-Nitrosourea (ENU)-induced Tyr265Stop mutation of the DNA Polymerase Accessory Subunit Gamma 2 (Polg2) is associated with renal calcification in mice. J Bone Miner Res 2019; 34(3):497-507.
23. Michiels S, Danoy P, Dessen P, et al. Polymorphism discovery in 62 DNA repair genes and haplotype associations with risks for lung and head and neck cancers. Carcinogenesis 2007; 28(8):1731-39.
24. Nakano M, Tashiro K. Association studies getting broader: a commentary on 'A polymorphism of the POLG2 gene is genetically associated with the invasiveness of urinary bladder cancer in Japanese males'. J Hum Genet 2011; 56(8):550-51.
25. Datta S, Ray A, Roy R, Roy B. Association of DNA sequence variation in mitochondrial DNA polymerase with mitochondrial DNA synthesis and risk of oral cancer. Gene 2016; 575(2 Pt 3):650-54.
26. Zuo X, Deguchi Y, Xu W, et al. PPARD and interferon gamma promote transformation of gastric progenitor cells and tumorigenesis in mice. Gastroenterology 2019; 157(1):163-78.
27. Wang P, Guo X, Zong W, et al. PGC-1alpha/SNAI1 axis regulates tumor growth and metastasis by targeting miR-128b in gastric cancer. J Cell Physiol 2019; 234(10):17232-34.

Radio-sensitizing effects of microRNA-27a elevation in lung cancer cells by inhibiting ZEB1 expression and activating DNA damage repair pathway

YL. Ge, FL. Jin and DH. Zhang

Department of Radiotherapy, Dongyang People's Hospital of Zhejiang Province, Jinhua, Zhejiang, P.R. China

Received August 10, 2020 – Accepted December 15, 2020

MicroRNAs (miRNAs or miRs) exert either as tumor-inhibiting or oncogenic roles in tumorigenesis of lung cancer. In the present study, we identified a novel microRNA (miR)-27a as being involved in the radiosensitivity of lung cancer cells. Therefore, we sought to characterize its potential underlying mechanism in lung cancer cell sensitivity to radiotherapy. To this end, A549 and H460 cells irradiated with 8 Gy irradiation (IR) were used as a cell model. RT-qPCR exhibited that the expression of miR-27a increased, whereas ZEB1 was poorly expressed in A549 and H460 cells exposed to IR. As reflected by dual-luciferase reporter gene assay, miR-27a could target and inversely modulate ZEB1 expression. Gain- and loss-of-function experiments exhibited that miR-27a inhibition promoted proliferation of IR-treated A549 and H460 cells and reduced the sensitivity of A549 and H460 cells to radiotherapy, which was rescued by silencing of ZEB1. Further, miR-27a inhibition disrupted the homologous recombination (HR)-mediated DNA repair, evidenced by reduced ATM, pCHK2 and Rad51 levels. Collectively, miR-27a activates HR-mediated DNA repair by inhibiting ZEB1 expression to enhance the radiosensitivity of lung cancer cells, highlighting a therapeutic target for lung cancer radiosensitivity.

Lung cancer is the most frequently diagnosed malignancy (11.6% of the total cases) and the major cause of cancer-related death (18.4% of the total cancer deaths) worldwide in 2018, with a dismal prognosis (only 18%) (1, 2). Lung cancer is historically clarified into two main histological subtypes: small cell lung cancer (SCLC) and non-small cell lung cancer (NSCLC) (3). Smoking serves as the preliminary risk for lung cancer and might interrupt epithelial barrier integrity accompanied by enhanced susceptibility to infection (4). The mainstay of treatment option for lung cancer is radical surgery, while definitive radiotherapy with stereotactic techniques can control the disease from metastasis dissemination, making it suitable for medically inoperable patients (5). However, the resistance of lung cancer cells to radiotherapy remains to be a challenging obstacle for patients, and it is of great importance to enhance lung cancer cell radiosensitivity during the treatment (6, 7).

MicroRNAs (miRNAs or miRs), small 20-24 nucleotides molecules, exert pivotal roles on tumorigenesis, and their tumor-inhibiting and oncogenic roles have been suggested in lung cancer (8). With the help of miR signature-associated

Key words: lung cancer; radiosensitivity; microRNA-27a; zinc-finger E-box-binding homeobox 1; homologous recombination-mediated DNA repair

Corrresponding Author:
Dr Dahai Zhang,
Department of Radiotherapy,
Dongyang People's Hospital of Zhejiang Province,
No. 60, Wuning West Road, Dongyang City,
Jinhua 322100, Zhejiang, P.R. China
Tel./Fax: +86 13806779173
e-mail: zhangdhai4221@163.com

0393-974X (2021)
Copyright © by BIOLIFE, s.a.s.
This publication and/or article is for individual use only and may not be further reproduced without written permission from the copyright holder.
Unauthorized reproduction may result in financial and other penalties
DISCLOSURE: ALL AUTHORS REPORT NO CONFLICTS OF INTEREST RELEVANT TO THIS ARTICLE.

stratification, radiotherapy may possibly be personalized beyond present treatment methods (9). Intriguingly, polymorphisms of miR-5197, miR-605, miR-146a, and miR-27a induced the chemotherapy toxicity of lung cancer, which may be conducive for the suppression of platinum-based chemotherapy-induced toxicity (10). The miR-27 family is broadly distributed in vertebrates and basically comprises of two homologs: miR-27a and miR-27b (11). The expression of miR-27a is markedly reduced in the serum of NSCLC patients (12). miR-27a rs895819 is proposed to be correlated with neutropenia toxicity in patients with gallbladder carcinoma undergoing chemo-radiotherapy (13). In addition, miR-27a was deregulated by the combined action of radiation and modeled microgravity in human peripheral blood lymphocytes (14). However, the relevance of miR-27a to lung cancer radiosensitivity has been rarely reported. Based on the microarray analysis, we identified zinc-finger E-box-binding homeobox 1 (ZEB1) to be targeted by miR-27a. As a transcription factor, ZEB1 promotes epithelial-mesenchymal transition (EMT), tumor metastasis, and resistance to therapies (15). Elevation of ZEB1 is associated with the enhanced migratory and invasive capabilities of NSCLC cells (16). A recent study emphasized upregulation of ZEB1 as a possible modulator of chemoresistance via a direct interaction with ataxia-telangiectasia mutated (ATM) kinase, an important component of the DNA damage repair pathway which has been linked to radio-resistance (17). Moreover, ATM phosphorylates serine/threonine residues of hundreds of substrate proteins and can subsequently catalyze phosphorylation via their activation of other kinases such as checkpoint kinase 2 (CHK2) (18). Homologous recombination (HR), which modulates the repair of DNA double-strand breaks, is of paramount importance for enhancing survival in response to both chemotherapy and radiotherapy in human cancers, including lung cancer (19). DNA repair protein RAD51 homolog 1 (Rad51) plays a central role in HR (20, 21). In this study, we sought to investigate the relationship between miR-27a, ZEB1 and HR-mediated DNA damage repair pathway as well as their effects on lung cancer cell sensitivity to radiotherapy.

MATERIALS AND METHODS

Cell treatment

Human normal lung epithelial cells BEAS-2B and lung cancer cells A549 and H460 were from the Cell Bank of Chinese Academy of Sciences (Shanghai, China). After validating that cells were not infected with mycoplasma, BEAS-2B and A549 cells were plated in Dulbecco's modified Eagle's medium (DMEM, Thermo fisher, Austin, TX, USA) and H460 cells in Roswell Park Memorial Institute (RPMI)-1640 medium (Thermo Fisher) supplemented with 10% fetal bovine serum (FBS) according to previous studies (22, 23). Cells were cultured in a humidified incubator at 37°C and 5% CO_2. When above 80% cell confluence was reached, A549 and H460 cells were trypsinized in a 1:3 ratio and irradiated with different doses of γ ray (0 Gy, 2 Gy, 4 Gy, 6 Gy, 8 Gy or 10 Gy) using a Gamma cell 40 Exactor (Atomic Energy of Canada Limited, Canada). The cells were irradiated only once with the dose rate of 1 Gy/min. After the irradiation (IR), the cells were collected for study.

Flow cytometry

Annexin-V/propidium iodide (PI) double-stained flow cytometry was performed as per the instructions of the Annexin-V/PI detection kit (Solarbio, Beijing, China). In brief, cells were trypsinized (0.25%) and centrifuged at 1000 r/min for 5 min before the pellet was added with 200 μL binding buffer to prepare cell resuspension solution at 1×10^6 cells/mL. Thereafter, cells were incubated with 10 μL Annexin V-fluorescein isothiocyanate (FITC) for 15 min, and then with 300 μL binding buffer as well as 5 μL PI for 5 min in the dark. Finally, cells were analyzed with a flow cytometer (BD Biosciences, Franklin Lakes, New Jersey, USA), and data were analyzed with Modfit LT (Verity Software House, Topsham, ME, USA) software.

For cell cycle assay, cells were fixed overnight in 70% ethanol at -20°C, centrifuged at 1000 r/min for 5 min and prepared in a cell suspension at a concentration of 1×10^6 μmol/L. After the cell suspension was added with RNaseA, the final concentration was adjusted to 50 mg/L. Cells were treated with 50 μg/mL PI (Solarbio) for 30 min in the dark and filtered with a 300-mesh nylon mesh before the cell cycle was assayed using red fluorescence at the excitation wavelength of 488 nm with a flow cytometer (Beckman Coulter, Inc., Brea, CA, USA).

Microarray analysis

miRNA differential analysis was performed by Affymetrix microarray data (Themo Fisher, Waltham, MA, USA). Total RNA was extracted from cells using TRIzol reagent (Thermo Fisher) and purified using RNeasy kit (Qiagen, Valencia, CA, USA). RNA was subjected to sodium dodecyl sulfate polyacrylamide gel electrophoresis and reversely transcribed into cDNA with a PrimeScript RT reagent Kit (Takara, Tokyo, Japan). miRNA labeled with NAEZLabel Antibody Cy3 Labeling Kit (Biovision, Milpitas, CA, USA) was hybridized with Human Gene Expression Assay (Themo Fisher) and scanned with ScanArray Express Microarray Scanner (PerkinElmer, Boston, MA, USA). $|FoldChange| > 2$ and $p < 0.01$ were set as the standard, and a heatmap was plotted.

Cell transfection

Plasmids containing miR-27a inhibitor and miR-27a control, ZEB1-negative control (NC) and small interfering RNA (si)-ZEB1 were synthesized by GenePharma (Shanghai, China). Next, the synthesized sequence was inserted into pcDNA3.1(+) vector (Promega, Madison, WI, USA) to construct expression plasmid. Afterwards, the cells to be transfected were seed into a 6-well plate. Upon 50% cell confluence, 200 nm synthesized fragments were loaded into plasmids using Lipofectamine RNAiMAx (Thermo Fisher), and 2 μg plasmid was transfected into cells using Lipofectamine 2000 (Thermo Fisher). The cells stably transfected for at least 48 h were stored for subsequent use.

Reverse transcription quantitative polymerase chain reaction (RT-qPCR)

Total RNA was isolated from the cells using TRIzol reagent (Takara), and the concentration of RNA was measured with an ultraviolet spectrophotometer and adjusted to 1 g/L. Next, reverse transcription was performed using PrimeScript RT Master Mix and Mir-X miRNA First-Strand Synthesis Kit (Takara). RT-qPCR was performed on cDNA using SYBR Premix Ex Taq II Kit (Takara). The relative expression of ZEB1 or miR-27a was normalized to glyceraldehyde-3-phosphate dehydrogenase (GAPDH) or snRNA U6 expression and calculated using the $2^{-\Delta\Delta Ct}$ method. The primers were listed as follows: miR-27a forward: 5'-CCGCTCGAGACTGGCTGCTAGGAAGGTG-3', miR-27a reverse: 5'-GCGAATTCTTGCTGTAGCCTC CTTGTC-3'; U6 forward: 5′-GCACCTTAGGCTGAACA-3', U6 reverse: 5'-AGCTTATGCCGAGCTCTTGT-3'; ZEB1 forward: 5'-GCTTCTCACACTCTGGGTCTTA-3', ZEB1 reverse: 5'-CCTCATTCTCTGCCTCTTCTACC-3'; GAPDH forward: 5'-GTCACCTTCACCGTTC-CAGTTTT-3', GAPDH reverse: 5'- CTTAGTTGCGTTA-CACCCTTTCTT-3'.

Colony formation assay

After transfection, the cells at logarithmic growth phase were dispersed into a single cell suspension. After the cells were adherent to the wells, cells were irradiated with 8 Gy γ ray. The cells were seeded in 60-mm culture dishes (500 cells/dish) and incubated in a constant temperature incubator for 7 days. The medium was renewed every other day. Next, cells were fixed with 4% paraformaldehyde for 0.5 h and stained with 0.2% crystal violet staining solution for 15 min before cell colonies were counted under a microscope (DM500, Leica, Weztlar, Germany).

Cytotoxicity assay

The cells were plated into 96-well plates (5×10^3 cells/well). Cell cytotoxicity was assayed using a cell counting kit-8 (CCK-8, Beyotime, Shanghai, China). The cells were incubated for 1, 2, 3 or 4 weeks and then with 10 μL CCK-8 solution for 4 h in an incubator. The optical density (OD) of the cells at 450 nm were detected using a microplate reader (RT-6100, Rayto, Shenzhen, Guangdong, China), and a growth curve was plotted.

Transwell assays

Cell migration assay was performed in 24-well Transwell chambers (Corning, Midland, MI, USA). Briefly, A549 and H460 cells (1×10^5 cells/well) were added to the apical chamber. The cells incubated with 0.1 nM medium for 24 h were exposed to 8 Gy ray. Next, the medium in apical chamber was renewed with RPMI-1640 medium containing 1% FBS, while RPMI 1640 medium containing 10% FBS was added to the lower chamber to induce cell migration. After a 24-h of culture, cells were fixed with paraformaldehyde (4%) and stained with crystal violet (0.1%). Finally, the migrated cells were counted in 4 random microscopic fields under an inverted fluorescence microscope (IX73, Olympus, Tokyo, Japan).

Cell invasion assay was performed basically as above. Prior to experiment, the apical chamber was pre-coated with a layer of Matrigel (Corning). Serum-free

RPMI-1640 medium was added into the apical chamber, while RPMI-1640 medium containing 10% FBS into the basolateral chamber.

Dual-luciferase reporter gene assay

The wild-type (WT) sequence of ZEB1 3'untranslated region (3'-UTR) and its mutated (MUT) sequence in the absence of miR-17a binding sites were inserted into the firefly luciferase pEZX-MT01 vector (GeneCopoeia, Guangzhou, Guangdong, China). Thereafter, vectors were transfected into A549 or H460 cells using lipo2000 Transfection Reagent (Thermo Fisher) with miR-27a control and miR-27a inhibitor for 24 h. Firefly luciferase activity and Renilla luciferase activity were measured, and the fluorescence activity was expressed as the normalization of firefly luciferase activity to Renilla luciferase activity.

Immunoblotting

The stably transfected cells were cultured for 48 h and resuspended at a concentration of 1×10^6 cells/L. After cells were adherent to the wells, cells were irradiated and lysed with 1 mL radio-immunoprecipitation assay (Solarbio) before the protein samples were collected. After the protein samples were quantified by Coomassie brilliant blue, 20 μL protein was electrophoresed and transferred to a polyvinylidene fluoride membrane (Millipore, Billerica, MA, USA). The membrane was blocked with 5% skim milk and probed overnight with primary antibodies against ZEB1 (ab203829, 1: 500, Abcam, Cambridge, UK), ATM (sc-135663, 1:800, Santa Cruz Biotechnology Inc., Santa Cruz, CA, USA), phosphorylated CHK2 (pCHK2; ab32148, 1: 2000, Abcam), Rad51 (sc-398587, 1:2000, Santa Cruz Biotechnology), GAPDH (#5174, 1:1000, Cell Signal Technology, Beverly, MA, USA). The membrane was re-probed with a secondary antibody (ab150077, 1:4000, Abcam) at 37°C on a shaker for 2 h. Development was conducted using an electrogenerated chemiluminescence luminescence kit (Beyotime), and protein was quantitatively analyzed using Image Quant software (Molecular Dynamics, Minnesota, USA).

Statistical analysis

Statistical analysis was performed with SPSS software 21.0 (IBM SPSS Statistics, Chicago, IL, USA). Measurement data were summarized by mean ± standard deviation of three independent tests. The statistical significance of unpaired data with normal distribution and equal variance was calculated using unpaired *t*-test. Differences among multi-groups were analyzed by one-way or two-way analysis of variance (ANOVA) with Tukey's post hoc test. The rank sum test was conducted if the data did not meet the normality of data or the homogeneity of the variance. A value of $p < 0.05$ indicated statistical significance.

RESULTS

IR treatment induces lung cancer cell apoptosis

A549 and H460 cells were irradiated with different doses of γ ray (0 Gy, 2 Gy, 4 Gy, 6 Gy, 8 Gy or 10 Gy), and flow cytometry (Fig. 1A) exhibited that IR induced marked increase in the apoptosis of A549 and H460 cells in an IR dose-dependent manner. We further examined the cell cycle of A549 and H460 cells by flow cytometry (Fig. 1B), and IR treatment induced cell cycle arrest at G0/G1 phase, especially after the 8 Gy dose of IR. The A549 and H460 cells at G0/G1 phase also increased upon 10 Gy dose of IR, whereas the growth rate reduced, which is in agreement with the study by Pawilk et al. (24). Therefore, cells irradiated with 8 Gy were used in the subsequent experiments.

miR-27a inhibition promotes proliferation of IR-treated lung cancer cells

To screen differentially expressed miRs, microarray analysis was performed on A549 cells treated with IR at different doses. We observed that the expression of miR-27a in A549 cells increased with increasing IR dose, with the most significant differences in expression (Fig. 2A). We then performed the same experiment and analysis on H460 cells and found that the expression of miR-27a in H460 was slightly lower than that of A549 cells, but still showed an increase in expression with increasing IR doses (Fig. 2B). This led us to find whether miR-27a affects the radiosensitivity of lung cancer cells.

The expression of miR-27a in normal lung epithelial cells and lung cancer cells was examined, and revealed that miR-27a was significantly downregulated in lung cancer cells (Fig. 2C).

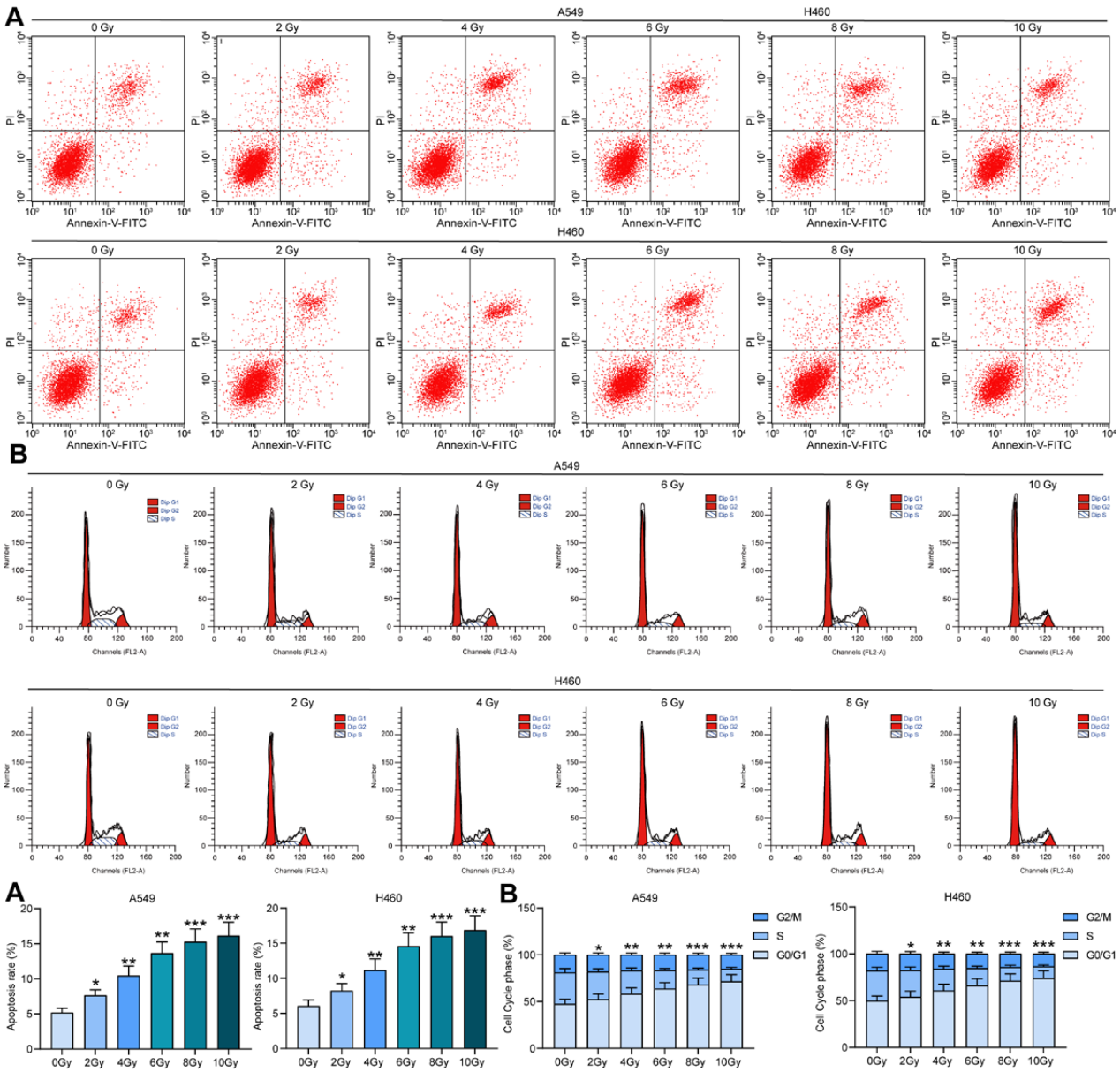

Fig. 1. *IR treatment promotes lung cancer cell apoptosis.* ***A****) The apoptosis of lung cancer cells after different doses of IR treatment determined using flow cytometry.* ***B****) The cell cycle after different doses of IR determined using flow cytometry. * p < 0.05, ** p < 0.01, ***p < 0.001 according to the one-way (panel A) or two-way ANOVA (panel B).*

Thereafter, miR-27a expression was downregulated in A549 and H460 cells using three miR-27a inhibitors. RT-qPCR revealed that the miR-27a inhibitor#2 transfection led to the lowest miR-27a level among the three miR-27a inhibitors (Fig. 2D), which was selected for the following experiments. Colony formation and cytotoxicity assays (Fig. 2E, F) were conducted to determine OD values and colony formation after cells were transfected with miR-27a inhibitor and then subjected to 8 Gy IR treatment. Marked enhanced OD values and increased number of colonies formed were observed in response to miR-27a inhibitor compared with miR-27a control, indicating enhanced cell proliferation.

Downregulation of miR-27a reduces the sensitivity of lung cancer cells to radiotherapy

Transwell assays (Fig. 3 A, B) identified marked

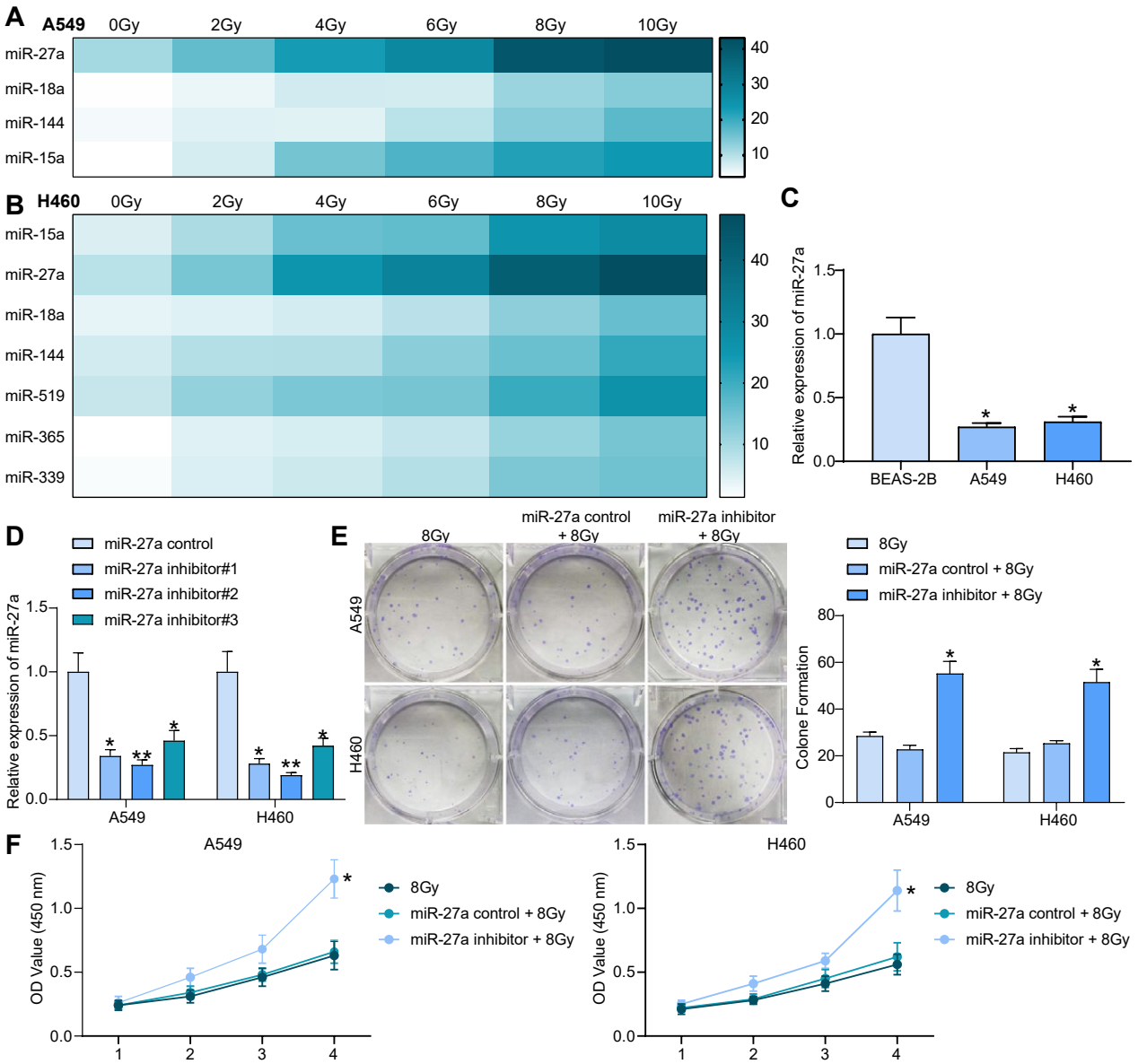

Fig. 2. *miR-27a knockdown enhances proliferation of IR-treated lung cancer cells.* ***A)*** *The differentially expressed miRs screened by microarray analysis in A549 cells after IR treatment.* ***B)*** *The differentially expressed miRs screened by microarray analysis in H460 cells after IR treatment.* ***C)*** *The expression of miR-17a in lung cancer cells and control cells detected by RT-qPCR.* ***D)*** *The silencing efficiency of miR-27a inhibitors in lung cancer cells validated with RT-qPCR.* ***E)*** *The number of colonies formed detected by colony formation assay.* ***F)*** *Cell viability detected by cytotoxicity assay (OD values were detected every other week) * $p < 0.05$, ** $p < 0.01$ according to the one-way (Panel C) or two-way ANOVA (Panel D-F).*

rise in migrated and invasive cells in response to miR-27a inhibitor following IR treatment. Flow cytometry further exhibited that miR-27a depletion reduced cell apoptosis compared with miR-27a control (Fig. 3C). As expected, the results of cell cycle assays also demonstrated that miR-27a knockdown contributed to more cells in S phase and less cells in G0/G1 phase (Fig. 3D).

miR-27a targets ZEB1 and inversely regulates ZEB1 expression in lung cancer cells

StarBase (http://starbase.sysu.edu.cn), Targetscan (http://www.targetscan.org), PITA (https://genie.weizmann.ac.il/pubs/mir07/mir07_data.html), RNA22 (https://cm.jefferson.edu/rna22/) and miRWalk (http://mirwalk.umm.uni-heidelberg.de/)

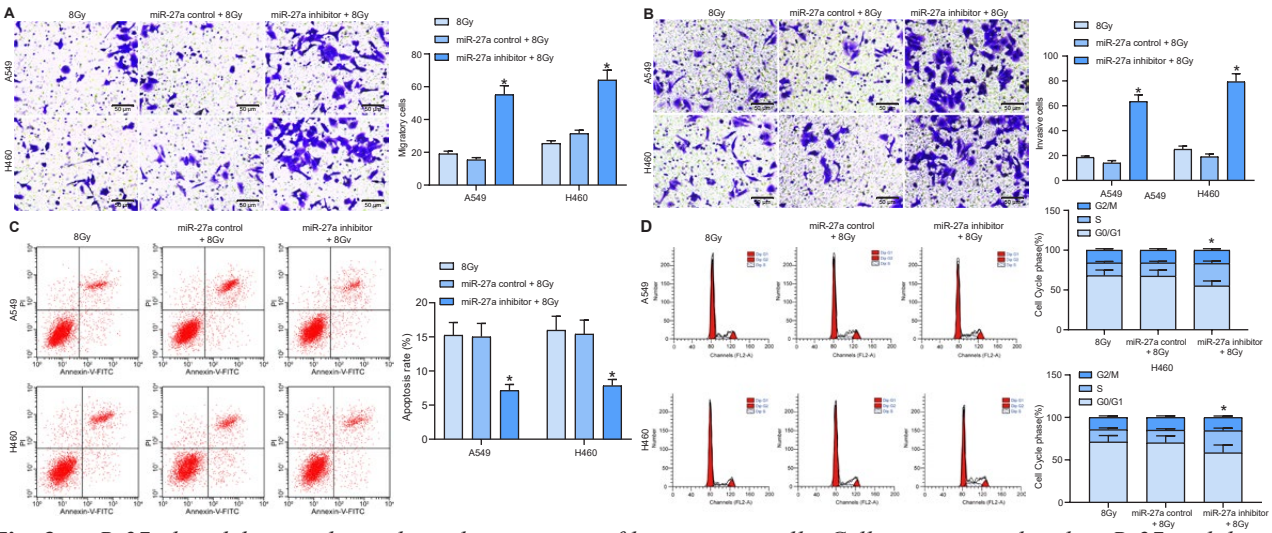

Fig. 3. *miR-27a knockdown reduces the radiosensitivity of lung cancer cells. Cells were treated with miR-27a inhibitor or miR-27a control following IR treatment.* ***A****) The migration of lung cancer cells determined using Transwell assays.* ***B****) The invasion of lung cancer cells determined using Transwell assays.* ***C****) The apoptosis of lung cancer cells determined using flow cytometry.* ***D****) The cell cycle determined using flow cytometry. * $p < 0.05$ according to the two-way ANOVA.*

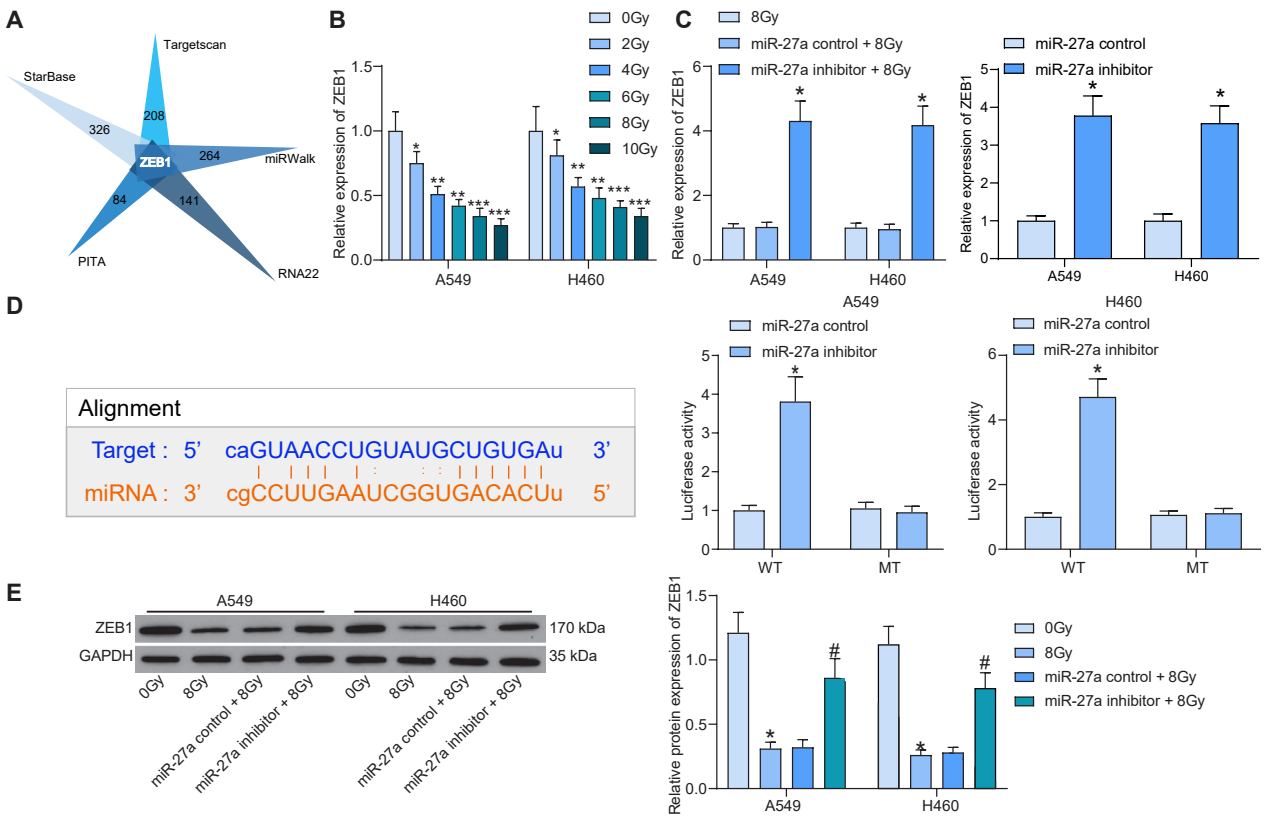

Fig. 4. *miR-27a could negatively regulate ZEB1 expression in lung cancer cells.* ***A****) Venn map of target genes of miR-27a.* ***B****) ZEB1 expression determined with RT-qPCR after cells were irradiated with 8 Gy IR.* ***C****) ZEB1 expression determined with RT-qPCR in cells treated with miR-27a inhibitor or miR-27a control following 8 Gy IR.* ***D****) Targeting relationship between miR-27a and ZEB1 validated using dual-luciferase reporter gene assay.* ***E****) ZEB1 protein expression determined with immunoblotting in cells treated with miR-27a inhibitor or miR-27a control following 8 Gy IR. * $p < 0.05$ according to the two-way ANOVA. * $p < 0.05$, ** $p < 0.01$, *** $p < 0.001$ vs 0 Gy; # $p < 0.05$ vs miR-27a control + 8Gy.*

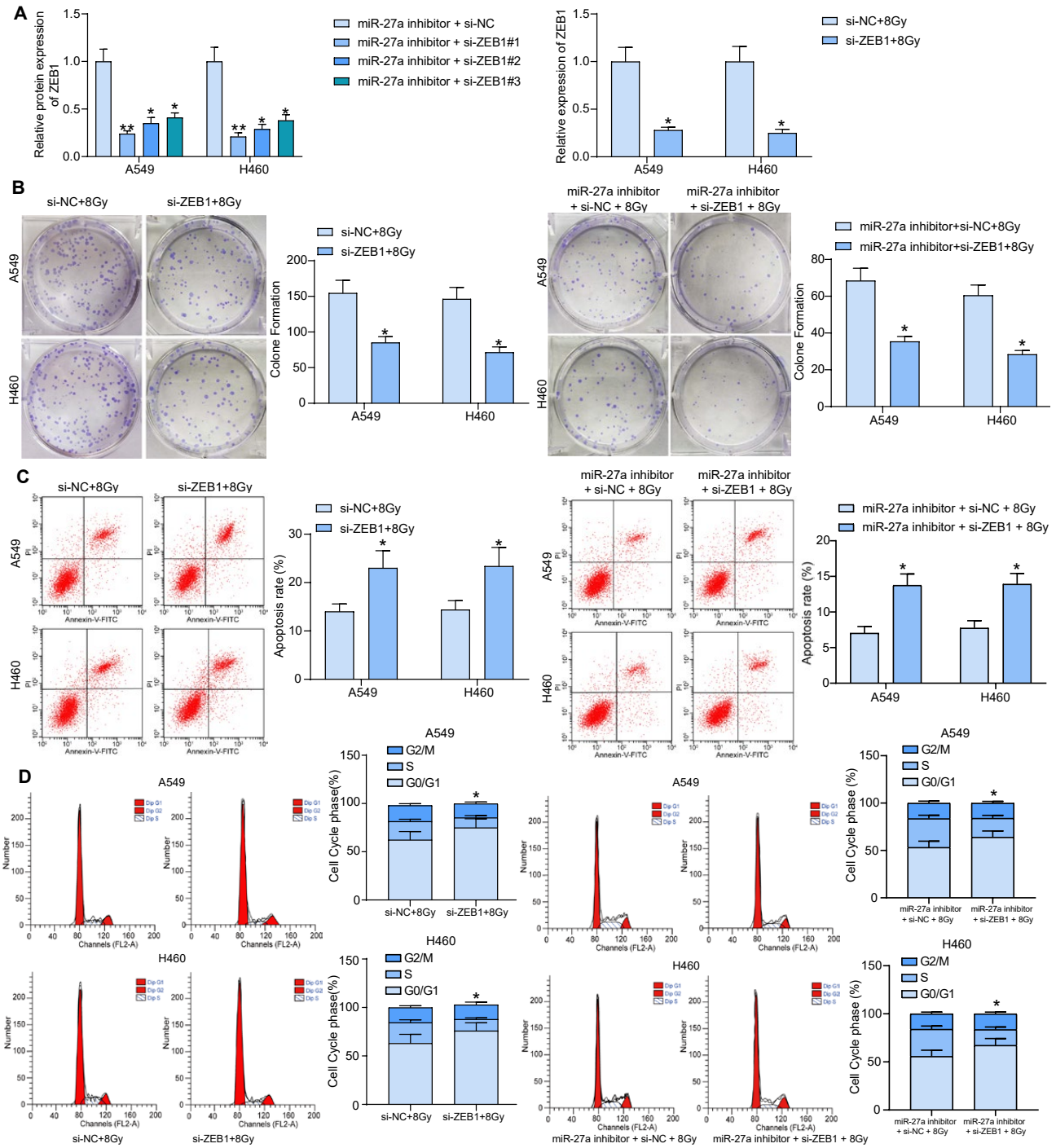

Fig. 5. *ZEB1 knockdown abrogates the effects of miR-27a inhibitor on radiosensitivity of lung cancer cells.* ***A****) The silencing efficiency of ZEB1 in lung cancer cells validated with RT-qPCR.* ***B****) The number of colonies formed detected by colony formation assay in cells treated with si-ZEB1 and miR-27a inhibitor following 8 Gy IR.* ***C****) The apoptosis of lung cancer cells determined using flow cytometry in cells treated with si-ZEB1 and miR-27a inhibitor following 8 Gy IR.* ***D****) The cell cycle determined using flow cytometry in cells treated with si-ZEB1 and miR-27a inhibitor following 8 Gy IR.* * $p < 0.05$ *according to the two-way ANOVA.*

were employed to predict the putative targets of miR-27a. ZEB1 was found in the intersection (Fig. 4A). RT-qPCR exhibited ZEB1 mRNA expression reduced in an IR dose-dependent manner (Fig. 4B) and its expression was partially restored in miR-27a inhibitor-treated cells following 8 Gy IR and cells only transfected with miR-27a inhibitor (Fig. 4C). As validated by dual-luciferase reporter gene assays, miR-27a inhibitor transfection resulted in an enhancement in luciferase activity of ZEB1-WT (Fig. 4D). As reflected in Fig. 4E, immunoblotting results displayed a reduction in ZEB1 protein expression after cells were treated with 8 Gy IR, while an opposite trend was observed by the further treatment of miR-27a inhibitor. Taken together, miR-27a could inversely modulate ZEB1 expression.

ZEB1 knockdown rescues the effects of miR-27a inhibitor on lung cancer cell radiosensitivity

We downregulated ZEB1 expression using three siRNAs targeting ZEB1 in cells transfected with miR-27a inhibitor or without transfection. miR-27a inhibitor + si-ZEB1#1 with the best silencing efficiency was chosen for subsequent experiments (Fig. 5A). As revealed by colony formation assay and flow cytometry (Fig. 5 B-D), silencing of ZEB1 sensitized cells to radiation therapy and induced cell apoptosis. In addition, co-transfection of miR-27a inhibitor and si-ZEB1 resulted in diminished ability of colony formation, promoted apoptosis and induced G0/G1 phase arrest in lung cancer cells, accompanied by reduced cell mitosis.

miR-27a activates HR-mediated DNA repair pathway by inhibiting ZEB1 expression to enhance lung cancer cell radiosensitivity

The levels of DNA damage repair-related proteins ATM, pCHK2 and Rad51 were determined after cells were subjected to 8 Gy IR. Based on the results of immunoblotting, IR caused a significant increase in the activity of the DNA damage repair pathway in cells, where ATM is a marker of DNA damage, CHK2 has an important role in the regulation of DNA double strand break-induced apoptosis and cell cycle arrest (25), and Rad51 and ATM are both key kinases of HR-mediated DNA repair. Therefore, we suggested that miR-27a modulates the radiosensitivity of lung cancer cells by activating the HR-mediated DNA repair (Fig. 6A). The activities of key kinases in this process in cells with si-ZEB1 were determined, which was found to increase the activity of HR-mediated DNA repair in cells with si-ZEB1 (Fig. 6B). The cells transfected with miR-27a inhibitor and IR treatment exhibited reduced levels of ATM, pCHK2 and Rad51 levels, while the trend was reversed by further treatment of si-ZEB1 (Fig. 6C). Therefore, miR-27a activates HR-mediated DNA repair by inhibiting ZEB1 expression to enhance the radiosensitivity of lung cancer cells.

DISCUSSION

Lung cancer is the major cause of cancer-related death worldwide, and many surgical techniques have been developed but are basically available to patients diagnosed at early stage (26). Radiotherapy is an important modality applied for the treatment of lung cancer, which can be used as curative or palliative treatment across all stages of disease (27). However, resistance blunts the therapeutic effect of radiotherapy for NSCLC patients with RAS-mutant, which leads to only a 5-10% survival rate in some cases (28). The present study illustrated that miR-27a activates HR-mediated DNA damage repair pathway by reducing ZEB1 expression to enhance the radiosensitivity of lung cancer cells.

Initially, miR-27a expression was silenced in lung cancer cells and its knockdown enhanced proliferation of IR-treated lung cancer cells. Consistently, miR-27a-5p expression was suppressed in SCLC clinical samples and enforced expression of miR-27a-5p suppressed cancer cell aggressiveness (29). Depletion of miR-27a led to proliferation, self-renewal, and the ratio of undifferentiated cells in SCLC, and promoted stem-like properties of SCLC cells (30). Moreover, elevation of miR-27a contributed to enhanced chemotherapy sensitization in alveolar rhabdomyosarcoma cells (31). miR-27 mimic was found to enhance the pro-apoptotic ability of cisplatin drugs in oral squamous cell carcinoma cells (32). In subsequent experiments, we also revealed that downregulation of miR-27a reduced the sensitivity

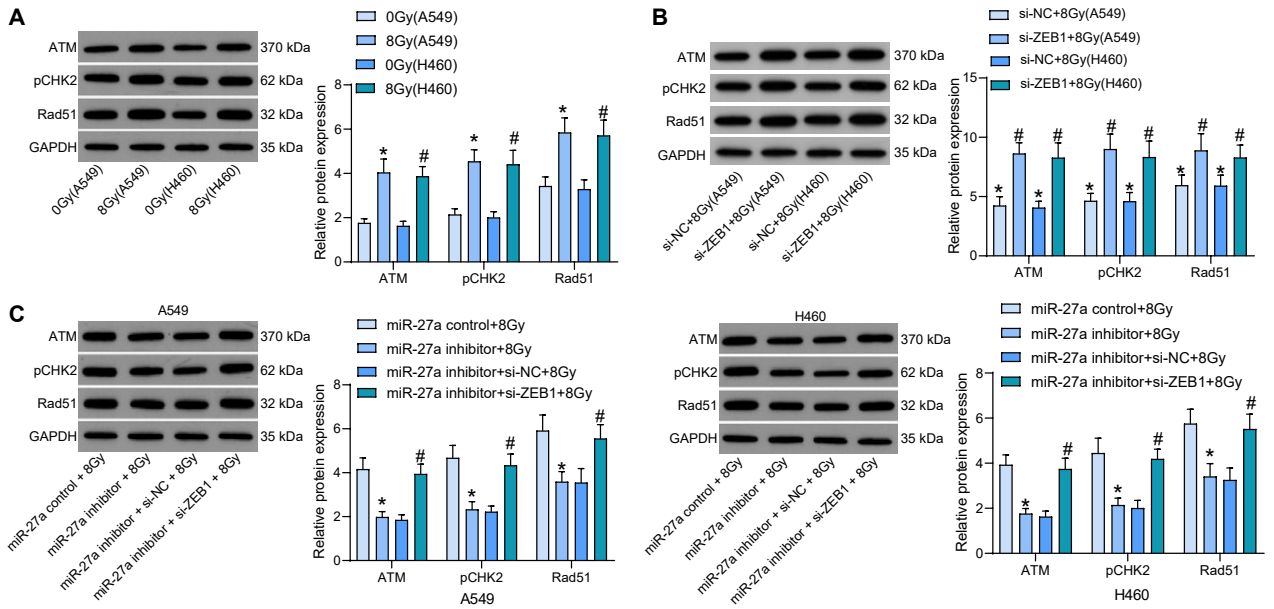

Fig. 6. *miR-27a activates HR-mediated DNA repair pathway to sensitize lung cancer cells to radiotherapy. A, The levels of ATM, pCHK2 and Rad51 after cells were subjected to 8 Gy IR determined using immunoblotting. B, The levels of ATM, pCHK2 and Rad51 in response to si-ZEB1 determined using immunoblotting. C, The levels of ATM, pCHK2 and Rad51 in response to miR-27a inhibitor and si-ZEB1 determined using immunoblotting. * $p < 0.05$ according to the two-way ANOVA. * $p < 0.05$ vs A549 cells treated with 0 Gy, si-NC + 8 Gy, miR-27a control + 8 Gy; # $p < 0.05$ vs H460 cells treated with 0 Gy, si-NC + 8 Gy, miR-27a inhibitor + si-NC + 8Gy.*

of lung cancer cells to radiotherapy. Likewise, esophageal squamous cell carcinoma (ESCC) patients exhibited suppressed miR-27a level and its elevation promoted IR-induced apoptosis, delayed cell cycle transition and increased ESCC radiosensitivity (33).

Another key finding is that miR-27a could target and inversely regulate ZEB1 expression in lung cancer cells. Similarly, miR-199a-3p elevation was proposed to suppress ZEB1 expression to inhibit tumor growth, cell proliferation and promote apoptosis in NSCLC (34). Concordant with our study, ZEB1 expression was elevated in NSCLC cell lines (35). Moreover, elevation of ZEB1 was also reported to abrogate the suppressive effects of miR-455 overexpression on the malignant phenotype of NSCLC cell lines (36). Furthermore, our study revealed that silencing of ZEB1 flattened the effects of miR-27a knockdown on radiosensitivity of lung cancer cells. Consistently, in a previous study reported by Liu et al., the loss of ZEB1 was correlated with the attenuated IR-triggered EMT of lung cancer cells (37).

DNA damage repair deficiency was harbored by a number of aggressive high-grade carcinoma, and inactivation of core HR and HR-associated genes, such as ATM, CHEK2, RAD54L, and RAD51B, occurs in many localized and metastatic prostate cancers (38). We hypothesized that miR-27a-ZEB1 axis may regulate the radiosensitivity of lung cancer cells *via* HR-mediated DNA damage repair pathway, which has been validated by the reduced levels of ATM, pCHK2 and Rad51 after miR-27a inhibition. The activation of ATM transcription could be targeted by DNA, contributing to the reactivation of hepatitis B virus replication (39). DNA repair genes including PARP and ATM/ATR exert radio-sensitizing effects and ATM level is associated with reduced IR response (40). The upregulation of pCHK2 is suggestive of triggered DNA damage (41). The HR-mediated DNA repair is characterized by DNA damage-triggered Rad51 focus formation (42). Furthermore, the activation

of the DNA repair pathway, as manifested by ATM, pCHK2, and Rad51 elevation, is correlated with the promoted radiosensitivity via miR-146a-5p/RPA3 axis in hepatocellular carcinoma (43). In the context of NSCLC, enhancement of IR-triggered DNA damage could increase sensitivity of NSCLC cells to radiotherapy (44). Intriguingly, the upregulation of ZEB1 as a possible modulator of chemoresistance via direct interaction with ATM kinase, an important component of the DNA damage repair pathway which has been linked to radio-resistance (17), which further supported our hypothesis.

In conclusion, our results indicated that miR-27a was inhibited while ZEB1 was elevated in lung cancer cells, while an opposite trend was observed upon IR administration. miR-27a targets and regulates ZEB1 expression. miR-27a inhibition enhances proliferation of IR-treated lung cancer cells and reduces sensitivity of lung cancer cells by disrupting HR-mediated DNA damage repair pathway, while silencing of ZEB1 abolishes the effects of miR-27a knockdown on lung cancer cell radiosensitivity. These findings may serve as a promising therapeutic target in lung cancer. At present, the effects and mechanisms of miR-27a/ZEB1/HR-mediated DNA damage repair pathway axis remains scantly identified in lung cancer radiosensitivity, which still requires further validation.

REFERENCES

1. Bray F, Ferlay J, Soerjomataram I, Siegel RL, Torre LA, Jemal A. Global cancer statistics 2018: GLOBOCAN estimates of incidence and mortality worldwide for 36 cancers in 185 countries. CA Cancer J Clin 2018; 68:394-424.
2. Quintanal-Villalonga A, Molina-Pinelo S. Epigenetics of lung cancer: a translational perspective. Cell Oncol (Dordr) 2019; 42:739-56.
3. Duffy MJ, O'Byrne K. Tissue and blood biomarkers in lung cancer: a review. Adv Clin Chem 2018; 86:1-21.
4. Greathouse KL, White JR, Vargas AJ, et al. Interaction between the microbiome and TP53 in human lung cancer. Genome Biol 2018; 19:123.
5. Indini A, Rijavec E, Bareggi C, Grossi F. Novel treatment strategies for early-stage lung cancer: the oncologist's perspective. J Thorac Dis 2020; 12:3390-8.
6. Li H, Jiang M, Cui M, et al. MiR-365 enhances the radiosensitivity of non-small cell lung cancer cells through targeting CDC25A. Biochem Biophys Res Commun 2019; 512:392-8.
7. Ren J, Liu T, Han Y, Wang Q, Chen Y, Li G, Jiang L. GSK-3beta inhibits autophagy and enhances radiosensitivity in non-small cell lung cancer. Diagn Pathol 2018; 13:33.
8. Iqbal MA, Arora S, Prakasam G, Calin GA, Syed MA. MicroRNA in lung cancer: role, mechanisms, pathways and therapeutic relevance. Mol Aspects Med 2019; 70:3-20.
9. Verma V, Lautenschlaeger T. MicroRNAs in non-small cell lung cancer invasion and metastasis: from the perspective of the radiation oncologist. Expert Rev Anticancer Ther 2016; 16:767-74.
10. Fang C, Li XP, Gong WJ, et al. Age-related common miRNA polymorphism associated with severe toxicity in lung cancer patients treated with platinum-based chemotherapy. Clin Exp Pharmacol Physiol 2017; 44 Suppl 1:21-9.
11. Ma M, Yin Z, Zhong H, Liang T, Guo L. Analysis of the expression, function, and evolution of miR-27 isoforms and their responses in metabolic processes. Genomics 2019; 111:1249-57.
12. Heegaard NH, Schetter AJ, Welsh JA, Yoneda M, Bowman ED, Harris CC. Circulating micro-RNA expression profiles in early stage nonsmall cell lung cancer. Int J Cancer 2012; 130:1378-86.
13. Gupta A, Sharma A, Yadav A, et al. Evaluation of miR-27a, miR-181a, and miR-570 genetic variants with gallbladder cancer susceptibility and treatment outcome in a North Indian population. Mol Diagn Ther 2015; 19:317-27.
14. Girardi C, De Pitta C, Casara S, Sales G, Lanfranchi G, Celotti L, Mognato M. Analysis of miRNA and mRNA expression profiles highlights alterations in ionizing radiation response of human lymphocytes under modeled microgravity. PLoS One.
15. Zhou Z, Zhang P, Hu X, et al. USP51 promotes deubiquitination and stabilization of ZEB1. Am J Cancer Res 2017; 7:2020-31.
16. Jia X, Wang Z, Qiu L, et al. Upregulation of

LncRNA-HIT promotes migration and invasion of non-small cell lung cancer cells by association with ZEB1. Cancer Med 2016; 5:3555-63.
17. Drapela S, Bouchal J, Jolly MK, Culig Z, Soucek K. ZEB1: a critical regulator of cell plasticity, DNA damage response, and therapy resistance. Front Mol Biosci 2020; 7:36.
18. Sun Y, McCorvie TJ, Yates LA, Zhang X. Structural basis of homologous recombination. Cell Mol Life Sci 2020; 77:3-18.
19. Chen G, Chen J, Qiao Y, et al. ZNF830 mediates cancer chemoresistance through promoting homologous-recombination repair. Nucleic Acids Res 2018; 46:1266-79.
20. Jin ZL, Shen XH, Shuang L, Kwon JW, Seong MJ, Kim NH. Inhibition of DNA repair protein RAD51 affects porcine preimplantation embryo development. Reproduction 2019; 157:223-34.
21. Mueck K, Rebholz S, Harati MD, Rodemann HP, Toulany M. Akt1 Stimulates Homologous Recombination Repair of DNA Double-Strand Breaks in a Rad51-Dependent Manner. Int J Mol Sci 2017; 18.
22. Huang C, Huang M, Chen W, et al. N-acetylglucosaminyltransferase V modulates radiosensitivity and migration of small cell lung cancer through epithelial-mesenchymal transition. FEBS J 2015; 282:4295-306.
23. Wu D, Li Y, Zhang H, Hu X. Knockdown of Lncrna PVT1 enhances radiosensitivity in non-small cell lung cancer by sponging Mir-195. Cell Physiol Biochem 2017; 42:2453-66.
24. Pawlik TM, Keyomarsi K. Role of cell cycle in mediating sensitivity to radiotherapy. Int J Radiat Oncol Biol Phys 2004; 59:928-42.
25. van Jaarsveld MTM, Deng D, Ordonez-Rueda D, Paulsen M, Wiemer EAC, Zi Z. Cell-type-specific role of CHK2 in mediating DNA damage-induced G2 cell cycle arrest. Oncogenesis 2020; 9:35.
26. Hoy H, Lynch T, Beck M. Surgical Treatment of Lung Cancer. Crit Care Nurs Clin North Am 2019; 31:303-13.
27. Vinod SK, Hau E. Radiotherapy treatment for lung cancer: current status and future directions. Respirology 2020.
28. Chen K, Shang Z, Dai AL, Dai PL. Novel PI3K/Akt/mTOR pathway inhibitors plus radiotherapy: Strategy for non-small cell lung cancer with mutant RAS gene. Life Sci 2020; 255:117816.
29. Mizuno K, Mataki H, Arai T, et al. The microRNA expression signature of small cell lung cancer: tumor suppressors of miR-27a-5p and miR-34b-3p and their targeted oncogenes. J Hum Genet 2017; 62:671-8.
30. Miao Y, Li J, Qiu X, Li Y, Wang Z, Luan Y. miR-27a regulates the self-renewal of the H446 small cell lung cancer cell line in vitro. Oncol Rep 2013; 29:161-8.
31. Bharathy N, Berlow NE, Wang E, et al. The HDAC3-SMARCA4-miR-27a axis promotes expression of the PAX3:FOXO1 fusion oncogene in rhabdomyosarcoma. Sci Signal 2018; 11.
32. Liu B, Cao G, Dong Z, Guo T. Effect of microRNA-27b on cisplatin chemotherapy sensitivity of oral squamous cell carcinoma via FZD7 signaling pathway. Oncol Lett 2019; 18:667-73.
33. Wang X, An D, Liu X, Wang X, Li B. MicroRNA-27a downregulates the expression of Hsp90 and enhances the radiosensitivity in esophageal squamous cell carcinoma. Onco Targets Ther 2019; 12:5967-77.
34. Bai J, Jiao WY. Down-Regulation of ZEB1 by miR-199a-3p Overexpression restrains tumor stem-like properties and mitochondrial function of non-small cell lung cancer. Onco Targets Ther 2020; 13:4607-16.
35. Yao YH, Cui Y, Qiu XN, Zhang LZ, Zhang W, Li H, Yu JM. Attenuated LKB1-SIK1 signaling promotes epithelial-mesenchymal transition and radioresistance of non-small cell lung cancer cells. Chin J Cancer 2016; 35:50.
36. Li YJ, Ping C, Tang J, Zhang W. MicroRNA-455 suppresses non-small cell lung cancer through targeting ZEB1. Cell Biol Int 2016; 40:621-8.
37. Liu W, Huang YJ, Liu C, et al. Inhibition of TBK1 attenuates radiation-induced epithelial-mesenchymal transition of A549 human lung cancer cells via activation of GSK-3beta and repression of ZEB1. Lab Invest 2014; 94:362-70.
38. Burdak-Rothkamm S, Mansour WY, Rothkamm K. DNA damage repair deficiency in prostate cancer. Trends Cancer 2020.
39. Kostyusheva A, Brezgin S, Bayurova E, et al. ATM and ATR expression potentiates HBV replication and contributes to reactivation of HBV infection upon DNA Damage. Viruses 2019; 11.
40. Reda M, Bagley AF, Zaidan HY, Yantasee W.

Augmenting the therapeutic window of radiotherapy: A perspective on molecularly targeted therapies and nanomaterials. Radiother Oncol 2020; 150:225-35.
41. Nair VA, Valo S, Peltomaki P, Bajbouj K, Abdel-Rahman WM. Oncogenic potential of bisphenol A and common environmental contaminants in human mammary epithelial cells. Int J Mol Sci 2020; 21.
42. Suhane T, Bindumadhavan V, Fangaria N, et al. Glu-108 in Saccharomyces cerevisiae Rad51 is critical for DNA damage-induced nuclear function. MSphere 2019; 4.
43. Luo J, Si ZZ, Li T, et al. MicroRNA-146a-5p enhances radiosensitivity in hepatocellular carcinoma through replication protein A3-induced activation of the DNA repair pathway. Am J Physiol Cell Physiol 2019; 316:C299-C311.
44. Ma W, Ma CN, Zhou NN, Li XD, Zhang YJ. Up-regulation of miR-328-3p sensitizes non-small cell lung cancer to radiotherapy. Sci Rep 2016; 6:31651.

Leptin reduces ventilator-induced lung injury in rats by regulating NLRP3, NLRC4 and NLRC3

X. Zhang[1*], WW. Qin[1*], FG. Ma[1], LX. Sun[1] and W. Han[2]

[1]Department of Anesthesia, Qingdao Municipal Hospital, Qingdao University, Qingdao, PR China; [2]Department of Respiratory and Critical Medicine,Qingdao Municipal Hospital, Qingdao University, Qingdao, PR China

Received May 7, 2020 – Accepted January 7, 2021

[*]These Authors contributed equally to this work

Leptin has been linked to acute lung injury (ALI) through its regulation of immune responses. We aimed to scrutinize the effects of leptin on nucleotide oligomerization domain–like receptors containing pyrin domain 3 (NLRP3), nucleotide oligomerization domain–like receptors with caspase activation and recruitment domain 4 (NLRC4), and nucleotide oligomerization domain–like receptors with caspase activation and recruitment domain 3 (NLRC3), as an essential part of the immune system, in ventilator-induced lung injury (VILI) of rats. In the present study, pathogen-free adult male SD rats were given saline or leptin, followed by ventilation. Lung tissue samples, bronchoalveolar lavage fluids (BALF), and blood were collected four hours after installation. Notable acute lung inflammation induced by mechanical ventilation is well-characterized by a massive increase in lung injury score and wet/dry weight (W/D) ratio. We also observed VILI was associated with interleukin (IL-1β and IL-18). Rats that received ventilation showed a decrease in the levels of NLRP3 and NLRC4, and an increased level of NLRC3. Pre-treatment with leptin could abolish all of these effects induced by VILI. It has been suggested that the regulation of NLRP3, NLRC4, and NLRC3 may underlie the protection observed during VILI by exogenous leptin.

The experimental evidence has shown that mechanical ventilation, life-saving support for patients suffering from lung injury, may injure the lungs through the introduction of excessive volume of air (1). Severe inflammation of the lungs during mechanical ventilation is closely associated with length of hospital stay (2, 3). Inflammation also increases vascular permeability, leading to pulmonary edema, and disrupts the alveolar-capillary interface, reducing pulmonary compliance, eventually leading to severe consequences called acute lung injury (ALI) (4). Therefore, suppressing inflammation and the production of cytokine intermediates may reduce mechanical ventilation-related pulmonary dysfunction and degeneration. Various lung-protective interventions have been shown to reduce activation of inflammation and thus reduce lung dysfunction (5–7).

Adipokines, adipose tissue-synthesized hormones, play a significant role in the regulation of various inflammatory and immune pathways (8). Leptin is a hormone mainly derived from adipose tissue, and it can mediate ventilator-induced lung injury (VILI) by regulating innate and adaptive immune responses

Key words: leptin; NLRP3; NLRC3; NLRC4; ventilator-induced lung injury

Corresponding Author:
Dr Lixin Sun,
Department of Anesthesia, Qingdao Municipal Hospital,
Qingdao University, No. 5 Donghai Middle Road,
Shinan District, Qingdao, 266071, PR China
Tel.: +86 15621022955
e-mail: sunlixin1221@126.com

0393-974X (2021)
Copyright © by BIOLIFE, s.a.s.
This publication and/or article is for individual use only and may not be further reproduced without written permission from the copyright holder.
Unauthorized reproduction may result in financial and other penalties
DISCLOSURE: ALL AUTHORS REPORT NO CONFLICTS OF INTEREST RELEVANT TO THIS ARTICLE.

(9). Leptin partially reduces LPS-induced lung injury by inhibiting the activation of NF-κB, p38, and ERK pathways, which is consistent with the obesity paradox phenomenon in lung injury by mechanical ventilation (10), which is consistent with the obesity paradox phenomenon in lung injury by mechanical ventilation. Obese individuals present distinct survival advantages for *in vivo* modelling of VILI (11). Leptin, a protein hormone, could reduce the activation and the influx of inflammatory factors into the lungs, thus inhibiting LPS-induced lung injury (10). In this study, leptin deficiency in mice reduced survival and enhanced LPS-induced ALI, but the exact mechanism is not clear.

One study showed that interleukin-18 (IL-18) derived from the activation of nucleotide oligomerization domain–like receptors containing pyrin domain 3 (NLRP3) inflammasome in macrophages could be triggered by leptin, raising the possibility that inflammasome activation could modulate inflammatory responses through leptin (12). Nucleotide oligomerization domain–like receptors (NLRs) consisted of NLRA, NLRB, NLRC, and NLRP (13), which were initially studied as critical regulators in immune responses. All of these NLRs act as vital factors that are directly or indirectly employed in inflammatory production once the infection or cell damage is enabled (14), especially NLRP3 (15), nucleotide oligomerization domain–like receptors with caspase activation and recruitment domain 4 (NLRC4) (16), and nucleotide oligomerization domain–like receptors with caspase activation and recruitment domain 3 (NLRC3) (17). They can sense the imbalance of intracellular environment caused by cellular damage or stress.

However, the role of leptin in reducing lung injury because of the interaction between NLRs has not been completely elucidated. To evaluate the effects of leptin on NLRs in VILI of rat model, leptin was applied as a pre-treatment before ventilation stimulation. Production of NLRP3, NLRC4, and NLRC3 were efficacy measures in leptin treatment for VILI.

MATERIALS AND METHODS

Animals

Adult male Wistar rats weighing 240–260 g (6–8 weeks old) were purchased from Pengyue Experimental Animals Center of Shandong (Jinan, China). All experimental treatments and procedures on adult male Wistar rats were performed in strict accordance with the requirements of the Medical Ethics Committee in Qingdao Municipal Hospital. Rats were housed in a regular animal room (room temperature: 20–25°C, humidity: 40–60%) for 12 h, with free access to water and food. The animals were maintained in keeping with the guidelines of the experimental animal centre of Qingdao University, and protocols were approved by the medical ethics committee of Experimental Animals of Qingdao Municipal Hospital (number 2018034).

Model of VILI

VILI model was established by ventilation as previously described with minor modifications (18). The rats were anaesthetized with an intraperitoneal injection of 40 mg/kg sodium pentobarbital, and then endotracheally intubated using 18-gauge endotracheal cannula. Mechanical ventilation settings: a tidal volume of 30 ml/kg with 4 h, a ventilatory frequency of 60 times/min, an inspired oxygen fraction (FiO_2) of 21%, and a positive end-expiratory pressure (PEEP) of 0 cm H_2O. The additional anaesthetics of sodium pentobarbital were intraperitoneally injected continuously according to the demand.

Experimental groups

The rats were randomly allocated into three groups: non-ventilated group (group A, n = 12) treated with 200 μl saline; ventilated with mechanical ventilation group (group B, n = 12) treated with 200 μl saline; ventilated with mechanical ventilation group (group C, n = 12) treated with leptin [500 μg/kg ip dissolved in 200 μl saline; (Calbiochem, MA, USA)] according to our preliminary experiment. Rats in group A were injected intraperitoneally with 200 μl saline, anesthetized with an injection of 40 mg/kg sodium, and intubated endotracheally using an 18-gauge endotracheal cannula for non-ventilation. Rats in group B were injected intraperitoneally with 200 μl saline, anesthetized with an injection of 40 mg/kg sodium, and intubated endotracheally using 18-gauge endotracheal cannula for mechanical ventilation. Rats in group C were injected intraperitoneally with 500 μg/kg leptin, anesthetized with an injection of 40 mg/kg sodium, and intubated endotracheally using 18-gauge endotracheal cannula for mechanical ventilation. The rats were

sacrificed by arterial bleeding to obtain corresponding test specimen after 4 h (Fig. 1).

Histopathological examination

The right upper lungs were collected for Routine H&E staining. Summarily, the upper lobe of the right lung tissue samples was immersed in 10% formalin, then treated for paraffin embedding. The embedded lung tissues were sliced subsequently at a thickness of 5 μm for observation under a light microscope at a magnification of 200×. The tissues were examined, and the pathological changes were assessed using defined criteria from previous studies (15).

Wet/dry weight (W/D) ratio

The middle lobe of the right lung tissue samples was removed to determine W/D ratio. The lung tissues were put on an electronic balance to ascertain the wet lung weight. The lung tissues were then dried at 65°C for 48 h and weighed again to determine the dry weight.

ELISA

Blood samples taken from the femoral artery at 4 h of mechanical ventilation were moved to procoagulant tubes, and instantly placed in a pre-cooled 4°C low-temperature centrifuge and spun at 1500 rpm/min for 10 min to detect inflammatory factor IL-18 and interleukin-1β (IL-1β) as measured by ELISA kits (eBiosciences, Vienna, Austria). The rats were sacrificed by arterial bleeding at the end of mechanical ventilation. Using 2 ml phosphate-buffered saline, the airways were flushed twice to collect about 3 ml bronchoalveolar lavage fluid (BALF). Then the BALF was centrifuged at 3000 rpm/min for 10 min to collect the plasma for detecting inflammatory factor IL-18 and IL-1β using ELISA kits obtained from eBiosciences (Vienna, Austria) according to the manufacturer's instructions.

Western blotting

Right lower lung tissue was homogenized in protease inhibitor cocktail containing RIPA buffer to detect the expression of NLRP3, NLRC4, and NLRC3. The membranes were blocked with 5% skim milk in PBS/Tween20 for 40 min, and equal quantities of proteins (50–60 **μg**) were given to each group and separated onto 10% SDS-PAGE gels (Keygen Biotech, Nanjing, China) and then transferred to polyvinylidene fluoride (PVDF) membrane (Millipore, Temecula, CA, US). Then, the membranes were treated with the proper primary antibody: anti-NLRP3 (1:1000 dilution; Abcam, Cambridge, UK), anti-NLRC4 (1:1000 dilution; Abcam, Cambridge, UK), anti-NLRC3 (1:1000 dilution; Abcam, Cambridge, UK), and β-actin (1:5000 dilution; easybio, Shenzhen, China). Bound antibody was envisaged using horseradish peroxidase-labelled secondary antibodies (goat anti-rabbit, bioeasy, Shenzhen, China). Eventually, each strip of protein was probed using an ECL chromogenic substrate (Millipore,USA).

Real-time quantitative PCR

Trizol reagent (Tiangen Biotech, Beijing) was used and reverse transcription was performed with the Prime Script™ RT reagent kit (TaKaRa, Japan) to extract RNA from the right lower lung tissues. Total RNA 1 **μg** was treated to eliminate genomic DNA contamination, followed by compositing the first-strand using the reverse transcription system (TaKaRa, Japan). SYBR Premix Ex Taq (TaKaRa, Japan) was used for polymerase chain reaction. The following primers were applied: NLRP3 forward primer, 5′-AGAAGGACCAGCCAGAGTGGAATGA-3′ and reverse primer 5′-TTTTTACAAATCGAGATGCGGGAGA-3′; NLRC4 forward primer, 5′-GTCTGTGCTGCC GTCTTTTAT-3′andreverseprimer5′-GCTTTTCTTGTTCCG ATTCAT-3′; NLRC3 forward primer, 5′-CAGATTGGTAA CAAAGGAGCCA-3′ and reverse primer 5′-CGTTCGGTTTATCTTCAGAGCA-3′; β-actin forward primer, 5′-TCCTGTGGCATCCATGAAACT-3′ and reverse primer, 5′-GAAGCATTTGCGGTGCACGAT-3′. Real-time quantitative PCR was handled in a 20 **μl** reaction solution including SYBR Premix Ex Taq, primers, and cDNAs. The cycles for PCR were: 95°C for 30 s, 40 periods at 95°C for 5 s and 60°C for 34 s. The melting curves were decided by the heat denature and the relative amount of mRNA, based on the $2^{-\Delta\Delta CT}$ method. The relative mRNA levels were normalised to β-actin control.

Statistical analyses

Due to the normal distribution and uniform variance of the data, One-way ANOVA and Bonferroni test were calculated with SPSS 19.0 statistical software. All variables used in this experiment were represented by mean ± standard deviation. Multiple groups were evaluated with One-way ANOVA procedures for continuous variables and multiple comparisons with the Bonferroni test.

RESULTS

Leptin prevented VILI

H&E staining was used to assess the pathological changes in lung tissues to observe lung injury. The conspicuous features of the lung tissues in group B were severe alveolar edema, destruction of the pulmonary architecture, thickened alveolar septa, hyaline membrane formation, alveolar haemorrhage, and infiltration of inflammatory cells. The features mentioned above were less pronounced in group C (Fig. 2A). Moreover, lung injury score from the different groups was in keeping with the above results (Fig. 2B). As shown in Fig. 2C, we observed a substantial increase in lung W/D ratio harvested from lung tissues compared with group A. Leptin pre-treatment inhibited the VILI. Moreover, group B exhibited a lower PaO_2 level than group A. In contrast, group C showed a decrease in PaO_2 values by the end of the ventilation period (Fig. 2D).

Leptin ameliorated IL-18 and IL-1β in serum and BALF induced by VILI.

The expression levels of IL-18 and IL-1β were investigated in serum and BALF respectively, after ventilation by ELISA kits. We assessed whether leptin could inhibit IL-18 and IL-1β induced by VILI. The differences were found between group A, group B, and group C in the expression of IL-18 and IL-1β in serum and BALF (Fig. 3 A–D). Rats treated with mechanical ventilation showed an increase in the expression of cytokines analyzed; leptin pre-treatment before mechanical ventilation prevented this effect.

Leptin regulated the expression of NLRP3, NLRC3, and NLRC4 protein in lung tissue.

NLRP3, NLRC3, and NLRC4 protein were quantified by using Western blotting. Group B showed increased NLRP3 expression, but pre-treatment with leptin abolished the effect in group C. The NLRC3 expression decreased in lung tissue in group B.

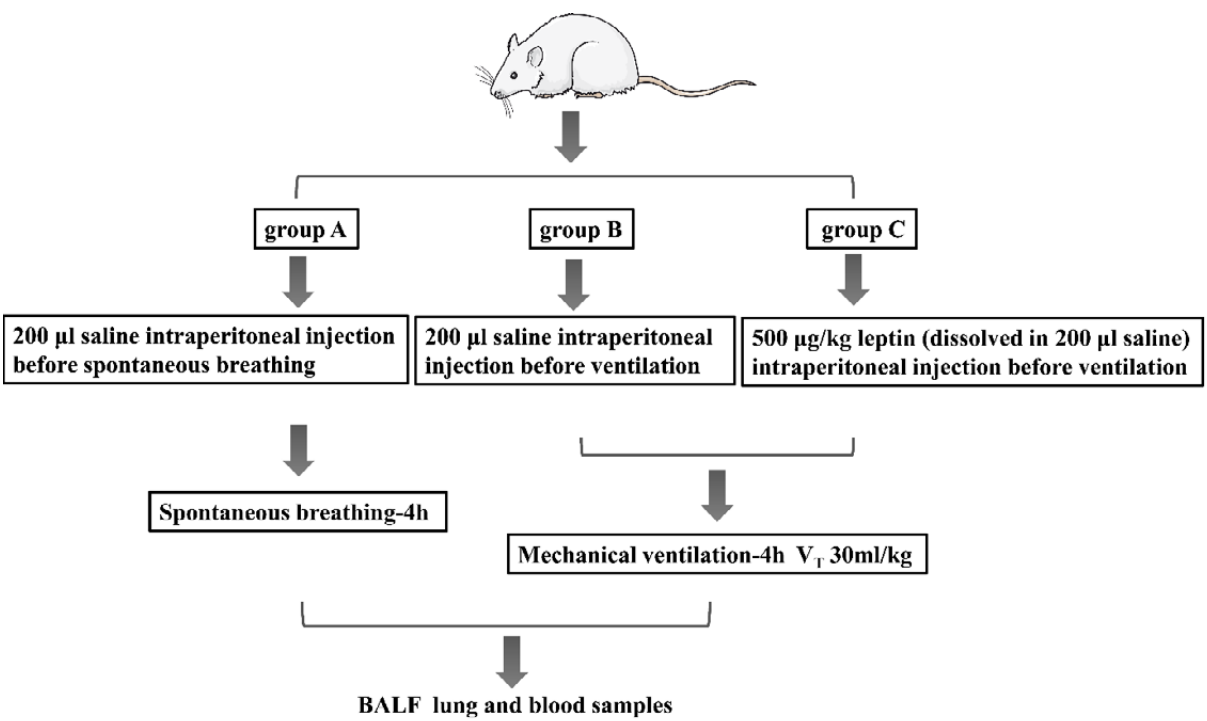

Fig. 1. *The flow diagram of mechanical ventilation lung injury model.*

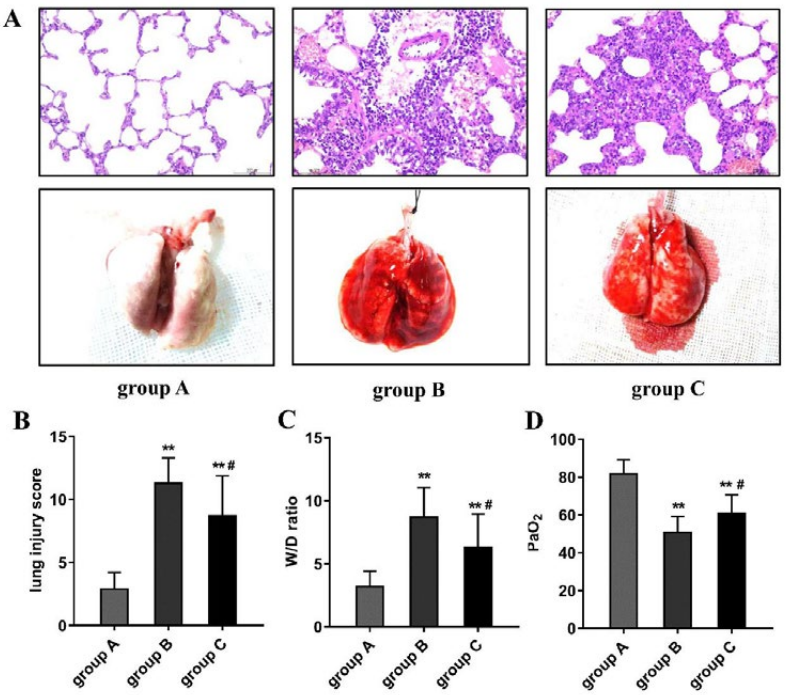

Fig. 2. *Prior leptin administration had lessened lung injury induced by ventilation. A) Representative pathological and histological analysis of the lungs (200×). B) Lung injury score. C) wet/dry ratio. D) Levels of PaO2 in blood gas analysis. Data are expressed as mean ± SD, n = 12/group. **P<0.01 group B and group C versus group A; #P<0.05 group C versus group B.*

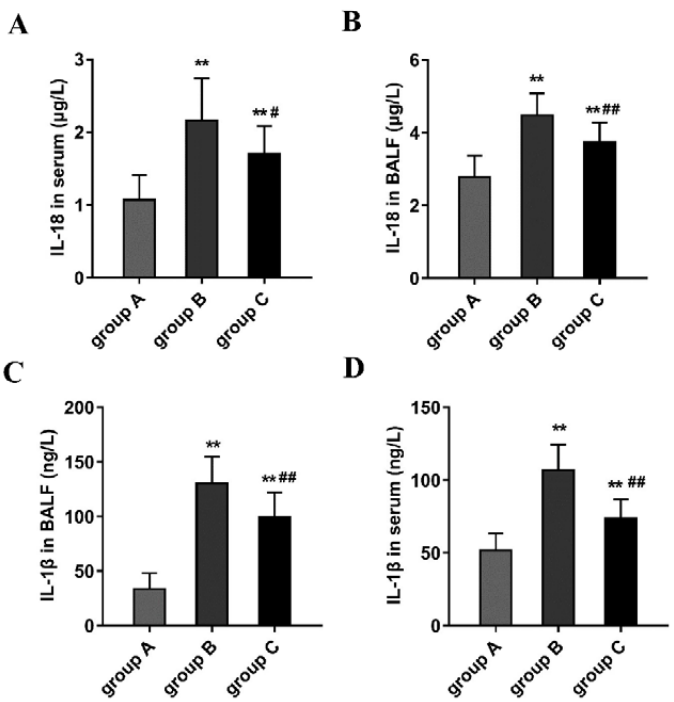

Fig. 3. *Enhanced leptin ameliorated inflammation in ALI Induced by ventilation. A) Serum cytokine IL 18. B) BALF cytokine IL 18. C) BALF cytokine IL 1β. D) Serum cytokine IL 1β. Data are expressed as mean ± SD, n =12/group. **P<0.01 group B and group C versus group A;#P<0.05 group C versus group B,##P<0.01 group C versus group B.*

In contrast, an increased NLRC3 expression was observed in group C. Mechanical ventilation-treated rats had increased levels of NLRC4 protein. Prior leptin administration attenuated the action of mechanical ventilation on NLRC4 expression (Fig. 4 A–D).

Leptin regulated the expression of NLRP3, NLRC3, and NLRC4 mRNA in lung tissue.

NLRP3, NLRC3, and NLRC4 mRNA were quantified in lung tissue using real-time quantitative PCR. Group B showed increased NLRP3 mRNA expression, and prior leptin administration to VILI abolished this effect in group C. NLRC3 expression was decreased in the lung tissues in group B. An increase in NLRC3 expression was observed in group C. Mechanical ventilation-treated rats had increased levels of NLRC4 mRNA, but leptin administration attenuated the effect of mechanical ventilation on NLRC4 expression (Fig. 5A–C). The possible role of NLRs in leptin-related VILI is summarized in Fig. 6.

DISCUSSION

The mechanisms by which treatment with exogenous leptin is involved in the development of ALI as induced by ventilation are not fully understood and need to be investigated through basic research and further clinical practice. We have established that high volume ventilation significantly increased inflammatory response, including high lung injury score and W/D ratio, production of IL-18 and IL-1β in BALF and serum, increased expression of NLRC3, decreased expression of NLRP3, NLRC4, and total lung injury. Importantly, this indicated that pre-treatment with leptin could protect rats against VILI and reverse the ventilation-induced effects.

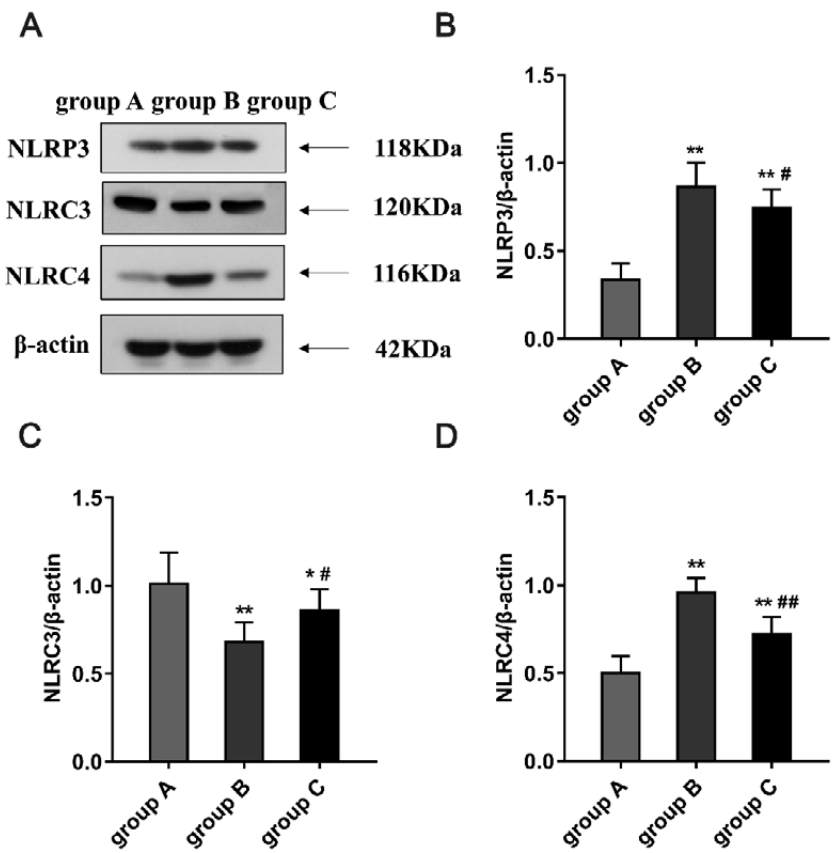

Fig. 4. *Leptin regulated the expression of NLRP3, NLRC3, and NLRC4 protein in lung tissue. A) NLRP3, NLRC3, and NLRC4 protein expression in three groups. B) Level of NLRP3 expression. C) Level of NLRC3 expression. D) Level of NLRC4 expression. Data are expressed as the ratio of NLRP3, NLRC3and NLRC4 to β actin. Data are expressed as mean ± SD, n = 12/group. **P<0.01 group B and group C versus group A; #P<0.05 ##P<0.01 group C versus group B.*

Regional lung deformation (19) and overinflation (20) of the alveoli induced by large tidal volume ventilation could exacerbate pulmonary inflammation through the release of cytokines and increased lung permeability, leading to lung edema and abnormality. In the present study, the ability of NLRs, a kind of pattern recognition receptors (PRRs), to mediate initial innate immune response to tissue or cellular injury and stress was investigated (5). Members of the NLRs family of proteins all contain C-terminal leucine-rich repeat (LRR) domains and central nucleotide-binding domains (NBD). The NLRs

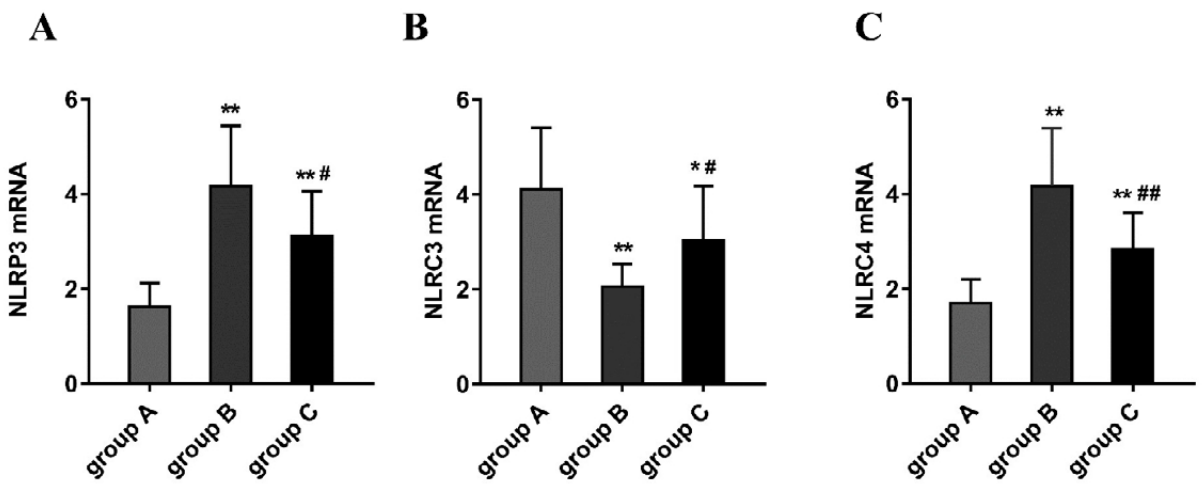

Fig. 5. *Leptin regulated the expression of NLRP3, NLRC3, and NLRC4 mRNA in lung tissue. A) Level of NLRP3 mRNA expression. B) Level of NLRC3 mRNA expression. C) Level of NLRC4 mRNA expression. Data are expressed as the ratio of NLRP3, NLRC3 and NLRC4 to β actin. Data are expressed as mean ± SD, n = 12/group. *P<0.05 **P<0.01 group B and group C versus group A; #P<0.05 ##P<0.01 group C versus group B.*

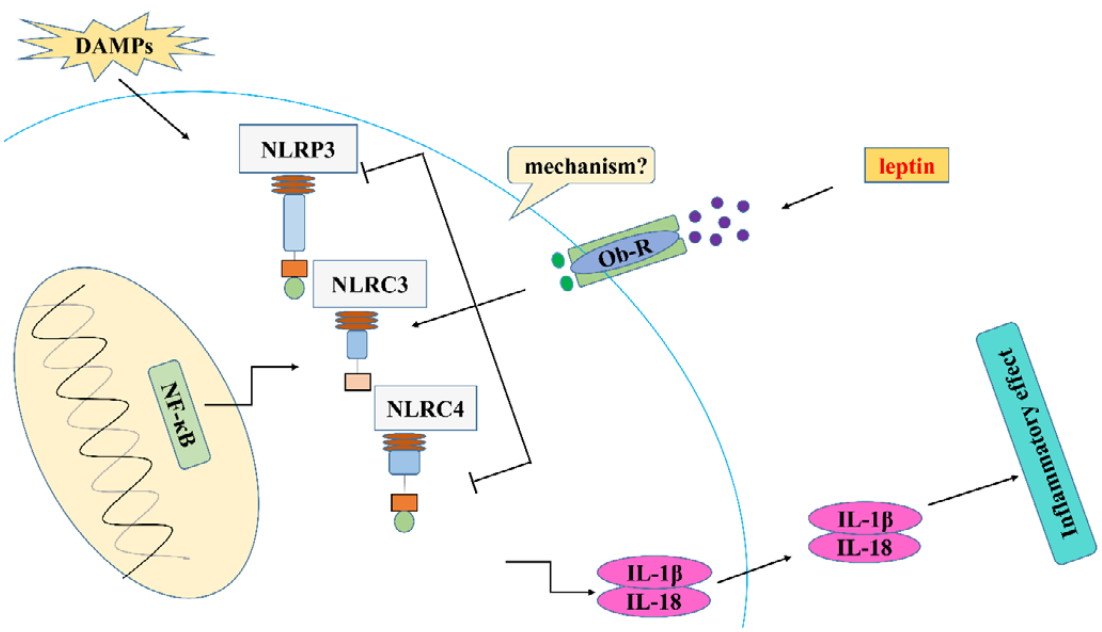

Fig. 6. *Role of NLRs in leptin related VILI.*

family is divided into a variety of subfamilies by their N-termini, and the NLRC and NLRP groups are the two most prominent among them. The NLRC proteins have caspase recruitment domains (CARD) at their N-termini, but the NLRP proteins have pyrin domains (PYD) instead. Both IL-1β and IL-18 are effective pro-inflammatory cytokines that have multiple effects on the innate or adaptive immune system. Under certain disordered internal circumstances, the NLR family of proteins can cleave and upgrade pro-IL-1β and pro-IL-18 into their mature and active biologically form. Furthermore, IL-1β and IL-18 are potentially considered as salient cytokines that induce ALI (21). The releasing of IL-1β and IL-18 can further amplify inflammatory responses by bringing about other proinflammatory cytokine production, such as tumor necrosis factor (TNF)-α, and monocyte chemotactic protein (MCP)-1 (22). Multiple statistical reviews have proved that keeping high concentrations of IL-1β and IL-18 is associated with the development of ALI (23–25). We discovered that leptin decreased the seriousness of VILI, in part due to reducing the release of inflammatory mediators of IL-1β and IL-18.

Leptin is a monomeric nonglycosylated protein, secreted by the ob gene. Whether leptin associated with obesity plays a role in mediating the inflammatory process underlying ALI is unclear. Several lines of evidence were coupled with the function of leptin, which conferred a proinflammatory effect. For example, pulmonary leptin contributes directly to the development of pulmonary neutrophilia during ALI (26) and patients with ALI had elevated leptin concentrations in BALF (27). Other sets of evidence suggested that leptin has anti-inflammatory effects. For example, exogenous administration of leptin ameliorated lung injury partly through restraining the activation of NF-**κ**B, p38, and ERK pathways (4). Leptin could ameliorate ALI by regulating insulin and corticosterone (28). In our work, leptin existed regarding the impact on the expression of inflammatory molecules. Protective effects of leptin on VILI may be at least partially related to downregulating the expression of IL-18 and IL-1β.

A role for NLRs in the regulation of inflammation has been identified, especially NLRC3 (29), NLRP3 (15, 30–31), and NLRC4 (32). They all can regulate the activation of cysteinyl aspartate specific proteinase 1 (caspase-1) by causing secretion of biologically active inflammatory cytokines, such as IL-1β and IL-18. Among them, NLRC3, which negatively regulates NLRs-mediated inflammatory responses through suppression of NLRP3/cryopyrin-induced apoptosis-associated speck-like protein containing CARD (ASC) speck formation and NF-**κB**-dependent transcriptional activity and signalling (29). Accumulating evidence shows that the mechanical stretch caused by ventilation can induce the activation of the NLRP3 inflammasome by numerous cellular and molecular alterations, including the activation of NIMA-related kinase 7 (NEK7), the degradation of cell junction proteins, and the release of cytokines (15). The pathway of NF-**κB**/TLR4/NLRP3 signals is the mechanism for the role of NLRP3 in the pathophysiology of lung injury (33). One of the mechanisms by which NLRC4 induce lung inflammation might involve AMP-activated protein kinase (AMPK) signalling, given that the inducible Drp1-mediated mitochondrial fission in LPS-induced sepsis model is responsible for the overproduction of ROS.

A recent large cohort study showed patients with high body mass index in ALI exhibited a reduction in proinflammatory cytokines in general (34). However, whether leptin was the important factor in regulating ventilator-induced pulmonary inflammation has not been discovered. Huang et al. (35) observed leptin-deficient mice exhibit significantly lower lung volume and lower alveolar surface area, similar to Maristella A. Landgraf (28) and Arteaga-Solis et al. (36). Similarly, we observed that augmented leptin levels in ventilation-treated mice decreased IL-18 and IL-1β secretion by regulating the expression of NLRP3, NLRC3, and NLRC4. We established that treating rats with leptin prior to ventilation may strengthen the importance of a regulatory loop in NLRs axis in VILI. Acute inflammatory response such as neutrophil aggregation is known to be regulated by the immune system. and some regulatory loops connected NLRs and circulating leptin. Nevertheless, no studies exploring the effects of leptin on the NLRP3, NLRC3, and NLRC4 levels have been performed.

Inflammasome activation leading to the

production of IL-1β has been proven to serve a pivotal role in leptin-induced growth of breast cancer cells (37). However, some other researchers have the exact opposite opinion as they found that leptin suppressed local immune responses. As reported by Landgraf, Arteaga-Solis, and Huang, who demonstrated a negative correlation between inflammasomes and leptin, we showed that leptin extenuated the ventilator-induced increase in pro-inflammatory inflammasome. The increased inflammasome expression triggered by stress and injury of macrophages was associated with IL-18 and IL-1β. Leptin-deficient ob/ob mice exhibited greater lethality and less pulmonary bacterial removal than db/db mice (38) and, as such, exogenous leptin administration to ob/ob mice improved survival rate and greatly improved pulmonary bacterial clearance. Taken together, these biological results and studies established the mechanisms of leptin on VILI. We conclude that leptin treatment before ventilation had protective effects in lung injury, reducing the following: a) pulmonary edema, destruction of pulmonary architecture, thickening of the alveolar septa, hyaline membrane formation, alveolar haemorrhage and infiltration of inflammatory cells in lung tissue; b) expression of cytokines IL-18 and IL-1β in lung tissue; c) expression of NLRP3, NLRC3, and NLRC4 in lung tissue. In conclusion, our present study establishes that leptin by exogenous administrating protects rat against VILI by regulating NLRs, including NLRP3, NLRC3, and NLRC4. In this way, leptin might be a better therapeutic strategy for preventing ALI induced by ventilation.

ACKNOWLEDGEMENTS

We are genuinely grateful to the Laboratory Research Center of Qingdao University for providing technical support for this study.

The study was supported by the Qingdao Outstanding Health Professional Development Fund (VDTR2017Y11)

REFERENCES

1. De Prost N, Dreyfuss D.How to prevent ventilator-induced lung injury? Minerva Anestesiol 2012; 78:1054-66.
2. Rhodes A, Evans LE, Alhazzani W, et al. Surviving Sepsis Campaign: International Guidelines for Management of Sepsis and Septic Shock:2016. Intensive Care Med 2017; 43: 304-77.
3. Rhee C, Dantes R, Epstein L, et al; CDC Prevention Epicenter Program. Incidence and trends of sepsis in US hospitals using clinical vs claims data 2009-2014. JAMA 2017; 318:12.
4. Herrero R, Sanchez G, Lorente JA. New insights into the mechanisms of pulmonary edema in acute lung injury.Ann Transl Med 2018; 6:32.
5. Luo M, Hong XQ, Zhu H, Li G, Tang L. The HO-1 signal prevents HMGB1-mediated activation of NLRP3 inflammasomes in lipopolysaccharide-induced acute lung injury in vitro. J Surg Res 2019; 4804: 30721-8.
6. He P, Guo Y, Wang J, Yan L, Feng A. Protection of ripasudil, a Rho kinase inhibitor,in lipopolysaccharides-induced acute pneumonia in mice. Am J Transl Res 2019; 11:6433-43.
7. Liu H, Hao J, Wu C, Liu G, Wang X, Yu J, Liu Y, Zhao H. Eupatilin alleviates lipopolysaccharide-induced acute lung injury by inhibiting inflammation and oxidative stress. Med Sci Monit 2019; 25:8289-96.
8. Hillenbrand A, Weiss M, Knippschild U, Wolf AM, Huber-Lang M. Sepsis-induced adipokine change with regard to insulin resistance.Int J Inflam 2012; 2012:972368.
9. Cortese L, Terrazzano G, Pelagalli A. Leptin and immunological profile in obesity and its associated diseases in dogs. Int J Mol Sci 2019; 20: pii: E2392.
10. Dong HY, Xu M, Ji ZY, et al. Leptin Attenuates lipopolysaccharide or oleic acid-induced acute lung injury in mice. Am J Respir Cell Mol Biol 2013; 49:1057-63.
11. Sakr Y, Alhussami I, Nanchal R, et al; Intensive care over nations investigators. being overweight is associated with greater survival in ICU patients: results from the intensive care over nations audit.Crit Care Med 2015; 43:2623–32.
12. Fu S, Liu L, Han L, Yu Y. Leptin promotes IL-18 secretion by activating the NLRP3 inflammasome in RAW 264.7 cells. Mol Med Rep 2017; 16:9770-6.
13. Liu P, Lu Z, Liu L, et al. NOD-like receptor signaling

in inflammation-associated cancers: from functions to targeted therapies. Phytomedicine 2019; 8:152925.
14. Velloso FJ, Trombetta-Lima M, Anschau V, Sogayar MC, Correa RG. NOD-like receptors: major players (and targets) in the interface between innate immunity and cancer. BiosciRep 2019; 39:BSR20181709.
15. Liu H, Gu C, Liu M, Liu G, Wang D, Liu X, Wang Y. Ventilator-induced lung injury is alleviated by inhibiting NLRP3 inflammasome activation. Mol Immunol 2019; 111:1-10.
16. Poh L, Kang SW, Baik SH, et al. Evidence that NLRC4 Inflammasome mediates apoptotic and pyroptotic microglial death following ischemic stroke. Brain Behav Immun 2019; 75:34-47.
17. Zhou Z, Wu Y, Zhang C, et al. Suppression of NF-κB signal pathway by NLRC3-like protein in stony coral Acropora aculeus under heat stress. Fish Shellfish Immunol 2017; 67:322-30.
18. Xia W, Li G, Pan Z, Zhou Q. Hypercapnia attenuates ventilator-induced lung injury through vagus nerve activation. Acta Cir Bras 2019; 34:e201900902.
19. Albaiceta GM, Blanch L. Beyond volutrauma in ARDS: the critical role of lung tissue deformation. Crit Care 2011; 15:304.
20. Caruso P. Ventilator-induced lung injury distribution: the key to understanding injury mechanisms.Am J Respir Crit Care Med 2007; 175 95–6.
21. dos Santos G, Kutuzov MA, Ridge KM. The inflammasome in lung diseases. Am J Physiol Lung Cell Mol Physiol 2012; 303:627–33.
22. Boraschi D, Italiani P, Weil S, Martin MU. The family of the interleukin-1 receptors.Immunol Rev 2018; 281:197-232.
23. Dolinay T, Kim YS, Howrylak J, et al. Inflammasome-regulated cytokines are critical mediators of acute lung injury. Am J Respir Crit Care Med 2012; 185:1225-34.
24. Makabe H, Kojika M, Takahashi G, et al. Interleukin-18 levels reflect the long-term prognosis of acute lung injury and acute respiratory distress syndrome. J Anesth 2012; 26:658-63.
25. Opal SM, Fisher CJ Jr, Dhainaut JF, et al. Confirmatory interleukin-1 receptor antagonist trial in severe sepsis: a phase III, randomized, double-blind, placebo-controlled, multicenter trial. The Interleukin-1 Receptor Antagonist Sepsis Investigator Group. Crit Care Med 1997; 25:1115-24.
26. Ubags ND, Vernooy JH, Burg E, et al. The role of leptin in the development of pulmonary neutrophilia in infection and acute lung injury. Crit Care Med 2014; 42:143-51.
27. Jain M, Budinger GR, Lo A, et al. Leptin promotes fibroproliferative acute respiratory distress syndrome by inhibiting peroxisome proliferator-activated receptor-γ.Am J Respir Crit Care Med 2011; 183:1490-8.
28. Landgraf MA, Silva RC, Corrêa-Costa M, Hiyane MI, Carvalho MH, Landgraf RG, Câmara NO. Leptin downregulates LPS-Induced lung injury: role of corticosterone and insulin. Cell Physiol Biochem 2014; 33: 835-46.
29. Gültekin Y, Eren E, Özören N. Overexpressed NLRC3 acts as an anti-inflammatory cytosolic protein. J Innate Immun 2015; 7:25-36.
30. Wang YC, Liu QX, Zheng Q, et al. Dihydromyricetin alleviates sepsis-induced acute lung injury through inhibiting NLRP3 inflammasome-dependent pyroptosis in mice model.Inflammation 2019; 42:1301-10.
31. Chen H, Ding Y, Chen W, Feng Y, Shi G. Glibenclamide alleviates inflammation in oleic acid model of acute lung injury through NLRP3 inflammasome signaling pathway. Drug Des Devel Ther 2019; 13:1545-54.
32. He Y, Xu K, Wang Y, et al. AMPK as a potential pharmacological target for alleviating LPS-induced acute lung injury partly via NLRC4 inflammasome pathway inhibition.Exp Gerontol 2019; 125:110661.
33. Wang B, Wang J, Lu D, Qi N, Liu Q. The defensive action of LYRM03 on LPS-induced acute lung injury by NF-κB/TLR4/NLRP3 Signals. J Invest Surg 2019; 5:1-13.
34. Martino JL, Stapleton RD, Wang M, Day AG, Cahill NE, Dixon AE, Suratt BT, Heyland DK. Extreme obesity and outcomes in critically ill patients.Chest 2011; 140:1198-206.
35. Huang K, Rabold R, Abston E, et al. Effects of leptin deficiency on postnatal lung development in mice. J Appl Physiol(1985) 2008; 105:249-59.
36. Arteaga-Solis E, Zee T, Emala CW, Vinson C, Wess J, Karsenty G. Inhibition of leptin regulation of parasympathetic signaling as a cause of extreme body

weight-associated asthma. Cell Metab 2013; 17:35-48.
37. Raut PK, Kim SH, Choi DY, Jeong GS, Park PH.Growth of breast cancer cells by leptin is mediated via activation of the inflammasome: Critical roles of estrogen receptor signaling and reactive oxygen species production. Biochem Pharmacol 2019; 161:73-88.
38. Hsu A, Aronoff DM, Phipps J, Goel D, Mancuso P. Leptin improves pulmonary bacterial clearance and survival in ob/ob mice during pneumococcal pneumonia. Clin Exp Immunol 2007; 150:332-9.

Pro-inflammatory and pro-fibrotic role of long non-coding RNA RMRP in pediatric asthma through targeting microRNA-206/CCL2 axis

H. Yin, MH. Liu, F. Gao and HM. Shang

Department of Pediatrics, Western Hospital of Qingdao Municipal Hospital, Qingdao, Shandong, P.R. China

Received August 24, 2020 – Accepted January 7, 2021

Asthma is an inflammatory pulmonary illness that plagues infants and young children. We carried out this investigation to examine the role of long noncoding RNA (lncRNA) RNA component of mitochondrial RNA processing endoribonuclease (RMRP) in an asthmatic mouse model induced by ovalbumin (OVA) and human airway smooth muscle cells (ASMCs). Eight-week-old mice were sensitized with OVA to simulate pediatric asthma. The expression patterns of RMRP, microRNA-206 (miR-206) and C-C motif ligand 2 (CCL2) in pulmonary tissues were evaluated by qPCR. In addition, the concentrations of interleukin (IL)-4, IL-5 and IL-13 cytokines in bronchoalveolar lavage fluid were detected by ELISA. The expression of RMRP and CCL2 was elevated, while miR-206 was reduced in OVA-induced mice. Our findings indicated that administration of RMRP overexpression in ASMCs increased the levels of biomarkers in asthma. RMRP functioned as a sponge for miR-206 to upregulate CCL2 expression. Blockade of the TGF-β/Smad2 signaling pathway in ASMCs overexpressing RMRP suppressed the inflammatory cytokines and cell viability, while enhancing apoptosis. The RMRP/miR-206/CCL2 regulatory axis is implicated in the occurrence of pediatric asthma.

Asthma is a chronic disorder related to inflammation that tends to demonstrate lifelong suffering, with various severity grades throughout the lifetime of sufferers (1). Asthma is estimated to affect more than 300 million people globally, contributing to around 0.4 million deaths each year (2). It is characterized by bronchial airways inflammation, and the main symptoms include cough, wheezing, dyspnea, obstruction of airflow as well as tightness in the chest (3). The majority of pediatric asthma patients are atopic, which means that they produce extra IgE in response to environmental allergens (4). Among all structural changes during asthma, enhanced number of airway smooth muscle cells (ASMCs) is among the most important processes for the consequences of airway remodeling (5).

The functional roles of three types of noncoding RNAs, including long noncoding RNAs (lncRNA), microRNAs (miRNA) as well as messenger RNA (mRNAs) have been recently emphasized in the immune system, and respiratory diseases as well as inflammation-associated disorders (6-8). Moreover, four lncRNAs (RP11-46A10.4, LINC00883, BCYRN1, and LINC00882) have been proposed to act as miRNA sponges for 4 miRNAs (miR-150, miR-371-5p, miR-940 and miR-1207-5p) to maintain primary AMSCs (9). In addition, T cells of patients with rheumatoid arthritis, another autoimmune disease, exhibited elevated expression (2.43-fold) of lncRNA RNA component of mitochondrial RNA processing endoribonuclease (RMRP) (10). RMRP

Key words: long noncoding RNA RMRP; pediatric asthma; CCL2; microRNA-206; TGF-β/Smad2 signaling pathway

Corresponding Author:
Dr Hongmei Shang,
Department of Pediatrics, Western Hospital of Qingdao Municipal Hospital, No.2, Chaocheng Road, Shinan District, Qingdao 266000, Shandong, P.R. China
Tel./Fax: +86-0532-87072752
e-mail: shanghm153@163.com

0393-974X (2021)
Copyright © by BIOLIFE, s.a.s.
This publication and/or article is for individual use only and may not be further reproduced without written permission from the copyright holder.
Unauthorized reproduction may result in financial and other penalties
DISCLOSURE: ALL AUTHORS REPORT NO CONFLICTS OF INTEREST RELEVANT TO THIS ARTICLE.

is overexpressed in a broad range of human and murine tissues and is indispensable for early murine development (11). RMRP has also been validated to function as a sponge for miR-1-5p in septic mice (12). In addition, RMRP acts as an onco-lncRNA in lung cancer and gastric cancer by binding to miR-206 (13, 14). Nevertheless, whether RMRP exerts a regulatory role in asthma through the miR-206 interaction requires to be revealed. Interestingly, circulating miR-206-3p was downregulated after 4,4'-methylene diphenyl diisocyanate exposure, leading to development of occupational asthma (15). Furthermore, miR-206 targeted SOD1 3'UTR to suppress its expression, and the decline of miR-206 was associated with aggravated inflammation and asthmatic symptoms in mice with asthma (16). Consequently, the expression of RMRP and miR-206 in AMSCs was examined in the current investigation, and their regulatory effects on the asthma progression were determined through asthmatic mice as well as in *in vitro* experiments. Furthermore, the underlying molecular mechanisms of RMRP and miR-206 in regulating asthma progression were also explored with the aim of providing possible molecular markers and therapeutic targets for asthma.

MATERIALS AND METHODS

Establishment of a mouse model with asthma

All animal care and experimental protocols were conducted following the Institutional Guidelines for Care and Use of Laboratory Animals of Western Hospital of Qingdao Municipal Hospital. During the present study, 16 8-week.old male C57BL/6 mice (Experimental Animal Center, Hangzhou Normal University, Hangzhou, Zhejiang, China) were maintained in a specific-pathogen-free (SPF) facility with free access to water and food. Ovalbumin (OVA) for the establishment of asthmatic mice was purchased from Sigma-Aldrich Inc. (Grade V, CAS: O1641, Shanghai). From week 0 to week 2, the mice were sensitized weekly via an intraperitoneal injection of 50 mg OVA and 2 mg aluminum hydroxide (Sigma-Aldrich) under SPF conditions. On days 15, 20, and 25, the mice were administered 50 μg OVA via aerosol (3 times a day). Similar procedures were performed on the control mice in the saline group with the OVA substituted by saline. Mice were sacrificed using an intraperitoneal injection of sodium pentobarbital at 150 mg/mL.

Histological staining

The pulmonary tissues of the mice were fixed with 4% paraformaldehyde for 24 h. After dehydration with 80%, 90% and 100% ethanol and n-butanol, the tissues were then embedded in paraffin at 60°C and cut into 5-μm sections. The sections were heated at 60°C for 1 h and dewaxed in xylene. Following the rehydration in an ethanol gradient, the samples were stained with hematoxylin (Beijing Solabio Life Sciences Co., Ltd., Beijing, China) for 2 min and then differentiated with 1% hydrochloric acid for 10 s. Subsequently, the sections were stained with eosin solution for 1 min, dehydrated with gradient ethanol, cleared with xylene, and then sealed. After that, the morphological changes of pulmonary tissues were observed under an optical microscope (XP330, Bingyu, Shanghai, China). The extent of pulmonary inflammation was assessed by infiltration of inflammatory cells around the bronchus as follows: 0, normal; 1, mild infiltration; 2, moderate infiltration; 3, moderate to severe infiltration; 4, great number of cell infiltration.

Detection of pulmonary fibrosis by Masson's trichrome staining

The pulmonary tissues of the mice were fixed in 4% paraformaldehyde for 24 h. After dehydration with 80%, 90% and 100% ethanol and n-butanol, the tissues were then embedded in paraffin at 60°C and dewaxed. After hydration, the tissues were stained with Regaud's hematoxylin solution for 5-10 min and thoroughly washed under distilled water. The tissues were stained with Masson Ponceau acid fuchsin for 5-10 min, then immersed in 2% glacial acetic acid aqueous solution and differentiated with 1% molybdate aqueous solution for 3-5 min. The tissues were stained with aniline blue for 5 min and then immersed in 0.2% glacial acetic acid aqueous solution. The tissues were dehydrated with gradient ethanol, cleared with xylene and sealed. Finally, the tissues were observed under a microscope, and the collagen deposition area was quantitatively analyzed using ImageJ image analysis software (NIH, Bethesda, MD, USA).

Immunohistochemical staining

The α-SMA expression in tissues was determined

using immunohistochemical staining. After paraffin-dewaxing, the sections were incubated in 0.01 mol/L citrate buffer (pH = 6.0) for 15 min for antigen revival. The sections were then cooled, incubated in 3 g/L H_2O_2 for 30 min to inactivate endogenous peroxidase and then blocked with normal horse serum (diluted at 1:10) for 30 min. After the removal of the supernatant, the sections were incubated with the α-SMA primary antibody (1:500, 19245, Cell Signaling Technology, Beverly, MA, USA) at 4°C followed by the addition of horseradish peroxidase (HRP)-labelled goat anti-rabbit antibody to IgG (ab6271, Abcam, Cambridge, UK) and streptavidin-scaprogen peroxidase. The stained cells were then loaded and observed using an optical microscope.

Enzyme-linked immunosorbent assay (ELISA)

Bronchoalveolar lavage (BAL) was washed three times with 1.2 mL phosphate buffered saline (PBS). The BAL was collected in a cryogenic centrifuge at 4°C and then centrifuged at 450 ×g for 10 min, and the supernatant was preserved at -20°C. Subsequently, IL-4 (ab221833), IL-5 (ab204523) and IL-13 (ab619434) levels in the supernatant were determined using ELISA kits (Abcam). In short, each well was blocked with a blocking buffer for 2 h and washed with a buffer. Antibodies against IL-4, IL-5 and IL-13 were added to the medium and incubated for 1 h. The substrate solution and termination solution were supplemented, and an automated microplate reader (BioTek Instruments, Winooski, VT, USA) was applied to determine the optical density (OD) value of each well within 30 min.

BAL fluid neutrophil counts

The BAL fluid was centrifuged at 225 ×g for 10 min, and then the supernatant was removed. The cell precipitate was resuspended to prepare glass slides for staining. The percentage of eosinophils (EOS) in total leukocytes was calculated by counting cells under an optical microscope.

Real-time reverse transcription-quantitative polymerase chain reaction (RT-qPCR)

Total RNA was isolated from cells or tissues using Trizol reagent (Takara Bio, Shiga, Japan). The cDNA was synthesized using the Prime Script RT kit (Takara) and the miRNA reverse transcription was performed using a PrimeScript miRNA cDNA synthesis kit (Takara). Then, real-time qPCR was performed using SYBR Premix ExTaq (Takara). The primer sequences are displayed in Table I. Relative mRNA expression of all genes was normalized to control glyceraldehyde-3-phosphate dehydrogenase (GAPDH), while that of miRNA was normalized to U6. The relative expression of target genes was calculated by using the comparative $2^{-\Delta\Delta Ct}$ method.

Western blot analysis

Proteins were extracted from tissues or cells after 20 min of lysis and centrifugation in radio immunoprecipitation assay buffer (Santa Cruz Biotechnology Inc., Santa Cruz, CA, USA). The concentration of protein samples was quantified using the Bradford method. After sodium dodecyl sulfate polyacrylamide gel electrophoresis to isolate the equal amount of protein, the protein was then transferred to a polyvinylidene difluoride membrane (Millipore, Bedford, MA, USA) and probed at 4°C for 24 h with the primary antibodies. The membrane was cultured with the secondary antibody for 2 h at room temperature. Antibodies applied for Western blot analysis included transforming growth factor-β (TGF-β, 5544, Cell Signaling Technology), Smad2 (5339, Cell Signaling Technology) and phospho-Smad2 (Ser 465/Ser 467, 18338, Cell Signaling Technology).

Luciferase reporter assay

The bioinformatics prediction website StarBase (http://starbase.sysu.edu.cn/) was applied to predict the sequence of binding sites between miR-206 and RMRP or CCL2, which was verified using a dual-luciferase reporter gene assay. H293T cells were co-transfected with RMRP or CCL2 recombinant plasmids, including RMRP-wild type (WT), RMRP-mutant (MT), CCL2-WT and CCL2-MT and miR-206 mimic or mimic control. The luciferase activity was measured using a dual-luciferase assay kit (Promega, Madison, WI, USA) with the addition of a firefly or renilla luciferase reagent following the manufacturer' s instructions.

Culture and treatment of human AMSCs

AMSCs were obtained from the Cell Bank of Shanghai Institute of Cells, Chinese Academy of Science (Shanghai, China). The cells were grown in Dulbecco's modified Eagle's medium containing 10% fetal bovine serum, 100 IU/mL penicillin,100 μg/mL streptomycin, 2 mM L-glutamine and 20 mM hydroxyethyl piperazine ethanesulfonic acid, and cultured at 37°C in humidified air

containing 5% CO_2. Subsequently, the well-grown AMSCs were treated with empty plasmid pcDNA3.1, pcDNA3.1-RMRP overexpression plasmid (100 nmol), scramble siRNA (100 nmol), three siRNAs targeting RMRP (100 nmol), RMRP + Mock (transfected with 50 nmol mimic control in the presence of RMRP overexpression), RMRP + miR-206 (transfected with 50 ng miR-206 mimic in the presence of RMRP overexpression), si-RMRP + Empty (transfected with empty plasmid pcDNA3.1 in the presence of RMRP knockdown), si-RMRP + CCL2 (transfected with pcDNA3.1-CCL2 overexpression plasmid in the presence of RMRP knockdown), RMRP + dimethylsulfoxide (treated with DMSO in the presence of RMRP overexpression), RMRP + 5-methyl-1-phenyl-2-(1H)-pyridone (treated with 0.3 mg/mL Pirfenidone, the TGF-β/Smad2 signaling pathway inhibitor, in the presence of RMRP overexpression) (17-20). RMRP overexpression plasmids, small interfering RNA (siRNA) targeting RMRP, and miR-206 mimic and the corresponding mimic control were synthesized and obtained from Shanghai Sangon Biological Engineering Technology & Services Co., Ltd. (Shanghai, China). The sequence information is shown in the Table II.

Acridine orange/ethidium bromide (AO/EB) staining

AO/EB staining could identify survival cells, early apoptotic cells and late apoptotic cells. In short, AMSCs were treated with AO (150 μg/mL) at room temperature for 10 min and with EB (150 μg/mL) for 10 min. The cells were then examined under a fluorescence microscope (Leica Microsystems GmbH, Wetzlar, Germany). Orange-stained cells were dead cells and green-labeled cells were living cells.

Table I. *Primer sequences for RT-qPCR*

Targets	Sequence (5'- 3')
RMRP	Forward: CAAGGAAGTATTGAAGATGAAGCTATG
RMRP	Reverse: CCATAAGAACGGAGGGACATT
CCL2	Forward: GAAGTCTGGGAATCGATCTGG
CCL2	Reverse: TCCCATCAATCTTCAGCACTC
miR-206	Forward: CCCGCACGATTTCATTGAAC
miR-206	Reverse: GGCGGATTGGAAATGAACTTC
GAPDH	Forward: GAAGGTGAAGGTCGGAGTC
GAPDH	Reverse: GAAGATGGTGATGGGATTTC

Note: RMRP, RNA component of mitochondrial RNA processing endoribonuclease; CCL2, C-C motif ligand 2; miR-206, microRNA-206; GAPDH, glyceraldehyde-3-phosphate dehydrogenase; RT-qPCR, quantitative real-time polymerase chain reaction.

Table II. *Sequence*

RMRP-siRNA	5'-CTGAGGACGTGGGATGATCATGGACATGAGGATTACCCATGTACTAGAGATCTCGTACACCA TCAGGGTACGTTCCAGCTAGCT-3'
miR-206 mimic	3'-GGUGUGUGAAGGAAUGUAAGGU-5'
miR-206 inhibitor	3'-ACCUUACAUUCCUUCACACACC-5'

Note: siRNA, small interfering RNA; miR, microRNA.

Cell counting kit-8 (CCK-8) assay

The transfected cells were plated into a 96-well plate at a density of 1500 cells/well and cultured for up to 72 h. Subsequently, cells were treated with 20 mL CCK-8 (5 mg/mL) for another 4 h. The OD value was measured at the wavelength of 570 nm by a plate reader (Bio-Rad, Hercules, CA, USA) after the addition of 100 mL DMSO.

β-galactosidase staining

Cellular senescence-related β-galactosidase staining was carried out using a β-galactosidase staining kit (Beyotime, Shanghai, China) following the manufacturer' s instructions. In short, the cells were plated in a 6-well plate and pre-treated. The cells were gently washed with PBS and fixed with a fixing solution. Afterwards, the cells in each well were stained with 1 mL staining solution, then sealed with paraffin film and incubated at 37°C free of CO_2 overnight.

Cell apoptosis detection

The transfected cells under good growth condition were stained with an Annexin V- fluorescein isothiocyanate (FITC)/propidium iodide (PI) apoptosis detection kit as per the manufacturer's instructions. Cells were first detached with ethylenediaminetetraacetic acid-free trypsin in a cell culture dish, transferred to a 15 mL centrifuge tube and centrifuged at 3000 rpm for 5 min at 4°C. Subsequently, cells were gently mixed with 4 mL pre-cooled PBS, then reacted with 5 μL Annexin V-FITC and 5 μL PI reagent for 15 min under light-avoiding conditions and analyzed by a flow cytometer. The data were analyzed with FlowJo software.

Immunofluorescence staining

ASMCs were fixed with 4% paraformaldehyde for a period of 30 min. Then the cells were permeabilized with 0.2% Triton X-100 in 1% bovine serum albumin (BSA) for 10 min, sealed with 3% BSA for 1 h at room temperature, and then incubated overnight with anti-α-SMA (19245, Cell Signaling Technology) at 4°C. The cells were then probed with the secondary FITC-conjugated goat anti-rabbit antibody to IgG (1:200, ab6717, Abcam) for 1 h. The expression of α-SMA was analyzed using a microscope (Leica Microsystems GmbH, Wetzlar, Germany).

Statistical analysis

The data statistical analysis was performed by SPSS 22.0 software (IBM Corp., Armonk, NY, USA). Numerical data are displayed as mean ± standard deviation (SD). Two group comparisons were performed with an unpaired *t*-test. One-way or two-way analysis of variance (ANOVA) was applied to access the statistical significance between multiple groups and Tukey's to test significance between specific groups. $p < 0.05$ was considered as statistically significant differences between different groups.

RESULTS

RMRP is increased in asthmatic mice

We first simulated a mouse asthma model by treating mice with OVA. The results of HE staining showed that the airways of OVA-sensitized mice were extensively damaged, including cell infiltration in the upper subcutaneous space and obvious exfoliation of the epithelium. There were also a large number of neutrophils, macrophages and EOSs (Fig. 1A) in the airway. Subsequently, we performed Masson's staining on mouse pulmonary tissues to detect collagen production in pulmonary tissues for pulmonary fibrosis assessment. OVA-treated mice showed significant levels of pulmonary fibrosis (Fig. 1B). Moreover, we performed α-SMA immunohistochemical staining on mouse pulmonary tissues and found that the OVA-treated mice had higher levels of α-SMA expression in pulmonary tissues, indicating that the OVA-treated mice had significant fibrotic changes in pulmonary tissues (Fig. 1C). Subsequently, by detecting the expression of inflammatory factors in the mouse BAL fluid, we found that IL-4, IL-5 and IL-13 (Fig. 1D) were significantly increased in the mice treated with OVA. Moreover, after OVA treatment, the number of EOSs, neutrophils, lymphocytes and monocytes in mouse pulmonary tissues increased significantly (Fig. 1E). The above results indicated that the asthmatic mouse model was successfully induced by OVA. Afterwards, we evaluated the RMRP, miR-206, and CCL2 expression in mouse pulmonary tissues by RT-qPCR, which revealed that RMRP and CCL2 expression in mice treated with OVA was higher than that in control mice, whereas miR-206 was reduced in OVA-treated mice (Fig. 1F).

RMRP promotes CCL2 expression through competitively binding to miR-206

To verify the relationships between miR-206

and RMRP or CCL2, we predicted the binding site sequence between miR-206 and RMRP or CCL2 by using the bioinformatics prediction website StarBase (http://starbase.sysu.edu.cn/). Subsequently, we examined the binding relationships between miR-206 and RMRP or CCL2 with the dual-luciferase assays. It was found that miR-206 has binding relationships with RMRP and CCL2 3'UTR (Fig. 2A, B). To

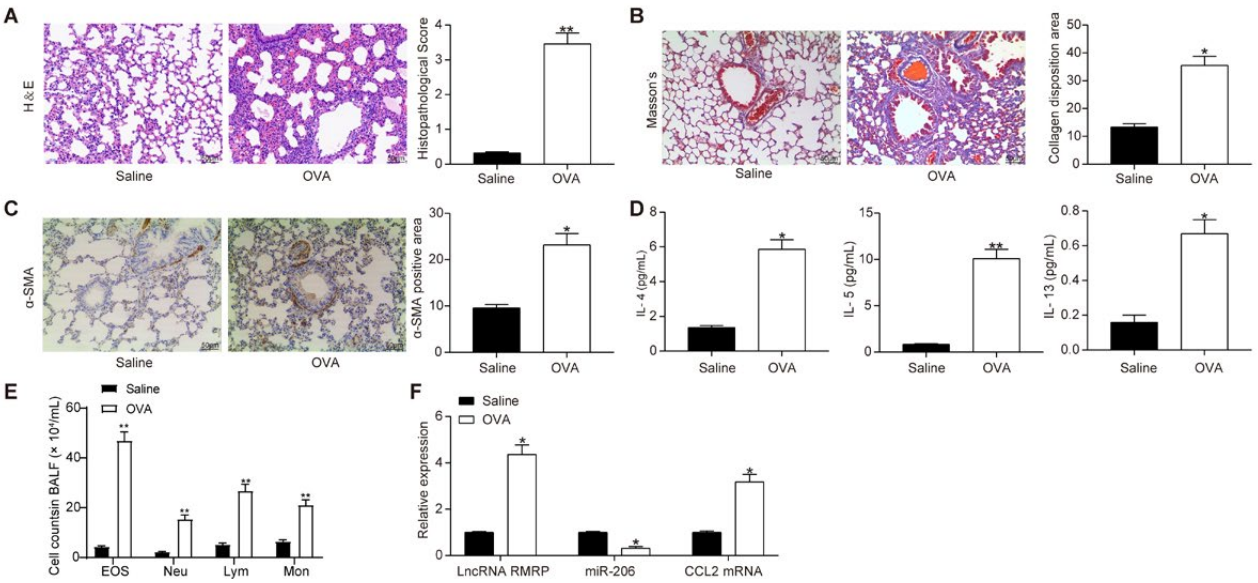

Fig. 1. *RMRP is highly expressed in pulmonary tissues of asthmatic mice. A total of 16 mice were either sensitized with OVA or treated with saline (n = 8).* ***A****)Oobservation of pathological structure in pulmonary tissues by HE staining;* ***B****) detection of collagen formation in pulmonary tissues by Masson's staining;* ***C****) immunohistochemical staining of α-SMA expression in mouse pulmonary tissue;* ***D****) the levels of inflammatory factors IL-4, IL-5 and IL-13 in mice detected by ELISA;* ***E****) number of EOS, neutrophils, lymphocytes and monocytes in mouse BAL fluids;* ***F****) the RMRP and miR-206 expression as well as CCL2 mRNA expression in mouse pulmonary tissues determined by RT-qPCR. Data are displayed as the mean ± SD of three independent experiments. Statistical significance was tested using unpaired t test (A-E) or two-way ANOVA (F) with the Tukey's multiple comparison post hoc test; *p < 0.05, **p < 0.01.*

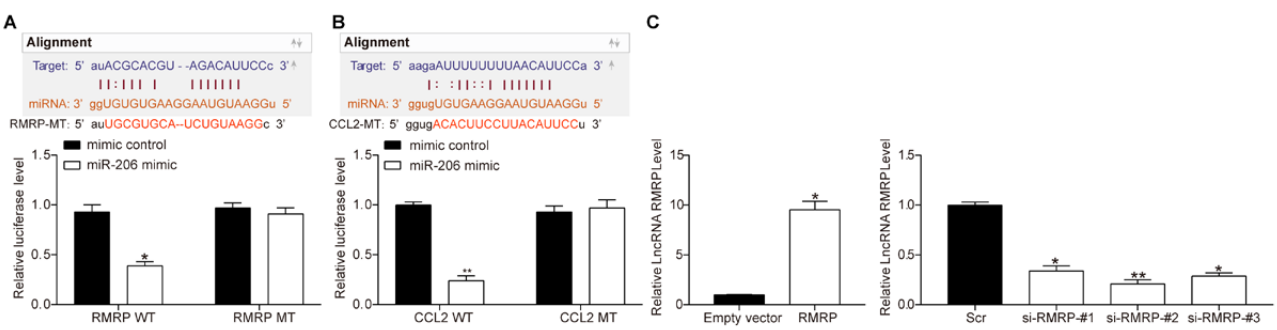

Fig. 2. *RMRP promotes CCL2 expression through competitively binding to miR-206.* ***A****) Binding sites between miR-206 and RMRP predicted by StarBase (http://starbase.sysu.edu.cn/) and verified through a dual-luciferase assay;* ***B****) the binding sites between miR-206 and CCL2 predicted by StarBase (http://starbase.sysu.edu.cn/) and verified through a dual-luciferase assay. Three siRNAs targeting RMRP and RMRP overexpression plasmids were transfected into AMSCs, respectively.* ***C****) the RMRP expression in the cells following transfection assessed by RT-qPCR. Data are displayed as the mean ± SD of three independent experiments. Statistical significance was tested using two-way (A, B) or one-way ANOVA (C) with the Tukey's multiple comparison post hoc test; *p < 0.05, **p < 0.01.*

further clarify the role of RMRP in pediatric asthma, we transfected RMRP overexpressing plasmid and three siRNAs targeting RMRP in human AMSCs, respectively, and collected cells at 48 h post-transfection. RT-qPCR results showed successful transfection (Fig. 2C).

RMRP knockdown promotes apoptosis of AMSCs and inhibits inflammatory response

First, we performed AO/EB staining on the cells. The results displayed that the number of orange cells in AMSCs with overexpression of RMRP was smaller than that in the control cells, whereas the number of orange cells in the cells with RMRP knockdown was increased, which proved that upregulation of RMRP in AMSCs inhibited cell apoptosis (Fig. 3A). Then, we further examined the proportion of apoptotic cells in each group of AMSCs by flow cytometry. We observed that after overexpression of RMRP, the levels of early or late apoptotic cells decreased significantly, but RMRP knockdown contributed to the opposite results (Fig. 3B). Moreover, we tested the levels of inflammatory factors produced by AMSCs using ELISA and found that overexpression of RMRP promoted AMSCs to secrete IL-4, IL-5 and IL-13. After RMRP knockdown, the IL-4, IL-5 and IL-13 levels were notably reduced in AMSCs (Fig. 3C).

RMRP knockdown represses fibrosis and cell viability of AMSCs

Subsequently, we examined AMSC viability through the CCK-8 kit and noted that overexpression of RMRP promoted cell proliferation, whereas RMRP knockdown inhibited AMSC proliferation (Fig. 4A). Moreover, we found by β-galactosidase staining that overexpression of RMRP inhibited cell senescence, whereas inhibition of RMRP increased the proportion of senescent cells in AMSCs (Fig. 4B). The determination of fibrocyte surface marker α-SMA expression by immunofluorescence staining

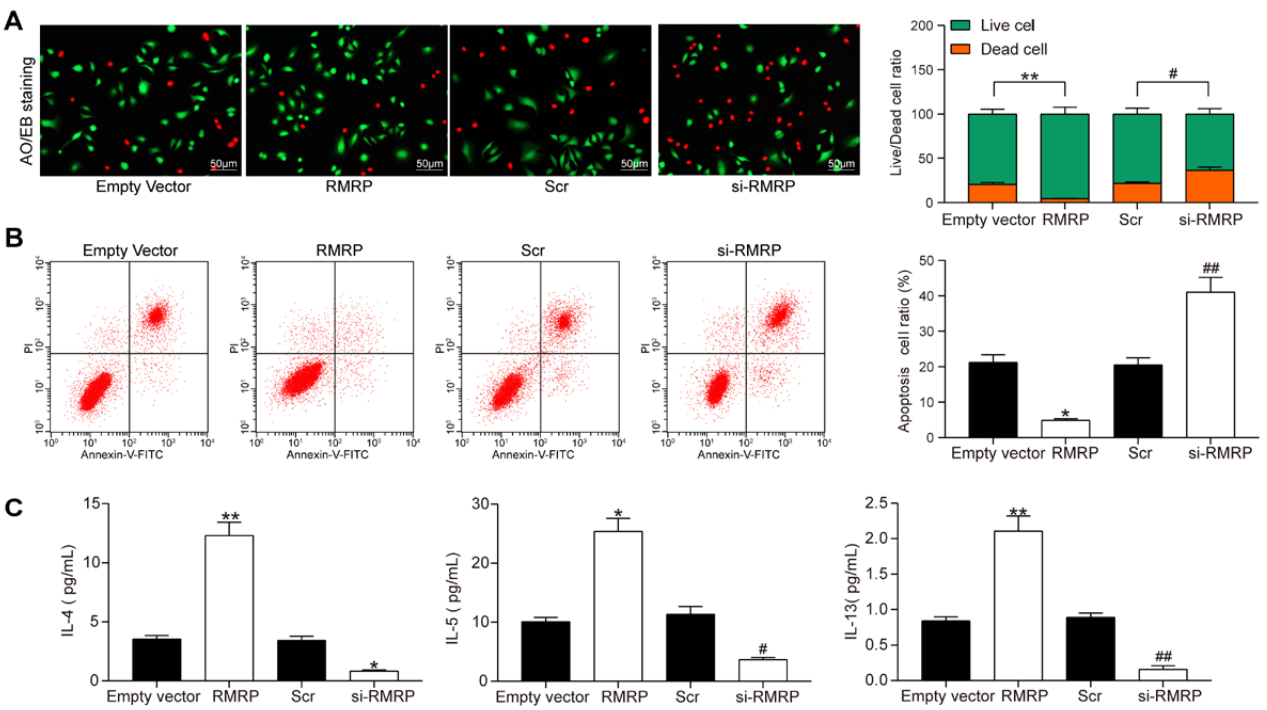

Fig. 3. *RMRP knockdown inhibits the recruitment of inflammatory cells and facilitates apoptosis in AMSCs.* ***A****) Proportion of living cells/dead cells detected by AO/EB staining;* ***B****) detection of apoptotic cells by flow cytometry;* ***C****) the levels of inflammatory factors IL-4, IL-5 and IL-13 in mice detected by ELISA. Data are displayed as the mean ± SD of three independent experiments. Statistical significance was tested using two-way (A) or one-way ANOVA (B, C) with the Tukey's multiple comparison post hoc test; *p < 0.05, **p < 0.01 vs. the empty vector group; #p < 0.05, ##p < 0.01 vs. the Scr group.*

illustrated that enhanced RMRP expression promoted α-SMA expression in AMSCs, while diminished RMRP expression reduced the α-SMA expression (Fig. 4C). Moreover, the miR-206 and CCL2 expression was assessed in cells under different treatments and found that miR-206 expression was inhibited in the cells overexpressing RMRP, while CCL2 expression was enhanced, and miR-206 and CCL2 expression in the ASMCs with RMRP knockdown illustrated an opposite trend (Fig. 4D).

miR-206 mimic weakens the promotive role of RMRP in AMSC apoptosis and inflammatory response

To further verify the role of the RMRP/miR-206/CCL2 axis in asthma, we overexpressed miR-206 in ASMCs overexpressing RMRP and overexpressed CCL2 in ASMCs with RMRP knockdown. After 48 h of transfection, the successful transfection was verified by RT-qPCR (Fig. 5A). After the simultaneous overexpression of miR-206 and RMRP, we found that ASMC apoptosis levels were promoted, while cell viability and the levels of inflammatory factors were significantly reduced (Fig. 5B-D). Moreover, after CCL2 restoration in the cells with RMRP knockdown, the number of apoptotic ASMCs was significantly reduced, whereas the cell viability and the level of inflammatory factors were significantly enhanced (Fig. 5B-D).

RMRP promotes the progression of asthma by activating the TGF-β/Smad2 signaling pathway

To further illustrate the downstream molecular mechanism of RMRP, we examined the expression of TGF-β1 and Smad2 in ASMCs through Western blot analysis. TGF-β1 was notably activated, while the phosphorylation of the Ser465/Ser467 site of Smad2 was significantly reduced in the cells expressing RMRP. Furthermore, the activation level of the signaling pathway was significantly reduced after further overexpression of miR-206. By contrast, in cells with RMRP knockdown, we found that the TGF-β/Smad2 signaling pathway was disrupted, but after further overexpression of CCL2, the activation level of the TGF-β/Smad2 signaling pathway was induced (Fig. 6A).

Thus, to excavate the effect of the TGF-β/Smad2 signaling pathway on asthma, we added a TGF-β/Smad2 signaling pathway-specific inhibitor, Pirfenidone, to ASMCs overexpressing RMRP. We monitored that apoptosis levels were significantly promoted, and the levels of inflammatory factors and cell viability were significantly reduced (Fig. 6 B-D).

DISCUSSION

Asthma, a heterogeneous disorder, is characterized by airway inflammation, obstruction, hyperresponsiveness and remodeling, and the

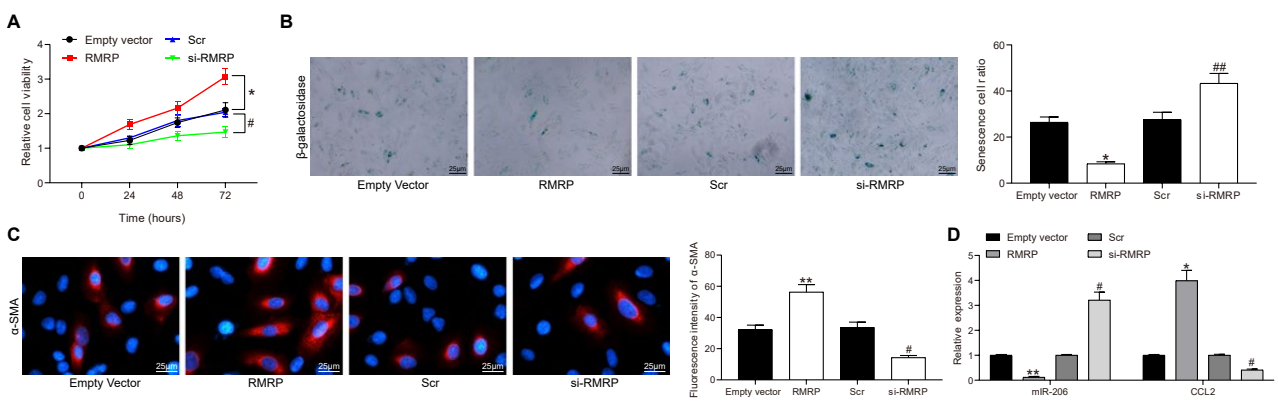

Fig. 4. *RMRP knockdown inhibits the viability and fibrosis of ASMCs.* ***A****) ASMC viability assessed by CCK-8 kits;* ***B****) detection of senescence ratio by β-galactosidase staining;* ***C****) immunofluorescence staining of α-SMA expression in ASMCs;* ***D****) the expression of miR-206 and CCL2 mRNA in cells after transfection measured by RT-qPCR. Data are displayed as the mean ± SD of three independent experiments. Statistical significance was tested using two-way (A, D) or one-way ANOVA (B, C) with the Tukey's multiple comparison post hoc test; *p < 0.05, **p < 0.01 vs. the empty vector group; #p < 0.05, ##p < 0.01 vs. the Scr group.*

relevance of lncRNAs has been indicated in pediatric airway diseases and asthma (21, 22). Herein, we show that the number of EOSs, neutrophils, lymphocytes and monocytes, the secretion of inflammatory factors and pulmonary fibrosis were enhanced in asthmatic mice compared with control mice. The RMRP and CCL2 expression was higher, while miR-206 was lower in asthmatic mice than in control mice. Knockdown of RMRP reduced inflammatory response, pulmonary fibrosis and ASMC proliferation. miR-206 mimic diminished the promotive role of RMRP in ASMCs, while CCL2 overexpression reversed the suppressive role of RMRP knockdown in ASMCs. Finally, RMRP significantly induced

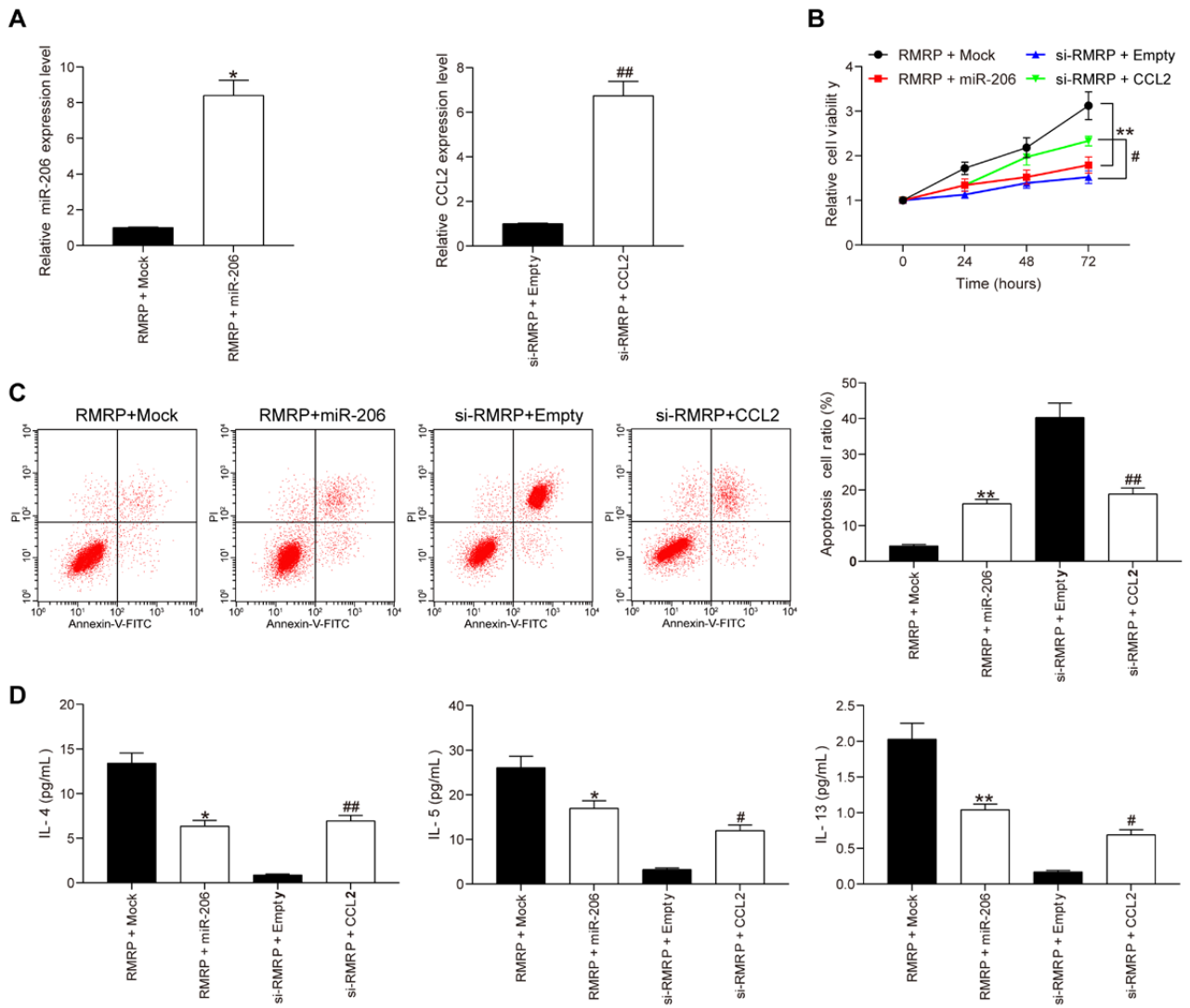

Fig. 5. *miR-206 mimic or CCL2 overexpression reverses the effects of RMRP overexpression or knockdown on ASMCs. ASMCs were co-transfected with RMRP + miR-206 or si-RMRP + CCL2. A) Expression of miR-206 and CCL2 mRNA in cells after transfection measured by RT-qPCR; B) ASMC viability assessed by CCK-8 kits; C) detection of apoptotic cells by flow cytometry; D) the levels of inflammatory factors IL-4, IL-5 and IL-13 in mice detected by ELISA. Data are displayed as the mean ± SD of three independent experiments. Statistical significance was tested using unpaired t test (A), two-way (B) or one-way ANOVA (C, D) with the Tukey's multiple comparison post hoc test; *p < 0.05, **p < 0.01 vs. the RMRP + Mock group; #p < 0.05, ##p < 0.01 vs. the si-RMRP + Empty group.*

the TGF-β/Smad2 signaling pathway, while the pathway-specific inhibitor abrogated the promotive effects of RMRP on inflammatory response and proliferation of AMSCs. Taken together, the results suggested that RMRP regulated ASMC proliferation and inflammatory response via miR-206/CCL2 in pediatric asthma with the participation of the TGF-β/Smad2 signaling pathway.

LncRNAs with more than 200 nucleotides have been implicated in several biological events through many mechanisms, involving chromatin modification, transcriptional translation, and post-transcriptional regulation (23). Various lncRNAs, such as TCF7, GAS5, BCYRN1 and TUG1 have been indicated to regulate the viability and migration of AMSCs through binding to different targets (24-27). Furthermore, silencing of RMRP impeded the growth and metastasis of papillary thyroid cancer cells by sponging miR-675 and downregulating mitogen-activated protein kinase 1 (28). RMRP has the potency to inversely modulate the miR-613 expression in hepatocellular carcinoma by performing as a competitive endogenous RNA (29). Notably, delivery of RMRP siRNA markedly ameliorated hypoxia-induced injury by enhancing cell viability and reducing cell apoptosis; whereas forced expression of RMRP exacerbated hypoxia-induced injury by serving as an endogenous sponge for miR-214-5p (30). In the current work, we provide strong evidence suggesting that depletion of RMRP by siRNA remarkably repressed inflammatory response and proliferation of AMSCs, while facilitating AMSC apoptosis. On the contrary, miR-206 mimic could counteract the promotive effects of RMRP on AMSC inflammation and proliferation. Interestingly, Kho et al. revealed that hsa-miR-206 was closely linked to asthma exacerbations in children with an odds ratio of 0.60 (31).

Bioinformatic analysis predicted that miR-206 targets CCL2. Hence, the regulatory effect of CCL2 on the function of AMSCs was also examined. CCL2 was markedly enhanced in pulmonary tissues of mice challenged with OVA, and overexpression of CCL2 was observed to reverse the role of RMRP repression on AMSC inflammation and proliferation enhancement. Consistently, increased levels of CCL2, correlated to an airway immune profile, have been identified as an independent predictor for the progression of asthma (32). Moreover, the protective effects of the CCL2/CCL2 receptor signaling deficits in inflammatory monocytes has been established in an OVA-induced asthmatic mouse model by inhibiting

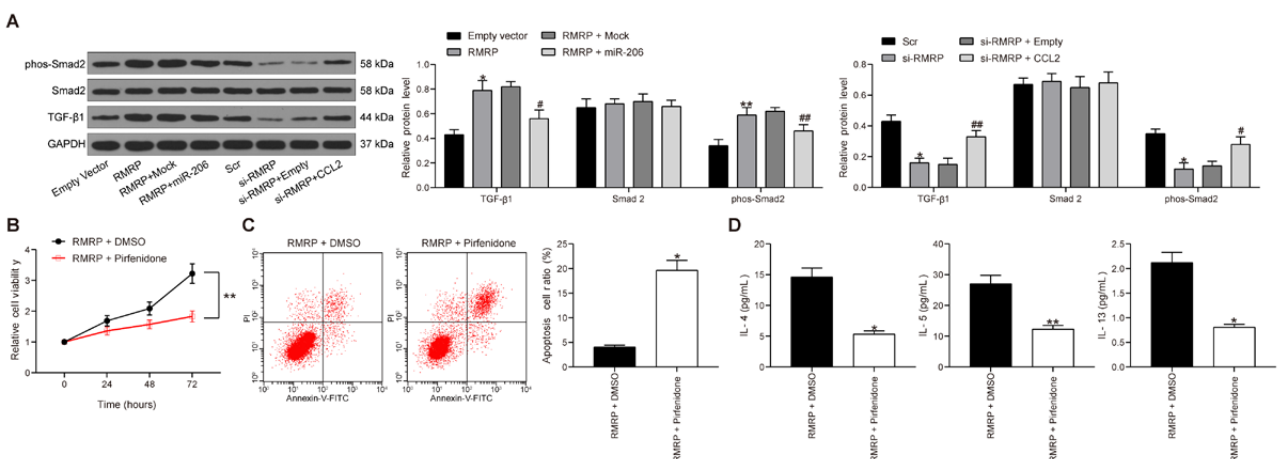

Fig. 6. *RMRP exerts its function through the TGF-β/Smad2 signaling pathway in AMSCs.* ***A****) Protein expression of TGF-β and Smad2 as well as Smad2 phosphorylation level in AMSCs tested by western blot analysis;* ***B****) ASMC viability assessed by CCK-8 kits;* ***C****) detection of apoptotic cells by flow cytometry;* ***D****) the levels of inflammatory factors IL-4, IL-5 and IL-13 in mice detected by ELISA. Data are displayed as the mean ± SD of three independent experiments. Statistical significance was tested using two-way (A, B) with the Tukey's multiple comparison post hoc test or unpaired t test (C, D); *p < 0.05, **p < 0.01 vs. RMRP + DMSO group (panel B-D).*

the inflammatory response of Th2 cells (33). More specifically, the TGF-β1/Smad2 signaling pathway was activated in AMSCs overexpressing RMRP, which was further impaired by miR-206 mimic. Moreover, the signaling was disrupted by RMRP knockdown in AMSCs, while further restored by CCL2 overexpression as evidenced by enhanced TGF-β1 expression and Smad2 phosphorylation. Consistently, administration of resveratrol during OVA sensitization suppressed airway inflammation and remodeling by inhibiting TGF-β1 signaling and suppressing the extent of Smad2/3 phosphorylation (34). In addition, Paw et al. believed that Fenofibrate impeded the activation of the TGF-β1/Smad signaling pathway in human bronchial fibroblasts, thus preventing bronchial remodeling in the process of asthma (35). Pirfenidone, a low-molecular weight compound, was first acknowledged as an anti-inflammatory drug agent and then developed as an anti-fibrotic drug, and has been approved by the Food & Drug Administration (US) as one of the two drugs for idiopathic pulmonary fibrosis (36). A previous study conducted by Mansoor et al. identified the anti-inflammatory role of Pirfenidone in a rat model of asthma (37). However, the particular role of Pirfenidone in AMSCs during asthma has not yet been clarified. We provided evidence in the present study that Pirfenidone could also accelerate AMSC apoptosis and inhibit its proliferation as well as inflammation.

In summary, these findings suggest that RMRP downregulated miR-206 expression and upregulated CCL2, and CCL2 expression was suppressed by miR-206, which suggests that RMRP could upregulate CCL2 through sponging miR-206. Even though additional research is necessary for clinical applications, this work has provided a basis for the important role of RMRP in abnormal ASMC proliferation and inflammation in asthma through the miR-206/CCL2/TGF-β1/Smad2 network.

REFERENCES

1. Nunes C, Pereira AM, Morais-Almeida M. Asthma costs and social impact. Asthma Res Pract 2017; 3:1.
2. Niespodziana K, Borochova K, Pazderova P, et al. Towards personalization of asthma treatment according to trigger factors. J Allergy Clin Immunol 2020; 145(6):1529-34.
3. Ingawale DK, Mandlik SK, Patel SS. Combination of Sarsasapogenin and Fluticasone attenuates ovalbumin-induced airway inflammation in a mouse asthma model. Immunopharmacol Immunotoxicol 2020; 42:128-37.
4. Sandford AJ. Asthma susceptibility: The role of transforming growth factor beta1. Respirology 2010; 15:583-84.
5. Salter B, Pray C, Radford K, Martin JG, Nair P. Regulation of human airway smooth muscle cell migration and relevance to asthma. Respir Res 2017; 18:156.
6. Booton R, Lindsay MA. Emerging role of MicroRNAs and long noncoding RNAs in respiratory disease. Chest 2014; 146:193-204.
7. Marques-Rocha JL, Samblas M, Milagro FI, Bressan J, Martinez JA, Marti A. Noncoding RNAs, cytokines, and inflammation-related diseases. FASEB J 2015; 29:3595-611.
8. Turner M, Galloway A, Vigorito E. Noncoding RNA and its associated proteins as regulatory elements of the immune system. Nat Immunol 2014; 15:484-91.
9. Perry MM, Tsitsiou E, Austin PJ, Lindsay MA, Gibeon DS, Adcock IM, Chung KF. Role of non-coding RNAs in maintaining primary airway smooth muscle cells. Respir Res 2014; 15:58.
10. Moharamoghli M, Hassan-Zadeh V, Dolatshahi E, Alizadeh Z, Farazmand A. The expression of GAS5, THRIL, and RMRP lncRNAs is increased in T cells of patients with rheumatoid arthritis. Clin Rheumatol 2019; 38:3073-80.
11. Rosenbluh J, Nijhawan D, Chen Z, Wong KK, Masutomi K, Hahn WC. RMRP is a non-coding RNA essential for early murine development. PLoS One 2011; 6:e26270.
12. Han Y, Cai Y, Lai X, et al. lncRNA RMRP Prevents mitochondrial dysfunction and cardiomyocyte apoptosis via the miR-1-5p/hsp70 axis in LPS-Induced sepsis mice. Inflammation 2020; 43:605-18
13. Meng Q, Ren M, Li Y, Song X. LncRNA-RMRP Acts as an Oncogene in Lung Cancer. PLoS One 2016; 11:e0164845.
14. Shao Y, Ye M, Li Q, et al. LncRNA-RMRP promotes

carcinogenesis by acting as a miR-206 sponge and is used as a novel biomarker for gastric cancer. Oncotarget 2016; 7:37812-24.
15. Lin CC, Law BF, Hettick JM. Acute 4,4'-Methylene Diphenyl diisocyanate exposure-mediated downregulation of miR-206-3p and miR-381-3p activates inducible nitric oxide synthase transcription by targeting calcineurin/NFAT signaling in macrophages. Toxicol Sci 2020; 173:100-113.
16. Wang L, Xu J, Liu H, Li J, Hao H. PM2.5 inhibits SOD1 expression by up-regulating microRNA-206 and promotes ROS accumulation and disease progression in asthmatic mice. Int Immunopharmacol 2019; 76:105871.
17. Brooks D, Zimmer A, Wakefield L, et al. Limited fibrosis accompanies triple-negative breast cancer metastasis in multiple model systems and is not a preventive target. Oncotarget 2018; 9:23462-81.
18. Chen C, Yao X, Xu Y, et al. Dahuang Zhechong Pill suppresses colorectal cancer liver metastasis via ameliorating exosomal CCL2 primed pre-metastatic niche. J Ethnopharmacol 2019; 238:111878.
19. Qin W, Liu B, Yi M, Li L, Tang Y, Wu B, Yuan X. Antifibrotic agent pirfenidone protects against development of radiation-induced pulmonary fibrosis in a murine model. Radiat Res 2018; 190:396-403.
20. Zhang Y, Zhou X, Yin C, Wu Y, Wang L. Overexpression of ERbeta inhibits the proliferation through regulating TNG-beta signaling pathway in osteosarcoma. Pathol Res Pract 2019; 215:152568.
21. Narozna B, Langwinski W, Szczepankiewicz A. Non-Coding RNAs in pediatric airway diseases. Genes (Basel) 2017; 8(12):348.
22. Zhang J, Zhu Y, Wang R. Long noncoding RNAs in respiratory diseases. Histol Histopathol 2018; 33:747-56.
23. Yu X, Zhe Z, Tang B, et al. alpha-Asarone suppresses the proliferation and migration of ASMCs through targeting the lncRNA-PVT1/miR-203a/E2F3 signal pathway in RSV-infected rats. Acta Biochim Biophys Sin (Shanghai) 2017; 49:598-608.
24. Fan M, Xu J, Xiao Q, Chen F, Han X. Long non-coding RNA TCF7 contributes to the growth and migration of airway smooth muscle cells in asthma through targeting TIMMDC1/Akt axis. Biochem Biophys Res Commun 2019; 508:749-55.
25. Lin J, Feng X, Zhang J, Tong Z. Long noncoding RNA TUG1 promotes airway smooth muscle cells proliferation and migration via sponging miR-590-5p/FGF1 in asthma. Am J Transl Res 2019; 11:3159-66.
26. Zhang XY, Tang XY, Li N, et al. GAS5 promotes airway smooth muscle cell proliferation in asthma via controlling miR-10a/BDNF signaling pathway. Life Sci 2018; 212:93-101.
27. Zhang XY, Zhang LX, Tian CJ, et al. LncRNAs BCYRN1 promoted the proliferation and migration of rat airway smooth muscle cells in asthma via upregulating the expression of transient receptor potential 1. Am J Transl Res 2016; 8:3409-18.
28. Wang J, Xiao T, Zhao M. MicroRNA-675 directly targets MAPK1 to suppress the oncogenicity of papillary thyroid cancer and is sponged by long non-coding RNA RMRP. Onco Targets Ther 2019; 12:7307-21.
29. Zhou N, He Z, Tang H, Jiang B, Cheng W. LncRNA RMRP/miR-613 axis is associated with poor prognosis and enhances the tumorigenesis of hepatocellular carcinoma by impacting oncogenic phenotypes. Am J Transl Res 2019; 11:2801-15.
30. Teng Y, Ding M, Wang X, Li H, Guo Q, Yan J, Gao L. LncRNA RMRP accelerates hypoxia-induced injury by targeting miR-214-5p in H9c2 cells. J Pharmacol Sci 2020; 142:69-78.
31. Kho AT, McGeachie MJ, Moore KG, Sylvia JM, Weiss ST, Tantisira KG. Circulating microRNAs and prediction of asthma exacerbation in childhood asthma. Respir Res 2018; 19:128.
32. Thorsen J, Rasmussen MA, Waage J, et al. Infant airway microbiota and topical immune perturbations in the origins of childhood asthma. Nat Commun 2019; 10:5001.
33. Jiang S, Wang Q, Wang Y, Song X, Zhang Y. Blockade of CCL2/CCR2 signaling pathway prevents inflammatory monocyte recruitment and attenuates OVA-Induced allergic asthma in mice. Immunol Lett 2019; 214:30-36.
34. Lee HY, Kim IK, Yoon HK, Kwon SS, Rhee CK, Lee SY. Inhibitory effects of resveratrol on airway remodeling by transforming growth factor-beta/smad signaling pathway in chronic asthma model. Allergy Asthma Immunol Res 2017; 9:25-34.

35. Paw M, Wnuk D, Kadziolka D, et al. Fenofibrate reduces the asthma-related fibroblast-to-myofibroblast transition by TGF-Beta/Smad2/3 signaling attenuation and connexin 43-dependent phenotype destabilization. Int J Mol Sci 2018; 19(9):2571.
36. Lachapelle P, Li M, Douglass J, Stewart A. Safer approaches to therapeutic modulation of TGF-beta signaling for respiratory disease. Pharmacol Ther 2018; 187:98-113.
37. Mansoor JK, Decile KC, Giri SN, et al. Influence of pirfenidone on airway hyperresponsiveness and inflammation in a Brown-Norway rat model of asthma. Pulm Pharmacol Ther 2007; 20:660-68.

Muscone alleviates myocardial ischemia-reperfusion injury via inhibition of oxidative stress and enhancement of SIRT3

C-J. Wei[1], F. Hua[1], Y-H. Chen[1], Z-W. Zhang[2] and Z-Y. Shen[3]

[1]Department of Cardiovascular Surgery, The First Affiliated Hospital of Soochow University, Wansheng Street, Suzhou Industrial District, Suzhou, China; [2]Department of Thoracic Surgery, The First Affiliated Hospital of Soochow University, Suzhou, China; [3]Department of Cardiovascular Surgery, The First Affiliated Hospital of Soochow University, Suzhou, China

Received February 20, 2020 – Accepted August 5, 2020

This study aimed at probing into the function of muscone in ameliorating myocardial ischemia-reperfusion (I/R) injury and exploring the underlying mechanism. To analyze the function of muscone, H9c2 cardiomyocytes were treated with hypoxia/reoxygenation (H/R) and Sprague-Dawley (SD) rats were treated with left anterior descending (LAD) of the coronary artery ligation for 30 min and reperfusion for 2 h to induce myocardial I/R injury. Quantitative real-time polymerase chain reaction (qRT-PCR) and Western blot were used to detect the expression of SIRT3. MTT assay and TUNEL assay were performed to investigate H9c2 viability and apoptosis, respectively. ELISA was employed to determine the expressions of inflammatory cytokines TNF-α, IL-6 and IL-1β, and myocardial injury markers CK and LDH. Oxidative stress markers MDA and SOD, and ROS expression levels were also detected. SIRT3 inhibitor 3-TYP was used to further confirm whether muscone worked via the augmentation of SIRT3. Herein, we found that muscone significantly inhibited inflammation and oxidative stress in H9c2 cardiomyocytes in a dose-dependent manner. H9c2 viability was promoted by muscone while apoptosis was inhibited. In SD rats, pre-treatment of muscone alleviated I/R injury-induced cardiac function dysregulation and left ventricle remolding. Furthermore, muscone increased SIRT3 expression at both mRNA and protein levels. With 3-TYP inhibiting SIRT3, the protective effects of muscone in H9c2 cardiomyocytes and SD rats were all significantly alleviated. In summary, muscone can attenuate inflammation, oxidative stress and cardiomyocytes injury in H9c2 cells treated with H/R and alleviate myocardial I/R injury of SD rats, which are dependent on SIRT3.

In the past decades, despite the greatly improved prognosis, myocardial infarction (MI) is still one of the leading causes of death and disability worldwide (1, 2). Currently, one of the most effective therapy strategies for MI is to restore the blood supply for the ischemic myocardium as soon as possible (3). However, reperfusion may cause changes in myocardial oxidative stress, inflammation, calcium overload, and pH, which will further aggravate myocardial damage caused by ischemia (4). At present, in the treatment of ischemic heart disease, how to minimize ischemia-reperfusion (I/R) injury is still a huge challenge (5). Therefore, it is vital to explore the potential drugs that can alleviate myocardial I/R injury.

Key words: muscone; ischemia-reperfusion; SIRT3

Corresponding Author:
Dr Zhen-ya Shen,
Department of Cardiovascular Surgery,
The First Affiliated Hospital of Soochow University,
No. 899, Pinghai Road, Suzhou 215000, China
Tel.: +86 0512-67972072
e-mail: lbfrm7043ks@163.com

0393-974X (2021)
Copyright © by BIOLIFE, s.a.s.
This publication and/or article is for individual use only and may not be further reproduced without written permission from the copyright holder.
Unauthorized reproduction may result in financial and other penalties
DISCLOSURE: ALL AUTHORS REPORT NO CONFLICTS OF INTEREST RELEVANT TO THIS ARTICLE.

times/min). Following that, the heart was exposed with thoracotomy, and LAD of the coronary artery was ligated for 30 min and reperfused for 2 h. At the end of the experiment, rats were euthanized by intraperitoneal injection and venous injection of sodium pentobarbital (200 mg/kg). All rats were randomly divided into 6 groups, with 10 in each group: (1) sham operation group: the rats were operated only without ligation of the coronary artery; (2) I/R group: the rats were operated and LAD was ligated; (3) I/R + L-muscone group: muscone (25 mg/kg, intravenous injection) was injected into the rat and then LAD was ligated; (4) I/R + M-muscone group: rats were intravenously injected with muscone (50 mg/kg) and then the LAD was ligated. (5) I/R+H-muscone group: muscone (75 mg/kg, intravenous injection) was injected into the rat and the LAD was ligated. (6) I/R + H-muscone + 3-TYP group: rats were first injected with muscone (75 mg/kg, intravenous injection) + 3-TYP (5 mg/kg, intravenous injection) and then LAD was ligated.

Determination of cardiac function

After the reperfusion for 2 h, the ejection fraction (EF), fractional shortening (FS), left ventricular end-diastolic pressure (LVEDP), left ventricular systolic pressure (LVSP) of rats were measured using Philips IE33 ultrasound system (Philips Healthcare, Amsterdam, Netherlands).

Enzyme-linked immunosorbent assay (ELISA)

H9c2 cells were inoculated into 6-well plates, and 4 wells were set in each group. 48 h after the culture, the supernatant was collected and centrifuged at 4°C for 10 min at 1000 × g. For tissues, rat myocardial tissues were homogenized, the homogenate was centrifuged with centrifugal radius of 13.5 cm at 2500 r/min for 20 min at 4°C. Subsequently, the supernatant was taken. Expressions of cytokines TNF-α, IL-1β, IL-6 and creatine kinase (CK) and lactate dehydrogenase (LDH) were detected according to the manufacturer's instructions using the ELISA kit [MultiSciences (Lianke) Biotech, Hangzhou, China].

Measurement of intracellular ROS

ROS expression level in cells was detected by 2, 7'-dichlorofluorescein (DCFDA) kit (Abcam, Shanghai, China). H9c2 cells were seeded into a 6-well plate, followed by being incubated with DCFDA (20 mM) for 30 min in the dark and washed with PBS, and ROS expression was detected using flow cytometry (Beckman Coulter). The content of ROS in rat myocardial tissue was detected employing ROS test kit (Jianbi Biological Co., Ltd., Nanjing, China) with a microplate reader after homogenization according to the manufacturer's instruction.

Activity of anti-oxidant enzymes

Superoxide dismutase (SOD) and malondialdehyde (MDA) kits (Jianbi Biological Co., Ltd., Nanjing, China) were used to determine the content of SOD and MDA according to the manufacturer's instruction.

Western blot

After the medium was discarded, the cells were washed once with PBS, and the protein was extracted using RIPA lysate (Sigma-Aldrich, Shanghai, China). After adding loading buffer, the protein sample was boiled and denatured. Subsequently, the protein samples were separated by 10% SDS-PAGE, transferred onto PVDF membrane (Millipore, Bedford, MA, USA), then blocked with defatted milk for 2 h at room temperature. After that, primary anti-SIRT3 antibody (rabbit anti-human polyclonal antibody, Abcam, 1:1000, ab189860) was added, with which the PVDF membrane was incubated at 4°C overnight. Afterward, the secondary antibody (goat anti-rabbit IgG, Abcam, 1:2000, ab205718) was used to incubate the membrane for 60 min at room temperature. After the membrane was washed, the bands were developed using ECL reagent (Millipore, Bedford, MA, USA). In this experiment, GAPDH was used as an internal reference, and ImageJ software was used to analyze the gray value of the bands.

Quantitative real-time polymerase chain reaction (qRT-PCR)

The total RNA was extracted using TRIzol (Thermo Fisher Scientific, MA, USA) method. Subsequently, the reverse transcription reaction was carried out with MMLV reverse transcriptase (Thermo Fisher Scientific, MA, USA). On the ABI7500 real-time PCR system, qRT-PCR was performed using SYBR premix EX TAQ II (TaKaRa, Dalian, China) in compliance with the manufacturer's instructions. SIRT3 primer sequences were as follows: forward: 5' -AGCTGCCTGCCTGTTTGC-3', reverse: 5'-GGGCCTCAAGACTACACTTCG-3'. GAPDH primer sequences were as follows forward: 5'-CCCACCACAGCTAGAACTTATC-3', reverse:

times/min). Following that, the heart was exposed with thoracotomy, and LAD of the coronary artery was ligated for 30 min and reperfused for 2 h. At the end of the experiment, rats were euthanized by intraperitoneal injection and venous injection of sodium pentobarbital (200 mg/kg). All rats were randomly divided into 6 groups, with 10 in each group: (1) sham operation group: the rats were operated only without ligation of the coronary artery; (2) I/R group: the rats were operated and LAD was ligated; (3) I/R + L-muscone group: muscone (25 mg/kg, intravenous injection) was injected into the rat and then LAD was ligated; (4) I/R + M-muscone group: rats were intravenously injected with muscone (50 mg/kg) and then the LAD was ligated. (5) I/R+H-muscone group: muscone (75 mg/kg, intravenous injection) was injected into the rat and the LAD was ligated. (6) I/R + H-muscone + 3-TYP group: rats were first injected with muscone (75 mg/kg, intravenous injection) + 3-TYP (5 mg/kg, intravenous injection) and then LAD was ligated.

Determination of cardiac function

After the reperfusion for 2 h, the ejection fraction (EF), fractional shortening (FS), left ventricular end-diastolic pressure (LVEDP), left ventricular systolic pressure (LVSP) of rats were measured using Philips IE33 ultrasound system (Philips Healthcare, Amsterdam, Netherlands).

Enzyme-linked immunosorbent assay (ELISA)

H9c2 cells were inoculated into 6-well plates, and 4 wells were set in each group. 48 h after the culture, the supernatant was collected and centrifuged at 4°C for 10 min at 1000 × g. For tissues, rat myocardial tissues were homogenized, the homogenate was centrifuged with centrifugal radius of 13.5 cm at 2500 r/min for 20 min at 4°C. Subsequently, the supernatant was taken. Expressions of cytokines TNF-α, IL-1β, IL-6 and creatine kinase (CK) and lactate dehydrogenase (LDH) were detected according to the manufacturer's instructions using the ELISA kit [MultiSciences (Lianke) Biotech, Hangzhou, China].

Measurement of intracellular ROS

ROS expression level in cells was detected by 2, 7'-dichlorofluorescein (DCFDA) kit (Abcam, Shanghai, China). H9c2 cells were seeded into a 6-well plate, followed by being incubated with DCFDA (20 mM) for 30 min in the dark and washed with PBS, and ROS expression was detected using flow cytometry (Beckman Coulter). The content of ROS in rat myocardial tissue was detected employing ROS test kit (Jianbi Biological Co., Ltd., Nanjing, China) with a microplate reader after homogenization according to the manufacturer's instruction.

Activity of anti-oxidant enzymes

Superoxide dismutase (SOD) and malondialdehyde (MDA) kits (Jianbi Biological Co., Ltd., Nanjing, China) were used to determine the content of SOD and MDA according to the manufacturer's instruction.

Western blot

After the medium was discarded, the cells were washed once with PBS, and the protein was extracted using RIPA lysate (Sigma-Aldrich, Shanghai, China). After adding loading buffer, the protein sample was boiled and denatured. Subsequently, the protein samples were separated by 10% SDS-PAGE, transferred onto PVDF membrane (Millipore, Bedford, MA, USA), then blocked with defatted milk for 2 h at room temperature. After that, primary anti-SIRT3 antibody (rabbit anti-human polyclonal antibody, Abcam, 1:1000, ab189860) was added, with which the PVDF membrane was incubated at 4°C overnight. Afterward, the secondary antibody (goat anti-rabbit IgG, Abcam, 1:2000, ab205718) was used to incubate the membrane for 60 min at room temperature. After the membrane was washed, the bands were developed using ECL reagent (Millipore, Bedford, MA, USA). In this experiment, GAPDH was used as an internal reference, and ImageJ software was used to analyze the gray value of the bands.

Quantitative real-time polymerase chain reaction (qRT-PCR)

The total RNA was extracted using TRIzol (Thermo Fisher Scientific, MA, USA) method. Subsequently, the reverse transcription reaction was carried out with MMLV reverse transcriptase (Thermo Fisher Scientific, MA, USA). On the ABI7500 real-time PCR system, qRT-PCR was performed using SYBR premix EX TAQ II (TaKaRa, Dalian, China) in compliance with the manufacturer's instructions. SIRT3 primer sequences were as follows: forward: 5' -AGCTGCCTGCCTGTTTGC-3', reverse: 5'-GGGCCTCAAGACTACACTTCG-3'. GAPDH primer sequences were as follows forward: 5'-CCCACCACAGCTAGAACTTATC-3', reverse:

5'-TGTATCCAAACTCATTGTCATAC-3'. The relative expression of SIRT3 was calculated by the $2^{-\Delta\Delta Ct}$ method.

TUNEL assay

TUNEL detection kit (Roche, Indianapolis, IN, USA) was used in this experiment. The medium was removed and the cells in each group were washed once with PBS. Then the cells were fixed with immunostaining fixative for 30 min before being rinsed with PBS. The immunostaining washing solution was then added and the cells were incubated for 2 min in an ice bath. Subsequently, 50 μL of TUNEL assay solution was added, with which the cells were incubated at 37°C for 60 min in the dark. Then the sample was washed 3 times with PBS. After that, the fluorescence was observed under a fluorescence microscope, and the excitation light was 450 to 500 nm, and the emission light was 515 to 565 nm (green fluorescence). A random field of 5 fields was selected for each sample to calculate the apoptotic rate (apoptotic cells/total cells × 100%). To evaluate the injury of heart tissues of the rats, heart tissue sections were baked at 70°C, then the paraffin sections were rehydrated with different gradients of ethanol, and then antigen repair was performed. Subsequently, H_2O_2 solution was added in order to inactivate endogenous enzymes at room temperature for 5 min, and then the sections were washed with PBS for 10 min. Then the immuostaining washing solution and TUNEL assay solution were added in sequence. The other procedures were as the same as the cell experiment.

MTT assay

The cells in the logarithmic growth phase were trypsinized to prepare single cell suspension with a density of 1×10^4/mL, and then the cells were seeded in a 96-well culture plate (200 μL per well). After being cultured for 24 h, fresh medium was added, and 20 μL of MTT solution (5 mg/ mL) was dripped into the wells for continuing the incubation for 4 h. After the medium was carefully discarded, 150 μL of DMSO was added to each well, and the culture plate was shaken for 10 min in the dark to dissolve the formazan. Ultimately, absorbance of each well was detected at a wavelength of 490 nm using a microplate reader.

Statistical analysis

SPSS 22.0 statistical software (SPSS Inc., Chicago, IL, USA) was used to analyze the data. Measurement data were expressed as mean ± standard deviation ($x \pm s$). Two groups of data were compared using *t*-test. $P < 0.05$ was statistically significant.

RESULTS

Muscone attenuated the inflammation and oxidative stress response of H9c2

Inflammation and oxidative stress play vital roles in myocardial I/R injury. Therefore, to preliminarily explore the role of muscone in I/R, we firstly examined the effect of muscone on inflammation and oxidative stress markers in cardiomyocytes. We found that muscone treatment reduced the expressions of the inflammatory factors TNF-α, IL-6 and IL-1β (Fig. 1 A-C), and also significantly decreased the production of oxidative stress markers MDA and ROS, while SOD expression was significantly increased (Fig. 1 D-F). These results suggested that muscone reduced the inflammation and oxidative stress in cardiomyocytes during H/R and had the potential to protect the myocardium in I/R.

Muscone reduced cardiomyocyte injury

To further pinpoint whether muscone has protective effects on H9c2 cardiomyocytes, the apoptosis and viability of H9c2 cells were detected by TUNEL and MTT assays, respectively, the findings of which revealed that H/R significantly enhanced H9c2 cell apoptosis and decreased cell viability, but muscone reversed this with a dose-dependent effect (Fig. 2 A, B). Furthermore, ELISA verified that the expression levels of myocardial injury markers CK and LDH were markedly decreased in the supernatant of H9c2 cells treated with muscone (Fig. 2 C, D). These results indicated that muscone ameliorated the injury of H9c2 cardiomyocytes after the H/R treatment.

Muscone increased the expression of SIRT3 in H9c2

Sirtuin 3 (SIRT3) regulates a range of genes involved in mitochondrial metabolic homeostasis and cell death, and functions prominently in oxidative stress-related diseases (16, 17). In the cardiovascular system, SIRT3 is also a protective factor. To further fathom the downstream mechanism by which muscone exerts its effects, the expression

of SIRT3 in H9c2 was examined. The results of qRT-PCR and Western blot showed that H/R injury observably reduced the expressions of SIRT3 mRNA and protein in H9c2 cells, while muscone promoted the expression of SIRT3 at the mRNA expression and protein levels. This effect could be significantly

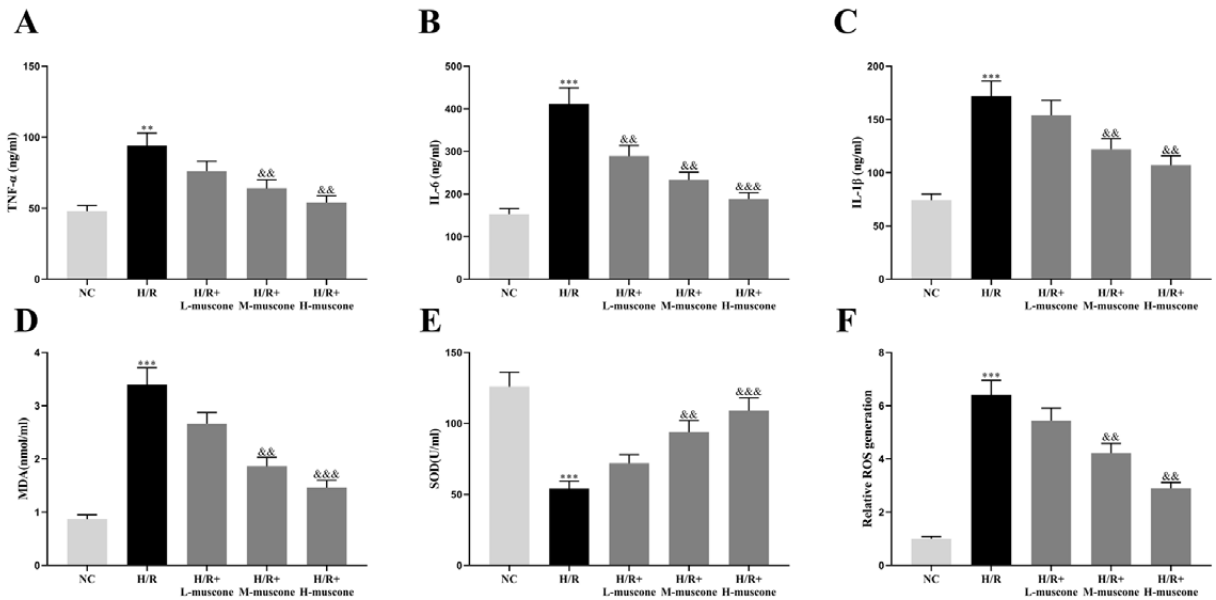

Fig. 1. *Effect of muscone on inflammation and oxidative stress of H9c2 cardiomyocytes.* ***A-C****) The expression levels of the inflammatory factors TNF-α, IL-6 and IL-1β were measured by ELISA.* ***D-E****) The expression of oxidative stress markers MDA and SOD were measured.* ***F****) The expression of ROS was detected by DCFDA method. ** and *** represent P < 0.01 and P < 0.001 respectively, the H/R group compared with the NC group; && and &&& represent P < 0.01 and P < 0.001 respectively, the H/R group compared with the H/R+muscone group.*

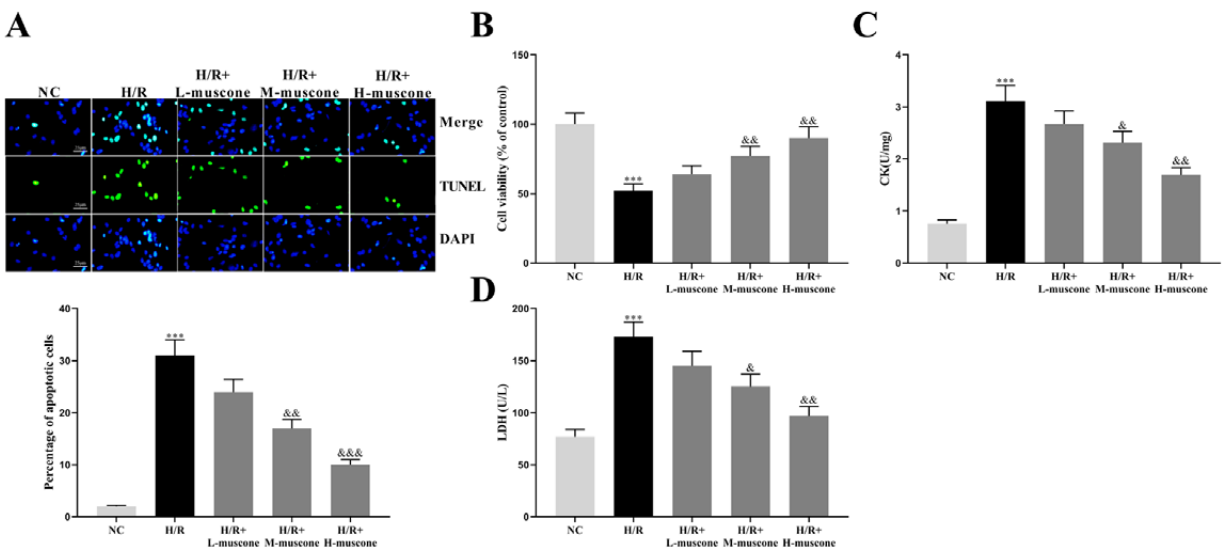

Fig. 2. *Effect of muscone on H9c2 cell injury.* ***A****) The apoptosis of H9c2 cells was monitored by TUNEL assay.* ***B****) viability of H9c2 cells was detected by MTT assay.* ***C-D****) The expression levels of myocardial injury markers CK and LDH were detected by ELISA. *** represents P < 0.001, H/R group compared with the NC group; &, && and &&& respectively represent P < 0.05, P < 0.01 and P < 0.001, H/R group compared with the H/R + muscone group.*

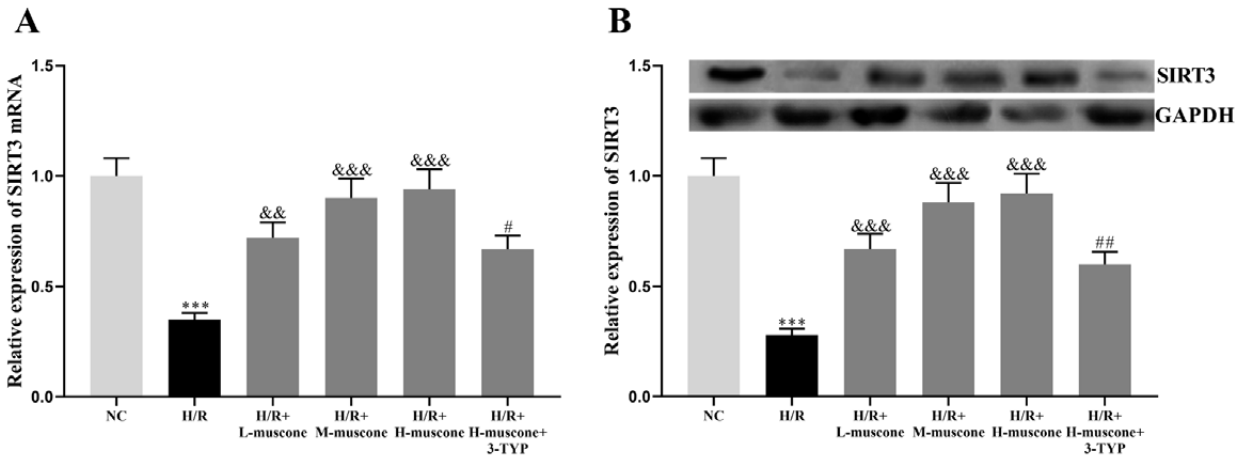

Fig. 3. *Effect of muscone on SIRT3 expression in H9c2 cells.* ***A****) The expression of SIRT3 mRNA in H9c2 cells was detected by qRT-PCR.* ***B****) Western blot was used to detect the expression level of SIRT3 in H9c2 cells. *** represents P < 0.001, H/R group compared with the NC group; && and &&& respectively represent P < 0.01 and P < 0.001, H/R group compared with the H/R+muscone group; # and ## respectively represent P < 0.05 and P < 0.01, H/R+muscone group compared with the H/R+H-muscone+3-TYP group,.*

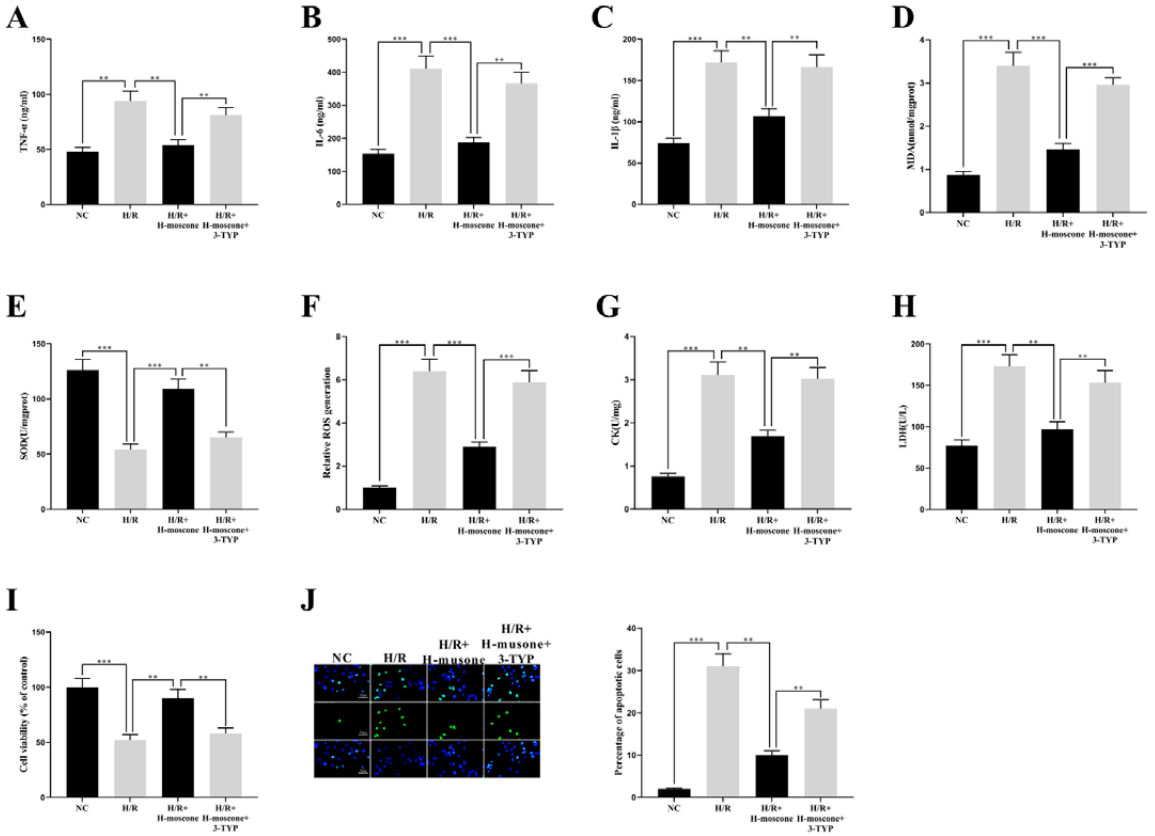

Fig. 4. *Inhibition of SIRT3 reversed the function of muscone in H9c2 cells.* ***A-C****) The expression levels of the inflammatory factors TNF-α, IL-6 and IL-1β were measured by ELISA.* ***D-E****) The expressions of cellular oxidative stress markers MDA and SOD were detected.* ***F****) The expression level of ROS was detected by DCFDA method.* ***G-H****) The expression levels of myocardial injury markers CK and LDH were detected by ELISA.* ***I****) H9c2 cell viability was detected by MTT assay.* ***J****) Apoptosis of H9c2 cells was detected by TUNEL assay. ** and *** represent P < 0.01 and P < 0.001, respectively.*

impeded by the addition of 3-TYP, a specific SIRT3 inhibitor (Fig. 3 A-B). Our results indicated that muscone could protect cardiomyocytes, probably by elevating SIRT3 expression.

Inhibition of SIRT3 reversed the role of muscone in protecting H9c2 cardiomyocytes

To further elaborate the mechanism by which muscone protects cardiomyocytes, the effect of 3-TYP on the function of muscone was observed. The results showed that the expressions of inflammatory factors TNF-α, IL-6, IL-1β, oxidative stress markers MDA, ROS, myocardial injury markers CK, and LDH were significantly increased by adding 3-TYP, while SOD expression was markedly decreased (Fig. 4 A-H). Meanwhile, 3-TYP also inhibited cell viability and promoted apoptosis (Fig. 4 I-J). These data proved that the function of muscone was reversed by 3-TYP, which validated that muscone protected H9c2 cardiomyocytes by activating SIRT3.

Muscone improved heart function of rat impaired by I/R.

To further verify the role of muscone, a rat model of myocardial I/R injury was established. Echocardiography demonstrated that I/R significantly reduced EF, FS, LVSP, and increased LVEDP of rats, while the injection of muscone partly abolished these effects (Fig. 5 A-D). This meant that muscone improved the cardiac function in rats with I/R.

Muscone ameliorated myocardial injury of rats.

To further investigate the effect of muscone on myocardial injury in rats, we tested the myocardial injury markers in rat serum and found that the serum CK and LDH expression levels were significantly reduced by muscone injection (Fig. 6 A, B). In rat myocardial tissue, muscone also markedly decreased the expressions of inflammatory factors TNF-α, IL-6

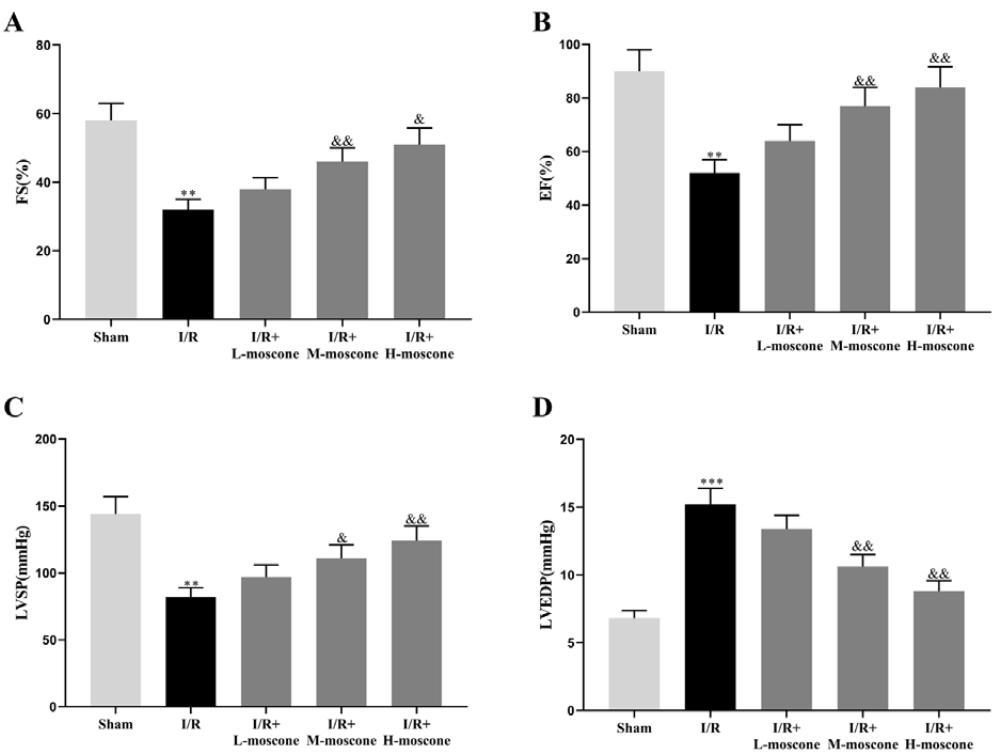

Fig. 5. *Effect of muscone on heart function in rats.* ***A-D****) Ejection fraction (EF), shortening fraction (FS), left ventricular end-diastolic pressure (LVEDP), left ventricular systolic pressure (LVSP) in rat hearts were measured by echocardiography. ** and *** respectively represent P < 0.01 and P < 0.001, sham group compared with I/R group; & and && respectively represent P < 0.05 and P < 0.01, I/R group compared with I/R+muscone group.*

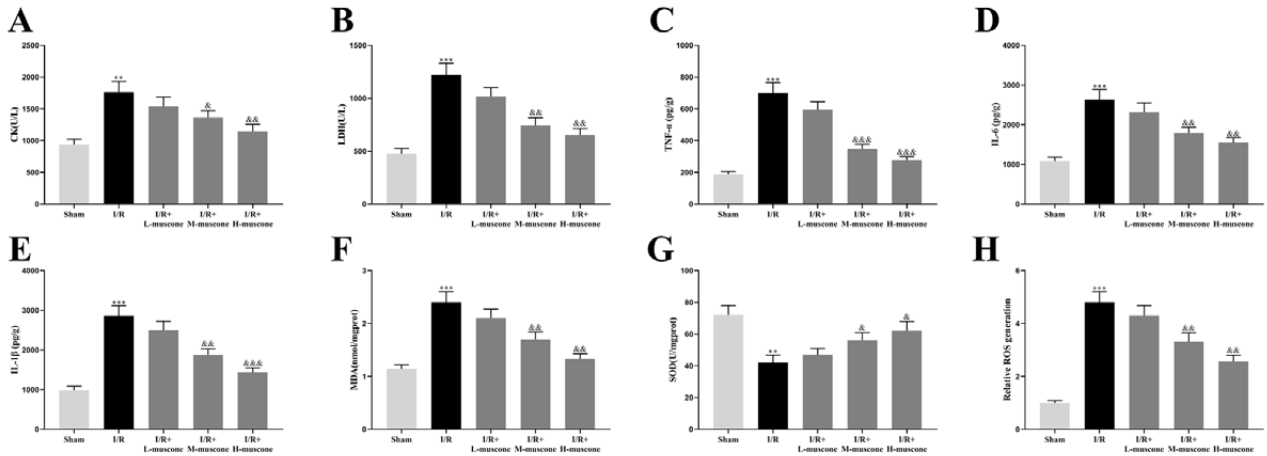

Fig. 6. *Protective effect of muscone on rat myocardium.* ***A, B****) The myocardial injury markers CK and LDH were detected by ELISA.* ***C-E****) The expressions of the inflammatory factors TNF-α, IL-6 and IL-1β were detected by ELISA.* ***F-G****) The oxidative stress response markers MDA and SOD of rat myocardium were detected.* ***H****) Myocardial ROS expression level in rats was detected by ROS detection kit. ** and *** represent P < 0.01 and P < 0.001 respectively, sham group compared with I/R group; &, && and &&& respectively represent P < 0.05, P < 0.01 and P < 0.001, I/R group compared with I/R+muscone group.*

and IL-1β (Fig. 6 C-E). In addition, the expressions of ROS and MDA were observably lower in the muscone group than that in the I/R group, and the expression of SOD was significantly higher than that in the I/R group (Fig. 6 F-H). Our results further demonstrated that muscone alleviated myocardial I/R injury in rats.

Muscone exerted its cardioprotective effect by up-regulating SIRT3 expression.

Next, we examined the expression of SIRT3 mRNA and protein in rat myocardial tissue by qRT-PCR and Western blot. It was observed that I/R reduced the expression of SIRT3, and muscone promoted SIRT3 expression, which was attenuated by SIRT3 inhibitor 3-TYP (Fig. 7 A, B). 3-TYP also inhibited the function of muscone in repressing myocardial inflammation and oxidative stress and reducing myocardial injury (Fig. 7 C-J). Additionally, the myocardial function was significantly reduced in the I/R+muscone+3-TYP group compared to in the I/R+muscone group (Fig. 7 K-N). Additionally, we used the TUNEL assay to detect the apoptosis of the cardiomyocytes of the rats in each group. As shown, muscone significantly reduced the injury of rat myocardial tissue, while after 3-TYP administration, the protective effects of muscone were abolished (Fig. 8). Collectively, we concluded that the high expression of SIRT3 was accompanied by the cardioprotective effect of muscone.

DISCUSSION

Myocardial I/R injury is one of the important causes of cardiac dysfunction (6). Little is known concerning the effect of muscone on alleviating myocardial I/R injury and its mechanism. Our study found that muscone could enhance the expression of SIRT3 in the myocardium, thereby reducing the inflammation and oxidative stress caused by I/R and protecting the cardiomyocytes.

Cellular inflammatory response and oxidative stress are the main mechanisms responsible for myocardial injury. I/R triggers a strong inflammatory reaction, and the infiltrated inflammatory cells exacerbate the ischemic injury. Meanwhile, the increase of inflammatory factors will further recruit leukocytes, resulting in secondary injury and increasing the risk of heart rupture (18). ROS can cause DNA damage, mitochondrial dysfunction, and lipid peroxidation. In addition, increased ROS

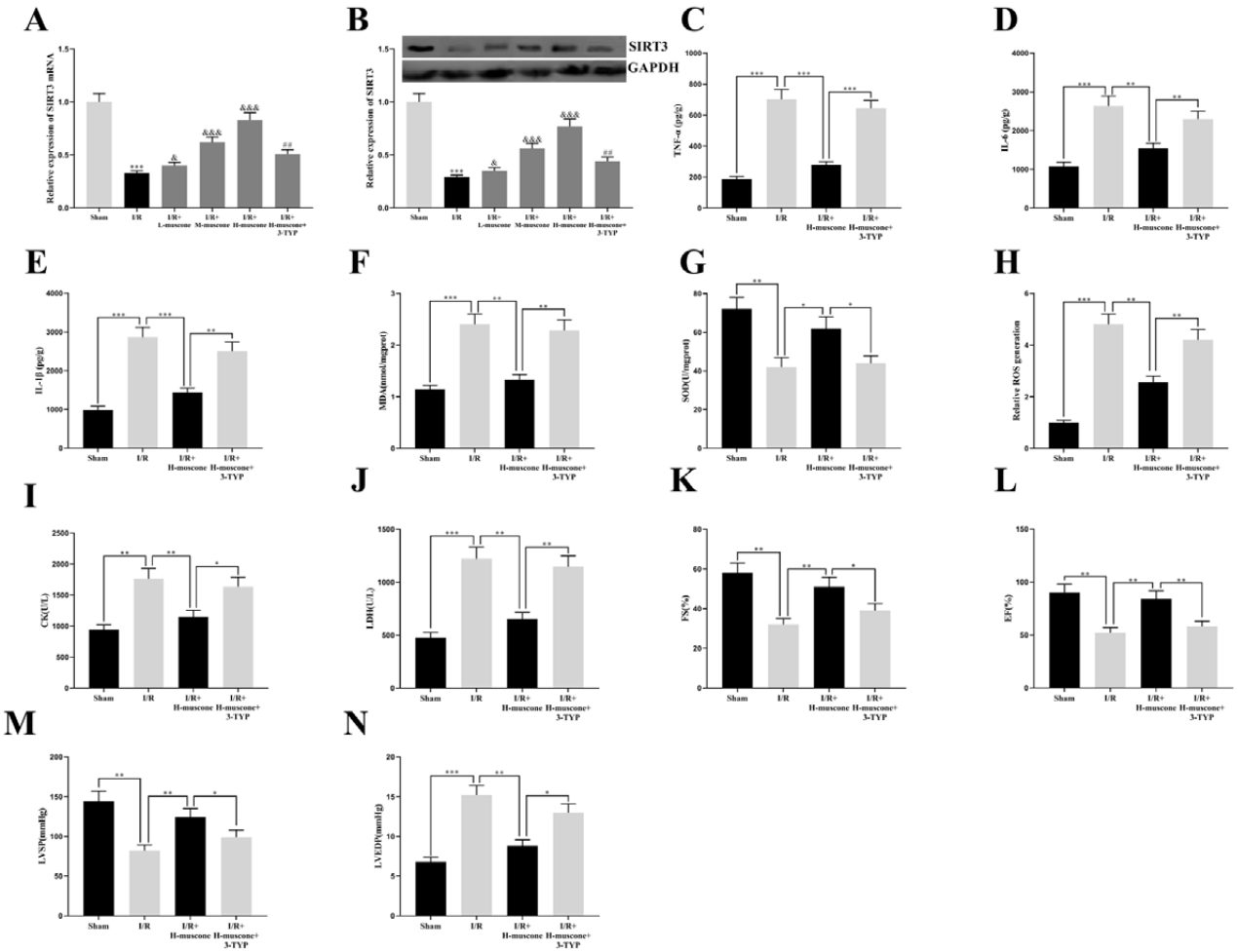

Fig. 7. *Musconee exerted protective effects on rat myocardium through SIRT3.* ***A, B****) The expression levels of SIRT3 mRNA and protein in rat heart tissue were detected by qRT-PCR and Western blot respectively.* ***C-E****) The expressions of the inflammatory factors TNF-α, IL-6 and IL-1β were detected by ELISA.* ***F, G****) The oxidative stress response markers MDA and SOD of rat myocardium were detected.* ***H****) Myocardial ROS expression level in rats was detected by ROS detection kit.* ***I, J****) The myocardial injury markers CK and LDH were detected by ELISA.* ***K-N****) Ejection fraction (EF), shortening fraction (FS), left ventricular end-diastolic pressure (LVEDP), left ventricular systolic pressure (LVSP) were examined by echocardiography. *, ** and *** represent P < 0.05, P < 0.01, and P < 0.001, respectively. In A and B, *** represents P < 0.001, sham group compared with I/R group; & and &&& represent P < 0.05 and P < 0.001, respectively, I/R group compared with I/R+musone group; ## represents P < 0.01, I/R+H-musone group compared with the I/R+H-musone+3-TYP group.*

expression in cardiomyocytes induces changes in proteins involved in excitatory-contraction coupling and enhances sensitivity to proteolysis, which also increases cardiomyocytes apoptosis (7). We found that muscone significantly reduced ROS and MDA production, and an increase in SOD was observed, suggesting that muscone deceased myocardial oxidative stress. Moreover, the expressions of the inflammatory factors TNF-α, IL-6 and IL-1β were also markedly decreased by the administration of muscone. These results suggested that muscone alleviated I/R induced myocardial inflammation. The inhibitory effect of muscone on inflammatory response and oxidative stress is reported in a variety of cells. For example, in the MI model of mice, muscone reduces the chronic inflammation induced

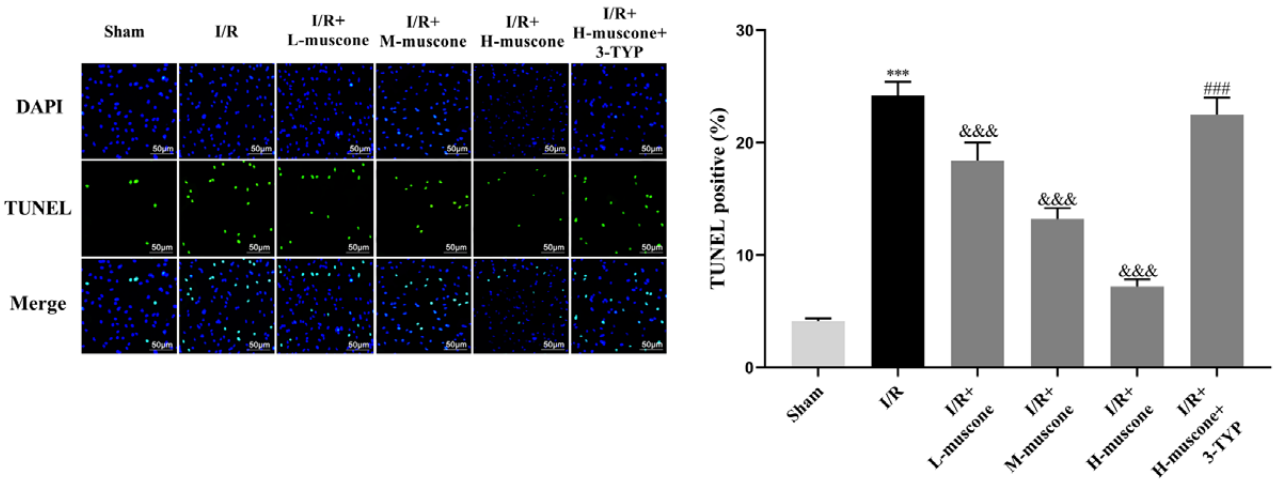

Fig. 8. *Muscone ameliorated the apoptosis of the cardiomyocytes of the rats. The apoptosis of the cardiomyocytes of rats was detected by TUNEL assay. *** represents p < 0.001, compared with Sham group; &&& respectively represents p < 0.001, compared with I/R group; ### respectively represents P < 0.001, compared with I/R+H-muscone group.*

by cardiac macrophages by inhibiting the activation of NF-κB and NLRP3 inflammasome, and has a certain improvement in the cardiac function of mice with MI (19). In PC12 cells, muscone significantly attenuates the increase in ROS caused by ischemia, suggesting the neuroprotective effect of muscone (20). Our work confirmed the role of muscone in ameliorating myocardial inflammation and oxidative stress, which is consistent with previous reports.

Cardiomyocyte apoptosis plays a prominent role in the pathophysiological process of MI and ischemic cardiomyopathy. The decrease in cardiomyocyte number means that the heart cannot effectively contract, which will directly contribute to a decline in cardiac function (6, 21, 22). Muscone has an inhibitory effect on apoptosis in a variety of cells. For instance, in high glucose-induced RSC 96 cells, muscone attenuates autophagy and apoptosis by modulating the AKT/mTOR signaling pathway (23). In a study on skin flap survival, muscone reduces cell apoptosis, inhibits the production of oxidative stress SOD and MDA, and promotes angiogenesis (24). In this study, TUNEL assay and MTT assay showed that muscone significantly attenuated the apoptosis of H9c2 cells and enhanced their viability. Consistent with *in vitro* experiments, echocardiography unearthed that muscone markedly improved cardiac function in rats, which further confirmed the role of muscone in alleviating myocardial injury caused by I/R.

(SIRT3) is one of the most active members of the Sirtuin family, whose coding gene is located on chromosome 11p15.5, and is found to have a protective effect on cardiovascular disease. SIRT3 regulates glycolipid metabolism, maintains myocardial ATP levels, prevents cardiac metabolic disorders, and inhibits oxidative stress (25). One study found that in the development of cardiac hypertrophy, SIRT3 improves mitochondrial function and inhibits oxidative stress (26). Another study suggests that the deficit of SIRT3 accelerates the formation of arterial thrombosis (27). In addition, inhibition of myocardial I/R injury by IPTC requires SIRT3-mediated deacetylation of cyclophilin D (28). It is also reported that inhibition of SIRT3 can counteract the protective effects of various substances such as curcumin on myocardial injury (29). Therefore, promotion of SIRT3 expression and activity is a promising therapeutic strategy which can delay the development of cardiovascular diseases. In our study, we found that the expression of SIRT3 in H9c2 cells treated with muscone or SD rats injected with muscone was significantly increased at both mRNA and protein expression levels. Furthermore, it was observed that the functions of muscone on inhibiting

oxidative stress, inflammatory response and apoptosis were eliminated by SIRT3 inhibitor 3-TYP. For the first time, our study demonstrated the expression of SIRT3 was regulated by muscone, further explaining the mechanism by which muscone exerted its anti-inflammatory and anti-oxidation functions.

In summary, with *in vitro* and *in vivo* experiments, we found that muscone alleviates the inflammatory response, oxidative stress and cardiomyocyte injury caused by I/R via increasing the expression of SIRT3, and improves the cardiac function of rats. Our study further clarifies the molecular mechanism of muscone to protect myocardium against I/R injury after MI, and proffers a theoretical basis for the application of moschus/muscone in clinical practice.

REFERENCES

1. Reed GW, Rossi JE, Cannon CP. Acute myocardial infarction. Lancet 2017; 389:197-210.
2. Piepoli MF, Corrà U, Dendale P, et al. Challenges in secondary prevention after acute myocardial infarction: A call for action. Eur J Prev Cardiol 2016; 23:1994-2006.
3. Rentrop KP, Feit F. Reperfusion therapy for acute myocardial infarction: Concepts and controversies from inception to acceptance. Am Heart J 2015; 170:971-80.
4. Hausenloy DJ, Yellon DM. Myocardial ischemia-reperfusion injury: a neglected therapeutic target. J Clin Invest 2013; 123:92-100.
5. Yang Q, He GW, Underwood MJ, Yu CM. Cellular and molecular mechanisms of endothelial ischemia-reperfusion injury: perspectives and implications for postischemic myocardial protection. Am J Transl Res 2016; 8:765-77.
6. Wang D, Zhang X, Li D, et al. Kaempferide protects against myocardial ischemia-reperfusion injury through activation of the PI3K/Akt/GSK-3β Pathway. Mediators Inflamm 2017; 2017:5278218.
7. Neri M, Riezzo I, Pascale N, Pomara C, Turillazzi E. Ischemia-reperfusion injury following acute myocardial infarction: a critical issue for clinicians and forensic pathologists. Mediators Inflamm 2017; 2017:7018393.
8. Mattera R, Benvenuto M, Giganti MG, et al. Effects of polyphenols on oxidative stress-mediated injury in cardiomyocytes. Nutrients 2017; 9:523.
9. Yu H, Guan Q, Guo L, et al. Gypenosides alleviate myocardial ischemia-reperfusion injury via attenuation of oxidative stress and preservation of mitochondrial function in rat heart. Cell Stress Chaperones 2016; 21:429-37.
10. Zhang JJ, Peng K, Zhang J, Meng XW, Ji FH. Dexmedetomidine preconditioning may attenuate myocardial ischemia-reperfusion injury by down-regulating the HMGB1-TLR4-MyD88-NF-κB signaling pathway. PLoS One 2017; 12:e0172006.
11. Wu Q, Li H, Wu Y, Shen W, Zeng L, Cheng H, He L. Protective effects of muscone on ischemia-reperfusion injury in cardiac myocytes. J Ethnopharmacol 2011; 138:34-39.
12. Cen W, Chen Z, Gu N, Hoppe R. Prevention of AMI induced ventricular remodeling: inhibitory effects of heart-protecting musk pill on IL-6 and TNF-Alpha. Evid Based Complement Alternat Med 2017; 2017:3217395.
13. Xu L, Cao Y. Native musk and synthetic musk ketone strongly induced the growth repression and the apoptosis of cancer cells. BMC Complement Altern Med 2016; 16:511.
14. Wang X, Meng H, Chen P, et al. Beneficial effects of muscone on cardiac remodeling in a mouse model of myocardial infarction. Int J Mol Med 2014; 34:103-11.
15. Du Y, Ge Y, Xu Z, et al. Hypoxia-Inducible Factor 1 alpha (HIF-1α)/Vascular Endothelial Growth Factor (VEGF) pathway participates in angiogenesis of myocardial infarction in muscone-treated mice: preliminary study. Med Sci Monit 2018; 24:8870-77.
16. Mihanfar A, Nejabati HR, Fattahi A, et al. SIRT3-mediated cardiac remodeling/repair following myocardial infarction. Biomed Pharmacother 2018; 108:367-73.
17. Chen Y, Luo HQ, Sun LL, et al. Dihydromyricetin attenuates myocardial hypertrophy induced by transverse aortic constriction via oxidative stress inhibition and SIRT3 pathway enhancement. Int J Mol Sci 2018; 19:2592.
18. Frangogiannis NG. The inflammatory response in myocardial injury, repair, and remodeling. Nat Rev Cardiol 2014; 11:255-265.

19. Du Y, Gu X, Meng H, et al. Muscone improves cardiac function in mice after myocardial infarction by alleviating cardiac macrophage-mediated chronic inflammation through inhibition of NF-κB and NLRP3 inflammasome. Am J Transl Res 2018; 10:4235-46.
20. Yu L, Wang N, Zhang Y, et al. Neuroprotective effect of muscone on glutamate-induced apoptosis in PC12 cells via antioxidant and Ca^{2+} antagonism. Neurochem Int 2014; 70:10-21.
21. Orogo AM, Gustafsson ÅB. Cell death in the myocardium: my heart won't go on. IUBMB Life 2013; 65:651-56.
22. Scarabelli TM, Gottlieb RA. Functional and clinical repercussions of myocyte apoptosis in the multifaceted damage by ischemia-reperfusion injury: old and new concepts after 10 years of contributions. Cell Death Differ 2004; 11: S144-52.
23. Dong J, Li H, Bai Y, Wu C. Muscone ameliorates diabetic peripheral neuropathy through activating AKT/mTOR signaling pathway. J Pharm Pharmacol 2019; 71:1706-13.
24. Kailiang Z, Yihui Z, Dingsheng L, Xianyao T. Effects of muscone on random skin flap survival in rats. J Reconstr Microsurg 2016; 32:200-207.
25. Sun W, Liu C, Chen Q, Liu N, Yan Y, Liu B. SIRT3: A new regulator of cardiovascular diseases. Oxid Med Cell Longev 2018; 2018:7293861.
26. 26.Meng G, Liu J, Liu S, et al. Hydrogen sulfide pretreatment improves mitochondrial function in myocardial hypertrophy via a SIRT3-dependent manner. Br J Pharmacol 2018; 175:1126-45.
27. Gaul DS, Weber J, van Tits LJ, et al. Loss of Sirt3 accelerates arterial thrombosis by increasing formation of neutrophil extracellular traps and plasma tissue factor activity. Cardiovasc Res 2018; 114:1178-88.
28. Bochaton T, Crola-Da-Silva C, Pillot B, et al. Inhibition of myocardial reperfusion injury by ischemic postconditioning requires sirtuin 3-mediated deacetylation of cyclophilin D. J Mol Cell Cardiol 2015; 84:61-69.
29. Wang R, Zhang JY, Zhang M, et al. Curcumin attenuates IR-induced myocardial injury by activating SIRT3. Eur Rev Med Pharmacol Sci 2018; 22:1150-60.

Wingless/int-1induced secreted protein-1: a new biomarker for renal fibrosis

Y. Zhou[1], P. Chai[2], J. Wang[1], L. Li[1] and MH. Chen[1]

[1]*Department of Nephrology, General Hospital of Ningxia Medical University, Yinchuan, China;*
[2]*Department of Ultrasonic, General Hospital of Ningxia Medical University, Yinchuan, China*

Received September 7, 2020 – Accepted November 26, 2020

This study aimed to detect the expression of Wnt-induced secreted protein-1 (WISP-1) in renal fibrosis (RF) and to clarify the underlying mechanism. An *in vivo* mousee model of unilateral ureteral obstruction (UUO) and *in vitro* model of fibrosis on renal tubular epithelial NRK52E cells after transforming growth factor-β1 (TGF-β1) stimulation were used. Quantitative real-time PCR (qRT-PCR), Western blot (WB), and immunohistochemistry were used to detect WISP-1 and fibrosis markers, including the expression of fibronectin (FN), collagen I (Col I), collagen IV (Col IV), and α-smooth muscle actin (α-SMA). *In vitro* experiments showed that the expression of WISP-1 and fibrosis markers FN, Col I, Col IV, and α-SMA in rat renal tubular epithelial cells were significantly higher than that in the control group after 48 h of TGF-β1 stimulation. *In vivo* experiments showed that the expressions of WISP-1 and fibrosis markers FN, Col I, Col IV, and α-SMA in the obstructed kidney of UUO animal models were significantly increased in mRNA and protein levels compared to normal mice. This study showed that WISP-1 may be an essential cytokine that promotes renal fibrosis, being involved in the development of renal fibrosis.

Renal fibrosis is a pathophysiological process determined by a complex interaction of multiple cells, cytokines, and growth factors, leading to increased synthesis of extracellular matrix (ECM), reduced degradation, and excessive deposition of ECM (1-3). The Wnt signaling pathway is involved in the physiopathological processes such as cell differentiation, apoptosis, immunity and oxidative stress (4). Wingless/int-1 (Wnt)-induced secreted protein-1 (WISP-1) is one of the downstream target genes after Wnt signalling pathway activation, and has biological functions such as promoting cell proliferation, mediating cell adhesion, and promoting ECM synthesis (5). Recent studies have shown that WISP-1 is involved in the repair of organ damage and is related to fibrosis of the lungs (6), myocardium (7), and liver (8). Exogenous recombinant WISP-1 protein can promote alveolar epithelial type II cell proliferation and epithelial-mesenchymal transition (EMT). It can also promote human lung fibroblasts to synthesize ECM. WISP-1 neutralizing antibodies can reverse the expression of EMT-related genes, reduce collagen deposition, and alleviate lung fibrosis in mice (9). It can be seen that WISP-1 may be the main cytokine that promotes fibrosis. However, there is little evidence of WISP-1 implication in renal fibrosis. In this study, we aimed to investigate the expression levels of WISP-1 and fibrosis indicators *in vivo* using an unilateral ureteral obstruction (UUO) murine model ,and *in vitro* on renal tubular epithelial cells after TGF-β1 stimulation.

Key words: Wnt induced secreted protein-1; renal fibrosis; TGF-β1; unilateral ureteral obstruction model

Corresponding Author:
Dr Menghua Chen,
Department of Nephrology,
General Hospital of Ningxia Medical University,
No. 804 Shengli South Street,
Xingqing District, Yinchuan, 750004, China
e-mail: chenmenghuanxmu@126.com

0393-974X (2021)
Copyright © by BIOLIFE, s.a.s.
This publication and/or article is for individual use only and may not be further reproduced without written permission from the copyright holder.
Unauthorized reproduction may result in financial and other penalties
DISCLOSURE: ALL AUTHORS REPORT NO CONFLICTS OF INTEREST RELEVANT TO THIS ARTICLE.

MATERIALS AND METHODS

In vitro experiment

Rat renal tubular epithelial NRK52E cells were purchased from Chengdu Zen BioScience Co., Ltd, China. The cells were cultured in DMEM (Dulbecco's modified eagle medium), high glucose medium containing 10% fetal bovine serum (Shanghai Sixin Biotechnology Co., Ltd., China) at 37°C and 5% CO_2. NRK52E cells were divided into a TGF-β1 group and a control group. The cells in the TGF-β1 group were treated with 6 ng/mL TGF-β1 (Pepreotech, USA) and incubated for 48 h. The cells from the control group were cultured for 48 h in the same conditions but without TGF-β1.

In vivo UUO mice model

Thirty healthy male 8-week-old C57BL/6 (20g-25g) mice of clean grade were purchased from Guangdong Medical Experimental Animal Center, China. The mice were separated into two groups, a UUO model group (UUO group) and a sham-operation control group (Sham group), with 15 animals per group. The mice in the UUO group underwent 12 h of fasting and water deprivation before the operation. For unilateral ureteral ligation, the mice were anaesthetized with 10% chloral hydrate (0.3-0.4 μL/100g) intraperitoneally, and the skin from the right side was disinfected. After disinfection, an incision of 0.5 cm was made below the spinal rib on the left-side of the back of the mouse. After opening the abdominal cavity, the left ureter was first freed, and $^1/_3$ of the ureter was double ligated with a 4.0 silk thread. Then, the muscles and skin were sutured and the wound was disinfected. Two h after the operation, mice received a normal diet and drinking water. In the Sham group, laparotomy was performed according to the method described above, however the left ureter was freed without ligation. The protocol was approved by the ethics committee of the General Hospital of Ningxia Medical University. The animal experiment followed the regulations of the State Science and Technology Commission on the management of laboratory animals.

After the UUO mouse model was obtained, the animals were kept for 2 weeks in standard laboratory conditions at 20-25℃, 40-60% humidity and 12 h light/dark cycle, with free access to feed and water. Animals were sacrificed by cervical dislocation two weeks after modelling. Kidneys were collected and separated into 2 parts: one part was fixed with 4% paraformaldehyde (Shanghai Yuchun Biotechnology Co., Ltd., China) for light microscopy observation (hematoxylin and eosin (H&E) and Masson staining) and immunohistochemical staining, and the other part was quick-frozen with liquid nitrogen and stored at -80°C for further determination of renal tissue proteins and mRNA.

Histopathological examination

Paraffin sections of 2 μm were subjected to Masson and H&E staining and examined under a light microscope (Thermo Fisher Scientific, USA). For Masson staining, 2-μm paraffin sections were dewaxed by water, stained with Weiger's hematoxylin for 10 min, and rinsed with distilled water several times. Then the sections were stained for 10 min with ponceau acid fuchsin, rinsed with distilled water treated with 1% phosphomolybdic acid for 5 min without washing, and stained with aniline blue for 5 min. After treatment with 1% glacial acetic acid for 1 min, conventional dehydration was performed, and the slides were sealed with transparent neutral gum.

For H&E staining, paraffin sections were routinely dewaxed by water followed by staining of cell nuclei with hematoxylin for 5 min and rinsed with tap water several times. Then the sections were successively treated with 1% hydrochloric acid - alcohol for 20 s, rinsed with tap water several times, treated with 1% ammonia treatment for 30 s and rinsed with tap water for 5 min. The eosin was used for cytoplasmic staining for 1 minand then rinsed with tap water for 10 s. After dehydration in gradient alcohol and xylene, the slides were sealed.

Immunohistochemical staining

A three-step immunohistochemical method was used for immunohistochemical analysis. The 4-μm paraffin sections were dewaxed and washed with water. The antigen retrieval for WISP-1 was made by autoclave heating repair method (the tissue sections were put in an autoclave at pH 6.0 with 0.01M sodium citrate buffer and pressurized at high temperature for 3 min followed by cooling to room temperature and rinsed with distilled water for 5 min and PBS (phosphate-buffered saline) twice for 5 min each time. The antigen retrieval for α-smooth muscle actin (α-SMA) was made by microwave repair method (the tissue sections were kept at 80°C for 5 min, then at 40°C for 10 min and then kept at room temperature for 2 h). The

antigen retrieval for fibronectin (FN), collagen I (Col I), collagen IV (Col IV) were performed by pepsin repair (the tissue sections were kept at 37°C for 15 min). After the repair, the PBS was used to rinse the sections for 5 min, 3 successive times and then incubated at room temperature for 15 min with 3% hydrogen peroxide-methanol solution to block the activity of endogenous peroxidase followed by PBS rinse for 5 min, 3 successive times. All the tissue sections pretreated as above were incubated with Goat serum at 37°C for 30 min and then with WISP-1 (1:500, AmyJet Scientific Inc, China), FN (1:200, Shanghai Yaji Biological Technology Co., Ltd., China), Col IV (1:100, Shanghai Xinyu Biological Technology Co., Ltd., China), Col I (1:100, Shanghai Xinyu Biological Technology Co., Ltd., China) and α-SMA (1:200, Hangzhou LinkMed Co., Ltd., China) antibody overnight at 4°C. Next day, the tissues were rinsed in PBS for 10 min, 4 successive times, incubated at 37°C for 30 min with biotin-labelled goat anti-rabbit IgG, rinsed with PBS, followed by incubation with horseradish peroxide-labelled streptavidin at 37°C for 30 min. Then, the slides were counterstained with hematoxylin counterstaining and sealed with gum. A light microscope (Thermo Fisher Scientific (China) Co., Ltd.) was used for observation.

Quantitative real-time PCR (qRT-PCR)

Kidney tissue RNA was extracted by the Trizol method. The reverse transcription reaction was performed according to the steps provided in the Takara reverse transcription kit instructions (Takara, Japan). Primer sequences were required for PCR amplification. SYRB Green mix 10 μl, upstream primer 0.4 μl, downstream primer 0.4 μl, ddH_2O 8.2 μl, and cDNA 1 μl, total system 20 μl. After mixing, it was put in a qRT-PCR instrument (Beckman, USA) for a reaction. The reaction conditions were 50°C for 5 min, 95°C for 10 min, 56°C for 30 s, and 72°C for 40 s.

Western blot (WB) detection for protein expression

The kidney tissue or renal tubular epithelial cells were collected for lysis. The total protein of the tissue or cells was extracted and the protein concentration was determined using bicinchoninic acid (BCA). The loading sample containing 50 μg proteins was subjected to sodium dodecyl sulfate polyacrylamide gel electrophoresis (SDS-PAGE). Then, the membrane was transferred. After it was sealed with 5% defatted milk powder (Jiangsu Caiwei Biotechnology Co., Ltd., China) for 1 h, the primary antibodies [WISP-1 (1:500, AmyJet Scientific Inc, China), FN (1:500, Shanghai Yaji Biological Technology Co., Ltd., China), Col IV (1:200, Shanghai Xinyu Biological Technology Co., Ltd., China), Col I (1:200, Shanghai Xinyu Biological Technology Co., Ltd., China) and α-SMA (1:500, Hangzhou LinkMed Co., Ltd., China)] and secondary antibodies [(goat anti-rabbit IgG-HRP (1:1000, Real-Times Biotechnology Co., Ltd., China)] were added for hybridization After the strips were incubated in the antibodies and washed, the exposure solution was applied to develop the strips. The images were analyzed using Image J software (National Institutes of Health, USA).

Statistical analysis

All data analysis was performed using SPSS 22.0 statistical software (IBM, USA). Measurement data were expressed as mean ± standard deviation ($\bar{x}\pm s$). Student's *t*-test and single-factor variance analysis were used for group comparison. Pearson correlation analysis was used to evaluate the correlation between different data. A value of $P < 0.05$ was considered statistically significant.

RESULTS

Expression of WISP-1 and fibrosis biomarkers in TGF-β1-induced fibrosis of rat renal tubular epithelial cells

After TGF-β1 treatment, the mRNA and protein level of WISP-1, FN, Col I, Col IV, snd α-SMA were significantly increased compared with the control group (Fig. 1).

In vivo study on the UUO mice model

Histological observation

The kidneys of the Sham group were normal in size and shape, reddish-brown, and the envelope was smooth. In the UUO group, kidneys of the mice were significantly enlarged, pale, and the envelope was tense. Renal light microscopy after H&E staining and Masson staining showed that the obstructed renal tissue of the UUO group presented varying degrees of fibrosis (Fig. 2A), mainly manifested as glomerular sclerosis, collagen fiber deposition, renal tubular dilatation, renal interstitial fibrosis, and

interstitial inflammatory cell infiltration. Routine staining results showed that UUO model was successfully modelled.

Results of immunohistochemical staining

The expression of WISP-1 and fibrosis indexes was analyzed by immunohistochemical staining. In the UUO group, the expression of fibrosis markers, such as Col I, Col IV, FN, and α-SMA, in the obstructed kidneys of the mice were significantly increased compared with the Sham group. At the same time, the expression of WISP-1 was also significantly increased and mainly distributed in the renal interstitial region, and a small part was expressed in the glomerular mesangial region. FN, Col I and Col IV proteins were mainly expressed in the glomerular mesangial region and the renal interstitium. Some renal tubular cytoplasm showed a small amount of expression. α-SMA protein was mainly expressed in renal tubular cells and renal interstitium (Fig. 2 B, C).

Expression of WISP-1 and fibrosis indexes detected by qRT-PCR and WB

At the mRNA (Fig. 3A) and protein (Fig. 3 B, C) levels, the expression of WISP-1 and fibrosis

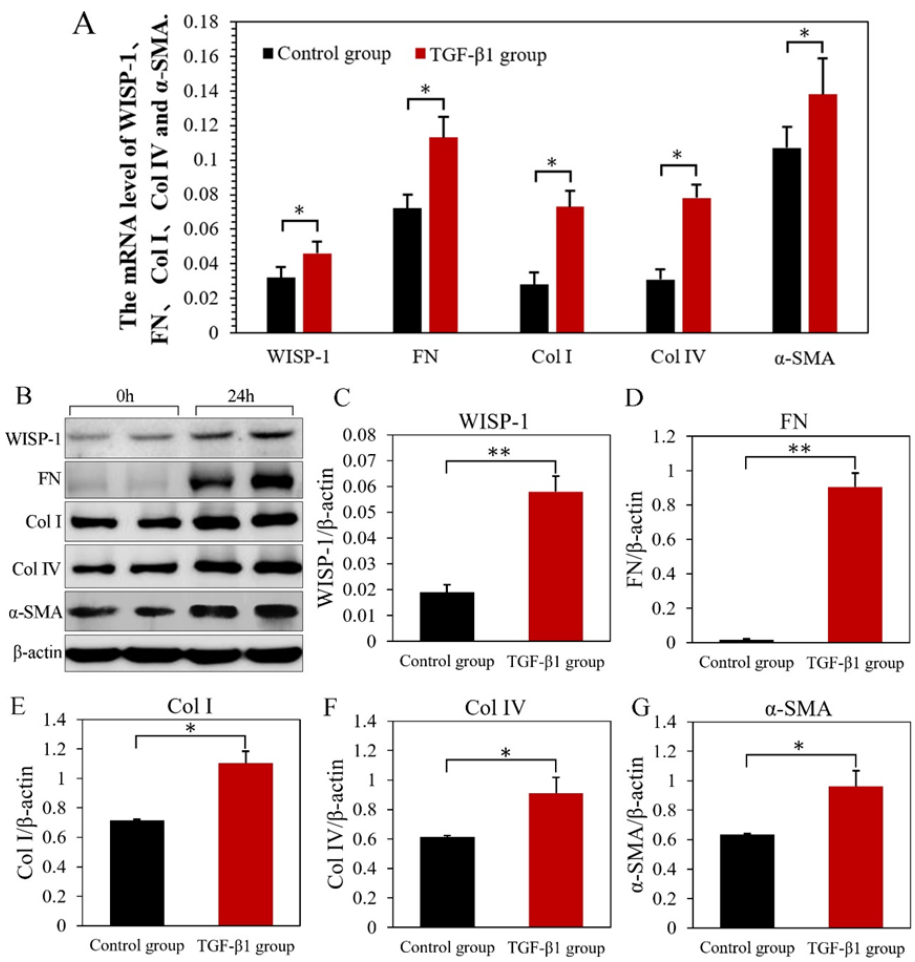

Fig. 1. *Expression of WISP-1, FN, Col I, Col IV, and α-SMA at the protein level in rat renal tubular epithelial cells.* ***A****) The expression of WISP-1, FN, Col I, Col IV, and α-SMA at the mRNA level in rat renal tubular epithelial cells;* ***B****) Western blot;* ***C****) WISP-1 relative gray statistics;* ***D****) FN relative gray statistics;* ***E****) Col I relative gray statistics;* ***F****) Col IV relative gray statistics; G: α-SMA relative gray statistics; *: vs control group P <0.05, **: vs control group P <0.01.*

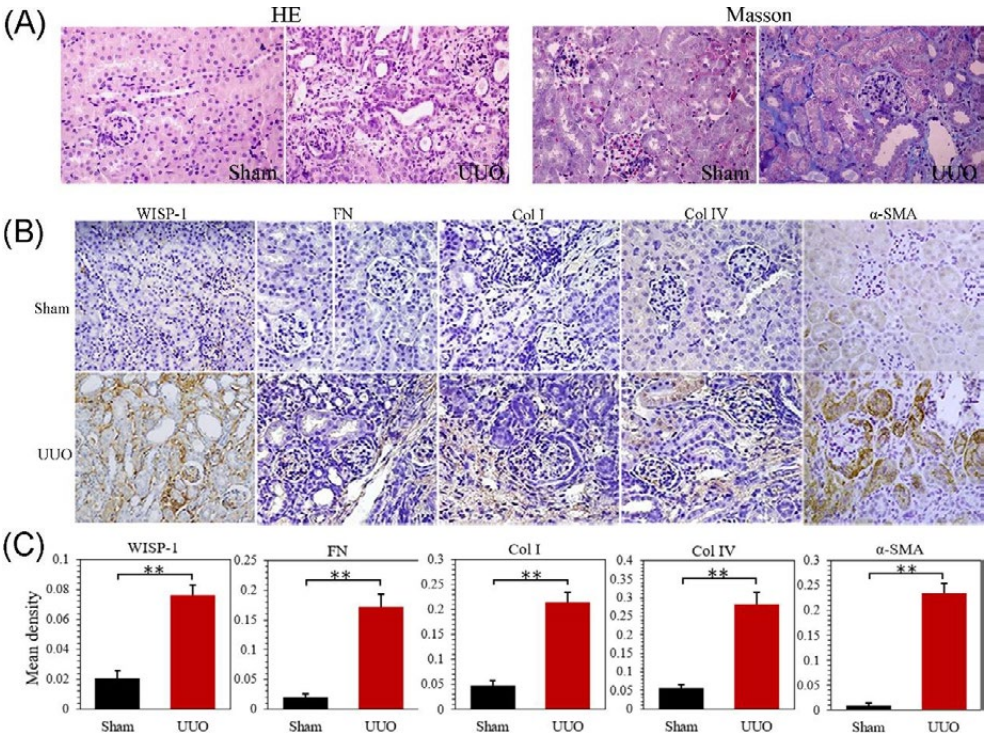

Fig. 2. ***A)*** *Morphological and structural changes of mouse kidney tissues observed by HE and Masson staining (×200);* ***B)*** *The expression of WISP-1, FN, Col I, Col IV, and α-SMA in mouse kidney tissue observed by immunohistochemical staining (×200);* ***C)*** *Average density statistics. ** vs Sham group P <0.01.*

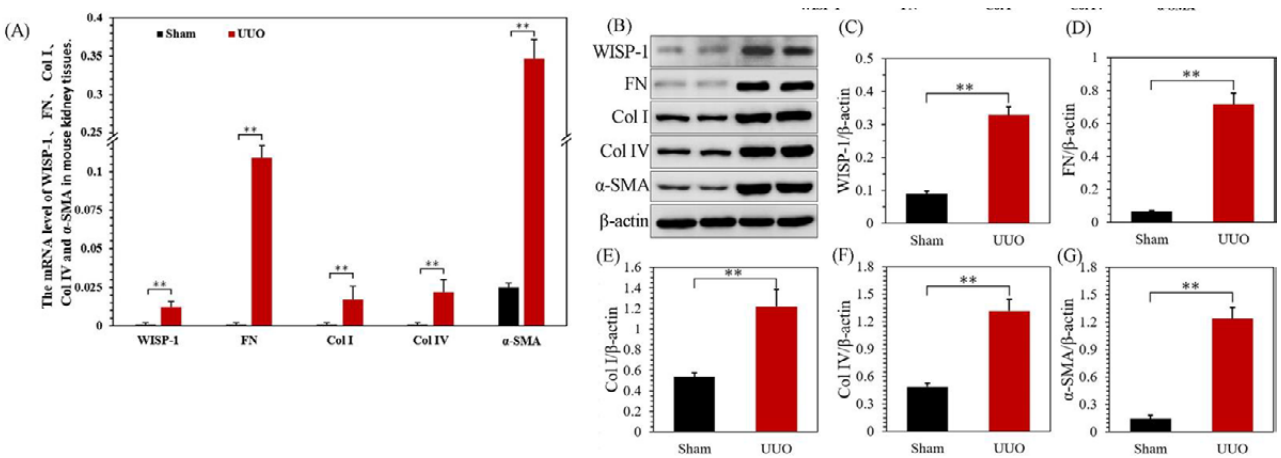

Fig. 3. *Expression of WISP-1, FN, Col I, Col IV, and α-SMA at the mRNA and protein level in mouse kidney tissues.* ***A)*** *The expression of WISP-1, FN, Col I, Col IV, and α-SMA at the mRNA level in mouse kidney tissues;* ***B)*** *Western blot;* ***C)*** *WISP-1 relative gray statistics;* ***D)*** *FN relative gray statistics;* ***E)*** *Col I relative gray statistics;* ***F)*** *Col IV relative gray statistics;* ***G)*** *α-SMA relative gray statistics; **: vs Sham group P <0.01.*

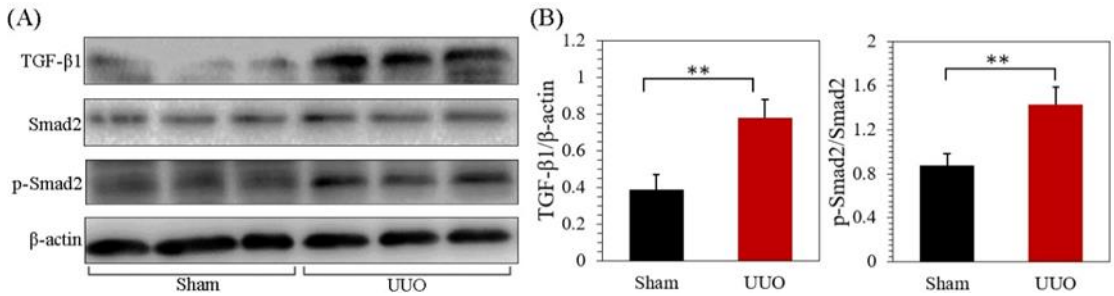

Fig. 4. *Expression of TGF-β1 and activation of Smad2 signaling pathway in mouse kidney tissues.* ***A)*** *Western blot;* ***B)*** *relative gray statistics; **vs Sham group P <0.01.*

indexes was higher than that in the Sham group. The consistency of the above results suggested that the expression of WISP-1 was enhanced in the renal fibrotic tissues of the UUO model.

TGF-β1 expression and activation of Smad2 signaling pathway

Compared with the Sham group, the expression of TGF-β1 and p-Smad2 protein in the UUO group was significantly increased (P <0.01) (Fig. 4).

DISCUSSION

The occurrence of renal fibrosis involves a variety of cytokines and signaling pathways. Many studies have proved that the TGF-β/Smad signaling pathway is the main pathway of renal fibrosis (10, 11). TGF-β1 plays an important role in the process of trans-differentiation of epithelial cells, endothelial cells and pericytes into myofibroblasts (12, 13). The UUO model is currently recognized as a model of tubulointerstitial fibrosis. There are reports in the literature that on the first day after UUO, α-SMA positive cells have already appeared in the renal interstitium, indicating that the activation of renal interstitial intrinsic fibroblasts in the early stage after UUO has been started (14, 15). In the UUO kidney model, the TGF-β1/Smad signaling pathway is significantly activated, which simultaneously causes a variety of lesions of renal interstitial fibrosis (16, 17). The results of this study indicate that TGF-β1, as a profibrotic factor, can stimulate fibrosis of renal tubular epithelial cells *in vitro*, also supported by *in vivo* data.

WISP-1 is related to fibrosis of the heart, lungs, liver and other organs (7-9, 18). It can be seen that WISP-1 may be a potential target for antifibrotic therapy, and inhibition of WISP-1 expression may reduce renal fibrosis. The present study showed that WISP-1 increases at the mRNA and protein levels in both *in vivo* and *in vitro* experiments, confirming its implication in renal fibrosis.

In summary, this study further confirms that WISP-1 expression is positively correlated with the degree of renal fibrosis and can be used as a new biomarker or potential therapeutic target.

REFERENCES

1. Zhou X, Bai C, Sun X, et al. Puerarin attenuates renal fibrosis by reducing oxidative stress induced-epithelial cell apoptosis via MAPK signal pathways in vivo and in vitro. Ren Fail 2017; 39(1):423-31.
2. Seif MM, Madboli AN, Marrez DA, Aboulthana WMK. Hepato-renal protective effects of Egyptian purslane extract against experimental cadmium toxicity in rats with special emphasis on the functional and histopathological changes. Toxicology Reports 2019; 6:625-31
3. Wang X, Fu W, Liu HY, Wang ZB, Kuang HX, Wang QH. The protective effect and the underlying mechanism of ephedra sinica stapf on renal injury in a murine model. Farmacia 2020; 68(3):476-82.
4. Wang Q, Zang W, Han L, et al. Wenyang Huazhuo Tongluo formula inhibits fibrosis via suppressing Wnt/β-catenin signaling pathway in a Bleomycin-induced systemic sclerosis mouse model. Chin Med 2018; 13:17.

5. Kerekes K, Bányai L, Trexler M, Patthy L. Structure, function and disease relevance of Wnt inhibitory factor 1, a secreted protein controlling the Wnt and hedgehog pathways. Growth Factors 2019; 37(1-2):29-52.
6. Soon LL, Yie TA, Shvarts A, Levine AJ, Su F, Tchou-Wong KM. Overexpression of WISP-1 down-regulated motility and invasion of lung cancer cells through inhibition of Rac activation. J Biol Chem 2003; 278(13):11465-70.
7. Venkatachalam K, Venkatesan B, Valente AJ, et al. WISP1, a pro-mitogenic, pro-survival factor, mediates tumor necrosis factor-alpha (TNF-alpha)-stimulated cardiac fibroblast proliferation but inhibits TNF-alpha-induced cardiomyocyte death. J Biol Chem 2009; 284(21):14414-27.
8. Jian YC, Wang JJ, Dong S, et al. Wnt-induced secreted protein 1/CCN4 in liver fibrosis both in vitro and in vivo. Clin Lab 2014; 60(1):29-35.
9. Königshoff M, Kramer M, Balsara N, et al. WNT1-inducible signaling protein-1 mediates pulmonary fibrosis in mice and is upregulated in humans with idiopathic pulmonary fibrosis. J Clin Invest 2009; 119(4):772-87.
10. Strutz F, Zeisberg M, Renziehausen A, Raschke B, Becker V, van Kooten C, Müller G. TGF-beta 1 induces proliferation in human renal fibroblasts via induction of basic fibroblast growth factor (FGF-2). Kidney Int 2001; 59(2):579-92.
11. Liu GX, Li YQ, Huang XR, et al. Disruption of Smad7 promotes ANG II-mediated renal inflammation and fibrosis via Sp1-TGF-β/Smad3-NF.κB-dependent mechanisms in mice. PLoS One 2013; 8(1):e53573.
12. Gu TT, Chen TY, Yang YZ, et al. Pterostilbene alleviates fructose-induced renal fibrosis by suppressing TGF-β1/TGF-β type I receptor/Smads signaling in proximal tubular epithelial cells. Eur J Pharmacol 2019; 842:70-78.
13. Zhang X, Bi-Cheng L, Al-Assaf S, Phillips G, Phillips A. Cordyceps sinensis decreases TGF-β1 dependent epithelial to mesenchymal transdifferentiation and attenuates renal fibrosis. Food Hydrocolloids 2012; 28:200-212.
14. Sato M, Muragaki Y, Saika S, Roberts AB, Ooshima A. Targeted disruption of TGF-beta1/Smad3 signaling protects against renal tubulointerstitial fibrosis induced by unilateral ureteral obstruction. J Clin Invest 2003; 112(10):1486-94.
15. Higashi AY, Aronow BJ, Dressler GR: Expression profiling of fibroblasts in chronic and acute disease models reveals novel pathways in kidney fibrosis. J Am Soc Nephrol 2019; 30(1):80-94.
16. Chen J, Li D. Telbivudine attenuates UUO-induced renal fibrosis via TGF-β/Smad and NF-κB signaling. Int Immunopharmacol 2018; 55:1-8.
17. Martínez-Klimova E, Aparicio-Trejo OE, Tapia E, Pedraza-Chaverri J. Unilateral ureteral obstruction as a model to investigate fibrosis-attenuating treatments. biomolecules 2019; 9(4):141. Tong Y, Yu Z, Zhang R, Ding X, Chen Z, Li Q. WISP1 mediates lung injury following hepatic ischemia reperfusion dependent on TLR4 in mice. BMC Pulm Med 2018; 18(1):189-89.
18. Tong Y, Yu Z, Zhang R, Ding X, Chen Z, Li Q: WISP1 mediates lung injury following hepatic ischemia reperfusion dependent on TLR4 in mice. BMC Pulm Med 2018, 18(1):189-89.

Lactate augments intramuscular triglyceride accumulation and mitochondrial biogenesis in rats

L. Zhou, SY. Chen, HJ. Han and JQ. Sun

Institute of Sports Science, Sichuan University, Chengdu, China PR

Received October 28, 2020 – Accepted January 15, 2021

Regular exercise induces intramuscular triglyceride accumulation with improved mitochondrial ability, but the mechanism remains unknown. The glycolytic product of exercise, lactate, has long been recognized to suppress lipolysis and promote lipogenesis in adipocytes through inhibition of the cAMP-PKA pathway by activation of the G protein-coupled receptor (GPR81). However, whether lactate results in a similar process in skeletal muscle is unclear. Here, by using intramuscular injection of lactate to the gastrocnemius, the lipid metabolism effects were investigated in rat skeletal muscle. Firstly, the lactate-injection effect was verified by comparing changes in blood lactate levels from injection and exercise (30 min, 31 m/min, treadmill running). After five weeks of lactate intervention, intramuscular triglyceride levels in the gastrocnemius and the proportion of epididymis adipose mass to body weight increased. Chronic intramuscular injection of lactate elevated lactate receptor, GPR81, and reduced cAMP response element-binding (CREB) and P-CREB abundance in the gastrocnemius. Additionally, there was a significant decline in lipolytic-related proteins (AMPK, P-AMPK, P-HSL, CPT-1B, TGF-β2, SDHA) and a significant increase in fat synthesis proteins (SREBP-1C, PPAR-γ). Surprisingly, mitochondrial biomarkers (PGC-1α, CS) were also increased in the gastrocnemius, suggesting that chronic lactate might promote mitochondria biogenesis. Together, these results demonstrated that lactate may play a crucial role in triglyceride storage and mitochondria biogenesis in the skeletal muscle of rat.

The role of lactate in inhibiting free fatty acid (FFA) and lipid metabolism has long been recognized (1), but the molecular pathway has been poorly understood for a long time (2). As early as the 1960s, researchers noted that lactate accumulation in the blood during intensive exercise coincides with decreases in fatty acid oxidation (3). Furthermore, exogenous lactate-injection to the circulation also causes a decline in circulating FFA in running dogs (4, 5). These experiments clearly show the effect of lactate on lipid metabolism and fatty acid release from adipocytes. However, whether these effects are achieved through the inhibition of lipolysis or the stimulation of lipogenesis is ambiguous. In recent years, several groups of researchers have found that lactate inhibits lipolysis in adipose tissue through activation of an orphan G protein-coupled receptor (GPR81), and this pathway has been tested in mouse, rat, and human adipocytes. In addition, the FFA-suppressing effect of lactate disappears in GPR81-deficient mice (6-9).

The lactate selectivity of GPR81 was discovered in adipose tissue where GPR81 is highly expressed and serves to downregulate the formation of cAMP,

Key words: Lactate; GPR81; cAMP; intramuscular triglyceride; skeletal muscle

Corresponding author:
Dr Jingquan Sun,
Institute of Sports Science,
Sichuan University, Chengdu, China PR
Tel.: +86 15114065276
e-mail: sunjingquan@scu.edu.cn

0393-974X (2021)
Copyright © by BIOLIFE, s.a.s.
This publication and/or article is for individual use only and may not be further reproduced without written permission from the copyright holder.
Unauthorized reproduction may result in financial and other penalties
DISCLOSURE: ALL AUTHORS REPORT NO CONFLICTS OF INTEREST RELEVANT TO THIS ARTICLE.

thereby curbing lipolysis and promoting the storage of lipid (8). GPR81 is also expressed in skeletal muscle, the primary site of lactate production, which forms and utilizes lactate continuously under resting conditions (6); however, the mechanism by which lactate functions in skeletal muscle is unclear. The adaptation of intramuscular triglyceride storage after training is a significant energy source during exercise; however, the molecular mechanism underlying this adaptation is unknown (2). Since there is a correlation between increased plasma lactate levels and decreased fatty acid mobilization during exercise, and since lactate inhibits lipolysis in adipocytes, we hypothesized that lactate might play a role in intramuscular triglyceride accumulation. A recent study reported that at the cellular level, lactate increases triglyceride accumulation in myotubes via the GPR81-cAMP signaling pathway (10). However, this effect has not been demonstrated in living animals.

The primary aim of this study was to investigate the long-term effect of lactate on intramuscular lipid metabolism. Thus, an experiment was designed to mimic exercise-induced lactate production in the gastrocnemius to investigate how lactate functions in rat skeletal muscle. Several muscular lipolytic proteins were selected, including adenosine monophosphate-activated protein kinase (AMPK), P-AMPK, hormone-sensitive lipase (HSL), transforming growth factor beta-2 (TGF-β2), succinate dehydrogenase (SDHA) and carnitine palmitoyltransferase-1B (CPT-1B). To further determine whether the accumulation of triglycerides was induced by lipogenesis, two crucial fat synthesis proteins, sterol regulatory element-binding protein-1c (SREBP-1C) and peroxisome proliferator-activated receptor gamma (PPAR-γ) (11), were detected. Moreover, growing evidence suggests that lactate acts as a signaling molecule and contributes to mitochondrial adaptation in skeletal muscle (12). Furthermore, exercise-induced intramuscular triglyceride accumulation is usually accompanied by the improvement of mitochondrial function to more efficiently breakdown triglycerides; recent studies have found a positive association between intramuscular triglyceride accumulation and the mitochondrial biogenesis protein, peroxisome proliferator-activated receptor-γ coactivator-1α (PGC-1α) (13). Therefore, the effect of lactate treatment on the mitochondrial biomarkers, PGC-1α and citrate synthase (CS), which are considered to be important in mitochondrial capacity, were investigated (14).

MATERIALS AND METHODS

Animals

The experiment was performed with Sprague Dawley rats (seven weeks of age, obtained from Chengdu DaShuo Biological Technology Co., Ltd. China). The rats were maintained on a standard rodent chow diet and water ad libitum under 12-h light/dark cycles. After an acclimation period of one week, the animals were assigned randomly into four groups according to their body weight: acute training group (n=5), which performed one single session of treadmill running (30min, 31m/min), and then blood lactate concentration was measured; acute lactate treated (n=14), subjected to a single dose of lactate-injection protocol, and then blood lactate concentration was measured; chronic lactate treated (CLT; n=10), subjected to a lactate-injection protocol for five weeks; chronic phosphate-buffered saline (PBS) treated (C; n=10). No death occurred during the experiment.

All procedures in the present study were approved by the Sichuan University animal ethics committee and carried out according to the criteria outlined in the "Guide for the Care and Use of Laboratory Animals."

Lactate treatment

Sodium lactate (C43922, Acros) solution was prepared in PBS (C0221A, Beyotime). For each injection, containers were aseptically processed, and the required solution was prepared. Local delivery of sodium lactate solution was performed by a single intramuscular injection in the gastrocnemius muscle of the left limb (0.64 mL/kg). According to a previous study, this value of lactate (0.25 M) was selected to elevate lactate levels in the gastrocnemius muscle to an average value of 25 mmol/L (15). To verify this protocol, we used two different lactate concentrations: 0.125 M and 0.25 M, to explore which concentration is more suitable for imitating exercise-induced lactate accumulation. Consequently, the 0.25 M

lactate solution was used for chronic intervention (five times/week for five weeks). The control animals were administered with PBS at the same volume (0.64 mL/kg each time, five times/week for five weeks).

Training protocol

All animals from the acute training group were initially familiarized with a motor-driven treadmill (Duan Animal Treadmill Co.Ltd, Huangzhou, China) for three days (5-10 m/min, 20 min/day) to avoid novelty and/or stress effects. Since chronic moderate-to-high intensity exercise has been well established to promote intramuscular triglyceride accumulation and mitochondria biogenesis in previous studies (16), a modified treadmill running protocol (30 min, 31 m/min, moderate to high intensity for rats) was used for the single session of training.

Determination of blood lactate concentration

Portable electrochemical devices Lactate Scout and Sensors (SensLab EKF, Germany) were used to determine the blood lactate level. The accuracy of this device has been proved in several studies (17). A drop of blood was excised from the aseptically treated wound of the rat's tail. After resting for 20 min, resting blood lactate concentration was determined. Then the rats were placed in a chamber to avoid external stimuli for the subsequent tests.

Western blot

After 6 h of fasting and 72 h after the final injection, the animals from C and CLT were anesthetized using chloral hydrate. The injected gastrocnemius was quickly excised on ice and frozen in liquid nitrogen, and stored at -80℃ for measurements. Approximately 180 mg of whole gastrocnemius muscle for each group (n=10) was homogenized in ice-cold RIPA buffer and then centrifuged at 12,000 RPM for 30 min at 4°C. The supernatant protein concentration was determined by BCA assay (Thermo) and trimmed by PBS for Western blotting analysis. 40-50μg protein for each lane was separated on a 10/12% SDS–PAGE gel and transferred onto a PVDF membrane, then blocked with 5% skimmed milk for 30-60min. Antibodies used for Western blotting were Secondary Antibody (31460, Invitrogen), GAPDH (AF7021, Affinity), GPR81 (PA5-75664, Invitrogen), P-CREB (AF3189, Affinity), CREB (AF6188, Affinity), SREBP-1C (AF4728, Affinity), PPAR-γ (AF6284, Affinity), AMPK (AF6423, Affinity), P-AMPK (AF3423, Affinity), TGF-β2 (ab113670, Abcam), CPT-1B (PA5-79065, Invitrogen), P-HSL (AF2206, Beyotime), SDHA (DF7043, Affinity), PGC1-α (AF7736, Beyotime), CS (DF13222, Affinity). Blots were developed using Western Lightning ECL (Affinity). All the bands were analyzed with Image J. GAPDH was used for the normalization of each protein to ensure the loading of equal quantities of protein.

Triglyceride assay

Intracellular triglycerides were assayed using a triglyceride assay kit (GPO-POD; Applygen Technologies Inc., Beijing, China) according to the manufacturer's recommended protocol. 50mg±5 of the gastrocnemius muscle of 7 rats each of each group were weighed and lysed on ice. After heating at 70℃ for 10 min, each sample was placed in a 96-well plate with two duplicates and then mixed with the kit's A+B solution. After 15-min incubation at 37°C and cooling to room temperature, the resultant purple color was measured using a spectrometer at 492 nm. Then the final values are calibrated by each sample's protein concentration measured by the BCA assay.

Weighing of epididymis adipose mass

After the rats were sacrificed by abdominal aorta blood sampling, the gastrocnemius muscle was excised, and epididymis adipose was stripped without connective tissue and weighed immediately. The proportion of epididymis adipose mass to body weight was calculated through each rat's epididymis adipose mass to body weight.

Statistical analysis

Statistical analyses were performed using GraphPad Prism software (version 8.0; GraphPad Software, Inc., La Jolla, CA, USA). The data were presented as the mean±standard deviation, and significant differences between the two groups were analyzed with the unpaired student test. $P<0.05$ was considered to indicate a statistically significant difference.

RESULTS

Time-dependent effect of different concentrations of intramuscular lactate-injection and the effect of acute training on the concentration of blood lactate

As shown in Fig. 1, the resting blood lactate

concentration of all rats in each group was 1.5±0.1 mmol/L. The peak value of injection-induced changes in blood lactate was reached (0.25 M lactate group = 4.63±1.11 mmol/L; 0.125 M lactate group = 2.4±0.26 mmol/L) after 5 min of injection. The exercise-induced changes in blood lactate were also determined after treadmill running (30 min, 31 m/min) for 5 min (one-time treadmill running group = 5.08±1.38 mmol/L). Therefore, to mimic exercise-induced lactate production, a 0.25 M sodium lactate solution was selected as the chronic intervention's concentration because the 0.25 M lactate solution caused changes in blood lactate to be close to exercise-induced changes in blood lactate levels (0.25 M lactate group = 4.63±1.11 mmol/L, one-time treadmill running = 5.08±1.38 mmol/L).

Effects of chronic lactate treatment

As shown in Fig. 2, chronic lactate intervention induces significantly increased in the abundance of triglycerides in the gastrocnemius (P = 0.0074) compared to that of the chronic phosphate-buffered saline intervention (the solvent of lactate solution). These data suggested that lactate might play a key role in intramuscular triglyceride accumulation.

Compared to the control rats, chronic lactate intervention induced significantly increased epididymis adipose mass percentage in body

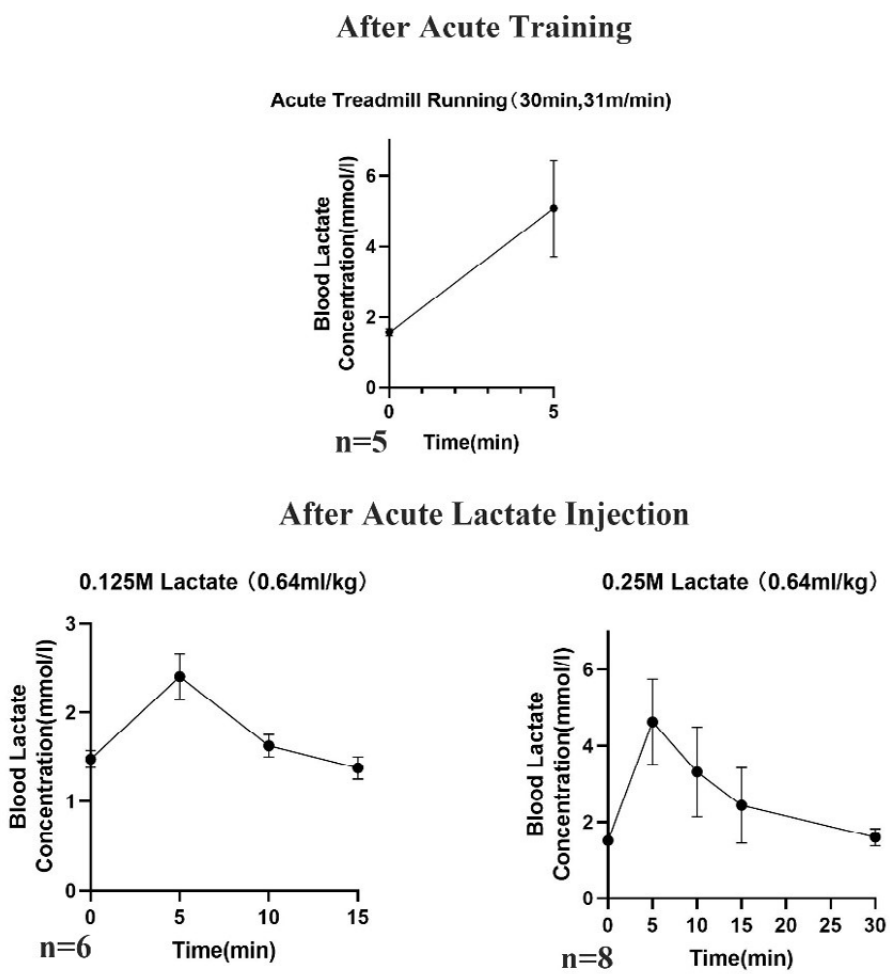

Fig. 1. *The time-dependent effect of intramuscular lactate-injection at different concentrations on blood lactate. Different rats were used in the three groups. The blood lactate of the acute 0.25 M lactate injection group (n = 8) was determined at rest and after the injection for 5, 10, 15, and 30 min. The blood lactate of the acute 0.125 M lactate injection group (n = 6) was determined at rest and after the injection for 5, 10, and 15 min. The blood lactate of the acute treadmill running (30 min, 31 m/min) group was determined at rest and after the training for 5 min. The data are presented as the mean±standard deviation.*

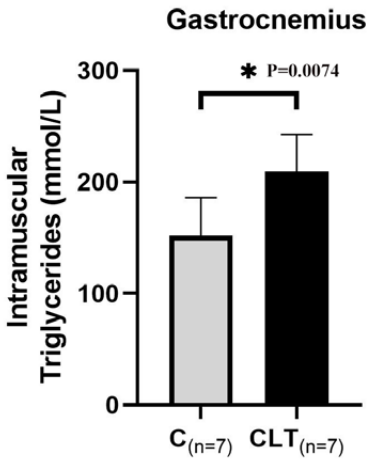

Fig. 2. *Effects of chronic lactate treatment on intramuscular triglycerides abundance in gastrocnemius. Experiments were performed with chronic PBS treated group (C, n=7) and chronic lactate treated group (CLT, n=7). Two replicates were used for each sample. The data were presented as the mean±standard deviation, and significant differences between the two groups were analyzed with the unpaired Student's t-test. *P < 0.05.*

weight (P = 0.0007) (Fig. 3), which suggests that intramuscular injection of lactate promoted lipid storage systemically.

Chronic lactate treatment at a concentration of 0.25 M elevated the expression of GPR81 (lactate's receptor) compared to that of the control group (P = 0.012) (Fig. 4). Consequently, the downstream GPR81 pathway, cAMP-PKA, was suppressed, as indicated by significant decreases in P-CREB (P = 0.0039) and CREB (P = 0.0013). These results suggested that the chronic intramuscular injection of lactate at concentrations of 0.25 M, 0.64 mL/kg, successfully activated GPR81 to inhibit the cAMP-PKA pathway in skeletal muscle.

SREBP-1C and PPAR-γ were examined to investigate the impact of lactate on lipogenesis, as they play a crucial role in the fatty acid synthesis and insulin-induced glucose metabolism (particularly in lipogenesis) (18). As shown in Fig. 5, after five weeks of lactate intervention, the abundance of SREBP-1C (P = 0.0183) and PPAR-γ (P = 0.0016)

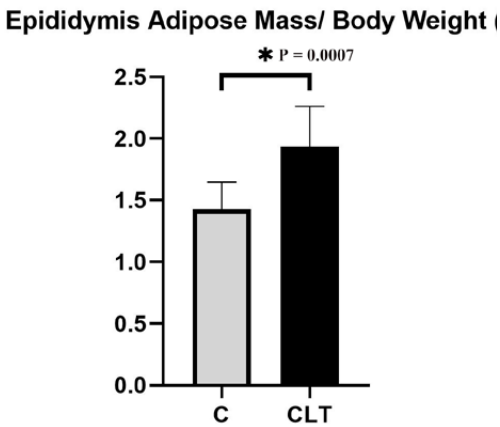

Fig. 3. *Changes in the proportion of epididymis adipose mass to body weight after chronic lactate intervention. Experiments were performed with the chronic PBS treated group (C, n=10) and chronic lactate treated group (CLT, n=10). The data were presented as the mean±standard deviation, and significant differences between the two groups were analyzed with the unpaired Student's t-test. *P < 0.05.*

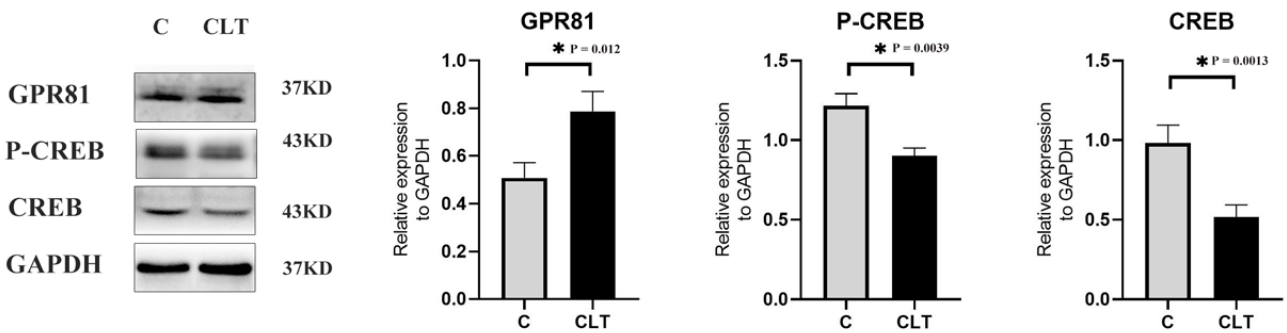

Fig. 4. *Western blot analysis and relative fold protein expression of GPR81, P-CREB, and CREB. Relative expression levels were normalized to GAPDH. Three bands are used for statistics. The data were presented as the mean±standard deviation, and significant differences between the two groups were analyzed with the unpaired Student's t-test. *P < 0.05. (GPR81, G-protein coupled receptor 81; CREB, cAMP response element-binding)*

was significantly increased, suggesting a mechanism by which lactate promotes lipogenesis in skeletal muscle. In summary, these data suggest that lactate might promote lipogenesis through SREBP-1C and PPAR-γ.

To determine whether the accumulation of triglycerides was induced by lipogenesis or inhibition of lipolysis, several proteins involved in the regulation of lipolysis in skeletal muscle were examined. As shown in Fig. 6A, CPT-1B, which is responsible for the transfer of free fatty acids into the mitochondria (19), was potently suppressed ($P < 0.0001$) in CLT rats. In addition, SDHA, which represents the activity of the tricarboxylic acid cycle (20), was also decreased ($P = 0.0337$) in the CLT group (Fig. 6B). Furthermore, the activity of AMPK and the AMPK-related protein (21), HSL, were also suppressed in CLT, as indicated by the reduction of levels of AMPK ($P = 0.0238$), P-AMPK ($P = 0.0012$), and P-HSL ($P = 0.012$) (Fig. 6 C, D). Lastly, TGF-β2, which plays a role in cellular energy uptake (22), also decreases ($P = 0.0017$) in the CLT group (Fig. 6E). In summary, these data indicated that lactate might induce triglyceride accumulation through inhibition of lipolysis.

Exercise-induced intramuscular triglyceride accumulation is often accompanied by the improved mitochondrial function that more effectively breaks down triglycerides (16); recent studies have found a direct association between the mitochondrial biogenesis protein PGC-1α and intramuscular triglyceride accumulation (13), therefore, biomarkers of mitochondrial biogenesis were included to investigate the impact of lactate on mitochondria. As presented in Fig. 7, levels of the PGC-1α protein, the classic biomarker of mitochondrial synthesis, increased ($P = 0.0017$) significantly in the CLT group compared to that of the control group. In addition, the CS protein, another mitochondrial marker, was significantly elevated ($P = 0.003$) after lactate intervention. These data suggested that lactate might play a key role in mitochondrial biogenesis.

DISCUSSION

In the current study, in order to investigate the physiological effects of lactate on rat skeletal muscle, an exogenous intramuscular lactate-injection method was used to simulate the transient elevation of systemic lactate levels after acute bouts of intensive exercise. After five weeks of lactate intervention, the intramuscular triglyceride levels in the gastrocnemius and the proportion of epididymis adipose mass to body weight were increased. Lactate

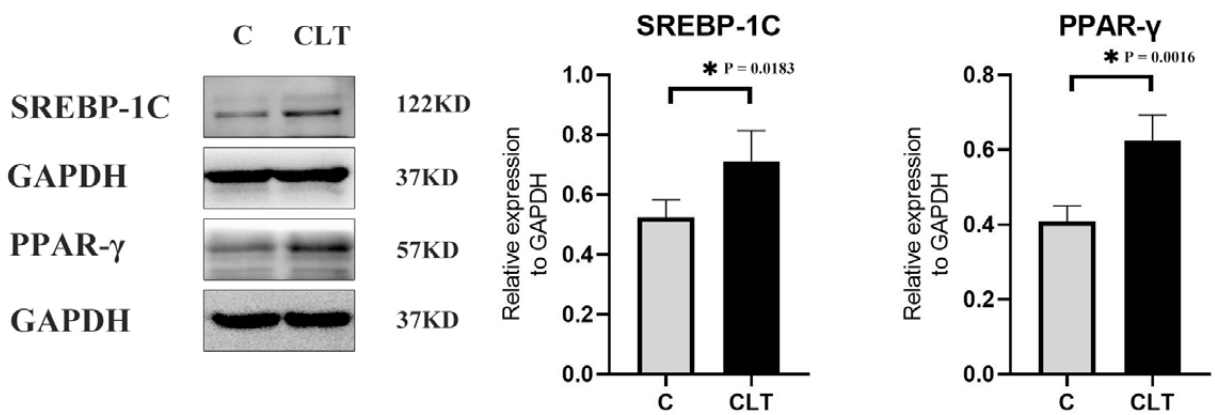

Fig. 5. *Western blot analysis and relative fold protein expression of SREBP-1C and PPAR-γ. Relative expression levels were normalized to GAPDH. Three bands are used for statistics. The data were presented as the mean±standard deviation. Significant differences between the two groups were analyzed with the unpaired Student's t-test. *P < 0.05.(SREBP-1C, sterol regulatory element-binding protein-1c; PPAR-γ, peroxisome proliferator-activated receptor-gamma)*

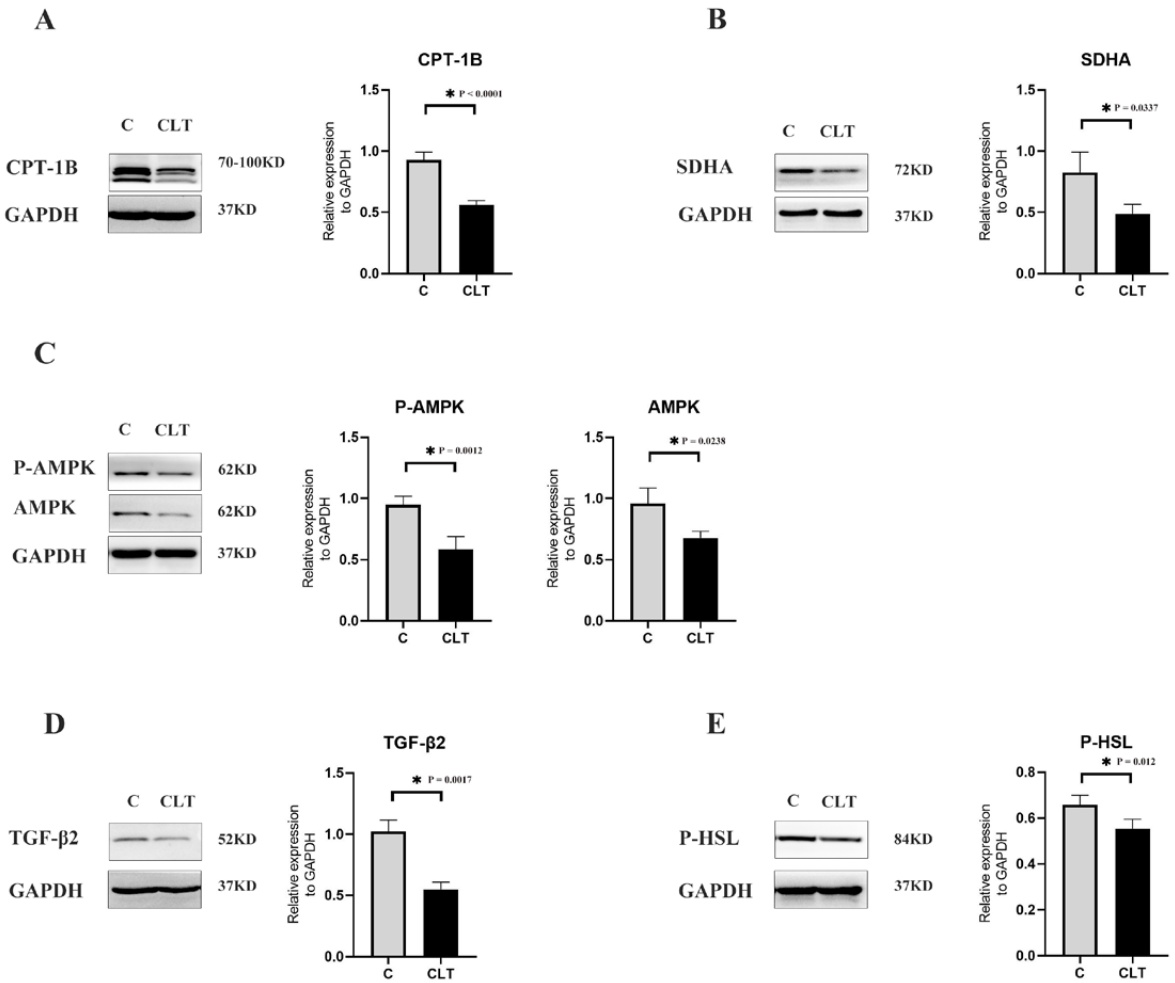

Fig. 6. *Western blot analysis and relative fold protein expression of (**A**) CPT-1B, (**B**) SDHA, (**C**) AMPK and P-AMPK, (**D**) TGF-β2, and (**E**) P-HSL. Relative expression levels were normalized to GAPDH. Three bands are used for statistics. The data were presented as the mean±standard deviation, and significant differences between the two groups were analyzed with the unpaired Student's t-test. *P < 0.05.(CPT-1B, carnitine palmitoyltransferase-1B; SDHA, succinate dehydrogenase; AMPK, adenosine monophosphate-activated protein kinase; TGF-β2, transforming growth factor beta-2; HSL, hormone-sensitive lipase).*

also elevated levels of its receptor, GPR81, and downregulated the abundance of its downstream protein, CREB, and P-CREB in the gastrocnemius. Meanwhile, there was a significant decline in lipolytic proteins and a significant increase in fat synthesis proteins, favoring intramuscular lipid accumulation. Furthermore, biomarkers of mitochondria (PGC-1α and CS) were also increased in the gastrocnemius, suggesting that chronic lactate treatment may promote mitochondrial biogenesis.

Fatty acid derived from intramuscular triglycerides is a significant energy source during exercise. Moderate to high intensity exercise results in a higher energy demand in the exercising muscle. Thus, the adaptation of intramuscular triglyceride storage after exercise may benefit exercising tissue by supplying free fatty acids at the site of the energy demand (23). However, the molecular mechanism underlying this adaptation is unknown (2). In this study, a new viewpoint was established that lactate plays a fundamental role in energy resource adaptation.

Independent of pH or sodium ions, lactate

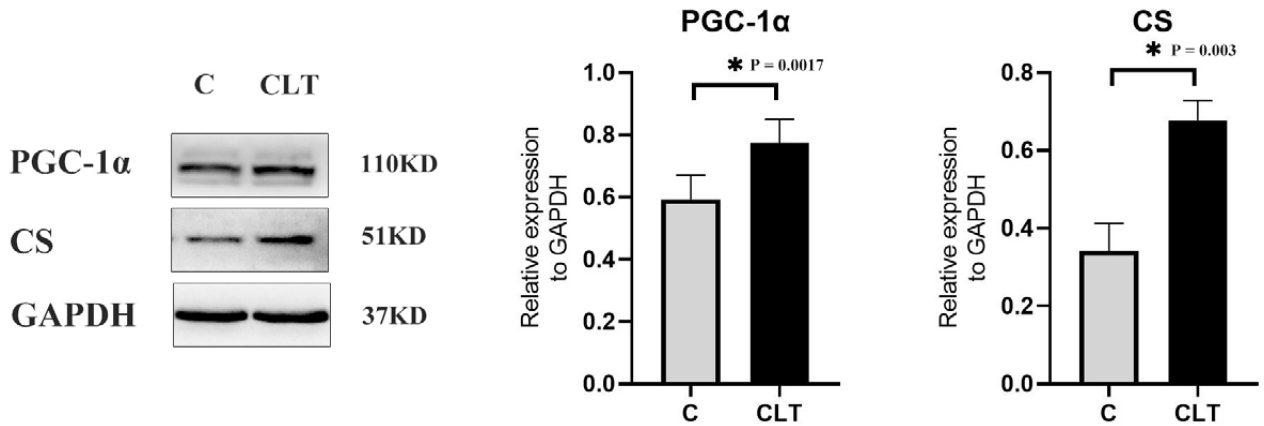

Fig. 7. *Western blot analysis and relative fold protein expression of PGC-1α and CS. Relative expression levels were normalized to GAPDH. Three bands are used for statistics. The data were presented as the mean±standard deviation, and significant differences between the two groups were analyzed with the unpaired Student's t-test. *P < 0.05. (PGC-1α, peroxisome proliferator-activated receptor-γ coactivator-1α; CS, citrate synthase)*

itself inhibits lipolysis in fat cells via activation of GPR81 (6). In mouse, rat, and human adipocytes, GPR81 appears to act as a lactate sensor with an inhibitory effect on lipolysis via cAMP and CREB (24), of which cAMP stimulates downstream genes via protein kinase A-mediated phosphorylation of CREB (25). However, the mechanism of whether lactate affects lipid metabolism in skeletal muscle was poorly understood. Here, these results demonstrated that using the intramuscular lactate-injection protocol (0.25 M sodium lactate, 0.64 mL/kg, five times/week for five weeks) to elevate lactate levels in the blood each time to an average value of 4.63±1.11 mmol/L, which is similar to moderate exercise-induced changes in blood lactate (Fig. 1), successfully activated the GPR81 signaling pathway to downregulate the cAMP-PKA signaling pathway in skeletal muscle (Fig. 4).

In line with previous cell experiments showing that lactate is associated with triglyceride accumulation (10), chronic lactate treatment also significantly increased the abundance of intramuscular triglycerides in living animals (Fig. 2). Surprisingly, it was also found that the intramuscular injection of lactate promoted systemic lipid storage, indicated by significant increases in the proportion of epididymis adipose mass to body weight (Fig. 3). Since the GPR81 signaling pathway is mobilized, which has been shown to promote fat production in adipocytes (6), and intramuscular triglycerides are elevated simultaneously, these results demonstrated the possibility that systemic triglyceride accumulation resulting from lactate injection may be attributed to the GPR81 signaling pathway.

Adipogenesis is a complex process that requires the synergistic action of various adipogenic enzymes, including SREBP-1C and PPAR-γ. SREBP-1C and PPAR-γ play a central role in adipocyte development, intramuscular lipid droplet programming, and exercise-induced lipid metabolism in mice and humans (13, 26). The cAMP/CREB pathway negatively regulates SREBP-1C expression at the transcriptional and post-translational levels (27). This is in line with our results, which show a significant increase in SREBP-1C and PPAR-γ following chronic lactate-induced suppression of the cAMP/CREB pathway. These results suggested that chronic lactate treatment promoted adipogenesis in rat skeletal muscle.

In addition to elevating levels of lipogenesis

proteins, lipid storage also requires numerous other processes, such as the reduction of lipolysis. These additional effects could also account for the effect of lactate on intramuscular triglyceride accumulation. To examine whether chronic lactate treatment affects lipolysis, a few key proteins involved in the regulation of lipolysis in skeletal muscle were detected. AMPK is involved in regulating intramuscular triglyceride breakdown during exercise via phosphorylation of the enzyme HSL, which is thought to be an important rate-limiting enzyme in intramuscular triglyceride breakdown (28). CPT-1B is responsible for the transfer of free fatty acids into the mitochondria (19), while SDHA plays a vital role in adenosine triphosphate production through the mitochondrial respiratory chain (20) and negatively correlates with circulating FFA (29). Furthermore, recent studies have shown that TGF-β2 stimulates cellular uptake of glucose and fatty acids (30). In this study, all of the lipolysis-related proteins mentioned above were significantly suppressed after chronic lactate treatment (Fig. 6). Therefore, these results suggested that lactate-induced triglyceride accumulation may be achieved through the inhibition of lipolysis.

Interestingly, although lipolysis in the gastrocnemius is suppressed by chronic lactate treatment, the classic mitochondrial biomarkers, PGC-1α and CS (31), are enhanced in this study, suggesting that lactate may promote mitochondrial biogenesis. PGC-1α plays a prominent role in regulating mitochondrial genesis, oxidative metabolism, and muscle adaption to exercise (32). Furthermore, PGC-1α may also promote intramuscular lipid storage (32). Therefore, according to our results, PGC-1α might be involved in mitochondrial biogenesis and intramuscular lipid storage simultaneously. At the cellular level, lactate stimulates the expression of the PGC-1α mRNA and promotes mitochondrial biogenesis (33). Here, the mitochondrial biogenesis effect of lactate was demonstrated in living animals (Fig. 7).

In summary, we hypothesize that lactate is involved in intramuscular triglyceride accumulation and mitochondrial biogenesis. These data indicate that lactate promoted the accumulation of intramuscular triglycerides by inhibiting lipolysis and stimulating lipogenesis. In addition, enhanced mitochondrial synthesis, which is usually accompanied by intramuscular triglyceride accumulation to breakdown triglycerides more efficiently after training, is also induced by lactate.

ACKNOWLEDGEMENT

This study is supported by The National Natural Science Foundation of China (31801002).

REFERENCES

1. Brooks GA, Mercier J. Balance of carbohydrate and lipid utilization during exercise: the "crossover" concept. J Appl Physiol (1985) 1994; 76(6):2253-61.
2. Bergman BC, Goodpaster BH. Exercise and muscle lipid content, composition, and localization: influence on muscle insulin sensitivity. Diabetes 2020; 69(5):848-58.
3. Issekutz B, Miller H. Plasma free fatty acids during exercise and the effect of lactic acid. Exp Biol Med 1962; 110(2):237-9.
4. Miller HI, Issekutz B, Jr., Rodahl K, Paul P. Effect of lactic acid on plasma free fatty acids in pancreatectomized dogs. Am J Physiol 1964; 207(6):1226-30.
5. Gold M, Miller HI, Issekutz B, Jr., Spitzer JJ. Effect of exercise and lactic acid infusion on individual free fatty acids of plasma. Am J Physiol 1963; 205(5):902-4.
6. Ahmed K, Tunaru S, Tang C, et al. An autocrine lactate loop mediates insulin-dependent inhibition of lipolysis through GPR81. Cell Metab 2010; 11(4):311-9.
7. Cai TQ, Ren N, Jin L, et al. Role of GPR81 in lactate-mediated reduction of adipose lipolysis. Biochem Biophys Res Commun 2008; 377(3):987-91.
8. Liu C, Wu J, Zhu J, et al. Lactate inhibits lipolysis in fat cells through activation of an orphan G-protein-coupled receptor, GPR81. J Biol Chem 2009; 284(5):2811-22.
9. Lauritzen KH, Morland C, Puchades M, et al. Lactate receptor sites link neurotransmission, neurovascular coupling, and brain energy metabolism. Cereb Cortex 2014; 24(10):2784-95.
10. Sun J, Ye X, Xie M, Ye J. Induction of triglyceride

accumulation and mitochondrial maintenance in muscle cells by lactate. Sci Rep 2016; 6(1):33732.
11. Wada S, Yamazaki T, Kawano Y, Miura S, Ezaki O. Fish oil fed prior to ethanol administration prevents acute ethanol-induced fatty liver in mice. J Hepatol 2008; 49(3):441-50.
12. Takahashi K, Kitaoka Y, Yamamoto K, Matsunaga Y, Hatta H. Oral lactate administration additively enhances endurance training-induced increase in cytochrome c oxidase activity in mouse soleus muscle. Nutrients 2020; 12(3).
13. Koves TR, Sparks LM, Kovalik JP, et al. PPARgamma coactivator-1alpha contributes to exercise-induced regulation of intramuscular lipid droplet programming in mice and humans. J Lipid Res 2013; 54(2):522-34.
14. Egan B, Zierath JR. Exercise metabolism and the molecular regulation of skeletal muscle adaptation. Cell Metab 2013; 17(2):162-84.
15. Nikooie R, Samaneh S. Exercise-induced lactate accumulation regulates intramuscular triglyceride metabolism via transforming growth factor-beta1 mediated pathways. Mol Cell Endocrinol 2016; 419:244-51.
16. Zacharewicz E, Hesselink MKC, Schrauwen P. Exercise counteracts lipotoxicity by improving lipid turnover and lipid droplet quality. J Intern Med 2018; 284(5):505-18.
17. Romanov AY, Prikhodko AM, Tysyachnyi OV, Baev OR, Yarotskaya EL, Sukhikh GT. Comparison of cord blood lactate measurement by gas analyzer and portable electrochemical devices. J Perinat Med 2020; 48(2):157-61.
18. Eberle D, Hegarty B, Bossard P, Ferre P, Foufelle F. SREBP transcription factors: master regulators of lipid homeostasis. Biochimie 2004; 86(11):839-48.
19. Ratner C, Madsen AN, Kristensen LV, et al. Impaired oxidative capacity due to decreased CPT1b levels as a contributing factor to fat accumulation in obesity. Am J Physiol Regul Integr Comp Physiol 2015; 308(11):R973-82.
20. Pollard PJ, Wortham NC, Tomlinson IP. The TCA cycle and tumorigenesis: the examples of fumarate hydratase and succinate dehydrogenase. Ann Med 2003; 35(8):632-9.
21. Gaidhu MP, Anthony NM, Patel P, Hawke TJ, Ceddia RB. Dysregulation of lipolysis and lipid metabolism in visceral and subcutaneous adipocytes by high-fat diet: role of ATGL, HSL, and AMPK. Am J Physiol Cell Physiol 2010; 298(4):C961-71.
22. Starling S. A new metabolic role for TGFbeta2. Nat Rev Endocrinol 2019; 15(4):191.
23. van Loon LJ, Koopman R, Stegen JH, Wagenmakers AJ, Keizer HA, Saris WH. Intramyocellular lipids form an important substrate source during moderate intensity exercise in endurance-trained males in a fasted state. J Physiol 2003; 553(Pt 2):611-25.
24. Langin D. Adipose tissue lipolysis revisited (again!): lactate involvement in insulin antilipolytic action. Cell Metab 2010; 11(4):242-3.
25. Brindle P, Nakajima T, Montminy M. Multiple protein kinase A-regulated events are required for transcriptional induction by cAMP. Proc Natl Acad Sci U S A 1995; 92(23):10521-5.
26. Horton JD, Goldstein JL, Brown MS. SREBPs: activators of the complete program of cholesterol and fatty acid synthesis in the liver. J Clin Invest 2002; 109(9):1125-31.
27. Zhou L, Li Y, Nie T, et al. Clenbuterol inhibits SREBP-1c expression by activating CREB1. J Biochem Mol Biol 2007; 40(4):525-31.
28. Kiens B. Skeletal muscle lipid metabolism in exercise and insulin resistance. Physiol Rev 2006; 86(1):205-43.
29. Petersson SJ, Christensen LL, Kristensen JM, Kruse R, Andersen M, Hojlund K. Effect of testosterone on markers of mitochondrial oxidative phosphorylation and lipid metabolism in muscle of aging men with subnormal bioavailable testosterone. Eur J Endocrinol 2014; 171(1):77-88.
30. Takahashi H, Alves CRR, Stanford KI, et al. TGF-beta2 is an exercise-induced adipokine that regulates glucose and fatty acid metabolism. Nat Metab 2019; 1(2):291-303.
31. Larsen S, Nielsen J, Hansen CN, et al. Biomarkers of mitochondrial content in skeletal muscle of healthy young human subjects. J Physiol 2012; 590(14):3349-60.
32. Summermatter S, Baum O, Santos G, Hoppeler H, Handschin C. Peroxisome proliferator-activated receptor {gamma} coactivator 1{alpha} (PGC-1{alpha}) promotes skeletal muscle lipid refueling in vivo by activating de novo lipogenesis and the

pentose phosphate pathway. J Biol Chem 2010; 285(43):32793-800.

33. Hashimoto T, Hussien R, Oommen S, Gohil K, Brooks GA. Lactate sensitive transcription factor network in L6 cells: activation of MCT1 and mitochondrial biogenesis. FASEB J 2007; 21(10):2602-12.

PADI4, negatively regulated by miR-335-5p, participates in regulating the proliferation, migration, invasion and radiosensitivity of nasopharyngeal carcinoma cells

LN. Wei[1*], M. Luo[2*], XP. Wang[2], T. Liang[2], CJ. Huang[2] and H. Chen[2]

[1]Department of Endoscopy, The Affiliated Tumor Hospital of Guangxi Medical University, Nanning Guangxi, China; [2]Department of Oncology, Nanning The Second People's Hospital, Nanning, Guangxi, China

Received October 26, 2020 – Accepted January 14, 2021

*These Authors contributed equally to this work

Peptidyl arginine deiminase 4 (PADI4), an enzyme that converts arginine residues to citrulline residues in the presence of calcium ions, affects the biochemical activities of proteins. The biological function of PADI4 as well as its mechanism in nasopharyngeal carcinoma (NPC) necessitates further investigation. PADI4 expression in NPC tissues and cells was detected using Western blot. qRT-PCR was used to determine the expression of miR-335-5p and PADI4 mRNA in NPC tissues and cells. BrdU assay and CCK-8 assay were employed to detect cell proliferation. Cell migration and invasion were evaluated using Transwell assay. NPC cells were exposed to different doses of radiation *in vitro*, and then colony formation assays were used to detect colony survival. The target relationship between miR-335-5p and PADI4 was verified using Western blot, qRT-PCR, and dual-luciferase reporter gene assays. Compared with normal mucosal epithelial tissues and cell lines, the expression level of PADI4 in NPC tissues and cells was significantly up-regulated. PADI4 overexpression promoted the proliferation, migration, and invasion of NPC cells. Under radiation, NPC cell survival was significantly promoted by the up-regulation of PADI4. Conversely, knock-down of PADI4 suppressed the above-mentioned malignant phenotypes. MiR-335-5p could bind with the 3' UTR of PADI4 mRNA, and suppressed the expression of PADI4. PADI4 down-regulated the expression of p21 and activated the mTOR signaling pathway. PADI4, which is negatively regulated by miR-335-5p, promotes the proliferation, migration, invasion and radioresistance of NPC cells by regulating the p21 and mTOR signaling pathways.

Nasopharyngeal carcinoma (NPC), which mainly occurs in southern China and Southeast Asia, is a solid tumor originating from nasopharyngeal epithelial cells (1). Moreover, its morbidity reaches up to 25 cases per 100,000 population in endemic regions, which is 25-fold higher than elsewhere in the world (1, 2). Due to the limited therapies, the prognosis is poor for NPC patients with recurrences, distant metastases, chemoresistance or radioresistance (3). Therefore, an in-depth exploration on the mechanism of NPC progression is necessary to discover novel therapeutic targets for NPC.

Peptidyl arginine deiminase (PAD) catalyzes the transformation from arginine residues in polypeptides to citrulline in the presence of Ca^{2+} (4). The molecular conformation of the citrullinated protein is frequently changed, followed by changes of the biochemical activity (5). At present, five PAD enzymes have been found in human tissues (4, 6). Among them, peptidyl arginine deiminase

Key words: miR-335-5p; PADI4; NPC

Corresponding Author:
Dr Hao Chen,
Department of Oncology,
Nanning The Second People's Hospital,
13 Dancun Road, Nanning 530021, Guangxi, China
Tel.: +86 18934717234/86 07712870627
e-mail: lanzaidu88@163.com.

0393-974X (2021)
Copyright © by BIOLIFE, s.a.s.
This publication and/or article is for individual use only and may not be further reproduced without written permission from the copyright holder.
Unauthorized reproduction may result in financial and other penalties
DISCLOSURE: ALL AUTHORS REPORT NO CONFLICTS OF INTEREST RELEVANT TO THIS ARTICLE.

4 (PADI4, PAD4), which is originally cloned in HL-60 cells, forming a dimer, consisting of 663 amino acids with a molecular mass of 74 kDa (7). The citrullinated protein catalyzed by PADI4 is involved in a variety of biological processes. For example, citrullinated nucleoprotein 1 (NPM1) is transferred from the nucleoli to the nucleus to inhibit apoptosis (8); cytokeratin (CK) is also a critical apoptosis-related protein, and citrullinated CK can suppress the cleavage of caspase, thereby inhibiting the apoptosis (9). In addition, PADI4, significantly over-expressed in lung cancer tissues, is involved in the promotion of epithelial-mesenchymal transition (EMT) (10). These studies suggest that PADI4 plays an oncogenic role in human tumors, but the role of PADI4 in the progression of NPC still warrants further investigation.

MicroRNA (miRNA), a type of endogenous non-coding small single-stranded RNA consisting of 18 to 24 nucleotides, is widely found in plants, animals, protozoa and viruses (11). MiRNAs are involved in the tumorigenesis and progression of tumors including NPC, by regulating the biological processes of cells, such as apoptosis, cell proliferation, DNA damage repair, metabolism, and they also act as carcinogens or tumor suppressors to regulate the expression of genes (12, 13). For example, miR-506 inhibits the metastasis of NPC cells by inactivating the Wnt/β-catenin signaling pathway and down-regulating LHX2 expression (14). MiR-122 exerts tumor-suppressing effects by regulating the PI3K/AKT signaling pathway (15). MiR-222 promotes NPC progression and increases radioresistance by regulating PTEN (16). Additionally, miR-335-5p plays a tumor-suppressing role in a variety of human tumors, such as non-small cell lung cancer, gastric cancer, thyroid cancer and NPC (17-20). However, the role of miR-335-5p in the progression of NPC needs further study.

In this study, we found that PADI4 expression was significantly up-regulated in NPC tissues. Over-expression of PADI4 in NPC cells remarkably promoted the proliferation, migration, and invasion of NPC cells, and reduced radiosensitivity. Mechanistically, PADI4 was negatively regulated by miR-335-5p, and it could regulate p21 and mTOR pathways. This study is expected to provide potential targets for NPC treatments.

MATERIALS AND METHODS

Tissue samples

Our study was approved by the Ethics Review Board of The Affiliated Tumor Hospital of Guangxi Medical University. According to the Declaration of Helsinki, human tissue samples were collected and used. The written informed consent was signed by all participants. The tumor tissues and normal nasopharyngeal mucosa derived from 45 newly diagnosed NPC patients were collected. There were 27, 13, and 5 cases of non-keratinized squamous cell carcinoma, keratinized squamous cell carcinoma, and undifferentiated carcinoma, respectively, and the samples were stored in liquid nitrogen at -196°C.

Inclusion criteria are as follows: newly diagnosed patients with nasopharyngeal carcinoma diagnosed by histopathological examination and hospitalized in our hospital; patients who plan to complete the radiotherapy plan. Exclusion criteria: patients with incomplete clinical data. None of the patients had received anticancer treatment before tissue samples were collected.

Cell lines

Human immortalized nasopharyngeal epithelial cell lines (NP69 cells) and NPC cell lines (CNE1, S18, S26, CNE2 and SUNE2 cells) were procured from the BeNa Culture Collection (BNCC, Beijing, China). The above cells were cultured in Dulbeccos Modified Eagles Medium (DMEM) (HyClone, Logan, UT, USA) supplemented with 10% fetal bovine serum (FBS) (Hyclone, Waltham, MA, USA), 100 U/mL penicillin and 0.1 mg/mL streptomycin (Invitrogen, Carlsbad, CA, USA) in 5% CO_2 at 37°C.

Cell transfection

Empty plasmid (Ctrl), pcDNA-PADI4 (PADI4), non-targeting siRNA (si-Ctrl, sense strand, 5'-UUCUCCGAACGUGUCACGUTT-3' and antisense strand, 5'-ACGUGACACGUUCGGAGAATT-3'), siRNAs against PADI4 (si-PADI4, sense strand, 5'-GCAAGACAGUGUCUGUUAAGA-3' and antisense strand, 5'- UUAACAGACACUGUCUUGCUG-3'), scrambled miRNA negative control (miR-Ctrl, 5'-CACUGGUACAAGGGUUGGGAGA-3'),

miR-355-5p mimics (miR-355-5p, 5'-UCAAGAGCAAUAACGAAAAAUGU-3'), and miR-355-5p inhibitors (miR-355-5p in, 5'-ACAUUUUUCGUUAUUGCUCUUGA-3') were purchased from GenePharma (Shanghai, China). CNE1 and SUNE2 cells were transferred into 24-well plates (3×10^5 cells/well) and then cultured at 37°C in 5% CO_2 for 24 h. After that, NPC cells were transfected with the siRNAs (50 nM), mimics (20 nM), or inhibitors (20 nM) using Lipofectamine 3000 (Invitrogen, Carlsbad, CA, USA). Transfection efficiency was detected using quantitative real-time polymerase chain reaction (qRT-PCR) or Western blot 24 h after the transfection.

RNA isolation and qRT-PCR

Total RNA was extracted from tissues and cell lines using TRIzol Regent (Invitrogen, Carlsbad, CA, USA). NanoDrop Microvolume Spectrophotometer was then used to detect the concentration and purity of RNA and the extracted RNA was subjected to reverse transcription to obtain complementary DNA (cDNA). 2 μL of obtained cDNA was taken for the following PCR amplification with U6 and GAPDH as internal references. The sequences of the primers used are shown as follows: U6: forward primer: 5'-CTCGCTTCGGCAGCACA-3', reverse primer: 5'-AACGCTTCACGAATTTGCGT-3'; GADPH: forward primer: 5'-AACGGATTTGGTCGTATTG-3', reverse primer: 5'-GGAAGATGGTGATGGGATT-3'; miR-335-5p, forward primer: 5'-UGUUUUGAGCGGGGGUCAAGAGC-3', reverse primer: 5'-CUCUCAUUUGCUAUAUUCA-3'; PADI4, forward primer: 5'-CGAAGACCCCCAAGGACT-3', reverse primer: 5'-AGGACAGTTTGCCCCGTG-3'. The PCR reaction system was established with a total volume of 20 μL: 2 μL of cDNA, 10 μL of SYBR Green Mix (Takara, Dalian, China), 0.5 μL of primers, and 7.5 μL of ddH_2O. PCR amplification was conducted on Applied Biosystems 7500 detection system (Applied Biosystems, Foster City, CA, USA). The relative expressions of the genes were calculated using $2^{-\Delta\Delta Ct}$ method.

Western blot

NPC tissues and cell lines were lysed using RIPA lysis buffer (Pierce, Rockford, IL, USA) and the supernatant was collected after high-speed centrifugation. Then the protein concentration was determined using bicinchoninic acid (BCA) kit (Beyotime, Shanghai, China), and the protein in supernatant was denatured in boiling water at 100°C for 10 min. After that, the prepared protein sample (30 μg) was subjected to electrophoresis using 10% sodium dodecyl sulfate-polyacrylamide gel (SDS-PAGE) and then transferred to polyvinylidene fluoride (PVDF) membrane (Millipore, Billerica, MA, USA). After being blocked using 5% skimmed milk, the membrane was incubated with the primary antibody at 4°C overnight. Following that, the membrane was rinsed using TBST solution and then incubated with Goat Anti-Rabbit IgG H&L (Abcam, ab150077, 1: 1000) at room temperature for 1 h. After the rinse with TBST again, the protein bands on the membrane were visualized using enhanced chemiluminescence kit (Pierce, Waltham, MA, USA). The primary antibodies used in this study were as follows: anti-PADI4 antibody (Abcam, ab128086, 1: 1000), anti-p21 antibody (Abcam, ab218311, 1: 1000), anti-p-mTOR (Abcam, ab84400, 1: 1000), and anti-β-actin antibody (Abcam, ab20272, 1: 3000). Signal quantification was obtained using Quantity One software (Version 4.6.6; Bio-Rad Laboratories, Inc, Berkeley, CA, USA).

Cell counting kit-8 (CCK-8) assay

NPC cells were trypsinized, harvested, and resuspended to make cell suspension (1×10^4 cells / mL). Each well of the 96-well plate was supplemented with 100 μL of cell suspension and 3 replicate wells were set for each group. Thereafter, the 96-well plate was maintained at 37°C in 5% CO_2. 24 h later, 10 μL of CCK-8 solution (Dojindo, Kumamoto, Japan) was added to each well and incubated for 60 min. After the culture was terminated, the absorbance (OD value) of each well at a wavelength of 450 nm was measured using a microplate reader. The absorbance of each well was measured on the following 2nd, 3rd, 4th, and 5th day, respectively.

BrdU assay

NPC cells were seeded into 96-well plates (1×10^3 cells per well), and BrdU solution (Beyotime Biotechnology, Shanghai, China) was added to each well after 24 h of culture. After another 24 h of culture, 100 μL of fixative was added, and 30 min later, the fixed cells were rinsed 3 times and then blocked using 5% bull serum albumin for 30 min. Subsequently, 2 mol/L HCL was added to denature the DNA, and the cells were washed by PBS. Anti-BrdU antibody (Beyotime Biotechnology, Shanghai,

China) was used to incubate the cells at 4°C for 12 h before the cells were incubated with DAPI solution (Beyotime Biotechnology, Shanghai, China) for 30 min. After the solution was discarded and the cells were washed with PBS twice, 3 visual fields under a microscope were randomly selected to count the number of BrdU-positive cells and the number of DAPI positive cells, and the cell proliferation rate in each field was calculated.

Transwell assay

The membrane of the Transwell system (Corning, NY, USA) was coated using Matrigel for cell invasion detection (no Matrigel for cell migration detection). Following that, 100 μL of cell suspension (cell density of 2×10^5 cells / mL) was added to the upper chamber, and 250 μL of medium supplemented with 10% FBS was added to the lower chamber, and the cells were maintained at 37°C in 5% CO_2 for 48 h. After the upper chamber was removed, the cells that did not pass through the membrane were wiped off using a cotton swab, and the cells that passed through the membrane were fixed using 4% paraformaldehyde for 15 min and stained with crystal violet solution for 30 min. Subsequently, the cells were imaged in 6 randomly selected fields of view using an inverted light microscope (magnification, x200).

Colony formation assay

Transfected NPC cells were transferred into 6 cm culture dishes (1×10^3 cells/dish) and exposed to irradiation (4 Gy). The medium was then discarded and carefully washed twice using PBS. After 2 weeks of culture at 37°C in 5% CO_2, the colonies were fixed using 10% methanol, carefully washed 3 times using PBS, stained using 0.1% crystal violet for 15 min, and dried at room temperature. The colonies formed were observed and counted with the naked eye.

Dual-luciferase reporter gene assay

A bioinformatics analysis tool (http://www.microrna.org/microrna/home.do) was used to predict the binding site between miR-335-5p and PADI4, and the fragments containing the binding site between PADI4 and miR-335-5p were amplified using qRT-PCR and cloned into the pGL3 Luciferase Reporter Vectors (Promega, Madison, WI, USA) to construct a PADI4 wild-type (WT) reporter plasmid; PADI4 mutant (MUT) reporter plasmid was constructed by site-directed mutagenesis (Thermo Fisher Scientific, Shanghai, China). PADI4 WT reporter plasmid or PADI4 MUT reporter plasmid and miR-335-5p mimics or miR-Ctrl were co-transfected into NPC cells, respectively. 48 h after the transfection, the cells were harvested. Firefly luciferase activity was detected according to the instruction of the Dual-luciferase Reporter Assay System (Promega, Madison, WI, USA), with renilla luciferase activity value as internal reference.

Statistical analysis

Statistical analysis was performed using SPSS software (SPSS Inc., Chicago, IL, USA). Measurement data were expressed as x±s. The differences between the two groups were analyzed by Student's *t*-test. $P < 0.05$ signified statistical significance.

RESULTS

PADI4 was significantly overexpressed in NPC tissues and cell lines

First, we examined the expression characteristics of PADI4 in adjacent tissues and tumor tissues derived from 10 NPC patients using Western blot. As shown in Fig. 1A, among these 10 patients, most cases presented high expression of PADI4 in cancer tissues compared with adjacent tissues (1#, 2#, 4#, 5#, 7#, 8#, 10#). Furthermore, the expressions of PADI4 mRNA and protein in non-cancerous cell line NP69 and five NPC cell lines (CNE1, S18, S26, CNE2, and CNE2) were also examined by qRT-PCR and Western blot. The results of qRT-PCR and Western blot showed that the expression levels of PADI4 in five NPC cell lines were remarkably higher than that of non-cancerous cell line NP69 (Fig. 1 B, C).

PADI4 enhanced the proliferation, migration, invasion and radioresistance of NPC cells

Among the five NPC cell lines, the expression level of PADI was the lowest in CNE1 cells, while the expression level of PADI4 in SUNE2 cells was the highest (Fig. 1 B, C). Therefore, to investigate the role of PADI4 in NPC, CNE1 cells were transfected with PADI4 over-expression plasmid to establish PADI4 overexpression model, and PADI4 siRNA was transfected into SUNE2 cells to establish PADI4

knockdown model (Fig. 2 A, B). The results of BrdU assay and CCK-8 assay suggested that compared with the control group, PADI4 overexpression promoted CNE1 cell proliferation, while both of the two PADI4 siRNAs suppressed the proliferation of NPC cells (Fig. 2 C-E). Additionally, the results of Transwell assay indicated that overexpression of PADI4 significantly promoted the migration and invasion of CNE1 cells compared to the control group; conversely, compared with the control group, knock-down of PADI4 significantly inhibited the migration and invasion of SUNE2 cells (Fig. 2 F-H). Radiotherapy is the most important therapy strategy for NPC, so whether PADI4 regulated the radiosensitivity of NPC cells was also explored. It was found that PADI4 over-expression significantly

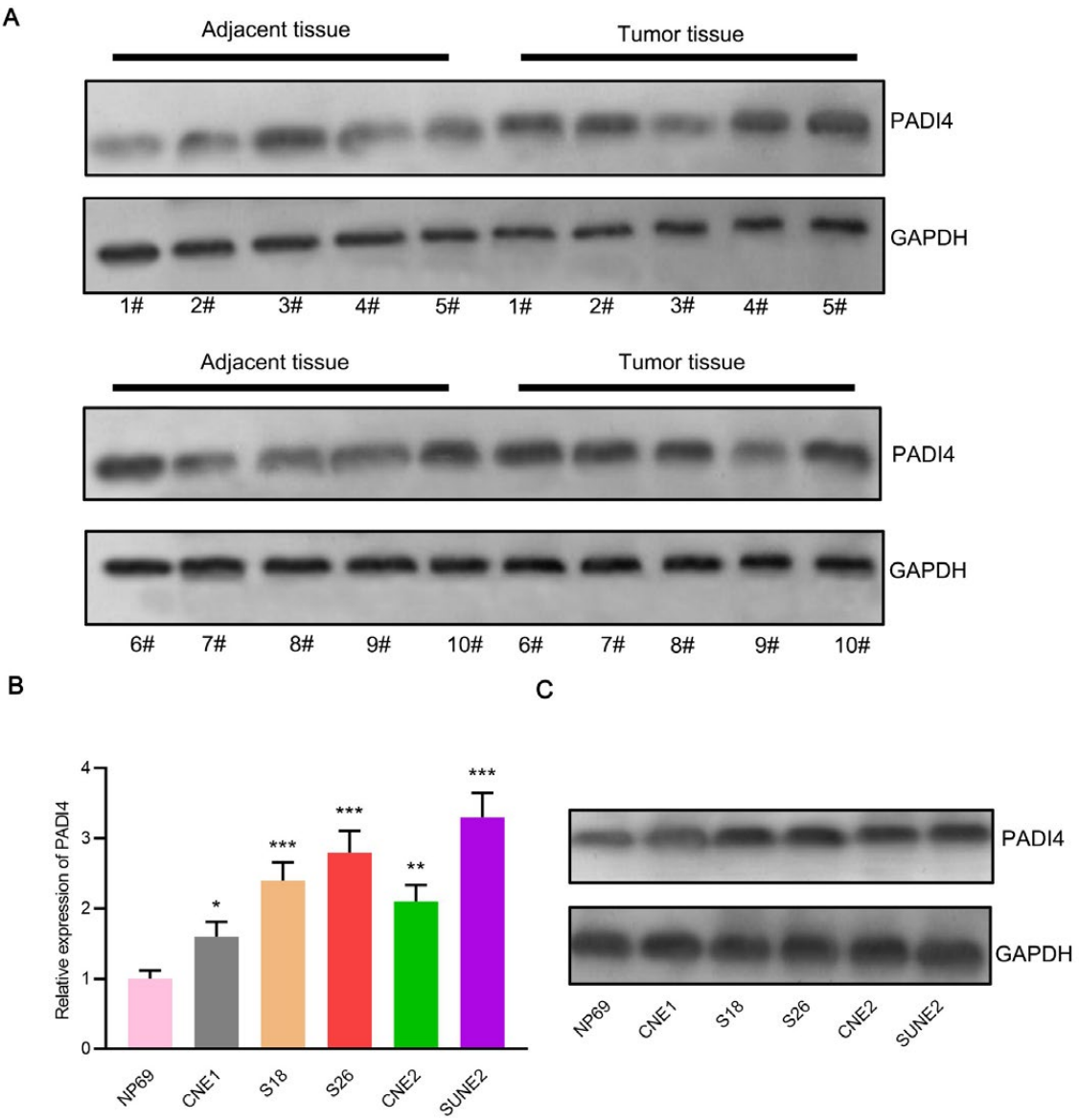

Fig. 1. *PADI4 expression was significantly up-regulated in NPC.* ***A****) Western blot was used to detect the expression of PADI4 in human NPC tissues and adjacent tissues.* ***B, C****) qRT-PCR and Western blot were used to detect the expression level of PADI4 in human NPC cell lines and NP69 cells. All of the experiments were performed in triplicate. * P < 0.05, ** P < 0.01, *** P < 0.001.*

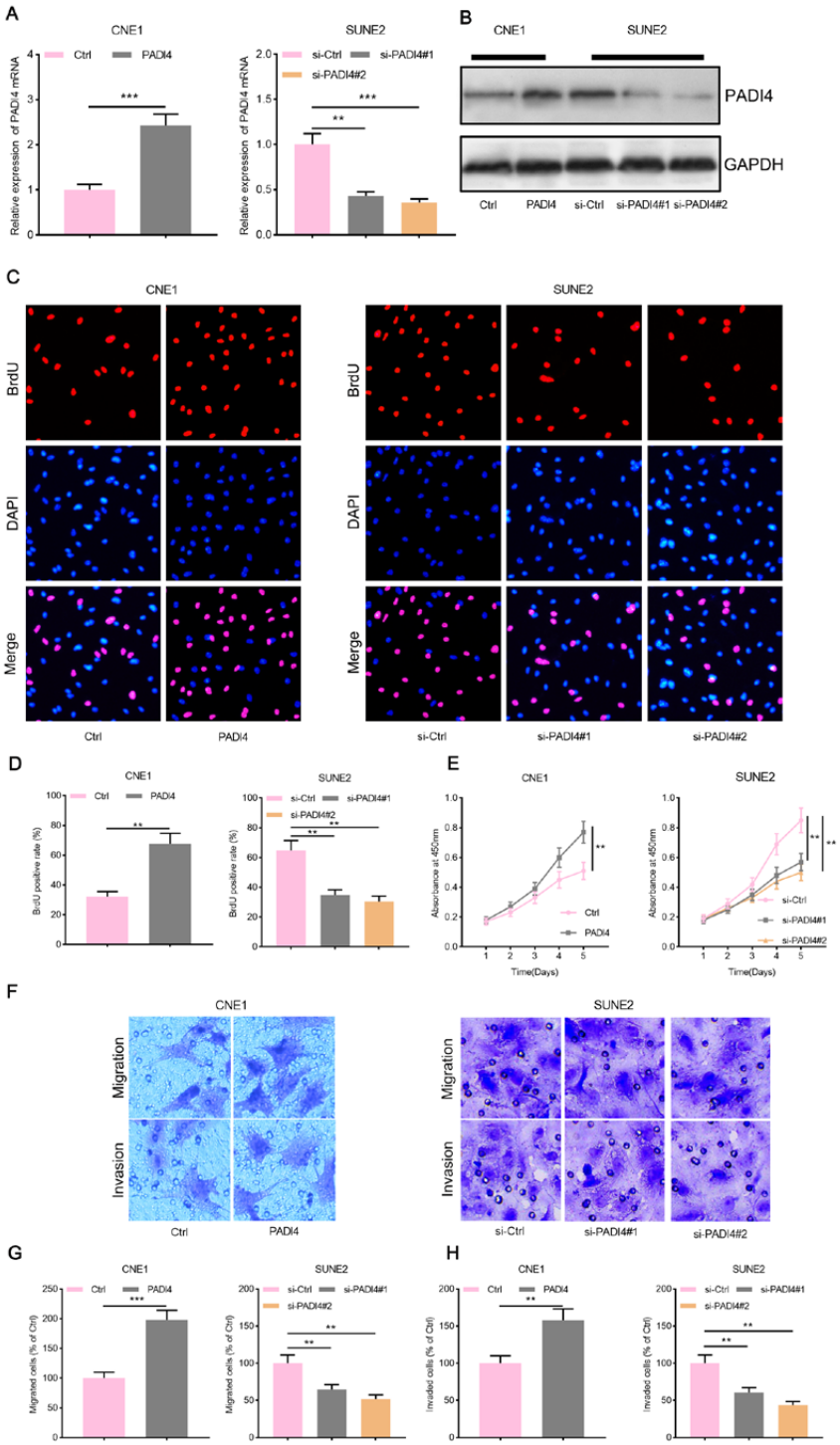

Fig. 2. *PADI4 promoted the proliferation, migration, and invasion of NPC cells.* ***A, B****) CNE1 cells were transfected with PADI4 overexpression plasmid and empty vector plasmid, respectively. SUNE2 cells were transfected with PADI4 siRNAs (#1 and #2) and control siRNA, respectively. qRT-PCR and Western blot were used to detect the expression of PADI4 mRNA and protein in CNE1 and SUNE2 cells after transfection.* ***C-E****) BrdU assay and CCK-8 assays were used to detect the proliferation of NPC cells.* ***F-H****) Transwell assays were used to detect the migration of invasion of NPC cells. All of the experiments were performed in triplicate. ** $P < 0.01$, *** $P < 0.001$.*

increased the number of colonies formed by CNE1 cells under radiation at a dose of 4 Gy; conversely, knockdown of PADI4 in SUNE2 cell led to less colony formed under irradiation (Fig. 3A). A previous study indicated that PADI4 plays a cancer-promoting role by suppressing p21 transcription (21). Consistently, in the present work, it was found that over-expression of PADI4 significantly inhibited p21 expression (Fig. 3B). In addition, the radiosensitivity of NPC cells can be promoted by inducing autophagy, which is regulated by the mTOR signaling pathway (22). Interestingly, the results of Western blot also suggested that over-expression of PADI4 could promote the expression of p-mTOR (Fig. 3B). Conversely, compared with the control group, knock-down of PADI4 induced the up-regulation of p21 and the inactivation of mTOR signaling (Fig. 3B). These results indicated that PADI4 enhanced the proliferation, migration, invasion and radioresistance of NPC cells, probably by inhibiting p21 expression and activating the mTOR signaling pathway.

miR-335-5p directly targeted PADI4

To investigate the mechanism of aberrant expression of PADI4 in NPC, miRanda database (http://www.microrna.org) was used to screen the potential miRNAs that could potentially regulate

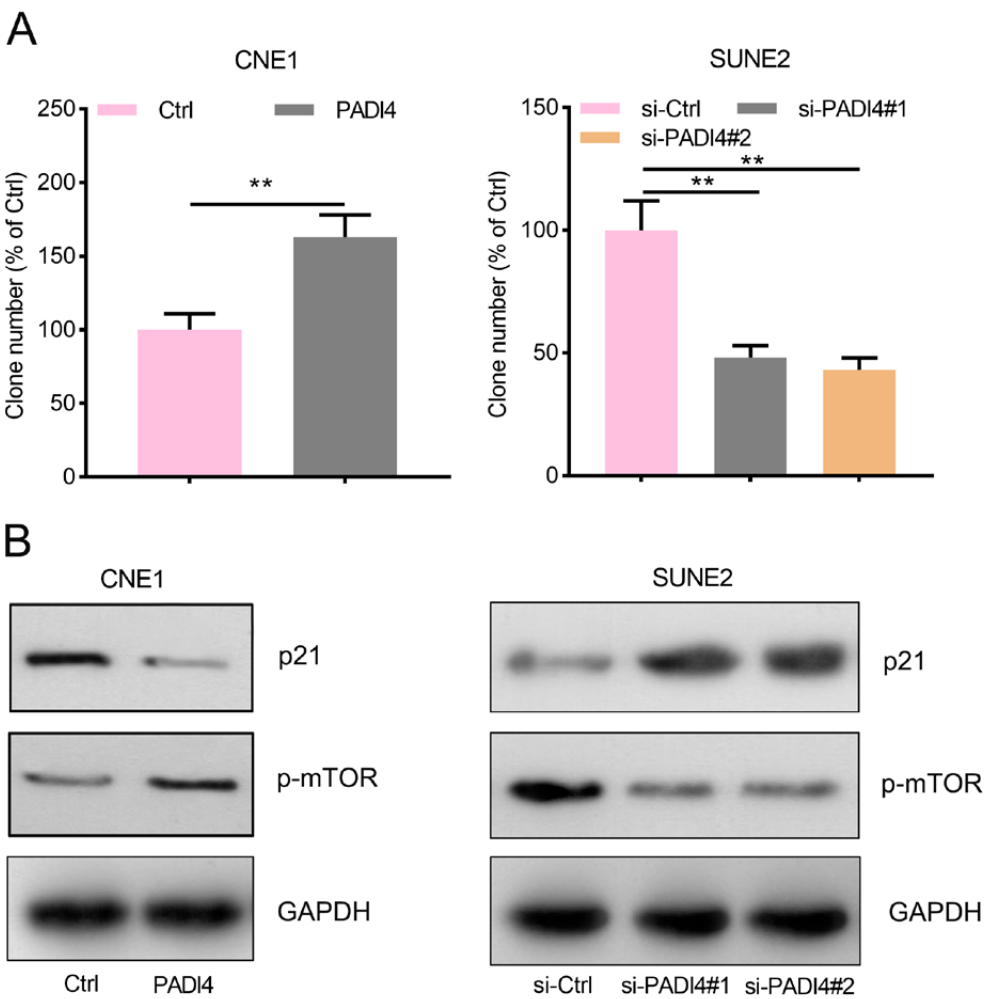

Fig. 3. *PADI4 regulated the radioresistance of NPC cells, and it regulated p21 and p-mTOR expression. Under the irradiation of 4Gy, the radiosensitivity of NPC cells was detected using colony formation assay. Western blot was used to detect the expression of p21 and p-mTOR in NPC cells. All of the experiments were performed in triplicate. ** P < 0.01.*

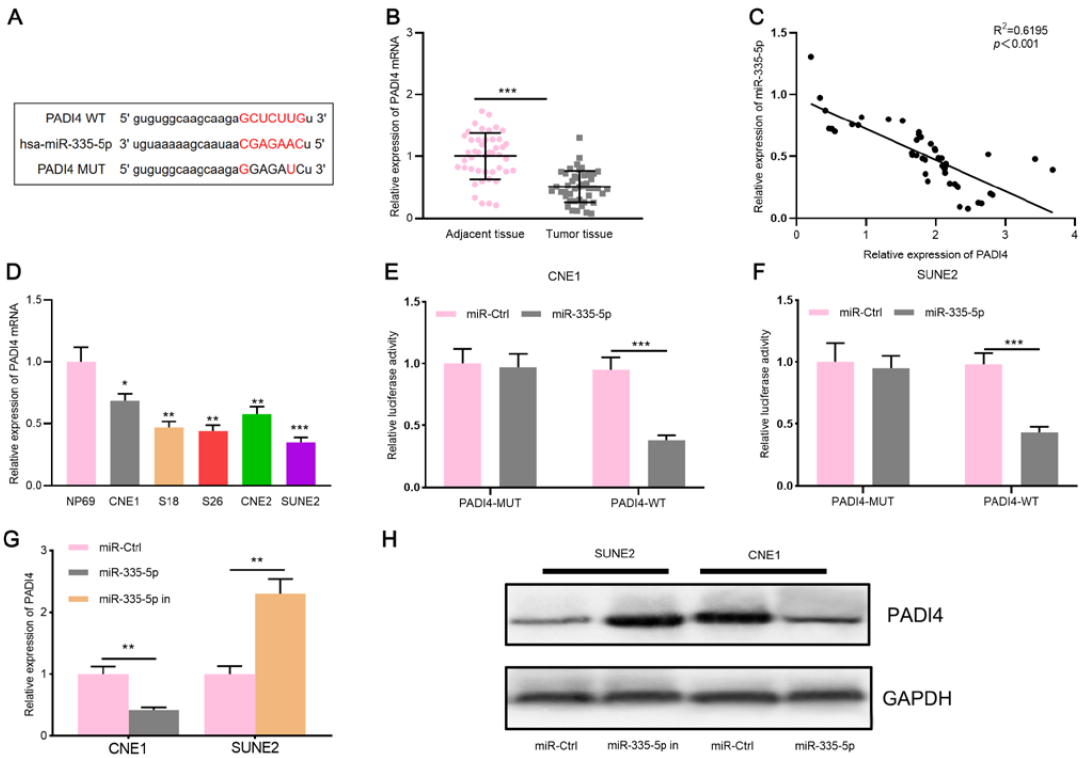

Fig. 4. *PADI4 was the downstream target of miR-335-5p in NPC.* ***A)*** *Bioinformatics was used to predict the potential binding site between miR-335-5p and PADI4 3' UTR.* ***B)*** *qRT-PCR was used to detect the expression of miR-335-5p in cancer tissues and adjacent tissues derived from NPC patients.* ***C)****Pearson's correlation analysis showed that miR-335-5p was significantly negatively correlated with PADI4 expression in NPC tissues.* ***D)****qRT-PCR was used to detect the expression level of miR-335-5p in NPC cell lines and NP69 cells.* ***E, F)*** *Dual-luciferase reporter gene assay was performed to validate the predicted binding site between miR-335-5p and PADI4 3' UTR.* ***G, H)****The results of qRT-PCR and Western blot showed that miR-335-5p mimics inhibited the expression of PADI4 in CNE1 cells, while miR-335-5p inhibitors induced a significant increase of PADI4 expression in SUNE2 cells. All of the experiments were performed in triplicate. * P < 0.05, ** P < 0.01, *** P < 0.001.*

PADI4. It was found there was a potential binding site between miR-335-5p and the 3'UTR of PADI4 (Fig. 4A). qRT-PCR suggested that the expression level of miR-335-5p in NPC tissues was significantly lower than that in adjacent tissues (Fig. 4B). Furthermore, the results of Pearson's correlation analysis suggested a significant negative correlation between miR-335-5p expression and PADI4 expression in NPC tissues (Fig. 4C). Compared with NP69 cells, the expression levels of miR-335-5p in five NPC cell lines were significantly down-regulated (Fig. 4D). Dual luciferase reporter gene assay was performed to verify the binding relationship between miR-335-5p and PADI4 3'-UTR. It was found that over-expression of miR-335-5p remarkably reduced the luciferase activity of wild-type PADI4 reporter but did not significantly change the luciferase activity of mutant PADI4 reporter (Fig. 4 E, F). The results of qRT-PCR and Western blot also showed that miR-335-5p mimics markedly inhibited PADI4 expression at both mRNA and protein expression levels, while PADI4 expression was significantly up-regulated after transfection of miR-335-5p inhibitors (Fig. 4 G, H). These data revealed that miR-335-5p, served as an upstream regulator of PADI4, negatively regulated PADI4 expression in NPC cells.

miR-335-5p inhibited the proliferation, migration, invasion and radioresistance of NPC cells

As mentioned above, miR-335-5p expression was significantly reduced in NPC tissues and cells, which suggested that miR-335-5p played a tumor-

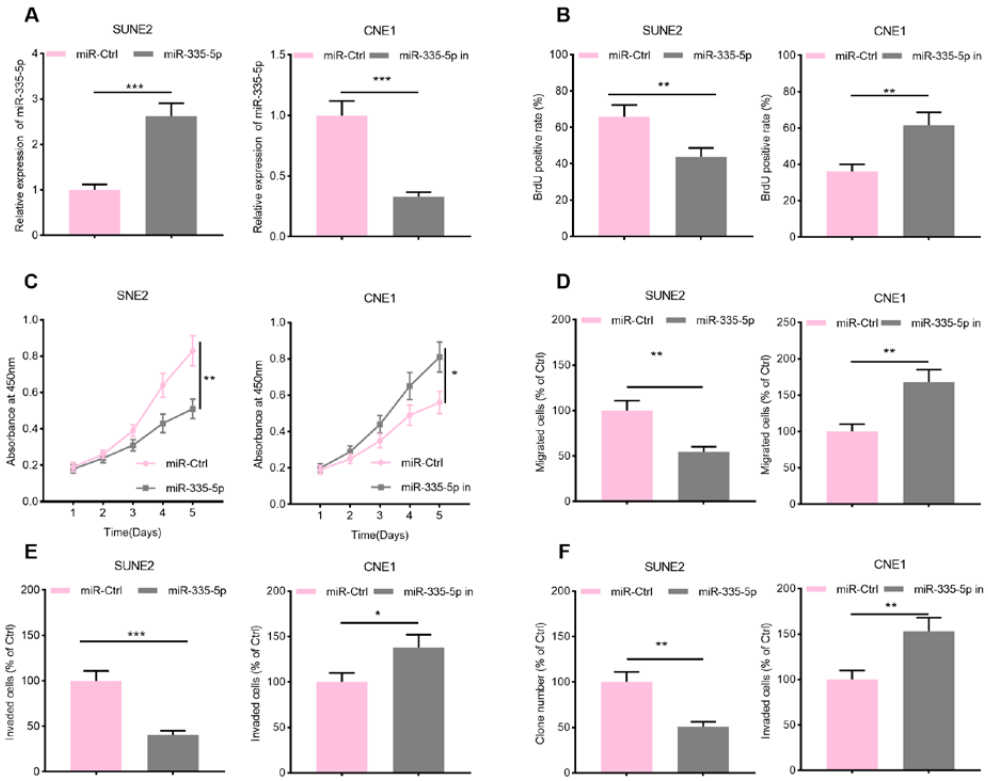

Fig. 5. *miR-335-5p significantly inhibited proliferation, migration, and invasion and promotes radiosensitivity of NPC cells.* ***A)*** *MiR-335-5p mimics and miR-335-5p inhibitors were transfected into SUNE2 and CNE1 cells, respectively. Transfection efficiency was detected using qRT-PCR.* ***B, C)*** *BrdU assay and CCK-8 assays were used to detect the proliferation of NPC cells.* ***D, E)*** *Transwell assays were used to detect the migration of invasion of NPC cells.* ***F)*** *Under the irradiation of 4Gy, the radiosensitivity of NPC cells was detected using colony formation assay. All of the experiments were performed in triplicate. * P < 0.05, ** P < 0.01, *** P < 0.001.*

suppressive role in NPC (Fig. 4 B-D). To further investigate the role of miR-335-5p in NPC, we transfected SUNE2 cells with miR-335-5p mimics and negative control, respectively, and the miR-335-5p inhibitors and negative control were transfected into CNE1 cells, respectively. qRT-PCR results confirmed the successful transfection (Fig. 5A). The results of the CCK-8 assay and BrdU assay showed that miR-335-5p mimics significantly inhibited the proliferation of SUNE2 cells compared to the control group (Fig. 5 B, C). Through Transwell assays, it was found that compared with the control group, miR-335-5p up-regulation remarkably inhibited the migration and invasion of SUNE2 cells (Fig. 5 D, E). In addition, under the irradiation of 4Gy, the number of colonies formed by SUNE2 cells was significantly reduced after transfection of miR-335-5p mimics (Fig. 5F). Nevertheless, compared with the control group, miR-335-5p inhibitors significantly promoted the above malignant phenotypes of CNE1 cells (Fig. 5 C-H). These data indicated that miR-335-5p inhibited the proliferation, migration, invasion and radioresistance of NPC cells.

miR-335-5p / PADI4 axis was involved in the regulation of the proliferation, migration, invasion and radiosensitivity of NPC cells

Considering the distinct roles of miR-335-5p and PADI4 in regulating malignant phenotypes of NPC cells and their regulatory relationship, it was hypothesized that the function of miR-335-5p in NPC was mediated by PADI4. Next, we co-transfected

miR-335-5p mimic and PADI4 over-expression plasmid or control plasmid into SUNE2 cells, and meanwhile co-transfected miR-335-5p inhibitors and PADI4 siRNA or control siRNA into CNE1 cells. As shown, restoring PADI4 expression counteracted the inhibitory effects of miR-335-5p over-expression on the proliferation, migration, invasion, and radioresistance of NPC cells; knock-down of PADI4 partially reversed the cancer-promoting effects of miR-335-5p inhibitors in NPC cells (Fig. 6 A-E). Therefore, it was confirmed that miR-335-5p/PADI4 axis was involved in promoting the proliferation, migration, invasion and radioresistance of NPC cells.

DISCUSSION

NPC is a highly invasive and metastatic malignancy (23). Substantial progress has been made in the treatments of NPC, but local recurrence, distant metastasis, chemoresistance and radioresistance are still important reasons for treatment failure (24). Therefore, an in-depth elucidation of the mechanism by which NPC progresses is essential for developing novel effective treatment of NPC. For the first time, this study found that PADI4 was highly expressed in NPC tissues and cells. PADI4, negatively regulated by miR-335-5p, was involved

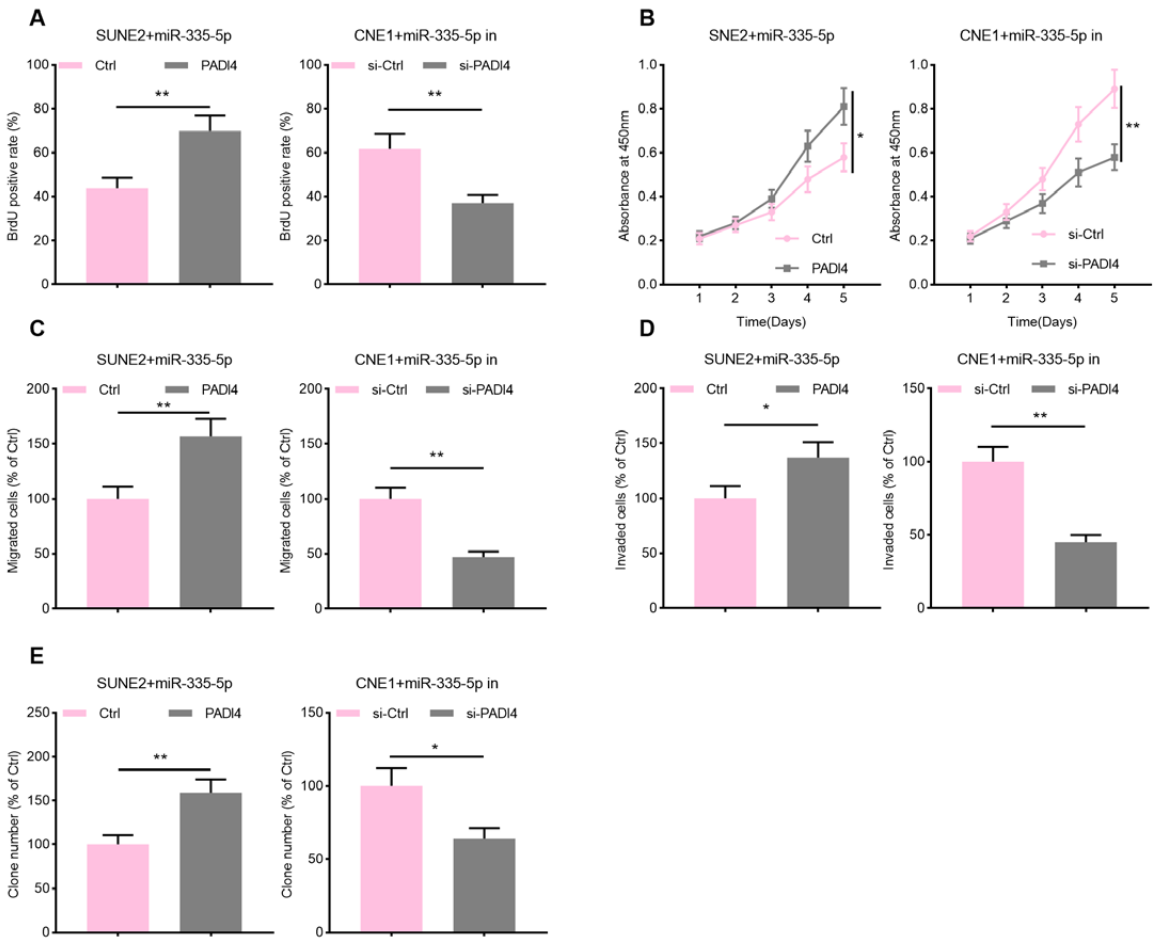

Fig. 6. *miR-335-5p/PADI4 axis was involved in regulation of the malignant phenotypes of NPC cells.* ***A, B****) MiR-335-5p mimic and PADI4 over-expression plasmid (or control plasmid) were co-transfected into SUNE2 cells, and miR-335-5p inhibitors and PADI4 siRNA (or control siRNA) were co-transfected into CNE1 cells. Subsequently, BrdU assay and CCK-8 assays were used to detect the proliferation of NPC cells.* ***C, D****) Transwell assays were used to detect the migration of invasion of NPC cells.* ***E****) Under the irradiation of 4Gy, the radiosensitivity of NPC cells was detected using colony formation assay. All of the experiments were performed in triplicate. * P < 0.05, ** P < 0.01.*

in promoting the proliferation, migration, invasion, and radioresistance of NPC cells.

PADI4 is a key enzyme that catalyzes the citrullination of arginine residues, which can post-translationally modify a wide range of proteins in cells (6). Accumulating studies have found that PADI4, highly expressed in cancer tissues and patients' serum, plays an important role in tumorigenesis and disease progression of many cancers, including esophageal squamous cell carcinoma, colonic cancer, gastric cancer, etc (25-28). Specifically, in gastric cancer, PADI4 can activate the angiogenesis, proliferation, migration and invasion of cancer cells by up-regulating the expression of CXCR2, KRT14 and TNF-α (27). PADI4-driven citrullination of the extracellular matrix accelerates liver metastasis of colorectal cancer (28). Furthermore, PADI4 suppresses the expression of p53 downstream genes (including OKL38, p21, CIP1, and WAF1) by deaminating the methylated arginine sites in histone H3, thereby inhibiting the cell apoptosis (29). It is worth noting that the expression level of PADI4 in non-neoplastic tissues of some benign diseases (including cholecystitis, cervicitis and osteoarthritis) is within the normal range (30). This implies that PADI4 is promising to be a specific biomarker for tumor diagnosis. In this study, we found that PADI4 expression levels were significantly increased in NPC tissues and cells. Over-expression of PADI4 significantly promoted the proliferation, invasion, and radioresistance of NPC cells. Conversely, compared with the control group, knocking down PADI4 significantly inhibited the aforementioned malignant phenotypes of NPC cells. For the first time, we identify that PADI4 is a novel cancer-promoting gene in NPC.

MiRNAs regulate the malignant biological behaviors of cancer cells such as proliferation, apoptosis, migration, invasion, stemness and so on. MiRNAs serve as the biomarkers for early diagnosis and assessment of prognosis, and it also provides targets for the treatment of tumors (31). Recent research has found that miR-335-5p plays different roles in a variety of tumors, and miR-335-5p expression is down-regulated in cervical cancer, osteosarcoma, gastric cancer, NPC and other cancers (20, 32-34). MiR-335-5p inhibits TGF-β1-induced EMT through specific regulation of ROCK1 expression in non-small cell lung cancer (17). In NPC, miR-335-5p inhibits the proliferation and metastasis of NPC cells by binding to the 3' UTR of TRIM29 and regulating the transduction of PTEN/AKT/mTOR signaling. Consistently, the present study also found that miR-335-5p inhibited the proliferation, migration, invasion, and radioresistance of NPC cells, which is consistent with the previous report (20). Additionally, the results of qRT-PCR and Western blot indicated that miR-335-5p negatively regulated the expression of PADI4. Furthermore, the results of dual-luciferase reporter gene assay suggested miR-335-5p specifically bound to PADI4 3' UTR. In addition, the restoration of PADI4 expression reversed the anti-cancer effect of miR-335-5p in NPC. Collectively, it is concluded that miR-335-5p/PADI4 axis is involved in NPC progression.

In summary, we demonstrate for the first time that PADI4 expression is significantly up-regulated in NPC tissues and cells, and miR-335-5p/PADI4 axis is involved in regulating the malignant biological behaviors of NPC cells in vitro. This study provides a novel theoretical basis for further understanding NPC progression. However, this study is limited to in vitro experiments, and in vivo experiments will further validate our demonstrations. Additionally, in the present work, our data implied that p21 signaling and mTOR signaling were regulated by PADI4 in NPC cells, indicating that PADI4 can probably modulate the cell cycle and autophagy to promote NPC progression, which also requires further investigations in the following work.

ACKNOWLEDEGMENTS

We thank Hubei Yican Health Industry Co., Ltd. for its linguistic assistance during the preparation of this manuscript.

Our study was supported by Guangxi Key Research Project (grant number: AB17195005), the Guangxi Zhuang Autonomous Region Health and Family Planning Commission Self-financing Research Project (grant number: Z20190381), the Natural Science Foundation of Guangxi Province

(grant number: 2017GXNSFBA198072), Science Research and Technology Development Key Program of Nanning City (grant number: 20173018-4), and Nanning Excellent Young Scientist Program (grant number: 2017GXNSFBA198072).

REFERENCES

1. Jiang H, Jun P, Zhiguo L, Qiwen D, Dan W. Long non-coding RNA FOXD3-AS1 silencing exerts tumor suppressive effects in nasopharyngeal carcinoma by downregulating FOXD3 expression via microRNA-185-3p upregulation. Cancer Gene Ther 2020; doi: 10.1038/s41417-020-00242-z.
2. Sheng JP, Wang LQ, Han YJ. Dual roles of protein as a template and a sulfur provider: a general approach to metal sulfides for efficient photothermal therapy of cancer. Small 2018; 14(1). doi: 10.1002/smll.201702529.
3. Duan B, Shi S, Yue H, et al. Exosomal miR-17-5p promotes angiogenesis in nasopharyngeal carcinoma via targeting BAMBI. J Cancer 2019; 10:6681-92.
4. Chang X, Fang K. PADI4 and tumourigenesis. Cancer Cell Int 2010; 10:7.
5. Koushik S, Joshi N, Nagaraju S et al. PAD4: pathophysiology, current therapeutics and future perspective in rheumatoid arthritis. Expert Opin Ther Targets 2017; 21:433-47.
6. Anzilotti C, Pratesi F, Tommasi C, Migliorini P. Peptidylarginine deiminase 4 and citrullination in health and disease. Autoimmun Rev 2010; 9:158-60.
7. Nakashima K, Hagiwara T, Ishigami A et al. Molecular characterization of peptidylarginine deiminase in HL-60 cells induced by retinoic acid and 1alpha,25-dihydroxyvitamin D(3). J Biol Chem 1999; 274:27786-792.
8. Tanikawa C, Ueda K, Nakagawa H, Yoshida N, Nakamura Y, Matsuda K. Regulation of protein Citrullination through p53/PADI4 network in DNA damage response. Cancer Res 2009; 69:8761-69.
9. Chang X, Han J. Expression of peptidylarginine deiminase type 4 (PAD4) in various tumors. Mol Carcinog 2006; 45:183-96.
10. Liu M, Qu Y, Teng X Xing Y, Li DD, Li CH, Cai L. PADI4mediated epithelialmesenchymal transition in lung cancer cells. Mol Med Rep 2019; 19:3087-94.
11. Polli A, Godderis L, Ghosh M, Ickmans K, Nijs J. Epigenetic and miRNA expression changes in people with pain: a systematic review. J Pain 2019; 21:763-80
12. Yang CX, Sedhom W, Song J, Lu SL. The role of MicroRNAs in recurrence and metastasis of head and neck squamous cell carcinoma. Cancers (Basel) 2019; 11:395.
13. Wang S, Claret FX, Wu W. MicroRNAs as therapeutic targets in nasopharyngeal carcinoma. Front Oncol 2019; 9:756.
14. Liang TS, Zheng YJ, Wang J, Zhao JY, Yang DK, Liu ZS. MicroRNA-506 inhibits tumor growth and metastasis in nasopharyngeal carcinoma through the inactivation of the Wnt/beta-catenin signaling pathway by down-regulating LHX2. J Exp Clin Cancer Res 2019; 38:97.
15. Cheng C, Xiaohua W, Ning J, et al. MiR-122 exerts anti-proliferative and apoptotic effects on nasopharyngeal carcinoma cells via the PI3K/AKT signaling pathway. Cell Mol Biol (Noisy-le-grand) 2018; 64:21-25.
16. Wu W, Chen X, Yu S, Wang R, Zhao R, Du C. microRNA-222 promotes tumor growth and confers radioresistance in nasopharyngeal carcinoma by targeting PTEN. Mol Med Rep 2018; 17:1305-10.
17. Du W, Tang H, Lei Z, Zhu J, Zeng YY, Liu Z, Huang J-A. miR-335-5p inhibits TGF-beta1-induced epithelial-mesenchymal transition in non-small cell lung cancer via ROCK1. Respir Res 2019; 20:225.
18. Zou J, Wu K, Lin C, Jie ZG. LINC00319 acts as a microRNA-335-5p sponge to accelerate tumor growth and metastasis in gastric cancer by up-regulating ADCY3. Am J Physiol Gastrointest Liver Physiol 2020; 318(1):G10-G22.
19. Luo L, Xia L, Zha B et al. miR-335-5p targeting ICAM-1 inhibits invasion and metastasis of thyroid cancer cells. Biomed Pharmacother 2018; 106:983-90.
20. Zhou XM, Sun R, Luo DH et al. Upregulated TRIM29 promotes proliferation and metastasis of nasopharyngeal carcinoma via PTEN/AKT/mTOR signal pathway. Oncotarget 2016; 7:13634-50.
21. Fan L, Zong M, Gong R, et al. PADI4 Epigenetically suppresses p21 transcription and inhibits cell apoptosis in fibroblast-like synoviocytes from rheumatoid arthritis patients. Int J Biol Sci 2017; 13:358-66.

22. Chang L, Huang Z, Li S, et al. A low dose of AZD8055 enhances radiosensitivity of nasopharyngeal carcinoma cells by activating autophagy and apoptosis. Am J Cancer Res 2019; 9:1922-37.
23. Jiang N, Jiang X, Chen Z, et al. MiR-203a-3p suppresses cell proliferation and metastasis through inhibiting LASP1 in nasopharyngeal carcinoma. J Exp Clin Cancer Res 2017; 36:138.
24. Tsang CM, Lui VWY, Bruce JP, Pugh TJ, Lo KW. Translational genomics of nasopharyngeal cancer. Semin Cancer Biol 2019; 61:84-100.
25. Liu C, Tang J, Li C, Pu G, Yang D, Chang X. PADI4 stimulates esophageal squamous cell carcinoma tumor growth and up-regulates CA9 expression. Mol Carcinog 2019; 58:66-75.
26. Xin J, Song X. Role of peptidylarginine deiminase type 4 in gastric cancer. Exp Ther Med 2016; 12:3155-60.
27. Zheng Y, Zhao G, Xu B, et al. PADI4 has genetic susceptibility to gastric carcinoma and upregulates CXCR2, KRT14 and TNF-alpha expression levels. Oncotarget 2016; 7:62159-76.
28. Yuzhalin AE, Gordon-Weeks AN, Tognoli ML, et al. Colorectal cancer liver metastatic growth depends on PAD4-driven citrullination of the extracellular matrix. Nat Commun 2018; 9:4783.
29. Chang X, Hou X, Pan J, Fang K, Wang L, Han J. Investigating the pathogenic role of PADI4 in oesophageal cancer. Int J Biol Sci 2011; 7:769-81.
30. Chang X, Han J, Pang L, Zhao Y, Yang Y, Shen Z. Increased PADI4 expression in blood and tissues of patients with malignant tumors. BMC Cancer 2009; 9:40.
31. Ding L, Gu H, Xiong X et al. Micrornas involved in carcinogenesis, prognosis, therapeutic resistance and applications in human triple-negative breast cancer cells 2019; Cells 2019; 8(12):1492.
32. Liang H, Zhang C, Guan H, Liu J, Cui Y. LncRNA DANCR promotes cervical cancer progression by upregulating ROCK1 via sponging miR-335-5p. J Cell Physiol 2019; 234:7266-78.
33. Wang Y, Yang T, Zhang Z et al. Long non-coding RNA TUG1 promotes migration and invasion by acting as a ceRNA of miR-335-5p in osteosarcoma cells. Cancer Sci 2017; 108:859-67.
34. Li H, Xie S, Liu M et al. The clinical significance of downregulation of mir-124-3p, mir-146a-5p, mir-155-5p and mir-335-5p in gastric cancer tumorigenesis. Int J Oncol 2014; 45:197-208.

Endovascular treatment of visceral aneurysms and pseudoaneurysms

YX. He[1], G. Li[1], Y. Liu[2], H. Tang[3], ZY. Chong[1], XJ. Wu[1], X. Jin[1], SY. Zhang[1] and M. Wang[1]

[1]Department of Vascular Surgery, Shandong Provincial Hospital Affiliated to Shandong First Medical University, Jinan, China, [2]Department of General Surgery, Qilu Hospital of Shandong University, Jinan, China; [3]Shandong Center for Disease Control and Prevention, Shandong Center for Disease Control and Prevention, Jinan, China

Received June 16, 2020 – Accepted January 26, 2021

Visceral artery aneurysm (VAA) is a rare and potentially life-threatening condition, defined as true artery aneurysms and pseudoaneurysms of splanchnic circulation and renal artery. This study reports our experience in the diagnosis and endovascular treatment of visceral artery aneurysms (VAAs) over a 10-year period. Between 2008 and 2018, a total of 24 VAAs in 21 patients were diagnosed by clinical symptoms and a combination of imaging techniques, such as Doppler ultrasound, computed tomography angiogram, and catheter angiogram. All patients underwent endovascular treatment to exclude aneurysms. Oral antiplatelet medicine was administered, and imaging examination was performed during follow-up. Technical success was achieved in all 21 patients, and no periprocedural complications occurred. Endovascular coiling alone was employed in 10 aneurysms. Coiling was combined with gelfoam in 2 aneurysms. Coiling was assisted by stent in 4 aneurysms. Covered stents were deployed in 8 aneurysms individually. Clinical symptoms disappeared or highly improved in all patients after treatment. None of the patients showed recurrent symptoms after discharge. However, two cases with new aneurysms after 6 and 8 months, respectively, and one case with in-stent thrombosis after 12 months were reported during follow-up. This study may justify the efficacy of percutaneous endovascular coil embolization and stent deployment. It also provides beneficial experience about how to choose appropriate various endovascular strategies based on both clinical symptoms and aneurysm anatomy condition.

Visceral artery aneurysm (VAA) is a rare and potential life-threatening condition, defined as true artery aneurysms and pseudoaneurysms of splanchnic circulation and renal artery (1-3). VAA develops as a result of atherosclerosis, fibromuscular dysplasia, collagen disorders, inflammation, infection, vasculitis, trauma, etc (1, 2). The incidence rate of VAA ranges from 0.1%-2% (4, 5). However, the increased application of imaging examination modalities in recent years, such as Doppler ultrasound, computed tomography angiography and magnetic resonance imaging, have resulted in overtreatment in asymptomatic patients.

VAA is considered as a life-threatening disease because of the potential risk of rupture and hemorrhage (6, 7). Therefore, surgery is indicated for patients with symptomatic aneurysm, a rapidly-growing aneurysm, a VAA of diameter greater than 2 cm, mycotic aneurysm, and women of childbearing age (1, 7-9). Conventional open surgery strategies

Key words: vascular visceral aneurysm; endovascular treatment; coil; stent

Corresponding Author:
Dr Mo Wang,
Department of Vascular Surgery, Shandong Provincial Hospital,
Affiliated to Shandong First Medical University,
No.324, Jingwuweiqi Road, Jinan 250021, China
Tel.: 86015168889826
e-mail: doctorwangmo@126.com

0393-974X (2021)
Copyright © by BIOLIFE, s.a.s.
This publication and/or article is for individual use only and may not be further reproduced without written permission from the copyright holder.
Unauthorized reproduction may result in financial and other penalties
DISCLOSURE: ALL AUTHORS REPORT NO CONFLICTS OF INTEREST RELEVANT TO THIS ARTICLE.

for VAA have included aneurysmal resection with or without vascular reconstruction, and aneurysm ligation with or without end-organ resection. However, open surgery treatment is associated with a rate of perioperative mortality and morbidity, especially in patients with severe comorbidities (10-13). Recently, endovascular treatment has become a widely-accepted first-line choice for VAA in many centers (14-17). Either coil embolization or stent placement can be performed with a high rate of success and low mortality and morbidity. The immediate exclusion of aneurysms and short-term outcomes are also satisfactory. However, the indication and long-term durability of endovascular treatment are not well clarified.

In this retrospective study, we present our experience with endovascular management in a single center, focusing on procedural techniques, perioperative morbidity and mortality, and long-term durability.

MATERIALS AND METHODS

Between 2008 and 2018, in 21 patients (including 24 VAAs), 17 males and 4 females, underwent endovascular treatment in our department. The clinical characteristics, including age, gender, presenting symptoms, comorbidities, aneurysm features, endovascular treatment strategies, postoperative complications, re-intervention, length of hospital stay, and follow-up outcomes, were reviewed and summarized. Specific attention was paid to the technique point and long-term prognosis.

The general endovascular inclusion criteria included symptomatic and ruptured aneurysm, aneurysm diameter (greater than 2 cm, or smaller than 2 cm in fertile women), significant medical comorbidities, no contraindication to intravenous contrast, gender, age (18, 19). The aneurysm morphology inclusion criteria were based on suitable anatomic location, adequate caliber and course of vessels to allow for catheter passage, adequate proximal and distal anchoring zone for covered stent, and adequate collateral circulation to the end organ for coil embolization. We excluded the VAA in patients with aortic dissection or concomitant aortic aneurysm (18, 19).

In order to confirm the diagnosis of VAA and the aneurysm features and observe prognosis, a combination of perioperative imaging examination modalities was performed, consisting of computed tomography angiography (CTA), magnetic resonance imaging (MRI), Doppler ultrasound scanning, and sometimes selective percutaneous catheter-directed angiography.

Endovascular management was performed to exclude the aneurysm from the parent artery in several ways. For aneurysms involving large arteries (e.g., the splenic artery), coils were deployed in the parent artery distal and then proximal to the aneurysm, in order to eliminate blood flow to the aneurysm. For patients with VAA involving smaller arteries, large particles or glue were applied to occlude the distal parent artery or its branches, followed by coil deployment in the proximal parent artery. For patients presenting with a wide-neck aneurysm, stent-assisted coil embolization was performed, or a cover stent was deployed in selected cases, to prevent migration of the coils from the aneurysm sac.

Technical success was defined as follows: the successful deployment of coils or glue or stent within the aimed artery, exclusion of the aneurysmal arterial segment without evident contrast extravasation, preservation of flow within the intended parent artery, and blocking of initial hemorrhage (15).

The follow-up imaging examination was performed to evaluate aneurysm sac perfusion, aneurysm size change, end-organ blood perfusion, and coil or stent. After discharge, all patients underwent a clinical and Doppler ultrasound follow-up at 1, 6, 12 months, and then annually. The CTA scan was performed at least once during the first year. For patients undergoing covered stent placement, lifelong oral antiplatelet medicine was administered.

Statistical analysis

Statistical analysis was performed using Statistical Product and Service Solutions (SPSS) 22. 0 software (IBM, Armonk, NY, USA). Data were represented as mean ± SD (Standard Deviation). The *t*-test was used for analyzing measurement data. Differences between two groups were analyzed by using the Student's *t*-test. Comparison between multiple groups was made using One-way ANOVA test followed by Post Hoc Test (Least Significant Difference). $p<0.05$ indicated asignificant difference.

RESULTS

Baseline characteristics of all patients are shown in

Table I. During the study period, a total of 21 patients with a mean age of 54.78±13.43 years (17 males, 4 females) were admitted into our department. Except VAAs observed in 2 patients incidentally, VAAs resulted in associated symptoms in the other patients at the time of treatment, such as abdominal pain, rupture and hemorrhage. The comorbidities in these patients included atherosclerosis, coronary artery disease, pancreatitis, hypertension, hyperlipidemia, arteritis. No drug therapy was administered to 2 patients with arteritis as biochemical indicators were normal.

The diagnosis of VAA was confirmed based on a combination of imaging examination modalities. All patients underwent Doppler ultrasound and CTA in order to evaluate the aneurysm features, location and collateral circulation. There were 24 aneurysms in 21 patients, including 15 true VAAs and 9 pseudoaneurysms. VAAs involved various splanchnic arteries, such as 4 in splenic artery, 2 in hepatic artery, 2 in renal artery, 2 in celiac artery, 10 in superior mesenteric artery, 2 in inferior mesenteric artery, 1 in gastroduodenal artery and 1 in pancreaticoduodenal artery. The imaging examinations revealed 16 aneurysms were 10–20 mm in diameter, 5 aneurysms were larger than 20 mm, and 3 ruptured pseudoaneurysms were smaller than 20 mm in diameter.

All patients underwent endovascular treatment. Femoral approach was applied in 19 patients, and brachial approach in 2 patients. The endovascular intervention was performed in patients under local anesthesia. Coil embolization, stent-assisted coil embolization, coil embolization combined with gelfoam, and covered stent were performed individually based on aneurysm feature, location and collateral circulation. (Figs. 1 and 2). The treatment strategies are presented in Table II. Sole endovascular coiling was employed in 10 aneurysms. Coiling was combined with gelfoam in 2 aneurysms. Coiling was assisted by stent in 4 aneurysms. Covered stents (6×40, 8×40, 8×60, 9×40 mm) were deployed in 8 aneurysms individually.

The technical success was achieved in all patients. Oral aspirin 100 mg/d was administered

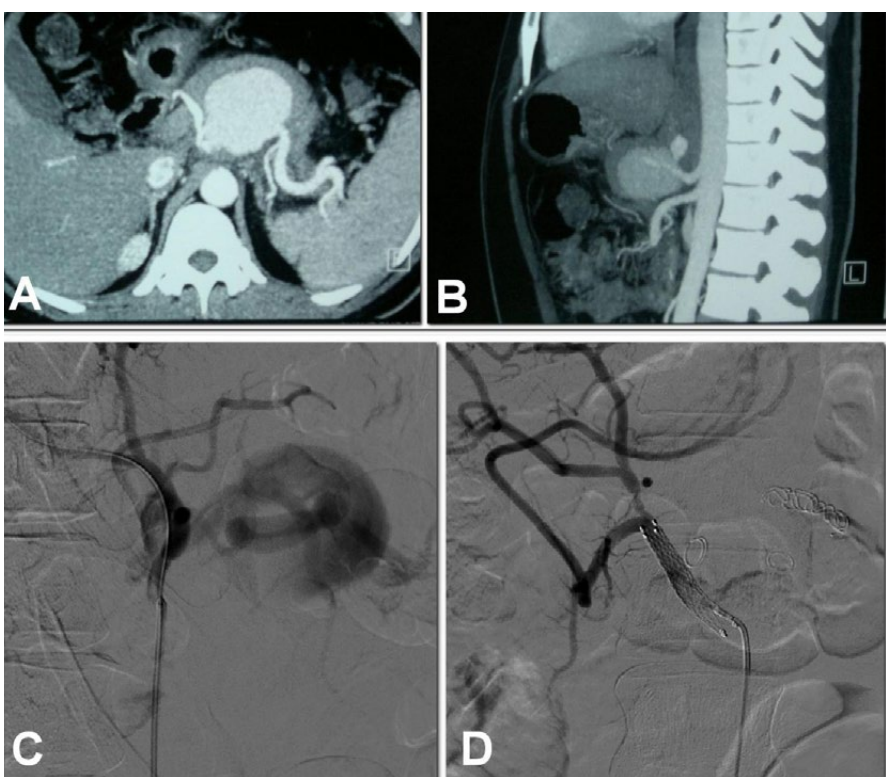

Fig. 1. *A) The axial image of CTA showing a celiac arterial pseudoaneurysm.* ***B****) Sagittal image of celiac arterial pseudoaneurysm.* ***C****) Intraoperative angiogram.* ***D****) Completion angiogram after stent-assisted coil embolization.*

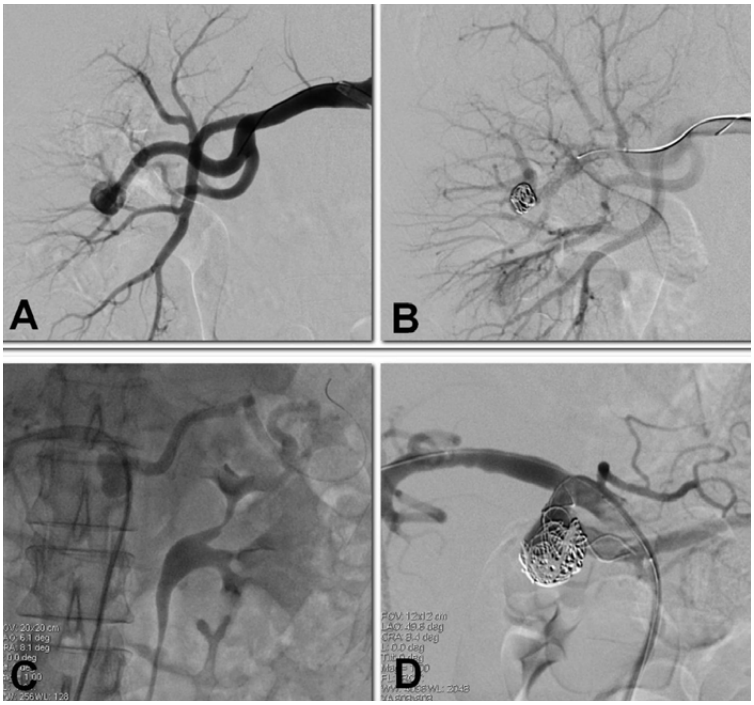

Fig. 2. ***A****) Intraoperative angiogram showed a renal artery aneurysm.* ***B****) Completion angiogram after coil embolization for the renal aneurysm.* ***C****) Intraoperative angiogram showed a splenic artery pseudoaneurysm.* ***D****) Completion angiogram after coil embolization for the splenic aneurysm.*

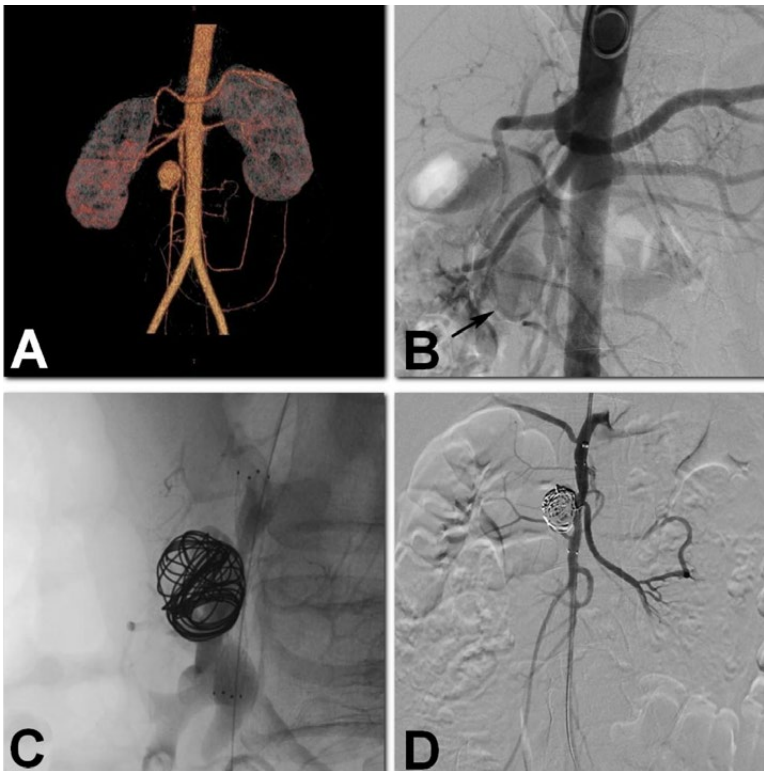

Fig. 3. ***A****) CTA showed a SMA aneurysm.* ***B****) Intraoperative angiogram for the SMA aneurysm.* ***C****,* ***D****) Completion angiogram after stent-assisted coil embolization for the SMA aneurysm.*

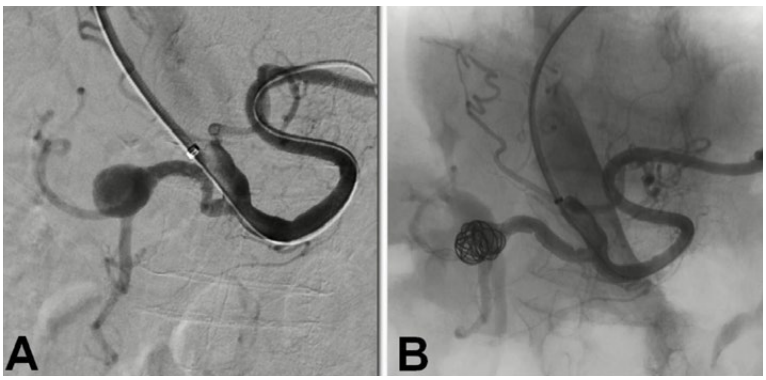

Fig. 4. *A) Intraoperative angiogram showed a hepatic artery aneurysm.* ***B****) Completion angiogram after coil embolization for the hepatic artery aneurysm.*

Table I. *Clinical characteristics of patients with VAA*

Gender	**Total (n=21)**
Male	17
Female	4
Age	Mean 54.78±13.43y, Range 26-77y
Hospital stay	Mean 15.97±5.42d, Range 3-49d
Follow-up duration	Mean 17.75±3.12m, Range 12-51m
Comorbidities	
Atherosclerosis	11
CAD*	17
Pancreatitis	5
Hypertension	14
Hyperlipidemia	15
Arteritis	2
Symptoms	
Pain	16
Incidental finding	2
Rupture and Hemorrhage	3
Aneurysm feature	Total (*n*=24)
True aneurysm	15
False aneurysm	9
Aneurysm location	
Splenic artery	4
Hepatic artery	2
Renal artery	2
Celiac artery	2
SMA	10
IMA	2
GAD*	1
PAD*	1

**CAD: coronary artery disease; SMA: superior mesenteric artery; IMA: inferior mesenteric artery; GAD: gastroduodenal artery; PAD: pancreaticoduodenal artery; y: year; d: day; m: month.*

Table II. *Endovascular strategies by anatomic location*

Location	No	Treatment	End-organ infarction	Re-intervention	Follow-up outcome
Splenic artery	4	Coil/gelfoam(1),coil(2) , covered stent(1)	—	—	—
Hepatic artery	2	Coil/gelfoam(1),coil(1)	—	—	new aneurysm (1)
Renal artery	2	Coil(2)	—	—	—
Celiac artery	2	Coil(1),Coil/stent(1)	—	—	—
SMA*	10	Coil/stent(3), covered stent(7)	—	1	Stent thrombosis(1), new aneurysm(1)
IMA*	2	coil(2)	—	—	—
GAD*	1	coil(1)	—	—	—
PAD*	1	coil(1)	—	—	—

**SMA: superior mesenteric artery; IMA: inferior mesenteric artery; GAD: gastroduodenal artery; PAD: pancreaticoduodenal artery.*

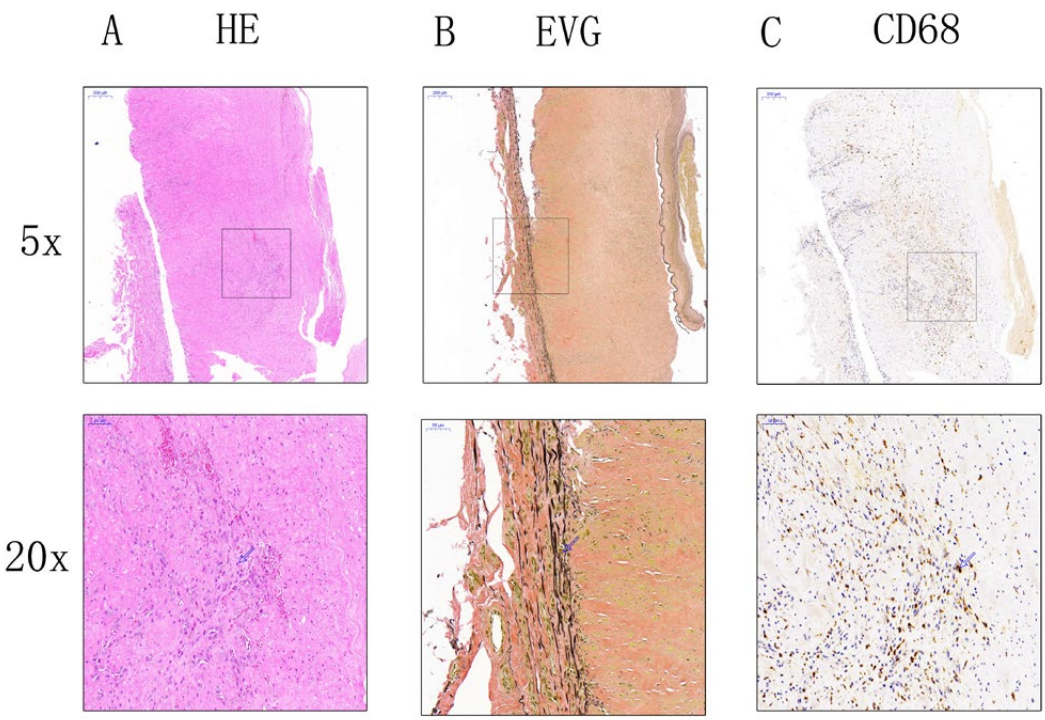

Fig. 5. *Histopathologic changes of aneurysm: **A)** Representative hematoxylin and eosin (HE)–stained micrographs (original magnification) 5X and 20X). Substantial expansion and inflammatory cell (arrow) infiltration into the artery wall. **B)** Representative elastica van Gieson–stained micrographs (original magnification) 5X and 20X). Elastica van Gieson–stained elastic lamellae of aneurysm exhibited the elastin fragmentation (arrow). **C)** Immunohistochemical staining for CD68 in aneurysmal tissues (original magnification) 5X and 20X). There was increased number of CD68-positive macrophages (arrow) in the mural of aneurysm tissue.*

for 3 months to patients undergoing stent placement. No perioperative complications or morbidities were observed during hospital stay (mean 15.97±5.42 days, range 3-49 days) (Fig. 3). The symptoms were improved obviously or disappeared after treatment. During the follow-up (mean 17.75±3.12 months, range 12-51 months), no recurrent symptoms or long-term complications were reported. The follow-up imaging examination revealed totally excluded aneurysms, except new aneurysms in 2 patients at the 6th and 8th months of follow-up, and in-stent thrombosis in 1 patient at the 12th month. Because of the small diameter (< 20 mm) and asymptomatic situation, re-intervention was replaced by regular imaging examination (Fig. 4).

Molecular biological examination was performed of the excised part of these aneurysms. The result of hematoxylin and eosin (H&E)–stained micrographs showed substantial expansion and inflammatory cell (arrow) infiltration into the artery wall as shown in Fig. 5. The elastica van Gieson–stained elastic lamellae of aneurysm exhibited the elastin fragmentation. Immunohistochemical staining showed that there was an increased number of CD68-positive macrophages in the mural of aneurysm tissue. These histopathologic changes were consistent with with the major characteristic of intracranial aneurysm and abdominal aortic aneurysm.

DISCUSSION

Visceral artery aneurysms (VAAs) were considered a life-threatening disease because of potential rupture with a low incidence rate; however, increased imaging examination and frequency of percutaneous intra-arterial intervention has resulted in overtreatment of VAAs in recent years. True VAA represents an uncommon degenerative arterial disease, characterized by all three layers of the artery, while pseudo-aneurysms are surrounded by incomplete elements of artery wall, fibrous tissue, and neighbouring stroma (2, 20, 21). Both true VAAs and pseudoaneurysms may present life-threatening clinical emergencies when they rupture.

The occurrence of VAAs is equal among males and females. Up to 95–98% of VAAs are observed in splenic (60%), hepatic (20%), superior mesenteric (5.5%), celiac (4%), and gastroduodenal artery aneurysms (4%) (1, 2, 22). The remaining 2–5% of VAAs involves the pancreaticoduodenal, gastric, colic, ileal, and jejunal arteries. Renal artery aneurysms are regarded as a consequence of hypertension and present a slightly different natural history, so they are usually described separately.

True VAA represents a degenerative artery disease, the etiology of which includes atherosclerosis, arterial medial degeneration, and fibromuscular dysplasia (20, 21). It comprises all three layers of artery wall and can present an emergency of rupture. Pseudoaneurysm is characterized by its structure, contributed by partial artery wall, fibrous tissue or adjacent stroma. Iatrogenic intervention, trauma, infection, inflammation, intra-vascular drug use, and vasculitis may result in a pseudoaneurysm (20, 21).

The importance of VAA is related to the potential risk of rupture, which can result in a high mortality rate (12). Pseudoaneurysms are more likely to rupture than true aneurysms and require emergency treatment (2). Compared with the rare ruptured splenic artery aneurysm, hepatic artery rupture is much more frequent (2). In this study, 1 patient with hepatic aneurysm and 2 patients with SMA aneurysms presented with emergences of rupture.

Patients with VAAs usually presented with abdominal pain, depending on the aneurysm location and hemorrhage (1, 2). However, asymptomatic VAAs also can be observed as a result of widely-applied imaging examinations. The general indications of surgical management depend on both the aneurysm feature and symptoms. The diameter size greater than twice the artery caliber, rapidly increasing aneurysm size, symptomatic aneurysm, aneurysms in female patients of child-bearing age and mycotic aneurysms require either open surgery or endovascular surgery (1, 10). There is no consensus on the specific indication of endovascular treatment in VAA patients, however, favorable anatomy is necessary for successful treatment.

Most previous studies on animals and humans indicate a major role of chronic aortic inflammation in abdominal aortic aneurysm (AAA) pathogenesis. Evidence suggests that inherited and haemodynamic

factors also have an important role in AAA pathogenesis. According to the inflammation theory of AAA, chronic aortic inflammation leads to aortic wall destruction. A wide array of innate immune cells, such as neutrophils and macrophages, and adaptive immune cells, such as T and B lymphocytes, enter the aortic wall via adventitial vasa vasorum or from periadventitial lymph nodes, intimal atherosclerotic plaque and the intraluminal thrombus. Cytokines produced by these cells can potentiate the inflammatory response. Oxygen-derived free radicals and other products from the inflammatory cells can induce apoptosis and phenotypic changes of vascular smooth muscle cells (VSMCs) in the media, which leads to partial loss of the matrix-producing and matrix-repair capacity of the media. Proteases released from the infiltrating inflammatory cells can induce fragmentation of the microfibrils of the media, leading to loss of wall elasticity. Ultimately, these effects can lead to the medial thinning and aortic weakening typical of end-stage AAA (23).

We have carried out surgical resection in some cases of open of VAA, such as splenic aneurysm, superior mesenteric aneurysm, popliteal aneurysm, etc. We performed molecular biological examination of the excised part of these aneurysms. The elastica van Gieson–stained elastic lamellae of aneurysm exhibited the elastin fragmentation. Immunohistochemical staining showed an increased number of $CD68^+$ macrophages in the mural of aneurysm tissue. These histopathologic changes were consistent with the major characteristic of intracranial aneurysm and abdominal aortic aneurysm. Currently, no drug therapy is available for AAA. The conventional open surgical treatment includes ligation of proximal and distal parent artery, aneurysmal resection, with or without vascular reconstruction, and end-organ resection (1, 10, 12). However, open surgery is related to a certain rate of mortality and morbidity and is not suitable for patients who cannot tolerate surgical intervention, especially for those with severe comorbidities. In recent years, endovascular treatment has become the first-line choice for VAA patients. The high technical success rate, satisfactory short-term outcome and minimally procedural wound make it a popular and highly cost-effective treatment modality. For patients in this study, we performed endovascular treatment based on the above considerations.

Endovascular treatment includes embolization (coil, gelfoam, particles, NBCA glue, thrombin, vascular plug, etc) and covered stent placement (15, 16, 19). The occlusion of aneurysm sac with coil should be performed in this situation. When the coils are at a high risk of migration from a wide-neck aneurysm sac, a metal stent can be deployed in the parent artery to assist coil embolization. We do not recommend coil embolization for pseudoaneurysm, as the coil pack in aneurysm sac may increase the risk of rupture because of the incomplete arterial wall surrounding the pseudoaneurysm.

The purpose of interventional embolization is to eliminate the aneurysm from the arterial circulation, while ensuring that the collateral circulation continues to perfuse the terminal organs to prevent the occurrence of serious complications such as terminal organ ischemia and infarction due to excessive embolization (18, 20, 21). However, this technique also needs specific and appropriate anatomic conditions, such as adequate arterial caliber for stent delivery device, adequate proximal and distal anchoring zone. The number of input veins and afferent vessels may influence the successful exclusion of aneurysm by covered stent, as multiple efferent and afferent vessels may not be bridged by stent-graft and become a source of type II endoleak. We successfully placed eight covered stents in splenic (n=1) and SMA (n=7) and no stent-related complications were observed.

Endovascular techniques provide various advantages, such as the ability to perform with local anesthesia, detailed assessment of collateral circulation, a low rate of postoperative complications, a shorter hospital stay compared with open surgery. However, percutaneous endovascular treatment is also associated with many complications, including intra-procedural aneurysm rupture, end organ infarction, sacrifice of the visceral vessel, non-target vessel embolization, coil migration, access site hematomas, aneurysm recurrence, arterial disruption, in-stent thromboembolic event, stent rupture or migration, contrast nephropathy, pain, and fever (19, 24). However, no periprocedural complications occurred in our patients. Moreover, the follow-up outcomes of

our patients were satisfactory in general, except for two cases of aneurysm recurrence and one case of in-stent thrombosis, as shown in Table II.

As VAAs are uncommon, literature focusing on comparing open surgery with endovascular treatment is very limited. Hislop et al. (25) reported reductions in complication rate, in-hospital stay, and overall costs in an endovascular treatment group based on a review of VAA patients in the state of New York between 2000 and 2006. Tulsyan et al. (15) reported 98% of technical success rate and 8.3% of 30-day periprocedural mortality rate in 48 VAA patients undergoing endovascular treatments. However, Sachdev et al. (26) reported there was no significant difference in early mortality or morbidity between endovascular treatments and visceral arteries. In our study, the technical success rate was up to 100% and relatively long-term follow-up outcomes were also satisfactory. This may provide a beneficial experience to justify the long-term durability of endovascular treatment.

In conclusion, long-term follow-up after endovascular intervention is important for either coil embolization or stent deployment. For coil embolization, Doppler ultrasound or CTA is essential to evaluate coil position, aneurysm size, collateral circulation, and blood flow to end-organ. For covered stent placement, a consecutive imaging examination by ultrasound or CTA at 1 month, 6 months, and then yearly after discharge is recommended. Moreover, oral antiplatelet medicine should be administered to patients undergoing covered stent placement.

These cases of endovascular treatment may justify the efficacy of percutaneous endovascular coil embolization and stent deployment. This study also provides beneficial knowledge (based on our experience) on how to choose appropriate various endovascular strategies based on both clinical symptoms and aneurysm anatomy condition. However, a control group of open surgery and further investigation may be still needed to justify the advantages of endovascular treatment.

ACKNOWLEDGEMENT

This work was supported by Shandong province key research and development plan (2016GSF201227).

REFERENCES

1. Yoshioka Y, Yoshioka K, Ikeyama S. Large gastric intramural hematoma mimicking a visceral artery aneurysm: a case report. J Med Case Rep 2018; 12:61.
2. Dawson J, Fitridge R. Update on aneurysm disease: current insights and controversies: peripheral aneurysms: when to intervene - is rupture really a danger? Prog Cardiovasc Dis 2013; 56:26-35.
3. Jana M, Gamanagatti S, Mukund A, et al. Endovascular management in abdominal visceral arterial aneurysms: A pictorial essay. World J Radiol 2011; 3:182-7.
4. Koganemaru M, Abe T, Nonoshita M, Iwamoto R, Kusumoto M, Kuhara A, Kugiyama T. Follow-up of true visceral artery aneurysm after coil embolization by three-dimensional contrast-enhanced MR angiography. Diagn Interv Radiol 2014; 20:129-35.
5. Stanley JC, Thompson NW, Fry WJ. Splanchnic artery aneurysms. Arch Surg 1970; 101:689-97.
6. Gehlen JM, Heeren PA, Verhagen PF, Peppelenbosch AG. Visceral artery aneurysms. Vasc Endovascular Surg 2011; 45:681-7.
7. Ferrero E, Viazzo A, Ferri M, et al. Management and urgent repair of ruptured visceral artery aneurysms. Ann Vasc Surg 2011; 25:981 e7-11.
8. Kawai T, Shimohira M, Suzuki K, et al. Time-resolved magnetic resonance angiography as a follow-up method for visceral artery aneurysm treated with coil-embolisation. Pol J Radiol 2018; 83:e137-e42.
9. Choi JY, Kwon OJ. Approaches to the management of spontaneous isolated visceral artery dissection. Ann Vasc Surg 2013; 27:750-7.
10. Sachdev-Ost U. Visceral artery aneurysms: review of current management options. Mt Sinai J Med 2010; 77:296-303.
11. Pulli R, Dorigo W, Troisi N, Pratesi G, Innocenti AA, Pratesi C. Surgical treatment of visceral artery aneurysms: A 25-year experience. J Vasc Surg 2008; 48:334-42.
12. Marone EM, Mascia D, Kahlberg A, Brioschi C, Tshomba Y, Chiesa R. Is open repair still the gold standard in visceral artery aneurysm management?

Ann Vasc Surg 2011; 25:936-46.
13. Van Petersen A, Meerwaldt R, Geelkerken R, Zeebregts C. Surgical options for the management of visceral artery aneurysms. J Cardiovasc Surg (Torino) 2011; 52:333-43.
14. Uberoi R, Chung D. Endovascular solutions for the management of visceral aneurysms. J Cardiovasc Surg (Torino) 2011; 52:323-31.
15. Tulsyan N, Kashyap VS, Greenberg RK, Sarac TP, Clair DG, Pierce G, Ouriel K. The endovascular management of visceral artery aneurysms and pseudoaneurysms. J Vasc Surg 2007; 45:276-83.
16. Fankhauser GT, Stone WM, Naidu SG, et al. The minimally invasive management of visceral artery aneurysms and pseudoaneurysms. J Vasc Surg 2011; 53:966-70.
17. Cordova AC, Sumpio BE. Visceral Artery Aneurysms and Pseudoaneurysms—Should They All be Managed by Endovascular Techniques? Ann Vasc Dis 2013; 6:687-93.
18. Ferrero E, Ferri M, Viazzo A, et al. Visceral artery aneurysms, an experience on 32 cases in a single center: treatment from surgery to multilayer stent. Ann Vasc Surg 2011; 25:923-35.
19. Saltzberg SS, Maldonado TS, Lamparello PJ, et al. Is endovascular therapy the preferred treatment for all visceral artery aneurysms? Ann Vasc Surg 2005; 19:507-15.
20. Carroccio A, Jacobs TS, Faries P, et al. Endovascular treatment of visceral artery aneurysms. Vasc Endovascular Surg 2007; 41:373-82.
21. Kunzle S, Glenck M, Puippe G, Schadde E, Mayer D, Pfammatter T. Stent-graft repairs of visceral and renal artery aneurysms are effective and result in long-term patency. J Vasc Interv Radiol 2013; 24:989-96.
22. Huang YK, Hsieh HC, Tsai FC, Chang SH, Lu MS, Ko PJ. Visceral artery aneurysm: risk factor analysis and therapeutic opinion. Eur J Vasc Endovasc Surg 2007; 33:293-301.
23. Golledge J. Abdominal aortic aneurysm: update on pathogenesis and medical treatments. Nat Rev Cardiol 2019; 16:225-42.
24. Kolvenbach RR, Yoshida R, Pinter L, Zhu Y, Lin F. Urgent endovascular treatment of thoraco-abdominal aneurysms using a sandwich technique and chimney grafts--a technical description. Eur J Vasc Endovasc Surg 2011; 41:54-60.
25. Hislop SJ, Patel SA, Abt PL, Singh MJ, Illig KA. Therapy of renal artery aneurysms in New York State: outcomes of patients undergoing open and endovascular repair. Ann Vasc Surg 2009; 23:194-200.
26. Sachdev U, Baril DT, Ellozy SH, et al. Management of aneurysms involving branches of the celiac and superior mesenteric arteries: a comparison of surgical and endovascular therapy. J Vasc Surg 2006; 44:718-24.

Protective effects of NLRP3 inhibitor MCC950 on sepsis-induced myocardial dysfunction

S. Li[1], Z. Guo[2] and Z.-Y. Zhang[1]

[1]Department of Liver Intensive Care Unit, Beijing Tsinghua Changgung Hospital, School of Clinical Medicine, Tsinghua University, Beijing, China; [2]Department of Intensive Care Unit, Beijing Tsinghua Changgung Hospital, School of Clinical Medicine, Tsinghua University, Beijing, China

Received November 12, 2020 – Accepted January 26, 2021

Sepsis-induced myocardial dysfunction (SIMD) leads to poor prognosis or even death in severe sepsis cases, therefore, exploring its pathogenesis and new therapeutic targets has become the focus of current research. Specifically, an SIMD rat model was constructed by cecal ligation and puncture (CLP) method. At 24 h after intraperitoneal injection of the NLRP3 selective inhibitor MCC950, the levels of serum cardiac troponin I (cTnI) and Lactate dehydrogenase (LDH) in serum were detected, and the cardiac function of rats was examined via echocardiography. In addition, the pathological changes of myocardial tissues were observed by histological method, and the expression changes of inflammatory factors were detected in the tissue and serum. At the same time, H9C2 cells were treated with lipopolysaccharide (LPS) to simulate the *in vitro* model, and the expressions of inflammation and pyroptosis-related factors were detected. The results manifested that in the CLP group, the levels of serum cTnI and LDH were obviously increased, the myocardial tissue structure was disordered, the cell edema was severe, and the cardiac function was markedly reduced. Meanwhile, the expressions of inflammatory factors IL-6, IL-8 and TNF-α rose remarkably. On the contrary, MCC950 effectively reversed the above situation. Moreover, MCC950 inhibited LPS-induced inflammation and pyroptosis of H9C2 cells. In conclusion, the NLRP3 inhibitor MCC950 can reduce the release of LDH and other cellular inflammatory factors in the cytoplasm, thereby improving the cardiac function and slowing down the apoptosis of cardiomyocytes, which may be related to the inhibition of NLRP3/Caspase-1/IL-1β pathway.

Sepsis is a systemic inflammatory response syndrome caused by infection. It is a common complication in critically ill patients and one of the main causes of death in intensive care unit (ICCU) patients (1). In severe cases, sepsis is accompanied by organ dysfunction or inadequate tissue perfusion. Moreover, it is a vital risk factor for the safety and life of patients. Millions of patients worldwide are infected with this disease every year, and the mortality rate is higher than 25%. Even with the increase of iatrogenic resuscitation and organ support, its incidence rate is still rising (2). Sepsis often attacks the heart, and sepsis-induced myocardial dysfunction (SIMD) has become an important cause of poor prognosis or even death in severe sepsis cases (3). In the earliest stage, the disease is clinically manifested as left ventricular dilation and decreased ejection fraction, accompanied by cell autophagy (4), apoptosis (5), inflammation and pyroptosis (6). As the central link of sepsis, the production of a large number of

Key words: sepsis-induced myocardial dysfunction; MCC950; pyroptosis; inflammation; NLRP3/Caspase-1/IL-1β pathway

Corresponding Author:
Zhenyu Zhang, MD
Department of Liver Intensive Care Unit,
Beijing Tsinghua Changgung Hospital, School of Clinical Medicine,
Tsinghua University, No.168 Litang Road, Changping District
102218, Beijing, China
Tel.: 86 010-56119391
e-mail: mbfsg7@163.com

0393-974X (2021)
Copyright © by BIOLIFE, s.a.s.
This publication and/or article is for individual use only and may not be further reproduced without written permission from the copyright holder.
Unauthorized reproduction may result in financial and other penalties
DISCLOSURE: ALL AUTHORS REPORT NO CONFLICTS OF INTEREST RELEVANT TO THIS ARTICLE.

inflammatory mediators and cytokines plays an important role in the occurrence and development of SIMD, and is one of the pathological foundations of myocardial tissue damage. At present, exploring the pathogenesis of SIMD has become a hotspot in critical care research.

Current research has found that the NLRP3 inflammatory body plays an important role in a variety of autoimmune and inflammatory diseases. NLRP3 is a pattern recognition receptor of the innate immune system, capable of sensing pathogen-associated molecular patterns (PAMPs) and damage-associated molecular patterns (DAMPs) (7). When the danger signal of damaged cells is detected, NLRP3 recruits apoptosis-related proteins containing CARD-CARD domain, and then combines pro-caspase-1 to form the NLRP3 inflammatory response complex. The NLRP3 inflammasome promotes the enzymatic hydrolysis of pro-caspase-1 to produce active caspase-1. Then active caspase-1 can cleave the inactive inflammatory factors pro-IL-1β and pro-IL-18 in the cell, be transformed into activated forms of IL-1β and IL-18, and secrete to the outside of the cell to participate in immunity response and inflammatory response (8, 9). MCC950 is a selective NLRP3 inhibitor. Studies have shown that MCC950 has a significant effect in regulating the inflammatory response induced by myocardial infarction (10) and cardiomyopathy (11), and whether treatment with the NLRP3 inhibitor MCC950 can sufficiently reduce SIMD, and its specific mechanism of action and efficacy still need to be further clarified.

Pyroptosis is a type of cell death associated with inflammation discovered in recent years. It is also a regulated necrosis driven by pathological stimuli, namely proinflammatory programmed death. The morphological characteristics of cell pyroptosis are DNA cleavage, nuclear concentration, and cell membrane rupture (12). In the classical pathway, activated caspase-1 can cleave Gasdermin D (GSDMD), and its product GSDMD-N can form pores in the cell membrane. Later, the destruction of ion gradients inside and outside the cell membrane and the increase in osmotic pressure cause water to enter the cell, which eventually leads to membrane rupture and cell cleavage, resulting in cell pyroptosis (13). After the cell membrane ruptures, DAMPs and other cell contents are released into the extracellular environment, recruit more cytokines, and further extend the inflammatory cascade reaction, thereby aggravating cell damage (14).

However, the function of MCC950 in SIMD has rarely been researched, and whether it also plays a similar role has not been studied. Based on previous research, this study explored the role and molecular regulation mechanism of MCC950-dependent cell pyroptosis in SIMD through the combination of cell and animal experiments.

MATERIALS AND METHODS

Laboratory animals

SPF-grade healthy male SD rats aged 6-8 weeks (Slake Experimental Animal, Shanghai, China) were housed in the SPF animal room of the Experimental Animal Center of School of Clinical Medicine, Tsinghua University. All animal experiments were conducted in accordance with animal experiment guidelines. This study was approved by the Animal Ethics Committee of the School of Clinical Medicine, Tsinghua University.

Animal model

A rat model of sepsis was established by cecal ligation and puncture (CLP). The rats fasted for 12 h before surgery and had free access to water. They were anesthetized with intraperitoneal injection of 2% pentobarbital sodium (Boaigang, Beijing, China). After anesthesia, the rats were placed in the supine position on the operating table with the limbs fixed, and a 1.5-cm longitudinal incision was made in the middle of the abdomen. The skin and muscle layers were cut layer by layer. After the abdominal cavity was opened, the cecum was exposed, and its terminal mesentery was freed. Subsequently, a 4-0 line (Boaigang, Beijing, China) was applied to ligate the intestinal canal from the ileocecal part to the end 1/3 of the cecum. A 21G sterile needle (Boaigang, Beijing, China) was used to penetrate the intestinal canal, and a small amount of content was gently squeeze out to ensure that the perforation was unblocked. Then, the rat cecum was put back, the abdominal wall was sutured layer by layer, and the incision was disinfected with iodophor (Boaigang, Beijing, China). According to

previous research, MCC950 (3mg/kg) (15) was injected intraperitoneally within 30 min after the end of modeling, and the corresponding volume of normal saline was injected intraperitoneally in the Sham group and CLP group. At 24 h after intraperitoneal injection of MCC950, the serum was retained for the next study.

Echocardiographic evaluation of rat cardiac function

Rats were anesthetized with 2% pentobarbital sodium by intraperitoneal injection at a dose of 3.5 mg/100 g, and the epicardial area was depilated. High-frequency ultrasound imaging system (Nuohai Life Science, Shanghai, China) was used to detect cardiac function indicators, including left ventricular shortening rate (LVFS) and left ventricular ejection fraction (LVEF). Each indicator was measured 3 times and the average value was recorded.

Tissue extraction

Rats in both the Sham group and CLP group were sacrificed after echocardiographic testing, the chest was quickly opened along the sternum to expose the heart, and 4 mL of blood was extracted with a syringe. After standing for 1 h, the blood was subjected to centrifugation at 3000 r/minute for 10 min, and the upper serum was stored at -80°C. Then, the heart was quickly removed, the residual blood was rinsed with physiological saline, the surface water was absorbed by the filter paper, the apex part was stored in the prepared 10% neutral formaldehyde solution, and the remaining myocardial tissue was stored at -80°C.

Hematoxylin & eosin (H&E) staining

The myocardial tissues were dehydrated by gradient ethanol, transparentized using xylene, and then embedded with liquefied paraffin. After the cooling of paraffin blocks, a microtome was used to cut the tissues into 4-μm thick sections. Then the sections were treated with xylene and gradient ethanol in sequence. After hematoxylin staining, the tissues were rinsed with running water for 5 min, and 10% hydrochloric acid alcohol was used for differentiation. After sufficient washing, eosin (Jian Cheng, Nanjing, China) was applied for counterstaining. Later, tissue sections were dehydrated by gradient ethanol in turn, transparentized using xylene and then mounted with mounting reagent. Finally, the pathological changes were observed under an optical microscope (Bio, New York, NY, USA).

Immunohistochemical staining

The sections were deparaffinized in xylene and rehydrated under an ethanol gradient. Then they were rinsed 3 times with phosphate buffer saline (PBS), incubated with 3% hydrogen peroxide for 30 min, and blocked by 10% goat serum for 1 hour. Next, the main antibody (IL-α, 1:500, Abcam, Cambridge, MA, USA) was incubated overnight at 4°C. The next day, the secondary antibody (1:500, Abcam, Cambridge, MA, USA) was incubated at room temperature for 1 hour. Next, the slices were sequentially dehydrated by gradient ethanol, xylene was transparent, and then mounted with a mounting reagent. Finally, positive cells were counted under an optical microscope.

LDH activity and Malondialdehyde (MDA) content detection

The LDH activity and MDA content of rat serum and H9C2 cell supernatant were measured according to the instructions of LDH and MDA kit (Jian Cheng, Nanjing, China).

Serum cardiac troponin I (cTnI) content detection

Immediately after the serum was collected, the cTnI content in the serum of each group of rats was detected through the cTnI kit.

Cell culture and processing

H9C2 cells (American type culture collection, Manassas, VA, USA) were cultured in Dulbecco's Modified Eagle's Medium (DMEM; Life Technology, Wuhan, China) containing 10% fetal bovine serum (FBS; Life Technology, Wuhan, China) and placed in a 5% CO_2, 37°C incubator. When the cells were grown and fused to 90%, they were digested with trypsin (Life Technology, Wuhan, China) and passaged. When the cell growth density reached about 50%, they were synchronized for 24 h. In this experiment, the rats were divided into 3 groups: control group; LPS group (1 mg/L LPS treatment for 24 h) (16); and LPS+MCC950 group (1 μmol/L MCC950 and 1 mg/L LPS co-treatment for 24 h) (17).

Cell Counting Kit-8 (CCK8) Assay

H9C2 cells were inoculated in 96-well plates at 5000

cells/well. After 24 h, the cells were added with CCK-8 reagent (Camilo, Nanjing, China) in the dark, and placed in the incubator for 2 h. After terminating the reaction, the absorbance at 450 nm was detected with a microplate reader (Life Technology, Wuhan, China), and the cell activity was calculated according to the formula.

Western blotting (WB)

RIPA Lysis Buffer (Camilo, Nanjing, China) was used to lyse rat heart tissues and H9C2 cells. BCA method (Camilo, Nanjing, China) was used to quantify protein concentration. A total of 15 μg protein samples were separated using a 10% sodium dodecyl sulfate-polyacrylamide gel. Then, the dispersed proteins were transferred onto a polyvinylidene difluoride (PVDF, Thermo Fisher Scientific, Waltham, MA, USA) membrane for 2 h. Next, 10% skim milk was used to block the membrane for 1 h, and the primary antibodies were used for incubation at 4°C overnight. The next day, the corresponding secondary antibody (Camilo, Nanjing, China, 1:2000) was used to incubate the proteins at room temperature for 2 h. Later, the enhanced chemiluminescence (ECL) kit (Camilo, Nanjing, China) was used for chemiluminescence development. Primary antibodies included antibodies against IL-6 (Abcam, Cambridge, MA, USA, Rabbit, 1:2000), IL-8 (Abcam, Cambridge, MA, USA, Mouse, 1:2000), TNF-α (Abcam, Cambridge, MA, USA, Rabbit, 1:3000), NLRP3 (Abcam, Cambridge, MA, USA, Rabbit, 1:2000), caspase-1 (Abcam, Cambridge, MA, USA, Rabbit, 1:2000) GSDMD (Abcam, Cambridge, MA, USA, Mouse, 1:2000), GSDMD-N (Abcam, Cambridge, MA, USA, Mouse, 1:2000) and GAPDH (Abcam, Cambridge, MA, USA, 1:3000).

Quantitative Real-Time Polymerase Chain Reaction (qRT-PCR)

TRIzol reagent (Thermo Fisher Scientific, Waltham, MA, USA) was utilized to extract the total RNAs of myocardial tissues and H9C2 cells, and then ultraviolet spectrophotometry was applied to determine the RNA purity (Beckman Coulter, Miami, FL, USA). The RNAs with the purity of 1.9-2.1 were used for the following assays. Next, the RNAs were subjected to reverse transcription and PCR, using GAPDH as an internal reference, and the target gene mRNA expression level was calculated according to the $2^{-\Delta\Delta Ct}$ method. The primer list is shown in Table I.

Table I. *RT-PCR primers*

Gene name	Forward (5'>3')	Reverse (5'>3')
IL-1β	GCAACTGTTCCTGAACTCAACT	ATCTTTTGGGGTCCGTCAACT
IL-6	TAGTCCTTCCTACCCCAATTTCC	TTGGTCCTTAGCCACTCCTTC
IL-8	CAAGGCTGGTCCATGCTCC	TGCTATCACTTCCTTTCTGTTGC
TNF-α	CCCTCACACTCAGATCATCTTCT	GCTACGACGTGGGCTACAG
NLRP3	CCATCGGCCTTTGAGAAAGTG	ACACATGAATAACGGGGTTTCC
Caspase-1	CAGGCAAGCCAAATCTTTATCAC	TCCAACCCTCGGAGAAAGTC
GSDMD	ATTACCCGCCCGAGAAAGG	TCGCAGCAAAGATCCACACAG
GAPDH	ACAACTTTGGTATCGTGGAAGG	GCCATCACGCCACAGTTTC

RT-PCR: quantitative real-time polymerase chain reaction

Enzyme Linked Immunosorbent Assay (ELISA)

H9C2 cells were seeded in 96-well plates at 5000 cells/well. After treating the cells with LPS and MCC950 for 24 h, the cell supernatant was collected and the cell protein concentration was detected. Next, the coating buffer (Kaiji, Nanjing, China) was added and left overnight at 4°C. The next day, the cells were washed with phosphate buffered saline with Tween 20 (PBST)for 3 times, and blocked with BSA reagent (Kaiji, Nanjing, China) for 1 h. Then the cell supernatant was added, and incubated at room temperature. After 2 h, the cells were washed with PBST 3 times, and antibodies against IL-1β IL-6, IL-8 and TNF-α antibody were added separately for incubation at room temperature. After 1 h, the cells were washed with PBST 3 times. Subsequently, substrate liquid was added for color development, and 15 min later, stop buffer was added. Finally, the absorbance at 450 nm was detected with a microplate reader.

Statistical analysis

Statistical Product and Service Solutions 22.0 (SPSS IBM, Armonk, NY USA) statistical software was used to analyze the experimental data. The mean ± standard deviation ($\bar{x}\pm s$) was used to represent the measurement data. Comparisons among multiple groups were made using One-way ANOVA, followed by Post Hoc Test (least significant difference). $P<0.05$ indicated that the difference was significant

RESULTS

Protective effect of MCC950 on sepsis-induced cardiac structure and function

In order to explore the effect of sepsis on heart injury, a sepsis model was established by CLP method. The results showed that the myocardial cells in the Sham group were generally normal, while those in the CLP group suffered from obvious interstitial edema and degeneration of granules, with disappearance of some cell lines and stripes, and disordered muscle fibers. After treatment with MCC950, the above changes were obviously alleviated (Fig. 1A). Echocardiography was performed 24 h after modeling, and it was found that there was no

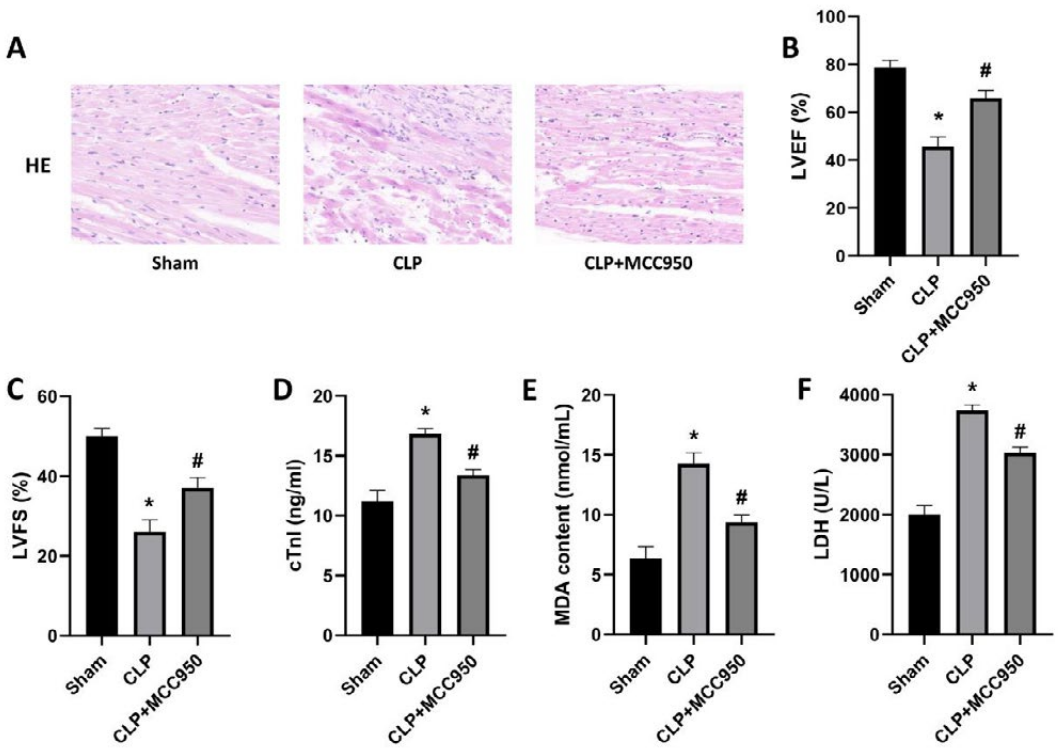

Fig. 1. *Protective effect of MCC950 on sepsis-induced cardiac structure and function.* ***A)*** *HE staining.* ***B, C)*** *Echocardiography detected the LVEF% and LVFS%.* ***D~F)*** *The content of cTnI, MDA, LDH in serum. *statistical difference from the Sham group P<0.05; # statistical difference from the CLP group P<0.05*

obvious abnormality in the echocardiography of the Sham group. The LVEF and LVFS of rats in the CLP group were obviously reduced. However, CLP-induced cardiac dysfunction was improved after CLP+MCC950 treatment (Fig. 1 B, C). At the same time, the cTnI content in the serum of the 3 groups of rats was detected. The results manifested that the cTnI content of the CLP group was obviously higher than that of the Sham group, while the cTnI content of the CLP+MCC950 group was obviously reduced compared with that in the CLP group (Fig. 1D). The above results confirmed that the sepsis model established by the CLP method was successful, and MCC950 could effectively relieve sepsis-induced

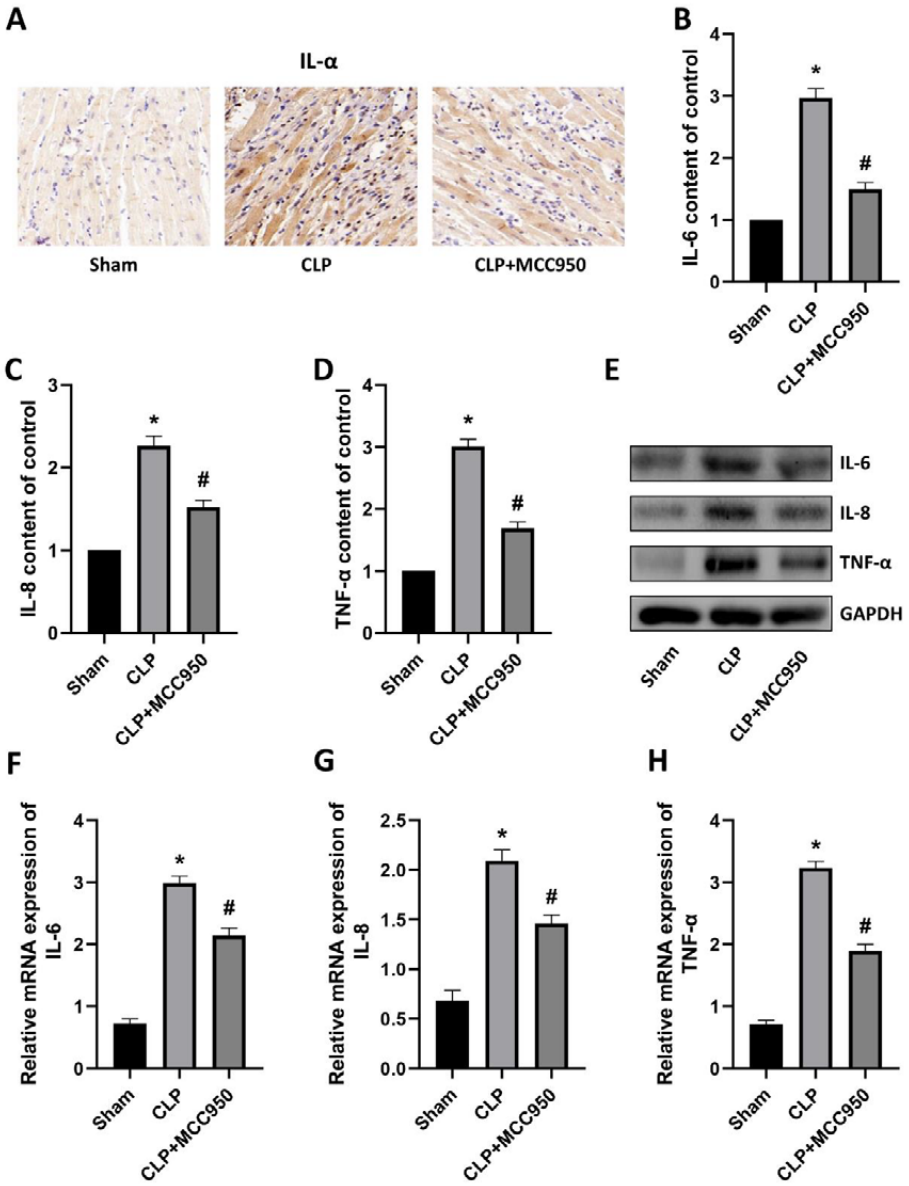

Fig. 2. *MCC950 inhibited sepsis-induced cardiomyocyte inflammation.* ***A)*** *Immunohistochemical staining was used to detect IL-α expression in heart tissues.* ***B-D)*** *ELISA method was used to detect the content of IL-6, IL-8 and TNF-α in serum.* ***E)*** *WB was used to detect the protein expression of IL-6, IL-8, TNF-α in heart tissues.* ***F-H)*** *qRT-PCR was used to detect the mRNA expressions of IL-6, IL-8 and TNF-α in heart tissues. * statistical difference from the Sham group P<0.05; # statistical difference from the CLP group P<0.05.*

cardiac structural destruction and dysfunction. In addition, MDA content and LDH activity in serum were detected, and it was found that MCC950 was able to effectively inhibit CLP-induced increase in MDA content and LDH activity (Fig. 1 E, F).

MCC950 inhibited sepsis-induced cardiomyocyte inflammation

In order to explore the effect of MCC950 on sepsis-induced cardiomyocyte inflammation, the expression of IL-α was first detected by immunohistochemical staining. The results revealed that the expression of IL-α in the myocardial tissues in the CLP group was obviously increased compared with that in the sham group, but in the CLP+MCC950 group, IL -α expression was obviously reduced compared with that in the CLP group (Fig. 2A). Next, the ELISA method was applied to detect the levels of IL-6, IL-8, and TNF-α in the serum. It was discovered that compared with those in the Sham group, the levels of IL-6, IL-8, and TNF-α in the CLP group were markedly increased. In comparison with the CLP group, the content of IL-6, IL-8 and TNF-α in the CLP+MCC950 group was obviously reduced (Fig. 2 B-D). At the same time, WB results also confirmed that the protein expressions of IL-6, IL-8, and TNF-α

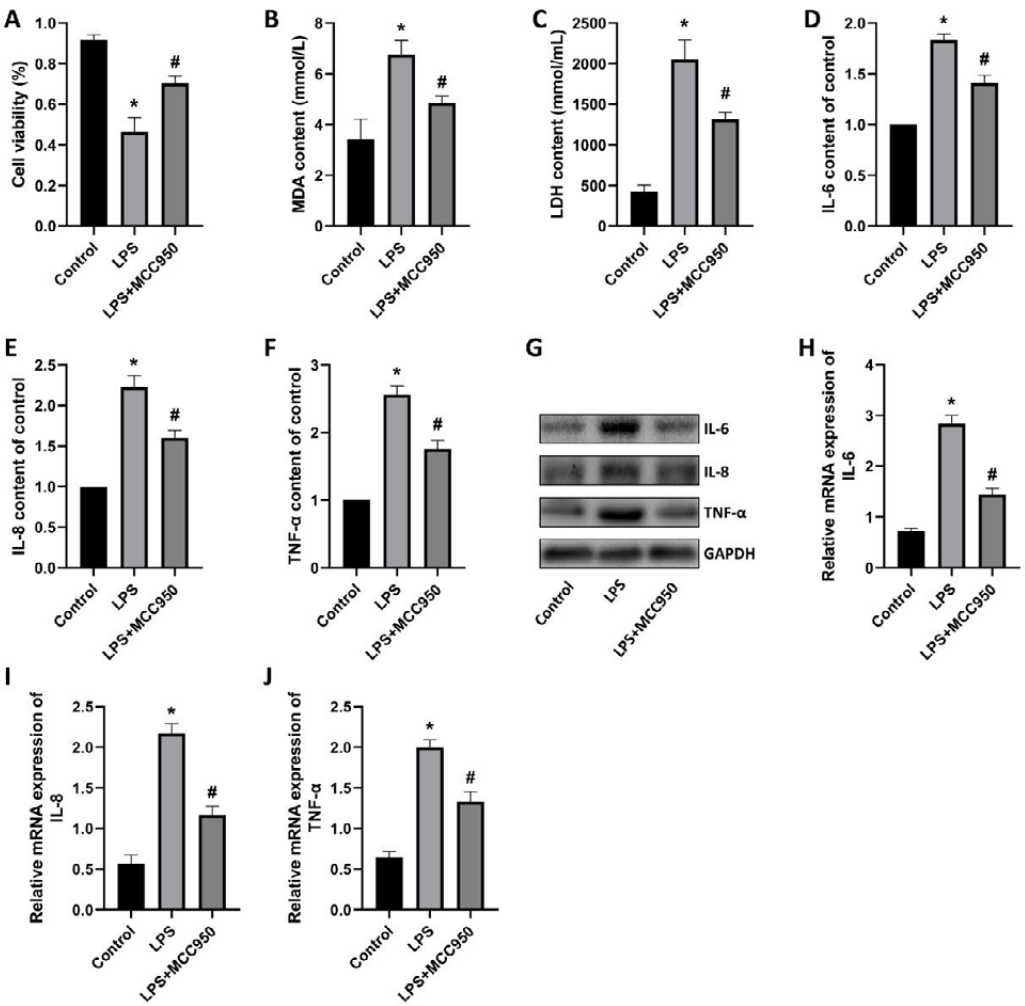

Fig. 3. *MCC950 inhibited LPS-induced H9C2 cytotoxicity and inflammation.* ***A)*** *CCK-8 method was used to detect the H9C2 cell activity.* ***B-C)*** *The content of MDA and LDH in cell supernatant.* ***D-F)*** *ELISA method was used to detect the content of IL-6, IL-8 and TNF-α in cell supernatant.* ***G)*** *WB was used to detect the protein expressions of IL-6, IL-8 and TNF-α in H9C2 cells.* ***H-J)*** *qRT-PCR was used to detect the mRNA expressions of IL-6, IL-8 and TNF-α in H9C2 cells. * statistical difference from the Control group P<0.05; # statistical difference from the LPS group P<0.05.*

protein in the CLP group were notably increased, and MCC950 could effectively inhibit the increased protein expressions of IL-6, IL-8, and TNF-α (Fig. 2E). At the same time, qRT-PCR also obtained similar results (Fig. 2 F-H).

MCC950 inhibited LPS-induced H9C2 cytotoxicity and inflammation

According to previous studies, 1 mg/L LPS and 1 μmol/L MCC950 were used to treat H9C2 cells. The CCK-8 method was utilized to examine cell activity, and showed that the cell activity in the LPS group remarkably declined at 24 h of incubation in comparison with that in the control group, while it was obviously enhanced in the LPS+MCC950 group in comparison with that in the LPS group (Fig. 3A). Meanwhile, the MDA content and LDH activity of the cell supernatant in the LPS group were increased obviously compared with those in the control group. On the contrary, the MDA content and LDH activity in the LPS+MCC950 group were decreased compared with those in the LPS group (Fig. 3B~3C). By detecting the content of IL-6, IL-8, and TNF-α in the cell supernatant, it was found that MCC950 was able to effectively suppress the increase of the above-mentioned inflammatory cytokine content induced by LPS (Fig. 3D-3F). Besides, WB and qRT-PCR also obtained similar results (Fig. 3G-3J). Moreover, the *in vitro* results were consistent with the *in vivo* results.

MCC950 suppressed LPS-induced pyroptosis of H9C2 cells

Next, the effects of MCC950 on LPS-induced

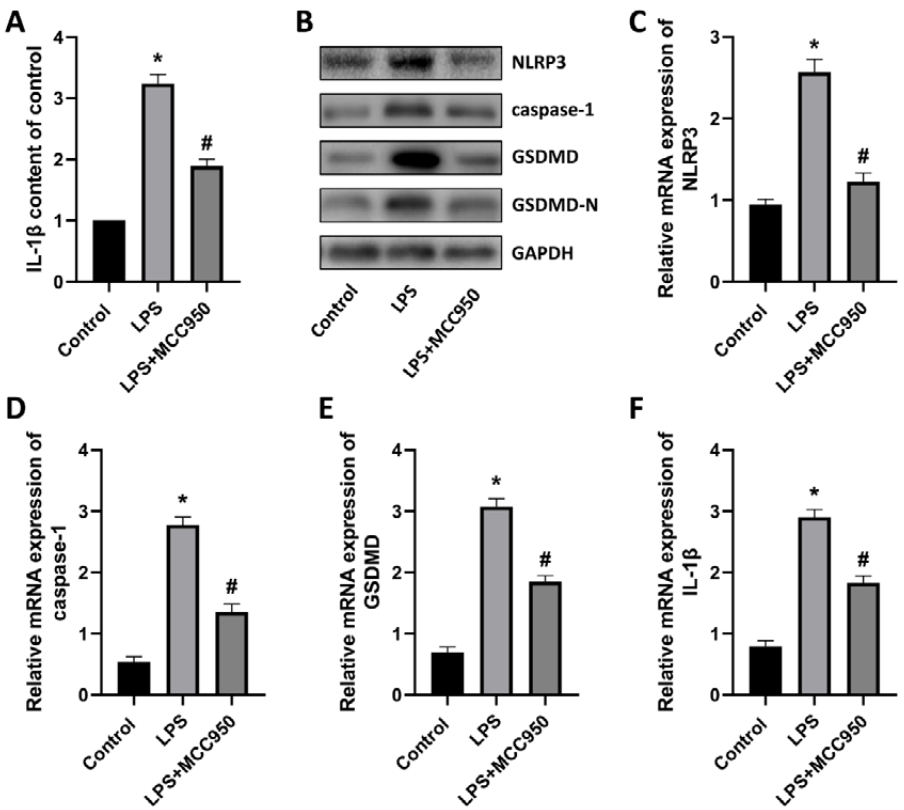

Fig. 4. *MCC950 inhibited LPS-induced pyroptosis of H9C2 cells.* ***A)*** *ELISA method was used to detect the content of IL-1β in cell supernatant.* ***B)*** *WB was used to detect the protein expressions of NLRP3, caspase-1, GSDMD and GSDMD-N in H9C2 cells.* ***C-F)*** *qRT-PCR was used to detect the mRNA expressions of NLRP3, caspase-1, GSDMD and IL-1β in H9C2 cells. * statistical difference from the Control group P<0.05; # statistical difference from the LPS group P<0.05.*

pyroptosis of H9C2 cells were explored. ELISA results showed that IL-1β content in the LPS group was obviously increased compared with that in the control group, while MCC950 could effectively inhibit the increase in IL-1β content compared with that in the LPS group (Fig. 4A). In addition, the protein expressions of NLRP3, caspase1, GSDMD and GSDMD-N in H9C2 cells were markedly higher in LPS group than in LPS+MCC950 group (Fig. 4B). qRT-PCR results showed that the expressions of NLRP3, caspase1, GSDMD and IL-1β mRNA in the LPS group were notably increased. In contrast, after the treatment of H9C2 cells treated with MCC950, NLRP3, caspase1, GSDMD and IL-1β mRNA expressions were obviously reduced (Fig. 4 C-F). On this basis, it could be speculated that MCC950 can suppress myocardial cell pyroptosis by inhibiting the NLRP3/caspase1/IL-1β pathway.

DISCUSSION

Sepsis and severe sepsis, because of their high ICU hospitalization and mortality rated, have been regarded as a huge burden on the health care system, so early diagnosis and treatment of the disease has become the focus of research. The heart, as a vital organ to maintain human activity and function, is easily affected during the development of sepsis. A large number of studies have shown that myocardial dysfunction is related to the poor prognosis of sepsis patients, which can cause hemodynamic instability and thus become an independent risk factor for the death of patients (18, 19). Despite the increasing research on sepsis in recent years, the complex pathogenesis of SIMD remains controversial (20, 21). In this study, a CLP-induced SIMD animal model was constructed. The NLRP3 selective inhibitor MCC950 was injected intraperitoneally to observe whether the cardiac dysfunction in sepsis rats was improved. *In vitro*, H9C2 cells were treated with LPS and the possible mechanism was explored. The results *in vivo* showed that the NLRP3 inhibitor MCC950 played an important role in SIMD and could reduce sepsis-induced myocardial structural damage and myocardial function damage.

Pyroptosis is a newly discovered method of programmed cell death of inflammatory cells, which mainly mediates the activation of a variety of Caspase, including caspase-1, through inflammatory bodies, causing a variety of GSDM family members including GSDMD to shear and polymerize, which results in cell membrane perforation. Caspase-1 plays an important role in cell pyroptosis. On the one hand, activated caspase-1 can cleave GSDMD, forming a peptide containing the N-terminal active domain of GSDMD, inducing cell membrane perforation and causing inflammation. On the other hand, activated caspase-1 cleaves pro-IL-1β and pro-IL-18 to form active IL-1β and IL-18, and releases them to the outside of the cell, recruiting inflammatory cells to aggregate and expand the inflammatory response. Compared with apoptosis, cell pyroptosis occurs faster and is accompanied by the release of a large number of pro-inflammatory factors (22). The results of this study also found that *in vivo*, CLP induced an inflammatory response in cardiomyocytes, and LPS could also induce an inflammatory response in H9C2 cells *in vitro*, thereby promoting increased expressions of IL-α, IL-6, IL-8 and TNF-α. *In vitro* studies have found that MCC950 can reduce the production of GSDMD-N by inhibiting the NLRP3/Caspase-1/IL-1β pathway, reduce its penetration into the cell membrane, and decrease the release of LDH and other cellular inflammatory factors in the cytoplasm, thereby slowing down LPS-induced pyroptosis of H9C2 cells.

The NLRP3 inflammatory body exerts crucial effects in sepsis-induced cardiomyocyte damage, and the NLRP3 inhibitor MCC950 can reduce the release of LDH and other cellular inflammatory factors in the cytoplasm, thereby improving the cardiac function and slowing down the apoptosis of cardiomyocytes, which may be related to the inhibition of NLRP3/Caspase-1/IL-1β pathway.

REFERENCES

1. Cecconi M, Evans L, Levy M, Rhodes A. Sepsis and septic shock. Lancet 2018; 392:75-87.
2. Uhle F, Lichtenstern C, Brenner T, Weigand MA. Pathophysiology of sepsis. Anasthesiol Intensivmed Notfallmed Schmerzther 2015; 50:114-22.

3. Walley KR. Sepsis-induced myocardial dysfunction. Curr Opin Crit Care 2018; 24:292-99.
4. Shi X, Liu Y, Zhang D, Xiao D. Valproic acid attenuates sepsis-induced myocardial dysfunction in rats by accelerating autophagy through the PTEN/AKT/mTOR pathway. Life Sci 2019; 232:116613.
5. Zhang WX, He BM, Wu Y, Qiao JF, Peng ZY. Melatonin protects against sepsis-induced cardiac dysfunction by regulating apoptosis and autophagy via activation of SIRT1 in mice. Life Sci 2019; 217:8-15.
6. Li N, Zhou H, Wu H, et al. STING-IRF3 contributes to lipopolysaccharide-induced cardiac dysfunction, inflammation, apoptosis and pyroptosis by activating NLRP3. Redox Biol 2019; 24:101215.
7. Mangan M, Olhava EJ, Roush WR, Seidel HM, Glick GD, Latz E. Targeting the NLRP3 inflammasome in inflammatory diseases. Nat Rev Drug Discov 2018; 17:588-606.
8. Haneklaus M, O'Neill LA. NLRP3 at the interface of metabolism and inflammation. Immunol Rev 2015; 265:53-62.
9. Kelley N, Jeltema D, Duan Y, He Y. The NLRP3 inflammasome: an overview of mechanisms of activation and regulation. Int J Mol Sci 2019; 20(13):3328.
10. van Hout GP, Bosch L, Ellenbroek GH, et al. The selective NLRP3-inflammasome inhibitor MCC950 reduces infarct size and preserves cardiac function in a pig model of myocardial infarction. Eur Heart J 2017; 38:828-36.
11. Wang H, Sun X, Hodge HS, Ferrario CM, Groban L. NLRP3 inhibition improves heart function in GPER knockout mice. Biochem Biophys Res Commun 2019; 514:998-1003.
12. Jia C, Chen H, Zhang J, et al. Role of pyroptosis in cardiovascular diseases. Int Immunopharmacol 2019; 67:311-18.
13. Schneider KS, Gross CJ, Dreier RF, et al. The inflammasome drives GSDMD-independent secondary pyroptosis and IL-1 release in the absence of caspase-1 protease activity. Cell Rep 2017; 21:3846-59.
14. Mathur A, Hayward JA, Man SM. Molecular mechanisms of inflammasome signaling. J Leukoc Biol 2018; 103:233-57.
15. Ward R, Li W, Abdul Y, et al. NLRP3 inflammasome inhibition with MCC950 improves diabetes-mediated cognitive impairment and vasoneuronal remodeling after ischemia. Pharmacol Res 2019; 142:237-50.
16. Shi Y, Jiang H, Yang X. PPARδ activation protects H9c2 cardiomyoblasts from LPS-induced apoptosis through the heme oxygenase-1-mediated suppression of NF-κB activation. Mol Med Rep 2017; 15:3775-80.
17. Zhang ZQ, Yang YF, Yan JR, et al. Advanced glycated albumin induces macrophage pyroptosis via upregulating nucleotide-binding oligomerization domain-like receptor protein 3. Sheng Li Xue Bao 2019; 71:846-54.
18. Merx MW, Weber C. Sepsis and the heart. Circulation 2007; 116:793-802.
19. Martin L, Derwall M, Thiemermann C, Schurholz T. Heart in sepsis : Molecular mechanisms, diagnosis and therapy of septic cardiomyopathy. Anaesthesist 2017; 66:479-90.
20. Ren J, Ren BH, Sharma AC. Sepsis-induced depressed contractile function of isolated ventricular myocytes is due to altered calcium transient properties. Shock 2002; 18:285-88.
21. Chagnon F, Bentourkia M, Lecomte R, Lessard M, Lesur O. Endotoxin-induced heart dysfunction in rats: assessment of myocardial perfusion and permeability and the role of fluid resuscitation. Crit Care Med 2006; 34:127-33.
22. Van Opdenbosch N, Lamkanfi M. Caspases in cell death, inflammation, and disease. Immunity 2019; 50:1352-64.

MicroRNA-1274a serves as a prognostic biomarker in patients with osteosarcoma and is involved in tumor progression via targeting ADAM9

XT. Feng[1], C. Wang[1], FJ. Zhang[2] and XQ. Wu[3] and Z. Zhang[2]

[1]Department of Joint Orthopaedics, Weifang Traditional Chinese Hospital, Weifang, Shandong, China; [2]Department of Joint Surgery, Weifang People's Hospital, Weifang, Shandong, China; [3]School of Public Health, Weifang Medical University, Weifang, Shandong, China

Received November 26, 2020 – Accepted January 28, 2021

Osteosarcoma (OS) is the most frequent primary malignancy in bone, and commonly occurs in children and adolescents. The aim of this study was to assess the aberrant expression of miR-1274a in OS patients, and to evaluate the role of miR-1274a as a prognostic biomarker and tumor suppressor in OS progression. miR-1274a expression was estimated using quantitative real-time polymerase chain reaction. The Kaplan-Meier method and Cox regression analysis were used to evaluate the prognostic value of miR-1274a in OS. Gain- and loss-of-function *in vitro* experiments were used to explore the functional role of miR-1274a in OS progression. A target gene of miR-1274a was analyzed using a dual-luciferase reporter assay. miR-1274a expression was decreased in OS tissues and associated with distant metastasis and clinical stages in OS patients. Low miR-1274a could predict poor overall survival and disease-free survival in OS. The overexpression of miR-1274a could inhibit OS cell proliferation, migration and invasion. Additionally, ADAM9 was demonstrated to serve as a direct target of miR-1274a in OS cells. In conclusion, reduced miR-1274a predicts poor prognosis and serves as a potential tumor suppressor in OS. ADAM9 is a target of miR-1274a, which may mediate the functional role of miR-1274a in OS progression.

Osteosarcoma (OS) is the most common primary malignancy in bone with a high degree of malignancy, and frequently occurs in children and adolescents (1). OS accounts for approximately 0.2% of the total incidence of human malignant solid tumors (2). The onset age is between 15 and 20 years, and males are more common than females (3). The most common site of OS is the dry and scaly end of the long tubular bone, the distal end of the femur and the proximal end of the tibia, followed by the proximal end of the humerus and fibula (4). Although the prognosis of patients with non-metastatic OS has been significantly improved by using surgical and neoadjuvant chemotherapy regimens in recent years, about one-third of the patients still have local recurrence and metastasis, contributing to poor prognosis (5). In addition, OS is very prone to local and distal metastasis after clinical treatment, which leads to lung micro-metastasis in most patients (6). In recent years, in addition to traditional anti-tumor treatment, gene targeted therapy has become a hot spot in research (7). However, the specific mechanisms involved in OS

Key words: MicroRNA-1274a; prognosis; proliferation; migration; osteosarcoma; ADAM9

Corresponding Author:
Dr Zhen Zhang,
Department of Joint Surgery,
Weifang People's Hospital,
No. 151, Guangwen Street,
Weifang, 261000, Shandong, China
Tel./Fax: 86-0536-8675736
e-mail: zhangzhen385@163.com

0393-974X (2021)
Copyright © by BIOLIFE, s.a.s.
This publication and/or article is for individual use only and may not be further reproduced without written permission from the copyright holder.
Unauthorized reproduction may result in financial and other penalties
DISCLOSURE: ALL AUTHORS REPORT NO CONFLICTS OF INTEREST RELEVANT TO THIS ARTICLE.

pathogenesis remain elusive. Thus, seeking effective therapeutic targets for the treatment of OS becomes a major problem to be urgently resolved.

MicroRNAs (miRNAs) are small non-coding RNAs with 21-25 nucleotides in length, which have been reported to be involved in a variety of key biological processes, including cell development, differentiation, cell apoptosis, and proliferation (8). The important functional roles of miRNAs are exerted by regulating various genes that generally serve pivotal roles in different pathological processes, by directly binding to the 3'-terminal untranslated region (3'-UTR) of target mRNAs (9). A large number of miRNAs exist in the human genome, and thousands of human protein-coding genes are co-regulated by miRNAs (10). In human malignancies, numerous miRNAs have been reported to be closely correlated with tumor development and progression (11). There are also some miRNAs involved in OS pathogenesis, such as miR-486 (12) and miR-124 (13). Studies in the related field have indicated that the expression of miRNA-1274a can be detected in OS samples, and miRNA-1274a may be correlated with the cell activity of OS (14). The deregulated expression of miR-1274a and its critical role have been reported in gastric cancer (15) and prostate cancer (16). However, the clinical significance and precise biological function of miR-1274a remain unclear in OS.

Therefore, this study takes miRNA-1274a as the research entry point, combined with the analyses of clinical and experimental data, to explore the prognostic value of miR-1274a, as well as its regulatory effects on tumor cell proliferation, migration and invasion in OS. In addition, a potential target gene of miR-1274a was predicted and analyzed, which may help to preliminarily understand the molecular mechanisms involved in the biological function of miR-1274a in OS progression. The results of this study may provide evidence for miRNA-1274a as a potential biomarker and therapeutic target for the treatment of OS.

MATERIALS AND METHODS

Patients and tissue collection

A total of 124 patients with OS who underwent surgical resection in Weifang Traditional Chinese Hospital were collected between 2010 and 2014. All patients were pathologically diagnosed with OS and did not receive any treatment in advance. Exclusion criteria were as follows: i) cases of systemic infection; ii) cases of other malignant tumors. During surgery, cancerous tissues and adjacent non-cancerous tissues of each patient were collected and cryopreserved with liquid nitrogen at -80°C. The demographic and clinicopathological characteristics of the patients, including gender, age, tumor size, differentiation, distant metastasis and clinical stage, were recorded and are listed in Table I. All patients had complete electronic medical record information. The experimental procedure of this study was approved by the Ethics Committee of Weifang Traditional Chinese Hospital, and each patient was required to sign a written informed consent. A follow-up was conducted for 5 years, and disease progression status and survival information were recorded.

Cell culture and transfection

Four OS cell lines SaOS2, MG63, U2OS, SW1353 and a normal cell line hFOB1.19 were purchased from the Shanghai Cell Bank of Chinese Academy of Science (Shanghai, China). The cells were cultured in RPMI-1640 medium and kept at 37°C in a humidified incubator containing 5% CO_2. After cells proliferated to a sufficient number, Lipofectamine™ 2000 (Invitrogen, MA, USA) was used for cell transfection with miRNA-1274a mimic (5'-GUCCCUGUUCAGGCGCCA-3'), miRNA-1274a inhibitor (5'-UGGCGCCUGAACAGGGAC-3') and their corresponding negative controls (mimic NC: 5'-UUCUCCGAACGUGUCACGU-3' and inhibitor NC: 5'-CAGUACUUUUGUGUAGUACAA-3') according to the manufacturer's protocol. The transfection vectors were synthesized from GenePharma (Shanghai, China). The subsequent cell experiments were carried out at 48 h post-transfection.

RNA extraction and quantitative Real-time PCR (qRT-PCR)

Total RNA was extracted from the obtained tissues and cells by TRIzol reagent (Invitrogen) according to the manufacturer's instructions. The collected RNA was quantified by NanoDrop 2000 (Thermo Fisher Scientific), then was reverse transcribed into cDNA using a Taqman MicroRNA Reverse Transcription Kit (Applied Biosystems, CA, USA) following the manufacturer's protocols. miR-1274a expression was examined using qRT-PCR, which was carried out using the SYBR Green I PCR Core

Reagent (Applied Biosystems, Foster City, CA) on an 7500 Real-Time PCR system (Applied Biosystems). U6 was used as an internal control, and the final expression data of miR-1274a were calculated using the $2^{-\Delta\Delta Ct}$ method. The sequences of primers were as follows: miR-1274a forward 5'-GCCGAGGTCCCTGTTCAGG-3', miR-1274a reverse 5'-CTCAACTGGTGTCGTGGA-3'; U6 forward 5'-CTCGCTTCGGCAGCACA-3', U6 reverse 5'-AACGCTTCACGAATTTGCGT-3'.

Cell proliferation assay

After 48 h of transfection, the cells were grown in complete medium in 96-well plates with 5×10^3 cells/well. Each well was added to 20 μL MTT (Sigma-Aldrich, MO, USA) after incubation for 24, 48 and 72 h, and was further cultured for 4 h at 37°C. The medium was then removed, and 150 μL of dimethyl sulfoxide (DMSO) was added to the wells to dissolve the formazan. Finally, the absorbance at 490 nm was detected to evaluate the cell proliferation by a microplate reader (Bio-Rad, model 550, Philadelphia, PA, USA).

Cell migration and invasion assay

The Transwell system with 8 μm pore size (Coring, USA) was used to analyze the migration and invasion abilities of OS cells. The system was divided into two types: one without Matrigel precoating (for migration assay) and another one with Matrigel coating (for invasion assay). The same composition in the upper and lower chambers was RPMI-1640 medium, and the difference was that the lower chamber was filled with 10% FBS and the upper lumen was serum-free RPMI-1640. Tumor cells were inoculated into the upper chambers. After 48 h of incubation at 37°C, the cells in the lower chambers were fixed with 4% paraformaldehyde for 10 min and stained with 0.1% crystal violet for 20 min at room temperature. The cells in the lower chamber were counted with an inverted microscope. The experiments were repeated at least three times.

Dual-luciferase reporter assay

The target genes of miR-1274a were predicted using the miRanda (http://www.microrna.org/microrna/home.do), and ADAM9 was found to have a binding site of miR-1274a.

Table I. *Association of miR-1274a expression and the clinical characteristics of OS patients*

Features	Total No. n = 124	miR-1274a expression		*P* values
		Low (n = 65)	High (n = 59)	
Age (years)				
≤ 20	61	31	30	0.726
> 20	63	34	29	
Gender				
Female	58	30	28	0.884
Male	66	35	31	
Tumor size (cm)				
≤ 8	61	27	34	0.074
> 8	63	38	25	
differentiation				
Well/moderate	74	35	39	0.165
Poor	50	30	20	
Distant metastasis				
Negative	76	32	44	0.004
Positive	48	33	15	
Clinical stage				
IA-IIA	69	29	40	0.009
IIB-III	55	36	19	

The 3'-UTR of ADAM9 containing the wild-type (WT) and mutant type (MUT) putative binding site of miR-1274a was cloned into the pmirGLO dual-luciferase reporter vector (Promega, WI, USA). The SaOS2 and U2OS cells were co-transfected with the combined vectors and miR-1274a mimic, miR-1274a inhibitor or the NCs by the Lipofectamine™ 2000 (Invitrogen, MA, USA). At 48 post-transfection, the relative luciferase activity was determined using the Dual-Luciferase Reporter Assay System (Promega, WI, USA) according to the instructions of the manufacturer.

Statistical analysis

All data were presented as mean ± SD, and all statistical analyses were performed using SPSS 21.0 software (SPSS, Inc., Chicago, USA) and GraphPad Prism 7.0 software (Inc., Chicago, USA). The data of two group or multiple groups were compared using Student's *t*-test or one-way ANOVA followed by Tukey's test. The relationship between miR-1274a expression and clinicopathological data was analyzed using *Chi*-squared test. Survival analysis was performed using Kaplan-Meier methods and log-rank test. Prognostic value of miR-1274a was confirmed by Cox regression analysis. Differences with $P < 0.05$ were considered statistically significant.

RESULTS

Downregulation of miR-1274a in OS tissues and cell lines

According to the results of qRT-PCR, miR-1274a expression was significantly downregulated in OS tissues compared with the normal controls ($P < 0.001$, Fig. 1A). In addition, the expression of miR-1274a in patients with different clinical stages was further compared. As shown in Fig. 1B, the OS patients with IIB-III clinical stages had significantly lower expression of miR-1274a than that in the cases with IA-IIA clinical stages ($P < 0.001$). In the four OS cell lines, the expression of miR-1274a was also decreased when compared to the expression data in the normal cells (all $P < 0.001$, Fig. 1C).

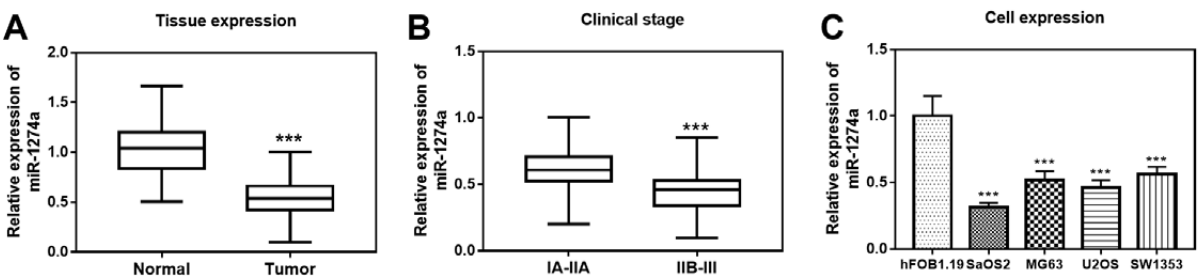

Fig. 1. *Expression of miR-1274a in OS tissues and cell lines.* ***A****) The expression of miR-1274a was downregulated in OS tissues compared with the normal controls.* ***B****) OS patients with IIB-III clinical stage had lower miR-1274a expression than the cases with IA-IIA stage.* ***C****) Lower expression level of miR-1274a was founded in four OS cell lines compared with the normal cells. ***P < 0.001.*

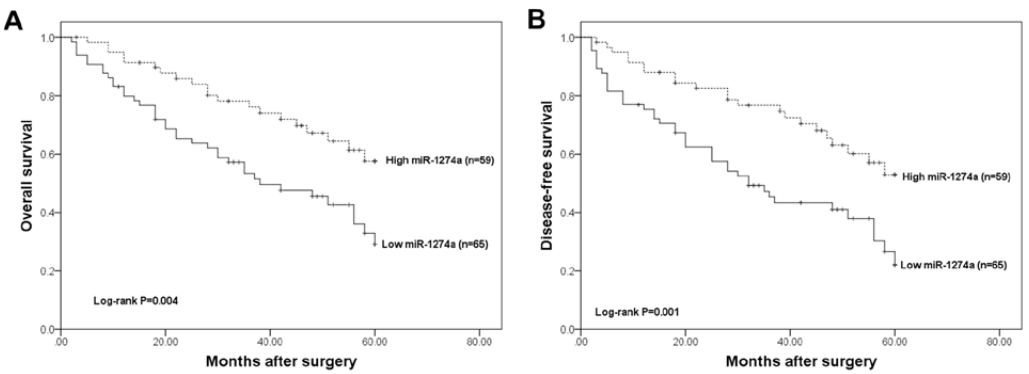

Fig. 2. *Kaplan-Meier survival curves in the patients with OS.* ***A****) The overall survival time of patients with low miR-1274a expression was shorter than those patients with high miR-1274a expression. (log-Rank P = 0.004).* ***B****) OS patients with low miR-1274a expression had poor disease-free survival compared with those with high miR-1274a (log-rank P = 0.001).*

Association of miR-1274a expression with the clinicopathological characteristics of OS patients

The relationship between miR-1274a expression and OS patients' clinical data was examined to discover the role of miR-1274a in the development of OS. The expression of miR-1274a was firstly divided into low (n = 65) and high (n = 59) expression groups based on the median value. From the data in Table I, the expression of miR-1274a was found to be associated with distant metastasis ($P = 0.004$) and clinical stage ($P = 0.009$), whereas no significant relationship was found between miR-1274a and age, gender, tumor size or differentiation (all $P > 0.05$).

Clinical significance of miR-1274a in the prognosis of OS

This study recorded and analyzed the disease progression status and survival information after surgery in OS patients, and the association of miR-1274a expression with overall survival and disease-free survival was evaluated. The Kaplan-Meier survival curves (Fig. 2) indicated that patients with low expression levels of miR-1274a had clearly shorter overall survival time than those with high expression levels of miR-1274a (log-rank $P = 0.004$). Moreover, the association of low miR-1274a with poor disease-free survival was also demonstrated in OS patients (log-rank $P = 0.001$, Fig. 2B). Furthermore, the multivariate Cox analysis was conducted to confirm the prognostic value of miR-1274a. The data listed in Table II show that miR-1274a was independently associated with the overall survival and disease-free survival of OS patients (overall survival: HR = 3.301, 95%CI = 1.863-5.847, $P = 0.001$; disease-free survival: HR =

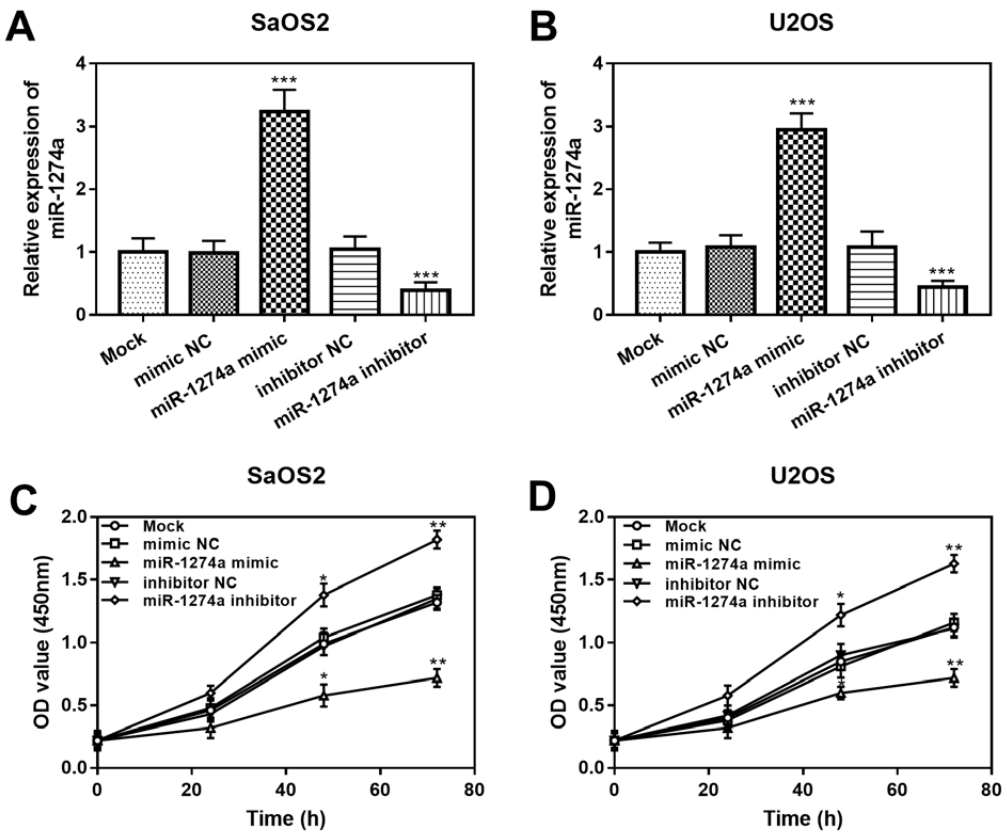

Fig. 3. *Effect of miR-1274a on proliferation of SaOS2 and U2OS cells. The expression of miR-1274a in (**A**) SaOS2 and (**B**) U2OS cells was significantly higher following transfection with miR-1274a mimic and significantly lower following transfection with miR-1274a inhibitor compared with untreated cells. The proliferation of (**C**) SaOS2 and (**D**) U2OS cells was inhibited when the expression of miR-1274a was increased, and was enhanced when the expression of miR-1274a was decreased. *P < 0.05, **P < 0.01, ***P < 0.001.*

3.587, 95%CI = 1.925-6.532, $P < 0.001$). In addition, distant metastasis and clinical stage of OS patients were also independently associated with overall survival and disease-free survival (all $P < 0.05$).

miR-1274a overexpression inhibits OS cell proliferation, migration and invasion

Considering the potential role of miR-1274a demonstrated in OS patients, gain- and loss-of-functional analyses were performed to examine the functional role of miR-1274a in OS progression. According to cell transfection, the expression of miR-1274a was successfully upregulated by the miR-1274a mimic and downregulated by the miR-1274a inhibitor (all $P < 0.001$, Fig. 3 A, B). Cell proliferation assay was carried out by the MTT method, and found that the high

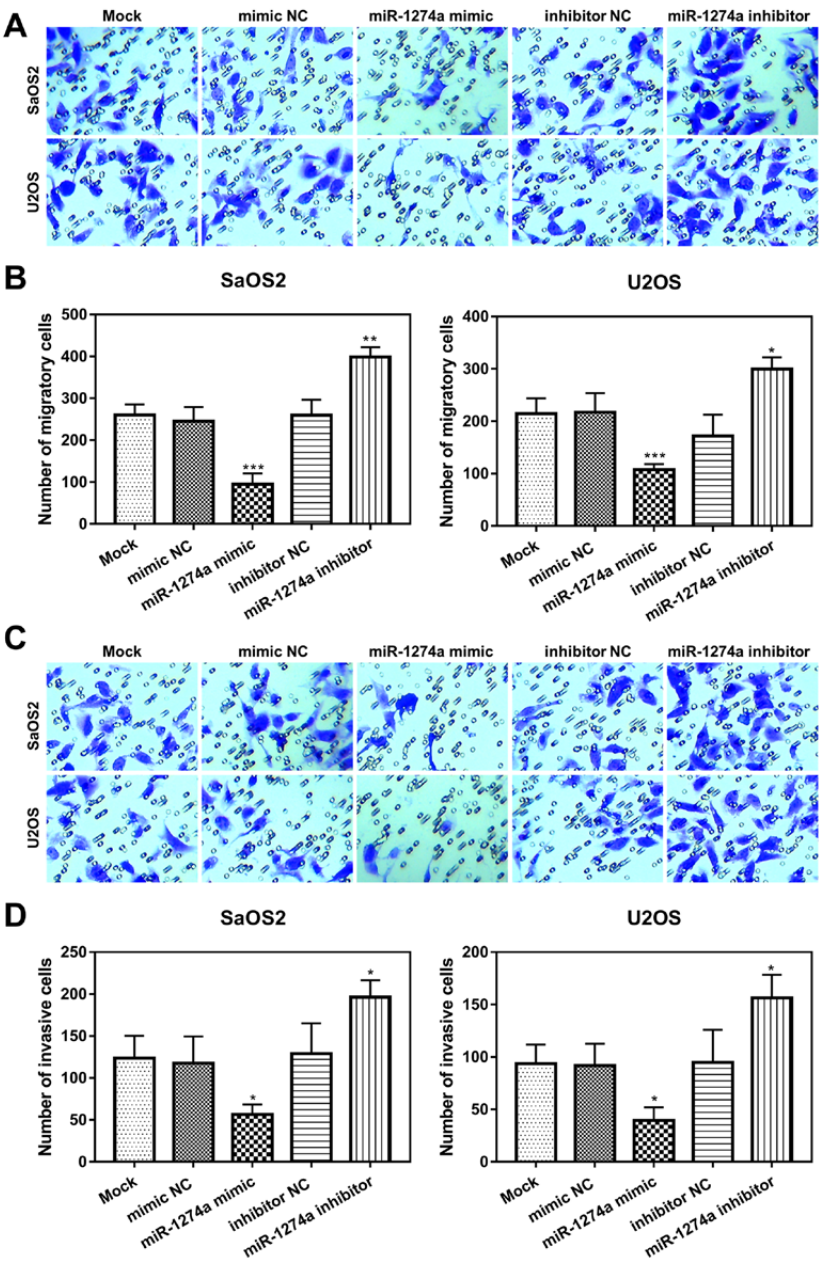

Fig. 4. *Effect of miR-1274a on the migration and invasion of SaOS2 and U2OS cells.* ***A, B****) The migration of SaOS2 and U2OS cells was inhibited by the upregulation of miR-1274a, but was enhanced by downregulation of miR-1274a.* ***C, D****) miR-1274a overexpression inhibited, whereas miR-1274a downregulation promoted the invasion of SaOS2 and U2OS cells. All experiments were repeated three times. *P < 0.05, **P < 0.01, ***P < 0.001.*

expression of miR-1274a inhibited the proliferation of SaOS2 and U2OS cells, but the low expression of miR-1274a promoted the proliferation of SaOS2 and U2OS cells (all $P < 0.05$, Fig. 3 C, D). From the results of Transwell analysis, OS cell migration and invasion were inhibited by the overexpression of miR-1274a, but was enhanced by the downregulation of miR-1274a in both SaOS2 and U2OS cells (all $P < 0.05$, Fig. 4).

ADAM9 is a direct target of miR-1274a in OS cells

According to the *in silico* prediction, a putative binding site of miR-1274a was found at the 3'-

Table II *Multivariate Cox analysis for miR-1274a in OS patients*

Variables	Overall survival			Disease-free survival		
	HR	95% CI	*P* value	HR	95% CI	*P* value
miR-1274a	3.301	1.863-5.847	0.001	3.587	1.925-6.532	< 0.001
Age	1.555	0.906-2.668	0.109	1.574	0.913-2.751	0.152
Gender	1.519	0.880-2.622	0.134	1.524	0.910-2.712	0.146
Tumor size	1.553	0.897-2.622	0.116	1.529	0.832-2.510	0.112
Differentiation	1.500	0.865-2.599	0.149	1.681	0.869-2.646	0.158
Distant metastasis	2.089	1.070-4.080	0.031	2.225	1.215-4.421	0.024
Clinical stage	1.982	1.067-3.680	0.030	2.123	1.099-3.817	0.028

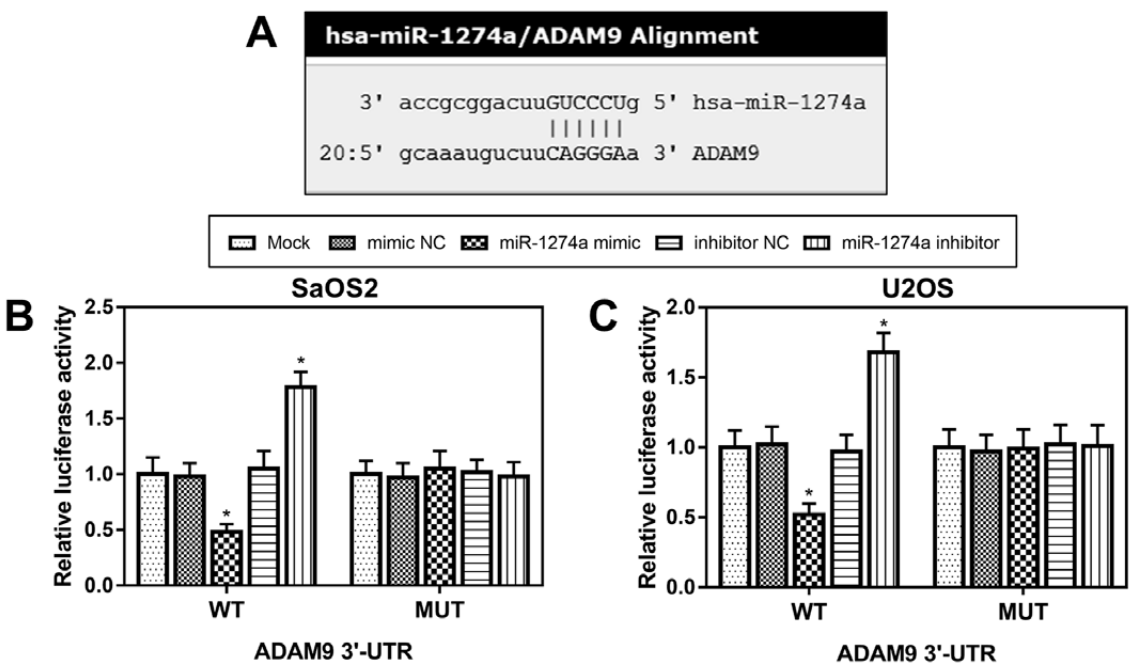

Fig. 5. *ADAM9 serves as a target gene of miR-1274a in OS cells.* ***A****) The putative binding site of miR-1274a at the 3'-UTR of ADAM9.* ***B, C****) The results of dual-luciferase reporter assay in SaOS2 and U2OS cell lines. *P < 0.05.*

UTR of ADAM9 (Fig. 5A). The subsequent dual-luciferase reporter assay results shown in Fig. 5 B, C revealed that the relative luciferase activity of SaOS2 and U2OS cells with WT 3'-UTR of ADAM9 was significantly inhibited by miR-1274a overexpression, but was increased by the knockdown of miR-1274a (all $P < 0.05$), while no significant luciferase activity changes were observed in the MUT group ($P > 0.05$).

DISCUSSION

MiRNAs play key roles in the regulation of various biological processes, such as cell differentiation, proliferation, apoptosis and stress (17). In addition, they are involved in the pathogenesis of many diseases, including tumors (18). The discovery of miRNAs has led to a global search for their roles in tumors. Currently, a consensus has been reached that miRNA plays a very important role in the occurrence, development, proliferation, apoptosis, invasion, metastasis and drug resistance of tumors (19). In 2002, with the study of the role of miR-15 and miR-16 in chronic lymphoma, the important roles of miRNAs in tumorigenesis and progression were gradually revealed (20). Further experiments showed that miR-15 and miR-16 negatively affected chronic lymphoma by targeting an oncogene BCL2 (21). In contrast, miR-21 is highly expressed as a very typical oncogene in many tumors, such as breast cancer. Its overexpression *in vivo* can lead to tumor growth, proliferation and repair (22). All these studies indicate that miRNAs can be used as novel targets for targeted cancer therapy.

With advances in medicine, especially in the molecular field, tumors have been given the opportunity for personalized treatment. Globally, more than 2,000 genes are being tested and explored for personalized therapies for a variety of diseases, but only one of them is miRNA therapy (23). Song et al. found that miRNA-215 played a role in the development of drug resistance to OS (24). However, miR-21 was closely related with the apoptosis, proliferation and metastasis of tumor cells. MiR-199a-3p was negatively correlated with the proliferation of tumor cells (25). These experiments proved that miRNAs play regulatory roles in the proliferation, apoptosis and metastasis of OS cells.

A growing body of evidence suggest that miRNAs play important roles in the development of OS by regulating the biological functions of OS cells. For example, the overexpression of miR-24 significantly enhanced NSCLC cell migration and invasion by inhibiting ZNF367 (26). miR-451a inhibited the migration and invasion of NSCLC cells by accelerating AFT2 (27). miR-135a inhibits the proliferation, migration, and invasion of NSCLC cells by targeting the igf-1 gene (28). miR-185 inhibited the proliferation, migration and invasion of NSCLC cells by targeting KLF7 (29). A study in the field of OS indicated that the expression of miR-1274a could be detected in OS samples, and miRNA-1274a might be correlated with the cell activity of OS (14). The present study found that the expression level of miR-1274a in OS tissues and cell lines was down-regulated, which led to further explore the relationship between miR-1274a and OS. The relationship analysis data showed the association between miR-1274a and distant metastasis and clinical stage of OS patients, and the expression of miR-1274a was found to be significantly decreased in OS cases with advanced clinical stage. Thus, it was considered that miR-1274a may be involved in the development of OS. Distant metastasis frequently occurs in OS patients, leading to the increased mortality, and the lung is the most common metastatic site (30). This study found the significant relationship between low miR-1274a expression with positive distant metastasis in OS patients, which further suggested the role of miR-1274a with the aggressiveness of OS.

The clinical value of miR-1274a dysregulation has been documented in human cancers. For example, the aberrant expression of miR-1274a in prostate cancer patients has been proposed as a biomarker to distinguish cancer patients from healthy controls (16). By analyzing the 5-year follow-up information in OS patients, this study also discussed the prognostic value of miR-1274a. The Kaplan-Meier survival curves plotted in this work showed that patients with low miR-1274a expression had shorter overall survival time and poorer disease-free survival than those with high miR-1274a expression.

The multivariate Cox regression data demonstrated that the expression of miR-1274a was an independent prognostic factor to predict OS overall survival and disease-free survival. In conclusion, the decreased expression of miR-1274a may predict a poor prognosis of OS.

The functional role of miR-1274a has been investigated in several human cancers. Wang et al. provided evidence for miR-1274a as an oncogene to facilitate gastric cancer cell proliferation and migration via targeting FOXO4 (15). The decreased miR-1274a in clear cell renal cell carcinoma cells led to enhanced cell apoptosis through inhibiting BMPR1B (31). In the current study, OS cell proliferation, migration and invasion abilities were all inhibited by the overexpression of miR-1274a, while were enhanced by the reduction of miR-1274a, which implied that miR-1274a might serve as a tumor suppressor in OS progression. Furthermore, a putative binding site of miR-1274a was predicted at the 3'-UTR of ADAM9, and we demonstrated that ADAM9 might be a direct target gene of miR-1274a in OS cells. ADAM9 has been reported to function as an oncogene, which can mediate the regulatory effects of miR-302a and miR-126 on OS cell proliferation, migration and invasion (32, 33). Consequently, we deduced that miR-1274a might inhibit OS progression by targeting ADAM9. These hypotheses need to be confirmed in further studies. In addition, A previous study by Zhou et al. documented that miR-1274a was involved in the anti-tumor therapy of sorafenib in hepatocellular carcinoma by targeting ADAM9 (34). Given the dysregulation of miR-1274a in OS progression and its relationship with ADAM9, we suspected that miR-1274a might also be correlated with the anti-tumor effects of sorafenib in OS, which warrants further investigations.

In summary, this study indicated that the expression level of miR-1274a is reduced in OS tissues, and serves as an independent prognostic biomarker of OS. The upregulation of miR-1274a could suppress OS cell proliferation, migration and invasion, which demonstrates that miR-1274a may function as a tumor suppressor in OS progression. All the findings of this study provide a potential novel biomarker and therapeutic target for the treatment of OS. However, the biological function and potential target of miR-1274a were only examined by *in vitro* experiments, further studies are needed to confirm our findings using *in vivo* investigations.

REFERENCES

1. Bishop MW, Janeway KA, Gorlick R. Future directions in the treatment of osteosarcoma. Curr Opin Pediatr 2016; 28:26-33.
2. Vineis P, Wild CP. Global cancer patterns: causes and prevention. Lancet 2014; 383:549-57.
3. Kansara M, Teng MW, Smyth MJ, Thomas DM. Translational biology of osteosarcoma. Nat Rev Cancer 2014; 14:722-35.
4. Park HJ, Bae JS, Kim KM, et al. The PARP inhibitor olaparib potentiates the effect of the DNA damaging agent doxorubicin in osteosarcoma. J Exp Clin Cancer Res 2018; 37:107.
5. Spraker-Perlman HL, Barkauskas DA, Krailo MD, et al. Factors influencing survival after recurrence in osteosarcoma: A report from the Children's Oncology Group. Pediatr Blood Cancer 2019; 66:e27444.
6. Zhang Y, Zvi YS, Batko B, et al. Down-regulation of Skp2 expression inhibits invasion and lung metastasis in osteosarcoma. Sci Rep 2018; 8:14294.
7. Jiao GJ, Zhang SJ, Li Y, Wu WL, Liu HC. MicroRNA-645 promotes metastasis of osteosarcoma via targeting tumor suppressor NM23 nucleoside diphosphate kinase 2. Clin Exp Pharmacol Physiol 2018; 45:1317-24.
8. Garofalo M, Leva GD, Croce CM. MicroRNAs as anti-cancer therapy. Curr Pharm Des 2014; 20:5328-35.
9. Zhang P, Hou Q, Yue Q. MiR-204-5p/TFAP2A feedback loop positively regulates the proliferation, migration, invasion and EMT process in cervical cancer. Cancer Biomark 2020; 28(3):381-390
10. Liu B, Shyr Y, Cai J, Liu Q. Interplay between miRNAs and host genes and their role in cancer. Brief Funct Genomics 2018; 18:255-66.
11. Jerez S, Araya H, Hevia D, Irarrazaval CE, Thaler R, van Wijnen AJ, Galindo M. Extracellular vesicles from osteosarcoma cell lines contain miRNAs associated with cell adhesion and apoptosis. Gene 2019; 710:246-57.

12. Liu Y, Zhang J, Xing C, Wei S, Guo N, Wang Y. miR-486 inhibited osteosarcoma cells invasion and epithelial-mesenchymal transition by targeting PIM1. Cancer Biomark 2018; 23:269-77.
13. Cong C, Wang W, Tian J, Gao T, Zheng W, Zhou C. Identification of serum miR-124 as a biomarker for diagnosis and prognosis in osteosarcoma. Cancer Biomark 2018; 21:449-54.
14. Kobayashi E, Satow R, Ono M, et al. MicroRNA expression and functional profiles of osteosarcoma. Oncology 2014; 86:94-103.
15. Wang GJ, Liu GH, Ye YW, Fu Y, Zhang XF. The role of microRNA-1274a in the tumorigenesis of gastric cancer: accelerating cancer cell proliferation and migration via directly targeting FOXO4. Biochem Biophys Res Commun 2015; 459:629-35.
16. Said R, Garcia-Mayea Y, Trabelsi N, et al. Expression patterns and bioinformatic analysis of miR-1260a and miR-1274a in prostate cancer Tunisian patients. Mol Biol Rep 2018; 45:2345-58.
17. Yu H, Song H, Liu L, et al. MiR-92a modulates proliferation, apoptosis, migration, and invasion of osteosarcoma cell lines by targeting Dickkopf-related protein 3. Biosci Rep 2019; 39.
18. Hayes J, Peruzzi PP, Lawler S. MicroRNAs in cancer: biomarkers, functions and therapy. Trends Mol Med 2014; 20:460-9.
19. Si W, Shen J, Zheng H, Fan W. The role and mechanisms of action of microRNAs in cancer drug resistance. Clin Epigenetics 2019; 11:25.
20. Cimmino A, Calin GA, Fabbri M, et al. miR-15 and miR-16 induce apoptosis by targeting BCL2. Proc Natl Acad Sci U S A 2005; 102:13944-9.
21. Calin GA, Dumitru CD, Shimizu M, et al. Frequent deletions and down-regulation of micro- RNA genes miR15 and miR16 at 13q14 in chronic lymphocytic leukemia. Proc Natl Acad Sci U S A 2002; 99:15524-9.
22. Schetter AJ, Leung SY, Sohn JJ, et al. MicroRNA expression profiles associated with prognosis and therapeutic outcome in colon adenocarcinoma. JAMA 2008; 299:425-36.
23. Yue J. miRNA and vascular cell movement. Adv Drug Deliv Rev 2011; 63:616-22.
24. Song B, Wang Y, Titmus MA, Botchkina G, Formentini A, Kornmann M, Ju J. Molecular mechanism of chemoresistance by miR-215 in osteosarcoma and colon cancer cells. Mol Cancer 2010; 9:96.
25. Duan Z, Choy E, Harmon D, Liu X, Susa M, Mankin H, Hornicek F. MicroRNA-199a-3p is downregulated in human osteosarcoma and regulates cell proliferation and migration. Mol Cancer Ther 2011; 10:1337-45.
26. Liu Z, Jiang L, Zhang G, Li S, Jiang X. MiR-24 promotes migration and invasion of non-small cell lung cancer by targeting ZNF367. J BUON 2018; 23:1413-9.
27. Shen YY, Cui JY, Yuan J, Wang X. MiR-451a suppressed cell migration and invasion in non-small cell lung cancer through targeting ATF2. Eur Rev Med Pharmacol Sci 2018; 22:5554-61.
28. Zhou Y, Li S, Li J, Wang D, Li Q. Effect of microRNA-135a on cell proliferation, migration, invasion, apoptosis and tumor angiogenesis through the IGF-1/PI3K/Akt signaling pathway in non-small cell lung cancer. Cell Physiol Biochem 2017; 42:1431-46.
29. Zhao L, Zhang Y, Liu J, Yin W, Jin D, Wang D, Zhang W. miR-185 Inhibits the Proliferation and Invasion of Non-Small Cell Lung Cancer by Targeting KLF7. Oncol Res 2019; 27:1015-23.
30. Marko TA, Diessner BJ, Spector LG. Prevalence of metastasis at diagnosis of osteosarcoma: an international comparison. pediatr blood cancer 2016; 63:1006-11.
31. Yoshino H, Yonezawa T, Yonemori M, et al. Downregulation of microRNA-1274a induces cell apoptosis through regulation of BMPR1B in clear cell renal cell carcinoma. Oncol Rep 2018; 39:173-81.
32. Yang X, Cui Y, Yang F, Sun C, Gao X. MicroRNA302a suppresses cell proliferation, migration and invasion in osteosarcoma by targeting ADAM9. Mol Med Rep 2017; 16:3565-72.
33. Jiang L, He A, Zhang Q, Tao C. miR-126 inhibits cell growth, invasion, and migration of osteosarcoma cells by downregulating ADAM-9. Tumour Biol 2014; 35:12645-54.
34. Zhou C, Liu J, Li Y, et al. microRNA-1274a, a modulator of sorafenib induced a disintegrin and metalloproteinase 9 (ADAM9) down-regulation in hepatocellular carcinoma. FEBS Lett 2011; 585:1828-34.

Comparative surface detail reproduction for elastomeric impression materials: Study on reproducibility performance

G. Varvara[1], B. Sinjari[1], S. Bernardi[2], I. Turkyilmaz[3], V. Malvezzi[1], M. Piattelli[1] and S. Caputi[1]

[1]Department of Medical, Oral and Biotechnological Sciences, Dental School, 'G. D'Annunzio' University of Chieti–Pescara, Chieti, Italy; [2]Department of Life, Health and Environmental Sciences, University of L'Aquila, L'Aquila, Italy; [3]Department of Prosthodontics, New York University College of Dentistry, New York, NY, USA

Received September 14, 2020 - Accepted October 16, 2020

For dental impression of a prepared tooth, the goal is a void-free negative representation from which an accurate cast of a tooth and its surrounding tissue can be reproduced. This *in-vitro* study assessed and compared the reproduction accuracies of surface detail obtained with three different dental elastomeric impression materials: vinyl polysiloxane (VPS), vinyl polyether silicone (VPES), and polyether (PE). A stainless-steel model with two abutments was used, with impressions taken 10 times for each material, for 20 abutment impressions per group, using a two-phase, one-step technique (heavy body/light body). The impressions were removed and assessed for numbers of enclosed voids and open voids visible on the surface. The defect frequency was 95% for impressions with the VPS and VPES materials, and 30% for the PE material. No significant differences were seen for number of impressions with defects for VPS *versus* VPES. Significant differences were seen for VPS and VPES *versus* the PE material (P <.05). No significant differences were seen for the defect type distributions across these three impression materials. The PE impression material showed better accuracy for reproduction of surface detail of these dental impressions compared to the VPS and VPES impression materials.

The fabrication of well-fitting indirect prosthetic restorations is a complex process where the making of the dental impression is of particular importance. The combination of the impression material and the method is essential for the production of a successful impression, mainly in terms of dimensional accuracy and detail reproduction (1). Although there have been various technical improvements in computer-aided design and manufacturing systems and in three-dimensional imaging procedures with digital impressions (direct intraoral or indirect extraoral), the standard impression processes continue to have an important role for the transfer of information from the clinic to the dental laboratory (2, 3).

In making an impression, the goal is to provide a negative representation of the prepared tooth that is void free, thus providing an accurate cast of both the prepared tooth and its surrounding tissue (4). The ability to reproduce the surface detail in impressions of partially fixed dental prostheses in the dental laboratory has been evaluated in a number of studies. For example, Samet et al. (5) carried out a clinical study where >89% of their impressions had ≥1 visible errors. Indeed, 50.7% of their impressions

Key words: vinyl polysiloxane; vinyl polyether silicone; polyether; impression materials; prosthetics dentistry

Corresponding Author:
Giuseppe Varvara
Department of Medical, Oral and Biotechnological Sciences
University 'G. D'Annunzio' of Chieti–Pescara
Via dei Vestini, 31 - 66100 Chieti (CH), Italy
Tel./Fax: +39 0871 3554070
e-mail: gvarvara@unich.it

0393-974X (2021)
Copyright © by BIOLIFE, s.a.s.
This publication and/or article is for individual use only and may not be further reproduced without written permission from the copyright holder.
Unauthorized reproduction may result in financial and other penalties
DISCLOSURE: ALL AUTHORS REPORT NO CONFLICTS OF INTEREST RELEVANT TO THIS ARTICLE.

showed tears or voids in the finish, while 40.4% showed air bubbles at the margin line, and 26.9% showed both; thus, their recommendation was that dentists are more critical in their evaluation of such impressions. Also, a report by Raigrodski et al. (6) indicated that small defects, including tears, voids, and bubbles, were present in the preparation areas of 92-96% of their control impressions, following analysis by a clinician and a dental technician.

A number of factors can have an influence on the quality and accuracy of impressions, with the most important being the mechanical properties of the elastomeric impression material (6) and the technique (7). Some studies indicated previously that the more recent improvements in the mechanical properties of elastomeric impression materials that are now available mean that the reproduction quality for surface detail is more affected by the technique used than by the impression material (4, 7-9). However, further studies have shown that the impression technique has no significant effects on the reproduction quality for surface detail of dental impressions (10-12). Thus, despite various previous studies on the quality and accuracy of impressions in terms of the importance of the materials and/or techniques used, controversy remains. These contradictory data in the literature can potentially be explained by the types of elastomeric impression materials and their related mechanical properties, along with the various protocols used to determine the quality and accuracy of impressions.

A number of impression materials are commercially available. Vinyl polysiloxane (VPS) and polyether (PE) are two impression materials that are widely used for indirect restoration in restorative dentistry, such as for inlays, onlays, veneers, fixed dental protheses, and implant-supported restorations. Previous studies have indicated the accuracy and dimensional stability of VPS and PE (13-17).

As a hydrophobic material, the correct control of moisture with VPS is of great importance for clinically acceptable impressions to be obtained, with the need to avoid the formation of voids at the margins of the tooth preparation surfaces in the impression, and thence of bubbles in gypsum casts. However, this hydrophobicity might affect the initial efficiency obtained with the impression material soon after mixing, in terms of the wet environment and its penetration into narrow spaces (14). The latest generation of VPS impression materials used clinically are known as hydrophilic or hydrophilized VPS, where there is the addition of extrinsic surfactant material. In being described as hydrophilic, this suggests that they should perform adequately when used under moist or wet conditions, by providing enhanced precision during complex clinical procedures, and thus minimizing potential clinical problems caused by voids and bubbles, and by pulls and tears (17). This enhanced hydrophilicity should improve the accuracy of impressions, as it should provide improved flow and finer detail for impressions of the moist dentinal surfaces, and also around the gingival sulcus (13). Thus, the addition of these surfactants should facilitate the making of improved impressions with better surface qualities (18), which should provide fewer defects and thus improve the stone dies (6). Furthermore, the changes to the rheological and flow characteristics of these newer hydrophilized VPS impression materials have been reported to improve their handling and adaptation to both soft and hard tissues (17).

Polyether is a hydrophilic material, composed of a relatively low molecular weight polyether, with a silica filler, and a plasticizer, which also indicates its use in moist environments. The wetting properties of PE are good, and thus gypsum casts are easier to make (18). Dimensional stability and wettability represent the most important features of such PE materials, which should result in reduced numbers of voids and more detailed reproduction of intraoral structures. On the other hand, removal of impression materials made of PE from the mouth can be difficult, and this also comes with increased risk of die breakage and might be associated with the greater rigidity of such PE materials compared to VPS (19). Of note, the newer PE impression materials have been reported to be more flexible than the previously used products, which should make it easier to remove them from the mouth (18).

A relatively new class of impression materials has also become commercially available recently: a vinyl polyether silicone (VPES; also classified as

a vinyl siloxane ether or vinyl polyether siloxane) (1, 20). This was developed by combining the PE polymers and vinyl groups of VPS. It has been indicated by the manufacturer that this VPES has good mechanical properties, which includes high elastic recovery and high tear and tensile strength, along with good dimensional accuracy and flow properties. These are combined with particularly good wetting characteristics when applied to a prepared tooth under unset conditions, and also when under set conditions (1). VPES should thus combine the ease of removal of VPS and the hydrophilicity (i.e., the wetting properties) of PE, which should make it a promising material for use in complex situations where moisture control is an issue. This applies particularly to narrow, deep gingival crevices (21), where the excellent flowability through its thermosensitive rheology system allows this material to get into narrow sulcus crevices without losing its high stability (21). The accuracy of this new VPES impression material has not been established, and there are few data in the literature relating to its use (1, 18-22).

The aim of this *in-vitro* study was to examine the reproduction of surface detail of these impression materials according to their different mechanical properties, specifically through the comparison of this relatively new VPES with both the VPS and PE impression materials. The study was designed to analyze the visible defects on the surface of impressions obtained using the conventional two-phase (heavy/light body impression material), one-step impression technique. The null hypothesis here indicated that no differences would be seen for reproduction of defect-free surface detail of impressions made using these three materials despite their different mechanical properties.

MATERIALS AND METHODS

For this evaluation of the production of defect-free surface detail, impressions were made with stainless-steel abutments using stock metal trays and the three different materials with different mechanical properties. These were then examined for open voids and enclosed voids. The master model comprised a stainless-steel die with two shouldered complete-crowns, with a tapered abutment, which was constructed using a lathe, as described previously (4, 7). Each abutment had a base diameter of 12 mm, a height from the shoulder margin of 8 mm, a shoulder width of 3 mm (and thus a diameter at the shoulder margin of 6 mm), and a taper of 6 degrees; the centers of the two abutments were separated by 20 mm (Fig. 1). This standardized master model was used for comparison of the defects associated with the three impression materials used in this study. This master model was positioned manually in an autopolymerizing acrylic resin (Orthojet, Ravelli, Italy). This acrylic resin device containing the master model was then prepared for the reproducible positioning of the tray. The impressions were all made using stock metal trays (size 6; ASA Dental). For 20 experimental impressions for each of the investigated impression materials, 10 impressions of the master model (each with two abutment impressions) were made, using: VPS (Aquasil Ultra; Dentsplay International, Milford, DE); VPES (Exa'lence; GC Corporation, Tokyo, Japan); and PE (Impregum Penta Super Quick; 3M Deutschland GmbH, Neuss, Germany). All of the impressions were made using a two-phase, one-step technique with the impression materials (heavy-body and light-body) applied simultaneously, using a perforated stock metal tray for VPS and VPES, and a non-perforated stock metal tray for PE. For PE, adhesive (Polyether Adhesive; 3M Deutschland GmbH, Germany) was applied to the non-perforated stock metal tray (for 15 min), following the manufacture's instructions, for good bond strength between the PE and the metal tray. The impressions were made using the VPS, VPES and PE impression materials as detailed in Table I, with all of the impressions made by the same operator. An automatic mixing device was used to dispense the heavy-body material (Pentamix 3, 3M Deutschland GmbH, Germany), with a dispensing gun used for the light-body material (Automix; Dentsply International), along with the corresponding tips. The heavy-body mixed material was loaded into the impression tray and the light-body material was syringed around the prepared abutments and above the heavy-body material previously loaded into the impression tray. The impression tray was positioned by hand until its periphery touched the acrylic resin; it was then maintained in this position using hand pressure. As the impressions were made at room temperature (20°C) rather than mouth temperature, the polymerization times

Fig. 1. *The stainless-steel die containing 2 complete-crown, tapered abutment preparations abutments that provided the standardized master model to compare the defects associated with each of the elastomeric impression materials (base diameter of 12 mm; height from the shoulder margin of 8 mm; shoulder width of 3 mm; taper of 6 degrees; distance between the centers of the abutments of 20 mm).*

for each impression material were twice those defined by the manufacturer. The setting times used were thus 12, 14, and 8 minu for VPS, VPES and PE, respectively. After removal of the impressions, assessment of the surfaces of the abutment impressions was carried out by an examiner who had been trained in a standardized technique to recognize and classify any surface defects. For all of the surfaces of the abutment impressions, the examiner examined and counted any "bubble-like" enclosed voids (<2 mm) and any open voids (~2-4 mm) that it was possible to see with the naked eye using a working distance of ~150 mm. All of the impressions were also photographed (digital camera: Fine Pix S2pro; Fuji; AF Micro Nikkor (105 mm, 1:2.8D); Nikon). The examiner included only the defects in the impressions in and around the prepared abutments in this assessment. Clinically, precise detail registration during impression of the margin design and finish line of prepared tooth is an important factor that affects the survival of the restoration (Fig. 2). The abutment impressions were each ranked according to the number of defects: type #0, absence of defects (e.g., Fig. 3); type #1, 1 or 2 enclosed voids (e.g., Fig. 4); type #2, >2 enclosed voids (e.g., Fig. 4); and type #3, open voids seen (e.g., Fig. 5).

To evaluate the differences between the frequencies of defects across the experimental groups, the non-parametric data were analyzed using Fisher's exact tests

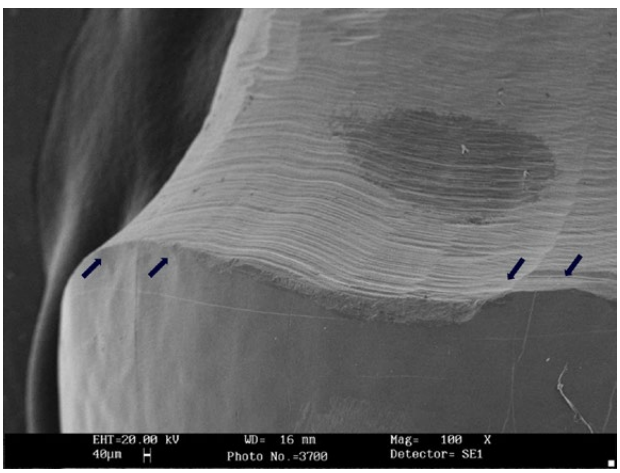

Fig. 2. *Representative image (X100) under scanning electron microscopy (Evo 50; Carl Zeiss, Oberkochen, Germany) of a prepared tooth with a chamfer margin design. It appears clear a sharp and defined finish line (arrows) on enamel. The margin was prepared by a diamond rotary cutting bur (#198 018; Komet, Lemgo, Switzerland) with an air turbine (SP 405; Faro SpA, Ornago, Italy) at 300,000 rpm.*

Table I. *Technical characteristics of the impression materials used. ISO, International Organization for Standardization (https://www.iso.org/standard/60586.html)*

Impression material	Body type	ISO 4823 type	Consistency	Lot N°	Proprietary name	Supplier
Vinyl polysiloxane	Heavy Light	2 3	Medium Light	00006234 170131	Aquasil Ultra	Dentsplay International, Milford, DE, USA
Vinyl Polyether silicone	Heavy Light	1 3	Heavy Light	1809071 1808271	Exa'lence	GC Corporation,Tokyo, Japan
Polyether	Heavy Light	1 3	Heavy Light	44058269 4405295	Impregum Penta Super Quick	3M Deutschland GmbH, Neuss, Germany

on contingency tables. The medians were obtained for each experimental group. To explore significance among the types of defects in the three impression materials, ANOVA tests were performed. The results obtained were considered significant for P <.05.

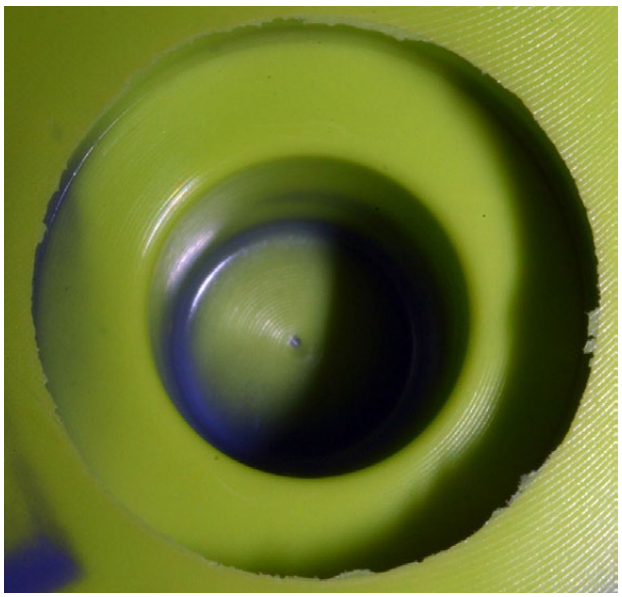

Fig. 3. *Representative impression with an absence of bubble-like enclosed voids or open voids (polyether impression material).*

RESULTS

Table II provides a summary of the identification (type) and quantification (number) of defects according to the three impression materials with different mechanical properties used here. The frequencies of the defects ranged from 95% for the VPS and VPES impression materials, to 30% for the PE impression material, with the tested groups showing a statistically significant difference (P <.05). For VPS *versus* VPES, there were no statistically significant differences between these defect assessments, while the differences seen for the VPS and VPES groups versus the PE group were statistically significant (P <.05). The data gathered here in this study thus indicated rejection of the null hypothesis. Each of the VPS and VPES impression materials produced worse results in comparison with the PE impression material. Although there were no statistically significant differences among the distributions of the defect types across each of the three impression materials, the data indicate that the PE impression material provided better results that the VPS and VPES impression materials. Here, open voids (type #3 defects) were the most frequent type

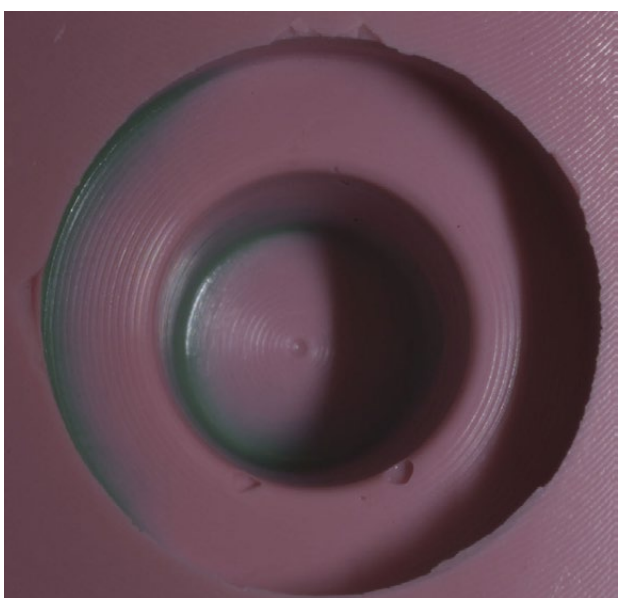

Fig. 4. *Representative impression showing some bubble-like enclosed voids (vinyl polyether silicone impression material).*

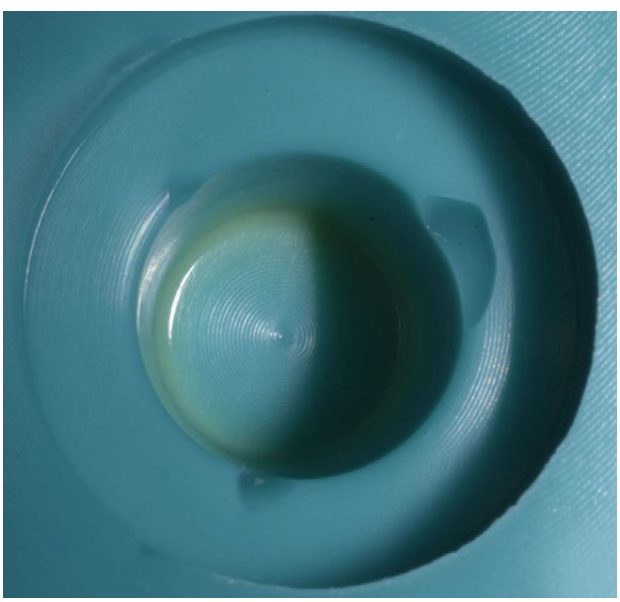

Fig. 5. *Representative impression showing some open voids (vinyl polysiloxane impression material).*

Table II. *Quantification and typing of the defects recorded for each impression material*

Impression material	Number of specimens with defects (n)	Defect frequency (%)	Defect type (n)# #1	#2	#3	Median†
Vinyl polysiloxane	19[a]	95[a]	5	2	12	3
Vinyl polyether silicone	19[a]	95[a]	5	5	9	3
Polyether	6[b]	30[b]	3	2	1	1
Significance	**[a] vs [b] <.05 (within columns)**		**>.05**			
Test	**Fisher exact test (P value)**		**ANOVA (P value)**			

#Defect type #1 (1-2 enclosed voids), type #2 (>2 enclosed voids), type #3 (presence of open voids); †Number of defect ranking.

of defect for the silicone impression materials (VPS, VPES), with enclosed voids (types #1, #2 defects) mainly seen for the PE impression material.

DISCUSSION

The present study investigated the defect frequencies of three impression materials with different mechanical properties, which showed significant differences between them. Furthermore, while the defect types for the VPS and VPES impression materials showed a fairly even distribution across enclosed voids (types #1, #2 defects) and open voids (type #3 defect), the PE impression material produced the best set of results for reproduction of detail.

To limit the number of factors that might influence the results obtained here, stock trays were applied for the three experimental groups, with the same operator making all of the impressions. Furthermore, the same technique was applied for the three impression materials examined. This appears, to the best our knowledge, to be the first *in-vitro* study to investigate the reproduction of surface detail of impression materials with different mechanical properties, in terms of VPES compared with VPS and PE, according to the types and numbers of defects that were visible on these surface impressions, including enclosed, bubble-like, voids and open voids.

Vinyl polysiloxane and PE appear to be the most accurate materials for making dental impressions on the basis of their surface reproduction and dimensional stability (23). Indeed, Lee et al. (24) did not find any significant differences in the accuracy of these impression materials. Johnson et al. (25) also showed no significant differences under dry conditions in terms of the dimensional distortion between VPS and PE when used with full-arch disposable impression trays. An *in-vitro* study has also demonstrated that the VPS and PE impression materials can penetrate and remain entrapped inside the dentinal tubules during the impression procedures, although again, this phenomenon was essentially superimposable for these two impression materials (26). In showing no significant differences between these two types of elastomeric materials, this study (26) demonstrated that both VPS and PE have high intrinsic characteristics and provide a high degree of accuracy, such that they concluded that both of these materials can reproduce the required details. Further *in-vitro* studies investigating VPS have also shown similar reproduction of detail for moist surfaces in comparison with PE (27, 28).

However, several studies have shown differences between these two impression materials (15, 29-32). VPS was reported to provide better reproduction of detail compared to PE (29, 31). On the other hand, other studies have indicated that PE is moderately hydrophilic and can provide more accurate impressions in the presence of saliva or blood, compared to VPS (18). As the wetting angle of PE is low, it can capture and reproduce the fine detail more accurately than VPS, to provide better performance (18). However, although VPS impression material has shown good enough quality in terms of detail reproduction, control

of its moisture remains crucial for taking adequate impressions (6).

This study also confirms these data, whereby the PE impression material showed the lowest total number of voids among these three experimental groups, and was thus significantly better than both the VPS and VPES impression materials. In particular, the PE impression material also showed the lowest numbers of enclosed and open voids in the finish line. This will be due to the higher hydrophilicity and wettability of the PE impression material. Indeed, in the present study, PE showed defects in only 30% of the impressions. This would appear to be related to the greater liquidity of the heavy-body and light-body PE; even though these are classified as ISO viscosity types 1 and 3, respectively, a rheological study showed that at initial mixing, they are more liquid (have a higher tan δ) than the respective consistencies of VPS (32). Thus, the combination of the viscosities of the PE phases used in the present study might be better suited to avoid the creation of bubbles and open voids on the finish line. Further investigations are needed to better understand the full reasons behind this.

As indicated above, the use of VPES has been introduced more recently for conventional prosthodontics. According to the manufacturers, the chemical formulations of the VPES impression materials include a combination of both VPS and PE, purportedly to combine the best characteristics of both VPS and PE into this single, more versatile, material (1, 24, 33, 34). In an *in-vivo* study, Enkling et al. (20) showed that the performance of the VPES impression material was significantly better when compared to PE. In contrast, a further recent investigation on the accuracy of VPES, VPS, and PE as dental impression materials in implantology reported that VPS was significantly better than VPES (34). Then Baig et al. (35) concluded that the pouring of complete-arch multi-implant casts from VPES impressions provided comparable accuracy to PE.

Some studies have indeed examined the accuracy of such combinatory impression materials as compared to VPS and PE for impressions of fixed dental prostheses (1, 34); however, limited data are available at present on the accuracy of VPES used as an impression material in terms of defect-free reproduction of detail. Furthermore, to the best of our knowledge, the literature does not contain any evidence supporting the accuracy of such new hybrid materials for defect-free reproduction of detail for prosthodontic impressions. In the present study, both VPS and VPES resulted in higher numbers of voids compared to PE. Although no significant difference was seen between VPS and VPES, both of these experimental groups showed significant differences to PE. The VPS and VPES materials thus resulted in higher numbers of enclosed and open voids in the impressions, and especially in the finish line. This would appear to be due to their lower hydrophilicity and wettability, whereby in the present study the VPS and VPES impression materials resulted in defects in 95% of the impressions.

In the present study, the best outcome was, however, obtained with the PE impression material. Here, only 30% of the impressions had defects, reflecting the higher hydrophilicity and wettability of this impression material. PE is a particularly fluid material that provides good reproduction of the preparation finish line, and also of the subgingival margins. This impression material is known to have a low surface tension, which will improve the wettability of the prepared teeth. Analysis of the data in the present study indicates that this PE material can provide improved defect-free reproduction of detail compared to the other two impression materials examined here, VPS and VPES.

As well as the *in-vitro* nature of the present study, a limitation is seen in terms of the different temperature and humidity conditions to those present physiologically in the oral cavity. During standard impression making, saliva and blood might be present. Therefore, it is essential that the impression material used can sufficiently wet the surface of the dentition and gingiva when they contain moisture. In addition, the present investigation was conducted by taking impressions with only one impression technique. It would be interesting to know the behavior of these materials when tested with other impression techniques, such as the two-phase, two-step and three-phase, two-step impression injection techniques. Of note, *in-vitro* studies supported by *in-vivo* studies are needed to further explore the relative merits of the PE impression material regarding, in particular, the dimensional accuracy and how it performs in an oral environment

under conditions that include saliva.

Within the above-mentioned limitations of the present *in-vitro* study, we can conclude that these different impression materials differentially affect the reproduction detail of such dental impressions. In particular, the PE impression material showed fewer defects in the reproduction of detail for these impressions compared to the VPS and VPES impression materials, based on a two-phase, one-step technique, and in terms of enclosed (bubble-like) and open voids.

REFERENCES

1. Stober T, Johnson GH, Schmitter M. Accuracy of the newly formulated vinyl siloxanether elastomeric impression material. J Prosthet Dent 2010; 103:228-39.
2. Atieh MA, Ritter AV, Ko CC, Duqum I. Accuracy evaluation of intraoral optical impressions: a clinical study using a reference appliance. J Prosthet Dent 2017; 118:400-405.
3. Lo Russo L, Caradonna G, Biancardino M, De Lillo A, Troiano G, Guida L. Digital versus conventional workflow for the fabrication of multiunit fixed prostheses: a systematic review and meta-analysis of vertical marginal fit in controlled in-vitro studies. J Prosthet Dent 2019; 122:435-40.
4. Varvara G, Murmura G, Sinjari B, Cardelli P, Caputi S. Evaluation of defects in surface detail for monophase, 2-phase, and 3-phase impression techniques: an in-vitro study. J Prosthet Dent 2015; 113:108-13.
5. Samet N, Shoha M, Livny A, Weiss EI. A clinical evaluation of fixed partial denture impressions. J Prosthet Dent 2005; 94:112-17.
6. Raigrodski AJ, Dogan S, Mancl LA, Heindl H. A clinical comparison of two vinyl polysiloxane impression materials using the one-step technique. J Prosthet Dent 2009; 102:179-86.
7. Caputi S, Varvara G. Dimensional accuracy of resultant casts made by a monophase, one-step and two-step, and a novel two-step putty/light-body impression technique: an in-vitro study. J Prosthet Dent 2008; 99:274-81.
8. Lee IK, DeLong R. Pintado, M.R.; Malik, R. Evaluation of factors affecting the accuracy of impressions using quantitative surface analysis. Oper Dent 1995; 20:246-52.
9. Kotsiomiti E, Tzialla A, Hatjivasiliou K. Accuracy and stability of impression materials subjected to chemical disinfection - a literature review. J Oral Rehabil 2008; 35:291-99.
10. Luthardt RG, Walter MH, Weber A, Koch R, Rudolph H. Clinical parameters influencing the accuracy of 1- and 2-stage impressions: a randomized controlled trial. Int J Prosthodont 2008; 21:322-27.
11. Hung SH, Purk JH, Tira DE, Eick JD. Accuracy of one-step versus two-step putty wash addition silicone impression technique. J Prosthet Dent 1992; 67:583-89.
12. Idris B, Houston F, Claffey N. Comparison of the dimensional accuracy of one- and two-step techniques with the use of putty/wash addition silicone impression materials. J Prosthet Dent 1995; 74:535-41.
13. Petrie CS, Walker MP, O'mahony AM, Spencer P. Dimensional accuracy and surface detail reproduction of two hydrophilic vinyl polysiloxane impression materials tested under dry, moist, and wet conditions. J Prosthet Dent 2003; 90:365-72.
14. German MJ, Carrick TE, McCabe JF. Surface detail reproduction of elastomeric impression materials related to rheological properties. Dent Mater 2008; 24:951-56.
15. Sinjari B, D'Addazio G, Murmura G, Di Vincenzo G, Semenza M, Caputi S, Traini T. Avoidance of interaction between impression materials and tooth surface treated for immediate dentin sealing: an in-vitro study. Materials 2019; 12: E3454.
16. Gökçen-Rohlig B, Ongül D, Sancakli E, Sermet B. Comparative evaluation of the effects of implant position, impression material, and tray type on implant impression accuracy. Implant Dent 2014; 3:283-88.
17. Dogan S, Schwedhelm ER, Heindl H, Mancl L, Raigrodski AJ. Clinical efficacy of polyvinyl siloxane impression materials using the one-step two-viscosity impression technique. J Prosthet Dent 2015; 114:217-22.
18. Punj A, Bompolaki D, Garaicoa J. Dental impression materials and techniques. Dent Clin N Am 2017; 61:779-96.

19. Re D, De Angelis F, Augusti G, Augusti D, Caputi S, D'Amario M, D'Arcangelo C. Mechanical properties of elastomeric impression materials: an in-vitro comparison. Int J Dent 2015; 2015:428286.
20. Enkling N, Bayer S, Jöhren P, Mericske-Stern R. Vinylsiloxanether: a new impression material. Clinical study of implant impressions with vinylsiloxanether versus polyether materials. Clin Implant Dent Relat Res 2012; 14:144-51.
21. Walker MP, Alderman N, Petrie CS, Melander J, McGuire J. Correlation of impression removal force with elastomeric impression material rigidity and hardness. J Prosthodont 2013; 22:362-66.
22. Siadat H, Saeidi Z, Alikhasi M, Zeighami S. Comparative evaluation of the effect of impression materials and trays on the accuracy of angulated implants impressions. J Clin Exp Dent 2018; 10:e1096-102.
23. Hoods-Moonsammy VJ, Owen P, Howes DG. A comparison of the accuracy of polyether, polyvinylsiloxane, and plaster impressions for long-span implant-supported prostheses. Int J Prosthodont 2014; 27:433-38.
24. Lee H, So JS, Hochstedler J, Ercoli C. The accuracy of implant impressions: a systematic review. J Prosthet Dent 2008; 100:285-91.
25. Johnson GH, Lepe X, Aw TC. The effect of surface moisture on detail reproduction of elastomeric impressions. J Prosthet Dent 2003; 90:354-64.
26. Sinjari B, D'Addazio G, Xhajanka E, Caputi S, Varvara G, Traini T. Penetration of different impression materials into exposed dentinal tubules during the impression procedure. Materials 2020; 13:E1321.
27. German MJ, Carrick TE, McCabe JF. Surface detail reproduction of elastomeric impression materials related to rheological properties. Dent Mater 2008; 24:951-56.
28. Michalakis KX, Bakopoulou A, Hirayama H, Garefis DP, Garefis PD. Pre- and post-set hydrophilicity of elastomeric impression materials. J Prosthodont 2007; 16:238-48.
29. Hamalian TA, Nasr E, Chidiac JJ. Impression materials in fixed prosthodontics: influence of choice on clinical procedure. J Prosthodont 2011; 20:153-60
30. Gonçalves FS, Popoff DA, Castro CD, Silva GC, Magalhães CS, Moreira AN. Dimensional stability of elastomeric impression materials: a critical review of the literature. Eur J Prosthodont Restor Dent 2011; 19:163-66.
31. Nassar U, Oko A, Adeeb S, El-Rich M, Flores-Mir C. An in-vitro study on the dimensional stability of a vinyl polyether silicone impression material over a prolonged storage period. J Prosthet Dent 2013; 109:172-78.
32. Berg JC, Johnson GH, Lepe X, Adan-Plaza S. Temperature effects on the rheological properties of current polyether and polysiloxane impression materials during setting. J Prosthet Dent 2003; 90:150-61.
33. Kronström MH, Johnson GH, Hompesch RW. Accuracy of a new ring-opening metathesis elastomeric dental impression material. J Prosthet Dent 2010; 103:23-30.
34. Kurtulmus-Yilmaz, S, Ozan O, Ozcelk TB, Yagiz A. Digital evaluation of the accuracy of impression techniques and materials in angulated implants. J Dent 2014; 42:1551-59.
35. Baig MR, Buzayan MM, Yunus N. Accuracy of a new elastomeric impression material for complete-arch dental implant impressions. J Investig Clin Dent 2018; 9:e12320.

Clinical and diagnostic findings in COVID-19 patients: an original research from SG Moscati Hospital in Taranto Italy

M. Balzanelli[1*], P. Distratis[1*], O. Catucci[1], F. Amatulli[1], A. Cefalo[1], R. Lazzaro[1], K.S. Aityan[2], G. Dalagni[3], A. Nico[3], A. De Michele[4], E. Mazza[4], M. Tampoia[4], P. D'Errico[5], G. Pricolo[5], A. Prudenzano[5], E. D'Ettorre[6], C. Di Stasi[6], L.F.P. Morrone[7], KCD. Nguyen[8], HV. Pham[9], F. Inchingolo[10], D. Tomassone[11#], and C. Gargiulo Isacco[1,8#]

[1]SET-118, Department of Pre-hospital and Emergency, SG Giuseppe Moscati Hospital, Taranto, Italy; [2]Department of Multidisciplinary Research Centre, Lincoln University, Oakland CA, USA; [3]Department of Pneumology, SG Giuseppe Moscati Hospital, Taranto, Italy; [4]Department of Clinical Pathology, SS. Annunziata and SG Giuseppe Moscati Hospital, Taranto, Italy; [5]Department of Hematology, SS. Annunziata, Taranto, Italy; [6]Department of Diagnostic Imaging, SG Giuseppe Moscati Hospital, Taranto, Italy; [7]Department of Nephrology, SS. Annunziata, Taranto, Italy; [8]American Stem Cells Hospital Ho Chi Minh, Vietnam; [9]Phan Chau Trinh University of Medicine and Nam-Khoa Biotek, Ho Chi Minh, Vietnam; [10]"Aldo Moro", University of Bari, School of Medicine D.I.M. (Department of Interdisciplinary Medicine), Bari, Italy; [11]Foundation of Physics Research Center, Celico, Italy

Received October 14, 2020 – Accepted January 11, 2021

*Contributed equally as first authors

[#]Joint last authors

The coronavirus disease 2019 (COVID-19) pandemic is a worldwide medical challenge due to the scarcity of proper information and remedial resources. The ability to efficiently avoid a further SARS-CoV-2 pandemic will, therefore, depend on understanding several factors which include host immunity, virus behavior, prevention measures, and new therapies. This is a multi-phase observatory study conducted in the SG Moscati Hospital of Taranto in Italy that was converted into COVID-19 Special Care Unit for SARS-Co-V2 risk management. Patients were admitted to the 118 Emergency Pre-Hospital and Emergency Department based on two diagnostic criteria, the nasopharyngeal swab assessed by reverse-transcriptase–polymerase-chain-reaction (RT-PCR) and CT-scan image characterized by ground glass opacity. Patients were divided into four groups, positive-positive (ER-PP), negative-positive (ER-NP), negative-negative (ER-NN) and a group admitted to the ICU (ER-IC). A further control group was added when the T and B lymphocyte subsets were analyzed. Data included gender, age, vital signs, arterial blood gas analysis (ABG), extensive laboratory results with microbiology and bronchoalveolar lavage fluid (BALF) which were analyzed and compared. Fundamental differences were reported among the groups. Males were significantly higher in PP, ICU, and NP groups, from 2 to 4-fold higher than females, while in the NN group, the number of females was mildly higher than males; the PP patients showed a marked alkalotic, hypoxic, hypocapnia ABG profile with hyperventilation at the time of

Corresponding Author:
Dr C. Gargiulo Isacco,
SET-118, Department of Pre-hospital and Emergency,
SG Giuseppe Moscati Hospital,
Taranto, 74100, Italy
Tel.: +39 3273736805
e-mail: drciroisacco@gmail.com

0393-974X (2021)
Copyright © by BIOLIFE, s.a.s.
This publication and/or article is for individual use only and may not be further reproduced without written permission from the copyright holder.
Unauthorized reproduction may result in financial and other penalties
DISCLOSURE: ALL AUTHORS REPORT NO CONFLICTS OF INTEREST RELEVANT TO THIS ARTICLE.

admission; finally, the laboratory and microbiology results showed lymphopenia, fibrinogen, ESR, CRP, and eGFR were markedly anomalous. The total number of CD4$^+$ and CD8$^+$ T cells was dramatically reduced in COVID-19 patients with levels lower than the normal range delimited by 400/µL and 800/µL, respectively, and were negatively correlated with blood inflammatory responses.

Key words: SG Moscati Hospital; 118 Pre-Hospital Medical System-Emergency Department; COVID-19, Sars-CoV-2; Arterial Blood Gas (ABG); bronchioalveolar lavage fluid (BALF)

COVID-19 as an atypical pneumonia infectious disease is caused by the severe acute respiratory syndrome coronavirus 2 (SARS-CoV-2) and shares 79.6% of its genome with SARS-CoV-1. COVID-19 as a disease was first acknowledged in isolated patients of Hubei Province in Wuhan City from China mainland and soon reached planetary proportions (1). SARS-CoV-2 belongs to the CoV phylogeny which includes two novel human coronaviruses, NL63 and HKU1, and recent findings have confirmed that it has evolved and tripled the number of full-length genome sequences. SARS-CoV-2 binds to host cell receptor-like Angiotensin-Converting Enzyme 2 receptor (ACE_2) thanks to its external spikes made of proteins composed of highly specific glycoprotein domain (possible therapeutic target) (1, 2).

Despite SARS-CoV-2 sharing the 3′–5′ exonuclease RNA proof-reading activity encrypted within nsp14 with other Coronavirus family members, it seems to be capable of "self-repairing", adjusting and adapting its RNA to environmental changes and during stress replicative process (3).

At present, what is known about COVID-19 disease is still based on data and outcomes coming from clinical experience. The transmission takes place via respiratory saliva droplets, and close contacts are considered the main mode of transmission. Clinically, the overall picture describes a blend of inflammatory and infectious patterns that may rapidly shift into typical systemic inflammatory response syndrome (SIRS) or into acute respiratory distress syndrome (ARDS), and eventually may conclude with multi-organ failure (MOF) and death (3-10).

Differences seen in disease incidence and severity are related to insufficiencies of both innate and adaptive immune responses also linked to definite gene polymorphisms (SNPs) that facilitate the virus binding capacity on cells receptors such as the ACEr. The presence of pre-existing comorbidities also plays a key role in enhancing viral invasion (10, 11).

Lymphopenia has been seen as an additional feature in the totality of screened COVID-19 patients and could be considered a determinant marker in cause-specific mortality among the general population. In COVID-19, CD4$^+$ helper T cells (Th) and CD8$^+$ cytotoxic T cells (CTLs) were markedly reduced, ascribed to the persistent viral stimulation that induce an earlier apoptosis of either CD4$^+$ or CD8$^+$ T-cells leading to a reduced immune modulatory responses (12).

Recent studies observed a decline of CD4$^+$ (70.56%), CD8+ T (95%) in a total of 499 COVID-19 patients hospitalized in non-ICU and ICU departments. These findings are attributed to the penetrating modality of the virus via lymphocyte ACE-$_2$r and, its direct to assaults on lymphatic organs, thymus, spleen and lymph nodes (9-14).

The presence of necrotic tissues assessed in COVID-19 deceased patients reflected a generalized amplification of inflammatory and infectious patterns as the main cause of multiple organ involvement. Microscopic autopsy confirmed massive micro-vascular thromboembolism and the presence of non-specific neutrophil and macrophage infiltrates, indicative of an auto-generating necroinflammatory loop arrangement. Conclusions that highlight the silent progression of the disease characterized by the "happy hypoxia" in which a patient's health degenerates silently, almost unnoticeably, up to the point of a sudden irreversible cardiorespiratory blockage (4, 16-20).

The current study focused on data collected from patients admitted to the 118 Emergency Department

of the SG Moscati Hospital in Taranto, Italy (Table I). The patients (n=181) were divided into four groups based on two main criteria, positivity to nasopharyngeal swab analyzed by RT-PCR and, positive to lung/thorax CT-scan imaging technique in compliance with the "typical" ground-glass opacity configuration (PP), patients negative to swab but positive to CT-scan, patients negative to both swab and CT-Scan (NN without "ground glass opacity" but affected by different diseases) and a COVID-19 patient group admitted into the ICU (PP-ICU). The average age of all patients admitted to the 118 Emergency Department and ICU was significantly higher than the average age of the general population of Taranto province (confidence level 95%). The overall outcomes suggested the elderly were more susceptible to COVID-19 disease and likely to have a poor prognosis (20). The age curve of ICU-PP and PP was marked from 60 to 79 years and the curve of NP was from 80 to 99 years, with a total peak that reached 80 to 99 years. Eventually, an alarming distribution rate was noted of the age for normal population of Taranto province; the peak was seen in the age group between 40 to 59 years (about 30% of the entire population); the younger generation (0-19, 20-39 years) showed a much lower percentage for the same age intervals which forecasted a decline of the general population, data confirmed by the general trend for Italy. The percentage of emergency patients grew exponentially with age. The relatively low number of emergency patients for the age group over 100 years was still the highest percentage age group adjusted for the age distribution of the population (Fig. 1 a,b; Fig. 2 a.b) (Table I). All confirmed COVID-19 patients admitted to our facility showed typical signs of respiratory distress with or without detectable comorbidities with an increase of alveolar-capillary permeability with interstitial edema of lung parenchyma, anomalies then confirmed by "ground-glass opacities" CT-scan. All patients showed an increase of classic inflammatory and infectious markers such as the IL-6, troponin, D-dimer, ESR, fibrinogen, and CRP.

MATERIALS AND METHODS

The patients admitted for COVID-19 diseases were informed, and consented to share clinical data for this study research that was conducted per the World Medical Association Declaration of Helsinki. From March 27th, 2020 to May 25th (the considered period), a total of 381 patients were screened at the 118 Emergency Department of the SG Moscati Hospital of Taranto, most of whom were male [n=22 (61%)], 19 deceased (2 in 118 Department, 5 in Pneumology Department, 5 in ICU and 7 in the Infectious Diseases Department [n=19 (5%)], over 80% of older age (mean age 72 years). The patients (n=181) enrolled in the study were divided into four groups, PP (n=46), NP (n=51), the NN (n=63), and PP-ICU (20).

Statistical analysis

Descriptive statistics were used to summarize the data; results are reported as distribution and correlation ranges and values as appropriate. Categorical variables were summarized as counts and percentages. Statistical analysis was supported by Student's *t*-test. The null hypothesis H0 was calculated by using t-statistics. The significance level, denoted as alpha (α) was used to indicate the probability of rejecting the "null hypothesis" when it was true. Confidence level=1-significance level; the p-value was calculated by using Student's *t*-Distribution, if p-value > alpha, the test failed to reject the null hypothesis (H0) and it was accepted (the result was considered not significant), if p-value < alpha it rejected the null hypothesis (the result was considered significant); the df or degree of freedom was 0.003671.

$$\text{t-score} = \frac{(\overline{X}_1 - \overline{X}_2) - (\mu_1 - \mu_2)}{\sqrt{\frac{S_1^2}{n_1} + \frac{S_2^2}{n_2}}}$$

$$df = \frac{\left(\frac{S_1^2}{n_1} + \frac{S_2^2}{n_2}\right)^2}{\frac{(S_1^2/n_1)^2}{n_1 - 1} + \frac{(S_2^2/n_2)^2}{n_2 - 1}}$$

$$\text{t-score} = \frac{\overline{X}_1 - \overline{X}_2}{\sqrt{\frac{S_1^2}{n_1} + \frac{S_2^2}{n_2}}} \quad \begin{array}{l} H0: \mu_1 = \mu_2 \\ HA: \mu_1 \neq \mu_2 \end{array}$$

RESULTS

The groups included both men and women; median age, 50 years (age range, 18-86 years). The results were then assessed and compared. The gender distribution between all patients COVID CT positive

(PP, NP, NN, ICU-PP) was statistically significant (with the significance level alpha = 0.05) from the total Table II; Figs 1, 2.

Age distribution including the total population of Taranto province

The average age of all four groups PP, NP, NN, and ICU-PP patients was significantly (confidence level 95%) higher than the average age of the general population of Taranto. The average age of PP and ICU-PP patients was statistically equal with the confidence level of 95%. The average age of NN and ICU patients was statistically equal with the confidence level of 95%. (A peculiar result. Possibly because ICU patients were suffering from general existing conditions as in the total population). The

Table I. *Population distribution - province of Taranto as of January 1 2019*

Age		Numbers			%		
From	**To**	**Male**	**Female**	**Total**	**Male**	**Female**	**Total**
0	19	54,081	51,347	105,428	19.3%	17.3%	**18.3%**
20	39	66,337	64,777	131,114	23.7%	21.8%	**22.7%**
40	59	83,441	87,999	171,440	29.8%	29.6%	**29.7%**
60	79	61,410	69,769	131,179	22.0%	23.5%	**22.7%**
80	99	14,365	23,121	37,486	5.1%	7.8%	**6.5%**
100		22	87	109	0.0%	0.0%	**0.0%**
	Total:	**279,656**	**297,100**	**576,756**	**100%**	**100%**	**100%**

Table II. *Covid-19 patients admitted to 118 Emergency Department*

(PaO_2)	**(PaO_2)**	**(PaO_2)**	**(PaO_2)**
up to 60 mmHg	**61 to 70 mmHg**	**71 to 90 mmHg**	**> 90 mmHg**
Patients n. 59	**Patients n. 64**	**Patients n. 132**	**Patients n. 55**
11 Swab +	**12 Swab +**	**17 Swab +**	**2 Swab +**
48 Swab -	**52 Swab -**	**115 Swab -**	**53 Swab -**
CT scan	**CT scan**	**CT scan**	**CT scan**
27 CT +	**20 CT +**	**22 CT +**	**5 CT +**
32 CT -	**44 CT -**	**110 CT -**	**50 CT -**

Covid-19 patients (n=310) admitted to the 118 Emergency Department were screened for arterial blood gas (ABG) analysis, Swab Buffer (oral-nasal-pharynx) analyzed by RT-PCR and thoracic CT scan were then performed and results were compared. Notably, based on the oxygen saturation level (PaO2) the CT scan revealed, in line with different published data, a better degree of accuracy compared to swab-RT-PCR outcomes, the PaO2 up to 60 mmHg on a total of 59 patients the CT+ was 27 vs 11 swab+ (column 1); the pO2 from 61 to 70 mmHg, total 64 cases, 20 CT+ vs 12 swab+ (column 2); the PaO2 from 71 to 90 mmHg, total 132 cases, 22 CT+ vs 17 swab+ (column 3); the PaO2 90 mmHg, total 55 cases, 5 CT+ vs 2 swab+ (column 4).

mean ages for all other groups PP, NP and NN and ICU-PP categories were significantly different with the confidence level 95%. The percentage of patients admitted to the 118-Department grows exponentially with age. The relatively low number of emergency patients for the age group over 100 years was still the highest percentage age group adjusted for the age distribution of the population. The percentage of emergency PP and NP patients by age did not exceed the percentage of other patients, and the percentage of IC-PP by the age of the population was lower than the percentage of ER-PP.

Distribution of 118-Pre-Hospital Department the NN, NP, and PP patients based on the evaluation of the CT, RT-PCR and ABG values

An alarming distribution by age was seen for the normal population of Taranto, the peak was related to the age group 40-59 (about 30% of all population, the younger generation (0-19, 20-39) showed a much lower percentage for the same age intervals, which indicated that the population would decline in the future. The majority of PP patients showed an alkaline shift in pH over NP and NN patients (with the significance level alpha = 0.05; Confidence level

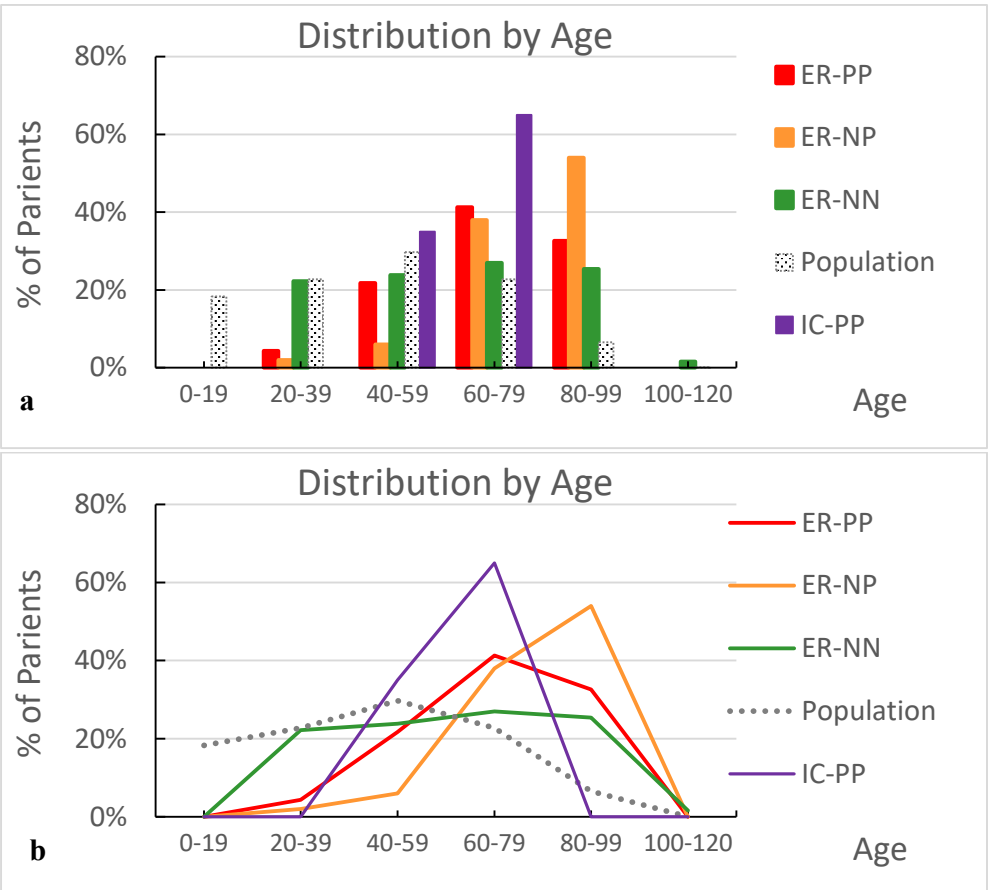

Fig. 1. *Number and percentage of emergency patients by age vs the age distribution of the Taranto population; (a) graph (b) histogram; the percentage of the elderly patients constitute the majority of the of patients admitted to 118 and then hospitalized. Younger patients with negative CT scan indicated that younger people handle COVID easier and call emergency for different health issues; an interesting fact, is the peak of PP: the ages varies between 60-79 and the peak of NP on 80-99 with total peak on 80-99, nevertheless, the age peak of ICU-PP of 60-79 results the same as for PP. The date revealed an alarming distribution by age for the general population of Taranto. It was found that the age group ranged between 40-59 (about 30% of all population) while the younger generation (0-19, 20-39) showed a much lower percentage for the same age intervals which indicates that the population is steadily declining.*

= 1-alpha =0.95). NP patients were more acidic than NN patients but this difference was statistically insignificant.

The PP (n=46) showed pH values alkalotic (>7,45) (n=33/72%), males were 26=59% and females 7=15%; the PaO2 value <75 mm/Hg (n=33/72%), males 27=59% and females 6=13%; the $PaCO_2$ value <75 mm/Hg (n=33/72%), males 26=57% and females 7=15%. The NP group (n=51) showed pH alkalotic (>7,45) (n=25/49%), males were 14=27% and females 11=22%; the PaO2 value <75 mm/Hg (n=35/69%), males 21=41% and females 14=27%; the $paCO_2$ value <75 mm/Hg (n=28/55%), males 20=39% and females 8=16%. The NN group (n=63) showed pH alkalotic (>7,45) (n=29/46%), males were 11=77% and females 18=29%; the PaO2 value <75 mm/Hg (n=27/43%), males 14=22% and females 13=21%; the $PaCO_2$ value <75 mm/Hg (n=32/51%), males 13=21% and females 19=30%.

Distribution by PaO_2 and $PaCO_2$. The oxygen level for PP and NP patients was similar (with the significance level alpha=0.05; Confidence level=1-alpha =0.95). The PaO_2 level in NN patients was significantly higher than the level of PP and NP patients (significance level 0.05). The $PaCO_2$ level for PP was significantly lower than the level for NN

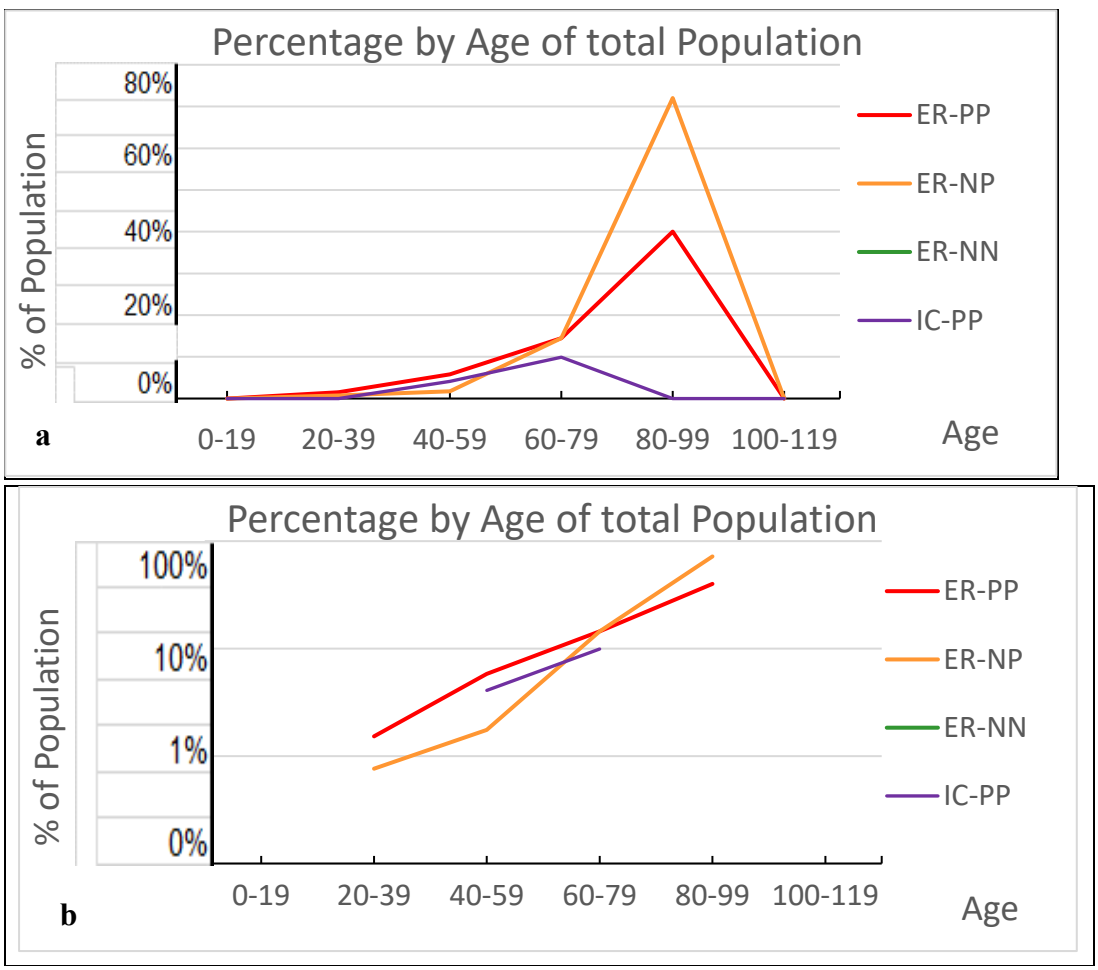

Fig. 2. *Percentage of patients of total population by age. a) Linear Graph; b) Logarithmic Graph. Percentage of emergency patients grows exponentially with age. The relatively low number of emergency patients for the age group over 100 years is still the highest percentage age group adjusted for the age distribution of the population. Percentage of emergency PP and NP patients by age does not exceed the percentage of other patients. Percentage of ICU-PP computed by the age of population is lower than that in PP.*

and NP patients (significance level 0.05); the CO_2 level for NP and NN patients are statistically the same (significance level 0.05). *Distribution by HCO_3.* There was no difference between HCO_3 levels for all 118 Emergency Department admitted patients including PP, NP, and NN (insignificance differences).

Distribution by BE. There was a significant difference between BE levels for PP and NP patients (significance level 0.05); there was no difference between BE levels for NN patients and NP patients (insignificance differences). *Distribution by FO_2HB.* There was a significant difference between FO_2Hb levels for PP and NP as well as for NP and NN patients (significance level 0.05); there was no difference between FO_2Hb levels for PP and NN patients (insignificant differences).

White blood cells, neutrophils, lymphocytes distribution significance for each group PP, NP and NN

Distribution by white blood cell count WBC. There was a significant difference in WBC levels for ICU-NP as well as for NP-NN patients (significance level 0.05); there was no difference in WBC levels for ICU-PP, ICU-NN, PP-NP, and PP-NN patients

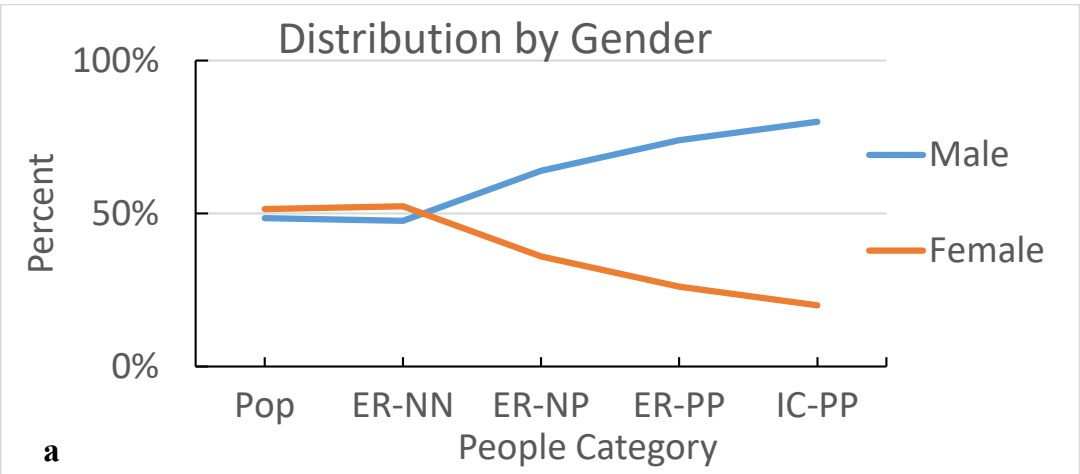

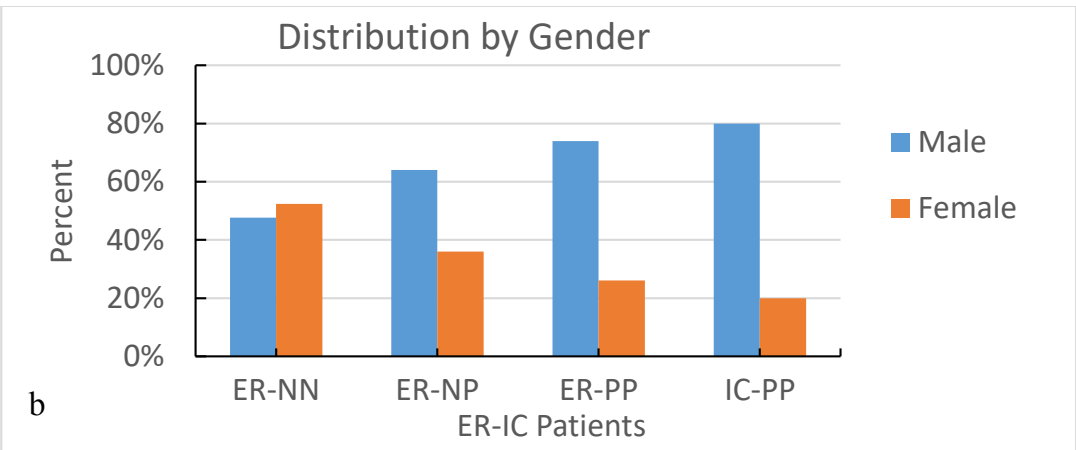

Fig. 3. ***a, b)*** *The gender distribution between the NN patients and the total population is statistically insignificant with the significance level alpha = 0.05. It means that all ER-NN patients are from the general population for different health reasons, a trait that has no impact on the gender differences; the gender distribution between all COVID CT positive patients (NP, PP, ICU-PP) is statistically significant (with the significance level alpha = 0.05) from the total population. Data clearly indicated that COVID-19 lung damage mostly impacts males compared to females. In addition, the number and percentage of emergency patients included in the totality of Taranto population show that the majority of affected patients are elderly. An interesting fact is that the peak of ICU-PP is between 60-79 the same as for PP (1-b).*

(insignificant differences). The WBC revealed the highest number in the NP group, 36 patients affected out of 51 (71%), 25males (49%) and 11 females (22%); the negative group had 29 patients with high WBC out of 63 (46%), 13 males (21%) and 16 females (25%); the PP was the less affected with only 16 patients out 46 (35%), 13 males (28%) and 3 females (6%).

Distribution by neutrophils. There was a significant difference in Neutrophils levels for PP- NP as well as for NP-NN patients (significance level 0.05); there was no difference in neutrophil levels for IC-PP, IC-NP, IC-NN, and PP-NN patients (insignificant differences level 0.05). An important presence was found of neutrophilia in the PP group, 27 patients out of 46 (59%) were found with a high neutrophil level, 21males (46%) and 6 females (13%); the NP group showed the highest presence of patients with high neutrophils 39 out of 51 (78%), 31 (61%) males and 13 (25%) females; the negative group showed the lowest patients affected by neutrophilia, 34 out of 63 (54%), 14 males (22%) and 20 females (32%).

Distribution by lymphocytes. There was a significant difference in lymphocyte levels for PP-NP as well as for NP-NN patients (significance level 0.05); there was no difference in lymphocyte levels for IC-PP, IC-NP, IC-NN, and PP-NN patients (insignificant differences). Lymphopenia was the major value that characterized the PP group, 35 patients, out of 46 (76%) were detected with a marked low count of lymphocytes, 28 males (61%) and 7 females (15%); the NP lymphopenia was confirmed in 30 patients

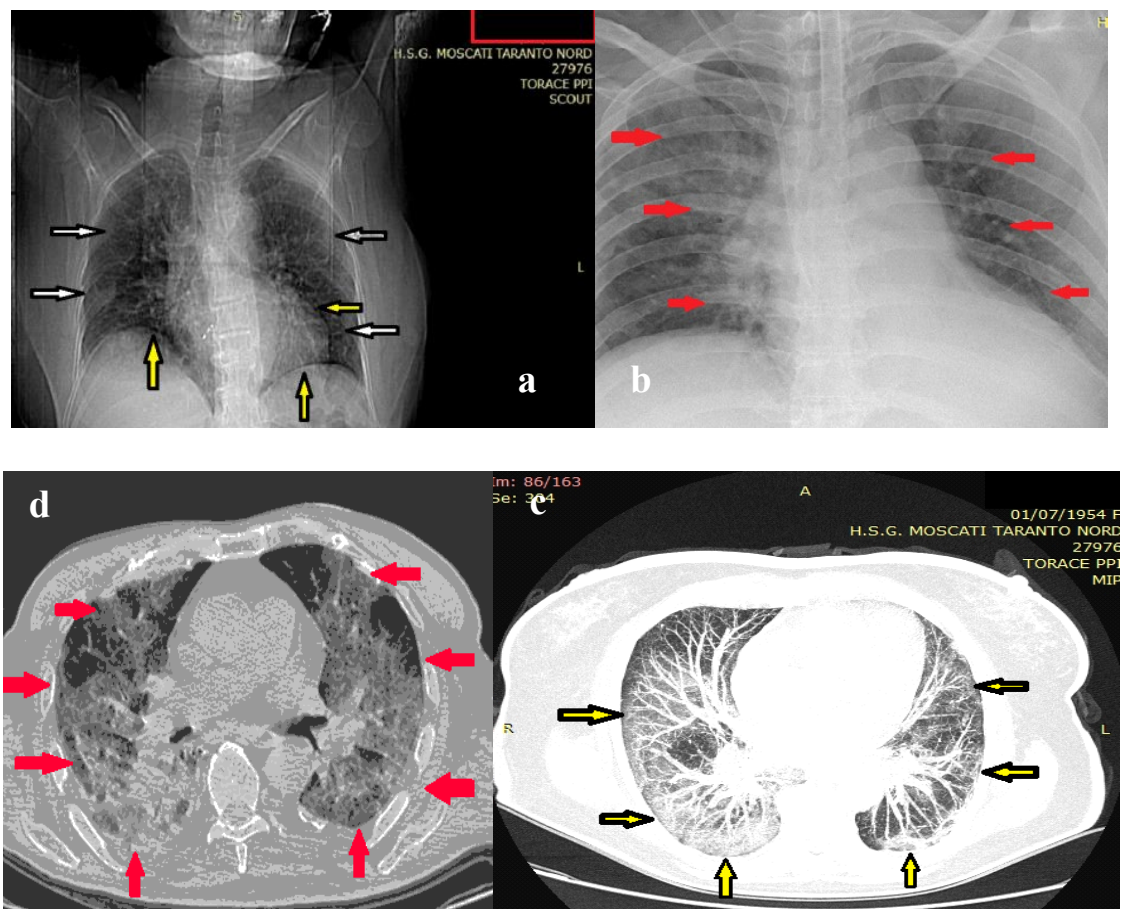

Fig. 4. *Chest CT of 38-year-old male with axial and coronal planes shows the progression of pneumonia with bilateral diffuse patchy mixed ground-glass opacities and linear opacities in the subpleural area (black/white arrow) associated with an anterior pericardial effusion (yellow arrows) (**a-b**); bilateral diffused ground-glass opacity (yellow arrows) from a 66-year-old man with predominant cardiomegaly (red arrows) (**c-d**).*

out 51 (60%), 3 1males (61%) and 14 females (27%); the lymphopenia was not a major problem in the NN- only 26 patients out of 63 (41%) were confirmed with the low level of lymphocytes, 20 males (32%) and 26 females (41%).

eGFR values and statistics analysis of the PP, NP and NN groups

There was a significant difference between eGFR levels for PP-NP as well as for NP-NN patients (significance level 0.05); there was no difference between eGFR levels for PP- NN patients (insignificant differences). The eGFR measurements were taken and divided into three different grades of severity, the eGFR % under 60 ml/min. (severe range), between 60-89 ml/min. (medium severity range) and over 90 ml/min. (mild range). The PP patients resulted to be the most affected in the medium severity range, 22 patients out of 46 (48%) 17 males (37%) and 5 females (11%); in the NP group 18 patients out of 51 were affected (36%), 14 males (28%) and 4 females (8%); in the NN group 19 patients were affected out 63 (30%), with 11 males and 8 females. In the lowest eGFR range (<60ml/min) the PP group had 14 patients out of 46 (31%) of which 10 males (21%) and 4 females (8%); the NP group had 25 patients out of 51 (50%) of which 15 males (30%) and 10 females (20%); the NN group had 21 patients out of 63 (34%) of which 10 males (8%) and 13 females (21%). In the mild range (>90 ml/min) the PP group had 10 patients out of 46 (21%) of which 8 males (17%) and 2 females (4%); the NP group had 8 patients out of 51 (16%) of which 4 males (8%) and 4 females (8%); the NN group had 23 patients out of 63 (36%) of which 11 males (17%) and 12 females (12%).

Statistical analysis and measurements of ESR, CRP, D-dimer, Fibrinogen and Troponin on PP, NP, and NN groups

There was a significant difference between ESR levels for PP-NN as well as for NP-NN patients (significance level 0.05); there was no difference between ESR levels for PP- NP patients (significance level 0.05). The values of erythrocyte sedimentation rate (ESR, >10 mm/h) in the PP were quite exclusive, patients with high ESR were 43 out of 46 (93%) of whom 32 males (70%) and 11 females (24%); in the NP group, patients with high ESR were 45 out of 51 (88%) of which 29 males (57%) and 16 females (31%); in the NN group patients with high ESR were 42 out of 63 (67%) of which 13 males (21%) and 29 females (46%).

There was a significant difference in CRP levels for all categories of ICU patients *vs* PP, NP, and NN, except for PP-NP patients (significance level 0.05); there was a significant difference in PP NN (significance level 0.05). The values of (CRP, >3.5 mg/L) in the PP were highly exclusive, patients with high CRP were 46 out of 46 (100%) of which 34 males (74%) and 12 females (26%); in the NP group patients with high CRP were 51 out of 51 (100%) of which 33 males (65%) and 18 females (35%); in the NN group patients with high CRP were 44 out of 63 (70%) of which 23 males (37%) and 21 females (33%).

There was a significant difference in D-dimer levels for PP-NP patients (significance level 0.05). The D-dimer values in the PP group did not show great relevance, 17 patients out 46 (37%) of which 11 males (24%) and 6 females (13 %); the D-dimer values in the NP group showed great relevance, 39 patients out 51 (76%) of which 27 males (53%) and 12 females (24 %); the D-dimer values in the NP group showed enough relevance, 43 patients out 63 (68%) of which 20 males (32%) and 23 females (37 %).

There was a significant difference in fibrinogen levels for PP-NN and NP-NN patients (significance level 0.05); there was no difference in fibrinogen levels for ICU patients with other patients and between PP-NP patients (insignificant differences). The values of fibrinogen (400 > mg/dl) in the PP were significant, patients with high fibrinogen were 44 out of 46 (96%) of which 33 males (72%) and 11 females (24%); in the NP group, patients with high fibrinogen were 45 out of 51 (88%) of which 31 males (61%) and 14 females (27%); in the NN group patients with high fibrinogen were 34 out of 63 (54%) of which 15 males (24%) and 19 females (30%).

There was a significant difference between Troponin levels for NP-NN patients (significance level 0.05); there was no difference between Troponin levels for PP-NP and PP-NN patients

(insignificant differences). The values of Troponin (14> ng/L) in the PP were less compared to the other groups, patients with high troponin were 14 out of 46 (30%) of which 11 males (24%) and 3 females (7%); in the NP group patients with high fibrinogen were 34 out of 51 (67%) of which 24 males (47%) and 10 females (20%); in the NN group patients with high troponin were 30 out of 63 (48%) of which 12 males (19%) and 18 females (29%).

Statistical analysis and measurements of T and B lymphocyte and their subsets in the Control, PP, NP, and NN groups

The T and B lymphocytes and their subsets were analyzed and compared among each group. There was a significant difference in levels for PP *vs* Control, NP, and NN patients (significance level 0.05). Lymphocytes (absolute count/ul) showed a significant difference of PP *vs* Control, NP and NN (significance level 0.05); both CD4 and CD8 (absolute count/ul) showed a significant difference of PP *vs* Control and NN (significance level 0.05) but not *vs* NP; B Lymphocytes (absolute count/ul) showed a significant difference of PP *vs* Control, NP and NN (significance level 0.05) but not *vs* NP; monocytes CD64++CD33++CD45++(absolute/ul) showed a significant difference of PP *vs* Control, NP and NN (significance level 0.05); T CD8+CD57- (cytotoxic CD8+%) showed a significant difference of PP *vs* NP and NN but not *vs* Control (significance level 0.05); CD4+CD45RA (T CD4+ naïve%) and CD8+CD45RA(T CD4+ naïve%) showed a significant difference of PP *vs* Control, NP and NN (significance level 0.05); CD8+CD38+DR+ (T CD8+ activated %) showed a significant difference of PP *vs* Control, NP and NN (significance level 0.05). The CD4+ and CD8+ T cells were negatively correlated with age and inflammatory responses (CRP, ESR, and fibrinogen) in both PP and ICU-PP groups *vs* Np and NN (coefficient rate of 0.70).

COVID-19 patients in ICU

A chest CT-scan was obtained in 20 patients (100%) at the time of ICU admission, and all the images showed bilateral pulmonary ground-glass opacities and pulmonary nodules. Seventeen pleural effusions were seen, BALF and blood microbiological analysis were obtained in 17 patients (96%); the whole 17 samples showed presence of different pathogens as follow, *Klebsiella spp* (n=7), *Candida albicans* (n=5), *Pseudomonas spp* (n=5), *Acinetobacter* (n=1), *Aspergillus* (n=1), *Staphylococcus aureus* (n=1), *Stenotrophomonas* (n=1); some patients (n=10) presented a positive blood culture for *Klebsiella spp* (n=5), *Candida albicans* (n=1), *Pseudomonas spp* (n=1), *Acinetobacter* (n=1), *Proteus spp* (n=1), *Staphylococcus hominis* (n=1), *Staphylococcus epidermis* (n=1).

DISCUSSION

The unpredictability of the SARS-CoV-2 could be related to the complexity of its inner structure, the virus possesses an envelope crucial for its pathogenicity as it also promotes viral assembly; it has four main structural proteins including spike (S) glycoprotein, small envelope (E) glycoprotein, membrane (M) glycoprotein, a nucleocapsid (N) protein, and is also equipped with accessory proteins that inhibit the host's innate immune response (2). The spiked glycoproteins are considered the most efficient weapons, composed of two subunits (S1 and S2), these homotrimers of the S proteins constitute the spears located on viral surface essential to dock on target host cells receptors (5, 6). In SARS-CoV-2, the S2 subunits contain a fusion peptide, a transmembrane domain, and a cytoplasmic domain, all highly conserved and could potentially be a target for antiviral therapy (anti-S2). Other structural elements on which research must necessarily focus are ORF3b, which has no homology with that of other members of the Corona family, and a secreted protein (coded by ORF8), which was also seen structurally different from those members (4-6). The wide presence of ACE2r located along the respiratory epithelium constitutes the main entrance for the Sars-CoV-2 body invasion and wide spectrum infection.

The over-expression of pro-inflammatory interleukins and cytokines led by IL-6 have been related to an uncontrolled neutrophil, T cell, and local polarized M1 macrophage activity in response to resilient virus stimuli. The excessive accumulation

of mucous within lung alveolar interstices, better known as neutrophil extracellular trap (NET), may certainly be considered one of the causes of bronchoalveolar blockage and the typical feature of "Ground glass opacity" seen in CT-scan images of patients affected by COVID-19 disease (Fig. 4 a-d) (21-23).

The arterial blood gas (ABG) analysis has remained a key marker in predicting COVID-19 from the very beginning. In general the majority of hospitalized patients showed acid-base anomalies, characterized by hypoxia (low O_2) and hypocapnia (low CO_2) with compensatory alkalosis (Table III). The age (>50 years), the gender (prevalently males) and the preexisting co-morbidities, such as chronic obstructive pulmonary diseases (COPD), chronic kidney failure, diabetes and cardiovascular diseases, have been proved to ease unfavorable course of COVID-19 (Figs. 1, 2). The low mortality rate (3-5% of the total of affected individuals), the speed, the unpredictability and the sudden aggravation of symptoms have been revealed to be the essential features of the tropism of SARS-CoV2, as patients have been seen to fall into a state of irreversible cardio respiratory arrest almost without warnings (11).

Pathologically, a secondary bacterial/mycotic infection could explain the full aggressiveness and inflating progression seen in many of the COVID-19-affected patients fully inherent to the rapidity of sepsis and multi-organ involvement. The BALF and blood specimen collected from PP-ICU patients seem to confirm the presence of several pathogens such as *Klebsiella spp*, *Candida albicans, Pseudomonas spp, Acinetobacter, Aspergillus, Staphylococcus aureus, Stenotrophomonas, Proteus spp, Staphylococcus hominis* and *Staphylococcus epidermis* (32-40).

The significantly reduced number of T-CD4+, T-CD8+, B cells and T-CD4 naïve with high level of activated T-CD8+ (CD8+CD38+DR+) has been seen a very peculiar immune dysfunction feature of COVID-19 as it was shown in the PP group, which makes this virus completely unique among the entire Corona family members. In addition, these outcomes lead us to hypothesize a certain affinity of sars-cov-2 with both HIV virus and severe influenza A virus (IAV) infection, either immunologically or genetically (41-53) (Table IV).

According to the latest Italian Health System guidelines, COVID-19 can be classified based on nasopharyngeal swab analyzed by RT-PCR as the main basis of disease confirmation, and other auxiliary examinations are used to distinguish the severity. Thoracic CT-scan, ABG and blood tests are easy, fast, and cost-effective. This study suggested that the ABG results and lymphocyte sub-sets can also be used as reliable indicators to classify and predict the moderate, severe, and critical course of the disease, independently of RT-PCR results. It follows that NP patients presenting with a COVID-like disease arrangement discharged as COVID-19 negative, which avoids the whole series of surveillance and controls, may eventually become a potential source of a larger scale infection in the future. To conclude, we are well aware that further studies are needed, mainly related to the scarcity of information regarding COVID-19.

REFERENCES

1 Bolles M, Donaldson E, Baric R. SARS-CoV and emergent coronaviruses: viral determinants of interspecies transmission. Curr Opin Virol 2011; 1(6):624-34.

2. Pepin KM, Lass S, Pulliam JRC, Read AF, Lloyd-Smith JO. Identifying genetic markers of adaptation for surveillance of viral host jumps. Nat Rev Microbiol 2010; 8:802-13.

3. Denison MR, Graham RL, Donaldson EF, et al. Coronaviruses: an RNA proofreading machine regulates replication fidelity and diversity. RNA Biol 2011; 8:270-79.

4. Couzin-Frankel J. The mystery of the pandemic's 'happy hypoxia. Science 2020; 368:455-56.

5. Zhang Y, Xiao M, Zhang S et al. Coagulopathy and antiphospholipid antibodies in patients with COVID-19. N Engl J Med 2020, doi: 10.1056/NEJMc2007575.

6. Yuen KS, Ye ZW, Fung SY, Chan CP, Jin DY SARS-CoV-2, and COVID-19: The most important research questions. Cell Biosci 2020; 10:40.

7. Lei J, Kusov Y, Hilgenfeld R. Nsp3 of coronaviruses:

Structures and functions of a large multi-domain protein. Antiviral Res 2018; 149:58-74.
8. Song W, Gui M, Wang X, Xiang Y Cryo-EM structure of the SARS coronavirus spike glycoprotein in complex with its host cell receptor ACE2. PLoS Pathog 2018; 14(8):e1007236.
9. Hamming I, Timens W, Bulthuwas ML, Lely AT, Navis G, Van Goor H. Tissue Distribution of ACE2 protein, the functional receptor for SARS coronavirus. A first step in understanding SARS pathogenesis. J Pathol 2004; 203(2):631-37.
10 Gao M, Yang L, Chen X, et al. A study on infectivity of asymptomatic SARS-CoV-2 carriers. Respir Med 2020; 169:106026.
11. Cascella M, Rajnik M, Cuomo A et al. Features, evaluation, and treatment of coronavirus (COVID-19). 2020 Aug 10. In: StatPearls [Internet]. Treasure Island (FL): StatPearls Publishing; 2020 PMID: 32150360.
12. Tan L, Wang Q, Zhang D et al. Lymphopenia predicts disease severity of COVID-19: a descriptive and predictive study. Sig Transduct Target Ther 2020; 5, 33.
13. Wherry EJ, Kurachi M. Molecular and cellular insights into T cell exhaustion. Nat Rev Immunol 2015; 15:486-99.
14. Diao B, Wang C, Tan Y et al. Reduction and functional exhaustion of T Cells in patients with coronavirus diseases 2019 (COVID-19). Front Immunol 2020; 11(827):1-7.
15. Zhu N, Zhang D, Wang W, et al. A novel coronavirus from patients with pneumonia in China 2019. N Engl J Med 2020; 382:727-33.
16. Belen-Apak FB, Sarialioglu F Pulmonary intravascular coagulation in COVID-19: possible pathogenesis and recommendations on anticoagulant/thrombolytic therapy. J Thromb Thrombolysis 2020; 1-3.
17. Moore H, Barrett CD, Moore EE et al. Is there a role for plasminogen activator (tPA) as a novel treatment for refractory COVID-19 associated with acute respiratory distress syndrome (ARDS)? J Trauma Acute Care Surg 2020; 88(6):713-14.
18. Xu Z, Shi L, Wang Y. Pathological findings of COVID-19 associated with acute respiratory distress syndrome. Lancet Respir Med 2020; 8:420-22.
19. Fox SE, Akmatbekov A, Harbert JL, Li G, Brown Q, Vander Heide RS Pulmonary and cardiac pathology in Covid-19: the first autopsy series from New Orleans. MedRxiv 2020; 1-8.
20. Liu J, Liu Y, Xiang P et al. Neutrophil-to-lymphocyte ratio predicts critical illness patients with 2019 coronavirus diseases in the early stage. J Transl Med 2020; 18:206.
21. Zhou F, Yu T, Du R, et al. Clinical course and risk factors for mortality of adult inpatients with COVID-19 in Wuhan, China: a retrospective cohort study. Lancet 2020; 395(10229):1054-62.
22. Mozzini C, Girelli D. The role of neutrophil extracellular traps in Covid-19: only a hypothesis or a potential new field of research? Thromb Res 2020; 191:26-27.
23. Meng H, Yalavarthi S, Kanthi Y, et al. In vivo role of neutrophil extracellular traps in antiphospholipid antibody-mediated venous thrombosis. Arthritis Rheumatol 2017; 69(3):655-67.
24. Jia HP, Look DC, Shi L, et al. ACE2 receptor expression and severe acute respiratory syndrome coronavirus infection depend on the differentiation of human airway epithelia. J Virol 2005; 79(23):14614-621.
25. Hoffmann M, Kleine-Weber H, Schroeder S, et al. SARS-CoV-2 Cell Entry depends on ACE2 and TMPRSS2 and was blocked by a clinically proven protease inhibitor cell 2020; 181(2):271-280.e8.
26. Pan F, Ye T, Sun P, et al. Time course of lung changes at chest CT during recovery from coronavirus diseases 2019 (COVID-19). Radiology 2020; 295(3):715-21.
27. Bernheim A, Mei X, Huan M, et al. Chest CT findings in Coronavirus Diseases-19 (COVID-19): relationship to duration of infection. Radiology 2020; 295(3):200463.
28. Papageorgiou C, Jourdi G, Adjambri E, et al. Disseminated intravascular coagulation: an update on pathogeneswas, diagnosis, and therapeutic strategies. Clin Appl Thromb Hemost 2018; 24(9):8S-28S.
29. Becker RC. COVID-19 update: COVID-19-associated coagulopathy. J Thromb Thrombolysis 2020; 50(1):54-67.
30. Levi M, Thachil J, Iba T, Levy JH. Coagulation abnormalities and thrombosis in patients with COVID-19. Lancet Haematol 2020; 7(6):e438-e440.
31. Santacroce, L.; Charitos, I.A.; Carretta, D.M.; De Nitto, E.; Lovero, R. The human coronaviruses (HCoVs) and the molecular mechanisms of SARS-

CoV-2 infection. Preprints 2020; doi: 10.20944/preprints202010.0041
32. Vall32. amkondu J, John A, Wani WY, et al. SARS-CoV-2 pathophysiology and assessment of coronaviruses in CNS diseases with a focus on therapeutic targets. Biochim Biophys Acta Mol Basis Dis 2020; 1866(10):165889.
33. DiMango E, Ratner AJ, Bryan R, Tabibi S, Prince A. Activation of NF-kappaB by adherent Pseudomonas aeruginosa in normal and cystic fibrosis respiratory epithelial cells. J Clin Invest 1998; 101(11):2598-605.
34. Mohamed A, Hassan T, Trzos-Grzybowska M, et al. Multi-triazole-resistant Aspergillus fumigatusand SARS-CoV-2 co-infection: a lethal combination [publwashed online ahead of print, 2020 Jun 26]. Med Mycol Case Rep 2020; doi:10.1016/j.mmcr.2020.06.005.
35. Almand EA, Moore MD, Jaykus LA. Virus-bacteria interactions: an emerging topic in human infection. Viruses 2017; 9(3):58.
36. Hoffmann J, Machado D, Terrier O, Pouzol S et al. Viral and bacterial co-infection in severe pneumonia triggers innate immune responses and specifically enhances IP-10: a translational study. Sci Rep 2016; 6:38532.
37. Gordon S, Taylor PR. Monocyte and macrophage heterogeneity. Nat Rev Immunol 2005; 5:953-64.
38. Merad M, Martin JC Pathological inflammation in patients with COVID-19: a key role for monocytes and macrophages. Nat Rev Immunol 2020; 20:355-62.
39. Schyns J, Bureau F, Marichal T. Lung interstitial macrophages: past, present, and future. J Immunol Res 2018; 2018:5160794.
40. Kazmaier S, Weyland A, Buhre W et al. Effects of respiratory alkalosis and acidosis on myocardial blood flow and metabolism in patients with coronary artery diseases. Anesthesiology 1998; 89(4):831-7.
41. Santacroce L, Bottalico L, Charitos IA. The impact of COVID-19 on Italy: a lesson for the future. Int J Occup Environ Med 2020; 11(3):151-52.
42. Liu Q, Zhou YH, Yang ZQ. The cytokine storm of severe influenza and the development of immunomodulatory therapy. Cell Mol Immunol 2016; 13(1):3-10.
43. Dunning J, Blankley S, Hoang LT, et al. Progression of whole-blood transcriptional signatures from interferon-induced to neutrophil-associated patterns in severe influenza [published correction appears in Nat Immunol 2019; 20(3):373.
44. Kliger Y, Levanon EY. Cloaked similarity between HIV-1 and SARS-CoV suggests an anti-SARS strategy. BMC Microbiol 2003; 3:20.
45. Cainelli F, Dzudzor B, Lanzafame M, Goushchi A, Chhem S, Vento S (2020) HIV and SARS-Coronavirus-2 epidemics: possible interactions and need for studies, especially in Africa. Front. Med 7:216.
46. Applegate WB, Ouslander JG. COVID-19 presents high risk to older persons. J Am Geriatr Soc 2020; 68(4):681.
47. Terpos E, Ntanaswas-Stathopoulos I, Elalamy I, et al. Hematological findings and complications of COVID-19. Am J Hematol 2020; 95(7):834-47.
48. Cazzolla AP, Lovero R, Lo Muzio L et al. Taste and smell disorders in COVID-19 Patients: role of the interleukin-6. ACS Chem Neurosc 2020; 11(17):2774-81.
49. Kazmaier S, Weyland A, Buhre W et al. Effects of respiratory alkalosis and acidosis on myocardial blood flow and metabolism in patients with coronary artery diseases. Anesthesiology 1998; 89(4):831-7.
50. Gabay C, Kushner I. Acute-phase proteins and other systemic responses to inflammation. N Engl J Med 1999; 340(6):448-54.
51. Santacroce L, Charitos IA, Ballini A, et al. The human respiratory system and its microbiome at a glimpse. Biology 2020; 9(10). DOI: 10.3390/biology9100318.
52. Passarelli PC, Passarelli G, Charitos IA, Rella E, Santacroce L, D'Addona A. COVID-19 and Oral Diseases: How can we Manage Hospitalized and Quarantined Patients while Reducing Risks? Electron J Gen Med 2020; 17(6):em238.

LETTER TO THE EDITOR

Effects of fast-tracking anesthesia on the surgical efficacy and cerebral oxygen saturation of children with congenital heart disease

XL. Wu[1], JH. Cao[1], CJ. Shan[1], B. Peng[1], RD. Zhang[2], JL. Cao[3] and FC. Zhang[1]

[1]Xuzhou Children's Hospital, Xuzhou Medical University, Xuzhou, P.R. China; [2]Shanghai Children's Medical Center, Shanghai, P.R. China; [3]Department of Anesthesiology, The Affiliated Hospital of Xuzhou Medical University, Xuzhou, P.R. China

Received April 3, 2020 – Accepted December 4, 2020

To the Editor,

At present, congenital heart disease in children is one of the most common congenital malformations in the world (1). Statistics have shown that congenital cardiovascular malformations account for 34% of neonates hospitalized for congenital malformations (2). Most patients will have developmental delay and are clinically characterized by dysplasia, cyanosis, and cardiac insufficiency. For children with congenital heart disease, some small ventricular septal defects may have the chance of self-healing before the age of 5, however, at present, most of the patients have to accept surgery for radical treatment (3). In the early implementations of cardiovascular surgeries, opioid pain medicines are used as anesthetic, and postoperative mechanical ventilation is needed for the recovery, and stability of indicators (4). However, this method delays the patient's postoperative extubation time, which not only leads to a longer hospital stay but also increases treatment costs. Fast-tracking anesthesia refers to the rational and scientific anesthesia drugs and methods for surgery. Extubation within 6 hours after surgery as far as possible can maintain the depth of anesthesia and ensure the stability of hemodynamics. Cerebral oxygen saturation (rScO2) can reflect brain oxygenation status in real time (5), and rScO2 can be reflected by detecting balance in brain tissues, cerebral blood flow changes and cerebral oxygenation (6). Therefore, this study focuses on the clinical effects of conventional anesthesia compared to fast-tracking anesthesia as well as the impact of postoperative rScO2, so as to provide clinical references.

MATERIALS AND METHODS

A total of 450 children with congenital heart disease who were admitted to Xuzhou Children's Hospital from January 2016 to December 2018 were retrospectively analyzed. Two hundred and twenty patients who received conventional anesthesia were considered as the control group, and 230 patients who received fast-tracking anesthesia were regarded as the study group. Among them, there were 117 males and 103 females in the control group, 80 cases had ventricular septal defect, 65 cases had patent ductus arteriosus, and 75 cases had atrial septal defect. The average age of patients was (4.72±1.62) years, the average height was (101.22±25.26) cm, and the average body weight was (21.82±13.42) kg. There were 128 males and 102 females in the study group, 70 cases had ventricular septal defect, 80 cases had patent ductus arteriosus, and 80 cases had atrial septal defect.

Key words: congenital heart disease in children; cerebral oxygen saturation; fast-tracking anesthesia; conventional anesthesia; efficacy

Corresponding Author:
Dr. Fengchao Zhang,
Department of Anesthesiology,
Xuzhou Children's Hospital,
No.18 Suti North Road, Quanshan District,
Xuzhou 221006, P.R. China
e-mail: zhangfengchao96@126.com

0393-974X (2021)
Copyright © by BIOLIFE, s.a.s.
This publication and/or article is for individual use only and may not be further reproduced without written permission from the copyright holder.
Unauthorized reproduction may result in financial and other penalties
DISCLOSURE: ALL AUTHORS REPORT NO CONFLICTS OF INTEREST RELEVANT TO THIS ARTICLE.

The average age of patients was (4.92±1.82) years, the average height was (98.52±23.15) cm, and the average body weight was (20.12±11.26) kg.

All patients met the diagnostic criteria for congenital heart disease in the International Classification of Diseases and International Disease Statistics 13. Congenital heart disease was diagnosed by relevant clinical features, laboratory tests and imaging examinations. The exclusion criteria were as follows: patients with pulmonary insufficiency, renal insufficiency, hepatic insufficiency, and brain function and brain central nervous system diseases affecting the results of this study. All the family members of patients signed informed consent forms. This study was approved by the ethics committee of Xuzhou Children's Hospital.

Patients in the study group underwent fast-tracking anesthesia. Penehyclidine hydrochloride anesthesia (Chengdu List Pharmaceutical Co., Ltd, SFDA approval number: H20020606) was used before surgery (intravenous injection, dose of 0.04 mg/kg). After the injection, sevoflurane (Xiamen Institute of Biotechnology Co., Ltd., Art.No. YKPPSJ-009985) and oxygen (inhalation method, oxygen 8 L/min, sevoflurane dose of 8%) were used via endotracheal intubation to induce anesthesia. Rocuronium (N.V.Organon, SFDA approval number: H20130486), propofol (Xi'an Libang Pharmaceutical Co., Ltd, SFDA approval number: H19990281) (50 mg), fentanyl (Jiangsu Enhua Pharmaceutical Co., Ltd., SFDA approval number: H20113508) (0.2 mg) and midazolam (Zhejiang Jiuxu Pharmaceutical Co., Ltd, SFDA approval number: H20113387) (3~5 mg) was intravenously infused. 1% sevoflurane and 50% oxygen were used with air to maintain anesthesia. Propofol was used for patients at the rate of 100-400 mg/h. Vecuronium bromide was added according to the actual situation of patients. If patients gave signs of restlessness, muscle relaxants were injected into the muscle. The probe of cerebral oxygen saturation was placed on the left forehead or right forehead of patients, the illuminating point was placed 2 to 3 cm above the eyebrow, and the midline of the probe was 1 cm. During the operation, the balance of brain tissues, cerebral blood flow changes and cerebral oxygenation were detected to monitor rScO2. During the extracorporeal circulation, the circulation of anesthetic drugs was completed by means of loops. After the patient's body temperature was restored, the dose of anesthetic drugs was gradually reduced until suture was completed. The extubation operation was performed 6 hours after the end of the operation or within 6 hours. Patients in the control group underwent routine anesthesia. When patients were inductively anesthetized with propofol, the micro-pump was continuously pumped at a speed of 1.0-3.0 mg/kg. When patients were in a sedated state, the micro-pump was pumped at a speed of 20-80 μg/ (kg·min) and at a speed of 100-300 μg/(kg·min) during anesthesia induction. When the target-controlled infusion was performed, the effect compartment or plasma concentration were controlled to 2~5 μg/ml. Muscle relaxants were injected into the muscle if patients had signs of restlessness (the cerebral oxygen saturation was measured in the same manner as the study group). The routine extubation operation was performed after surgery.

The postoperative pulmonary function, the preoperative, intraoperative and postoperative cerebral oxygen saturation, and time of postoperative extubation of patients were compared between the two groups. Postoperative adverse reactions of patients were recorded, including heart failure, pneumonia, continuous high fever and other complications. After patients were discharged from the hospital, a random home visit was conducted, and the prognosis survival of patients was statistically analyzed.

The patients were followed-up for 3 years, and the patient survival was recorded by telephone and outpatient medical records.

Statistical analysis

All data were processed and analyzed by SPSS 24.0 software system (Beijing Strong-Vinda Information Technology Co., Ltd.). The counting data were measured by χ^2 test, and the measurement data were measured by *t*-test, expressed as mean±standard deviation (x±s). The survival rate was calculated by the Kaplan-Meier method, and the survival rate was compared by the Log-rank test. Multiple time points were tested by analysis of variance with repeated measures and Bonferroni post hoc tests. When p was less than 0.050, differences were statistically significant.

RESULTS

Clinical data

As shown in Table I, there was no statistically significant difference in the basic clinical information between the study group and the control group in

terms of age, gender, height, weight, nationality, place of residence, way of birth, smoking history of parents, drinking history of parents, and genetic disease history of parents. (p >0.050).

Comparison between the two groups

In the study group, the time of extubation, hospitalization and intensive care unit was (105.27±22.63)/min, (5.9±2.1)/d and (18.52±2.15)/h, respectively. In the control group, the time of extubation, hospitalization and intensive care unit was (401.36±45.1)/min, (13.5±4.3)/d and (26.72±3.62)/h, respectively. As shown in Table II, the indicators of patients in the study group were significantly shorter than those in the control group (p <0.050).

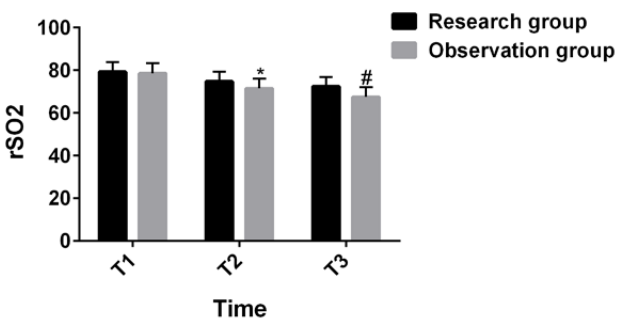

Fig. 1. *Comparison of cerebral oxygen saturation of patients before, during and after surgery between the two groups. Cerebral oxygen saturation at T1 (preoperative), T2 (intraoperative), and T3 (postoperative) were (79.28±4.65)%, (74.81±4.55)% and (72.43±4.43)%, respectively, in the study group. Cerebral oxygen saturation at T1, T2 and T3 were (78.63±4.8)%, (71.52±4.62)% and (67.52±4.59)%, respectively, in the control group. There was no significant difference in cerebral oxygen saturation between the study group and the control group at T1 (p > 0.050). The study group at T2 and T3 had significantly higher cerebral oxygen saturation than the control group (p < 0.050). Preoperative, intraoperative, and postoperative cerebral oxygen saturation between the two groups at each time point were compared, and the levels were higher in the study group than those in the control group (p <0.050).*

** represents the comparison of T2 between the control group and the study group (p < 0.050), and # represents the comparison of T3 between the observation group and the study group (p < 0.050).*

The cerebral oxygen saturation of the study group was (79.28±4.65)%, (74.81±4.55)% and (72.43±4.43)%, respectively, at T1 (preoperative), T2 (intraoperative), and T3 (postoperative). The cerebral oxygen saturation of the control group at T1, T2, and T3 was (78.63±4.8)%, (71.52±4.62)% and (67.52±4.59)%, respectively. There was no significant difference in cerebral oxygen saturation between the study group and the control group at T1 (p >0.050). The cerebral oxygen saturation of the study group at T2 and T3 was significantly higher than that of the control group (p <0.050). As shown in Fig. 1, the cerebral oxygen saturation at each time point before, during and after surgery was compared between the two groups, and the cerebral oxygen saturation of the study group was higher than that of the control group (p <0.050).

In the study group, the residual volume/total lung capacity of patients at T1 (preoperative), T2 (intraoperative), and T3 (postoperative) was (32.21±3.32)%, (33.62±3.83)% and (32.83±3.34)%, respectively. The residual volume/total lung capacity of patients at T1, T2 and T3 was (32.54±3.24)%, (48.55±4.25)% and (45.36±4.26%), respectively. The residual volume/total lung capacity of the study group was not significantly different from that of the control group at T1 (p >0.050). The residual volume/total lung capacity of the study group at T2 and T3 was significantly higher than that of the control group (p <0.050). As shown in Fig. 2, the residual volume/total lung capacity at each time point in the two groups was compared, the levels were lower in the study group than those in the control group before, during and after surgery (p <0.050).

The postoperative complications of the control group included 8 cases of heart failure, 12 cases of pneumonia, and 5 cases of continuous high fever. The postoperative complications of the study group included 2 cases of continuous high fever, and there was no heart failure or pneumonia. Comparing the postoperative complications of the two groups, it was concluded that the overall post-operative complication rate was significantly lower in the study group than that in the control group (p<0.050). See Table III for details.

Table I. *Comparison of clinical data of patients between the two groups*

	Study group (230)	Control group (220)	χ^2or *t*	*p*
Age (years)	4.92±1.82	4.72±1.62	1.229	0.220
Gender			0.277	0.599
Male	128(55.65)	117(53.18)		
Female	102(44.35)	103(46.82)		
Height/cm	98.52±23.15	101.22±25.26	1.183	0.238
Weight/kg	20.21±11.26	21.82±13.42	1.381	0.168
Nationality			3.589	0.058
Han	197(85.65)	201(91.36)		
Minority	33(14.35)	19(8.64)		
Place of residence			1.490	0.222
City	212(92.17)	209(95.00)		
Country	18(7.83)	11(5.00)		
Way of birth			1.016	0.313
Cesarean	128(55.65)	112(50.91)		
Eutocia	102(44.35)	108(49.09)		
Smoking history of parent			3.255	0.071
Yes	182(79.13)	158(71.81)		
No	48(20.87)	62(28.19)		
Drinking history of parents			0.025	0.873
Yes	171(74.35)	165(75.00)		
No	59(25.65)	55(25.00)		
Genetic disease history of parents			0.365	0.550
Yes	11(4.78)	8(3.64)		
No	219(95.22)	212(96.36)		

n (%)

Table II. *Comparison of time of postoperative extubation, hospitalization and intensive care unit of patients between the two groups*

Groups	Number of cases	Time of extubation/ min	Hospital stays/d	Time of intensive care unit /h
Study group	230	105.27±22.63	5.91±2.12	18.52±2.1
Control group	220	401.36±45.16	13.52±4.34	26.72±3.62
T value		89.070	23.790	22.200
p value		0.001	0.001	0.001

Table III. *Comparison of postoperative complications of patients between the two groups*

	Study group (230)	Control group (220)	χ^2	*p* value
Continuous high fever	2 (0.900%)	5 (2.300%)		
Heart Failure	0 (0.00%)	8 (3.600%)		
Pneumonia	0 (0.00%)	12 (5.500%)		
The overall incidence (%)	0.900%	11.400%	6.171	0.045

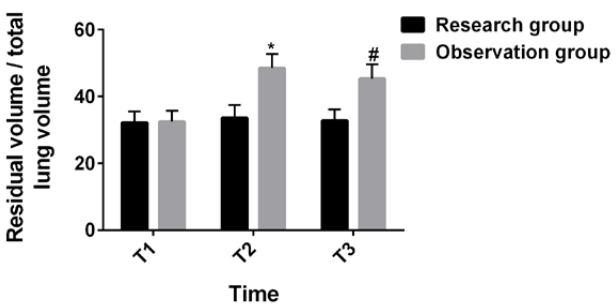

Fig. 2. *Comparison of the residual volume/total lung capacity of patients before, during and after surgery between the two groups. The residual volume/total lung capacity of patients at T1 (preoperative), T2 (intraoperative), and T3 (postoperative) was (32.21±3.32)%, (33.62±3.83)%, and (32.83±3.34)%, respectively, in the study group. The residual volume/total lung capacity of patients at T1, T2 and T3 was (32.54±3.24)%, (48.55±4.25)% and (45.36±4.26)%, respectively, in the control group. There was no significant difference in residual volume/total lung capacity at T1 between the study group and the control group (p > 0.050). The residual volume/total lung capacity in the study group at T2 and T3 was significantly higher than that in the control group (p < 0.050). Residual volume/total lung capacity at each time point was compared between the two groups, and the levels were lower in the study group than those in the control group before, during and after surgery (p <0.050).*
** represents the comparison of T2 between the control group and the study group (p < 0.050), and # represents the comparison of T3 between the observation group and the study group (p < 0.050).*

Prognosis

The success rate of 36-month randomized follow-ups was 97.11% (437/450) among 450 cases of children with congenital heart disease. Among these, 3 cases in the study group and 4 cases in the observation group were lost. In the control group, a total of 16 patients died, and the 36-month survival rate was 92.59%. The study group had a total of 8 patient deaths, and the 36-month survival rate of patients was 96.48%. There was no significant difference in the prognosis survival curves between the two groups (*p* =0.085) (Fig. 3).

DISCUSSION

Congenital heart disease in children is one of the most common causes of death in infants (7). Patients can be radically cured by interventional or surgical treatment (8). The effect of different anesthesia methods on postoperative cerebral oxygen saturation has become a hotspot in clinical

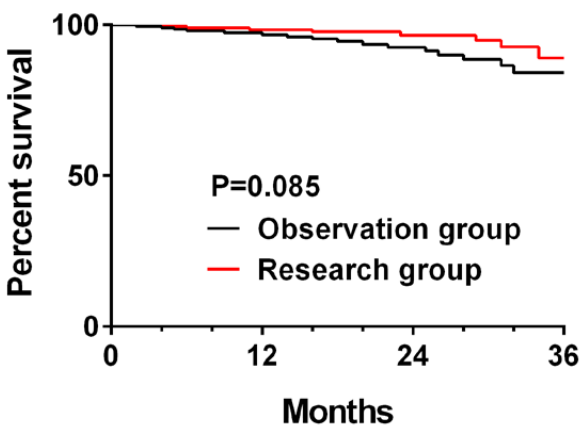

Fig. 3. *Comparison of prognosis and survival curves of patients between the two groups. There were 3 cases lost to follow-up in the study group and 4 cases lost to follow-up in the observation group. In the control group, a total of 16 patients died and the 36-month survival rate was 92.59%. In the study group, a total of 8 patients died and the 36-month survival rate was 96.47%. There was no significant difference in the prognosis and survival curves between the two groups (p =0.085).*

research. Cardiovascular surgeries involve many factors, and have certain complexity and specificity (9). Clinical research is needed to verify whether children with congenital heart disease can adapt to fast-tracking anesthesia. In relevant studies (10, 11), conventional anesthesia and fast-tracking anesthesia were used in congenital heart disease surgeries for children. The time of postoperative extubation, time of treatment in intensive care unit and hospitalization were reduced. The results of the studies showed that the postoperative cerebral oxygen saturation in the control group was lower than that in the study group. Patients in both groups had complications after surgery, but the number of complications in the study group was significantly less than that in the control group. In the control group, the extubation time after surgery was too long, and additional analgesic drugs were needed, which may cause postoperative complications (12). Moreover, in the daily diet of patients, excessive intake of oil, salt and water would increase the burden on the heart and affect the recovery of cardiac function. All indicators in fast-track anesthesia are higher than those of conventional anesthesia, which proved that fast-track anesthesia has better results.

To date, fast-tracking anesthesia has been widely used in various cardiovascular surgery, however, there are some limitations to this study. in this study, the clinical trials conducted have some limitations. Fast-tracking anesthesia cannot be applied to other types of cardiovascular surgeries. In the future, we will study the effects of fast-tracking anesthesia on patients in various cardiovascular surgeries, so as to provide references and suggestions for future clinical practice.

REFERENCES

1. Sun R, Liu M, Lu L, Zheng Y, Zhang P. Congenital heart disease: causes, diagnosis, symptoms, and treatments. Cell Biochem Biophys 2015: 72:857-860.
2. Marelli AJ, Ionescu-Ittu R, Mackie AS, Guo L, Dendukuri N, Kaouache M. Lifetime prevalence of congenital heart disease in the general population from 2000 to 2010. Circulation 2014; 130:749-756.
3. Macrae DJ. IV Fluids After Pediatric Cardiac Surgery. Pediatr Crit Care Med 2019; 20:385-387.
4. Branca P, McGaw P, Light R. Factors associated with prolonged mechanical
5. ventilation following coronary artery bypass surgery. Chest 2001; 119:537-546.
6. Kobayashi K, Kitamura T, Kohira S, et al. Factors associated with a low initial cerebral oxygen saturation value in patients undergoing cardiac surgery. J Artif Organs 2017; 20:110-116.
7. Lei L, Katznelson R, Fedorko L, et al. Cerebral oximetry and postoperative delirium after cardiac surgery: a randomised, controlled trial. Anaesthesia 2017; 72:1456-1466.
8. Shamshirsaz AA, Bateni ZH, Sangi-Haghpeykar H, et al. Cyanotic congenital heart disease following fertility treatments in the United States from 2011 to 2014. Heart 2018; 104:945-948.
9. Mukherjee S, Sharma M, Devgan A, Jatana SK. Iron deficiency anemia in children with cyanotic congenital heart disease and effect on cyanotic spells. Med J Armed Forces India 2018; 74:235-240.
10. Alam S, Shalini A, Hegde RG, Mazahir R, Jain A. Predictors and outcome of early extubation in infants postcardiac surgery: A single-center observational study. Ann Card Anaesth 2018; 21:402-406.
11. Iezzi F, Di Summa M, Sarto PD, Munene J. Fast-track extubation in pediatric cardiothoracic surgery in developing countries. Pan Afr Med J 2019; 32:55.
12. Mittnacht AJ, Hollinger I. Fast-tracking in pediatric cardiac surgery-the current standing. Ann Card Anaesth 2010; 13:92-101.
13. Lerman J, JÖhr M. Inhalational anesthesia vs total intravenous anesthesia (TIVA) for pediatric anesthesia. Paediatr Anaesth 2009; 19:521-534.

LETTER TO THE EDITOR

Effect of drug therapy on pregnancy rate, sex hormone levels and adverse reactions after laparoscopic surgery in patients with endometriosis and infertility

XY. Sun[1] and Z. Liang[2]

[1]Reproductive Medical Center, Yantaishan Hospital, Yantai, China; [2]Department of Breast Surgery, Yantaishan Hospital, Yantai, China

Received July 21, 2020 – Accepted December 9, 2020

To the Editor,

Endometriosis (EMT) refers to the appearance of biologically active endometrial tissues (including glands and stroma) outside the endometrium. The clinical manifestations include lower abdominal pain or dysmenorrhea, abnormal menstruation, and infertility. Studies have shown that 25-35% of infertility patients suffer from EMT, and 40% of EMT patients are infertile. Although EMT is a benign disease, its biological behavior is characterized by invasive growth and the condition is prone to relapse. It has been shown that the recurrence rate of EMT within 2 years of treatment is 30% (2). Improving the cure rate of EMT, EMT-associated infertility as well as pregnancy success rates is currently a research focus (3). The principle of clinical treatment for patients with EMT and infertility is to reduce and eliminate pathological changes, relieve and control pain, promote fertility, and to prevent and reduce recurrence (4). With ongoing developments in medical technology and continuous conceptual advancements in minimally invasive surgery, substantial results in the treatment of EMT have been achieved with the use of laparoscopic technology. The combination of laparoscopic diagnosis, surgery, and drug treatment represents the gold standard for the clinical treatment of EMT (5).

At present, gonadotropin-releasing hormone agonists, gestrinone and mifepristone are the predominant medications used following laparoscopic surgery (6). However, there are no reports on the study of combined treatment with these three drugs. Therefore, in this study, we investigated the efficacy of different drugs in the treatment of EMT with infertility following laparoscopic surgery between January 2015 and December 2017, in order to formulate a scientific basis for the selection of drug treatment in clinical settings.

MATERIALS AND METHODS

Clinical samples

One hundred and ninety-six cases of EMT with infertility were selected as subjects for this study. The age of the sample was (27.8±3.6) years, and the average course of disease was (4.1±2.3) years. According to the random single-blind method, the patients were divided into a control group and an observation group. The control group was treated with laparoscopic surgery, and the observation group was treated with laparoscopic surgery and drugs, with 98 cases in each group. There were no significant differences with regards to age, course of disease and other clinical data between the two groups.

Key words: endometriosis; sex hormone levels; gestrinone; triptorelin acetate; mifepristone

Corresponding Author:
Dr Zhi Liang
Department of Breast Surgery,
Yantaishan Hospital, No. 91 Jiefang Road,
Zhifu District, Yantai,
264001, China
e-mail: zhiliangyts@126.com

0393-974X (2021)
Copyright © by BIOLIFE, s.a.s.
This publication and/or article is for individual use only and may not be further reproduced without written permission from the copyright holder.
Unauthorized reproduction may result in financial and other penalties
DISCLOSURE: ALL AUTHORS REPORT NO CONFLICTS OF INTEREST RELEVANT TO THIS ARTICLE.

The study was approved by the ethics committee of Yantaishan Hospital. All patients included in this study participated on a voluntary basis and signed informed consent was obtained in each case.

Inclusion criteria were: diagnosis via laparoscopy and pathological biopsy; normal couples were infertile for more than 1 year. Exclusion criteria were: patients with genital malformations, ovarian malignant tumors, pelvic inflammatory masses, adenomyosis; patients with infertility caused by immune factors or other physical factors; infertility caused by abnormal male semen.

Surgical method

Conventional gauze was used for disinfection, routine establishment of pneumoperitoneum was achieved following general anesthesia, the four-port method was used to place a trocar, and a comprehensive inspection of pelvic structures as well as an investigation for adhesion sites were carried out. Subsequently, pelvic adhesions were released, sodium hyaluronate was placed to prevent adhesions, and the ovarian tissue was separated to perform cystectomy for those with ovarian cysts. Hysteromyoma resection was performed for uterine fibroids. If the fibrous end of the fallopian tube was closed, tubal stoma was feasible, and routine fallopian tube fluid inspection was performed to ensure that the fallopian tube was unobstructed. The pelvic cavity was rinsed with saline + gentamicin and the incision was closed.

Drug therapy

Triptorelin: intraperitoneal injection of triptorelin acetate (trade name: Dafilin, IPSENPHARMA, 3.75 mg, National Drug Standard: H20140298), 1. 75 mg once a month, was given for 3 months. Gestrinone: Gestrinone capsules (Hurun Zizhu Pharmaceutical Co., Ltd., National Pharmaceutical Standards: H19980020, 2.5 mg/capsule) were started 3 days after surgery, 2.5 mg orally, twice a week, continuously for 6 months. Mifepristone: Mifepristone tablets (Beijing Keyifeng Biotechnology Development Co., Ltd., National Pharmaceutical Standards: H20084624, 25 mg/tablet) were given, 25 mg orally, 2 times/day, for 3 months.

Observational index

The changes in subjective symptoms before and after treatment in the two groups of patients were assessed. The scores included pelvic symptoms (pelvic pain, pain during intercourse, dysmenorrhea) and physical signs (pelvic tenderness, induration); each item ranged from 0 to 3 points and the higher the score, the more serious the subjective symptoms. Using an automatic biochemical analyzer, radioimmunoassay was carried out to determine levels of follicle stimulating hormone (FSH) and luteinizing hormone (LH) on the 3rd day of preoperative menstruation, at the end of postoperative drug treatment and on the 3rd day of menstruation following the recovery of menstruation. Preoperative and postoperative estradiol (E2), and anti-Müllerian hormone (AMH) levels were determined and the number of antral follicles (AFC) was ascertained by vaginal ultrasound. Postoperative follow-up was conducted for 2 years, and recurrence in the two groups was monitored. Ovarian endometriosis cysts on pelvic ultrasonography, or progressive, periodic menstrual abdominal pain with elevated Ca125 were considered recurrences. The adverse reactions in the two groups were compared. Using telephone follow-up, outpatient follow-up, home follow-up and other methods, pregnancy outcome indicators in the two groups were statistically analyzed, and the differences in spontaneous pregnancy, spontaneous

Table I. Comparison of clinical efficacy between two groups of patients with endometriosis and infertility.

Group	Numbers	Significant effect	Effective	Relieved	Invalid
Control group	98	13	21	45	19
Observation group	98	21	36	33	8

Table II. *Comparison of subjective scores between the two groups before and after operation ($\bar{x}$±s)*

	Pelvic symptoms		Signs		Overall Score	
Group(n)	**Preoperative**	**postoperative for 6 months**	**Preoperative**	**postoperative for 6 months**	**Preoperative**	**postoperative for 6 months**
Control group	5.43±0.73	0.67±0.92	2.23±0.31	0.85±0.28	7.66±1.04	1.53±1.20
Observation group	5.56±0.80	1.45±1.02	2.26±0.45	1.61±0.74	7.82±1.25	3.06±1.76
t	0.075	5.304	0.389	10.304	0.323	11.340
p	>0.05	<0.05	>0.05	<0.05	>0.05	<0.05

abortion, ectopic pregnancy, spontaneous childbirth, cesarean section, etc. between the two groups were compared. Among them, poor pregnancy rate = spontaneous abortion rate + ectopic pregnancy rate + cesarean section rate.

Statistical analysis

SPSS 20. 0 Statistical software was used for data analysis; measurement data in accordance with the normal distribution were expressed as mean±standard deviation (x±s), *t*-test was adopted to facilitate comparison between the two groups; count data comparisons were made using χ^2 test; rank data comparison was conducted using the rank sum test. P <0. 05 was considered statistically significant.

RESULTS

Comparison of clinical efficacy between the two groups

The total effective rate in the observation group was higher than that in the control group [91.8% (90 /98) *vs* 80.6% (79 /98)] (χ^2 = 5.197, P = 0.02), and clinical efficacy in the observation group was better than that in the control group (Z = 4.295, P = 0.04) (Table I).

Comparison of subjective symptom scores before and after treatment between the two groups

Before treatment, there was no statistically significant difference in the subjective symptom scores between the two groups of patients (P>0.05); after treatment, the subjective symptom scores of both groups of patients were lower than those before treatment, and the scores in the observation group were lower than the those of the control group (P<0.05). The differences observed between the two groups in relation to pre- and post-operative symptoms, signs and overall scores were statistically significant (P <0.01) (Table II).

Changes in sex hormone levels

The levels of LH, FSH, and E2 decreased at 6 months after surgery in both groups compared with those before surgery, and the decrease in the observation group was significant (P<0.05). There was no difference in the level of AMH between the two groups before and after surgery (P>0.05). There was no difference in the AFC level between the two groups before surgery, and it wasdecreased after 6 months, but the level in the observation group was higher than that in the control group (P<0.05) (Table III). The total incidence of adverse reactions in the observation group after medication was higher than that in the control group (P<0.05) (Table IV).

Pregnancy outcomes

The ovulation rate and pregnancy rate in the observation group were significantly higher than those in the control group, and the difference between the two groups was statistically significant (P <0.05) (Table V). The rate of adverse pregnancy in the observation group was 4.76% (2/42) and the rate of adverse pregnancy in the control group was 21.42% (3/12). The difference between the two groups was statistically significant (P 0.05). The

Table III. *The levels of LH, FSH, and E2 before and after operation in both groups.*

Index		Observation group (98)	Control group (98)	*t*	*p*
LH(U/L)	Preoperative	6.13±122	6.34±1.30	0.375	>0.05
	Postoperative	2.34±0.76	4.20±0.94	6.356	<0.05
FSH(U/L)	Preoperative	5.15±1.21	5.33±0.85	0.104	>0.05
	Postoperative	2.34±0.23	3.95±0.56	15.244	<0.05
$E_{2(}$pmol/L)	Preoperative	195.34±0.90	198.45±1.35	0.566	>0.05
	Postoperative	96.07±0.36	153.65±1.04	31.745	<0.05
AMH(ng/mL)	Preoperative	2.49±0.56	2.40±1.23	0.733	>0.05
	Postoperative	2.16±0.37	2.21±0.88	0.435	>0.05
AFC	Preoperative	8.87±0.29	8.12±1.11	0.109	>0.05
	Postoperative	7.52±0.22	5.24±0.57	12.407	<0.05

Table IV. *The total incidence of adverse reactions in both group s after medication.*

Group (n)	Hot and sweaty	Vaginal discomfort	Joint pain	Skin Itch	Nausea and vomiting	Total incidence (%)
Control group	8	6	4	4	2	24.48
Observation group	0	0	0	2	4	6.12
χ^2						5.246
p						<0.05

Table V. *Comparison of ovulation induction outcomes between the two groups.*

Group (n)	Ovulation rate	Pregnancy rate
Control group (98)	91(92.85)	42(42.85)
Observation group (98)	75(76.53)	14(14.28)
χ^2	5.57	7.356
p	<0.05	<0.05

Table VI. *Comparison of pregnancy outcomes between the two groups.*

Group (n)	Spontaneous abortion	Ectopic pregnancy	Natural childbirth	Cesarean section
Control group (42)	0	2(4.76)	32(76.19)	8(19.04)
Observation group (14)	2(14.28)	1(7.14)	9(64.28)	2(14.28)
χ^2	3.77	0.23	6.35	0.21
p	<0.05	>0.05	<0.05	>0.05

Table VII. *Comparison of pregnancy outcomes between different groups of medicine.*

	Good pregnancy outcomes		Poor pregnancy outcomes	
Group(n)	**Natural childbirth**	**Cesarean section**	**Spontaneous abortion**	**Ectopic pregnancy**
Triptorelin (20)	12	6	0	2
Gestrinone (14)	7	3	1	3
Mifepristone (8)	2	1	1	4

spontaneous abortion rate in the observation group was significantly lower than that in the control group, and the natural delivery rate was significantly higher than that in the control group, with the differences between the two groups being statistically significant ($P<0.05$) (Table VI). The incidence of adverse pregnancy outcomes in the triptorelin group was lower than that of the other two groups, and the difference was statistically significant ($P <0.05$) (Table VII).

DISCUSSION

EMT is associated with various clinical manifestations and has a complicated etiology. The principle underlying treatment of EMT with infertility is to relieve symptoms, restore fertility and prevent recurrence (7). At present, laparoscopic surgery with its unique advantages of clinical application has become the first choice in the clinical treatment of EMT infertility. However, the range of lesions in patients with EMT and infertility is usually very extensive (8). Surgery is difficult because of the dense adhesion that exists between the lesions and surrounding tissues. Reports in the domestic literature indicate that the recurrence rate associated with laparoscopic conservative surgery for EMT was as high as 70% within 5 years after surgery. Postoperative adjuvant drug therapy can effectively reduce the risk of postoperative recurrence (10). Mifepristone is an anti-progesterone drug, which can cause amenorrhea and reduce ectopic lesions. Gestrinone is a 19 nortestosterone steroid with anti-progesterone, moderate anti-estrogen and anti-glandular effects. It can reduce the levels of sex hormone binding protein and inhibit follicle stimulating hormone (FSH) (6, 11). Triptorelin is a gonadotropin-releasing hormone agonist, which can promote the release of LH and FSH in the pituitary, inhibit the secretion of gonadotropin from the pituitary, and decrease the level of ovarian hormone (12). The results showed that the pregnancy success rate of the triptorelin group was higher than that of the other two groups ($P < 0.05$), and the incidence of adverse pregnancy outcomes was significantly lower than that of the other two groups ($P < 0.05$). In conclusion, laparoscopic surgery combined with gonadotropin-releasing hormone agonist can effectively improve the pregnancy success rate and pregnancy outcome, which is an approach that is worthy of clinical consideration and promotion.

REFERENCES

1. Kohl Schwartz AS, Wölfler MM, Mitter V, et al. Endometriosis, especially mild disease: a risk factor for miscarriages. Fertil Steril 2017; 108(5):806-14.
2. Tanbo T, Fedorcsak P. Endometriosis-associated infertility: aspects of pathophysiological mechanisms and treatment options. Acta Obstet Gynecol Scand 2017; 96(6):659-67.
3. Kuznetsov L, Dworzynski K, Davies M, Overton C; Guideline Committee. Diagnosis and management of endometriosis: summary of NICE guidance. BMJ 2017; 358:j3935.
4. Nezhat C, Lindheim SR, Backhus L, et al. Thoracic

Endometriosis Syndrome: A Review of Diagnosis and Management. JSLS 2019; 23(3):e2019.00029.
5. Brown J, Farquhar C. Endometriosis: an overview of Cochrane Reviews. Cochrane Database Syst Rev 2014; 2014(3):CD009590.
6. Song J, Wang Y, Yu L. Clinical comparison of mifepristone and gestrinone for laparoscopic endometriosis. Pak J Pharm Sci 2018; 31(5(Special)):2197-2201.
7. Yamanaka C, Wada H, Eguchi H, et al. Clinical significance of CD13 and epithelial mesenchymal transition (EMT) markers in hepatocellular carcinoma. Jpn J Clin Oncol 2018; 48(1):52-60.
8. Tulchinsky E, Demidov O, Kriajevska M, Barlev NA, Imyanitov E. EMT: A mechanism for escape from EGFR-targeted therapy in lung cancer. Biochim Biophys Acta Rev Cancer 2019; 1871(1):29-39.
9. Kasius A, Smit JG, Torrance HL, Eijkemans MJC, Mol BW, Opmeer B C, Broekmans FJM. Endometrial thickness and pregnancy rates after IVF: a systematic review and meta-analysis. Hum Reprod Update 2014; 20(4):530-41.
10. Chan JM, Sukumar AI, Ramalingam M, Ranbir Singh SS, Abdullah MF. The impact of endometrial thickness (EMT) on the day of human chorionic gonadotropin (hCG) administration on pregnancy outcomes: a 5-year retrospective cohort analysis in Malaysia. Fertil Res Pract 2018; 4:5.
11. Gugnoni M, Sancisi V, Gandolfi G, et al. Cadherin-6 promotes EMT and cancer metastasis by restraining autophagy. Oncogene 2017; 36(5):667677.
12. Klein K, Yang J, Aisenberg J, et al. Efficacy and safety of triptorelin 6-month formulation in patients with central precocious puberty. J Pediatr Endocrinol Metab 2016; 29(11):1241-48.

LETTER TO THE EDITOR

Differential expression and functional mechanism of TIMD4 gene in orbital adipose tissues of patients with thyroid-associated ophthalmopathy

YJ. Zhang[1*], LL. Zheng[2*], Y. Zhu[1], L. Zeng[3], Y. Xun[3] and SR. Deng[3]

[1]Department of Geriatric Endocrinology, Affiliated Haikou Hospital of Xiangya Medical College, Central South University, Haikou, China; [2]Central Laboratory, Affiliated Haikou Hospital of Xiangya Medical College, Central South University, Haikou, China; [3]Department of Endocrine, 928th Hospital of Joint service support force of the Chinese People's Liberation Army, Haikou, China

Received August 6, 2020 - Accepted December 10, 2020

[*]These authors contributed equally to this work

To the Editor,

Thyroid-associated ophthalmopathy (TAO) is an organ-specific autoimmune disease associated with thyroid insufficiency. It is the most common cause of proptosis in adults and is frequently associated with Graves' disease (1). Approximately 52% of patients with TAO have prolapse of the eyeball due to increased orbital fat. An increase in orbital fat in patients with TAO results from an increase in the number and volume of adipocytes (2). The deposition of extracellular matrix (ECM) in orbital tissues is one of the important pathological features of TAO. The T-cell immunoglobulin and mucin domain (TIMD) family is involved in innate immune responses, such as allergy, asthma, autoimmunity, and tolerance in transplantation (3). T-cell immunoglobulin and mucin domain containing 4 (TIMD4, also known as TIM4) was first identified as a receptor for phosphatidylserine and was shown to be involved in the phagocytosis of apoptotic cells by macrophages (4)Moreover, it was recently found to bind to extracellular vesicles (5). However, to date, no research has assessed the role of TIMD4 in orbital adipose tissues of TAO patients. The present study aimed to detect the expression level of TIMD4 in the orbital adipose tissue of TAO patients (hereinafter referred to as TAO group) and healthy controls (hereinafter referred to as control group), and to analyze the correlation of the proteins that may be involved in the underlying mechanism.

MATERIALS AND METHODS

Patients

In the present study, 78 TAO patients who were admitted to Haikou Hospital Affiliated to Xiangya Medical College (Haikou, China) from August 2016 to August 2019, as well as 53 healthy controls were included. The 78 TAO patients underwent orbital decompression. Tissue specimens were fixed in 10% neutral buffered formalin and then embedded into paraffin. There was no significant difference in gender ratio, age, and body mass index between the TAO group and the control group (P>0.05, Table I). All patients signed the written informed consent forms, and the research protocol was approved by the Ethics Committee of Affiliated Haikou Hospital of Xiangya Medical College.

Key words: thyroid-associated ophthalmopathy; TIDM4 gene; orbital adipose tissue; functional mechanism

Corresponding Author:
Dr Yanjiao Zhang
Department of Geriatric Endocrinology,
Affiliated Haikou Hospital
of Xiangya Medical College,
Central South University,
Haikou, 570208, China
e-mail: zhangyanjiaoyj2001@163.com

0393-974X (2021)
Copyright © by BIOLIFE, s.a.s.
This publication and/or article is for individual use only and may not be further reproduced without written permission from the copyright holder.
Unauthorized reproduction may result in financial and other penalties
DISCLOSURE: ALL AUTHORS REPORT NO CONFLICTS OF INTEREST RELEVANT TO THIS ARTICLE.

Quantitative reverse transcription polymerase chain reaction (RT-qPCR)

Total RNA was isolated by using TRIzol reagent (Thermo Fisher Scientific, Waltham, MA, USA). For this purpose, adipose tissues (50 mg) were incubated for 5 min in TRIzol at room temperature. Then, 0.2 ml of chloroform was added and shaken until thoroughly mixed. After the sample was incubated for 3 min at 4°C and centrifuged at 12,000 ×g for 15 min, the mixture was separated into low red phenol-chloroform, middle phase, and colorless upper water phase. The aqueous phase containing RNA was transferred to a new test tube, tilted at 45° and the solution was sucked out with a pipette. Next, 0.5 mL of isopropanol was added, and incubated for 10 min at 4°C, followed by centrifugation for 10 min (12,000 ×g). First strand cDNA synthesis was conducted by using a reverse transcription kit (TaKaRa Bio, Kusatsu, Japan) following the manufacturer's protocol with 2 mg of total RNA as a template. The resulting total RNA precipitate formed a white gel-like particle at the bottom of the test tube, and the supernatant was discarded with a micropipette. Afterwards, 1 mL of 75% ethanol was added, mixed well, and centrifuged at 7,500 ×g for 5 min. The supernatant was discarded. The RNA particles were dried by vacuum air for 10 min, and resuspended in 50 μL RNase-free ultrapure water, followed by incubation at 55-60°C for 15 min. Finally, the obtained RNA was reversely transcribed into cDNA by a Prime Script RT kit (Takara Bio Inc., Shiga, Japan).

The cDNA was obtained by the RevertAid First Strand cDNA Synthesis Kit (Thermo Fisher Scientific, Waltham, MA, USA), according to the manufacturer's instructions. Primer sequences are shown in Table II. RT-qPCR was performed with 1 μL cDNA, 10 μL 2× SYBR Green Master Mix on CFX96 RT-PCR system (Applied Biosystems, Foster City, CA, USA) under the following condition: at 95°C (pre-denaturation) for 10 min, at 95°C for 10 s, at 60°C for 20 s, and at 72°C for 30 s (40 cycles).

Isolation and cultivation of primary cells

The larger blood vessels and adipose tissues were removed with micro ophthalmic scissors and forceps, and washed with phosphate-buffered saline (PBS) for 3 times. The remaining fibrous connective tissue was placed in a dish containing a small amount of medium, and cut into sections (volume, 1 mm^3) with scissors and forceps. The cut tissue was carefully transferred into the culture bottle with tweezers, and Dulbecco's modified Eagle's medium (DMEM)/F12 complete medium containing 20% fetal bovine serum (FBS) and 1% penicillin streptomycin

Table I. *Baseline characteristics of TAO patients and healthy controls*

	TAO group (n=78)	Control group (n=53)	P
Male: female ratio	0.7	0.66	0.874
Age (years old)	43.32±10.19	38.63±8.17	0.317
BMI ($kg \cdot m^{-2}$)	19.86±3.57	22.18±3.89	0.134

Table II. *Primer sequences used for PCR*

Name	Primer sequence (5'-3')	
TIMD4	Upstream primers	CAAACACGTGCCTTTCACTAACC
	Downstream primers	GACTCAACACTACTCCAGGAATCAC
β-actin	Upstream primers	ATTCCTATGTGGGCGACGAG
	Downstream primers	AAGGTGTGGTGCCAGATTTTC

mixture was added. The final volume was 3 ml, and was mixed well. After that, the fluid was changed every 2-3 days to remove the remaining floating erythrocytes. According to different culture conditions and trypsin digestion time, relatively purified orbital fibroblasts were obtained. Human orbital fibroblasts were cultured for 3-8 passages.

Cell transfection

One day before transfection, 0.5-2 × 10^5 cells were inoculated into 24-well plates, and 500 µl of DMEM without antibiotics was added to ensure that the confluence of cells could reach 90-95%. Next, 0.8 µg DNA was diluted into 50 µl serum-free medium, and then was mixed gently. 2 µl Lipofectamine-2000 was diluted into 50 µl serum-free medium, gently mixed, and incubated at room temperature for 5 min. Afterwards, they were mixed gently and incubated at room temperature for 20 min. The culture medium was removed and the cells were washed twice with PBS. After the cells were incubated for 4-6 h, the medium was replaced to remove the complex. After 24-48 h, the expression of the transgenic gene was detected. The cells were subcultured with dilution of 1:10 after 24 h, and the medium was changed after 1 day. Plasmids were transiently transfected to TAO cells using Lipofectamine-2000 transfection reagent at a final concentration of 20 nmol/l/well. The serum-free DMEM was used to prepare transfection mixture. After TIMD4 was transfected into TAO cells, it was set as TIMD4 group.

Western blot assay

The cells in each group were collected and lysed with RIPA lysis buffer (Gibco, Carlsbad, CA, USA) supplemented with 1 mM benzenesulfonyl fluoride (Sigma-Aldrich, St. Louis, MO, USA). After centrifugation at 12,000 rpm, a BCA protein assay kit (SHanghai Biotechnology Co. Ltd., Shanghai, China) was applied to measure the total protein concentration of the supernatant cell lysates. Then, equal amounts of total protein were analyzed on sodium dodecyl sulfate-polyacrylamide gel electrophoresis (SDS-PAGE), transferred onto a polyvinylidene difluoride (PVDF) membrane, and blocked in 5% skim milk for 1 h. Then, the primary antibody was used to detect the expression

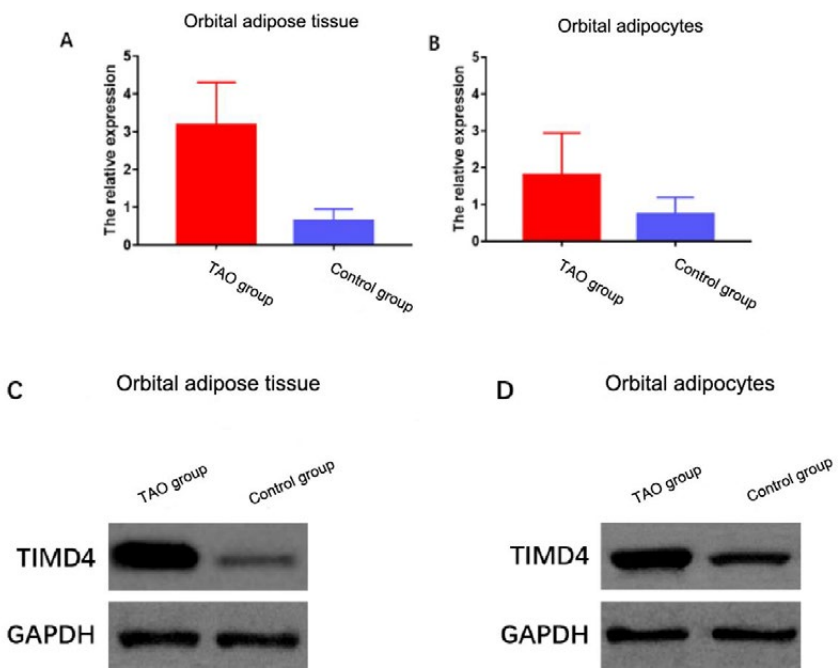

Fig. 1. *The expression of TIMD4 mRNA and protein in each group.* ***A)*** *Relative expression of TIMD4 mRNA in orbital adipose tissues.* ***B)*** *Relative expression of TIMD4 mRNA in orbital adipocytes on the 12th day after differentiation.* ***C)*** *Relative expression of TIMD4 protein in orbital adipose tissues.* ***D)*** *Relative expression of TIMD4 protein in orbital adipocytes on the 12th day after differentiation.*

levels of AP-1, IRF-4, CDX-2, Zic1, and glyceraldehyde 3-phosphate dehydrogenase (GAPDH) (1:100); then, the secondary antibody (1:100) was applied for incubation at room temperature for 2 h. Finally, the proteins were detected by enhanced chemiluminescence detection system (Millipore, Burlington, MA, USA). The protein levels were normalized to the corresponding GAPDH level.

Statistical analysis

SPSS 21.0 software (IBM, Armonk, NY, USA) was used to carry out statistical analysis, and data were expressed as mean ± standard deviation (SD). One-way analysis of variance (ANOVA) was used for making comparison among multiple groups. P<0.05 was considered statistically significant.

RESULTS

Relative expressions of TIMD4 mRNA and protein in orbital adipose tissues

Excluding the possible influences of age, gender, and body mass index (BMI), according to the results of RT-qPCR and Western blotting, the relative expressions of TIMD4 mRNA and protein in orbital adipose tissues in TAO group were higher than those in the control group (P < 0.05) (Fig. 1 A, C). The relative expression of TIMD4 mRNA in the intraorbital adipose tissues in the TAO group was 3.17±1.13 (without consideration of the influences of age, gender, and BMI), and it was 0.64-0.31 in the control group (P<0.05).

Rrelative expression of TIMD4 mRNA in orbital adipocytes

The *in-vitro* cultured preorbital adipose fibroblasts in the TAO group and control group could differentiate into adipocytes under the stimulation of 3-isobutyl-1-methylxanthine (IBMX), dexamethasone (DEX), and insulin. According to the results of RT-qPCR and Western blotting, the relative expression of TIMD4 mRNA and protein in orbital adipocyte tissues in the TAO group was higher than that in the control group (P < 0.05) (Fig. 1 B, 1D). The relative expression of TIMD4 mRNA in orbital adipocytes in the TAO group on the 12th day of differentiation was 1.78±1.16, and that of the control group on the 12th day of differentiation was 0.72±0.47, and the difference between the two expressions was statistically significant (P< 0.05) (Fig. 1B).

Culture, differentiation, and identification of pre-adipose fibroblasts in vitro

In the primary culture, there were cells around the tissue block within 3-5 days, and the cell growth reached the peak within 12 days. The cell passage was performed once every 3-4 days. Fibroblasts were found sensitive to trypsin and could be purified by multiple passages. Fig. 2A shows spindle or polygon-shaped cell bodies and the nuclei. During cellular differentiation, the cells became gradually round-shaped and further lipid droplets appeared. After 10 days of differentiation, the lipid droplets were marked in red according to the results of Oil Red O staining (Fig. 2B).

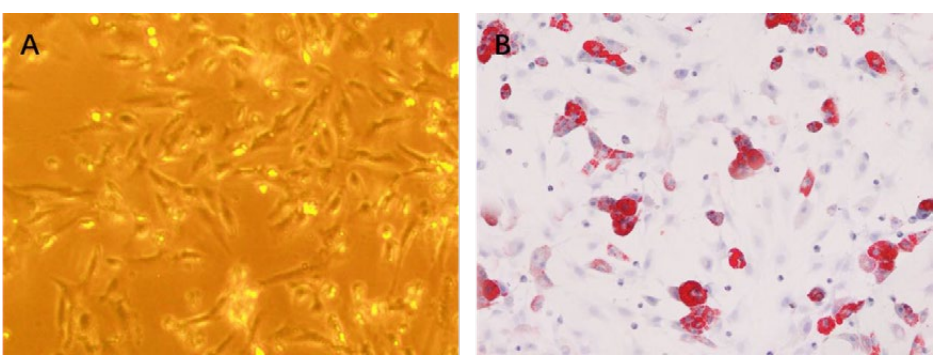

Fig. 2. ***A)*** *Pre-adipocytes cultured for 20 days and visualized under an inverted phase-contrast microscope;* ***B)*** *Lipid droplets of differentiated adipocytes stained with Oil Red O (× 100).*

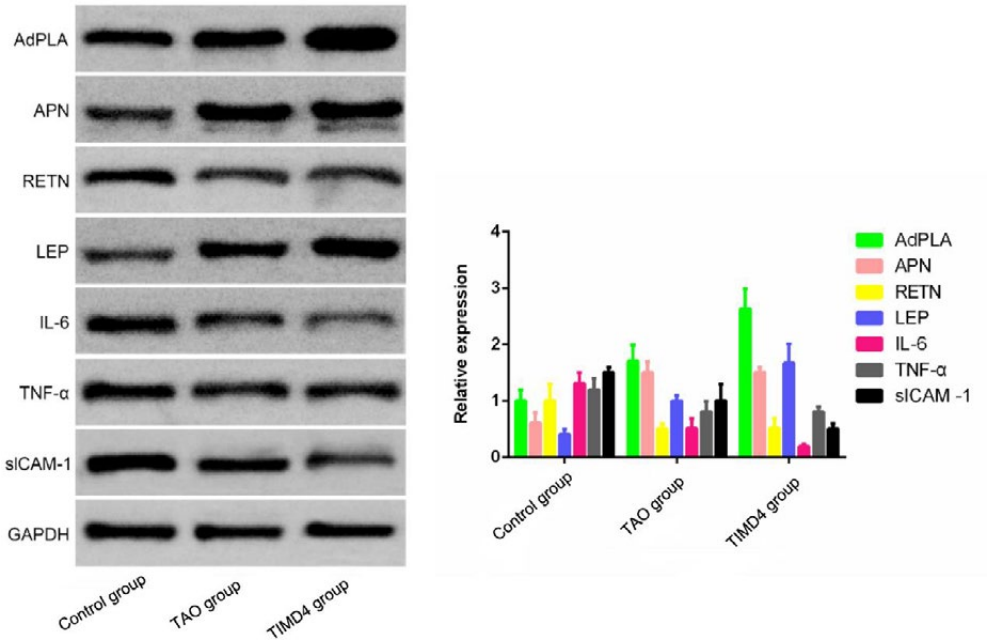

Fig. 3. *Relative expressions of adipose-specific phospholipase A2 (AdPLA), adiponectin (APN), resistin (RETN), leptin (LEP), IL-16, tumor necrosis factor-α (TNF-α), and soluble intercellular adhesion molecule (sICAM -1) in each group.*

Western blotting

Western blot assay detected the expressions of adipose-specific phospholipase A2 (AdPLA), adiponectin (APN), resistin (RETN), leptin (LEP), interleukin-16 (IL-16), tumor necrosis factor-α (TNF-α), and soluble intercellular adhesion molecule 1 (sICAM-1) in the control group, TAO group, and TIMD4 group. The results showed that the expressions of AdPLA, APN, and LEP were significantly elevated in the TAO group, while the expressions of RETN, IL-16, TNF-α, and sICAM-1 were remarkably decreased in the TAO group. At the same time, TIMD4 expression was positively correlated with the expressions of AdPLA and LEP, while TIMD4 expression was negatively correlated with the expressions of IL-6 and sICAM-1, and TIMD4 expression had no relationship with the expressions of APN, RETN, and TNF-α (Fig. 3).

DISCUSSION

The results of the present study showed that TIMD4 expression in orbital adipose tissues and differentiated orbital adipocytes in TAO patients was significantly higher than that in control group, suggesting that TIMD4 gene may be involved in the pathogenesis of TAO. TIMD4 gene expression can regulate cell proliferation, differentiation and apoptosis (6). In TAO, inflammatory cell infiltration in the host-tissue is noticeable, and orbital fibroblasts are proliferated under the action of inflammatory factors (7). Fibroblasts not only modulate the recruitment of immune cells, but also regulate their behavior, retention, and survival in damaged tissues (8), suggesting that TIMD4 indirectly promotes the proliferation of orbital fibroblasts through interacting with cytokines. The adipose tissues is a complex, essential, and highly active metabolic and endocrine organ, (9). It can secrete a series of adipokines, such as APN and LEP, as well as inflammatory factors (TNF- α and IL-6) (10). A recent study showed that orbital fibroblasts can interact with specific immune cells to promote TAO (11). In this process, inflammatory factors, including TNF-α, IL-6, and sICAM, participate in and promote the growth of lymphocytes, and then interact with fibroblasts (12).

The results of the present study suggest that the high TIMD4 expression in TAO patients and

its molecular mechanism may be related to the involvement of AdPLA, LEP, IL-6 and sICAM-1 in the pathological process of thyroid-associated ophthalmopathy, while the interaction among them remains to be further explored *in vitro*.

ACKNOWLEDGMENTS

This study was financially supported by Key Research and Development Projects of Hainan Province (Grant No. ZDYF2016160) and Haikou Key Science and Technology Plan Project (Grant No. 2014-072).

REFERENCES

1. Smith TJ, Kahaly GJ, Ezra DG, et al. Teprotumumab for thyroid-associated ophthalmopathy. N Engl J Med 2017; 376(18):1748-61.
2. Kumar S, Coenen MJ, Scherer PE, Bahn RS. Evidence for enhanced adipogenesis in the orbits of patients with Graves' ophthalmopathy. J Clin Endocrinol Metab 2004; 89(2):930-35.
3. Li Z, Ju Z, Frieri M. The T-cell immunoglobulin and mucin domain (Tim) gene family in asthma, allergy, and autoimmunity. Allergy Asthma Proc 2013; 34(1):e21-e26.
4. Miyanishi M, Tada K, Koike M, Uchiyama Y, Kitamura T, Nagata S. Identification of Tim4 as a phosphatidylserine receptor. Nature 2007; 450(7168):435-39.
5. Nakai W, Yoshida T, Diez D, et al. A novel affinity-based method for the isolation of highly purified extracellular vesicles. Sci Rep 2016; 6:33935.
6. Zhang Q, Wang H, Wu X, et al. TIM-4 promotes the growth of non-small-cell lung cancer in a RGD motif-dependent manner. Br J Cancer 2015; 113(10):1484-92.
7. Li W, Li X, Xu S, Ma X, Zhang Q. Expression of Tim4 in glioma and its regulatory role in LN-18 glioma cells. Med Sci Monit 2016; 22:77-82.
8. Yano H, Motoshima T, Ma C, et al. The significance of TIMD4 expression in clear cell renal cell carcinoma. Med Mol Morphol 2017; 50(4):220-26.
9. Yuan J, Tang ZL, Yang S, Cao JY, Li K. Molecular characteristics of the porcine TIMD4 gene and its association analysis. Biochem Genet 2012; 50(7-8):538-48.
10. Yang X, Yan L, Ha D, Qu L, Liu L, Tao Y. Changes in sICAM-1 and GM-CSF levels in skin tissue fluid and expression of IL-6, IL-17 and TNF-α in blood of patients with vitiligo. Exp Ther Med 2019; 17(1):408-12.
11. Son DH, Doan KV, Yang DJ, et al. FoxO1 regulates leptin-induced mood behavior by targeting tyrosine hydroxylase. Metabolism 2019; 91:43-52.
12. Tao P, Jing Z, Shou-Hong G, Shu-Juan P, Jian-Peng J, Wen-Quan L, Wan-Sheng C. Effects of leptin on norepinephrine in acute ischemic stroke. Pharmazie 2019; 74(8):477-480.

LETTER TO THE EDITOR

Correlation between the invasion mechanism of papillary thyroid carcinoma and expressions of NF-κB and the epithelial-mesenchymal transition-associated factors

Y. Chen[1], YT. Lv[2], JR. Chen[2] and HY. Zhang[2]

[1]Department of Pathology, Zhejiang Provincial People's Hospital, People's Hospital of Hangzhou Medical College, Hangzhou, Zhejiang, China; [2]Department of Pathology, Zhuji People's Hospital of Zhejiang Province, Zhuji, Zhejiang, China

Received August 6, 2020 – Accepted December 10, 2020

To the Editor,

Papillary thyroid carcinoma (PTC) is the most common type of malignant thyroid tumor, accounting for more than 70% of thyroid malignancies. PTC is originated from thyroid follicular epithelial cells. Epithelial-mesenchymal transition (EMT) encompasses dynamic changes in cellular organization from epithelial to mesenchymal phenotypes, leading to functional changes in cell migration and invasion. EMT involves the loss of cell–cell adhesion and the polarized epithelial morphology through the characteristic loss of epithelial cells, and a subsequent increase in mesenchymal markers. The hallmarks of EMT include loss of contact inhibition, remodeling of extracellular matrix, and reorganization of cytoskeleton, along with expression of mesenchymal markers and reduction of epithelial markers (1).

Previous studies (2, 3) reported that the activation of NF-κB can induce and maintain the occurrence of EMT. One study demonstrated that NF-κB can regulate the expressions of transcription factors (ZEB-1 and ZEB-2) to inhibit the expression of epithelial-specific gene (E-cadherin) (4). Moreover, it can induce the occurrence of EMT in mammary epithelial cells through inducing the expression of an interstitial specific gene (vimentin). The present study aimed to detect the expressions of NF-κB and EMT-associated factors (TTF-1, Thyroglobulin (Tg), N-cadherin, and E-cadherin) in PTC patients, and to explore the relationship between these expressions and clinicopathological characteristics of such patients. Our findings may not only provide new molecular markers for early detection of PTC invasion and metastasis and the assessment of prognosis, but also may guide clinicians for developing further effective therapies for thyroid cancer.

MATERIALS AND METHODS

From March 2018 to December 2019, 56 cases of thyroid cancer were admitted to Zhejiang Provincial People's Hospital (Hangzhou, China). None of the patients had undergone chemotherapy, radiotherapy, or immunotherapy preoperatively, and PTC was pathologically confirmed postoperatively. At the same time, the adjacent normal thyroid tissue (≥2 cm from the edge of the lesion area) was selected as the control group. The expressions of NF-κB, E-cadherin, thyroid transcription factor-1 (TTF-1), Tg, and N-cadherin in the PTC tissues were detected, and their correlations with clinicopathological characteristics were explored. The tissues were fixed with 10% formaldehyde

Key words: papillary thyroid carcinoma; NF-κB; epithelial-mesenchymal transition; immunohistochemistry

Corresponding Author:
Dr Haiyong Zhang,
Department of Pathology,
Zhuji People's Hospital of Zhejiang Province,
No.9 Jianmin Road, Taozhu Street, Zhuji,
311800, Zhejiang, China
e-mail: zhanghaiyongzhuji@163.com

0393-974X (2021)
Copyright © by BIOLIFE, s.a.s.
This publication and/or article is for individual use only and may not be further reproduced without written permission from the copyright holder.
Unauthorized reproduction may result in financial and other penalties
DISCLOSURE: ALL AUTHORS REPORT NO CONFLICTS OF INTEREST RELEVANT TO THIS ARTICLE.

(Shanghai Haling Biotechnology Co., Ltd., Shanghai, China), embedded into paraffin (Sakura, Tokyo, Japan), and cut into 4-μm thick sections by a microtome (Leica, Wetzlar, Germany). Informed consent was obtained from all patients, and this study was approved by the Ethics Committee of Zhejiang Provincial People's Hospital.

For each case, 6 pieces of wax blocks were sectioned continuously, with a thickness of 4 μm. One of the sections was used for H&E staining, 5 for immunohistochemical staining, and the remaining wax block was sectioned.

For H&E staining, paraffin-embedded sections were cleared in dimethylbenzene I and II (Henan Bafang Chemical Industry Co., Ltd., Xinxiang, China) for 8 min, respectively. Then, paraffin-embedded sections were immersed in 100% ethanol (Henan Bafang Chemical Industry Co., Ltd., Xinxiang, China), 95% ethanol, and 80% ethanol for 2 min, respectively. After washing with running tap water, the sections were stained with hematoxylin solution (Beijing Solarbio Science & Technology Co., Ltd., Beijing, China) for 5-10 min and washed by tap water for another 3 min. Afterwards, the sections were differentiated with 1% hydrochloric acid (Shanghai Rongbai Biotechnology Co., Ltd., Shanghai, China) for several seconds and washed with tap water. After immersing in 1% ammonia water for 5-10 min (Shanghai Ruji Biotechnology Co., Ltd., Shanghai, China) or warm water (around 50°C), the sections were re-washed with tap water. Afterwards, the sections were stained with eosin solution (Beijing Solarbio Science & Technology Co., Ltd., Beijing, China) for 2 min and washed with tap water. Next, the sections were immersed in 80% ethanol, 90% ethanol, and 95% ethanol, 2 min each, followed by absolute ethanol I for 1 min, absolute ethanol II for 2 min, dimethylbenzene I for 3 min, and dimethylbenzene II for 3 min.

Immunohistochemical staining of paraffin-embedded sections using SP method

The immunohistochemical staining of paraffin-embedded sections using the SP method was carried out to detect the expressions of TTF-1, Tg, and N-cadherin. The negative control was replaced with phosphate-buffered saline (PBS) rather than the primary antibody, and size-distinguishable samples were used as positive controls.

Five fields under a high-magnification microscope were randomly selected from each pathological section for scoring, and 100 cells were counted in each field. The normal expression of each factor was detected, and the expression of each factor was divided into four levels according to the percentage of positive staining and the intensity of staining, which were marked as "-", "+", "++", "+++", and then each factor was scored. The four grades were scored as 0, 1, 2, and 3, and the transitional area was scored as 0.5, 1.5, and 2.5, thus, the scores were divided into seven grades: 0, 0.5, 1, 1.5, 2, 2.5, and 3.

Statistical analysis

SPSS 20.0 software (IBM, Armonk, NY, USA) was used to perform statistical analysis, and the enumeration's positive rate was analyzed by the *chi*-squared test. Wilcoxon rank-sum test was employed for comparing two independent samples. The Spearman correlation coefficient was used to find the relationship between expressions of the above-mentioned factors (NF-κB, E-cadherin, TTF-1, Tg and N-cadherin) and clinicopathological characteristics of PTC patients. $P<0.05$ was considered statistically significant.

RESULTS

Results of morphological analysis

According to the morphological characteristics of PTC tissues stained with H&E, among the 56 cases, there were 38 cases of classic PTC (Fig. 1B), 7 cases of follicular variant of PTC (FV-PTC) (Fig. 1C), 5 cases of diffuse sclerosing variant of PTC (DSV-PTC) (Fig. 1E), and 6 cases of Hobnail variant of PTC (HV-PTC) (Fig. 1D).

The histological grades were divided into 3 groups, including well-differentiated, moderately-differentiated, and poorly-differentiated, in which there were 36 cases of well-differentiated grade, 14 cases of moderately-differentiated grade, 6 cases of poorly-differentiated grade.

Immunohistochemical staining

As shown in Fig. 2, the positive expression of NF-κB was mainly localized in the cytoplasm, which was positive or strongly positive in the PTC group, and was only poorly positive in the control group. The positive rate of NF-κB expression in the PTC and control groups was 80.36% (45/56) and 26.79%

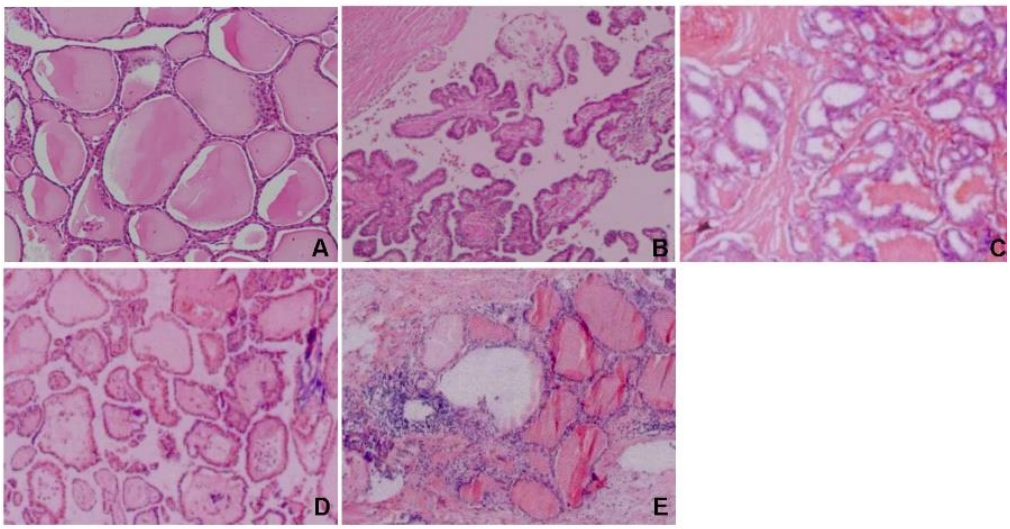

Fig. 1. *HE staining results.* ***A)*** *normal thyroid tissues;* ***B)*** *classic PTC;* ***C)*** *FV-PTC;* ***D)*** *HV-PTC;* ***E)*** *DSV-PTC (×200).*

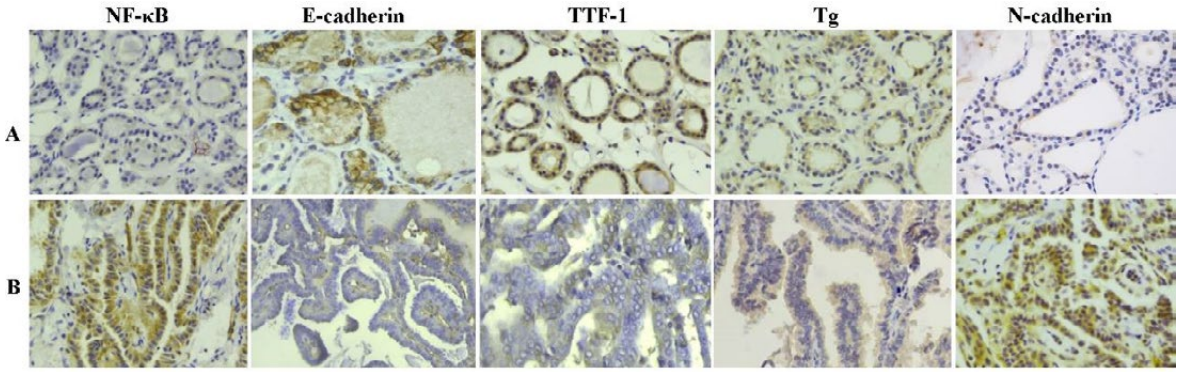

Fig. 2. *Immunohistochemical staining results.* ***A)*** *control group;* ***B)*** *PTC (×200).*

(15/56), respectively. The difference was statistically significant (P<0.01).

The positive expression of E-cadherin was mainly localized in the cell membrane, with TTF-1 in the nucleus, and Tg in the cytoplasm. The expressions of E-cadherin, TTF-1, and Tg in the PTC group were significantly lower than those in the control group (P<0.05).

The positive expression of N-cadherin was mainly localized in the cytoplasm, which was positive or strongly positive in the PTC group, while it was scarcely expressed in adjacent normal thyroid tissues. The difference between the two groups was statistically significant (P<0.01).

Correlation between clinicopathological characteristics of PTC patients and expressions of NF-kB and EMT-associated factors

The expressions of E-cadherin, TTF-1, and Tg in PTC tissues were all down-regulated compared with those in the control group (P<0.05). On the contrary, the expressions of NF-κB and N-cadherin were up-regulated (P<0.01) (Table I).

As shown in Table II, the expression of NF-κB was not correlated with gender, age, or extrathyroidal invasion (P>0.05), while correlated with tumor size, degree of differentiation, clinical stage, and lymph node metastasis (LNM) (P<0.05).

Table I. *Comparison of E-cadherin, TTF-1, Tg, and N-cadherin scores between the experimental group and the control group.*

Factor	Group	Grade							P
		0.0	0.5	1.0	1.5	2.0	2.5	3.0	
NF-Kb	Control group	3	4	8	13	25	2	1	0.007
	PTC group	0	0	2	4	5	10	35	
E-cadherin	Control group	0	0	3	11	25	14	3	0.009
	PTC group	1	1	6	20	17	10	1	
TTF-1	Control group	0	0	1	0	7	19	29	0.012
	PTC group	0	1	1	2	8	24	20	
Tg	Control group	0	0	2	6	13	20	15	0.036
	PTC group	0	0	1	8	18	23	6	
N-cadherin	Control group	0	0	7	17	24	7	1	0.003
	PTC group	1	1	2	3	10	15	24	

Note: Wilcoxon rank-sum test showed a statistically significant difference between any two groups (P < 0.05).group.

Table II. *Correlation between clinicopathological characteristics of PTC patients and expressions of NF-kB and EMT-associated factorsgroup.*

Characteristic	Classification	NF-κB	E-cadherin	TTF-1	Tg	N-cadherin
Age (years)	≥45	54.84±6.61	31.22±5.05	33.55±4.50	27.47±5.38	53.41±7.61
	< 45	60.35±4.19	26.91±4.93	26.61±4.28	29.62±4.81	61.32±5.19
	P	0.208	0.198	0.203	0.792	0.317
Gender	male	58.27±8.03	33.63±4.24	29.47±4.92	35.10±5.92	58.47±9.03
	female	59.11±7.39	28.35±3.88	28.29±4.03	28.84±5.36	59.01±8.39
	P	0.883	0.196	0.906	0.198	0.985
Size of the tumor	< 1cm	49.38±6.44	35.28±4.87	30.45±3.85	32.64±6.37	47.22±6.68
	1-3cm	60.38±7.93	25.53±5.22	28.28±5.01	26.52±4.74	59.31±9.15
	> 3cm	66.19±9.28	17.16±2.88	29.03±2.80	28.54±3.28	65.05±7.25
	P	**0.012**	**0.011**	0.853	0.775	**0.007**
Degree of differentiation	highly	64.26±6.28	33.77±4.03	33.36±4.05	33.78±4.08	66.61±7.51
	moderately	59.36±5.93	18.45±3.18	16.53±3.91	16.21±4.84	55.18±6.03
	low	48.37±5.03	4.40±3.92	4.28±2.03	5.59±4.03	44.35±6.16
	P	**0.013**	**0.002**	**0.001**	**0.002**	**0.001**
Stage of AJCC	I and II	52.34±7.29	31.54±5.37	31.35±3.87	26.42±6.11	50.26±8.07
	III and IV	67.73±6.89	17.38±7.51	9.57±3.25	30.83±5.38	68.13±6.19
	P	**0.026**	**0.029**	**0.004**	0.418	**0.008**
Extrathyroidal invasion	Yes	59.26±9.28	28.58±4.57	27.45±5.02	24.87±3.28	46.02±6.34
	No	58.31±5.24	30.93±6.74	31.61±4.77	25.24±5.04	59.11±7.69
	P	0.837	0.786	0.480	0.827	**0.031**
Lymph node metastasis	Yes	64.27±6.39	24.72±6.48	17.46±3.08	28.92±5.14	69.19±9.53
	No	51.48±8.38	30.02±5.33	32.98±4.89	28.78±5.28	53.15±8.21
	P	**0.032**	0.216	**0.023**	0.983	**0.027**

Table III. *Correlation analysis of the expressions of NF-κB and EMT-associated group.*

		E- cadherin	TTF-1	Tg	N-cadherin
NF-κB	**Correlation coefficient (r)**	-0.472	-0.397	-0.407	0.508
	P	0.006	0.012	0.008	0.005

E-cadherin was correlated with tumor size, clinical stage, and degree of differentiation. As the degree of differentiation decreased, E-cadherin expression decreased, while it was not correlated with gender, age, extrathyroidal invasion, or LNM (P>0.05).

The TTF-1 expression was correlated with the degree of differentiation (P<0.05). As the degree of differentiation decreased, TTF-1 expression was down-regulated. It was associated with LNM (P<0.05), and TTF-1 expression decreased in patients with LNM. TTF-1 expression was correlated with the American Joint Committee on Cancer (AJCC) TNM system (P<0.05), in which TTF-1 expression in stages III and IV was down-regulated compared with stages I and II. TTF-1 expression was not correlated with gender, age, tumor size, or extrathyroidal invasion (P>0.05).

Tg expression was correlated with the degree of differentiation (P<0.05). With decreasing the degree of differentiation, Tg expression decreased, and its expression was not correlated with gender, age, tumor size, clinical stage, extrathyroidal invasion, or LNM (P>0.05).

N-cadherin expression was not correlated with gender and age (P>0.05), while it was correlated with tumor size, degree of differentiation, clinical-stage, extrathyroidal invasion, or LNM (P<0.05).

As presented in Table III, NF-κB expression was negatively correlated with expressions of E-cadherin, TTF-1, and Tg (P<0.05), while it was positively correlated with N-cadherin expression (P<0.05).

DISCUSSION

PTC is often associated with LNM around the thyroid or distant organ metastasis, especially lung metastasis (5), and extensive direct infiltration of parathyroid tissues is an indicator of poor prognosis. In the EMT process, the morphological features may not only change, but also may be accompanied by changes in related phenotypic markers (6). More specifically, when EMT occurs, the expressions of E-cadherin and β-catenin are down-regulated, while the expressions of vimentin, N-cadherin, and fibronectin are up-regulated (7). These changes are mediated by related transcription factors, such as Snail, Slug, Twist1/2, and ZEB1/2, which also involve TGF-β, microRNAs, as well as Smad, NF-κB, Wnt/β-catenin, and Ras-MAPK/Snail/Slug signaling pathways (8, 9). The characteristic changes of EMT are mainly associated with the reduction of E-cadherin expression (10). In normal epithelial tissues, E-cadherin is highly expressed, thus, the characteristics of epithelial cells can be maintained (11). Ectopic expression of N-cad in epithelial tissues can affect the morphology and behavior of epithelial cells and induce their transformation into the mesenchyme, producing EMT (12). The *in-vivo* results of the present study revealed that E-cadherin expression in PTC tissues was significantly down-regulated, and N-cadherin expression in PTC tissues was markedly up-regulated compared with that in the control group, which is consistent with findings of previous studies. Moreover, the NF-κB expression in PTC tissues was significantly higher than that in the control group, indicating that NF-κB could promote the occurrence of EMT in cancer tissues. Therefore, it can be concluded that the EMT plays a role in promoting the occurrence, development, and infiltration of PTC.

REFERENCES

1. Lin X, Zhang H, Dai J, Zhang W, Zhang J, Xue G, Wu J. TFF3 Contributes to Epithelial-Mesenchymal

Transition (EMT) in papillary thyroid carcinoma cells via the MAPK/ERK signaling pathway. J Cancer 2018; 9(23):4430-39.
2. Lv N, Shan Z, Gao Y, Guan H, Fan C, Wang H, Teng W. Twist1 regulates the epithelial-mesenchymal transition via the NF-κB pathway in papillary thyroid carcinoma. Endocrine 2016; 51(3):469-77.
3. Han D, Wu G, Chang C, et al. Disulfiram inhibits TGF-β-induced epithelial-mesenchymal transition and stem-like features in breast cancer via ERK/NF-κB/Snail pathway. Oncotarget 2015; 6(38):40907-19.
4. Halytskiy V. Abnormalities in miRNAome contribute to epithelial-mesenchymal transition of breast cancer cells. Eur J Cancer 2017; 72(Suppl. 1): S24-S24.
5. An JH, Song KH, Kim SK, et al. RAS mutations in indeterminate thyroid nodules are predictive of the follicular variant of papillary thyroid carcinoma. Clin Endocrinol (Oxf) 2015; 82(5):760-6.
6. Ren L, Xu Y, Qin G, Liu C, Yan Y, Zhang H. miR-199b-5p-Stonin 2 axis regulates metastases and epithelial-to-mesenchymal transition of papillary thyroid carcinoma. IUBMB Life 2019; 71(1):28-40.
7. Fang CX, Ma CM, Jiang L, et al. p38 MAPK is Crucial for Wnt1- and LiCl-Induced Epithelial Mesenchymal Transition. Curr Med Sci 2018; 38(3):473-81.
8. Kurioka K, Wato M, Iseki T, Tanaka A, Morita S. Differential expression of the epithelial mesenchymal transition factors Snail, Slug, Twist, TGF-β, and E-cadherin in ameloblastoma. Med Mol Morphol 2017; 50(2):68-75.
9. Xu M, Li J, Wang X, et al. MiR-22 suppresses epithelial-mesenchymal transition in bladder cancer by inhibiting Snail and MAPK1/Slug/vimentin feedback loop. Cell Death Dis 2018; 9(2):209.
10. Luo CW, Wu CC, Chang SJ, et al. CHD4-mediated loss of E-cadherin determines metastatic ability in triple-negative breast cancer cells. Exp Cell Res 2018; 363(1):65-72.
11. Mitchell B, Leone D, Yang S, Khan A, Mahalingam M, Dhingra J. BRAF and epithelial-mesenchymal transition in papillary thyroid carcinoma - challenging the roles of Snail and E-Cadherin? Am J Transl Res 2016; 8(11):5076-86.
12. Selekman JA, Grundl NJ, Kolz JM, Palecek SP. Efficient generation of functional epithelial and epidermal cells from human pluripotent stem cells under defined conditions. Tissue Eng Part C Methods 2013; 19(12):949-60.

LETTER TO THE EDITOR

Erb-B2 receptor tyrosine kinase 2 knockdown inhibits retinoblastoma progression via Wnt/β-catenin signaling pathway *in vitro*

B. Liu[1], T. Gao[2], H-Y. Wu[3] and M. Wan[4]

[1]Department of Sports Medicine, Qingdao Municipal Hospital, Qingdao, China; [2]Department of Obstetricsn (III), Qingdao Municipal Hospital, Qingdao, China; [3]Department of Hematology, Qingdao Municipal Hospital, Qingdao, China; [4]Department of Ophthalmology and Stomatology, Qingdao Municipal Hospital, Qingdao, China

Received October 12, 2020 – Accepted December 17, 2020

To the Editor,

Retinoblastoma (RB) is an intraocular malignancy of early childhood and is a robust model of heritable predisposition to developing cancer (1). Recently, the most common treatment for patients includes chemotherapy combined with immunotherapy, which is cytotoxic to RB cells (2). Identifying the underlying mechanism of the development of RB is therefore urgent.

Erb-B2 receptor tyrosine kinase 2 (ERBB2), a member of the epidermal growth factor receptor (EGFR) family, is highly expressed in most tumors (3). Previous studies have found that patients with high expression of ERBB2 are prone to tumor metastasis and have short survival rate (4). Hedegger K et al. demonstrated that ERBB2 was elevated in pancreatic ductal adenocarcinoma and was involved in the tumor development (5). In RB, ERBB2 was found to be increased in RB cells (6). Previous studies have reported that hyperactivation of Wnt/β-catenin signaling is widely implicated in many types of cancers (7). Da Hyun Jung et al. discovered that ERBB2 modulated gastric cancer progression via the Wnt signaling pathway (8). The functional role and mechanism of ERBB2 in the modulation of RB progression, however, remains incompletely understood.

In the present study, ERBB2 was elevated in RB, and knockdown of ERBB2 impeded RB cell viability, migration and invasion. Furthermore, knockdown of ERBB2 blocked the activation of Wnt/β-catenin pathway. Taken together, the silence of ERBB2 attenuated RB progression via Wnt/β-catenin pathway.

MATERIALS AND METHODS

Patients and specimens

Human RB samples were extracted from 70 patients (age 0-7 years) diagnosed with RB who underwent surgery at Qingdao Municipal Hospital, Qingdao, China. Fifteen normal retinal specimens as controls were obtained from patients who died from non-ophthalmic diseases. The collected samples were stored at -80°C for further analysis. Written informed consent was signed by all RB patients, and the study was approved by the ethics committee of Qingdao Municipal Hospital, Qingdao, China.

Cell culture and cell transfection

RB cell lines (Y79 and SO-RB50) and retina epithelium cells ARPE-19 employed in the study were obtained from American Type Culture Collection (ATCC, Manassas, USA). The cells were cultured in RPMI1640

Key words: ERBB2; retinoblastoma; progression; Wnt/β-catenin

Corresponding Author:
Dr Mei Wan,
Department of Ophthalmology and Stomatology,
Qingdao Municipal Hospital, No. 5, Donghai Middle Road,
Shinan District,
Qingdao 266071, China
e-mail: lanshaizhi700673@163.com

0393-974X (2021)
Copyright © by BIOLIFE, s.a.s.
This publication and/or article is for individual use only and may not be further reproduced without written permission from the copyright holder.
Unauthorized reproduction may result in financial and other penalties
DISCLOSURE: ALL AUTHORS REPORT NO CONFLICTS OF INTEREST RELEVANT TO THIS ARTICLE.

medium containing 10% fetal bovine serum (FBS) and antibiotics and incubated at 37°C in a humidified incubator containing 5% CO_2.

The specific small interfering RNA for ERBB2 (siRNA ERBB2) or overexpression vector of ERBB2 (ERBB2 vector) were constructed by Shanghai Genechem Co. Ltd (Shanghai, China). The si-ERBB2 forward sequence was 5'-CAGC CCCAGAGGATTACAGA-3', and the reverse sequence was 5'-TCAGTCCTAGTGG GGTGTCC-3'. Cell transfection was conducted for 48 h using Lipofectamine 2000 reagent (Thermo Fisher Scientific, Waltham, MA, USA) following the manufacturer's protocol.

Real-time PCR (RT-PCR)

Total RNA was isolated from RB cells using TRIzol reagent (Invitrogen). cDNA was synthesized using a reverse transcription kit (Applied Biosystems). qPCR was performed using the Applied Biosystems 7500 instrument. GAPDH was used as an internal control, and data were calculated using the relative quantification ($2^{\Delta\Delta Cq}$) method.

The primers used were ERBB2, Forward: 5'-AGCCTTGCCCCATCAACT G-3', Reverse: 5'-AATGCCAACCACCGCAGA-3'; GAPDH, Forward: 5'-ATCTGGCA CCACACCTTCTACAAT-3', Reverse: 5'-CCGTCACCGGAGTCCATCA-3'.

Western blotting

RB tissues and cells were lysed as described previously (9). A bicinchoninic acid protein assay kit (Pierce; Thermo Fisher Scientific, Inc.) was used to detect total protein concentration. After SDS-polyacrylamide gel (SDSPAGE) electrophoresis and transferring to nitrocellulose filter (NC) membranes, the proteins were blocked with 5-10% skimmed milk, primary antibodies, and the corresponding secondary antibodies. Then the enhanced chemiluminescence detection system was applied for scanning the protein bands. GAPDH was used as a control.

CCK-8 assay

RB cells were seeded into 96-well microplates and incubated for 24 h. The cell viability was detected every 24 h for 96 h. Then, CCK-8 solution (10 µl) was added and cultured for another 2 h at 37°C. A Bio-Rad microplate reader (Hercules, CA, USA) was used to read the absorbance of the specimens at 490 nm.

Transwell assay

Transwell assays were used to detect RB cell migration and invasion. The experimental steps were almost the same except for the membranes with or without Matrigel-coating. RB cells were placed into the upper chamber, and the complete medium containing with 5% FBS was seeded in the lower chamber. After incubation for 24 h, RB cells were fixed and stained, and then photographed and calculated.

Statistical analysis

The data were presented as mean ± SD of triplicate experiments. Statistical analyses were performed using SPSS 22.0 software. Differences between the groups were analyzed using Student's *t*test or ANOVA followed by Tukey's multiple range post-hoc test. Log-rank test was carried out for determining survival analysis. A p value < 0.05 was considered to be a significant difference.

RESULTS

High expression of ERBB2 was associated with the prognosis of RB patients

To investigate whether ERBB2 was associated with RB progression, its expression was detected by RT-PCR in RB tissues. As shown in Fig. 1A, ERBB2 expression was increased significantly in RB tissues (n=70) compared to normal tissues (n=15). Kaplan-Meier survival analysis results showed that high ERBB2 exerted poor prognosis, while low ERBB2 predicted good prognosis of patients with RB (Fig. 1B). Then, ERBB2 expression was measured in RB cells by RT-PCR. As expected, ERBB2 was elevated significantly in both Y79 and SO-RB50 RB cell lines in comparison with normal control cells ARPE-19 (Fig. 1C). These data indicated that ERBB2 was increased in RB and its high expression predicted poor prognosis of RB patients, which suggests that ERBB2 might be a potential biomarker for diagnosing RB.

Knockdown of ERBB2 impeded RB cell viability, migration and invasion

To investigate the functional role of ERBB2 in RB progression *in vitro*, ERBB2 expression was inhibited by ERBB2 siRNA. As shown in Fig.

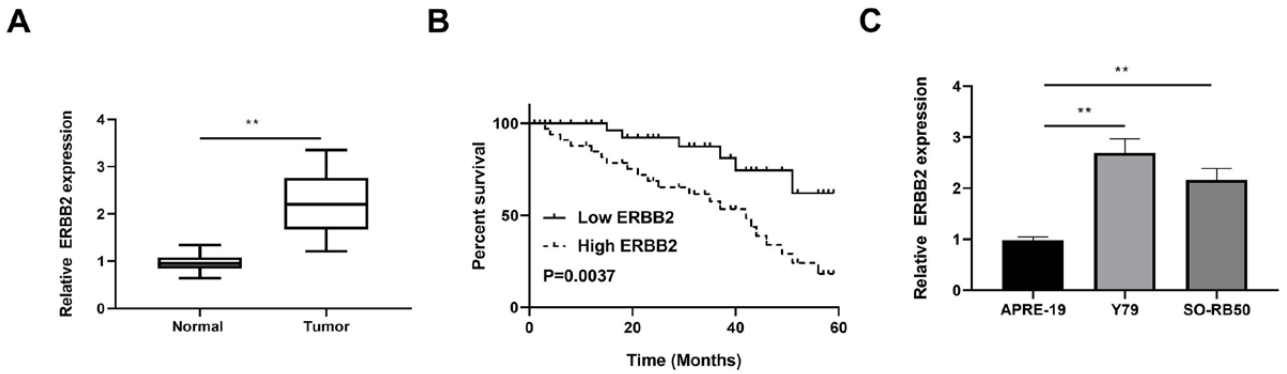

Fig. 1. *High expression of ERBB2 was associated with the prognosis of RB patients.* ***A****) Detection of ERBB2 mRNA expression in tumor tissues (n=70) and normal tissues (n=15) by RT-PCR.* ***B****) The relationship between ERBB2 and overall survival of RB patients.* ***C****) MiR-375 expression measured in Y79 and SO-RB50 cells via RT-PCR. *P<0.05, **P<0.01*

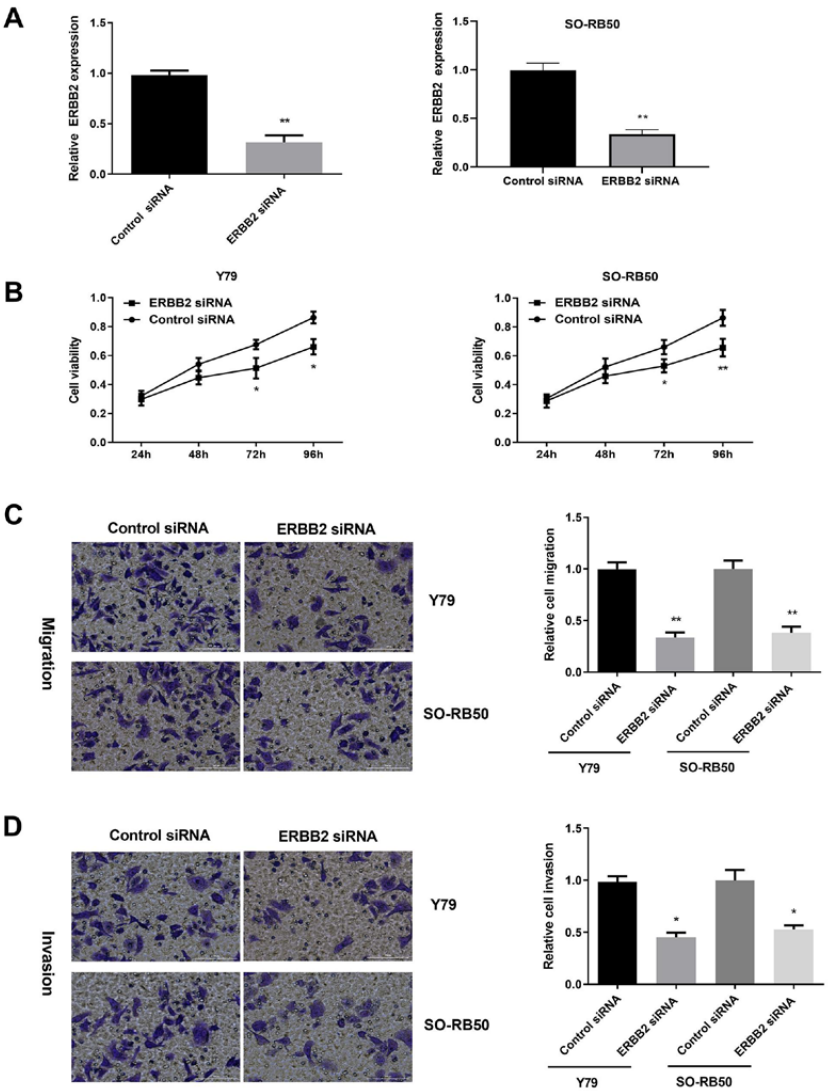

Fig. 2. *Decreasing ERBB2 inhibited RB progression. A) Relative ERBB2 mRNA expression measured in Y79 and SO-RB50 cells after treated with ERBB2 siRNA.* ***B****) Y79 and SO-RB50 cell viability tested after silencing ERBB2.* ***C****) Cell migration (****D****) cell invasion detected in Y79 and SO-RB50 cells after silencing ERBB2. *P<0.05, **P<0.01*

2A, ERBB2 expression was decreased by 68.4% in ERBB2 siRNA Y79 cells and reduced by 66% in ERBB2 siRNA SO-RB50 cells compared to the control group. CCK-8 assay results displayed that silence ERBB2 inhibited cell viability of Y79 and SO-RB50 cells (Fig. 2B). In addition, Transwell assays were applied to measure RB cell migration and invasion. The findings showed that silence ERBB2 suppressed RB cell migration and invasion in both RB cells (Fig. 2 C, D). These results demonstrated that down-regulation of ERBB2 suppressed RB progression.

Overexpression of ERBB2 promoted RB cell viability, migration and invasion

Then, ERBB2 expression was increased by ERBB2 vector. ERBB2 expression was increased notably in both Y79 and SO-RB50 cells after transfected with ERBB2 vector compared to the control group (Fig. 3A). CCK-8 assay results

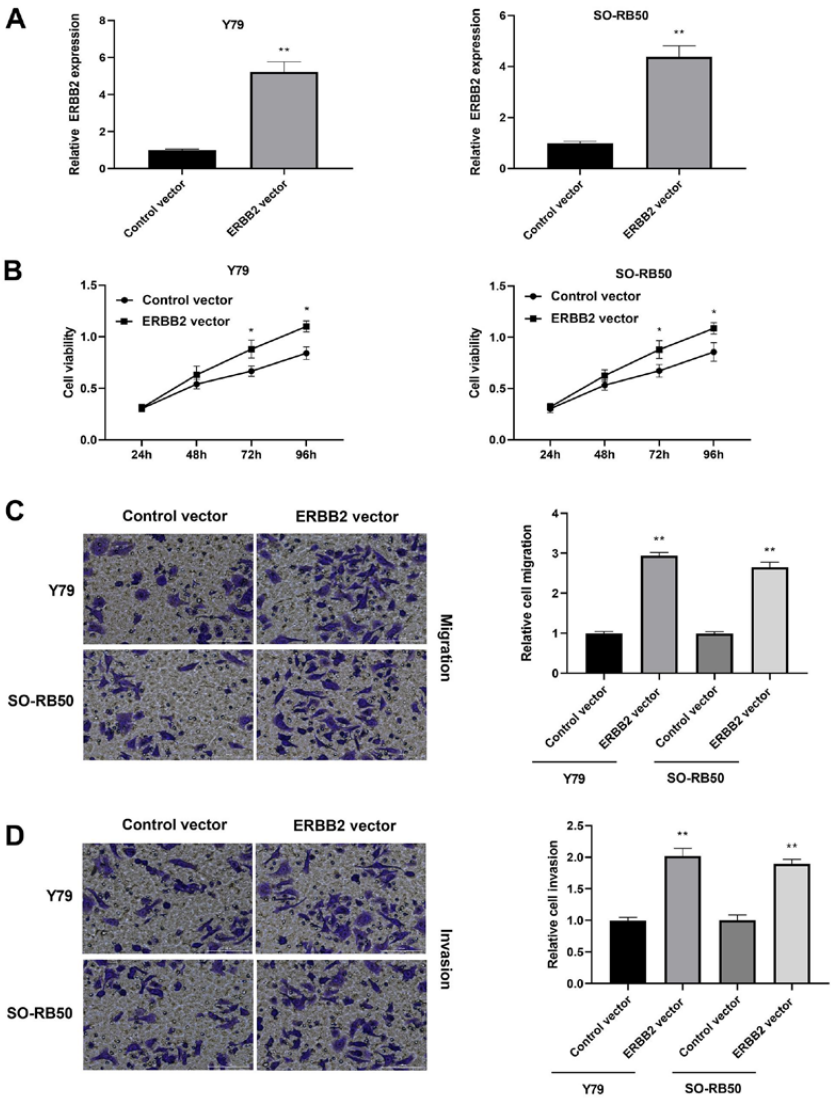

Fig. 3. *Increasing ERBB2 promoted RB progression.* ***A****) Relative ERBB2 expression measured in Y79 and SO-RB50 cells after treated with ERBB2 vector.* ***B****) Y79 and SO-RB50 cell viability tested after increasing ERBB2.* ***C****) Cell migration (****D****) cell invasion detected in Y79 and SO-RB50 cells after ERBB2 overexpression. *P<0.05, **P<0.01*

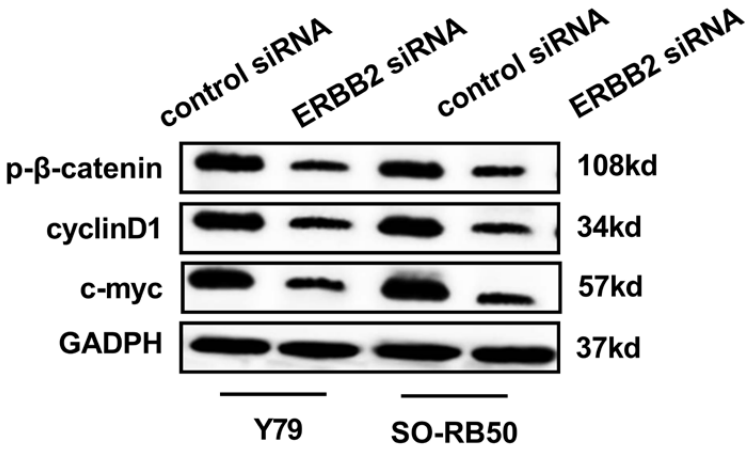

Fig. 4. *Silencing ERBB2 inhibited Wnt/β-catenin pathway. Detection of p-β-catenin, cyclind1 and c-myc protein level in Y79 and SO-RB50 cells after treated with ERBB2 sirna.*

displayed that overexpression of ERBB2 promoted cell viability of Y79 and SO-RB50 cells (Fig. 3B). In addition, Transwell assay results showed that overexpression of ERBB2 enhanced RB cell migration and invasion in both RB cells (Fig. 3 C, D). These results demonstrated that up-regulation of ERBB2 facilitated RB progression.

Knockdown of ERBB2 inhibited Wnt/β-catenin pathway

Previous study has found that ERBB2 could activate Wnt/β-catenin axis in tumors development (19). Here, we investigated whether the Wnt/β-catenin axis was involved in RB progression modulated by ERBB2. Down-regulation of ERBB2 repressed the downstream genes of Wnt/β-catenin pathway, including p-β-catenin, cyclinD1 and c-myc in both Y79 and SO-RB50 cells (Fig. 4). The data indicated that down-regulation of ERBB2 impedes RB cell progression through Wnt/β-catenin pathway.

DISCUSSION

Increasing evidence has shown that ERBB2 exhibited an important role in tumors development (11). Here, we demonstrated that ERBB2 was increased in RB and its up-regulation predicted the poor prognosis of RB patients. Moreover, decreasing ERBB2 repressed RB cell viability, invasion and migration. More importantly, Wnt/β-catenin pathway was involved in RB progression modulated by ERBB2.

ERBB2 was reported as an oncogene in various cancers. Yu X et al. reported that ERBB2 contributed to the promotion of proliferation and metastasis of lung cancer (12). Hedegger et al. showed that overexpression of ERBB2 enhanced cell viability of pancreatic ductal adenocarcinoma (5). Moreover, Hulit J et al. demonstrated that ERBB2 participates in mammary tumor growth through Wnt/β-catenin signaling pathway (10). However, the possible effects of ERBB2 on RB remains obscure. The present study, showed that ERBB2 was increased significantly in RB, and silencing ERBB2 inhibited RB cell viability, migration and invasion. Moreover, we further investigated the underlying mechanism of ERBB2 in RB progression, and the results showed that silencing ERBB2 inhibited the activation of Wnt/β-catenin signaling pathway, suggesting that ERBB2 might be a possible marker for treatment of RB.

Taken together, our findings demonstrated that ERBB2 was increased in RB and down-regulation of ERBB2 repressed RB progression through Wnt/β-catenin pathway, suggesting that ERBB2 might be a potential target for RB treatment.

REFERENCES

1. Dimaras H, Dimba EA, Gallie BL. Challenging the global retinoblastoma survival disparity through

a collaborative research effort. Br J Ophthalmol 2010; 94:1415-6.
2. Palma J, Sasso DF, Dufort G, et al. Successful treatment of metastatic retinoblastoma with high-dose chemotherapy and autologous stem cell rescue in South America. Bone Marrow Transplant 2012; 47:522-7.
3. Dahmke IN, Trampert P, Weinberg F, Mostajeran Z, Lautenschlager F, de Jonge N. Correlative fluorescence- and electron microscopy of whole breast cancer cells reveals different distribution of ErbB2 dependent on underlying actin. Front Cell Dev Biol 2020; 8:521.
4. Eldad S, Hertz R, Vainer G, Saada A, Bar-Tana J. Treatment of ErbB2 breast cancer by mitochondrial targeting. Cancer Metab 2020; 8:17.
5. Hedegger K, Algul H, Lesina M, Blutke A, Schmid RM, Schneider MR, Dahlhoff M. Unraveling ERBB network dynamics upon betacellulin signaling in pancreatic ductal adenocarcinoma in mice. Mol Oncol 2020; 14:1653-69.
6. Seigel GM, Sharma S, Hackam AS, Shah DK. HER2/ERBB2 immunoreactivity in human retinoblastoma. Tumour Biol 2016; 37:6135-42.
7. Polakis P. Wnt signaling and cancer. Genes Dev 2000; 14:1837-51.
8. Jung DH, Bae YJ, Kim JH, Shin YK, Jeung HC. HER2 Regulates cancer stem cell activities via the Wnt signaling pathway in gastric cancer cells. Oncology 2019; 97:311-18.
9. Lai YJ, Lin CI, Wang CL, Chao JI. Expression of survivin and p53 modulates honokiol-induced apoptosis in colorectal cancer cells. J Cell Biochem 2014; 115:1888-99.
10. Hulit J, Lee RJ, Li Z, et al. p27Kip1 repression of ErbB2-induced mammary tumor growth in transgenic mice involves Skp2 and Wnt/beta-catenin signaling. Cancer Res 2006; 66:8529-41.
11. Kunst N, Wang SY, Hood A, Mougalian SS, DiGiovanna MP, Adelson K, Pusztai L. Cost-effectiveness of neoadjuvant-adjuvant treatment strategies for women with ERBB2 (HER2)-positive breast cancer. JAMA Netw Open 2020; 3:e2027074.
12. Yu X, Lin Q, Liu F, Yang F, Mao J, Chen X. LncRNA TMPO-AS1 facilitates the proliferation and metastasis of NSCLC cells by up-regulating ERBB2 via sponging miR-204-3p. Int J Immunopathol Pharmacol 2020; 34:2058738420958947.

LETTER TO THE EDITOR

Role and mechanism of mirna-214-5p in myocardial injury in hypertensive rats

FJ. Qi[1], Z. Dong[1], XM. Zhang[1], RK.Yi[2], LY. Xie[1], HJ. Teng[1], JH. Lin[1] and C. Jia[3]

[1]The second ward of cardiovascular medicine, General Hospital of Fushun Mining Bureau of Liaoning Health Industry Group, Fushun, Liaoning, China; [2]The first ward of cardiovascular medicine, General Hospital of Fushun Mining Bureau of Liaoning Health Industry Group, Fushun, Liaoning, China; [3]Department of Dialysis, General Hospital of Fushun Mining Bureau of Liaoning Health Industry Group, Fushun, Liaoning, China

Received August 6, 2020 – Accepted December 21, 2020

To the Editor,

Long-term poor control of hypertension can cause changes in the structure and function of the heart, leading to hypertensive heart disease (1). The gradual impairment of cardiac systolic function eventually leads to cardiac insufficiency. It has been shown that 70% of heart failure is caused by hypertension. At the same time, cardiac complications, such as coronary heart disease and atrial fibrillation, may also occur (2). Cardiomyocyte damage caused by hypertension cannot be ignored. A growing number of studies have shown that the decrease in the number of cardiomyocytes caused by apoptosis is the main cause of ventricular dilatation and progressive heart dysfunction, and ultimately leads to end-stage heart failure (3).

However, a new mode of cell death, pyrolysis, has been discovered recently. Pyrolytic cells and apoptotic cells share some common morphological and biochemical changes, and the TUNEL test results of both types of cells are positive. Therefore, early studies tended to incorrectly identify pyrolysis as apoptosis (4). In a hypertensive rat model, electron microscopy results showed that a large number of cardiomyocytes displayed morphological features similar to pyrodecae cells, such as mitochondrial swelling, vacuolization, muscle fiber disorder and dissolution, cell swelling, and cell membrane irregularity (5). However, it is not clear whether the cells damaged by hypertension will undergo pyrolysis.

MiRNA is considered to be a key regulator of cardiovascular diseases, including myocardial infarction, heart failure, myocardial hypertrophy and arrhythmia. MiR-214-5p is processed from the 5' arm of miR-214 and can target p21 to activate protein kinase 4 (PAK4), a conserved serine/threonine protein kinase that phosphorylates downstream substrates to participate in the regulation of many cellular processes such as cell proliferation, differentiation, cytoskeleton remodeling and apoptosis (6). However, the effect and mechanism of miR-214-5p underlying myocardial pyrolysis caused by hypertension still remain unclear.

MATERIALS AND METHODS

Animals

Sixty healthy male Wistar rats, weighing 220-270g, were provided by Nanjing Junke Bioengineering Co., Ltd., China. Partial thermocoagulation was performed on the anterior branches of bilateral renal arteries in the rats (7). The rats were fed with a high-salt, high-fat, and high-cholesterol chow for 6 consecutive weeks to establish a rat

Key words: miR-214-5p; hypertensive rats; pyroptosis; myocardial injury

Corresponding Author:
Dr Fengjun Qi,
The Second Ward of Cardiovascular Medicine,
General Hospital of Fushun Mining Bureau
of Liaoning Health Industry Group,
Fushun, 113008, Liaoning, China
e-mail: qifengjunsgyy@163.com

0393-974X (2021)
Copyright © by BIOLIFE, s.a.s.
This publication and/or article is for individual use only and may not be further reproduced without written permission from the copyright holder.
Unauthorized reproduction may result in financial and other penalties
DISCLOSURE: ALL AUTHORS REPORT NO CONFLICTS OF INTEREST RELEVANT TO THIS ARTICLE.

hypertension model. An RBP-1B rat sphygmomanometer was used to measure the tail blood pressure once a week. After sacrifice by anesthesia, the hearts of rats were quickly removed by thoracotomy and washed with 0.9% sodium chloride. One part of the myocardium was fixed with paraformaldehyde to observe morphological changes. The remaining part of the myocardial tissue was stored at -70°C to detect the expression of related genes and proteins. All procedures of animal experiments were in compliance with international animal care and management regulations, and were approved by the Ethics Committee of the General Hospital of Fushun Mining Bureau of Liaoning Health Industry Group.

Pyroptosis detected by flow cytometry

The cells were seeded in 24-well plates at 5×10^5/well, and then treated with phosphate buffer saline (PBS) containing 5 μg/mL Hoechst 33342 and 10 μg/mL propidium iodide (PI). Cell pyroptosis was observed by flow cytometry, and the content of lactate dehydrogenase in the supernatant of each group was detected by a biochemical analyzer to reflect the extent of cell lysis.

Real-time PCR

The total RNA of each sample was extracted using a Trizol total RNA extraction kit. The obtained RNA was then reversely transcribed into cDNA using a reverse transcription kit. The reaction system was as follows: 1 μL of cDNA, 10 μL of SYBR® GREEN Master Mix, 0.5 μL each of upstream and downstream primers (Table I), and 8 μL of ddH_2O, for a total volume of 20 μL. Each sample was tested in triplicate wells, and U6 was used as the internal control. The reaction conditions were as follows: pre-denaturation at 95°C for 10 min, followed by 40 cycles of 10 s at 95°C, 20 s at 60°C, and 30 s at 72°C.

Primary cultured rat cardiomyocytes in the control group and the hypertension group

The rat heart was taken out via aseptic surgery along with the large blood vessels and atrial tissues attached to the heart, and washed 3-4 times with D-Hank's solution at 4°C to remove residual blood. After the tissues were cut into 1 mm^3 blocks, they were digested in 4 ml of 0.0625% trypsin solution at 37°C for 3 min in a constant temperature water bath, and the supernatant was discarded. After adding 5 mL of mixed digestion solution (0.0625% trypsin + 0.1% type II collagenase) to the remaining sediment and incubating in a 37°C water bath for 8-10 min (shaken 2 to 3 times during this period), a pre-cooled Dulbecco's Modified Eagle Medium/Ham's F-12 (DMEM/F-12) medium containing 10% fetal bovine serum was added to stop the digestion. The process was repeated 7-8 times until the tissue mass was completely digested. After each centrifugation at 1,000 r/min for 8 min, the supernatant was collected and the digestion was terminated, and then the supernatant was filtered with a nylon mesh to remove the remaining tissue mass, and the precipitate was suspended in the culture medium. The myocardial fibroblasts were removed by the differential adherence separation method every 2 hours. The non-adherent myocardial cell suspension was aspirated and the cell density was adjusted before seeding into cell culture plates. 0.1mmol/LBrdU was added to inhibit the growth of fibroblasts 3 days before culture, and the medium was changed within 48 h after the culture was started.

Cell transfection

When the confluence in the hypertensive group reached 60-80% after 24 h of culture, the Lipofectamine2000 transfection reagent was used to transfect the cells with miR-214-5p mimics or NC mimics at a final concentration

Table I. *Primer sequence.*

Name	Primer sequence (5'-3')	
miRNA-214-5p	Upstream primer	TGCGGACAGCAGGCACAGAC
	Downstream primer	CCAGTGCAGGGTCCGAGGT
β-actin	Upstream primer	CTCGCTTCGGCAGCACA
	Downstream primer	AACGCTTCACGAATTTGCGT

of 20 nmol/L. The transfection mixture was prepared using a serum-free DMEM. After transfecting miR-214-5p into the cells in the hypertensive group, the cells were named the miR-214-5p group.

Apoptosis detected by PI and Hoechst staining

PI was dissolved in PBS (pH 7.4) containing 0.1% TritionX-100 and 100μg/ml of RNase to a final concentration of 50μg/ml, and stored in the dark. Apoptotic cell suspension was prepared at a concentration of 10^6 cells/ml. 1 ml of cell suspension was mixed with 10 μl of PI staining solution and reacted for 10 min. Then, 5 ml of PBS were added and the mixture was centrifuged at 1,500r/min for 5 min. The supernatant was discarded and the washing was repeated twice. The cells were resuspended and placed on glass slides, stained with a 2μg/ml Hoechst dye at room temperature for 2 min, washed with water for 2 min, dried by baking the slides in an oven at 42°C to 55°C for 30 to 60 min, cooled to room temperature, and observed under a fluorescence microscope. The nuclei of normal live cells were stained red by PI, and all cells were stained blue by PI and Hoechst. The presence of complementary base pairs of miR-214-5p in PAK4 was predicted by Targetsacn 7.2.

Western blot assay

The myocardial tissue was collected, rinsed with PBS, added with a corresponding volume of lysate, and left on ice for 5 min. The lysate was then mixed and transferred to a new Eppendorf (EP) tube. Using a high-speed centrifuge,

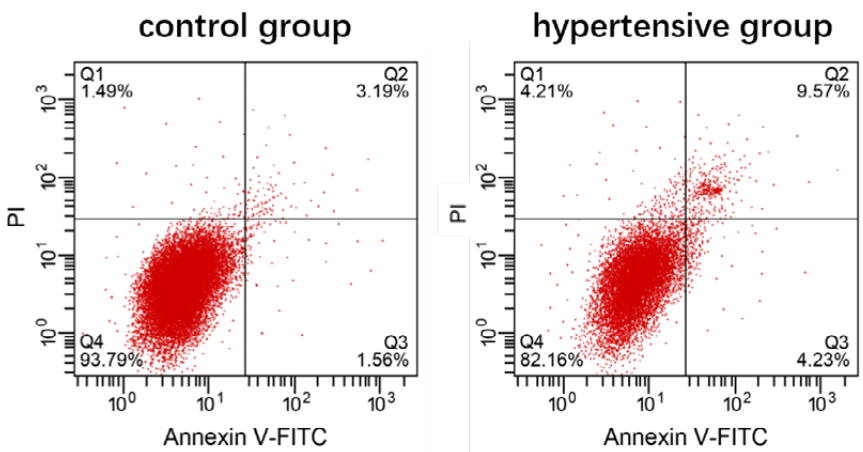

Fig. 1. *The pyroptosis in each group was analyzed by flow cytometry.*

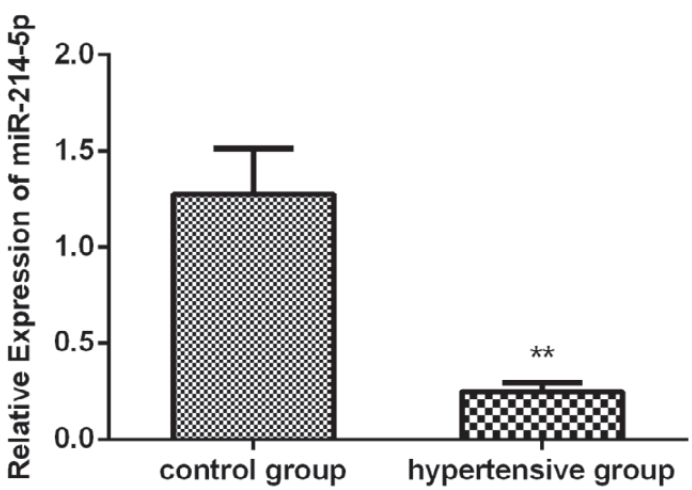

Fig. 2. *The expression level of miRNA-214-5p in myocardial tissues.*

the EP tube was centrifuged at 12,000 rpm and 4°C for 10 min. The obtained supernatant was the total protein extract of the cells. The protein concentration was determined by a bicinchoninic acid (BCA) assay. After diluting the supernatant of each group to the same protein concentration with a 1×SDS gel buffer, the protein samples were further diluted with a 5×loading buffer and PBS, boiled in water for 5 min and denatured. The denatured protein liquid was added to a 12% SDS-PAGE gel and electrophoresed for 60-120 min at 80V constant pressure. The SDS-PAGE gel was placed on a nitrocellulose membrane to carry out constant current transfer. 3% bovine serum albumin (BSA) was used for blocking at 4°C. After blocking, the nitrocellulose membrane was washed with PBS, and monoclonal anti-caspase-1, anti-IL-1β, and anti-GAPDH antibodies were added at a 1:500 dilution, respectively. The membrane was incubated at room temperature for 45 min, washed with PBS, and incubated with horseradish peroxidase labeled secondary antibodies (1:1000 dilution) at room temperature for 30 min. Then, the nitrocellulose membrane was washed with PBS, and an electrochemiluminescence (ECL) chemiluminescence agent was used to generate chemiluminescence. Kodak X was used to expose the nitrocellulose membrane for about 3 min. The X-ray film was scanned by a scanner, and the gray analysis of the strips was processed by the Gel-Pro Analyzer software. The gray value of each band was measured by the software in three independently repeated experiments, and the ratio of gray value of the target gene to that of GAPDH was used as the relative protein expression.

Statistical analysis

The data were analyzed with SPSS 22.0. The measurement data were shown in ($\bar{x}$ ±s). The comparison

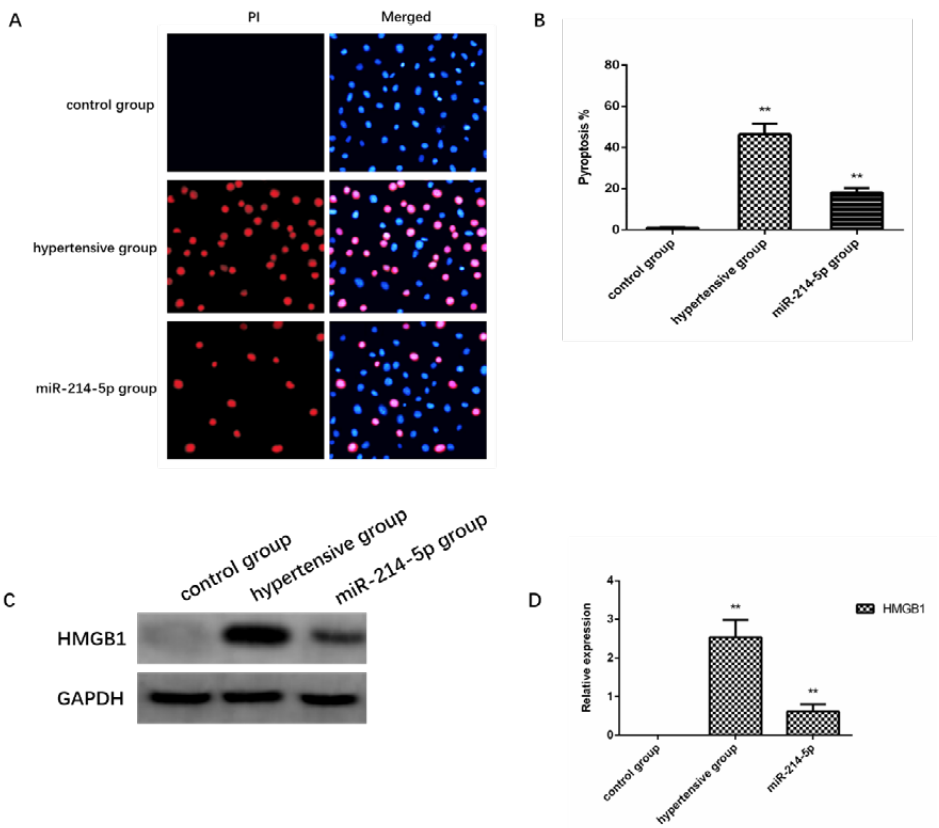

Fig. 3. *MiR-214-5p inhibited pyroptosis in the cardiomyocytes of hypertensive rats.* ***A****) Cell death was detected with PI (red in live cells) and Hoechst 33342 (blue in all cells);* ***B****) 5 randomly selected PI-positive cells in a field containing 100 cells for quantification ($\bar{x}$ ±s, n = 5);* ***C****) Western blot was used to detect the expression levels of HMGB1 in cell lysate and supernatant (Sup). Tubulin was used as the loading control of cell lysate;* ***D****) histogram of the relative intensity of HMGB1 in Western blot ($\bar{x}$ ±s, n = 3).*

between two groups was made with the paired *t*-test, and the comparison of three groups was carried out with one-way analysis of variance. P<0.05 indicated statistical difference.

RESULTS

The results of flow cytometry are shown in Fig. 1. The pyroptosis rate in the hypertension group was 9.57%, which was significantly higher than 3.19% in the normal control group (P<0.05).

The real-time quantitative PCR results in Fig. 2 showed that compared with the normal control group, the expression of miRNA-214-5p in tissues of myocardial injury was lower (p<0.05).

MiR-214-5p inhibited the pyroptosis of cardiomyocytes in hypertensive rats

Pyrolysis was analyzed using PI staining and the assay of the release of labeled HMGB1 proteins. As shown in Fig. 3 A and B, the cells in the hypertension group became round and swollen, and cell fragments could be seen. The PI dye penetrated the cell membrane and entered the nucleus, causing the surviving cells to emit red fluorescence. After statistical calculations, the pyrolysis rate was about 47%. However, after miR-214-5p transfection, cell pyrolysis was significantly reduced to a pyrolysis rate of about 18%. Western blot analysis showed that miR-214-5p could inhibit hypertension-induced secretion of HMGB1 in the supernatant of rat cardiomyocytes (Fig.s 3C, 3D). The above results indicated that miR-214-5p could inhibit the pyrolysis of myocardial cells in hypertensive rats.

Effect of miR-214-5p on the expression of PAK4, caspase-1 and IL-1β proteins

Using targetsacn7.2 to predict and analyze the target mRNAs of miRNA-214-5p, the potential mRNA targets of miRNA-214-5p were found. The Western blot results (Fig. 4) showed that, compared with the normal control group, PAK4 protein was down-regulated while caspase-1 and IL-1β proteins were up-regulated in the hypertension group. MiR-214-5p could up-regulate the expression of PAK4 protein and inhibit the expression of caspase-1 and IL-1β proteins.

DISCUSSION

Similar to necrosis, cell swelling, membrane

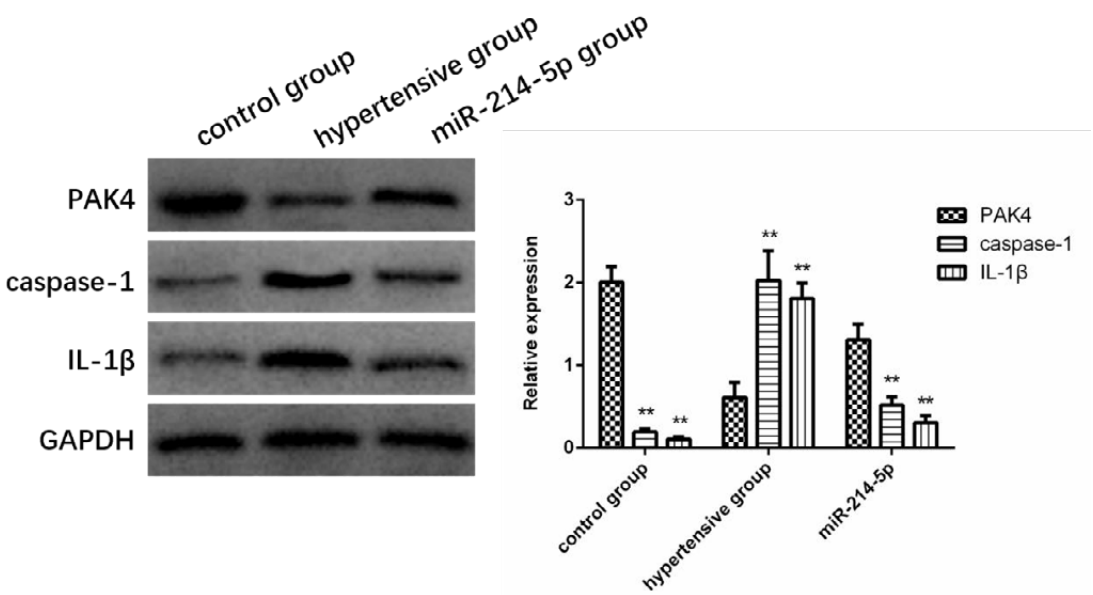

Fig. 4. *Relative expression of PAK4, caspase-1 and IL-1β proteins in each group.*

rupture, cytoplasm and content leakage can cause a series of inflammatory reactions (7). The results showed that when the cells pyrolyze, the integrity of the cell membrane was disrupted to form pores of 1 to 2 mm in diameter, which then disrupted the ion balance in the cells, leading to water inflow and osmotic dissolution of the cells (8). In the process of coronary heart diseases, such as myocardial infarction and heart failure, focal death of cardiomyocytes caused by inflammation is involved in myocardial injury and ventricular remodeling (9). A recent study has confirmed that miR-30d can regulate cardiomyocyte pyrolysis in diabetic cardiomyopathy by directly targeting foxo3a (10). MiR-9 can inhibit the carbonization of human ventricular myocytes treated with high glucose (11). It has been shown that the lack of miRNA-214 can lead to severe myocardial ischemia by promoting fibrosis and cardiomyocyte apoptosis (12), therefore, it is hypothesized that the overexpression of miR-214-5p can inhibit cell pyrolysis, suggesting that the low expression of miRNA-214-5p is related to elevated cell pyrolysis. In addition, the binding sites of miRNA-214-5p in PAK4-3'-UTR were screened in this study using genetic prediction. This study provides experimental data for targeted therapy of hypertensive myocardial injury. Overexpression of miRNA-214-5p can reduce myocardial injury, but its specific molecular mechanism needs further study.

ACKNOWLEDGMENT

This work was supported by the general project of Liaoning Province Science and technology fund (No. 2019-MS-188).

REFERENCES

1. Singh JP, Larson MG, Tsuji H, Evans JC, O'Donnell CJ, Levy D. Reduced heart rate variability and new-onset hypertension: insights into pathogenesis of hypertension: the Framingham Heart Study. Hypertension 1998; 32(2):293-97.
2. Klein I, Danzi S. Thyroid Disease and the Heart. Curr Probl Cardiol 2016; 41(2):65-92.
3. Franchi L, Eigenbrod T, Muñoz-Planillo R, Nuñez G. The inflammasome: a caspase-1-activation platform that regulates immune responses and disease pathogenesis. Nat Immunol 2009; 10(3):241-47.
4. Hilbi H, Moss JE, Hersh D, et al. Shigella-induced apoptosis is dependent on caspase-1 which binds to IpaB. J Biol Chem 1998; 273(49):32895-900.
5. Vande Walle L, Lamkanfi M. Pyroptosis. Curr Biol 2016; 26(13):R568-R572.
6. Doggrell SA, Brown L. Rat models of hypertension, cardiac hypertrophy and failure. Cardiovasc Res 1998; 39(1):89-105.
7. Duprez L, Wirawan E, Vanden Berghe T, Vandenabeele P. Major cell death pathways at a glance. Microbes Infect 2009; 11(13):1050-62.
8. Labbé K, Saleh M. Cell death in the host response to infection. Cell Death Differ 2008; 15(9):1339-49.
9. Wang Q, Ma S, Li D, et al. Dietary capsaicin ameliorates pressure overload-induced cardiac hypertrophy and fibrosis through the transient receptor potential vanilloid type 1. Am J Hypertens 2014; 27(12):1521-29.
10. Li X, Du N, Zhang Q, et al. MicroRNA-30d regulates cardiomyocyte pyroptosis by directly targeting foxo3a in diabetic cardiomyopathy. Cell Death Dis 2014; 5(10):e1479.
11. Jeyabal P, Thandavarayan RA, Joladarashi D, et al. MicroRNA-9 inhibits hyperglycemia-induced pyroptosis in human ventricular cardiomyocytes by targeting ELAVL1. Biochem Biophys Res Commun 2016; 471(4):423-29.
12. Ghaderi S, Alidadiani N, SoleimaniRad J, et al. DJ1 and microRNA-214 act synergistically to rescue myoblast cells after ischemia/reperfusion injury. J Cell Biochem 2018; 119(9):7192-203.

LETTER TO THE EDITOR

Expression of Disrupted-in-schizophrenia 1 protein and related inflammatory factors in refractory temporal lobe epilepsy in children

BH. Feng[1], CB. Huang[2] and ZF. Yuan[3]

[1]Department of Pediatrics, Ningbo Medical Center Lihuili Hospital, Ningbo, Zhejiang Province, China; [2]Department of Pediatrics, Yueqing Maternal and Child Health Care Hospital Wenzhou, Zhejiang Province, China;[3]Department of Neurology, The Children's Hospital of Zhejiang University School of Medicine, Hangzhou, Zhejiang Province, China

Received October 16, 2020 – Accepted December 21, 2020

To the Editor,

Epilepsy is a chronic disorder of the central nervous system (CNS) caused by disturbances in the electric brain activity (1). Temporal lobe epilepsy (TLE) is an important type of refractory epilepsy (RE) (1). Research has shown that activation of adaptive and innate immunity is implicated in RE (2). Activated T cells stimulate the microglial cells to produce pro-inflammatory factors and to cause neuronal damage (2). Necrotic neurons activate microglial cells, forming a vicious cycle, which is regarded as the critical cause of seizures and the persistence of epilepsy (3). Protein kinase B (PKB), also known as Akt, is a serine/threonine-protein kinase implicated in multiple cellular processes such as cell proliferation, apoptosis and cell migration (4). Numerous animal and human experiments have confirmed that the expression of AKT protein in epilepsy pathological tissues was increased (4, 5). Disrupted-in-Schizophrenia 1 (DISC1) is an important candidate gene associated with mental illness. Studies have shown that DISC1 is not only related to schizophrenia but also with various signaling pathways implicated in neurodevelopmental abnormalities and intracellular brain dysfunctions (6). DISC1 protein can inhibit AKT protein expression (7). Cognitive disorders, mental disorders, and other similar mental illness manifestations are expected to be observed in epileptic patients (8). DISC1 can therefore be a therapeutic target for mental illness and epilepsy that is worth investigating. This study aimed to investigate the expression of DISC1 protein and its related inflammatory factors in epileptic focus and non-epileptic focus brain tissues of RTLE pediatric patients, as well as to explore the influences of DISC1 on mental status and cognitive functions in patients with epilepsy.

MATERIALS AND METHODS

In this study, 16 pediatric patients with confirmed RTLE after surgical treatment were included between March 2018 and October 2019 in Ningbo Medical Center Lihuili Hospital. Their postoperative epileptogenic brain tissue archive wax blocks (the RTLE group) and peritumoral non-epileptic focus brain tissue wax blocks (the control group) were selected and used in the study. The patients had not received chemotherapy or other treatments prior to surgery. During surgery, the cerebral cortex and deep electrode monitoring results were used to obtain epileptic focus tissue samples from non-functional

Key words: temporal lobe epilepsy; DISC1 protein; inflammatory factors; mental state; cognitive function

Corresponding Author:
Dr Chongbin Huang,
Department of Pediatrics,
Yueqing Maternal and Child Health Care Hospital Wenzhou,
325600, Zhejiang Province, China
e-mail: huangcbcbwork@163.com

0393-974X (2021)
Copyright © by BIOLIFE, s.a.s.
This publication and/or article is for individual use only and may not be further reproduced without written permission from the copyright holder.
Unauthorized reproduction may result in financial and other penalties
DISCLOSURE: ALL AUTHORS REPORT NO CONFLICTS OF INTEREST RELEVANT TO THIS ARTICLE.

areas. The non-epileptic focus brain tissue around the tumor was considered the non-functional brain tissue that did not cause abnormal electroencephalography (EEG) during surgery and had no epilepsy focus tissue after surgery. Each legal tutor of the children included in the study signed informed consent for participation in the study. The study was approved by the Ethics Committee of Ningbo Medical Center Lihuili Hospital, China.

Sample tissues

The brain tissues were fixed with 4% paraformaldehyde (pH=7.4, 4°C) and placed in a solution containing 30% sucrose and stored at 4°C until the sample sank to the bottom. After being embedded with Optimal Cutting Temperature (OTC), the samples were continuously sectioned with a cryostat microtome (Beijing Shiji Kexin Scientific Instrument Co., Ltd, China) at a thickness of 16 μm. Then, the sections were stored at -20°C for further analysis.

Nissl staining

The tissue sections were brought from -20°C to room temperature for 30 min. After rewarming, the sections were washed with deionized water for 3 min and stained with violet A staining solution (Biofount, China) in a 56°C incubator for 1 h. Next, the sections were washed with deionized water for 3 min and differentiated with violet B differentiation solution (Biofount, China) for 1 min. Then, they were quickly dehydrated in 75%, 95%, and 100% alcohol, for 3 min each time. After the staining was completed, the sections were decoloured with xylene (Biofount, China) for 5 min × 2 times, covered with neutral resin, and observed and photographed under a microscope (IX53 type; Olympus, Japan).

Hematoxylin and Eosin (H&E) staining

The tissue sections were brought from -20°C for rewarming at room temperature for 30 min. The sections werethen washed with distilled water for 2 min and stained with hematoxylin staining solution (Coolaber Science and Technology Ltd., China) for 5 min. Next, the excess staining solution was washed with tap water. The sections were differentiated for 5s in 1% hydrochloric acid ethanol (Tianjin Bohua Chemical Reagent Co., Ltd., China) and then washed with tap water for 1 min. The sections were washed with 1% ammonia water (Foshan Huaxisheng Chemicals Co., Ltd., China) for 5s until coloured blue. Afterwards, they were washed with tap water for 2 min and then stained with eosin staining solution (Coolaber Science and Technology Ltd., China) for 10 s. The excess staining solution was washed with tap water. Successively, the sections were dehydrated in 80%, 95%, and 100% alcohol, respectively, for 3 min each time, decoloured with xylene (Biofount, China) for 5 min × 2 times, and covered with neutral resin. The sections were observed and photographed under a microscope (IX53 type; Olympus, Japan).

Immunohistochemical staining

Tissue sections were brought from -20°C for rewarming at room temperature for 3 h. The sections were trimmed to a size of 1 × 1 × 1 cm and fixed with 10% formalin for 24 h. After fixation, they were prepared into continuous 5-μm paraffin sections. The paraffin sections were de-waxed and dehydrated. The sections were placed in a container with antigen retrieval buffer and boiled for 1 h, then washed with 0.01M Phosphate Buffered Saline (PBS) for 5 min × 3 times. The water was dried. The antigen was blocked with 10% goat serum (Nanjing Shenghang Biotechnology Ltd., China), and the sections were incubated at 37°C for 1 h. Afterwards, the serum was decanted, and the first antibody (rabbit anti-DISC1-polyclonal antibody [1:200] (Signalway Antibody, USA); rabbit anti-AKT-monoclonal antibody [1:500] (Cell Signaling, USA); rabbit anti-HMGB1-monoclonal antibody [1:1,000] (Abcam, USA); mouse anti-IL-6-monoclonal antibody [1:500] (Abcam, USA) and rabbit anti-STAT-3-monoclonal antibody [1:500] (Abcam, USA)) was dripped at a concentration 50 μL/sheet. The sections were stored in a refrigerator at 4°C overnight. The next day, the sections were rewarmed at 37°C for 30 min, then washed with 0.01M PBS for 5 min × 3 times. The second antibody (IgG [1:100] (Beijing Zhongshan Golden Bridge Biotechnology Co., Ltd., China)) labeled with biotin was dripped at a concentration of 1 drop/sheet. Next, the sections were incubated at 37°C for 1 h and then washed with 0.01M PBS for 5 min × 3 times. Subsequently, the sections were dripped with horseradish-labelled streptavidin working solution (Beijing Zhongshan Golden Bridge Biotechnology Co., Ltd., China), incubated at 37°C for 20 min, and washed with 0.01M PBS for 5 min × 3 times. The color of the sections was developed with 3,3'-diaminobenzidine (DAB) (Shanghai Xinyu Biotechnology Co., Ltd.,

China). The reaction was observed under a microscope (IX53 type; Olympus, Japan). Once there were obvious brownish-yellow particles deposited, the sections were immediately washed with tap water. Afterwards, the sections were counterstained with hematoxylin staining solution for 30 s, decolored with hydrochloric acid, washed with tap water for 10 min, and washed with PBS for 5 min to stain blue. After gradient ethanol dehydration, the sections were decolored with xylene and covered with neutral gum. Ten visual fields were randomly selected for each section to count the positive cells in each sample. The average number of positive cells in 10 fields was chosen to calculate the number of positive cells in the sample.

Western blot

The samples were taken out from the refrigerator and chopped into pieces, and the proteins were extracted through the bicinchoninic acid (BCA) method (using BCA detection kits; Pierce, USA). After adding an appropriate amount of separation gel to the gel plate, the surface of the gum flattened with isopropanol. After being solidified at room temperature for 60 min, the upper gel was added. The sample stood at room temperature for 60 min, was boiled at 95°C for 8 to 10 min, and placed in an icebox. After the electrophoresis buffer was added, the protein samples were flattened by 60 V constant-voltage as pre-electrophoresis. When the bromophenol blue reached the junction of the stacking gel and the separation gel, the voltage was increased to 130 V. The electrophoresis was stopped when the bromophenol blue reached the bottom of the separation gel. The PVDF membrane was transferred using a steady current 170 mA for 2 h. Then, the membrane was blocked with 5% skimmed milk powder for 1 h (blocked with 5% BSA for phosphorylated proteins). The 1% BSA antibody diluent was utilized, and the membrane was incubated overnight at 4°C on a shaker after adding the antibody. The membrane was then taken out from 4°C and rewarmed at room temperature for 30 min. Then the membrane was incubated overnight for 2 h at room temperature on a shaker with the secondary antibody (hypothalamic regulatory peptides (HRP)-labeled secondary antibody (1: 5,000) (Abcam, USA)). The signal detection was performed by utilizing the Super Signal West Pico chemiluminescent substrate. The optical density of each band was measured by a gel imaging analysis system (American Eagle Eye II type gel image software (Siemon Company, USA)) and compared with the internal reference band. The ratio obtained was the expression of the target protein.

Statistical analysis

The IBM SPSS 22.0 (IBM, USA) was used for statistical analysis. The results of measurement data were expressed as mean ± standard deviation ($\bar{x}\pm s$). The comparison of the means of two independent samples was performed by using the Student's T-test. When the normal distribution was satisfied while the variances were not, the T' test was utilized. $P<0.05$ was considered statistically significant.

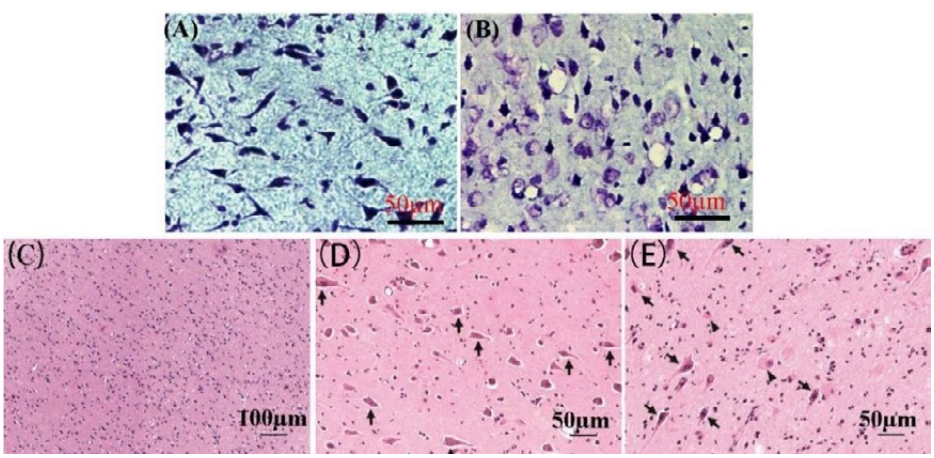

Fig. 1. ***A)*** *Nissl staining in control group tissues;* ***B)*** *Nissle staining in RTLE group tissues;* ***C)*** *H&E staining in brain tissue in the control group;* ***D, E)*** *H&E staining in epileptic focus brain tissues in RTLE group.*

RESULTS

Nissl staining

Abnormal neurons were observed in epilepsy tissues (Fig. 1 A, B). Staining showed that the Nissl bodies became lighter in color and decreased in number, or were dissolved and disappeared. Some neurons presented oedema and vacuole degeneration. In the control group, the nucleus, axons, and dendrites of neurons were easily distinguished. The nucleus of the neurons was dark blue, the Nissl bodies were purple-blue, and the Nissl bodies were massive or granular around the nucleus.

H&E staining

In the low-power visual field, H&E staining showed that in the control group, the lamellar columnar structure of the brain tissue was complete and orderly. Moreover, the unipolar apical dendrites of the neurons pointed uniformly to the pia mater surface (Fig. 1C). The epileptic focus brain tissue showed typical pathological changes presented as cortical laminar and columnar structural disorders (Fig.1 D, E). A large number of dysmorphic neurons (DNs) with different morphology and axon and dendritic polarity disorders were also been identified (Fig.1D) accompanied by balloon cells (BCs) that were larger in volume, mostly oval or elliptical, rich in cytoplasm, and often eccentrically distributed nuclei (Fig.1E).

Immunohistochemical staining

DISC1 positive immunohistochemical staining was located mainly in the cytoplasm, but also in the nucleus of nerve cells and glial cells. AKT positive immunohistochemical staining was located mainly in the cytoplasm, but also in the nucleus of nerve cells. The expression of DISC1 protein in the RTLE group was significantly decreased compared to the control group ($P<0.05$). Conversely, AKT protein expression increased significantly ($P<0.05$).

HMGB1, IL-6, and STAT-3 immuno-positive cells were present in the temporal lobe cortex of RTLE patients, and HMGB1 and STAT-3 were expressed in the nucleus and cytoplasm. IL-6 was widely expressed in cells. Moreover, the expressions

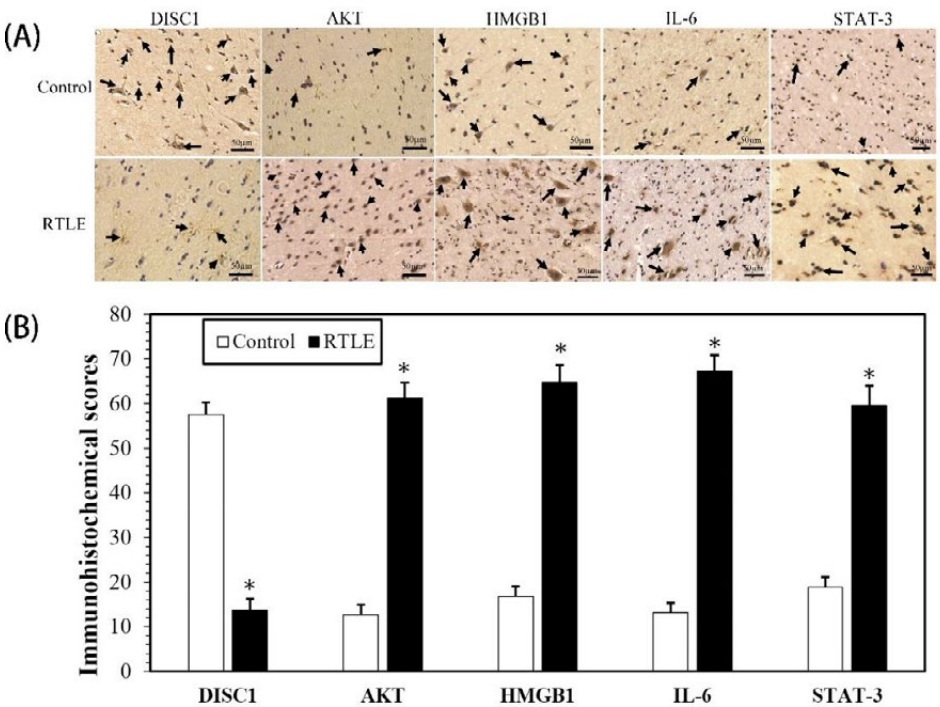

Fig. 2. *Immunohistochemical staining and immunohistochemical scores for DISC1, AKT, HMGB1, IL-6, STAT-3, and p-STAT-3 proteins.* ***A)*** *Images of immunohistochemical staining;* ***B)*** *Statistical chart of immunohistochemical scores. * $P<0.05$ compared with the control group.*

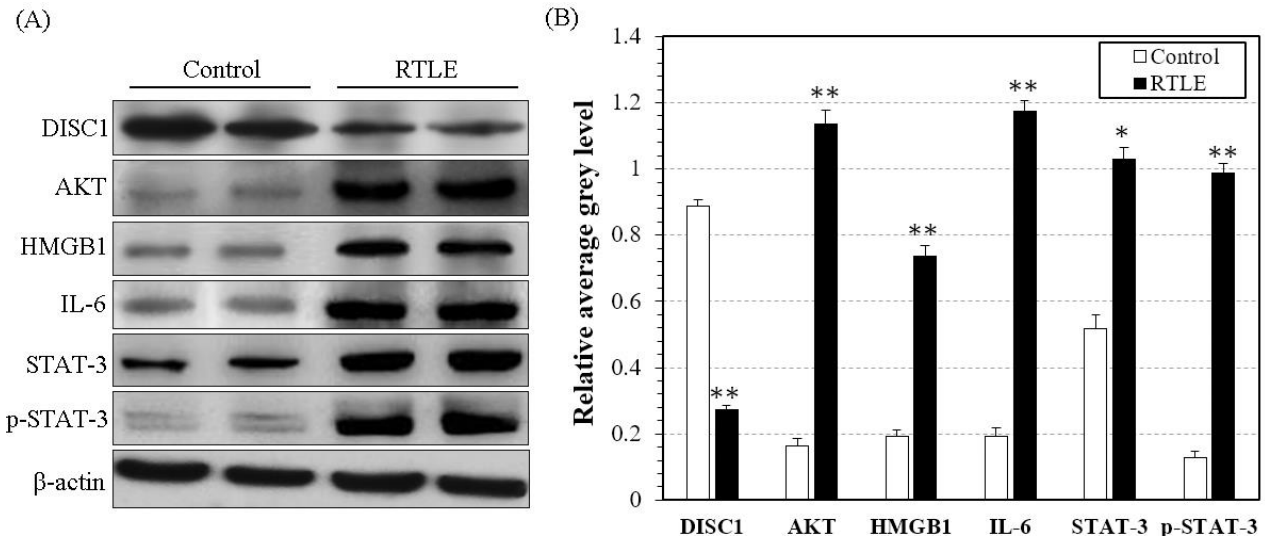

Fig. 3. ***A)*** *Western Blot results;* ***B)*** *Gray value of each protein band. *P<0.05, **P<0.01 compared with the control group.*

of HMGB1, IL-6, and STAT-3 in the RTLE group were significantly increased compared to the control group (P<0.05) (Fig.2).

Western blot

Western blot analysis showed that the expression of DISC1 protein in the RTLE group was significantly decreased compared with the control group (P<0.05). The expressions of AKT, HMGB1, IL-6, STAT-3, and phosphorylated STAT-3 (p-STAT-3) proteins in the RTLE group were significantly increased compared with the control group (P<0.05) (Fig.3).

DISCUSSION

DISC1 is an important candidate gene for mental illness, being a common risk factor for schizophrenia, bipolar disorder, depression, autism and Asperger's syndrome (6, 7). Studies have found that the pathological manifestations similar to epilepsy appear after the DISC1 gene is knocked out, suggesting that changes in DISC1 proteins may be implicated in the pathogenesis of temporal lobe epilepsy (9). Fournier et al. showed that the DISC1 mutation caused changes in the hippocampal dentate gyrus cell structure (10). In the present study, we observed a downregulation of the expression of DISC1 protein associated with an upregulation of AKT in the brain tissue of epileptic focus compared with the control group. This is in accordance with Kim et al. whose results that showed that DISC1 might regulate the AKT/mTOR signaling pathway through KIAA1212 (a complex of DISC1) and influence the occurrence of epilepsy by modulating the development of new neurons (11).

Furthermore, the expressions of inflammatory factors HMGB1, IL-6, STAT-3, and p-STAT-3 protein in epilepsy tissues were up-regulated compared with the control group. These findings are in accordance with studies showing an implication of immune-inflammatory response in the pathogenesis of epilepsy (10, 11). Recent studies have shown that abnormal JAK/STAT-3 signaling pathways in the central nervous system can cause epilepsy (12).

In conclusion, we showed that in RTLE epilepsy caused inflammatory cell infiltration, neuron degeneration, and neuronal death. The expression of DISC1 protein was downregulated and the related inflammation factors HMGB1, IL-6, and STAT-3 of DISC1 were up-regulated in tissues with RTLE showing their implication in pathophysiology of epilepsy.

REFERENCES

1. Sandu C, Magureanu SA, Iliescu C, Pomeran C, Craiu DC. Ketogenic diet treatment for status epilepticus. Farmacia 2019; 67(2):218-25.
2. Rosa DV, Rezende VB, Costa BS, et al. Circulating CD4 and CD8 T cells expressing pro-inflammatory cytokines in a cohort of mesial temporal lobe epilepsy patients with hippocampal sclerosis. Epilepsy Res 2016; 120:1-6.
3. Vinet J, Vainchtein ID, Spano C, et al. Microglia are less pro-inflammatory than myeloid infiltrates in the hippocampus of mice exposed to status epilepticus. Glia 2016; 64(8):1350-62.
4. Romero-Leguizamon CR, Ramirez-Latorre JA, Mora-Munoz L, Guerrero-Naranjo A. [Signaling pathways mTOR and AKT in epilepsy]. Rev Neurol 2016; 63(1):33-41.
5. Yang F, Ang WP, Shen DK, Liu XG, Yang YQ, Ma Y. [PI 3 K/Akt signaling pathway contributed to the protective effect of acupuncture intervention on epileptic seizure-induced injury of hippocampal pyramidal cells in epilepsy rats]. Zhen Ci Yan Jiu 2013; 38(1):20-25.
6. Rodríguez-Seoane C, Ramos A, Korth C, Requena JR. DISC1 regulates expression of the neurotrophin VGF through the PI3K/AKT/CREB pathway. J Neurochem 2015; 135(3):598-605.
7. Porteous D, Millar K. How DISC1 regulates postnatal brain development: girdin gets in on the AKT. Neuron 2009; 63(6):711-13.
8. Valente KDR, Busatto Filho G. Depression and temporal lobe epilepsy represent an epiphenomenon sharing similar neural networks: clinical and brain structural evidences. Arq Neuropsiquiatr 2013; 71(3):183-90.
9. Faulkner RL, Jang MH, Liu XB, et al. Development of hippocampal mossy fiber synaptic outputs by new neurons in the adult brain. Proc Natl Acad Sci U S A 2008; 105(37):14157-62.
10. Fournier NM, Caruncho HJ, Kalynchuk LE. Decreased levels of disrupted-in-schizophrenia 1 (DISC1) are associated with expansion of the dentate granule cell layer in normal and kindled rats. Neurosci Lett 2009; 455(2):134-9.
11. Kim JY, Duan X, Liu CY, et al. DISC1 regulates new neuron development in the adult brain via modulation of AKT-mTOR signaling through KIAA1212. Neuron 2009; 63(6):761-73.
12. Han CL, Ge M, Liu YP, et al. LncRNA H19 contributes to hippocampal glial cell activation via JAK/STAT signaling in a rat model of temporal lobe epilepsy. J Neuroinflammation 2018; 15(1):103.

LETTER TO THE EDITOR

Imperatorin inhibits the invasion and migration of breast cancer cells by regulating HMGB2

K-L. Gao[1], M. Li[2], K-P. Zhang[2]

[1]Breast and thyroid surgery, Zibo Central Hospital, Zibo, China; [2]Breast and Thyroid Surgery, Zibo No.1 Hospital, Zibo, China

Received November 9, 2020 – Accepted December 21, 2020

To the Editor,

Breast cancer (BC) is one of the most common female malignant tumors in the world, ranking second in the mortality rate of female cancers (1). The pathogenesis of BC is complex, the clinical manifestations are diverse, and tumor invasion and metastasis are the main causes of death in BC patients (2). Research on the molecular mechanism of the occurrence and development of BC and the exploration of effective therapeutic measures have therefore always been the hotspots in the field of BC. Imperatorin belongs to furanocoumarin compounds, which are mainly derived from the traditional Chinese medicines *Angelica dahurica*, *Peucedanum ostruthium*, *Cnidium monnieri*, *Radix angelicae pubescentis*, *Glehnia littoralis*, *Angelica sinensis*, etc. (3). Modern pharmacological research shows that imperatorin has an important role in anti-tumor, antibacterial, anti-viral treatment of cardiovascular diseases (4). HMGB2 is a relatively conservative member of the HMGB family. In recent years, many studies have proved that HMGB2 is highly expressed in gastric cancer, glioblastoma, pancreatic cancer, and other tumors, and plays an important role in tumor cell proliferation, invasion and metastasis 5-7). Studies have shown that overexpression of HMGB2 promoted the malignant behavior of BC (8). Whether imperatorin exerts an anti-tumor effect by affecting the expression of HMGB2 in BC cells has not been reported. This study explored the effects of different doses of imperatorin on the HMGB2 expression, invasion and migration of BC cells in order to clarify the mechanism and anti-tumor effects of imperatorin in BC.

MATERIALS AND METHODS

Cells

SKBR3 cells were purchased from Shanghai Institutes for Biological Sciences, Chinese Academy of Sciences (Shanghai, China). Cells were cultured in RPMI-1640 medium containing 10% fetal bovine serum (FBS) and 100U/mL double antibody (penicillin/streptomycin, Gibco, Grand Island, NY, USA), and cultivated in a humidified incubator at 37°C and 5% CO_2. The culture medium was replaced every 3 days, and 0.25% trypsin digestion was used for subculture. The cells in the logarithmic growth phase were used for subsequent experiments.

Cells were inoculated in a 96-well plate with 1×10^3 cells/well in 3 multiple wells. 25 μmol/L, 50 μmol/L, 100 μmol/L and 200 μmol/L imperatorin (purity > 99.5%, China Food and Drug Evaluation Institute) were added respectively and cultured for 48 h. The control group

Key words: imperatorin; HMGB2; invasion; migration; breast cancer cells

Corresponding Author:
Dr Min Li,
Breast and Thyroid Surgery,
Zibo No.1 Hospital,
No. 4 Mount Emei East Road,
Boshan District, Zibo 255200, China
e-mail: oudanglun69746843@163.com

0393-974X (2021)
Copyright © by BIOLIFE, s.a.s.
This publication and/or article is for individual use only and may not be further reproduced without written permission from the copyright holder.
Unauthorized reproduction may result in financial and other penalties
DISCLOSURE: ALL AUTHORS REPORT NO CONFLICTS OF INTEREST RELEVANT TO THIS ARTICLE.

was cultured for 48 h under the same conditions without imperatorin (0 μmol/L). Then 20 μL 5g/L MTT was added and cultured for 4 h. The supernatant was discarded, and 150 μL dimethyl sulfoxide (DMSO) was added to detect the OD value at the wavelength of 490 nm with a microplate reader. The inhibition rate of cell activity was calculated by the following formula: the inhibition rate = (OD control group - OD preimperatorin group)/OD control group × 100%.

After the cells reached about 80% confluence, the cells were starved for 12 h in serum-free medium, and then treated with the imperatorin. After treating cells for 24 h, the cells were resuspended in serum-free medium to 5×10^5/mL. 200μL cell suspension was added to the upper chamber, while 900 μL RPMI 1640 medium containing 10% FBS was added in the lower chamber. After culturing for 12 h, the upper chamber was taken out, and the non-migrated cells in the upper layer of the upper chamber were wiped with a cotton swab. Cells were fixed in anhydrous methanol at room temperature for 10 min, and stained with 0.1% crystal violet for 15 min. We selected 5 random field microscopes to take pictures and the cells were counted under microscopy. 100 μL Matrigel Matrix was spread on the membrane of each Transwell upper chamber. The rest of the operation was the same as the migration experiment.

qRT-PCR

After cells were treated with imperatorin for 24 h, total RNA was extracted with Trizol reagent (Invitrogen, Carlsbad, USA), and its concentration and purity were measured with a spectrophotometer. The RNA was reversely transcribed into cDNA using a reverse transcription kit (Applied Biosystems, Foster City, USA). All samples were then subjected to qRT-PCR with SYBR Green (Takara, Tokyo, Japan) on the ABI7500 system (Applied Biosystems). The relative expression was calculated by the $2^{-\Delta\Delta Ct}$ method and normalized to GAPDH expression. The primer sequences are listed in Table I.

Statistical analysis

All data were expressed as mean ± SD. GraphPad Prism 5 was used for statistical analysis. Student's *t*-test or ANOVA (parametric) with Tukey test was used to assess the statistical significance of differences. $P < 0.05$ was considered statistically significant.

RESULTS

Effects of imperatorin on cell viability, cell invasion, and cell migration

The MTT method was used to detect the effect of imperatorin (25 μmol/L, 50 μmol/L, 100 μmol/L and 200 μmol/L) on cell viability. As shown in Table II, the low concentration of imperatorin (25 μmol/L, 50 μmol/L) at three time points had no significant effect on SKBR3 cell activity, and the inhibitory effect was obvious when the concentration increased to 100 μmol/L and 200 μmol/L, and presented a dose-time dependent relationship. The inhibition rate at 72 h was 62.3% and 83.5%, respectively. In order to exclude the effect of imperatorin on SKBR3 cell migration and invasion caused by inhibition of cell activity, concentrations of 25 μmol/L and 50 μmol/L were selected in the following experiments.

Matrigel was spread on the upper Transwell chamber to detect the effect of different concentrations of imperatorin on the invasion ability of SKBR3 cells. After 24 h, cells treated with different concentrations of imperatorin (25 μmol/L,

Table I. *Primer sequences for real time fluorescence quantification PCR*

Gene Name		Primer sequences (5′-3′)
HMGB2	F	GGCTGAGGATTGCGTTAGAG
	R	GGGGTCTCCTTTACCCATGT
GAPDH	F	AGCCACATCGCTCAGACAC
	R	GCCCAATACGACCAAATCC

50 μmol/L) significantly inhibited the invasion of SKBR3 cells compared with the control group (Fig. 1A, $p<0.01$ or $p<0.001$). The difference between 25 μmol/L and 50 μmol/L groups was also statistically significant (Fig. 1A, $p<0.01$).

The Transwell chamber detects the effect of imperatorin on the migration ability of SKBR3 cells. After 24 h, cells treated with 25 μmol/L, 50 μmol/L imperatorin, the number of cells that penetrated the Transwell chamber was significantly less than the control group (Fig. 1B, $p<0.05$ or $p<0.01$). The comparison between the two different concentration of imperatorin was also statistically significant (Fig. 1B, $p<0.05$).

Effect of imperatorin on HMGB2 expression in BC cells

After 24 h, the expression of HMGB2 in SKBR3 cells with different concentrations of imperatorin was significantly down-regulated compared with the control group (Fig. 2, $p<0.01$ or $p<0.001$), and there was a statistical difference between the 25 μmol/L and 50 μmol/L groups (Fig. 2, $p<0.05$).

DISCUSSION

Tumor invasion and metastasis is a complex biological process, which is affected by the regulation of many genes, proteins and many other factors. At present, surgical resection is still the main treatment option for most solid tumors, but it is difficult to avoid postoperative recurrence and metastasis. As an important active component of *Umbelliferae* plants such as *Angelica dahurica*, imperatorin has shown a wide range of pharmacological effects. Another study also found that imperatorin has a significant inhibitory effect on cell proliferation of BC cell

Table II. *Effect of cell inhibition rate after imperatorin treatment in SKBR3 cells*

Group (μmol/L)	Cell inhibition rate (%)		
	24 h	48 h	72 h
0	0	0	0
25	4.5±1.9	8.6±2.2	10.2±3.1
50	13.5±4.3	20.3±5.4	26.8±5.7
100	31.6±6.9	49.9±6.4	62.3±6.0
200	56.4±5.8	70.7±5.9	83.5±8.6

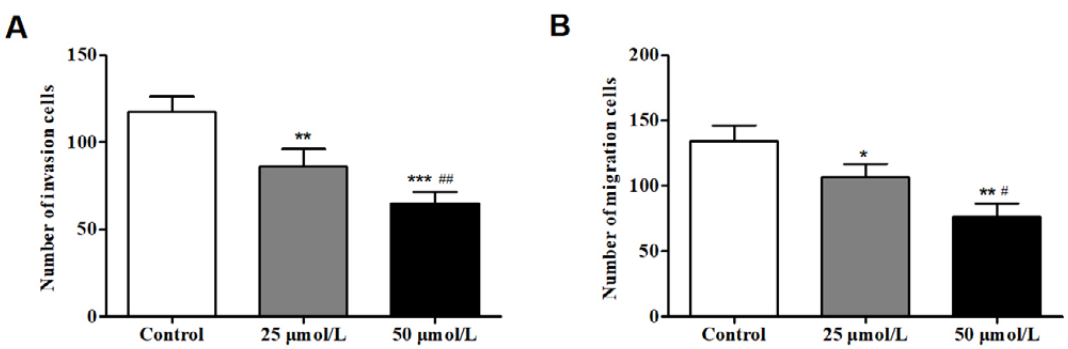

Fig. 1. *Effect of imperatorin on the invasion (A) and migration (B) of SKBR3 cells. *P < 0.05, **P < 0.01, ***P < 0.001 compared with control group; #P < 0.05, ##P < 0.01, compared with 25μmol/L group.*

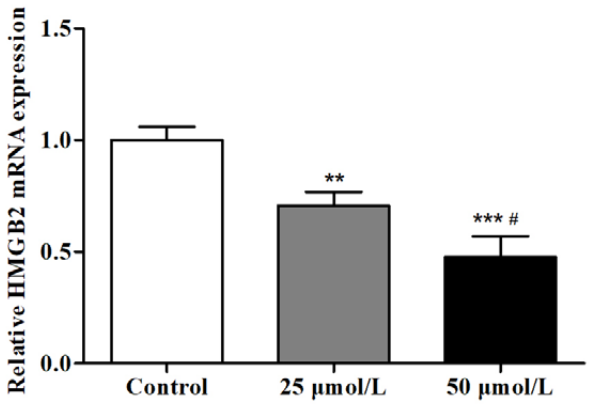

Fig. 2. *Effect of imperatorin on HMGB2 expression in SKBR3 cells. **P < 0.01, ***P < 0.001 compared with control group; #P < 0.05, compared with 25μmol/L group.*

MCF-7 in a concentration-dependent manner (9). Our results prove that imperatorin can significantly inhibit the migration and invasion of SKBR3 cells *in vitro*, and the higher the concentration, the more obvious the inhibitory effect of imperatorin, therefore it is dose-dependent. These results also suggested that down-regulating the expression of HMGB2 in tumor cells can inhibit tumor invasion and metastasis. Our experiments confirmed that imperatorin has a significant inhibitory effect on SKBR3 cell invasion and migration, and the invasion and migration viability of cells treated with imperatorin were significantly reduced. The molecular mechanism reduced the expression of HMGB2 in SKBR3 cells, resulting in a decrease in cell invasion and migration. The results of the study provide experimental evidence for imperatorin to inhibit BC metastasis.

In summary, imperatorin down-regulated the expression of HMGB2 in human BC SKBR3 cells to inhibit its migration and invasion process. These findings provide new insight into the underlying mechanism of the role of imperatorin in human BC. However, how imperatorin down-regulated the expression of HMGB2 in SKBR3 cells needs to be further studied. The application of imperatorin in the treatment of BC requires further animal and clinical experiments to support these findings.

REFERENCES

1. O'Sullivan CC, Loprinzi CL, Haddad TC. Updates in the evaluation and management of breast cancer. Mayo Clinic Proceedings 2018; 93:794-807.
2. Siegel RL, Miller KD, Jemal A. Cancer statistics, 2020. CA: Cancer J Clin 2020; 70:7-30.
3. Wu G, Chen J, Xu X, Mao Y, Zhong L, Lu X. Research progress on botanical and pharmacological properties of imperatorin. Guiding J Tradit Chin Medicine Pharmacol 2017; 023:54-56.
4. Deng M, Xie L, Zhong L, Liao Y, Liu L, Li X. Imperatorin: A review of its pharmacology, toxicity and pharmacokinetics. Eur J Pharmacol 2020; 879:173124.
5. Li J, Gao J, Tian W, Li Y, Zhang J. Long non-coding RNA MALAT1 drives gastric cancer progression by regulating HMGB2 modulating the miR-1297. Cancer Cell Int 2017; 17:44-44.
6. Wu ZB, Cai L, Lin SJ, et al. High-mobility group box 2 is associated with prognosis of glioblastoma by promoting cell viability, invasion, and chemotherapeutic resistance. Neuro-oncology 2013; 15:1264-75.
7. Cai X, Ding H, Liu Y, Pan G, Li Q, Yang Z, Liu W. Expression of HMGB2 indicates worse survival of patients and is required for the maintenance of Warburg effect in pancreatic cancer. Acta Bioch Bioph Sin 2017; 49:119-27.
8. Liu A, Li X, Wang G, Tang X, Dong Y, Ji N, Kang H. Effects of HMGB2 silencing on proliferation, apoptosis, invasion and migration of breast cancer cell line MDA-MB-231. Chin Clin Oncol 2017; 22:1-5.
9. Hong C. Imperatorin induces apoptosis of human breast cancer cell line MCF-7 in vitro. Zhejiang Practical Medicine June 2015; 20:177-79.

LETTER TO THE EDITOR

Expression of HSP60 in gastric lymphoma treated by a combination of trichosanthin and radiotherapy and its mechanism

JP. Hu[1*], HS. Jin[1*], ZF. Lang[2], L. Yan[1], J. Liang[3], KR. Cai[1], ZS. Jin[4] and BZ. An[5]

[1]Department of Histology and Embryology, Mudanjiang Medical University, Mudanjiang, China; [2]Department of Medical Function, Mudanjiang Medical University, Mudanjiang, China; [3]Stem Cell Institute, Mudanjiang Medical University, Mudanjiang, China; [4]Department of Pathology, Mudanjiang Medical University, Mudanjiang, China; [5]Department of Anatomy, Mudanjiang Medical University, Mudanjiang, China

Received August 6, 2020 – Accepted January 7, 2021

*These authors contributed equally to this work

To the Editor,

Primary gastric lymphoma (PGL) is the most common extranodal non-Hodgkin lymphoma and represents a wide spectrum of disease, ranging from indolent low-grade marginal zone lymphoma or mucosa-associated lymphoid tissue (MALT) lymphoma to aggressive diffuse large B-cell lymphoma (1). The highest incidence of PGL was reported in subjects who were aged 60-69 years. The main clinical manifestations of PGL are non-specific gastrointestinal symptoms, abdominal pain, nausea and vomiting. There may be an abdominal mass and cachexia in the late stage of PGL (2).

Trichosanthin (TCS) belongs to type 1 ribosome-inactivating protein (RIP), which is isolated from the root tuber of the Chinese medicinal herb *Trichosanthes kirilowii Maximowicz*, and consists of 247 amino acid residues (3). Preliminary studies have shown that TCS acts directly on syncytial trophoblast cells, resulting in cell degeneration and necrosis. *In vitro* and *in vivo* studies have shown that TCS has a potential antitumor activity, and can significantly prolong the average survival time of nude mice bearing human choriocarcinoma xenografts, however, the molecular mechanism of TCS has been poorly understood.

Heat shock protein 60 (HSP60) is a highly conserved protein abundantly expressed in both prokaryotic and eukaryotic cells, and is indispensable for maintaining the normal structure and function of mitochondrial proteins (4). HSP60 in mitochondria can act on apoptosis-associated factors and inhibit the activation of mitochondrial apoptotic pathway. Moreover, it can reduce the production of oxygen-free radicals in mitochondria. A small amount of HSP60 in the cytoplasm can also inhibit cell apoptosis through the interaction with apoptosis-associated factors. On the contrary, HSP60 can promote apoptosis under the action of some stimulating factors or when the location of HSP60 cells is abnormal. The dual-role of HSP60 in apoptosis and its significance in the diagnosis and treatment of tumor cells and other diseases have greatly attracted scholars' attention.

The present study aimed to assess the effects of TCS combined with radiotherapy on mice with gastric lymphoma, and detect the expression and molecular mechanism of HSP60.

Key words: gastric lymphoma; trichosanthin; HSP60; radiotherapy

Corresponding Author:
Dr Baizhu An,
Department of Anatomy,
Mudanjiang Medical University,
No.3 Tongxiang Road,
Mudanjiang 157011, China
e-mail: anbaizhu518518@163.com

0393-974X (2021)
Copyright © by BIOLIFE, s.a.s.
This publication and/or article is for individual use only and may not be further reproduced without written permission from the copyright holder.
Unauthorized reproduction may result in financial and other penalties
DISCLOSURE: ALL AUTHORS REPORT NO CONFLICTS OF INTEREST RELEVANT TO THIS ARTICLE.

MATERIALS AND METHODS

Animals

BALB/c-nu/nu nude mice were provided by Beijing Vital River Laboratory Animal Technology Co., Ltd. (Beijing, China). Mice were divided into blank control group, model group, and TCS group (n = 12 mice in each group), respectively. All animal experiments were approved by the Animal Ethics Committee of Hongqi Hospital Affiliated to Mudanjiang Medical University (Mudanjiang, China), and were carried out in accordance with the Declaration of Helsinki.

Fresh specimens of human malignant gastric lymphoma were collected from those cases who were admitted to hospital. There were 6 cases with diffuse microcrack B-cell lymphoma, 5 cases with diffuse large B-cell lymphoma, 2 cases with non-Hodgkin lymphocyte twisted cell type, and 2 cases with Hodgkin lymphoma. The living cancer cells derived from primary tumors and hepatic metastases from gastric cancer were collected. They were cultured in Roswell Park Memorial Institute (RPMI)-1640 medium at 4°C, and then transferred to a sterile environment. After removing non-tumor tissues, the tumor tissues were cut into 1mm^3 pieces for transplantation.

In the model group, nude mice were anesthetized by intravenous injection of pentobarbital sodium (30 mg/kg). The gastric antrum was approached through a midline incision along the gastric wall with a small curvature of 3 mm, and a deep-submucosal incision was made. Two pieces of 1 mm^3 tumor tissues were fixed in the submucosa of gastric wall with suture, the peritoneum was sutured with 7-0 silk thread, and the skin was sutured with 5-0 silk thread. After surgery, the mice were allowed free access to food and water, and were observed twice a week. In the TCS group, on the basis of the model group, rats were given TCS at a dose of 4.0 mg/kg every day.

Anatomical and histological examinations

All tumor-bearing nude mice were subjected to detailed anatomical examination, in which the volume of tumor was measured, the invasion of the surrounding organs was observed and the metastatic tumors of organs were observed. Tumor tissues were fixed with 10ml/L formaldehyde, embedded into paraffin, cut into slices, stained with hematoxylin and eosin (H&E), and were visualized under a light microscope.

H&E staining

After 12 weeks of administration, mice were sacrificed and their stomachs were taken, and fixed with 4% formaldehyde solution. After 24 h, they were embedded into paraffin and H&E staining was performed. The changes in gastric mucosa as well as angiogenesis and inflammatory cell infiltration were observed under a light microscope. According to the severity of the disease, the specimen was marked with "-" (0-point, no obvious lesion), "+" (1-point, low-risk lesion), "+ +" (2-point, moderate-risk lesion), and "+ + +" (3-point, high-risk lesion).

Immunohistochemistry (IHC)

HSP60 was detected by IHC. Firstly, paraffin-embedded tissues were cut into 5-μm thick slices. After dewaxing by xylene, tissues were dehydrated with gradient ethanol, washed three times with Tris-buffered saline (TBS), and subjected to antigen repair for 15 min. The sections were incubated at room temperature for 10 min in 3% H_2O_2 solution then blocked by endogenous peroxidase, washed with TBS for 3 times, 5 min each time, dried and sealed with 5% bovine serum albumin (BSA) for 20 min, after which BSA solution was removed. Next, 50 μl diluted primary antibody covering tissues were added to each section, and the section was washed with TBS for 3 times, 5 min each time. TBS was removed, and 50-100 μl secondary antibody was added to each slice, followed by incubation at 4°C for 50 min. After washing for 3 times, 5 min each time, TBS was removed. The diaminobenzidine (DAB)-photoconverted slices were washed with distilled water, stained with H&E for 25 s, air dried, dripped with neutral gum, and then sealed.

Quantitative analysis of the expressions of the above-mentioned proteins was carried out by an image analysis system. Three non-overlapping high-power fields (× 400) were randomly selected from each section, and the mean optical density, positive area and total area of all cells with a positive reaction under each view were measured, and the ratio of the positive area was calculated. The mean value of the optical density and positive area per case was used as the expression amount.

Radiation therapy

On the basis of the gastric lymphoma model, mice were exposed to 10 Gy whole-body gamma irradiation with a Theratron-780 60C0 radiotherapy machine. Mice were 75 cm away from the radiation source. Microwave-induced

biological effects observed in mice were interpreted after irradiation. Mice that received radiation therapy were allocated to the radiotherapy group.

On the basis of the gastric lymphoma model, 6 mice were treated with a combination of radiotherapy and TCS, and were allocated to the radiotherapy + TCS group.

Flow cytometry

The cells were collected and washed with phosphate-buffered saline (PBS; 0.01 M, pH 7.4). 5 L of 1 mg/mL propidium iodide (PI) stock solution was diluted to prepare 100 L of PI working solution. The washed cells were centrifuged, and the supernatant was discarded. The cells were resuspended in 1X Annexin binding buffer. The cell density was determined, and diluted with 1X Annexin binding buffer to reach a density of ~1×106 cells/ml. 100 µl of Annexin V-Dye conjugate/PI staining solution was added to each well with around 1×10^5 cells, and then the cells were resuspended. The cells were incubated at room temperature for 15 min. Then, 400 µl of 1X Annexin-binding buffer was added, and mixed gently. The sample was kept on ice. The stained cells were analyzed by flow cytometry and excitations of the luminescence at 530 and 575 nm were recorded.

Bioinformatics analysis was used to predict the target proteins of HSP60

We used the Targetscan7.2 (http://www.targetscan.org/vert_72/) to predict the target proteins of HSP60, review the literature, and select the preselected targets of BDNF, IL8, SEMA4C, and PPP3R1. Next, Western blotting was employed to detect the relevant protein levels of the three groups. The protein sample was extracted with radio-immunoprecipitation assay (RIPA) lysis buffer. The protein samples were separated through 10% sodium dodecyl sulfate polyacrylamide gel electrophoresis (SDS-PAGE), and were then transferred onto polyvinylidene fluoride (PVDF) membranes. The membranes were incubated with the primary antibody (Abcam, Cambridge, UK) overnight at 4°C, and were then incubated with the corresponding secondary antibody (Abcam, Cambridge, UK) for 1 h at room temperature. Enhanced chemiluminescence (ECL) was applied to detect the binding of antibodies to surface antigens on intact cells.

Statistical analysis

SPSS 19.0 software (IBM, Armonk, NY, USA) was used to perform statistical analysis. The measured data were expressed as mean ± standard deviation (SD). One-way analysis of variance (ANOVA) was utilized to make multiple comparisons among three groups, and the *Chi*-squared test was utilized for making comparison between two groups. $P < 0.05$ was considered statistically significant.

RESULTS

H&E staining

H&E staining results showed that the score of the model group and TCS group was higher than that in the blank control group, and that of the TCS group was lower than that in the model group, and the difference was statistically significant ($P < 0.05$; Table I). As shown in Fig. 1, the gastric mucosa epithelium in blank control group was intact, with smooth surface, no erosion and uniform cellular morphology, and glands were arranged orderly. There were few lymphocytes, no inflammatory cell infiltration in lamina propria, and no signs of submucosal edema. In the model group, the atrophy of some glands disappeared, and the smooth muscle cells of muscularis mucosa showed fascicular hyperplasia, which were inserted into the mucosa lamina propria. The lumen of glandular duct became larger, with chronic inflammatory cells infiltrated into lamina propria, into the muscularis mucosa, lymphocyte aggregation, lymphoid follicle formation, basal cell hyperplasia of the olfactory epithelium, goblet cells, and deep nuclear staining. In the TCS group, the thickness of gastric mucosa was moderate, and the glands were arranged in order. There were a limited number of lymphocytes and plasma cells in the lamina propria of some mucosa, and eosinophil infiltration could be occasionally observed. The morphology of both epithelial and glandular cells was normal.

Expression of HSP60 protein in each group was detected by immunohistochemistry and Western blotting

The expression of HSP60 protein in gastric mucosa in the model group was significantly higher than that in the blank control group ($P < 0.05$), and was markedly lower in the TCS group than that in the model group ($P < 0.05$) (Table II, Fig. 2).

Table I. *Comparison of H&E staining scores among the three groups.*

Group	HE staining scores
Blank control group	0±0
Model group	2.68±0.45
TCS group	1.89±0.33
F-value	32.22
P-value	0

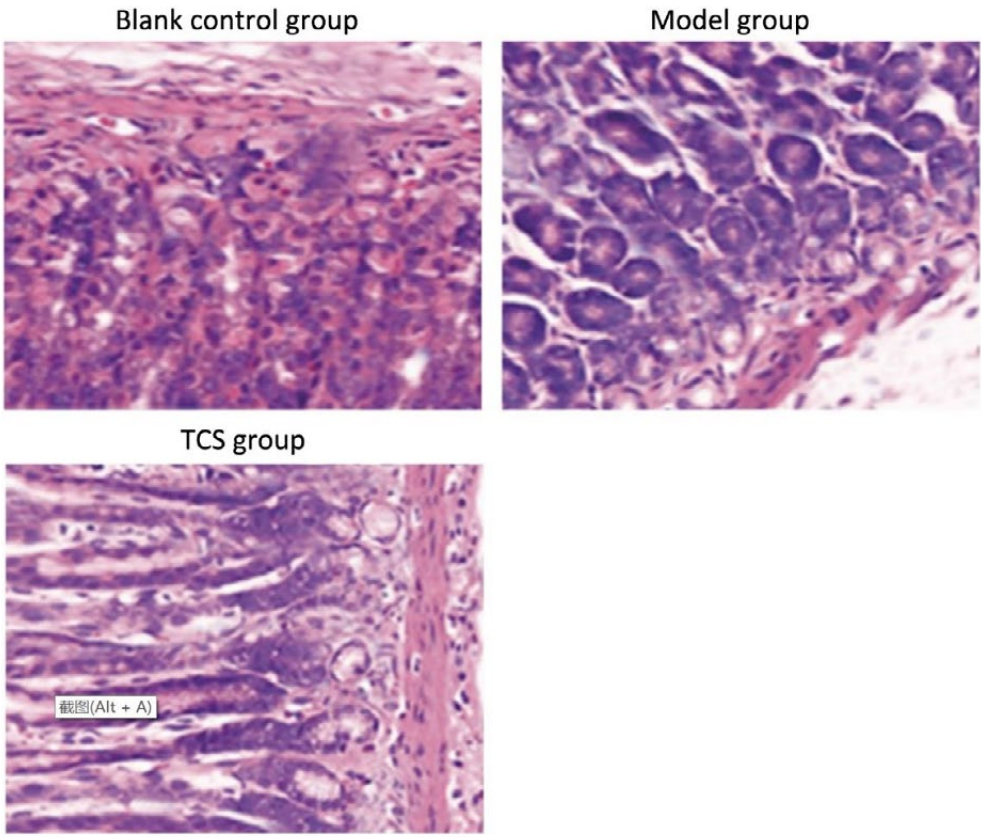

Fig. 1. *Pathological results of gastric mucosa in each group (HE staining, × 400).*

Flow cytometry

The combination of radiotherapy with TCS showed that both TCS and radiotherapy could promote the apoptosis of gastric lymphoma cells, and radiotherapy had a stronger inhibitory effect on apoptosis. At the same time, the combination of radiotherapy and TCS could enhance the apoptosis of gastric lymphoma cells, suggesting that TCS could improve the efficacy of radiotherapy (Fig. 3).

HSP60 could promote gastric lymphoma through HSP60-BCL6/nuclear factor-kappaB (NF-κB)/interleukin-6 (IL-6) pathway

HSP60 is highly expressed in gastric lymphoma. Five possible targets of HSP60 were selected for detection by bioinformatics analysis. Results of Western blotting showed that TCS combined with radiotherapy could inhibit the expressions of BCL6, NF-κB, and IL-6, while it had no effect on the

Table I. *Comparison of H&E staining scores among the three groups.*

Group	HSP60
Blank control group	24.98±3.33
Model group	63.45±9.19
TCS group	30.95±4.11
F-value	26.53
P-value	0

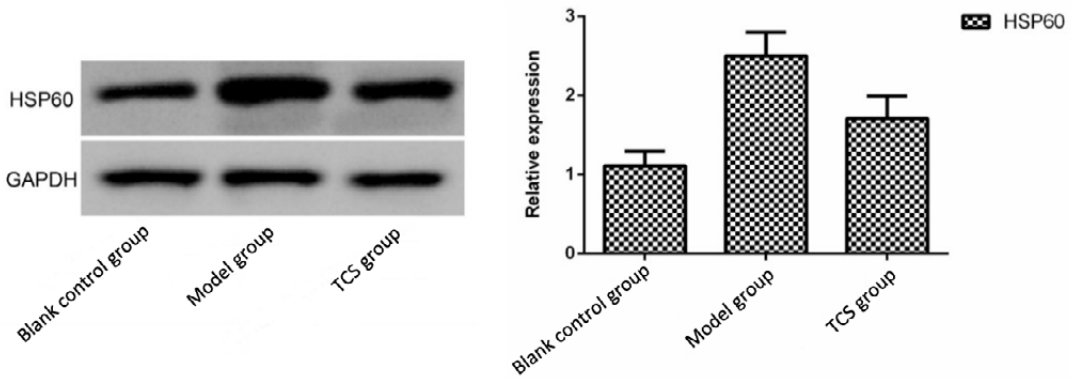

Fig. 2. *Expression of HSP60 protein was detected by Western blotting.*

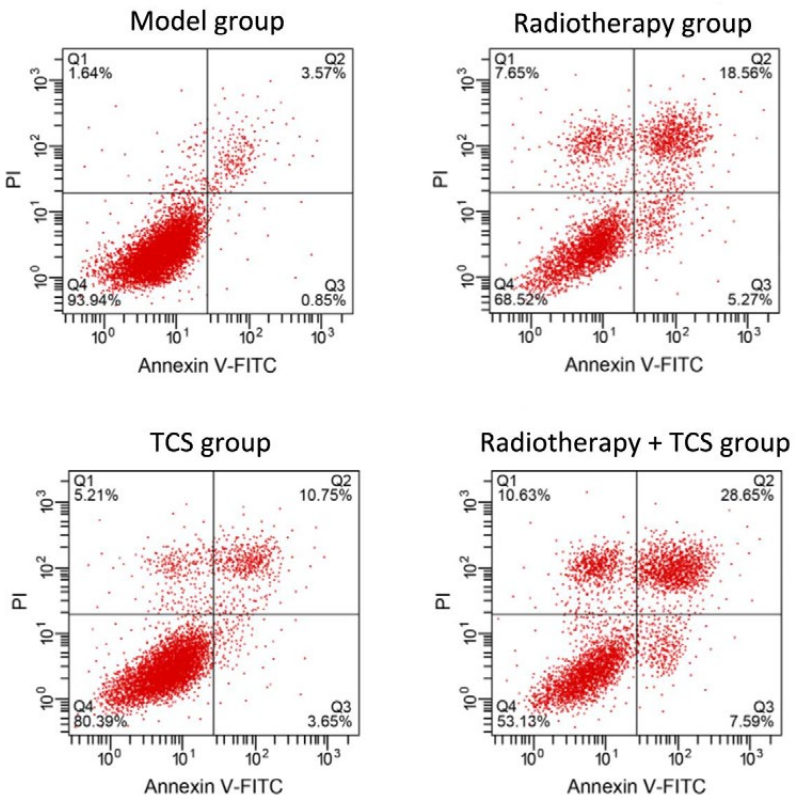

Fig. 3. *Results of flow cytometry.*

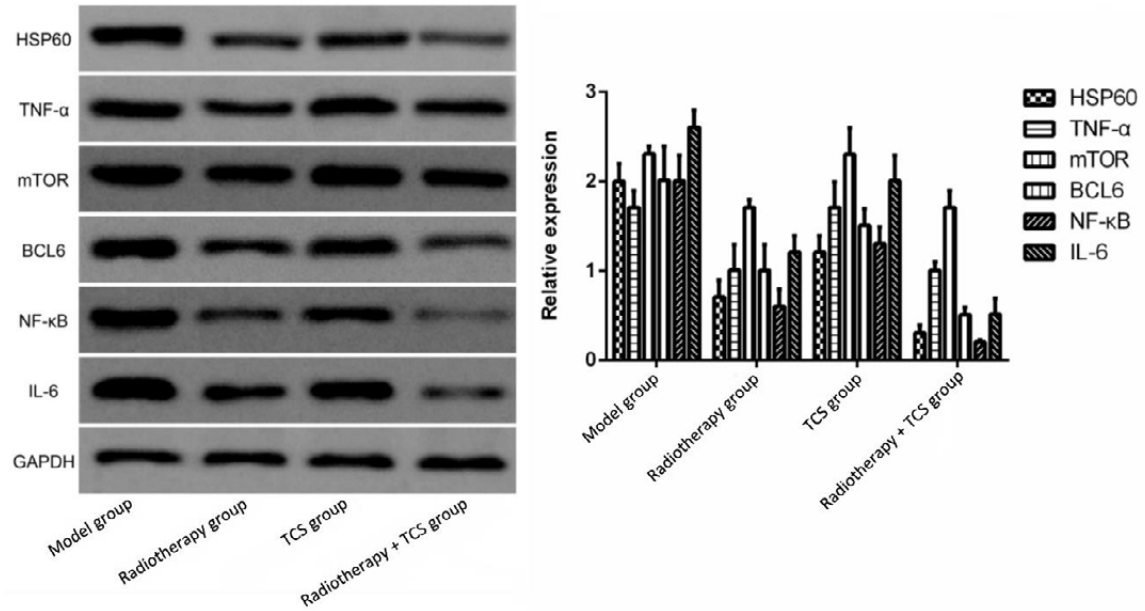

Fig. 4. *Expressions of HSP60 and related protein.*

expressions of tumor necrosis factor-α (TNF-α) and mammalian target of rapamycin (mTOR); however, radiotherapy could reduce the expressions of BCL-6, NF-κB, and IL-6. This suggests that TCS could promote gastric lymphoma through HSP60-BCL6/NF-κB/IL-6 pathway (Fig. 4).

DISCUSSION

In recent years, HSP60 has been shown to play a pivotal role in the inflammation, atrophy, and carcinogenesis of gastric mucosa. A previous study showed that silencing of HSP60 inhibits cell proliferation and promotes apoptosis in tumor cells, suggesting its pro-survival and anti-apoptotic functions (5). In addition, it participates in protein translocation, protein degradation, dissolution of pathologic protein aggregates, regulation of gene expression, cell differentiation, DNA replication, signal transduction, programmed cell death, cellular senescence and carcinogenesis (6). BCL6 protein is highly expressed in breast cancer cell lines and tissue specimens and expression of BCL6 protein is associated with disease progression and poor survival of breast cancer patients (7). NF-κB can significantly inhibit apoptosis, which is closely associated with the growth of tumor cells (8). Mutations of NF-κB family genes are frequent in human tumors, especially in lymphoid malignancies. Downstream genes of NF-κB include CyclinD1 and c-Myc, and sustain activation of NF-κB stimulating cell growth (9, 10). Recent studies have shown that IL-6 promotes tumor cell survival, and the IL-6 level is associated with poor prognosis in cancer patients (11, 12).

In summary, the expressions of BCL6, NF-κB, and IL-6 were inhibited by combined therapy of TCS + radiotherapy, whereas the expressions of TNF-α and mTOR were not significantly affected. However, radiotherapy could reduce the expressions of BCL-6, NF-κB, and IL-6. As a result, TCS could promote gastric lymphoma through HSP60-BCL6/NF-κB/IL-6 pathway.

ACKNOWLEDGEMENT

This study was financially supported by Heilongjiang Provincial Department of Education Overseas Scholars Project (Grant No. 1153h16).

REFERENCES

1 Juárez-Salcedo LM, Sokol L, Chavez JC, Dalia S. Primary gastric lymphoma, epidemiology, clinical diagnosis, and treatment. Cancer Control 2018; 25(1):1073274818778256.

2. Al-Akwaa AM, Siddiqui N, Al-Mofleh IA. Primary gastric lymphoma. World J Gastroenterol 2004; 10(1):5-11.

3. Xia Y, Zhou Z. Treatment of primary gastric lymphoma. Zhonghua Wei Chang Wai Ke Za Zhi 2017; 20(11):1227-30.

4. Li MX, Yeung HW, Pan LP, Chan SI. Trichosanthin, a potent HIV-1 inhibitor, can cleave supercoiled DNA in vitro. Nucleic Acids Res 1991; 19(22):6309-12.

5. Barreda B F, Gómez P R, Quispe L D, Sánchez LJ, Combe GJ, Casanova ML, Celis ZJ. Primary gastric lymphoma. Rev Gastroenterol Peru 2004; 24(3):238-62.

6. Duarte S, Momier D, Baqué P, et al. Preventive cancer stem cell-based vaccination reduces liver metastasis development in a rat colon carcinoma syngeneic model. Stem Cells 2013; 31(3):423-32.

7. Walker SR, Liu S, Xiang M, et al. The transcriptional modulator BCL6 as a molecular target for breast cancer therapy. Oncogene 2015; 34(9):1073-82.

8. Xanthoudakis S, Roy S, Rasper D, et al. Hsp60 accelerates the maturation of pro-caspase-3 by upstream activator proteases during apoptosis. EMBO J 1999; 18(8):2049-56.

9. Shan YX, Liu TJ, Su HF, Samsamshariat A, Mestril R, Wang PH. Hsp10 and Hsp60 modulate Bcl-2 family and mitochondria apoptosis signaling induced by doxorubicin in cardiac muscle cells. J Mol Cell Cardiol 2003; 35(9):1135-43.

10. Muschol-Steinmetz C, Jasmer B, Kreis NN, et al. B-cell lymphoma 6 promotes proliferation and survival of trophoblastic cells. Cell Cycle 2016; 15(6):827-39.

11. DiDonato JA, Mercurio F, Karin M. NF-κB and the link between inflammation and cancer. Immunol Rev 2012; 246(1):379-400.

12. Taniguchi K, Karin M. IL-6 and related cytokines as the critical lynchpins between inflammation and cancer. Semin Immunol 2014; 26(1):54-74.

LETTER TO THE EDITOR

lncRNA NEAT1 regulates cerebral ischemia/reperfusion injury through miR-1306-5p

XZ. Meng[1*], WW. Jiang[2*], HW. Guo[3], M. Li[3], MM. Zhao[3], FJ. Yu[4] and ZT. Gu[1]

[1]Department of Neurology, Weihai Haida Hospital, Weihai, China; [2]Spinal Surgery, Weihaiwei People's Hospital, Weihai, China; [3]Weihai Haida Hospital, Weihai, China; [4]Department of Neurology, Weihai Municipal Third Hospital, Weihai, China

Received October 22, 2020 – Accepted December 14, 2021

[*]These Authors contributed equally to this work

To the Editor,

The incidence of cerebral vascular disease (CVD) is continuously increasing, and ischemic cerebrovascular disease is the more common form. The interruption of blood flow and subsequent blood reperfusion can easily cause nerve damage, induce apoptosis, and can even lead to severe irreversible functional changes, namely cerebral ischemia reperfusion injury (CI/RI) (1). At present, there is no very effective treatment for CI/RI. Therefore, elucidating the pathogenesis is essential to discover new and effective treatments. In recent years, substantia evidence has shown that lncRNA is involved in the pathophysiological process of cerebral ischemia (2).

Long non-coding RNA (lncRNA) nuclear paraspeckle assembly transcript 1 (NEAT1) is an lncRNA that has been widely studied in various cancers, such as colorectal cancer, prostate cancer, glioma and ovarian cancer (3). Recent studies reported that NEAT1 overexpression exacerbated myocardial ischemia reperfusion injury (MI/RI) through multiple signaling pathways (4-6). For example, Du et al. suggested that MI/RI was promoted by the activation of MAPK pathway through NEAT1 upregulation (4). Moreover, NEAT1 also enhanced MI/RI by sponging miR-495-3p to regulate MAPK6 (5). Similarly, NEAT1 knockdown accelerated cell proliferation and hampered cell apoptosis of MI/RI via regulating miR-193a (6). However, there are few studies on the regulation network of NEAT1 and its mechanism in cerebral ischemia.

LncRNA can participate in ischemic brain injury by regulating some miRNAs (7). Thus, we further explored the target miRNA of NEAT1. The function of NEAT1 in protection of CI/RI and its relationship with miR-1306-5p in oxygen and glucose deprivation/recovery (OGDR) model were investigated in IMR-32 cells. The results revealed that NEAT1 could be an underlying biomarker for cerebral ischemia diagnosis and therapy, thus providing a novel mechanism for cerebral ischemia.

MATERIALS AND METHODS

Cell culture and transfection

Human IMR-32 cells (ATCC, USA) were cultured in DMEM/F12 medium (Hyclone, USA) containing 10% fetal bovine serum (FBS, Hyclone, USA), 10^6 IU/L streptomycin (Sigma, USA) and 10^5 IU/L penicillin (Sigma, USA). The cells were placed in an incubator with 95% air and 5% CO_2 at 37°C.

Key words: NEAT1; miR-1306-5p; cerebral ischemia/reperfusion injury

Corresponding Author:
Dr Zutao Gu,
Department of Neurology, Weihai Haida Hospital,
7-1 Zhuhai Road,
Economic and Technological Development Zone,
Weihai 264200, China
e-mail: tengqwxpnsu713578@163.com

0393-974X (2021)
Copyright © by BIOLIFE, s.a.s.
This publication and/or article is for individual use only and may not be further reproduced without written permission from the copyright holder.
Unauthorized reproduction may result in financial and other penalties
DISCLOSURE: ALL AUTHORS REPORT NO CONFLICTS OF INTEREST RELEVANT TO THIS ARTICLE.

Small interfering RNAs (siRNA) for NEAT1 (si-NEAT1) or si-NC, miR-1306-5p inhibitor (inhibitor) for interfering miR-1306-5p expression and inhibitor control (anti-NC), miR-1306-5p mimic (mimic) for overexpressing the miR-1306-5p and mimic control (miR-NC) were synthesized by GenePharma (Shanghai, China). Cells were seeded in a 6-well plate for 12-24 h, and then the transfection was performed by Lipofectamine™ 2000 transfection reagent (Invitrogen, USA) according to the instructions. After 12 h of transfection, OGDR was performed. The cells were then collected for subsequent experiments.

Construction of oxygen and glucose deprivation (OGD)/ recovery (OGDR) model in vitro

For the OGD model, Glucose-free Hank's balanced salt solution (Invitrogen, USA) was used to instead of the complete medium containing glucose. Cells were placed in hypoxic conditions (containing 5% CO_2, 0.3% O_2, and 94.7% N_2) for 4 h to simulate brain ischemic injury *in vitro*. For OGDR, after 4 h of OGD treatment, the sugar-free medium was replaced by complete medium containing glucose and 10% FBS. Cells were incubated with 95% air and 5% CO_2 at 37°C for 48 h. CI/RI was simulated *in vitro*. The cells of the control group were always cultured in complete medium and placed in the same conditions as the OGDR group.

Determination of related indicators

The cell viability was detected by the MTT method. In brief, cells were seeded in 96-well plates with 2×10^4 cells/ well. After treatments (transfection, OGDR and others), each well was added with 20 μL of MTT (5 g/L, Invitrogen, USA), and incubated for 4 h at 37°C. Then 150 μL diemthyl sulfoxide (DMSO, Invitrogen, USA) were added to each well, and the cells were incubated for 10 min in a shaker. After shaking and mixing, the absorbance value (OD) was measured with a microplate reader at 490 nm.

StarBase 3.0 software (http://starbase.sysu.edu.cn/ index.php) was used to predict miRNAs that could bind to NEAT1, and it was found that binding sites existed between NEAT1 and miR-1306-5p. Wild-type NEAT1 (NEAT1-wt) containing a putative miR-1306-5p binding site and NEAT1 (NEAT1-mut) containing a mutant binding site were synthesized and cloned into the luciferase reporter vector pmirGLO (Promega, USA). miR-1306-5p mimics or miR-NC sequences and NEAT1-wt or NEAT1-mut were co-transfected into cells by Lipofectamine 2000. After 48 h, the cells were collected and lysed by RIPA buffer. The relative luciferase activity was evaluated using a dual luciferase report analysis system.

The total RNA was extracted with Trizol reagents (Invitrogen, USA). The Nano-Drop ND1000 spectrophotometer (Wilmington, USA) was used to detect the ratio of D260/D280 and the concentration of RNA. The ratio of D260/D280 between 1.8 and 2.1 was used for the following experiment. 1 μg of total RNA was reverse transcribed into cDNA by Prime Script™ reverse transcription kit (Takara, USA). QRT-PCR was carried out using SYBR® Premix Ex Taq (Takara, USA) in CFX96 qPCR detection system (Bio-Rad, USA). We prepared the reaction system and set the reaction conditions according to the instructions of the corresponding kit. All steps were completed in the qRT-PCR instrument. GAPDH and U6 was used as internal reference. The relative expression was calculated by $2^{-\Delta\Delta CT}$ method. The experiment was repeated 3 times. Primers are listed in Table I.

After extracting the total protein of the cells by the RIPA lysis (Beyotime, China), the protein concentration of each sample was adjusted according to the result of the protein concentration determined by the bicinchoninic acid (BCA) method. After 20 μg proteins separated by 10% SDS-PAGE, they were transferred onto PVDF membrane. The membrane was incubated with a blocking solution containing 5% skimmed milk powder at room temperature for 1 h. Primary antibodies (Caspase-3, 1: 1000; Bcl-2, 1: 1000; Bax, 1: 2000; GAPDH, 1: 1500; Abcam, USA) were added and incubated at 4°C overnight. Then the membrane was incubated with HRP-labeled rabbit anti-mouse secondary antibody (1: 2000, Abcam) at 37°C for 2 h. Protein bands were detected by enhanced chemical fluorescence reagent (ECL, Millipore, USA) by automatic gel imaging system.

Statistical analysis

Statistical analysis was performed with GraphPad Prism 5 software, and the data was expressed as mean ± SD. Student's *t*-test was used for comparison between the two groups. $P < 0.05$ indicated statistically significant.

RESULTS

NEAT1 knockdown mediates cell viability and apoptosis in OGDR model cells

Firstly, the expression was detected of NEAT1

in an OGDR injury cell model that simulates CI/RI *in vitro*. QRT-PCR results showed that NEAT1 expression in IMR-32 cells was significantly up-regulated in the OGDR group compared to the control group, suggesting that the expression of NEAT1 was increased under OGDR conditions (Fig. 1A). Subsequently, the expression of NEAT1 was detected after si-NEAT1 transfected in the cells treated by OGDR. The results showed that NEAT1 expression was significantly reduced (Fig. 1B) in IMR-32 cells transfected with si-NEAT1/OGDR compared with the si-NC/OGDR group, indicating that NEAT1 was successfully inhibited by si-NEAT1.

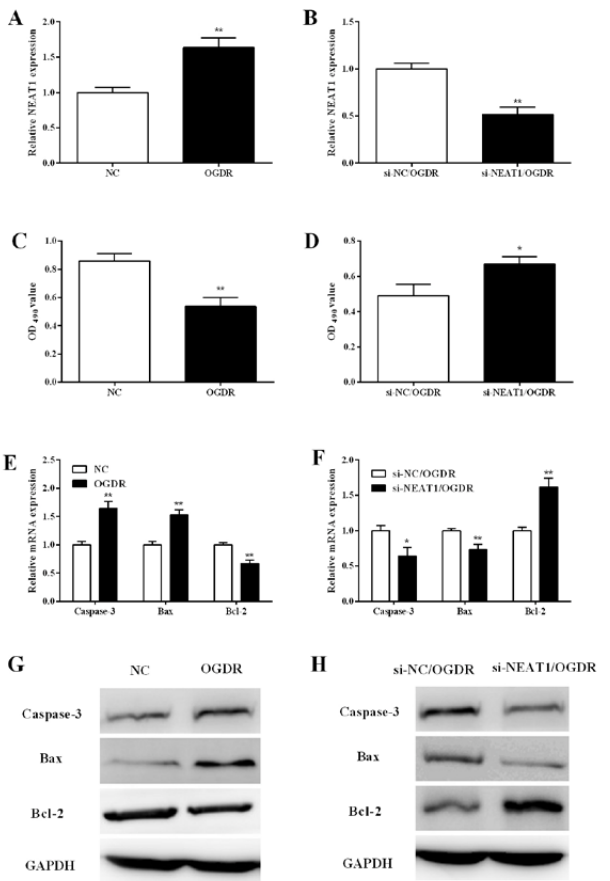

Fig. 1. *Effects of NEAT1 knockdown on cell viability and apoptosis of IMR-32 cells.* ***A)*** *NEAT1 expression was increased in OGDR model.* ***B)*** *NEAT1 was underexpressed in IMR-32 cells with OGDR treatment through si-NEAT1 transfection.* ***C, D)*** *MTT was performed to detect effects of OGDR treatment or NEAT1 knockdown on cell viability.* ***E, F)*** *Effect of OGDR treatment or NEAT1 knockdown on apoptosis associated gene (Caspase-3, Bax and Bcl-2) mRNA expression.* ***G, H)*** *Western blotting was performed to detect protein expression of Caspase-3, Bax and Bcl-2. *P < 0. 05, **P < 0. 01, compared with NC or si-NC/OGDR group.*

Based on the above results, the effect of NEAT1 on cell viability was detected by MTT method. The results showed that compared with the NC group, the cell viability was significantly reduced in the OGDR group (Fig. 1C). However, increasing cell viability was observed in the si-NEAT1/OGDR group *vs* si-NC/OGDR group (Fig. 1D). To further study the regulation of NEAT1 on apoptosis, qRT-PCR and Western blotting were used to detect the expression of mRNA and protein of apoptosis-related genes. The results showed that compared with the NC group, the mRNA expressions of Bax and Caspase-3 were notably increased, and Bcl-2 mRNA expression was significantly reduced in the OGDR group (Fig. 1E). Compared with the si-NC/OGDR group, the expression of Bax and Caspase-3 mRNA were markedly reduced, while the expression of Bcl-2 mRNA was dramatically increased in the si-NEAT1/OGDR group (Fig. 1F). Western blotting results showed that Bax, Bcl-2 and Caspase-3 protein expression had the same trend as their mRNAs (Fig. 1 G, H). The above results suggested that NEAT1 knockdown might inhibit OGDR-induced apoptosis, thereby promoting cell survival.

miR-1306-5p directly binds to NEAT1

StarBase3.0 online software prediction found that NEAT1 contains a complementary binding site with miR-1306-5p (Fig. 2A). The dual luciferase reporter gene experiment was used to detect the combination of NEAT1 to miR-1306-5p in IMR-32 cells. Results showed that the co-transfection of miR-1306-5p mimic and NEAT1-wt inhibited the luciferase activity, while miR-1306-5p mimic and NEAT1-mut co-transfection did not affect the luciferase activity (Fig. 2B). Compared with the NC group, the miR-1306-5p expression in IMR-32 cells of the OGDR group was significantly decreased (Fig. 2C). However, miR-1306-5p expression was significantly increased in si-NEAT1/OGDR group *vs* the si-NC/OGDR group (Fig. 2D). These results indicated that NEAT1 could target miR-1306-5p and regulate miR-1306-5p expression through binding sequence.

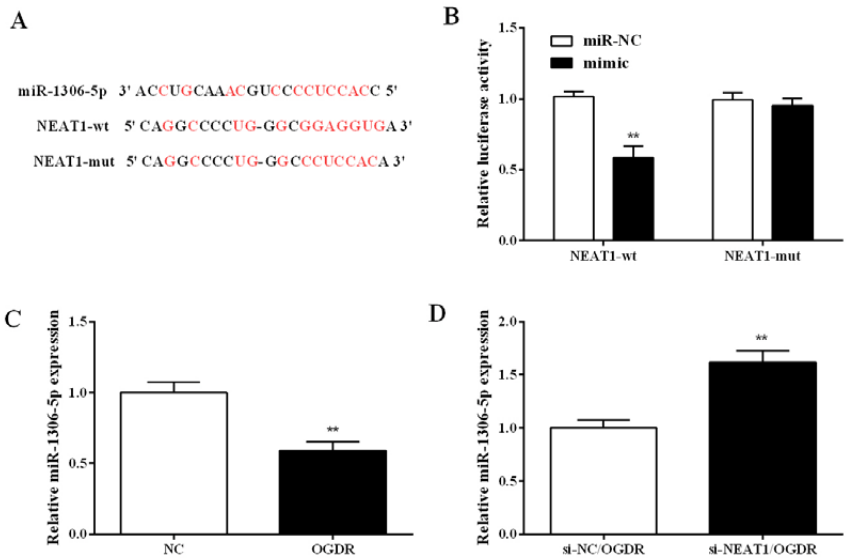

Fig. 2. *NEAT1 targets miR-1306-5p in IMR-32 cells.* ***A)*** *miR-1306-5p was predicted as a target of NEAT1 by bioinformatics analysis.* ***B)*** *The dual-luciferase assay was performed to determine whether NEAT1 binds to miR-1306-5p.* ***C)*** *miR-1306-5p expression was decreased in IMR-32 cells treated by OGDR using qRT-PCR analysis.* ***D)*** *miR-1306-5p expression was increased in IMR-32 cells treated with si-NEAT1 and OGDR. **P < 0. 01, compared with miR-NC, NC or si-NC/OGDR group.*

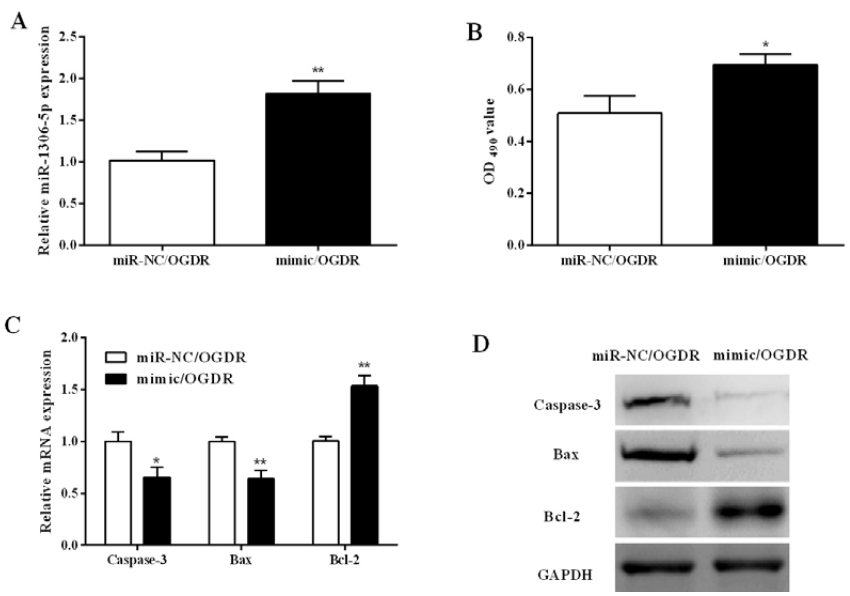

Fig. 3. *miR-1306-5p modulated IMR-32 cell viability and apoptosis.* ***A)*** *The expression of miR-1306-5p was increased in IMR-32 cells with the application of miR-1306-5p mimic and OGDR.* ***B)*** *Effects of miR-1306-5p overexpression on cell viability under OGDR condition.* ***C, D)*** *Effect of miR-1306-5p overexpression on apoptosis associated gene mRNA and protein expression. *P < 0. 05, **P < 0. 01, compared with miR-NC/OGDR group.*

miR-1306-5p involves in cell viability and apoptosis in OGDR model cells

To confirm the role of miR-1306-5p in CI/RI, miR-1306-5p mimic was transfected into IMR-32 cells of the OGDR group and tested the expression of miR-1306-5p. As shown in Fig. 3A, the miR-1306-5p expression in the mimic-transfected group was increased compared with the miR-NC/OGDR group.

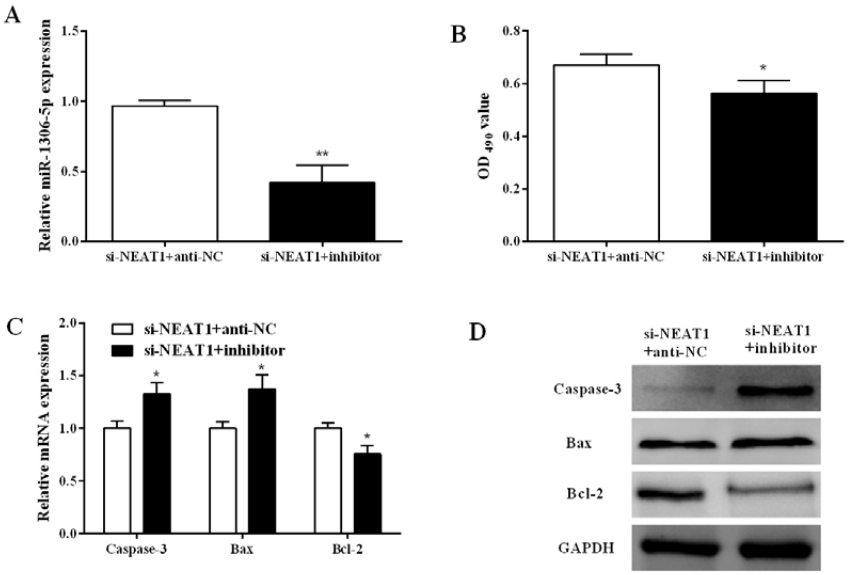

Fig. 4. *miR-1306-5p inhibitor reversed the protective effect of si-NEAT1 against OGDR injury.* ***A)*** *QRT-PCR analysis of miR-1306-5p expression.* ***B)*** *Cell viability was detected by MTT assay.* ***C, D)*** *Apoptosis associated gene mRNA and protein expression were detected by qRT-PCR and Western blotting, respectively. *P < 0. 05, **P < 0. 01, compared with si-NEAT1+anti-NC group.*

After OGDR treatment, we examined the effect of miR-1306-5p overexpression on cell viability. The mimic/OGDR group was found to have significantly higher IMR-32 cell activity than the miR-NC/OGDR group (Fig. 3B), suggesting that overexpression of miR-1306-5p could increase the cellular activity of oxygen-sugar deprived reperfusion cells. Moreover, we also detected the mRNA and protein expressions of apoptosis-related genes by qRT-PCR and Western blotting. The results showed that, compared with the miR-NC/OGDR group, the expressions of Bax and Caspase-3 mRNA were notably reduced, while the expression of Bcl-2 mRNA was obviously increased in the mimic/OGDR group (Fig. 3C). Western blotting results showed that Bax, Bcl-2 and Caspase-3 protein expression exhibited the same tendency as their mRNAs (Fig. 3D). Thus, we proposed miR-1306-5p had a protection of OGDR-induced cell damage.

NEAT1 regulates CI/R through targeting miR-1306-5p

NEAT1 could regulate OGDR-induced cell damage, but it was not known whether NEAT1 was mediated by miR-1306-5p to achieve this process. Therefore, si-NEAT1 and miR-1306-5p were co-transfected into IMR-32 cells treated by OGDR. Findings showed that the increasing expression of miR-1306-5p induced by si-NEAT1 was counteracted by miR-1306-5p inhibitor (Fig. 4A). Moreover, miR-1306-5p counteracted the promotion of si-NEAT1 on the cell viability of IMR-32 treated by OGDR (Fig. 4B). The effect of si-NEAT1 and miR-1306-5p co-transfection on mRNA and protein expressions of apoptosis-related genes was also detected. More importantly, the effect of si-NEAT1 on apoptosis-related gene mRNA and protein expressions was also reversed by miR-1306-5p inhibitor under OGDR conditions (Fig. 4 C, D). This showed that miR-1306-5p inhibitor could block the promotion of si-NEAT1 on cell viability and the protective effect of si-NEAT1 on OGDR-induced apoptosis.

DISCUSSION

The in-depth study of lncRNA in CI/R may also provide a new developmental direction for molecular treatment of CI/RI. In this study, the OGDR model was used to simulate the CI/RI

in vitro, and it was found that the expression of NEAT1 was increased in the OGDR group. And the knockdown of NEAT1 promoted the proliferation of IMR-32 cells with OGDR treatment, indicating that NEAT1 was involved in the CI/RI process, which was similar to a previous report (8). In the early stage of apoptosis, Caspase-3 is a key executive molecule (9). In the classic apoptotic pathway, Bcl-2 can inhibit the release of cytochrome C from the mitochondria into the cytoplasm, thereby inhibiting apoptosis (10). On the contrary, Bax can antagonize the role of Bcl-2, thereby promoting cell apoptosis (11). The present results showed that NEAT1 knockdown inhibited Bax and Caspase-3 expression, and promoted Bcl-2 expression in IMR-32 cells with OGDR treatment.

On the basis of the ceRNA hypothesis, we explored the target miRNA of NEAT1, and miR-1306-5p attracted our attention. MiR-1306-5p was downregulated in SH-SY5Y cells with OGDR treatment, and its overexpression could relieve OGDR-induced injury of SH-SY5Y by targeting BIK (12). We found that miR-1306-5p upregulation promoted cell proliferation and Bcl-2 expression, while inhibiting Bax and Caspase-3 expressions. These results were consistent with a previous study (12) showing that miR-1306-5p could regulate cell proliferation and apoptosis induced by OGDR. In the present study, NEAT1 was found to mediate the expression of miR-1306-5p. Moreover, the rescue experiments indicated that miR-1306-5p inhibition blocked the protection of NEAT1 knockdown in IMR-32 cells treated by OGDR. This shows that NEAT1 achieved the effect on CI/RI by regulating miR-1306-5p expression. However, animal experiments were not performed in the function of NEAT1 and miR-1306-5p *in vivo*. Thus, further studies should be performed to explore mechanisms of NEAT1 in CI/RI.

In conclusion, this study confirmed that NEAT1 knockdown could inhibit OGDR-induced apoptosis, possibly through regulating miR-1306-5p to affect Bax/Bcl-2-Caspase-3 pathway. The role of NEAT1 was observed in the process of apoptosis in a CI/RI cell model *in vitro*, and the results suggested that NEAT1 may be used as a potential target for the treatment of brain ischemia/reperfusion injury.

REFERENCES

1. Huang L, Chen C, Zhang X, et al. Neuroprotective effect of curcumin against cerebral ischemia-reperfusion via mediating autophagy and inflammation. J Mol Neurosci 2018; 64:129-39.
2. Ren W, Yang X. Pathophysiology of long non-coding RNAs in ischemic stroke. Front Mol Neurosci 2018; 11:96.
3. Yu X, Li Z, Zheng H, Chan MT, Wu WK. NEAT1: A novel cancer-related long non-coding RNA. Cell Prolif 2017; 50:e12329.
4. Du X, Wei J, Tian D, et al. NEAT1 promotes myocardial ischemia-reperfusion injury via activating the MAPK signaling pathway. J Cell Physiol 2019; 234:18773-80.
5. Luo M, Sun Q, Zhao H, Tao J, Yan D. Long noncoding RNA NEAT1 sponges miR-495-3p to enhance myocardial ischemia-reperfusion injury via MAPK6 activation. J Cell Physiol 2020; 235:105-13.
6. Ren L, Chen S, Liu W, Hou P, Sun W, Yan H. Downregulation of long non-coding RNA nuclear enriched abundant transcript 1 promotes cell proliferation and inhibits cell apoptosis by targeting miR-193a in myocardial ischemia/reperfusion injury. BMC Cardiovasc Disord 2019; 19:192.
7. Liu C, Yang J, Zhang C, Liu M, Zhao H. Analysis of long non-coding RNA expression profiles following focal cerebral ischemia in mice. Neurosci Lett 2017; 665:123-29.
8. Liu B, Xu T, Meng Y. IncRNA NEAT1 aggravates cerebral ischemia/reperfusion injury by sponging miR-874-3p. J Biol Regul Homeost Agents 2020; 34(2). doi: 10.23812/20-38A.
9. Porter AG, Janicke RU. Emerging roles of caspase-3 in apoptosis. Cell Death Differ 1999; 6:99-104.
10. Mignotte B, Vayssiere JL. Mitochondria and apoptosis. Febs J 2010; 252:1-15.
11. Vafaiyan Z, Gharaei R, Asadi J. The correlation between telomerase activity and Bax/Bcl-2 ratio in valproic acid-treated MCF-7 breast cancer cell line. Iran J Basic Med Sci 2015; 18:700-04.
12. Chen X, Li C, Li J, Sheng L, Liu X. Upregulation of miR-1306-5p decreases cerebral ischemia/reperfusion injury in vitro by targeting BIK. Biosci Biotechnol Biochem 2019; 83:2230-37.

LETTER TO THE EDITOR

Comparison of the therapeutic effects of metformin and glibenclamide on patients with gestational diabetes

Y-M. Lv[1], J. Fan[1], M-B. Li[2], Y. Ma[1], T-T. Li[3], G-R. Sun[4]

[1]Department of Pharmacy, Zhangqiu District People's Hospital, Jinan, China; [2]Intravenous Drug Deployment Center, Zhangqiu District People's Hospital, Jinan, China; [3]Operation Room, Zhangqiu District People's Hospital, Jinan, China; [4]Department of Pharmacy, Liaocheng People's Hospital of Shandong, Liaocheng, China

Received October 30, 2020 – Accepted January 18, 2021

To the Editor,

Gestational Diabetes Mellitus (GDM) affects approximately 5% of pregnant women (1). In particular, some newborn complications observed are often related to pregnant women with gestational diabetes, such as huge fetuses and hypoglycemia. It has been shown that these complications can be effectively reduced by strict control of blood sugar of pregnant women. Apart from the regulation of eating habits and exercise, the standard treatment for gestational diabetes is insulin therapy (2). Recent studies have revealed the feasibility of oral preparations in the treatment of gestational diabetes, such as metformin and glibenclamide (3, 4). Glibenclamide, as the second-generation oral sulfonylurea, can modulate blood sugar and insulin without the increase of side effects (5). In addition, metformin functions as a potential alternative to patients with gestational diabetes who are not sensitive to insulin (6). It was found that patients using metformin did not present any complications during the perinatal period. Metformin is thus regarded as a preferable medicine to gestational diabetes compared to insulin injection therapy. However, in gestational diabetes, the comparison of the therapeutic effects concerning metformin and glibenclamide remains to be determined. Therefore, the purpose of this study is to investigate the effects of metformin and glibenclamide in controlling blood sugar levels in the treatment of gestational diabetes.

MATERIALS AND METHODS

Study subjects

A total of 129 patients with gestational diabetes who received prenatal care in the obstetrics department of Zhangqiu District People's Hospital were included in the study. Inclusion criteria: fasting peripheral blood glucose concentrations higher than 105 mg/dL, or 2 hours postprandial peripheral blood glucose concentrations higher than 120 mg/dL. Exclusion criteria: patients who had a history of significant kidney or liver disease, chronic hypertension with drug therapy, or drug abuse. At the beginning of the study, all pregnant women included were given a healthy diet. They were provided with guidance and advice on diet and exercise (30 kcal/kg for normal weight or 25 kcal/kg for obese weight). Patients were recommended to walk for 30 minutes a day. The study was approved by the Ethics Committee of Zhangqiu District People's Hospital and all patients enrolled in this study gave written informed consent after a detailed explanation.

Key words: blood glucose; drug failure rate; gestational diabetes; glibenclamide; metformin

Corresponding Author:
Dr Guorui Sun,
Department of Pharmacy,
Liaocheng People's Hospital of Shandong,
No. 67 Dongchang West Road,
Liaocheng 252000, China
e-mail: xx84455@163.com

0393-974X (2021)
Copyright © by BIOLIFE, s.a.s.
This publication and/or article is for individual use only and may not be further reproduced without written permission from the copyright holder.
Unauthorized reproduction may result in financial and other penalties
DISCLOSURE: ALL AUTHORS REPORT NO CONFLICTS OF INTEREST RELEVANT TO THIS ARTICLE.

Grouping

The enrolled gestational diabetes patients were randomly divided into two groups, namely metformin-only treatment group (65 cases) and glibenclamide-only treatment group (64 cases). The blood glucose detection was conducted by a blood glucose counter under the guidance of a nurse. Each patient's blood glucose was measured 2 hours after meals every day.

Treatment

In the glibenclamide-only treatment group, the initial daily dose was 2.5 mg. Then, if necessary, the dose was increased to a maximum of 10 mg. Patients in the metformin-only treatment group received an initial dose of 500 mg per day. Then, if necessary, the dose was increased to a maximum of 2 g. Glucose levels were detected every week. Regardless of metformin or glibenclamide, after the maximum dose was applied, if the blood glucose level of patients exceeded the target value of 10 mg/dL under the same diet for two consecutive weeks, the treatment was considered as a failure and patients began to receive insulin therapy. Once insulin treatment started, oral medication was stopped. Fetal growth status was monitored monthly with ultrasound examination and prenatal diagnosis was performed twice a week from the 28th week.

Statistical analysis

The data were expressed as mean ± standard deviation. For measurement data, a Kolmogorov-Smirnov (KS) test was performed to identify normal distribution. If it was normally distributed, the independent-sample T-test or one-way ANOVA (one-way ANOVA) was used for

Table I. *Comparison of patient information and postprandial blood glucose levels between glibenclamide group and metformin group*

	Glibenclamide group (64 cases)	Metformin group (65 cases)	*P*
Age(years)	25.6±5.8	26.4±6.1	0.16
Body weight	55.1±19	58.6±21	0.47
Body weight index	32.4±6.0	32.9±7.2	0.79
<30	15(23.4%)	20(30.8%)	
≥30	49(76.6%)	45(69.2%)	
Gestational week at admission	28.1±4.0	26.5±5.8	0.14
Less than 24 weeks at the time of inclusion	9(14%)	14(22%)	0.42
Fasting blood glucose (mg/dL)	90.1±12	93.2±15	0.33
Blood sugar 2 hours after breakfast	103±16	100±21	0.14
Blood sugar 2 hours after lunch	112±23	108±17	0.33
Blood sugar 2 hours after dinner	118±16	125±17	0.29

Note: All data are expressed as mean plus or minus standard deviation, and the statistical test method used was independent sample T-test.

comparison between groups, and the Mann-Whitney test or the Kruskal-Wallis test was used for the non-normal distribution. The enumeration data was processed by *chi*-squared test. When the theoretical value was less than 5, Fisher's exact test was used. SPSS17.0 version software was used for the statistical analysis. When P<0.05, the difference was considered statistically significant.

RESULTS

There was no statistical difference between the two groups in terms of age, weight, body mass index (BMI) or pregnancy age (P>0.05). There were 14 patients (22%) in the metformin group and 9 patients (14%) in the glibenclamide group, the pregnancy of whom was less than 24 weeks at the time of randomization (Table I). There were 26 patients (40%) in the metformin group and 12 patients (18.8%) in the glibenclamide group, who did not meet requirement of the blood sugar reduction and needed insulin injections. There was a statistical difference between the two groups (P<0.05).

In this study, the failure rate of metformin was 2.8-fold higher than that of glibenclamide (95% CI 1.1-3.7, OR 2.7). There was no statistical difference of average fasting blood glucose or the blood glucose 2 hours after a meal between the two groups (P> 0.05). Three patients in the metformin treatment group and one patient in the glibenclamide treatment group had hypoglycemia. There was no statistical difference of maternal hypoglycemia between the two groups of patients (P=0.74). Except for the selective repeated cesarean section, there were 12 patients in the metformin treatment group and 2 in the glibenclamide treatment group who received cesarean section. The difference was statistically

Table II. *Comparison of pregnancy and neonatal outcomes between glibenclamide group and metformin group.*

	Glibenclamide group (64 cases)	Metformin group (65 cases)	*P*
Newborn weight (g)	3,397.6±350	3,102.4±200	0.02
Birth weight exceeds 4 kg	5(7.8%)	2(3.1%)	0.55
Neonatal intensive care	1(1.6%)	4(6.2%)	0.37
Neonatal hypoglycemia (<40mg/dL)	0	1(1.5%)	0.44
Maternal hypoglycemia (<60mg/dL)	1(1.6%)	3(4.6%)	0.61
Eclampsia	3(4.7%)	2(3.1%)	0.74
Shoulder dystocia	1(1.6%)	0	0.44
Cesarean section	2(3.1%)	12(18.5%)	0.01

Note: All data are expressed as mean plus or minus standard deviation, and the statistical test method used was Fisher's exact test.

significant (P = 0.01). The average infant weight in the metformin treatment group was significantly lower than that in the glibenclamide treatment group (P=0.02). There were no statistical differences in other neonatal indicators between the two groups (P>0.05). In the glibenclamide treatment group, macrosomia was observed in 5 patients (7.8%), while in the metformin treatment group, macrosomia was found in only 2 patients (3.1%) (Table II).

DISCUSSION

In terms of pregnancy outcome and neonatal outcome, in the present study, the two groups were very similar. The drug failure rate of glibenclamide was 16.2%. Although this was significantly higher than the result (4%) as firstly reported (7), it was basically consistent with the 20% failure rate of glibenclamide reported by a series of subsequent studies (8-10). The failure rate of metformin in this study was 34.7%, which was in line with the 46.3% failure rate as previously reported (11). Although there was no statistical difference in the incidence of macrosomia between the two groups, the average birth weight of the metformin group was significantly smaller than that of the glibenclamide group. It is probably implicated to the reason that metformin acts as an insulin sensitizer and can pass through the placenta to induce body weight loss (12). Strict control of gestational diabetes can be achieved through extensive use of insulin therapy. However, it is difficult for pregnant women to insist on this treatment that requires four injections a day. In addition, another problem with widespread insulin therapy is that it often leads to hypoglycemia in patients. In this case, oral preparations were well-tolerated during pregnancy and become increasingly accepted. However, the safety issues during lactation still need to be further studied. Although both drugs were well tolerated, the failure rate of metformin was twice that of glibenclamide. The limitation in the study is that the role of either metformin or glibenclamide needs to be clarified in a larger cohort. Also, the single treatment or "cocktail" therapy with insulin requires further investigation in clinical practice. Taken together, our data suggest that glibenclamide presents a favorable effect in the treatment of patients with gestational diabetes compared to metformin, which provides new insights for an alternative therapy for gestational diabetes in the future.

REFERENCES

1. Yeung RO, Savu A, Kinniburgh B, et al. Prevalence of gestational diabetes among Chinese and South Asians: A Canadian population-based analysis. J Diabetes Complications 2017; 31:529-36.
2. Brown J, Alwan N, West JMcKinlay CJ, Farrar D, Crowther CA. Lifestyle interventions for the treatment of women with gestational diabetes. Cochrane Database Syst Rev 2017; 5:CD011970.
3. Nachum Z, Zafran N, Salim R, et al. Glyburide versus metformin and their combination for the treatment of gestational diabetes mellitus: a randomized controlled study. Diabetes care 2017; 40:332-37.
4. Brown J, Martis R, Hughes B, Crowther CA. Oral anti-diabetic pharmacological therapies for the treatment of women with gestational diabetes. Cochrane Database Syst Rev 2017; 1:CD011967.
5. Langer O. Oral hypoglycemic agents: do the ends justify the means? Matern Health, Neonatol Perinatol 2015; 1:19.
6. Moore L, Clokey D, Rappaport V, Curet LB. Metformin compared with glyburide in gestational diabetes: a randomized controlled trial. Obstet Gynecol 2010; 115:55-59.
7. Langer O, Conway D, Berkus M, Xenakis EM, Gonzales O. A comparison of glyburide and insulin in women with gestational diabetes mellitus. N Engl J Med 2000; 343:1134-38.
8. Rochon M, Rand L, Roth L, Gaddipati S. Glyburide for the management of gestational diabetes: risk factors predictive of failure and associated pregnancy outcomes. Am J Obstet Gynecol 2006; 195:1090-94.
9. Jacobson G, Ramos G, Ching J, Kirby RS, Ferrara A, Field DR. Comparison of glyburide and insulin for the management of gestational diabetes in a large managed care organization. Am J Obstet Gynecol 2005;193:118-24.
10. Conway DL, Gonzales O, Skiver D. Use of glyburide for the treatment of gestational diabetes: the San Antonio experience. J Matern Fetal Neonatal Med 2004; 15:51-55.

11. Rowan J, Hague W, Gao W, Battin RM, Moore MP, MiG Trial Investigators. Metformin versus insulin for the treatment of gestational diabetes. N Engl J Med 2008; 358:2003-15.

12. Gandhi P, Bustani R, Madhuvrata P, Farrell T. Introduction of metformin for gestational diabetes mellitus in clinical practice: Has it had an impact? Eur J Obstet Gynecol Reprod Biol 2012; 160:147-50.

LETTER TO THE EDITOR

Double-target longitudinal puncture by freehand on elderly patients with hypertensive cerebral hemorrhage

CL. Hu, M. Xin, K. Zhang and LC. Zhang

Department of Neurosurgery, Langfang Fourth People's Hospital, Langfang, Hebei, China

Received November 3, 2020 – Accepted January 19, 2021

To the Editor,

The incidence rate of hypertensive cerebral hemorrhage (HICH) is increasing, and in recent years the age of patients has gradually become younger, especially in China. Moderate bleeding due to drainage of a punctured hematoma is the most commonly used treatment for HICH in hospitals at all levels, although opinions on positioning methods are mixed (1-3). In recent years, we designed a double-target, longitudinal, freehand puncture method for the treatment of elderly patients with HICH and achieved therapeutic effects. Data from patients with a blood loss between 25~40 mL were collected from May 2013 to May 2019. Patients treated in the Langfang Fourth People's Hospital from between 2013 and April 2016 were classified as the control group with the traditional positioning puncture, and those treated between May 2016 to May 2019 were classified into the observation group with double-target, longitudinal, freehand puncture (details in Fig. 1B).

The Authors have tried a variety of positioning methods in clinical practice, such as metal strip marking positioning, bimetal strip positioning, four-coordinate positioning, chord-distance positioning, six-line grid positioning, and double-X positioning (4-6). After synthesizing the advantages and disadvantages of multiple positioning methods, the authors designed the longitudinal, freehand puncture of a double-target treatment as illustrated in Fig. 1B. Results show that the hematoma clearance rate in the observation group was higher than in the control group on the 3rd, 7th, and 14th day after operation. The drainage tube indwelling time and complete hematoma absorption time were lower than that of the control group ($p<0.05$). There was no significant difference in perioperative mortality or complication rate between the two groups ($p>0.05$). The observation group scores at the first, second, and third months were lower than those of the control group ($p<0.05$). The authors therefore concluded that a longitudinal, freehand puncture of a double-target treatment can promote the rehabilitation of elderly patients with HICH. This treatment has the advantages of a high hematoma clearance rate, fast emptying, and improved patient prognosis and is worthy of clinical reference. However, patient cooperation and the dosage of sedatives may influence the value of this approach.

ACKNOWLEDGEMENT

This work was supported by Langfang S & T Support Project (Project number: 2017013135)

Key words: hypertensive cerebral hemorrhage; double-target puncture; hematoma clearance rate; NIHSS score

Corresponding Author:
Dr Meng Xin,
Department of Neurosurgery,
Langfang Fourth People's Hospital,
No.1128, East Jinkang Road, Bazhou District,
Langfang City, Hebei Province, China
e-mail: jaxn2742@163.com

0393-974X (2021)
Copyright © by BIOLIFE, s.a.s.
This publication and/or article is for individual use only and may not be further reproduced without written permission from the copyright holder.
Unauthorized reproduction may result in financial and other penalties
DISCLOSURE: ALL AUTHORS REPORT NO CONFLICTS OF INTEREST RELEVANT TO THIS ARTICLE.

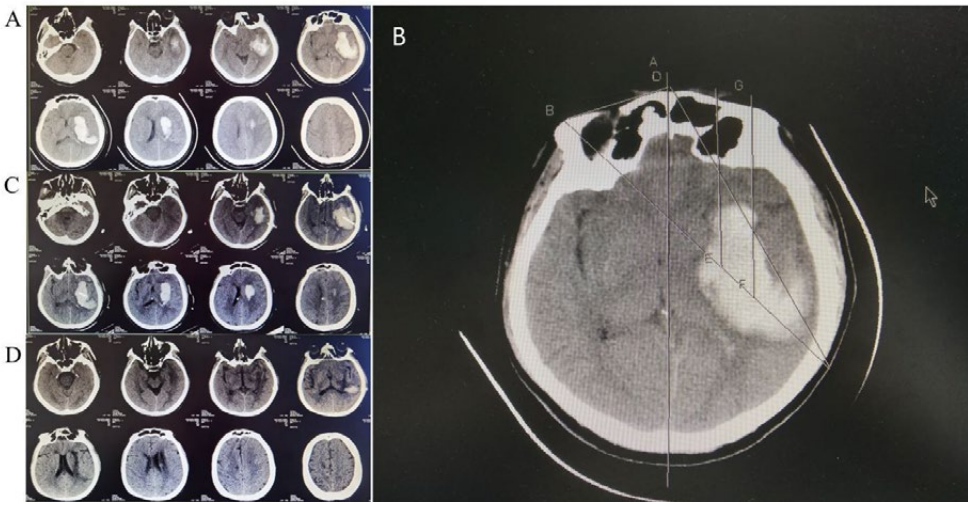

Fig. 1. *Procedure of double-target, longitudinal, freehand puncture **A**) Preoperative CT of patients. **B**) The double-target, longitudinal puncture method. The authors first determined the two target points, and then marked the frontal projection points to determine a plane. The long axis projection points define another plane. **C**) Postoperative view of drainage tube position. **D**) The removed hematoma 3 days after surgery when the drainage tube was pulled out.*

REFERENCES

1. Ranzani T, Cianchetti M, Gerboni G, Falco ID, Menciassi A. A soft modular manipulator for minimally invasive surgery: design and characterization of a single module. IEEE T Robot 2016; 32:187-200.
2. Hanley DF, Thompson RE, Muschelli J, et al. Safety and efficacy of minimally invasive surgery plus alteplase in intracerebral haemorrhage evacuation (MISTIE): a randomised, controlled, open-label, phase 2 trial. Lancet Neurol 2016; 15:1228-37.
3. Marescaux J, Diana M. Next step in minimally invasive surgery: hybrid image-guided surgery. J Pediatr Surg 2015;50: 30-36.
4. Park P, Wang MY, Lafage V, et al. Comparison of two minimally invasive surgery strategies to treat adult spinal deformity. J Neurosurg Spine 2015; 22:374-80.
5. Price JP, Dawson JM, Schwender JD, Schellhas KP. Clinical and radiologic comparison of minimally invasive surgery with traditional open transforaminal lumbar interbody fusion. Clin Spine Surg 2018; 31:E121-E126.
6. Lee L, Burke JP, deBeche-Adams T, et al. Transanal minimally invasive surgery for local excision of benign and malignant rectal neoplasia: outcomes from 200 consecutive cases with midterm follow up. Ann Surg 2018; 267:910-16.

LETTER TO THE EDITOR

Silencing of long noncoding RNA H19 inhibited invasion and migration of papillary thyroid cancer cells via microRNA-138-dependent regulating of LRRK2

ZY. Li[1], WZ. Liu[1], H. Guang[2], WC. Chen[3] and YH. Yang[1]

[1]Department of Ultrasound, Shenzhen Second people's Hospital, The First Affiliated Hospital of Shenzhen University, Shenzhen, Guangdong Province, China; [2]Department of pathology, Shenzhen Second people's Hospital, The First Affiliated Hospital of Shenzhen University, Shenzhen, Guangdong Province, China; [3]Department of Breast & Thyroid surgery, Shenzhen Second people's Hospital, The First Affiliated Hospital of Shenzhen University, Shenzhen, Guangdong Province, China

Received July 3, 2020 – Accepted January 19, 2021

To the Editor,

Papillary thyroid cancer (PTC) is the most common subtype of thyroid cancer, accounting for more than 80% of thyroid cancers (1). PTC has many risk factors, such as ionizing radiation exposure, a history of benign thyroid disease, and a family history of thyroid cancer (2). PTC is a long-term problem for patients as it requires lifelong medication, monitoring or both (3). It is therefore crucial to identify the underlying mechanisms of PTC and to develop novel biomarkers and targeted therapies (4). This study focuses on the interaction mechanism between H19/miR-138/ leucine-rich repeat kinase 2 (LRRK2).

Long non-coding RNAs are involved in the development or progression of various cancers. Relevant literature has reported that H19 can influence the spread, differentiation and cell movement of several cancers (5). H19 can be involved in monitoring DNA methylation and the regulation of intracellular miRNA patterns. Recent studies have shown that HIF-1, the hypoxic master regulator, binds directly to the H19 promoter and induces its transcription (6). MiRNAs play key roles in basic cellular processes, such as cell proliferation, apoptosis, development and inflammation. MiR-138 overexpression has been shown to inhibit the viability, migration, and invasion of retinoblastoma cells, as well as promoting apoptosis (7). The results of the present study results show that H19 could promote the growth of thyroid cancer cells by regulating LRRK2 through miR-138, indicating that thyroid cancer has a new regulatory mechanism and could be a potential therapeutic target.

MATERIALS AND METHODS

Cell culture and transfection

The human normal thyroid epithelial cell line Nthy-ori3-1 was purchased from the European Collection of Cell Culture (ECACC, Salisbury, UK). Thyroid cancer cells TPC-1 and FTC-133 were obtained from American type culture collection center (ATCC, Manassas, VA, USA). Cells were cultured in Dulbecco's Modified Eagle's Medium (Gibco BRL, Grand Island, NY, USA) containing 10% FBS, 100 U/ml penicillin and 100 g/ml streptomycin at 37°C with 5% CO_2.

Key words: PTC; LncH19; miR-138; LRRK2

Corresponding Author:
Dr Zhengyi Li,
Department of Ultrasound, Shenzhen Second People's Hospital
The First Affiliated Hospital of Shenzhen University,
3002 Sungang West Road,
Futian District, Shenzhen, 518035, China
e-mail: sheovwwv238@163.com

0393-974X (2021)
Copyright © by BIOLIFE, s.a.s.
This publication and/or article is for individual use only and may not be further reproduced without written permission from the copyright holder.
Unauthorized reproduction may result in financial and other penalties
DISCLOSURE: ALL AUTHORS REPORT NO CONFLICTS OF INTEREST RELEVANT TO THIS ARTICLE.

RT-qPCR

Total RNA was extracted from cells by Trizol reagent (TaKaRa, Dalian, China), and the RNA quality was detected by a Nanodrop spectrophotometer (Thermo Fisher Scientific, Wilmington, DE). Then, cDNA was converted into complementary DNAs (cDNAs) using the Primer-Script one-step RT-PCR kit (TaKaRa, Dalian, China) following the manufacturer's instruction. The cDNA templates were amplified by real-time PCR using the SYBR Premix Dimmer Eraser kit (TaKaRa, Dalian, China). Gene expression in each sample was normalized to GADPH. Primers were as follows: H19 forward 5′-CGC TTT TGA ACC AGC AGG G-3′, reverse 5′-TTC CCG AGG CTT TGG TGT G-3′; miR-138 forward 5′-GGA GCT GGT GTT GTG AAT CA-3′, reverse 5′-CAG TGC GTG TCG TGG AGT-3′; LRRK2 forward 5′-GAG CAC GCC TCC AAG TTA TTT-3′, reverse 5′-ACT GGC ATT ATG AAC TGT TAG CA-3′; U6 forward 5′-CTC GCT TCG GCA GCA CA-3′, reverse 5′-AAC GCT TCA CGA ATT TGC GT-3′; GAPDH forward 5′-GGA GGG AGA TCC CTC CAA AAT-3′, reverse 5′-GGC TGT TGT CAT ACT TCT CAT GG-3′.

Transwell experimental

Transwell chambers (Corning Incorporated, Corning, NY, USA) with or without Matrigel (BD Biosciences, San Jose, CA, USA) were used to determine invasion and migration of PTC cells, respectively. Forty-eight hours post-transfection, cells were collected and resuspended in FBS-free DMEM. In total, 5×10^4 cells/200μl suspension were plated onto the upper compartments of chambers. Simultaneously, 500 μl of DMEM supplemented with 20% FBS was added to the lower compartments to act as a chemoattractant. Cells remaining on the upper chambers were gently removed with a cotton swab. Cells adhering to the lower surface of the chambers were fixed with 4% paraformaldehyde for 10 min and stained with 0.05% crystal violet for 10 min. Finally, the number of invasive and migratory cells in five random fields of view was counted under an IX83 Olympus inverted light microscope (Olympus, Tokyo, Japan).

Western blot

After the cells were collected by Western blot assay, the total protein was extracted with RIPA lysate (Beyotime Biotechnology, Haimen, China), and the protein concentration was detected by BCA protein assay kit (Beyotime, Jiangsu, China). The proteins in the lysate were separated by 10% SDS-polyacrylamide gel and transferred to polyvinylidene fluoride (PVDF) membranes (0.22 or 0.45μm; Millipore, Billerica, MA). After blocking with 5% skim milk, the membranes were incubated with specific primary rabbit polyclonal anti-LRRK2 antibody (dilution, 1:1,000; cat. no. ab133518; Abcam, Cambridge, MA, USA) at 4°C overnight. After washing with PBST, HRP-labeled secondary antibody was added and incubated at room temperature for 1 h. The signals were detected using the Western Bright ECL detection system (Bio-Rad, Hercules, CA, USA).

Dual luciferase reporter gene experiment

The H19 and LRRK2 fragments that included miR-138 binding sites were mutated, and then the H19 and LRRK2 fragments with original or mutated sequences were, respectively, cloned into the pGL3 dual-luciferase vector (pGL3-empty; Promega Corp.). With the aid of Lipofectamine 2000 (Invitrogen; Thermo Fisher Scientific, Inc.), miR-138 mimic, miR-138 inhibitor and NC were then, respectively, transfected into the PTC cells that had been transfected with pGL3-H19-WT, pGL3-H19-MUT. After a 48-h transfection, luciferase activity was examined using the Dual Luciferase Reporter Assay System (Promega Corp.). The values were normalized to those obtained for pre-miR negative control transfection. The above experiments were performed at least 3 times.

Statistical analysis

Statistical analyses were performed using SPSS 16.0 software package (SPSS Inc., Chicago, IL, USA). All data from three independent experiments were expressed as mean ± SD, and *t*-test was used for comparison between the two groups. $P < 0.05$ was considered statistically significant.

RESULTS

We found that the expression level of H19 in PTC cell lines (TPC-1 and FTC-133) was significantly higher than that in Nthy-ori3-1 cells (Fig. 1A). Then the si-H19 was transfected into TPC-1 and FTC-133 cells. As the result of RT-qPCR shown, the expression of H19 was significantly reduced after transfecting with si-H19 (Fig. 1B). In addition, we

detected the metastasis of PTC-1 and FTC-133 cells. We found that the number of migration and invasion cells was reduced by H19 knockdown (Fig. 1 C, D). After knockdown of H19, the expression of LRRK2 was analyzed by Western blot, and the expression of LRRK2 was significantly reduced after transfection with si-H19 (Fig. 1E).

To further study the mechanism of miR-138 regulation in thyroid cancer cell lines, we generated WT-H19 3'-UTR luciferase report vector (WT-H19) and sites in MUT-H19 3'-UTR luciferase report vector (MUT-H19) H19 3'-UTR by predicted binding of miR-138 (Fig. 2A). miR-138 mimic, miR-138 inhibitor and NC were then, respectively, transfected into the PTC cells that had been transfected with pGL3-H19-WT, pGL3-H19-MUT. We detected the expression of miR-138 in normal thyroid cells and PTC cell lines (TPC-1 and FTC-133). As shown in Fig. 2B, the expression levels of miR-138 in TPC-1 and FTC-133 cells were significantly decreased compared to those in Nthy-ori3-1 cells. In order to detect the relationship between miR-138 and H19,

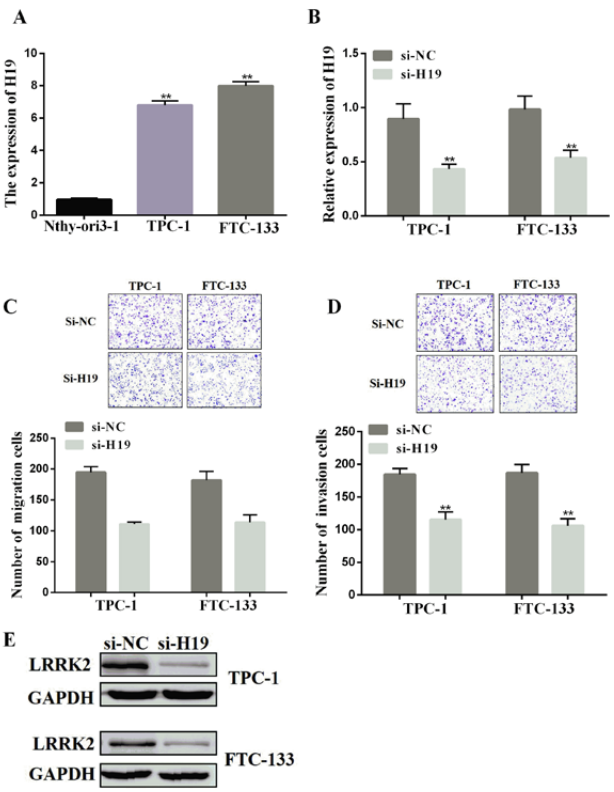

Fig. 1. *Knockdown of H19 reduced LRRK2 expression. **A)** RT-qPCR showed low expression of lnc H19 in normal thyroid cells, and conversely, significantly increased expression in tumor cells. **B)** The expression of knockdown H19 was expressed in two thyroid cancer cell lines. Compared with the control group, the expression level of H19 in si-H19 group was significantly decreased. **C, D)** After H19 knockdown, the invasion and migration of the two types of thyroid cancer cells were inhibited, and the number of cells was significantly reduced. **E)** After H19 knockdown was detected by protein western blot, the protein expression level of LRRK2 was also significantly reduced in the two cell lines.*

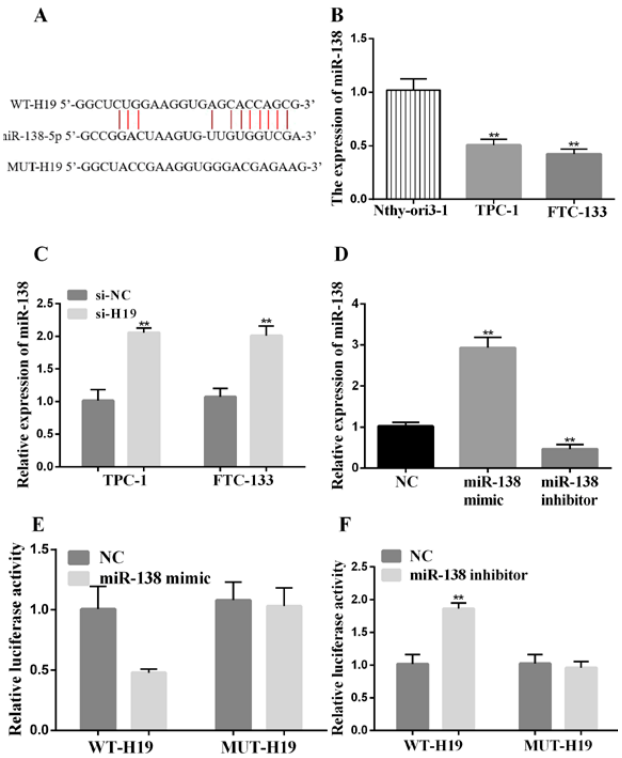

Fig. 2. *LncRNA H19 competitively binds with miR-138. **A)** The putative binding sites of H19 on miR-138. **B)** RT-qPCR was used to detect the expression of miR-138 in thyroid cancer cells. Repeat all experiments three times. **C)** After knocking down H19, the expression level of miR-138 was detected by RT-qPCR in the two thyroid cancer cell lines. Repeat all experiments three times. **D)** After cells were transfected with miR-138 mimic or miR-138 inhibitor, RT-qPCR was used to detect the transfection success or failure. **E, F)** To verify the interaction between miR-138 and H19, luciferase activity was detected after transfection with miR-138 mimic.*

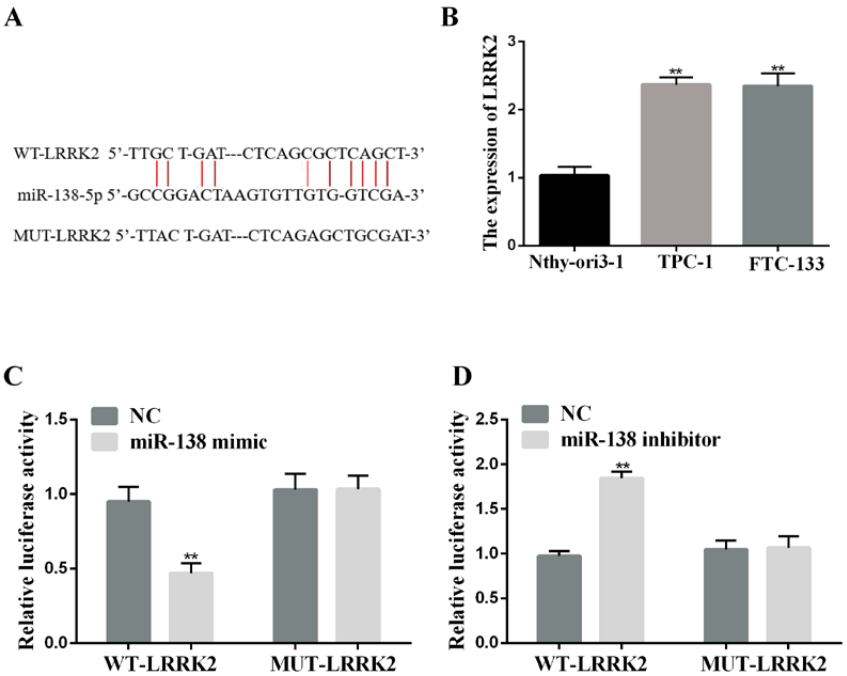

Fig. 3. *LRRK2 is the direct target of miR-211 in cervical cells.* ***A)*** *The putative binding sites of miR-138 on LRRK2.* ***B)*** *Compared with normal thyroid cells, the expression level of LRRK2 was detected by RT-qPCR.* ***C, D)*** *Luciferase reporter assay with the pGL3-LRRK2-3'-UTR-WT or pGL3-LRRK2-3'-UTR-MT were co-transfected with miR-138 mimics /NC.*

we used RT-qPCR to detect the expression of miR-138 after transfecting with si-H19 or si-NC in PTC cell lines (TPC-1 and FTC-133). The expression of miR-138 was higher in the si-H19 group than that in the si-NC group (Fig. 2C). To further investigate the role of miR-138 in PTC cells, we transfected miR-138 mimic and inhibitor into PTC cells, respectively, and the transfection effect was detected by RT-qPCR (Fig. 2D). After maintaining or mutating the binding sites within H19, the results of luciferase reporter gene assay displayed that miR-138 mimic could significantly reduce the luciferase activity under the presence of H19-WT, and miR-138 inhibitor could promote the luciferase activity under the presence of H19-WT, however, it failed to affect the luciferase activity of H19-MUT group (Fig. 2 E, F).

We identified LRRK2 mRNA as one of the putative miR-138 targets by using the Targetscan 7.2 (http://www.targetscan.org/vert 72/) (Fig. 3A). We used RT-qPCR to detect LRRK2 expression in PTC cell lines (TPC-1 and FTC-133) and Nthy-ori3-1 cells, and found that the expression of LRRK2 was higher in TPC-1 and FTC-133 cells than that in Nthy-ori3-1 cells (Fig. 3B). In order to further prove miR-138 and LRRK2, dual luciferase reporter assay was carried out. As shown in Fig. 3 C, D, luciferase activity was remarkedly reduced by miR-138 mimic and promoted by miR-138 inhibitor, but not the MUT- LRRK2 3'-UTR.

After LRRK2 was knocked down in PTC cells, the expression level of LRRK2 was significantly decreased (Fig. 4A). The expression of LRRK2 was partially restored by transfection with miR-138 inhibitor + LRRK2 knockdown (Fig. 4B). In order to verify the relationship between the three, we set up four groups of controlled experiments for testing Si-NC + inhibitor NC, si-NC + miR-138 inhibitor, si-H19 + inhibitor NC and si-H19 + miR-138 inhibitor. We first measured the expression levels of LRRK2 mRNA in two cell lines in the four groups and found that the MiR-138 inhibitor promoted LRRK2 expression. However, when

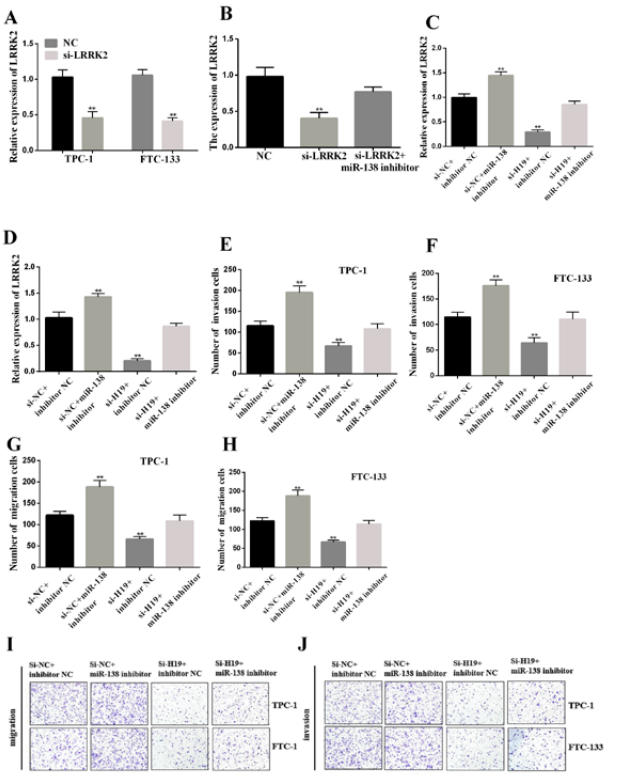

Fig. 4. *H19/miR-138 /LRRK2 regulates survival and metastasis of PTC cells.* ***A)*** *The level of LRRK2 was detected by RT-qPCR after transfected with si-H19.* ***B)*** *After transfection with miR-138 inhibitor on the basis of knockdown LRRK2, the level of LRRK2 was detected by RT-qPCR.* ***C, D)*** *LRRK2 expression level was detected by RT-qPCR in both thyroid cancer lines.* ***E-J)*** *Transwell assay was used to detect the invasion and migration of both thyroid cancer lines.*

H19 was knocked down simultaneously, LRRK2 expression level was relatively higher (Fig. 4 C, D). Cell invasion and migration were measured by MTT at morphological level, and miR-138 inhibitor was found to promote the cell invasion and migration. In contrast, knockdown H19 significantly reduced the cell invasion and migration. Inhibition of miR-138 and H19 expression at the same time can partially save cell invasion and migration(Fig. 4F and J).

DISCUSSION

PTC is a common secretory malignancy (8), and its incidence has been increasing in recent years (9). LncRNA has been shown to play an important role in the occurrence and development of human tumors (10). Silencing H19 can inhibit the proliferation, invasion and migration of breast cancer cells by regulating the expression of miR-138 and its targeted gene SOX4, as well as inducing cell cycle stagnation and apoptosis. Studies have shown that lncRNA RP11-476D10.1 can be combined with miR-138 to promote the expression of LRRK2; in addition, inhibiting the expression of lncRNA can inhibit the occurrence and development of tumor cells (11). This study focused on the ability of lncH19 to regulate the invasion and migration of PTC cells by regulating the targeted binding of miR-138-5p and LRRK2. Our experimental results showed that lncRNA H19 was highly expressed in PTC cell lines. Our study also showed that down-regulation of lncRNA H19 could inhibit PTC cell proliferation by decreasing the expression of LRRK2.

The present research found that both H19 and LRRK2 were highly expressed in thyroid cancer cell lines in vitro. H19 binds to miR-138 to regulate LRRK2. One study demonstrated that the expression level of LRRK2 in thyroid carcinoma tissues was significantly higher than that in normal thyroid tissues (12). Moreover, Tanswell assay was used to detect the invasion and migration of thyroid tumor cells, which was consistent with the results of RNA level, and the cell invasion and migration in the miR-138 inhibited group were significantly increased. However, the cell invasion and migration in the knockout H19 group were significantly reduced compared with the control group. Furthermore, after H19 knockdown and miR-138 suppression, the invasion and migration of the two cell lines increased compared with that of miR-138 suppression alone. In summary, these findings provide novel insight into the potential regulatory roles of H19 in PTC, and suggest that this pathway may prove to be a promising therapeutic target for the treatment of patients with PTC. The safety and efficacy of H19 based therapies remain to be demonstrated in clinical trials.

ACKNOWLEDGEMENTS

This study was supported by grants from the

Project of Shenzhen Science and Technology Plan (No. JCYJ20150330102720125, application of gene detection combined with interventional ultrasound in the diagnosis and treatment of papillary thyroid carcinoma).

REFERENCES

1. Wang ZH, Hao Z, Liang H, Dong W, Jing L, Shan Z, Teng W. Association between the expression of four upregulated miRNAs and extrathyroidal invasion in papillary thyroid carcinoma. Onco Targets Ther 2013; 6:281-87.
2. Leux C, Truong T, Petit C, Baron-Dubourdieu D, Guénel P. Family history of malignant and benign thyroid diseases and risk of thyroid cancer: a population-based case-control study in New Caledonia. Cancer Causes Control 2012; 23(5):745-55.
3. Nexo MA, Watt T, Cleal B, et al. Exploring the experiences of people with hypo- and hyperthyroidism. Qual Health Res 2015; 25:945-53.
4. Lubitz CC, Sosa JA. The changing landscape of papillary thyroid cancer: Epidemiology, management, and the implications for patients. Cancer 2016; 122(24): 3754-3759.
5. Toshiyuki I. Expression and role of long non-coding RNA H19 in carcinogenesis. Front Biosci 2018; 23:614-25.
6. Barbara M, Pilar DLP, Feda A, Azab AK. The role of hypoxia in cancer progression, angiogenesis, metastasis, and resistance to therapy. Hypoxia 2015; 83-92.
7. Wang Z, Yao Y-J, Zheng F, Guan Z, Qin W-J. Mir-138-5p acts as a tumor suppressor by targeting pyruvate dehydrogenase kinase 1 in human retinoblastoma. Eur Rev Med Pharmacol Sci 2017; 21(24):5624-29.
8. Yip L, Kelly L, Shuai Y, Armstrong MJ, Nikiforov YE, Carty SE, Nikiforova MN. MicroRNA signature distinguishes the degree of aggressiveness of papillary thyroid carcinoma. Ann Surg Oncol 2011; 18:2035-41.
9. Kowalska A, Walczyk A, Kowalik A, Payga I, Kamiński G. Increase in papillary thyroid cancer incidence is accompanied by changes in the frequency of the BRAF(V600E) mutation: A single-institution study. Thyroid 2016; 26(4):543-51.
10. Dai J, Li Q, Bing Z, et al. Comprehensive analysis of a microRNA expression profile in pediatric medulloblastoma. Mol Med Rep 2017; 15(6):4109-15.
11. Zhao Y, Zhao L, Li J, Zhong L. Silencing of long noncoding RNA RP11-476D10.1 enhances apoptosis and autophagy while inhibiting proliferation of papillary thyroid carcinoma cells via microRNA-138-5p-dependent inhibition of LRRK2. J Cell Physiol 2019; 234(11):20980-91.
12. Looyenga BD, Furge KA, Dykema KJ, et al. Chromosomal amplification of leucine-rich repeat kinase-2 (LRRK2) is required for oncogenic MET signaling in papillary renal and thyroid carcinomas. Proc Natl Acad Sci U S A 2011 25; 108(4):1439-44.

LETTER TO THE EDITOR

Endovascular electrocoagulation via microguidewire for treating intracranial aneurysms

C. Qiu, JB. Zhao, HC. Lu and J. Ma

Nanjing Comprehensive Stroke Center, Affiliated Nanjing Brain Hospital of Nanjing Medical University, Najing, Jiangsu China

Received October 27, 2020 – Accepted January 19, 2021

To the Editor,

Embolization and vessel occlusion are usually achieved using devices such as a detachable coil or balloon. However, in this study, good results were obtained using a microguidewire to perform endovascular electrocoagulation for the treatment of intracranial aneurysms. This abandoned technique was historically developed by Guglielmi Guido for vessel occlusion (1).

A 61-year-old woman visited the emergency department of the Affiliated Nanjing Brain Hospital of Nanjing Medical University on December 5, 2019. Her condition was severe when she was referred to Nanjing Comprehensive Stroke Center. She was then transferred to the intensive care unit (ICU) after obtaining her family members' consent. During the course of the disease, she presented with loss of consciousness, respiratory failure, which was managed by tracheal intubation and ventilation, and urinary and fecal incontinence. Computed tomography revealed subarachnoid and intracerebral hemorrhage. She was also diagnosed with lung infection, liver function impairment, and hypertension. Cerebral angiography was conducted under general anesthesia, with embolization of an aneurysm of the second segment (P2) of the right posterior cerebral artery (PCA). This procedure was performed on the same day to prevent intracranial aneurysm re-rupture and bleeding that would have endangered the patient's life. Signed and dated informed consent documents indicating that the subject has been informed of all pertinent aspects of the study were collected.

The following specific steps were carried out. Tthe patient was positioned in the supine position and intubated under general anesthesia, the right femoral artery was punctured with the Seldinger technique, a 6F sheath was inserted, and systemic heparinization was performed. Digital subtraction angiography with a 5F vertebral (angled) catheter revealed bilateral internal carotid artery occlusion, neovascularization in the skull base, and two right PCA aneurysms, both distal to P2 (Fig. 1). The proximal aneurysm on the right PCA was approximately 2.2 × 3.6 mm in size, irregularly shaped, and its neck was approximately 0.6-mm wide. The distal aneurysm on the right PCA was approximately 2.1 × 2.1 mm, but the size of its neck was unclear, therefore it was suspected to be a dissecting aneurysm. The bleeding in the distal aneurysm was considered to be closely related to the proximal aneurysm. After the angiography, the 5F catheter was placed in the right vertebral artery at the level of the C1−C2 vertebrae. An attempt to use a microcatheter (Prower-14) to select the cavity of the proximal right PCA aneurysm under the guidance of a microguidewire was unsuccessful.

Key words: intracranial aneurysms; endovascular electrocoagulation; microcatheter

Corresponding Author:
Dr Jun Ma,
Nanjing Comprehensive Stroke Center,
No.264 Guangzhou Road,
Gulou District, Nanjing,
Jiangsu, 210000, China
e-mail: jemt91@163.com

0393-974X (2021)
Copyright © by BIOLIFE, s.a.s.
This publication and/or article is for individual use only and may not be further reproduced without written permission from the copyright holder.
Unauthorized reproduction may result in financial and other penalties
DISCLOSURE: ALL AUTHORS REPORT NO CONFLICTS OF INTEREST RELEVANT TO THIS ARTICLE.

Thereafter, the microcatheter was replaced followed by repeated shaping, but an attempt to place it into the cavity of the aneurysm was unsuccessful (Fig. 2). The microcatheter (Prower-14) was then placed near the neck of the proximal right PCA aneurysm, and microguidewire selection into the aneurysm cavity was performed, followed by electrocoagulation with the microguidewire (5 times, 2 minutes each). The proximal right PCA aneurysm was no longer visible on the angiogram (Fig. 3). Another microcatheter (Prower-14) was used to select the cavity of the distal aneurysm of the right PCA, guided by a microguidewire. A 2 mm × 2.5 cm Codman coil and 1.5 mm × 2 cm HydroCoil were deployed. When the 1.5 mm × 2 cm HydroCoil was inserted, the microcatheter was ejected from the aneurysm cavity. After the coil and catheter were replaced, the microcatheter was inserted into the residual cavity

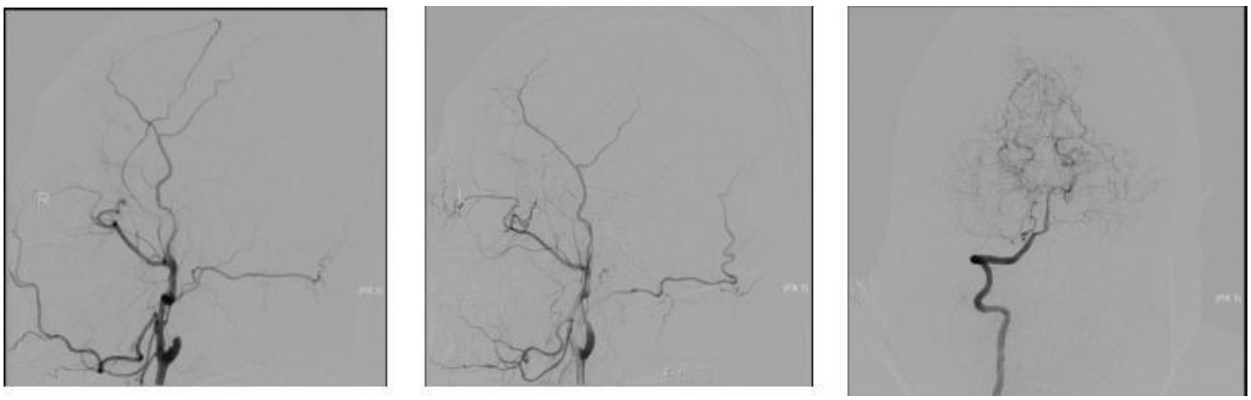

Fig. 1. *Digital subtraction angiography (DSA) imaging of carotid arteries (antero-posterior (AP) & lateral (LAT) view) (left), imaging of left carotid arteries (AP and LAT view) (middle), and imaging of 2 aneurysms distal to the right posterior cerebral artery (PCA) (P2), indicating bilateral internal carotid artery occlusion (right). Occlusion appears in the initial segment of the patient's right middle cerebral artery (MCA) and in the left internal carotid artery. Bleeding may be caused by the right PCA aneurysm.*

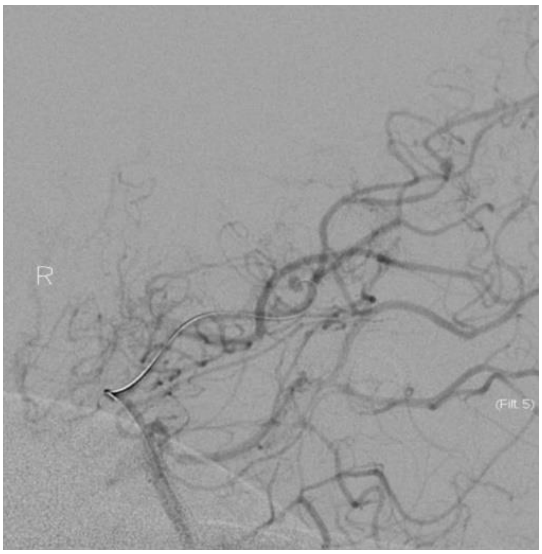

Fig. 2. *Failure of insertion of the microcatheter to the aneurysm neck via repeatedly shaped microguidewire followed by electrocoagulation of the aneurysm via microguidewire.*

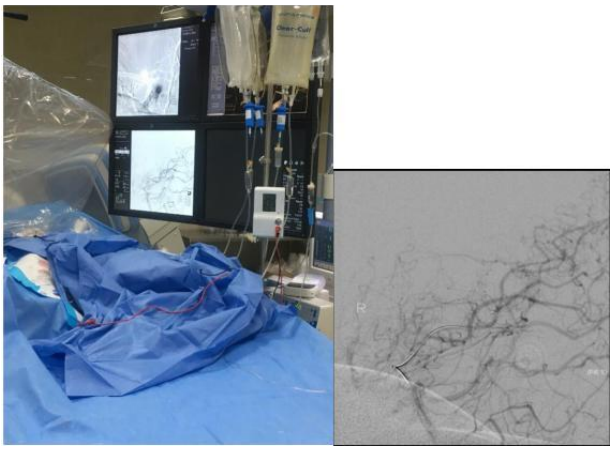

Fig. 3. *Intraoperative image. The red wire is connected to the guide wire, and the black wire is connected to the patient, thus forming a circuit. Digital subtraction angiography (DSA) was performed and evaluated after each electrocoagulation until the aneurysm was completely occluded (left); after 5 times of electrocoagulation and DSA, aneurysms no longer developed (right).*

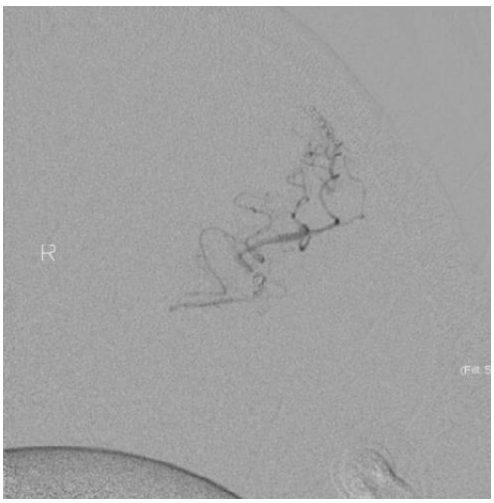

Fig. 4. *Embolization of an aneurysm via coils*

distal to the right PCA aneurysm. A 1 mm × 1 cm HydroCoil was then deployed and, upon deployment, the resistance became strong, and the embolization was terminated. All the coils were confirmed to be in the right position before release according to the angiogram (Fig. 4). The operation was successful, and further treatment was provided in the ICU.

However, because of the prolonged duration of tracheal intubation and unsuccessful extubation, the patient underwent a bedside tracheotomy 1 week later (2). The patient's condition was stabilized, and she was transferred to our department for further treatment. The patient's general condition was fair with stable vital signs, and she was discharged on December 24, 2019 (3). During her follow-up, angiography revealed that the right PCA aneurysms were barely visible, and both the aneurysm-bearing arteries and peritumoral vessels were clearly visible.

It is difficult to select the microcatheter for some aneurysms with extremely narrow necks, making it impossible to fill the aneurysm with conventional coils. This study highlighted the possibility that this long-abandoned technique might have a place in current treatment strategies for ruptured aneurysms. Nevertheless, the efficacy of this theory needs to be verified.

REFERENCES

1. Ji C, Guglielmi G, Chen H. Endovascular electrocoagulation: concept, technique, and experimental results. AJNR Am J Neuroradiol 1997; 18(9):1669-78.
2. Cho Y D, Kim C H, Kang H S, et al. Trapping of endovascular microguidewire: a rare and serious complication during therapeutic microcatheterization for cerebrovascular disease. Clinical Neuroradiology 2015; 25(1):73-77.
3. Lee SJ, Cho YD, Kang HS, Kim JE, Han MH. Coil embolization using the self-expandable closed-cell stent for intracranial saccular aneurysm: a single-center experience of 289 consecutive aneurysms. Clin Radiol 2012; 68:256-63.

LETTER TO THE EDITOR

Vitamin D_3 supplementation in controlling metabolic changes associated with non-alcoholic steatohepatitis

H-M. Han[1*], X-Z. Song[2*], M-H. Cui[3], X. You[4] and X-X. Piao[5]

[1]Department of Gastroenterology, Affiliated Hospital of Yanbian University, Yanji, China; [2]Department of Gastroenterology, Jilin Provincial People's Hospital, Changchun, China; [3]Department of Pathology and Cancer Research Center, Yanbian University Medical College, Yanji, China; [4]Department of Laboratory Medicine, Affiliated Hospital of Yanbian University, Yanji, China; [5]Department of Gastroenterology, Affiliated Hospital of Yanbian University, Yanji, China

Received November 3, 2020 – Accepted January 20, 2021

[*]These authors contributed equally to this project

To the Editor,

With the rate of occurrence of up to 30%, non-alcoholic fatty liver disease (NAFLD) represents a serious public health problem. In particular, it may potentially progress into non-alcoholic steatohepatitis (NASH). The liver of NASH patients is characterised by steatosis, intralobular inflammation, hepatocellular ballooning, perisinusoidal fibrosis in zone 3 and, often, susceptibility to liver tumors. Furthermore, the patients show metabolic abnormalities such as obesity, insulin resistance, fasting hyperglycemia, dyslipidemia, and altered adipokine profile. NASH animal models have been developed for detailed studies of the pathogenesis and appropriate therapeutic interventions of this disease (1). Although the models reflect certain features of human NASH, none replicates the full spectrum. The choline-deficient (CD) model shows low fasting blood glucose, peripheral insulin sensitivity, low serum insulin and leptin levels, which appear to be more consistent with those observed in human NASH. The model can, however, be very good for more probing studies of metabolic changes associated with NASH. In a recent study, a typical model was established of NASH liver with a CD-diet, increased hepatic lipid content, inflammation, lipid peroxidation and fibrosis, but no significant changes in body weight and lipid profile. Many authors suggest that Vitamin D_3 (VD_3) supplementation decreases blood glucose levels, ameliorates insulin/leptin resistance and NASH progression (2), but there is a lack of association between plasma vitamin D levels and blood glucose, insulin resistance, or the severity of NASH (2). The role of vitamin D supplementation remains poorly studied. We recently reported that supplementation of vitamin D_3 ameliorated lipid accumulation, lipid peroxidation, inflammation, hepatocyte apoptosis and fibrosis in the liver caused by CD-diet with alteration of the levels of serum vitamin D_3–hydroxyvitamin D (25-(OH)D_3) and hepatic vitamin D receptor (VDR), but higher doses of VD_3 may lead to adverse effects. In the present study, the metabolic changes were further studied in an animal model kept on CD-diet, and the effect of VD_3 supplementation on the NASH progression.

Key words: vitamin D_3; choline; non-alcoholic steatohepatitis; insulin resistance; leptin resistance

Corresponding Author:
Dr Hongmei Han,
Department of Gastroenterology,
Affiliated Hospital of Yanbian University,
No.1327, Juzi St.,Yanji, Jilin province, China
Tel.: +86 4332660009 - Fax:+86 4332513160
e-mail: hongmei_h@aliyun.com

0393-974X (2021)
Copyright © by BIOLIFE, s.a.s.
This publication and/or article is for individual use only and may not be further reproduced without written permission from the copyright holder.
Unauthorized reproduction may result in financial and other penalties
DISCLOSURE: ALL AUTHORS REPORT NO CONFLICTS OF INTEREST RELEVANT TO THIS ARTICLE.

MATERIALS AND METHODS

Animals and experimental treatments

All experimental procedures on animals were approved by the Ethics Committee of Yanbian University. The Ethical Guidelines of the China Association of Laboratory Animal Care were strictly followed in the experiments.

Six-week-old male Wistar rats (150-180 g) were obtained from Yisi Experimental Animal Technology Company (Changchun, China). After a 1-week acclimation period, the animals were randomly assigned into three groups: a control group (CG, $n = 5$) with adequate level of dietary choline content, a CD group (CDG, $n = 5$) which was kept on CD-diet, and a VD_3 supplementation group (CDVDG, $n = 15$) with CD-diet plus intraperitoneal (IP) VD_3 injection. The choline-adequate diet and the CD-diet were both the L-amino acid-defined diets based on AIN93 standard (3), but had different choline contents (1000 mg/kg (TP 1R810) and 0 mg/kg (TP 1R800, Trophic Animal Feed High-Tech Company, China), respectively).

To explore the effects of different doses of VD_3 on the progression of NASH, the animals in CDVDG group were randomly assigned into three subgroups : CDVDG1 ($n = 5$), CDVDG5 ($n = 5$) and CDVDG10 ($n = 5$), and subjected to IP injections of VD_3 (General Pharmaceutical Ltd, China) with a dosage of 1, 5, or 10 **μg/kg of body weight,** respectively, twice a week (Tuesdays and Saturdays). The same amount of saline (10 ml/kg) was administrated to the rats in the CG and CDG groups.

At the end of the experimental period (12 weeks), the rats were fasted for 12-13 h and, under anaesthesia, blood was withdrawn from the abdominal aorta. Thereafter, the animals were euthanized (CO_2 gas in an induction chamber). The blood was snap frozen in liquid nitrogen and stored at –80°C (Froilabo Bio-Memory BM 690, France) until analysed.

Measurement of serum fasting blood glucose, fasting insulin, HOMA-IR and leptin

Serum levels of fasting blood glucose (FBG) were detected by Hexokinase (HK) method using Modular PPI testing system (Roche Diagnostics, Mannheim, Germany).

Serum levels of fasting insulin (FINS) were measured using rat insulin ELISA kit (Xinlebio, China). Homeostasis model of assessment for insulin resistance index (HOMA-IR) = (FBG × FINS)/22.5 (4). Serum levels of leptin (LEP) were measured using rat leptin ELISA kit (Xinlebio, China).

Statistical analysis

Data were presented as means ± standard error of mean (SEM). For multiple comparisons, one-way analysis of variance (ANOVA) was used. In case ANOVA showed an overall significant difference, post hoc analysis was performed with the least significant difference test. Differences were considered significant at $p < 0.05$.

RESULTS

After 12 weeks of the experimental period, as compared with the CG, the CDG had an increased in the serum FINS (29.50±0.34 mU/L *vs* 26.49±0.76 mU/L, $p < 0.05$), HOMA-IR (11.07±0.20 *vs* 9.07±0.34, $p < 0.05$) and leptin (569.71±38.97 ng/L *vs* 408.24±43.71 ng/L, $p < 0.01$), with no significant difference in the serum FBG (8.44±0.11 mM *vs* 7.70±0.22 mM, $p = 0.07$).

As compared with the CDG, the CDVDG had significantly decreased FBG (CDVDG5: 7.70±0.03 mM *vs* 8.44±0.11 mM, $p < 0.05$), FINS (CDVDG1, 5, 10 *vs* CDG: 27.20±0.91 μIU/mL, 22.94±0.90 μIU/mL, 21.47±0.77 μIU/mL *vs* 29.50±0.34 μIU/mL, respectively, $p<0.05$, $p<0.01$, $p<0.01$) , HOMA-IR (CDVDG5, 10 *vs* CDG: 7.85±0.32, 7.56±0.59 *vs* 11.07±0.20, respectively, $p<0.01$, $p<0.05$) and leptin (CDVDG5 *vs* CDG: 445.87±14.98 ng/L *vs* 569.71±38.97 ng/L, $p<0.05$) (Fig. 1). In addition, serum FBG, FINS, HOMA-IR and leptin levels in the CDVDG were significantly decreased upon treatment with VD_3 in a dose-dependent manner (respectively, $p<0.01$, $p<0.01$, $p<0.01$, $p<0.05$), but the dosage of 10 μg of VD_3 per kg of body weight could not further decrease the serum FBG, FINS, HOMA-IR and leptin levels.

These results showed that VD_3 supplementation could effectively decrease the FBG, FINS, HOMA-IR and leptin, suggesting that VD_3 ameliorates FBG and insulin/leptin resistance caused by CD-diet.

DISCUSSION

NASH is a disease closely related to metabolism, stress and genetic environment. Fasting hyperglycemia, insulin and leptin resistance are important metabolic factors in NASH progression (2). In recent years, phototherapy has been reported to improve insulin

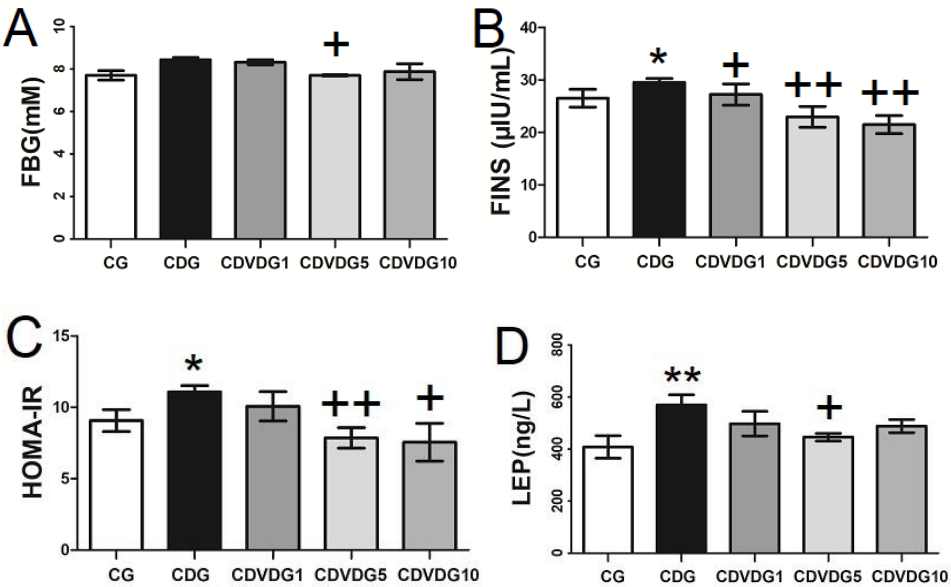

Fig. 1. *Effects of VD3 supplementation on the serum FBG, FINS, HOMA-IR and leptin.* ***A, B, C, D****) serum FBG, FINS, HOMA-IR and leptin levels, respectively. * p < 0.05 vs CG; ** p < 0.01 vs CG; + p < 0.05 vs CDG, ++ p < 0.001 vs CDG.*

and LEP resistance in NASH rats induced by CD-diet combined with iron supplementation diet (5). It was also demonstrated that VD3 supplementation regulates insulin sensitivity (6), reduces FBG and HOMA-IR levels (6) in NASH. Several experimental studies point towards a direct role of VD3 in modulating liver inflammation, fibrogenesis and improving hepatic response to insulin, likely through the binding to specific VD receptor expressed by different cell types in the liver (7). The results of this study showed that VD3 slightly reduces serum HOMA-IR and leptin levels in NASH rats induced by the CD-diet and improves insulin and leptin resistance.

The prevalence of metabolic syndrome components in the low VD group was significantly higher than that in the non-low VD group (8). VD3 has been reported to reduce blood glucose levels in type 2 diabetic rats (9). The mechanism may be related to VD3 promoting insulin secretion by increasing Ca2+ levels in pancreatic beta cells through non-genomic effects (8). It may also be related to the down-regulation of TLR4 expression through antigen-presenting cells, such as dendritic cells and macrophages, so as to reduce Thl-mediated inflammatory response and autoimmune damage and improve the inflammatory damage of islets (10). It has also been reported that VD3 increases the number of insulin receptors and up-regulates the insulin receptor gene, thereby increasing the glucose uptake capacity of the liver and improving glucose metabolism (11). In this study, FBG was slightly increased in rats (p = 0.07). After VD3 supplementation, FBG level was decreased in a dose-dependent manner, which is consistent with the previous reports. No significant weight gain or lipid changes in CD-diet-induced NASH rats were observed throughout our study. Our results demonstrate the role of VD3 in inhibiting the progression of NASH in rats induced by CD-diet by increasing the expression of VD receptor in liver tissue. In conclusion, our results suggest that VD3 supplementation is expected to be an effective measure for the treatment of patients with clinical NASH.

ACKNOWLEDGEMENT

This research was funded by the grant from the National Natural Science Foundation (No. 81860110).

REFERENCES

1. Takahashi Y, Soejima Y, Fukusato T. Animal models

of nonalcoholic fatty liver disease/nonalcoholic steatohepatitis. World J Gastroenterol 2012; 18:2300-8.
2. Nakano T, Cheng YF, Lai CY, et al. Impact of artificial sunlight therapy on the progress of non-alcoholic fatty liver disease in rats. J Hepatol 2011; 55:415-25.
3. Reeves PG, Rossow KL, Lindlauf J. Development and testing of the AIN-93 purified diets for rodents: results on growth, kidney calcification and bone mineralization in rats and mice. J Nutr 1993; 123:1923-31.
4. Matthews DR, Hosker JP, Rudenski AS, Naylor BA, Treacher DF, Turner RC. Homeostasis model assessment: insulin resistance and beta-cell function from fasting plasma glucose and insulin concentrations in man. Diabetologia 1985; 28:412-9.
5. Bril F, Maximos M, Portillo-Sanchez P, Biernacki D, Lomonaco R, Subbarayan S, et al. Relationship of vitamin D with insulin resistance and disease severity in non-alcoholic steatohepatitis. J Hepatol 2015; 62:405-11.
6. Foroughi M, Maghsoudi Z, Askari G. The effect of vitamin D supplementation on blood sugar and different indices of insulin resistance in patients with non-alcoholic fatty liver disease (NAFLD). Iran J Nurs Midwifery Res 2016; 21:100-4.
7. Beilfuss A, Sowa JP, Sydor S, et al. Vitamin D counteracts fibrogenic TGF-beta signaling in human hepatic stellate cells both receptor-dependently and independently. Gut 2015; 64:791–9.
8. Chiu KC, Chu A, Go VL, Saad MF. Hypovitaminosis D is associated with insulin resistance and beta cell dysfiinction. Am J Clin Nutr 2004; 79:820-5.
9. Tai K, Need AG, Horowitz M, Chapman IM. Vitamin D, glucose, insulin, and insulin sensitivity. Nutrition 2008; 24:279-85.
10. Erridge C. Endogenous ligands of TLR2 and TLR4:agonists or assistants? J Leukoc Biol 2010; 87:989-99.
11. Leung PS. The potential protective action of vitamin D in hepatic insulin resistance and pancreatic islet dysfunction in type 2 diabetes mellitus. Nutrients 2016; 8:147.

LETTER TO THE EDITOR

Changes and significance of serum sMICA levels in patients with recurrent miscarriage before and after lymphocyte infusion therapy

L-P. Wang[1], G-L. Luo[2], J. Liu[3], J-X. Xu[1], K. Liu[1], F-T. Sun[1] and Q-L. Zhou[1]

[1]Department of Blood Transfusion, Weifang People's Hospital, Weifang, Shandong Province, China; [2]Department of Obstetrics and Gynecology, Jiyang People's Hospital, Jinan, Shandong Province, China; [3]Health Management Department, Jiyang People's Hospital, Jinan, Shandong Province, China

Received October 30, 2020 – Accepted January 21, 2021

To the Editor,

Unexplained recurrent spontaneous abortion (URSA) refers to those who have had two or more consecutive spontaneous abortions with the same sexual partner (1). After clearly excluding genetic, endocrine, infectious, and psychological factors, the diagnosis of URSA can be made. URSA accounts for about 50% of the total prevalence, 80% of which are related to immune factors (2). Lymphocyte infusion therapy (URSA method) has been used clinically for nearly 20 years, and has achieved good therapeutic effects and relieved the suffering of many patients. However, the treatment mechanism of URSA has not been revealed in previous studies. It has been proposed that lymphocyte infusion therapy can regulate peripheral immune tolerance and make the mother resistant to paternal antigens. It has also been reported that the relationship between the function of natural killer cells (NK cells) and the pathogenesis of URSA is clear (3). In addition, sMICA was found to down-regulate the expression of NKG2D receptors on the surface of NK cells (4) and reduce their killing activity, which is an important factor in the immune tolerance mechanism. However, the correlation between sMICA and lymphocyte infusion therapy has not been reported in previous studies.

Recurrent miscarriages have many adverse effects on the physiology and psychology of women of childbearing age. From an immunological point of view, the rejection of antigens from the paternal line by the mother is a major cause of miscarriage. After nearly 30 years of clinical application, lymphocyte infusion has been proven to be a safe and effective method for the treatment of URSA, which relieves the suffering of many patients. However, the exact mechanism of lymphocyte infusion therapy remains unclear. It has been shown that lymphocyte infusion therapy can induce the maternal immune tolerance to the embryo (5) and make the second pregnancy successful.

The purpose of this study is to investigate the alternation of sMICA level before and after lymphocyte infusion therapy, and to confirm the correlation between sMICA levels and treatment effects of lymphocyte infusion.

MATERIALS AND METHODS

Patients

From May 2014 to August 2019, a total of 110 patients were selected to receive lymphocyte infusion therapy at Weifang People's Hospital. These patients were 28 to 36 years old, with an average age of 32.6 years. According to

Key words: recurrent spontaneous abortion; lymphocyte infusion therapy; sMICA

Corresponding Author:
Dr Qinglin Zhou,
Department of Blood Transfusion, Weifang People's Hospital,
No. 151 Guangwen Street, Weifang, 261041,
Shandong Province, China
Tel.: +86 0536-8192599
e-mail: kjb57x@163.com

0393-974X (2021)
Copyright © by BIOLIFE, s.a.s.
This publication and/or article is for individual use only and may not be further reproduced without written permission from the copyright holder.
Unauthorized reproduction may result in financial and other penalties
DISCLOSURE: ALL AUTHORS REPORT NO CONFLICTS OF INTEREST RELEVANT TO THIS ARTICLE.

the pregnancy outcome after treatment, they were divided into a success group and a failure group. The inclusion criterion are based on a previous study (6). Written informed consents were obtained from all patients. This study was approved by the Institutional Ethics Committee of Weifang People's Hospital.

Lymphocyte infusion therapy

The lymphocyte infusion therapy URSA treatment method was performed based on a previous study (6).

Detection of serum sMICA by ELISA

The human sMICA ELISA kit (Abcam, UK) was used to detect serum sMICA levels. Experimental procedure was strictly performed based on the reagent instructions. Each sample was repeated three times. The absorbance was detected with a microplate reader and the serum sMICA concentration was calculated according to the standard curve.

Statistical analysis

All experiments were repeated three times. The data are shown as mean ± SD and analyzed by Graphpad Prism 6. Student's t-test was used to analyze the difference between the two groups. The differences between multiple groups were detected by ANOVA. $P < 0.05$ was considered statistically significant.

RESULTS

Serum sMICA levels in patients before and after lymphocyte infusion

In this study, there were 84 successful pregnancies and 26 unsuccessful pregnancies in the 110 patients after treatment. The treatment success rate was 76.4%. The results showed that the serum sMICA levels of patients in the success group and failure group were higher than before the treatment. The differences between the two groups were statistically significant ($P<0.01$, Fig. 1).

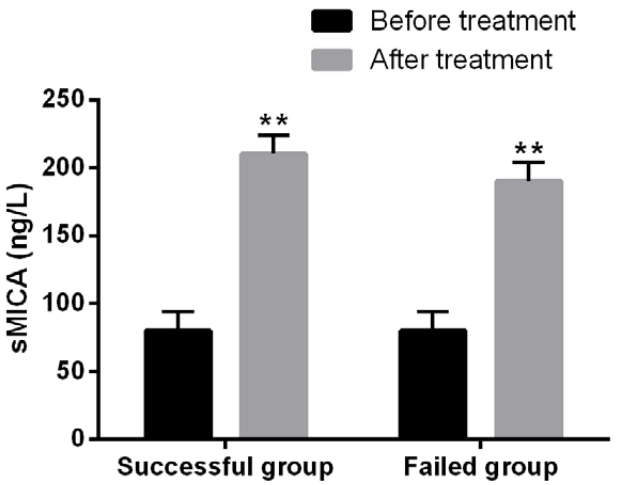

Fig. 1. *Comparison of serum sMICA concentration between the successful group and the failed group before and after treatment. **P < 0.01.*

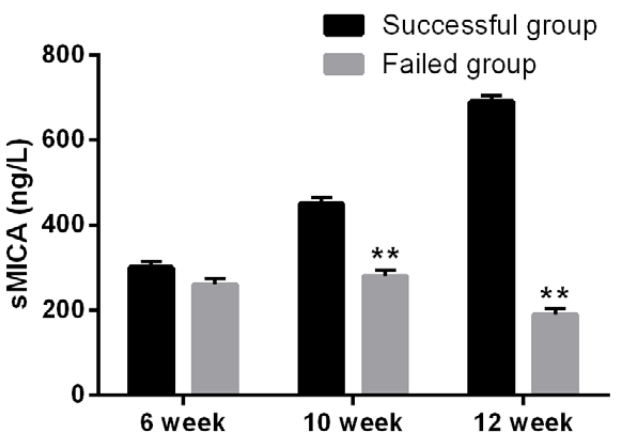

Fig. 2. *The levels of serum sMICA were compared in the successful group and the failed group ** P <0.01*

Comparison of serum sMICA levels in different gestational weeks between the successful group and the failed group of pregnant patients after treatment

The results showed that there was no significant difference in serum sMICA levels between the success group and the failure group at 6 weeks of pregnancy ($P>0.01$, Fig. 2). However, the difference in serum sMICA levels between the success group and the failure group at the 10th week and the 12th week was statistically significant ($P<0.01$, Fig. 2). Most cases in the failure group experienced a miscarriage again around 12 weeks of pregnancy, therefore, serum sMICA levels were not detected in this group after 12 weeks.

Trend of serum sMICA levels in different gestational weeks after pregnancy

As shown in Fig. 3, the serum sMICA level of the

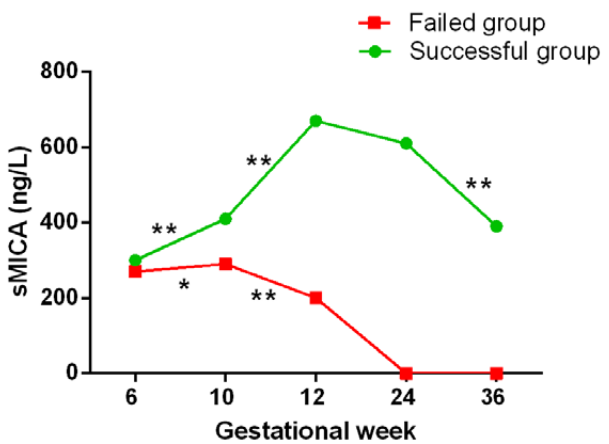

Fig. 3. *The trend of serum sMICA level in the successful group and the failed group at different gestational weeks ** P <0.01*

successful group gradually increased after pregnancy and reached its peak at 12 weeks of pregnancy. Serum sMICA levels remained high from 12 to 24 weeks, and then gradually decreased. In addition, the serum sMICA level of the failure group increased significantly after pregnancy compared to the success group. The serum sMICA reached the highest level at 10 weeks, and then rapidly decreased. The overall sMICA level of the failure group was lower than that of the success group.

DISCUSSION

The major histocompatibility complex class I chain-related protein (MIC) has multiple gene families, of which only MICA and MICB have the function of encoding and transcripting proteins. MICA is located at 6p21.31 on the short arm of human chromosome 6. There are two types of membranes (mMICA) and soluble (sMICA) in the body.

NK cells are a group of lymphocytes that can directly act on target cells and are important parts of the human innate immune system. mMICA is the first ligand binding to NKG2D, which can help NK cells recognize and kill target cells. In addition, NK cells present in peripheral blood and endometrium are closely related to the immune mechanism of the maternal-fetal interface that causes URSA. The expression of mMICA was not detected in the placental trophoblast tissue of normal pregnancy, but was increased in the placental trophoblast cells of URSA patients . The results indicate that the decrease in mMICA level may be one of the reasons for URSA. In addition, it has been found that sMICA can induce the internalization and degradation of NKG2D on the surface of T cells, and reduce the killing activity of NK cells , which is an important part of the human immune tolerance mechanism.

This study showed that the success rate of lymphocyte infusion therapy in URSA patients reached 76.4%, which is consistent with a previous study . The sMICA level after treatment was significantly higher than before treatment. The serum sMICA levels of the success group were increased significantly at 10 and 12 weeks of gestation. In addition, the serum sMICA level of the success group gradually increased after pregnancy and reached its peak at 12 weeks of pregnancy. Serum sMICA levels remained high from 12 to 24 weeks, and then gradually decreased. The serum sMICA level of the failure group after pregnancy was significantly higher than that of the success group. It can reach the highest level at 10 weeks, and then rapidly decreased. The results indicate that serum sMICA plays an important role in regulating the immune tolerance of pregnant women to paternal antigens and protecting the stable development of embryos in the early and middle pregnancy. The sMICA has been proved to be an important immune tolerance factor in the human body, and its correlation with treatment and pregnancy proves that lymphocyte infusion therapy can induce the maternal immune tolerance to the paternal antigens, so that the second pregnancy can be successful. However, this study is not clear enough to explain the role of sMICA in pregnancy. Therefore, further research is still needed.

In conclusion, the serum sMICA level was increased significantly after lymphocyte infusion therapy, and the serum sMICA level was increased with the increase of gestational age after pregnancy. It is suggested that a certain increase in serum sMICA levels after treatment and pregnancy may be a key factor for successful pregnancy. It can be used as an important indicator to predict the success of treatment after pregnancy.

ACKNOWLEDGEMENT

This study is supported by Weifang City Health Research Project (2014, No. 026).

REFERENCES

1. Luo L, Zeng X, Huang Z, Luo S, Qin L, Li S. Reduced frequency and functional defects of CD4(+) CD25(high)CD127(low/-) regulatory T cells in patients with unexplained recurrent spontaneous abortion. Reprod Biol Endocrinol 2020; 18:62.
2. Kwak-Kim J, Gilman-Sachs A. Clinical implication of natural killer cells and reproduction. Am J Reprod Immunol 2008; 59:388-400.
3. Sokolov DI, Mikhailova VA, Agnayeva AO, et al. NK and trophoblast cells interaction: cytotoxic activity on recurrent pregnancy loss. Gynecol Endocrinol 2019; 35:5-10.
4. Boukouaci W, Al-Daccak R, Dulphy N, et al. Soluble MICA-NKG2D interaction upregulates IFN-gamma production by activated CD3-CD56+ NK cells: potential impact on chronic graft versus host disease. Hum Immunol 2013; 74:1536-41.
5. Wu L, Luo LH, Zhang YX, et al. Alteration of Th17 and Treg cells in patients with unexplained recurrent spontaneous abortion before and after lymphocyte immunization therapy. Reprod Biol Endocrinol 2014; 12:74.
6. Achilli C, Duran-Retamal M, Saab W, Serhal P, Seshadri S. The role of immunotherapy in in vitro fertilization and recurrent pregnancy loss: a systematic review and meta-analysis. Fertil Steril 2018; 110:1089-100.
7. Hizem S, Mtiraoui N, Massaoudi S, et al. Polymorphisms in genes coding for the NK-cell receptor NKG2D and its ligand MICA in recurrent miscarriage. Am J Reprod Immunol 2014; 72:577-85.
8. Wang H, Yang D, Xu W, et al. Tumor-derived soluble MICs impair CD3(+)CD56(+) NKT-like cell cytotoxicity in cancer patients. Immunol Lett 2008; 120:65-71.
9. Sereshki N, Andalib A, Ghahiri A, Mehrabian F, Sherkat R, Rezaei A. Can the decreased expression of human leukocyte antigen class and by spermatozoa lead to recurrent spontaneous abortion? Iran J Pathol 2020; 15:19-22.

LETTER TO THE EDITOR

Vaginal bipolar radiofrequency as non-surgical treatment of stress urinary incontinence: Case series study

P. Gonzalez Isaza[1] and D.L. Velez Rizo[2]

[1]Department of Obstetrics and Gynecology, Division of Urogynecology and Pelvic Reconstructive Surgery, Hospital Universitario San Jorge, Pereira, Colombia; [2]Department of Women Health Fundación Cardioinfantil, Bogotá, Colombia

Received November 4, 2020 – Accepted January 21, 2021

To the Editor,

Stress Urinary Incontinence (SUI) is a common condition that consists in involuntary urine leakage caused by increased intra-abdominal pressure (e.g. during physical exercises, sneezing, coughing or laughing) in the absence of a bladder contraction (1). Risk factors include childbirth, advancing age, hysterectomy, recurrent urinary tract infections, smoking, medications such as diuretics and weight changes (2). Urinary incontinence affects up to 50% of women worldwide and 77% of elderly women. Non-ablative radiofrequency (RF) has been used as a minimally invasive technique, generating heat inside the tissue in the range of 40-45°C to stimulate activation of fibroblasts and synthesis of new collagen and elastin fibers by heat shock protein-mediated inflammatory cascade (3). Transcutaneous temperature-controlled RF resulted in significant improvements in SUI with histological changes such as increase in collagen, elastin, vascularity, and small nerve fibers (4). There are several devices in the market for RF-based intravaginal and vulvar treatments which do not require anaesthesia. Patients report a tolerable sensation of warmth without downtime (5). These devices can be either monopolar or bipolar, with Bipolar Radiofrequency (BPRF) intrinsically more safe. Millheiser et al. conducted a pilot study on 24 women using RF energy, delivered through the vaginal mucosa. Post-treatment assessments were at 10 days and 1, 3, and 6 months. Results showed that after 1-month, post-treatment self-reported vaginal tightness significantly improved in 67% of subjects and in 87% at 6 months. Mean sexual function scores also improved, and no adverse events were reported (6). Validated scales such as International Consultation on Incontinence Questionnaire - Short Form (ICIQ-SF) have a maximum degree of recommendation for use in urinary incontinence (7). The aim of this study was to investigate the efficacy and safety of RF Touch (DEKA M.E.L.A. Calenzano, Italy) BPRF device for transvaginal treatment of SUI. RF Touch consists in an RF Generator (500 Hz of frequency and 50 W of maximum power) placed in the driver box of some DEKA laser systems. A temperature controlled disposable handpiece (RF Touch), is used to deliver the RF energy to the targeted tissues. The system's software has the possibility of setting range of temperatures and a time of treatment.

The present study was conducted between August and November 2019. The patients were volunteers from the Primary Urogynecology Unit, Obstetrics

Key words: urinary incontinence; energy based devices; radiofrequency; bipolar radiofrequency.

Corresponding Author:
Pablo Gonzales Isaza,
Avenida Juan B Gutierrez, 18-60 Consultorio 702,
Edificio Oval Medica, Codigo Poatal 660002,
Pereira Colombia
Tel.: +573207887509
e-mail: pagonza@gmail.com

0393-974X (2021)
Copyright © by BIOLIFE, s.a.s.
This publication and/or article is for individual use only and may not be further reproduced without written permission from the copyright holder.
Unauthorized reproduction may result in financial and other penalties
DISCLOSURE: ALL AUTHORS REPORT NO CONFLICTS OF INTEREST RELEVANT TO THIS ARTICLE.

Table I. *Demographics.*

N° of patients	12
Age	35.5
Parity	1.8
Vaginal deliveries	1.5
BMI	24.33
PELVIC FLOOR EXAMINATION: Stages of POP–Q (Pelvic Organ Prolapse Quantification) system measurement	
Stage ≤1	12

Table II. *Inclusion/exclusion criteria*

INCLUSION CRITERIA	EXCLUSION CRITERIA
● Volunteers complaining about stress urinary incontinence.	● Volunteers with POP-Q stage> 1; ● Volunteers with a history of a recto-vaginal or vesicovaginal fistula; ● Volunteers unable to follow-up for a period of 9 months post-treatment; ● Abnormal HPV DNA test and subsequent abnormal liquid based cytology; ● Volunteers with undiagnosed uterine bleeding; ● Volunteers undergoing pelvic floor rehabilitation or surgical treatment for the management of their vaginal laxity.

Fig. 1. *Schematic handpiece use for SUI treatment protocol*

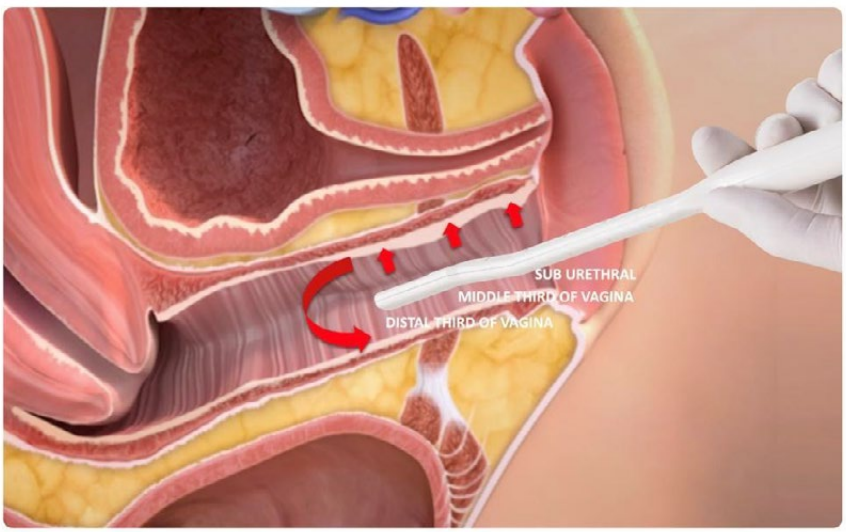

Table III. *Scores before and after protocol*

SCORE	BASELINE	END OF PROTOCOL
ICQ-SF	14.2	9.4
QUID	13.25	2.6

and Gynecology Department, Hospital Universitario San Jorge Pereira, Colombia. A total of 12 patients with an average age of 35.5 years, multi-parity and without overweight, as shown in the demographic distribution (Table I), were seen for a standardized BPRF protocol. Inclusion criteria were: patients complaining of SUI who offered to participate prior to obtaining informed consent and a written authorization to be included in their medical records according to the Helsinki declaration, Belmont report, CIOMS rules, GPC/ICH and 008430 resolution of Colombia government stabilised on 4th October 1993.

The exclusion criteria were: patients with previous pelvic organ prolapse surgery, patients with POP-Q stage> 1 (according with the Pelvic Organ Prolapse Quantification (POP-Q) system), smokers, non-compliant with protocol and other comorbidities (Table II).

Validated scales such as ICQ-SF and visual analogue scale VAS were measured before and after protocol. After photo documentation, the patients were placed in dorsal lithotomy position, and a clear water-based gel was used as conductive medium. Vaginal treatment was performed dividing the vagina into 3 quadrants (Fig. 1). BPRF energy was applied passing in a lateral motion from arcus tendineus to arcus tendineus with wide movements over each treated area for 15 minutes to the anterior vaginal wall (urethro-vesical junction). Power from the RF source was set to 40 W, temperature setting from 42°C to 45°C depending on the patient tolerance; no medications were administered after the treatment. Scheduled visits were set at 2-3-week intervals. ICIQ-SF and QUID questionnaires were filled in by the patients before and after BPRF. This was a small population pilot observational study, useful as a starting point for further studies. 90% (10.8 of 12) patients who met the criteria for SUI reported to have 70% improvement in SUI, and it was correlated with important changes in the scores of ICIQ-SF/QUID (Table III).

Paired Student's *t*-test was used to demonstrate, a statistically significant difference for all scores $p < 0.01$. None of the 12 patients included in the protocol presented adverse events or undesired symptoms related to the treatment. This experimental protocol demonstrates the safety and efficacy of using this energy device for stress urinary incontinence in a group of voluntary patients. We consider this non-surgical alternative as safe, easy to apply with minimal risk. Bipolarity and temperature control characteristics make it even safer. Larger series with longer follow-up are needed to confirm our findings.

REFERENCES

1. Lalji S, Lozanova P. Evaluation of the safety and efficacy of a monopolar nonablative radiofrequency device for the improvement of vulvo-vaginal laxity and urinary incontinence. J Cosmet Dermatol 2017; 16(2):230-4.
2. Costa AALFD, Vasconcellos IM, Pacheco RL, Bella ZIKJD, Riera R. What do Cochrane systematic reviews say about non-surgical interventions for urinary incontinence in women? Sao Paulo Med J

2018; 136(1):73-83.
3. Qureshi AA, Tenenbaum MM, Myckatyn TM. Nonsurgical vulvovaginal rejuvenation with radiofrequency and laser devices: a literature review and comprehensive update for aesthetic surgeons. Aesthet Surg J 2018; 38(3):302-11.
4. Vanaman M, Bolton J, Jones I, Wu D, Calame A, Goldman M. Histologic and clinical changes in vulvovaginal tissue after treatment with a transcutaneous temperature-controlled radiofrequency device. Dermatol Surg 2018; 0:1-9
5. Karcher C, Sadick N. Vaginal rejuvenation using energy-based devices. Int J Womens Dermatol 2016; 2(3):85-8.
6. Millheiser LS, Pauls RN, Herbst SJ, Chen BH. Radiofrequency treatment of vaginal laxity after vaginal delivery: nonsurgical vaginal tightening. J Sex Med 2010; 7(9):3088–3095.
7. Donovan JL, Badia X, Corcos J, et al. Symptom and Quality of Life Assessment, In: Abrams P, Cardozo L, Khoury S, Wein A, editors. Incontinence. Plymouth: Health Publication Ltd 2002; p. 270-316.

LETTER TO THE EDITOR

Comparison between diagnostic value of SPECT whole-body bone imaging and magnetic resonance imaging in bone metastasis of prostate cancer

J. Li*, ZX. Zou*, CJ. Hao*, YX. Shi* and YB. Sui

Department of Medical Image, The Affiliated Yantai Yuhuangding Hospital of Qingdao University, Yantai, P.R.China

Received June 11, 2020 – Accepted January 22, 2021

*These Authors contributed equally to this study

To the Editor,

Prostate cancer is an epithelial cancer of the prostate, which has a high incidence rate and increases with age (1, 2). Eventually, it can metastasize to bone and seriously threaten the health and life of patients (3). Pathological tissue diagnosis is the gold standard of clinical staging diagnosis of bone metastasis of prostate cancer while imaging technology used for clinical diagnosis is constantly upgraded (4). Nowadays, MRI (Magnetic Resonance Imaging) and SPECT (Single-Photon Emission Computed Tomography) are new imaging technologies used in diagnosis of bone metastasis of the disease (5). Of note, MRI is an advanced imaging device that has no radiation effects on the human body. SPECT is the most common examination tool for whole-body bone imaging. Compared with conventional imaging technology, the image quality of SPECT has been improved, and the shape of the bones can be clearly displayed, which facilitates the timely detection of the nidus of early bone metastasis (6). Moreover, bone metabolism and blood supply can be indicated in SPECT whole-body bone imaging. In this study, we investigated the application values of MRI diffusion-weighted SPECT whole-body bone imaging, magnetic resonance imaging and the combination of the two technologies in the diagnosis of bone metastasis of prostate cancer.

MATERIALS AND METHODS

Patients

A total of 136 patients with bone metastasis of prostate cancer, who were admitted to the Affiliated Yantai Yuhuangding Hospital of Qingdao University from March 2016 to April 2018, were enrolled. Their ages ranged from 55 to 89 years (average 68.46±10.94 years). Ninety patients were diagnosed with bone metastasis of prostate cancer by pathological biopsy. This study was approved by the Ethics Committee of the Affiliated Yantai Yuhuangding Hospital of Qingdao University. The patients who were included and their family members signed an informed consent form in advance.

Inclusion criteria: patient tissue samples were confirmed as bone metastasis of prostate cancer; patients had not received radical resection, endocrine therapy, radiotherapy or other related treatment; patients with no other malignant tumor; according to the preoperative PSA value, T stage and Gleason score, the patients were rated as medium or high risk according to D'Amico grading standard (7).

Exclusion criteria: After selection, MRI and SPECT

Key words: bone metastasis of prostate cancer; combined diagnosis; diagnostic value; MRI; SPECT

Corresponding Author:
Dr. Yanbin Sui,
Department of Medical Image,
The Affiliated Yantai Yuhuangding Hospital
of Qingdao University, No.20 Yuhuangding East Road,
Yantai 264000, P.R.China
e-mail: liyanzq000@126.com

0393-974X (2021)
Copyright © by BIOLIFE, s.a.s.
This publication and/or article is for individual use only and may not be further reproduced without written permission from the copyright holder.
Unauthorized reproduction may result in financial and other penalties
DISCLOSURE: ALL AUTHORS REPORT NO CONFLICTS OF INTEREST RELEVANT TO THIS ARTICLE.

examination were incomplete, or the image quality was poor, for the reason of contraindication of examination or patient non-cooperation, which affected the evaluators; patients with allergic reactions to contrast agents, claustrophobia; patients lost to follow-up.

Imaging equipment and methods

For SPECT, GCA-7200A/DI dual probe SPECT (TOSHIBA company) was used. A bone imaging agent (Chengdu Syncor Pharmaceutical Co., Ltd) with technetium (99mTc) methylene diphosphonate (MDP) injection was adopted with the dose of 40-925 MBq. After the patients were intravenously injected with imaging agent (the dose was adjusted according to the patient's body weight), they needed to drink more than 500 ml of distilled water as it was necessary for the patients to evacuate urine; after 3 hours, the imaging was carried out. The scanning speed was (15 20) cm/min, the acquisition matrix was 256×1024. Local imaging or tomographic imaging was carried out at the site of bone metastasis of some patients.

For MRI, patients began fasting 4 hours before the examination, and all patients were examined by MRI alone in the imaging department of our hospital (GE Signa Excite 3.0TMR, USA). The head and neck coil and external coil were used in the examination coil. The scanning sequence was divided into conventional sequence and whole body sequence. For the whole body sequence scanning process, the scanning range was from the top of the skull to the middle of the thigh, for patients over 180 cm in height, the fifth segment was added, and then each segment of the image was automatically stitched into a whole body image after scanning. The whole body sequence included coronal T_1WI and transverse RESOLVE-DWI (b = 0 and 800). The process of pelvic sequence scanning mainly included axial T_1WI and T_2WI fat suppression imaging, ordinary DWI sequence of prostate (b = 1500). When suspicious bone metastases were found during the scanning, T_1WI and T_2WI were added to scan the lipid suppression phase. Finally, Gd DTPA was injected intravenously to enhance the chest, abdomen and pelvis (chest axial, abdominal coronal, pelvic axial and sagittal). The scanning time of all sequences was about 1 hour.

Image interpretation: MRI and SPECT images were independently interpreted by three experienced radiologists and nuclear medicine physicians, respectively, none of whom knew the clinical data such as serum PSA level, Gleason score, or the examination results of other imaging. According to the results, the consistency principle was adopted to draw the initial conclusions of the two tests, and then the patients with metastases were divided into single metastasis and multiple metastases. For patients with single metastasis, the specific metastatic sites were recorded according to the spine, sternum, bones of the four limbs, bones of the pelvic cavity.

Diagnostic criteria

The diagnostic criteria of bone metastasis in SPECT imaging are shown in Table I. SPECT imaging features were identified in groups of presence and absence of bone metastasis of prostate cancer.

In imaging features, T_1WI indicated a low signal in SE sequence, T_2WI showed an increase of the signal. The signal which implied bone metastasis was equivalent to or higher than the surrounding bone marrow signal. All

Table I. *SPECT imaging features of presence and absence of bone metastasis of prostate cancer*

Groups	SPECT imaging features
The presence of bone metastasis of prostate cancer	There are many agminated niduses with high concentration in imaging agent, patients have unexplained bone pain.
The absence of bone metastasis of prostate cancer	There is no agminated nidus with high concentration in imaging agent. After the suspected nidus is repeatedly examined, it is found that there is no change in agminated nidus with high concentration or that it gradually decreases and disappears.

the patients were examined by MRI at 1 week before and after they were examined by SPECT whole-body bone imaging. The examination results of the two technologies were compared with the final diagnosis results.

Statistical analysis

SPSS 17.0 (Beijing Bizinsight Information Technology Co., Ltd.) software system was used to carry out statistical analysis. The enumeration data were expressed by [n(%)], the diagnostic value of bone metastasis of prostate cancer was compared by using χ^2 test. When P<0.05, the difference was considered to be statistically significant.

RESULTS

Of 136 patients, 30 (22.06%) had family history of prostate cancer. The niduses were distributed in spine, sternum, bones of the four limbs, bones of the pelvic cavity, skull of 90 patients with lymph node metastasis (Table II). Seventy-three patients were

Table II. *Clinical data of the patients [n (%)]*

Factors		n=136[n(%)]
Age (years)		
	≤68	30 (22.06)
	>68	106 (77.94)
Weight (kg)	(68.11±6.42)	136 (100.00)
Family history of prostate cancer		
	Yes	30 (22.06)
	No	106 (77.94)
Glycemic index (mmol/L)	<7.8mmol/L	136 (100.00)
Metastasis and distribution of the nidus		
	Spine	14 (10.29)
	Sternum	26 (19.12)
	Bones of the four limbs	28 (20.59)
	Bones of the pelvic cavity	10 (7.35)
	Skull	12 (8.82)
Clinical staging		
	I-II stage	26 (19.12)
	III-IV stage	110 (80.88)
Lymph node metastasis		
	Yes	90 (66.18)
	No	46 (33.82)

Table III. *Comparison between results of MRI and results of pathological diagnosis*

	Pathology confirmed that there was bone metastasis	Pathology confirmed that there was no bone metastasis	Total
confirmed that there was bone metastasis	73	14	87
onfirmed that there was no bone metastasis	17	32	49
Total	90	46	136

Table IV. *Comparison between results of SPECT and results of pathological diagnosis*

	Pathology confirmed that there was bone metastasis	Pathology confirmed that there was no bone metastasis	Total
SPECT confirmed that there was bone metastasis	86	8	94
SPECT confirmed that there was no bone metastasis	4	38	42
Total	90	46	136

Table V. *Comparison between results of MRI combined with SPECT and results of pathological diagnosis*

	Pathology confirmed that there was bone metastasis	Pathology confirmed that there was no bone metastasis	Total
MRI combined with SPECT confirmed that there was bone metastasis	89	8	97
MRI combined with SPECT confirmed that there was no bone metastasis	1	38	39
Summation	90	46	136

Table VI. *Comparison between diagnostic efficacy of MRI, SPECT and their combination in bone metastasis of prostate cancer*

	MRI[n (%)]	SPECT[n (%)]	SPECT combined with MRI	χ^2	P
Diagnostic coincidence rate	105 (77.21)	124 (91.18)	127 (93.38)	18.820	<0.001
Sensitivity	73 (81.11)	86 (95.56)	89 (98.89)	21.480	<0.001
Specificity	32 (69.57)	38 (82.61)	38 (82.61)	3.067	0.216

diagnosed with bone metastasis of prostate cancer by MRI, and the detection rate was 81.11%; 86 patients were diagnosed with bone metastasis of prostate cancer by SPECT, with detection rate of 95.56%. The different diagnostic results of 13 patients screened by MRI and SPECT was further confirmed by pathological method as bone metastasis (Table III, IV, Fig. I).

In this study, the sensitivity of MRI was 81.11%, specificity was 69.57%, diagnostic coincidence rate was 77.21%, negative predictive value was 69.57%, and positive predictive value was 81.11%. By contrast, screening sensitivity of SPECT was 95.56%, specificity was 82.61%, diagnostic coincidence rate was 91.18%, positive predictive value was 95.56%, and negative predictive value was 82.61%. There were significant differences of sensitivity, negative predictive value, positive predictive value, diagnostic coincidence rate between SPECT and of MRI ($P<0.05$). No statistical difference of

specificity between SPECT and MRI was observed (P>0.05). The sensitivity, specificity and diagnostic coincidence rate of MRI combined with SPECT in diagnosis of bone metastasis of prostate cancer were 98.89%, 82.61%, and 93.38%, respectively. The sensitivity and diagnostic coincidence rate of

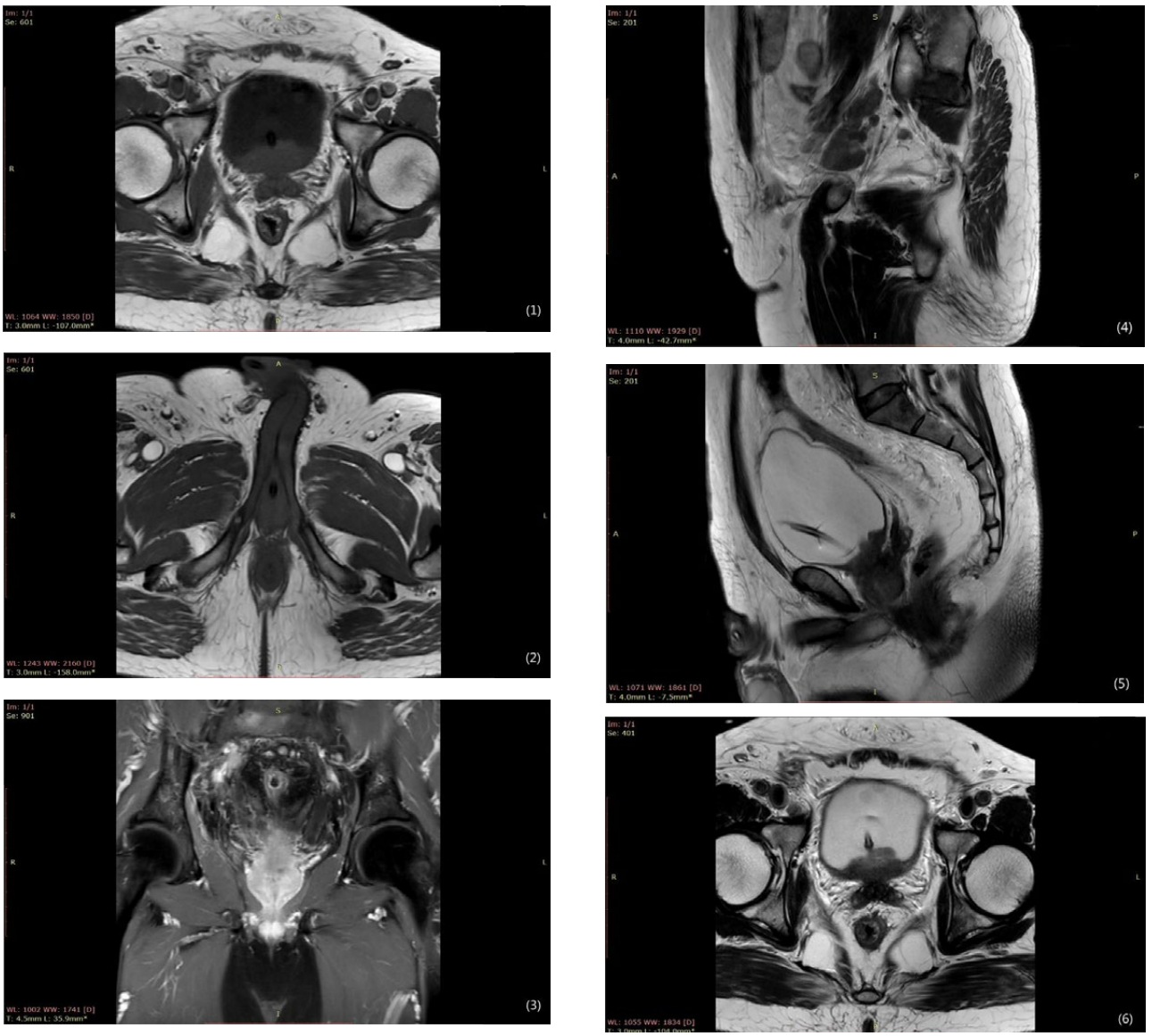

Fig. I. *Representative MR images [(1)-(3) shows the T1W images; (4)-(6) shows the T2W images] Gender: Male, Age: 66. MRI findings were as follows: The volume of prostate gland increased, and the size was about 3.2 * 3.4 * 4.2 cm. The internal signal was not uniform, the peripheral zone signal was decreased, the diffusion image showed high signal, enhanced scanning showed uneven obvious enhancement, the mass involved the posterior wall of bladder, the posterior wall of bladder was thickened, bilateral ureter was dilated, patchy and slightly short T2 signal was seen in bilateral seminal vesicle glands, which was obviously enhanced after enhancement. The bladder was well filled, and drainage tube shadow was seen in the bladder. Multiple nodular and patchy high signal changes were found in the sacrum, bilateral ilium and bilateral ischium, and the enhancement scanning was more obvious. Enlarged inguinal lymph nodes were seen on both sides. The fat space of pelvic floor was fuzzy, and a small amount of long T2 signal was seen in pelvic floor.*
Imaging diagnosis results were as follows: Prostate cancer involved posterior bladder wall, bilateral ureteral entrance, seminal vesicle gland with multiple bone metastasis and lymph node metastasis.

combination methods were significantly higher than those of single use of either MRI or SPECT ($P<0.05$) (Tables V, VI).

DISCUSSION

As an advanced medical imaging technology, MRI is not harmful, however, a limitation of MRI is that lesion sites may be missed. In particular, MRI is unsuitable for patients with residual metal objects in the body and pregnant women, besides the high cost. In whole-body bone imaging technologies, in terms of imaging, SPECT showed potential in early diagnosis of nidus compared to MRI (8). It has been found that the image of SPECT is much clearer than that of MRI in the nidus of patients (9). Similarly, in this study, sensitivity, specificity and diagnostic coincidence rate of SPECT were significantly increased compared to those of MRI. It has been demonstrated that, compared with other imaging technologies, SPECT has relatively high sensitivity, and can detect the site and size of the nidus when the bone metastasis nidus appears in early stage (10, 11). In a large number of studies, SPECT is recommended as an effective indicator for evaluating bone metastasis nidus in prostate cancer (12, 13). Our data further indicated that the sensitivity, specificity and diagnostic coincidence rate of MRI combined with SPECT were significantly higher than those of single use of MRI or SPECT, which may provide information for the timely treatment of bone metastasis and increase the survival rate of patients (14). The limitation of this study is that the small cohort is insufficient, and needs to be improved with advanced equipment in the future. In summary, the diagnostic efficacy of SPECT is superior to that of MRI in diagnosis of bone metastasis of prostate cancer. The combination of SPECT and MRI can further improve the diagnosis of bone metastasis with comparably high sensitivity, specificity and diagnostic coincidence rate.

REFERENCES

1. Cohen JH, Kristal AR, Stanford JL. Fruit and vegetable intakes and prostate cancer risk. J Natl Cancer Inst 2016; 92:61-68.
2. Wong MC, Goggins WB, Wang HH, et al. global incidence and mortality for prostate cancer: analysis of temporal patterns and trends in 36 countries. Eur Urol 2016; 70:862-74.
3. Heidenreich A, Bastian PJ, Bellmunt J, et al. EAU guidelines on prostate cancer. Part 1: screening, diagnosis, and local treatment with curative intent-update 2013. Eur Urol 2013; 65:124-37.
4. Prosper K, Sean R, James D. Immunochemical assays and nucleic-acid detection techniques for clinical diagnosis of prostate cancer. J Cancer 2016; 7:523-31.
5. Freitag MT, Radtke JP, Hadaschik BA, et al. Comparison of hybrid (68)Ga-PSMA PET/MRI and (68)Ga-PSMA PET/CT in the evaluation of lymph node and bone metastases of prostate cancer. Eur J Nucl Med Mol Imaging 2015; 43:70-83.
6. Narimatsu H, Nakahara T, Kodama S, et al. Bone SPECT/CT Localizes Increased Bone Metabolism and Subsequent Bone Resorption in Reflex Sympathetic Dystrophy. Clin Nucl Med 2017; 42:784-86.
7. Huang S, Guo Y, Jacobi A, et al. Aromatic hydrocarbon receptor suppresses prostate cancer bone metastasis cells-induced vasculogenesis of endothelial progenitor cells under hypoxia. Cell Physiol Biochem 2016; 39:709-20.
8. Rescigno P, de Bono JS. Immunotherapy for lethal prostate cancer. Nat Rev Urol 2019; 16:69-70.
9. Pickett CA, Cheezum MK, Kassop D, Villines TC, Hulten EA. Accuracy of cardiac CT, radionucleotide and invasive ventriculography, two-and three-dimensional echocardiography, and SPECT for left and right ventricular ejection fraction compared with cardiac MRI: a meta-analysis. Eur Heart J Cardiovasc Imaging 2015; 16:848-52.
10. Nozaki T, Yasuda K, Akashi T, Fuse H. Usefulness of single photon emission computed tomography imaging in the detection of lumbar vertebral metastases from prostate cancer. Int J Urol 2008; 15:516-19.
11. Umeda T, Koizumi M, Fukai S, Miyaji N, Motegi K, Nakazawa S, Takiguchi T. Evaluation of bone metastatic burden by bone SPECT/CT in metastatic prostate cancer patients: defining threshold value

for total bone uptake and assessment in radium-223 treated patients. Ann Nucl Med 2017; 32:105-13.

12. Jung K, Miller K, Wirth M, Albrecht M, Lein M. Bone turnover markers as predictors of mortality risk in prostate cancer patients with bone metastases following treatment with zoledronic acid. Eur Urol 2010; 59:604-12.
13. Gourtsoyianni S, Hwang S, Panicek DM, et al.Reproducibility and clinical correlations of post-treatment changes on CT of prostate cancer bone metastases treated with chemotherapy. Br J Radiol 2012; 85: 1243-49.
14. Even-Sapir E, Metser U, Mishani E, Lievshitz G, Lerman H, Leibovitch I. The detection of bone metastases in patients with high-risk prostate cancer: 99mTc-MDP planar bone scintigraphy, single- and multi-field-of-view SPECT, 18F-fluoride PET, and 18F-fluoride PET/CT. J Nucl Med 2006; 47:287-97.

LETTER TO THE EDITOR

Long non-coding RNA GAS5 inhibits the proliferation and induces the apoptosis of hypertrophic scar fibroblasts by sponging miR-21

HB. Luo[1], Y. Cao[1], MC. Tao[1], XH. Yang[1] and J. Chen[2]

[1]Department of Dermatology, The First Affiliated Hospital of Zhejiang Chinese Medical University, Hangzhou, China; [2]Department of Dermatology, Zhuji People's Hospital of Zhejiang Province, Zhuji, China

Received November 12, 2020 – Accepted January 25, 2021

To the Editor,

Hypertrophic scar (HS), a common complication caused by malfunctioned wound healing process after burn injury or other soft tissue injuries, is featured by excessive deposition of extracellular matrix (ECM) and invasive growth of fibroblasts (1). HS often affect the patient's quality of life because of both physical and psychosocial reasons (2). Accordingly, it is extremely necessary to identify the mechanisms underlying HS formation.

Long non-coding RNAs (lncRNAs), which refer to a large group of RNA transcripts with length more than 200 nucleotides and limited protein-coding potential, regulate a variety of physiological and pathophysiological processes (3). LncRNA growth arrest-specific transcript 5 (GAS5) is widely accepted as a tumor suppressor in many human cancers (4). Moreover, some studies also reported that activation of GAS5 attenuates kidney fibrosis and hepatic fibrosis (5, 6). The present study aimed to investigate the functional roles of lncRNA GAS5 in HS.

MATERIALS AND METHODS

Clinical samples

Twenty-five HS tissue samples and 25 normal skin tissue samples were obtained from 50 individuals who underwent scar excision and flap transplantation at The First Affiliated Hospital of Zhejiang Chinese Medical University (Hangzhou, China). All resected tissues were immediately snap-frozen in liquid nitrogen and stored at −80°C for further use. This study was performed in strict accordance with the approval of the Ethics Committee of The First Affiliated Hospital of Zhejiang Chinese Medical University. Written informed consents were obtained from all participants.

Cell culture and transfection

Human HS fibroblasts, obtained from Shanghai Guandao Biological Engineering Co., Ltd. (Shanghai, China), were cultured in RPMI-1640 medium (Thermo Fisher Scientific, Inc., Waltham, MA, USA) supplemented with 10% fetal bovine serum (FBS; HyClone, Logan, UT, USA) and 1% penicillin-streptomycin at 37°C in a humidified atmosphere containing 5% CO_2.

miR-21 mimics and negative control (NC) mimics were designed and synthesized by Guangzhou RiboBio Co., Ltd. (Guangzhou, China). The full length sequence of human GAS5 cDNA was amplified by PCR and cloned into the vector pcDNA3.1 (Invitrogen, Carlsbad, CA, USA). An empty vector was used as the negative control. Cells were cultured to 70–80% confluence, and transfection was performed using Lipofectamine 2000 (Invitrogen). Forty-eight hours post-transfection, the transfection efficiency was analyzed by RT-qPCR analysis.

Key words: long non-coding RNA GAS5; miR-21; hypertrophic scar fibroblasts; proliferation; apoptosis

Corresponding Author:
Dr Jie Chen,
Department of Dermatology,
Zhuji People's Hospital
of Zhejiang Province,
Zhuji 311800, China
e-mail: chenjieluckier@sina.com

0393-974X (2021)
Copyright © by BIOLIFE, s.a.s.
This publication and/or article is for individual use only and may not be further reproduced without written permission from the copyright holder.
Unauthorized reproduction may result in financial and other penalties
DISCLOSURE: ALL AUTHORS REPORT NO CONFLICTS OF INTEREST RELEVANT TO THIS ARTICLE.

RT-qPCR analysis

Total RNA was isolated using TRIzol reagent (Invitrogen), and reverse transcribed to cDNA using the PrimeScript™ RT reagent kit (TaKaRa, Dalian, China). PCR amplifications were then carried out using a SYBR Green PCR Kit (TaKaRa) on an iCycleriQ™ Real-Time PCR Detection System (Bio-Rad Laboratories, Hercules, CA, USA). The primers used here were listed as following: GAS5, forward, 5′-CGACTCCTGTGAGGTATGGTG-3′, reverse, 5′-ATCCTTCCTTGGGGACACAAC-3′; miR-21, forward, 5′-CTAAGACCTGTGGAATGGC-3′, reverse, 5′-CTCAAAGATGTCATTGCC-3′; GAPDH, forward, 5′-CAGGAGGCATTGCTGATGAT-3′, reverse, 5′-GAAGGCTGGGGCTCATTT-3′; U6, forward, 5′-GTGGACCGCACAAGCTCGCT-3′, reverse, 5′-TTGTTGAACGGCACTGTGTATAGCA-3′. Relative gene expression levels were calculated using $2^{-\Delta\Delta Ct}$ method. GAPDH or U6 was used as an internal reference.

MTT assay

Cell proliferation was determined by 3-(4,5-dimethylthiazol-2-yl)-2,5-diphenyltetrazolium bromide (MTT) assay. Cells were incubated in 96-well-plates at a density of 3×10^3 cells/well. At the indicated time points, 20 μl of MTT (5 mg/ml; Sigma-Aldrich, St. Louis, MO, USA) were added to each well. After incubation for additional 4 h, 150 μl of DMSO (Sigma-Aldrich) were added to dissolve the purple formazan. The absorbance of each well was measured at 570 nm on an ELx808 microplate reader (BioTek Instruments, Inc., Winooski, VT, USA).

Cell apoptosis analysis

Cells were washed in PBS and re-suspended in 100 μl of binding buffer. Then, the cells were stained with 5 μl of Annexin V-FITC and 1 μl of PI using Annexin V-FITC Apoptosis Detection Kit (BD Biosciences, San Jose, CA, USA). The stained cells were then subjected to FACScan flow cytometer (BD Biosciences) equipped with Cell Quest software.

Western blot analysis

Total protein was extracted using RIPA protein extraction reagent (Beyotime, Shanghai, China). The protein concentration was determined using a BCA protein quantification kit (Beyotime). An equivalent amount of protein was separated by SDS-polyacrylamide gel electrophoresis, and transferred to polyvinylidene difluoride membranes (Millipore, Bedford, MA, USA). After blocking in 5% nonfat milk for 1 h, the membranes were incubated with the primary antibodies overnight at 4°C. Primary antibodies used were as following: anti-α-SMA (1:1,000 dilution; Abcam, Cambridge, MA, USA), anti-Col I (1:500 dilution; Abcam), anti-Col III (1:500 dilution; Abcam) and anti-GAPDH (1:1,000 dilution; Santa Cruz Biotechnology, Santa Cruz, Dallas, TX, USA). Then, the membranes were incubated with the HRP-conjugated secondary antibody (1:8,000 dilution; Abcam) for 1 h at room temperature. The protein bands were visualized using an electrogenerated chemiluminescence kit (Pierce Biotechnology, Rockford, IL, USA). GAPDH serves as a loading control.

Dual-luciferase reporter assay

The GAS5 sequence containing the putative target sites for miR-21 was amplified from human genomic DNA, and then cloned into the psiCHECK-2 luciferase reporter vector (Promega, Madison, WI, USA). The mutant constructs were generated using a Mut Express II Fast Mutagenesis kit (Vazyme, Piscataway, NJ, USA). Cells seeded in 24-well plates were co-transfected with the luciferase reporters and miR-21 mimics or NC mimics using Lipofectamine 2000. After 48 h, the cell lysates were harvested, and the luciferase activities were analyzed with the Dual Luciferase Reporter Assay System (Promega).

RNA immunoprecipitation (RIP) assay

RIP assay was performed using a Magna RIP RNA-Binding Protein Immunoprecipitation kit (Millipore). Cell lysates were incubated with magnetic beads conjugated with anti-Ago2 or control IgG (Millipore). The immunoprecipitated RNAs were then subjected to RT-qPCR analysis.

Statistical analysis

All statistical analyses were performed using GraphPad Prism 6.0 software (GraphPad Software Inc., San Diego, CA, USA). All experiments were repeated three times. All continuous variables are presented as the mean ± standard deviation (SD). The significance of differences between two groups was analyzed using *t*-test and several sets of data were analyzed using one-way analysis of variance (ANOVA) test. The correlation

between GAS5 and miR-21 expression was tested by Pearson correlation coefficient analysis. *P* values of less than 0.05 were considered as statistically significance.

RESULTS

GAS5 is downregulated in HS samples

As indicated by RT-qPCR analysis, the expression levels of GAS5 were significantly decreased in HS tissues compared with those in normal skin tissues (Fig. 1).

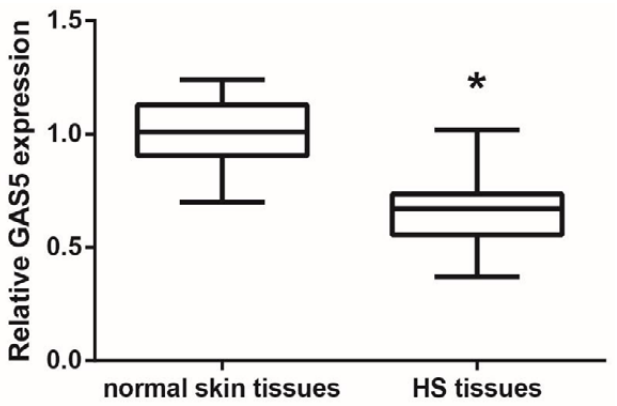

Fig. 1. *GAS5 is downregulated in HS samples. The expression of GAS5 in 25 HS tissues and 25 normal skin tissues, detected by RT-qPCR analysis. *P<0.05 vs HS tissues.*

GAS5 inhibits HF fibroblast proliferation and ECM-related protein expression

To understand the regulatory functions of GAS5 in HS fibroblasts, we overexpressed GAS5 in HS fibroblasts by transfection with pcDNA3.1-GAS5. The transfection efficiency was validated by RT-qPCR analysis (Fig. 2A). MTT assay indicated that GAS5 overexpression notably retarded the proliferation of HS fibroblasts (Fig. 2B). Moreover, as shown in Fig. 2C, the apoptosis rate of HS fibroblasts was also markedly enhanced by GAS5 overexpression. Furthermore. Western blot analysis demonstrated that the protein expression levels of α-SMA, Col I and Col III were also significantly decreased by GAS5 overexpression in HS fibroblasts (Fig. 2D).

GAS5 sponges miR-21 in HS fibroblasts

Through the RNA22 program (http://cbcsrv.

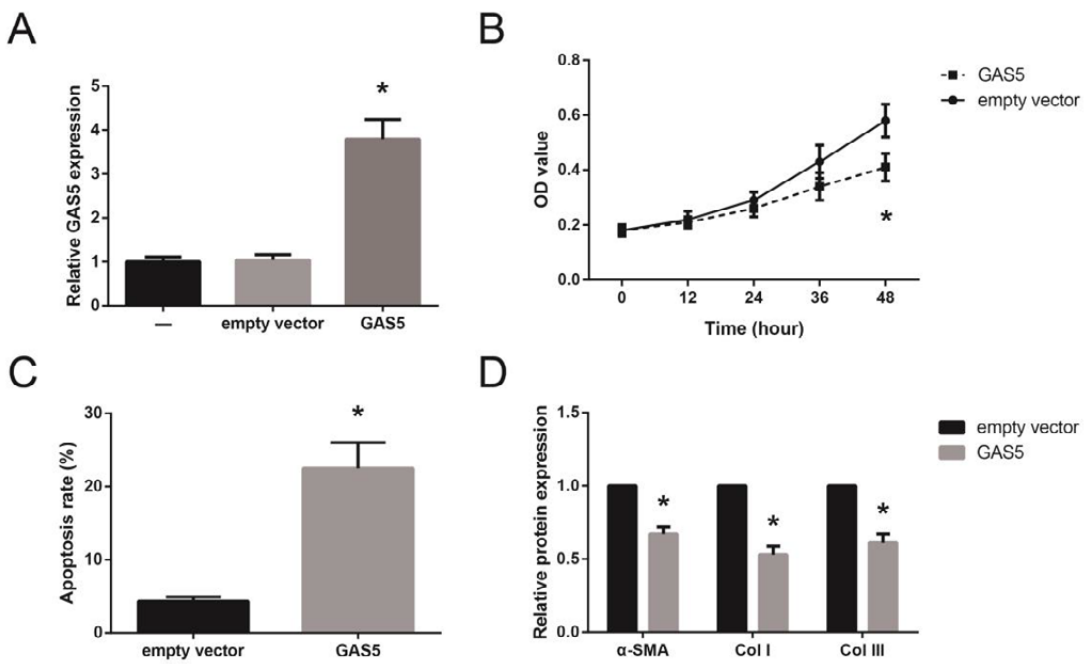

Fig. 2. *GAS5 inhibits HF fibroblast proliferation and ECM-related protein expression.* ***A****) The expression of GAS5 in HS fibroblasts after transfection.* ***B****) The proliferation of HS fibroblasts after GAS5 overexpression, detected by MTT assay.* ***C****) The apoptosis of HS fibroblasts after GAS5 overexpression, detected by flow cytometer analysis.* ***D****) The expression of ECM-related proteins in HS fibroblasts after GAS5 overexpression, detected by Western blot analysis. *P<0.05 vs empty vector-transfected cells.*

watson.ibm.com/rna22.html), miR-21 was identified to potentially bind to GAS5 (Fig. 3A). Dual-luciferase reporter assay was then performed to validate the binding relation, and the results indicated that miR-21 mimics could notably inhibit the luciferase activity of GAS5-WT, while they had no obvious effect on GAS5-MUT in HS fibroblasts (Fig. 3B). RIP assay also showed that GAS5 was strikingly enriched by Ago2 antibody in HS fibroblasts transfected with miR-21 mimics (Fig. 3C). In addition, as shown in Fig. 3D, GAS5 overexpression remarkably decreased miR-21 expression in HS fibroblasts. Moreover, the expression levels of miR-21 were notably increased in HS tissues compared with those in normal skin tissues (Fig. 3E), and an inverse correlation between GAS5 and miR-21 expression in HS tissues was also identified ($r=-0.421$, $P=0.036$; Fig. 3F).

miR-21 restoration blocks the role of GAS5 in HS fibroblasts

We then performed rescue experiments, and as indicated by MTT assay, the restrained proliferation of GAS5-overexpressing HS fibroblasts was notably reversed by miR-21 restoration (Fig. 4A), accompanied by the inhibition of apoptosis in HS fibroblasts (Fig. 4B). In addition, as shown in Fig. 4C, the inhibitory effects of GAS5 overexpression on the expression of ECM-related proteins in HS fibroblasts were also markedly diminished by miR-21 restoration.

DISCUSSION

In recent years, an increasing number of studies have suggested that lncRNAs can participate in the pathophysiological processes of HS. For example, Tu et al. identified the profiles of differentially expressed lncRNAs between fibroblasts derived from HS and normal skin samples (7). In addition, Chen et al. reported that lncRNA AC067945.2 was downregulated in HS tissues, and its overexpression inhibited collagen expression (8).

Our results, for the first time, showed that GAS5 is downregulated in HS samples. In the process of

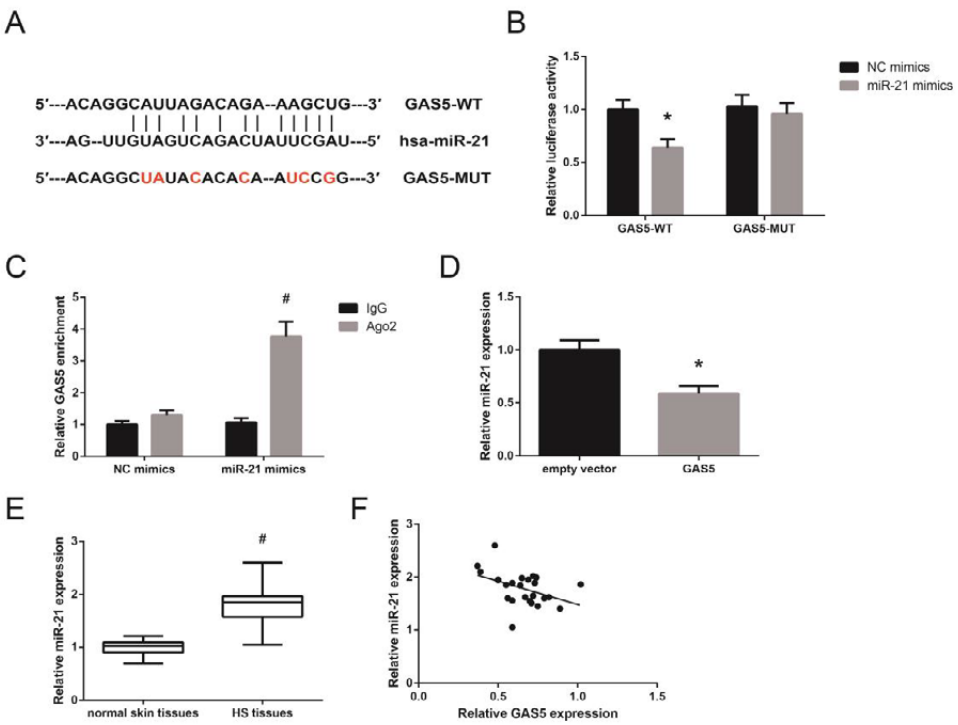

Fig. 3. *GAS5 sponges miR-21 in HS fibroblasts. **A)** The predicted binding sites between miR-21 and GAS5. B) The binding relation between miR-21 and GAS5 in HS fibroblasts, validated by dual-luciferase reporter assay. **C)** The binding relation between miR-21 and GAS5 in HS fibroblasts, validated by RIP assay. **D)** The expression of miR-21 in HS fibroblasts after GAS5 overexpression. E) The expression of miR-21 in 25 HS tissues and 25 normal skin tissues. F) The correlation between miR-21 and GAS5 expression in HS tissues. *P<0.05 vs NC mimics or empty vector-transfected cells; #P<0.05 vs HS tissues or IgG group.*

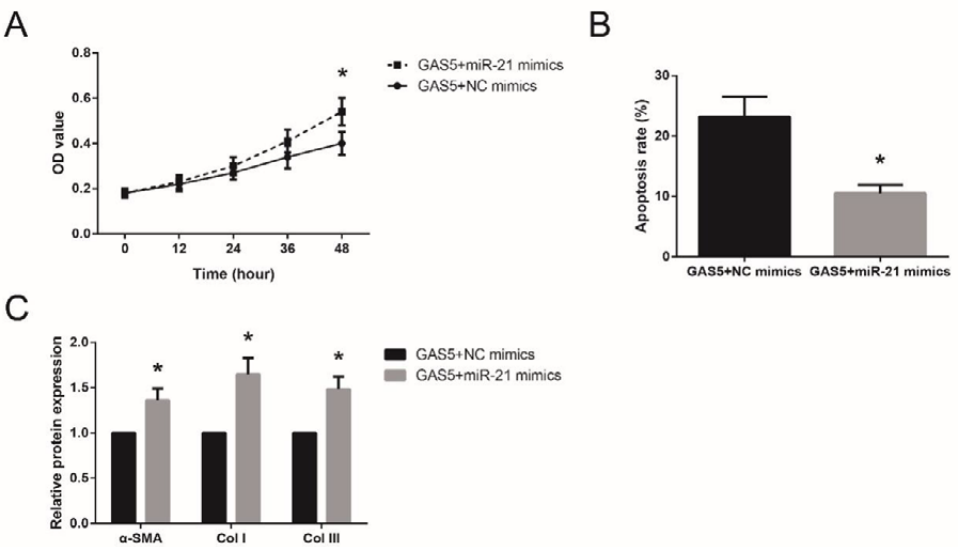

Fig. 4. *miR-21 restoration blocks the role of GAS5 in HS fibroblasts.* ***A****) The proliferation of HS fibroblasts after miR-21 restoration.* ***B****) The apoptosis of HS fibroblasts after miR-21 restoration.* ***C****) The expression of ECM-related proteins in HS fibroblasts after miR-21 restoration. *P<0.05 vs pcDNA3.1-GAS5+NC mimics-transfected cells.*

HS formation, fibroblasts typically exhibit excessive proliferation and secrete abundant ECM. Functional assays further revealed that GAS5 overexpression markedly inhibited the proliferation and induced the apoptosis of HS fibroblasts. Collagen is the most important ECM component and its disorganized accumulation can lead to HS formation (9). α-smooth muscle actin (α-SMA) is a key regulator of ECM metabolism in many tissues (10). Here, we found that the expression of ECM-related proteins, including α-SMA, Col I and Col III, were notably decreased by GAS5 overexpression in HS fibroblasts.

LncRNAs and miRNAs are two major subgroups of ncRNAs. In recent years, mounting articles have shown that lncRNAs can serve as competing endogenous RNAs (ceRNAs) and interact with specific miRNAs (11). We then hypothesized that GAS5 may also serve as a ceRNA in HS. The functional roles of miR-21 in HS have been previously reported (12), therefore it was selected as a candidate for further analysis. Through experimental validation, we showed that GAS5 could directly bind to miR-21 and inhibit its expression in HS fibroblasts. Rescue assays further confirmed that miR-21 restoration could largely diminish the effects of GAS5 overexpression in HS fibroblasts.

In conclusion, the present study provides promising evidence that GAS5 inhibited the proliferation and ECM-related protein expression in HS fibroblasts, partly by sponging miR-21. Our research points to a new way to the treatment of HS.

REFERENCES

1. Gauglitz GG. Management of keloids and hypertrophic scars: current and emerging options. Clin Cosmet Investig Dermatol 2013; 6:103-14.
2. Brown BC, McKenna SP, Siddhi K, McGrouther DA, Bayat A. The hidden cost of skin scars: quality of life after skin scarring. J Plast Reconstr Aesthet Surg 2008; 61(9):1049-58.
3. Mercer TR, Dinger ME, Mattick JS. Long non-coding RNAs: insights into functions. Nat Rev Genet 2009; 10(3):155-9.
4. Ma C, Shi X, Zhu Q, Li Q, Liu Y, Yao Y, Song Y. The growth arrest-specific transcript 5 (GAS5): a pivotal tumor suppressor long noncoding RNA in human cancers. Tumour Biol 2016; 37(2):1437-44.
5. Yu Y, Jiang H, Niu Y, et al. Long noncoding RNA-GAS5 retards renal fibrosis through repressing miR-21 activity. Exp Mol Pathol 2020; 116:104518.
6. Dong Z, Li S, Wang X, Si L, Ma R, Bao L, Bo A.

lncRNA GAS5 restrains CCl4-induced hepatic fibrosis by targeting miR-23a through the PTEN/PI3K/Akt signaling pathway. Am J Physiol Gastrointest Liver Physiol 2019; 316(4):G539-G550.
7. Tu L, Huang Q, Fu S, Liu D. Aberrantly expressed long noncoding RNAs in hypertrophic scar fibroblasts in vitro: A microarray study. Int J Mol Med 2018; 41(4):1917-30.
8. Chen L, Li J, Li Q, et al. Overexpression of LncRNA AC067945.2 down-regulates collagen expression in skin fibroblasts and possibly correlates with the VEGF and Wnt signalling pathways. Cell Physiol Biochem 2018; 45(2):761-71.
9. Zhu Z, Ding J, Shankowsky HA, Tredget EE. The molecular mechanism of hypertrophic scar. J Cell Commun Signal 2013; 7(4):239-52.
10. Satish L, Gallo PH, Baratz ME, Johnson S, Kathju S. Reversal of TGF-β1 stimulation of α-smooth muscle actin and extracellular matrix components by cyclic AMP in Dupuytren's-derived fibroblasts. BMC Musculoskelet Disord 2011; 12:113.
11. Salmena L, Poliseno L, Tay Y, Kats L, Pandolfi PP. A ceRNA hypothesis: the Rosetta Stone of a hidden RNA language? Cell. 2011; 146(3):353-8.
12. Li G, Zhou R, Zhang Q, Jiang B, Wu Q, Wang C. Fibroproliferative effect of microRNA-21 in hypertrophic scar derived fibroblasts. Exp Cell Res 2016; 345(1):93-9.

LETTER TO THE EDITOR

Predictive value of ABCD^3 score combined with vascular stenosis in the progression of TIA to cerebral infarction

L. Wang[1], HL. Dai[1], X. Tang[2], YJ. Yang[1], KY. Sun[1] and L. Yu[1]

[1]*Department of Neurology, The No.2 Hospital of Baoding, Baoding, Hebei Province, China;*
[2]*Department of Ultrasonography, Baoding No.1 Hospital, Baoding, Hebei Province, China*

Received November 9, 2020 – Accepted January 25, 2021

To the Editor,

Transient ischemic attack (TIA) is a recoverable and transient neurological defect caused by focal ischemia of the spinal cord, brain or retina. As a common clinical ischemic cerebrovascular disease, the presence of its clinical symptoms generally does not exceed 1 hour, and the longest does not exceed 24 hours, and there is no specific evidence of responsible lesions. In addition, it is the most important risk factor for the onset of acute cerebral infarction and a very early warning signal for cerebral infarction (1). Clinically, one-third of TIA patients develop cerebral infarction, and two-thirds of these patients develop the disease within 1 week, which means that the first 7 days after the onset of TIA is a high-risk period of cerebral infarction (2). Therefore, in the early stage of the onset of TIA, rapid and accurate risk stratification of TIA patients is essential. ABCD^3 score is one of the most common ischemic stroke risk assessment tools after TIA. Compared with ABCD^2, it has better predictive value for cerebral infarction within 1 week after TIA (3, 4). However, the ABCD^3 score has its limitations for recent secondary cerebral infarction of TIA, which makes the inefficient. In addition, TIA and MRI examinations are very common on admission. Therefore, the ABCD^3 score combined with magnetic resonance examination has the feasibility and objectivity in predicting recent secondary cerebral infarction in patients with TIA. However, it is unclear whether the ABCD^3 score combined with the degree of vascular stenosis is valuable in predicting cerebral infarction within 7 days after TIA. Therefore, this study aimed to explore the value of the ABCD^3 score combined with the degree of vascular stenosis in predicting cerebral infarction within 7 days after TIA.

MATERIALS AND METHODS

A total of 157 patients with TIA admitted to the Baoding Second Hospital from October 2017 to October 2019 were selected as the research subjects. The inclusion criteria were in accordance with the TIA diagnostic criteria developed by the American Heart Association/American Stroke Association in 2009: the first symptoms and signs of sudden neurological deficits, and the symptoms and signs completely disappeared within 24 hours; CT or MRI imaging of the head excluded patients with bleeding lesions and other responsible brain lesions. The exclusion criteria were: clinical diagnosis of cerebral infarction and cerebral hemorrhage; non-cerebrovascular events including tumors, intracranial infections, seizures, Meniere's disease, hypoglycemia, hypercalcemia; non-first TIA attacks; patients who could undergo MRI due to various technical devices installed in the body; patients who did not cooperate with treatment. A total of 157 patients

Key words: ABCD^3 cerebral infarct; MRA; TIA; vascular stenosis

Corresponding Author:
Dr Hailin Dai,
Department of Neurology,
The NO.2 Hospital of Baoding,
Baoding 071000,
Hebei Province, China
e-mail: chaomuyongsi14259@163.com

0393-974X (2021)
Copyright © by BIOLIFE, s.a.s.
This publication and/or article is for individual use only and may not be further reproduced without written permission from the copyright holder.
Unauthorized reproduction may result in financial and other penalties
DISCLOSURE: ALL AUTHORS REPORT NO CONFLICTS OF INTEREST RELEVANT TO THIS ARTICLE.

were included, 96 males and 61 females, aged 41 to 81 years, with an average age of (63.8±6.7) years. According to the medical history and clinical manifestations, each patient received an $ABCD^3$ score during hospitalization. All patients underwent head magnetic resonance imaging (MRI) and magnetic resonance angiography (MRA) examinations within 24 hours. This study was approved by the hospital ethics committee, and the patients voluntarily signed informed consent.

$ABCD^3$ score

The clinical data of the patients were recorded and used for scoring with the $ABCD^3$ scoring method. $ABCD^3$ score: (A) Age: 1 for age > 60; (B) Blood pressure: 1 for systolic blood pressure ≥ 140mmHg or diastolic blood pressure ≥ 90 mmHg; (C) Clinical symptoms: 2 for unilateral weakness and speech impairment 1 for joint weakness and 0 for other symptoms; (D) Duration of symptoms: 0 for 10 min, 1 for 59 to 59 min, and 2 for 60 min or more; (D) Diabetes: Scoring 1 point for patients with, 0 point for patients without. (D) Dual TIA episode: There was at least one additional TIA episode within 7 days of this TIA episode. The scores of ABCDDD are added up as a total score, with a total score of ≤ 3 being classified as low risk, a total score of 4 to 5 being classified as intermediate risk, and a total score of 6-7 being classified as high risk. All patients' $ABCD^3$ scores were independently evaluated by the same investigator on admission. If the patient had multiple attacks, the longest attack time was taken as the duration of the symptoms; the blood pressure was based on the blood pressure first obtained at the time of admission. Patients completed relevant imaging examinations within 24 hours after admission to exclude cerebral infarction.

Clinical treatment

After TIA was diagnosed according to the diagnostic criteria, aspirin (Bayer, 100mg/D) combined with clopidogrel hydrochloride (Sanofi, 75mg/D) was used to treat all patients. According to the neuroimaging features of the patients, they were given dual antiplatelet agglutination therapy for 21 days or 90 days. At the same time, they were given statins to stabilize plaque.

With the Siemens 3.0 MRI system, all patients were examined with MRI and MRA at the time of admission as diffusion-weighted imaging (DWI) sequence of brain MRI can show early ischemic tissue. When DWI images show focal high signal corresponding to clinical manifestations, it is considered as DWI abnormality. According to the warfarin aspirin symptomatic intracranial disease test standard, the three-dimensional time-of-flight MRA imaging method was used to measure the degree of intracranial stenosis (5). The head and neck vessels including internal carotid artery, basilar artery, anterior cerebral artery, middle cerebral artery and posterior cerebral artery were examined and evaluated.

According to the North American symptomatic carotid endarterectomy test (NASCET), the stenosis rate (%) = (1-diameter of stenosis segment/diameter of normal distal stenosis) × 100%, stenosis < 50% was mild stenosis, and the stenosis rate ≥ 50% was moderate or severe.

The diagnosis of cerebral infarction is based on the results of CT and MRI, as well as the clinical symptoms and signs. The diagnostic criteria are in accordance with the Chinese guidelines for the prevention and treatment of cerebrovascular diseases compiled by the Chinese society of Neurology, Chinese Medical Association in 2007. All TIA patients underwent MRI and MRA. MRI can clearly show the early infarct, T1 is low signal, T2 is high signal, and DWI can show the ischemic focus within a few minutes of symptoms. According to the clinical manifestations and imaging data of the patients, the neurologist judges whether there is cerebral infarction. The main manifestations of the TIA patients are unilateral limb weakness, dysphonia or aphasia, dizziness, hemisensory disorder, consciousness disorder, blurred vision, diplopia, etc. The end point for all patients was day 7.

Statistical analysis

All statistical analyses were performed by SPSS (SPSS Inc, Chicago, IL, USA). Data were expressed as mean ± SD from more than three independent experiments. Student's *t*-test and one-way ANOVA were used to calculate the difference between two or more groups. P value of 0.05 or less was regarded as significance.

RESULTS

A total of 157 patients with TIA were enrolled in this study. Among them, those who did not develop into cerebral infarction within 7 days were in the TIA group (31 cases), and those who developed cerebral infarction were in the cerebral infarction group (126

cases). The age, gender, TIA onset time, diabetes, hypertension and other general data of the two groups were compared, in which age was statistically significant ($P < 0.05$, Table I). The other items were not statistically significant ($P>0.05$, Table II).

The $ABCD^3$ of 157 TIA patients who were admitted to hospital were evaluated. Of these patients, within 7 days after TIA, there was 1 with cerebral infarction in TIA low-risk group, with the incidence of 1.6 %, 4 with cerebral infarction in TIA moderate-risk group, with the incidence of 16.7%, 26 with cerebral infarction in TIA high-risk group, with the incidence of 74.3%. The incidence rate of the high-risk group was significantly higher than that of the moderate-risk group and low risk group, with significant difference ($P<0.05$, Table III).

Among the 157 TIA patients there were: 81 cases with vascular stenosis <50% group, 5 cases of ischemic stroke occurred within 7 days (accounting for 6.2% of the 81 patients); 76 cases in the vascular stenosis ≥50% group, there were 26 patients with ischemic stroke within 7 days (accounting for 34.2% of 76 patients). The difference between the two groups was statistically significant ($P<0.05$).

When $ABCD^3$ score ≥ 4, there were 24 patients with secondary cerebral infarction in the TIA group with stenosis ≥ 50% within 7 days, accounting for 60%, which was significantly higher than that in TIA group with stenosis < 50% (11.8%), and the difference was statistically significant ($P < 0.05$). When $ABCD^3$ < 4, there was no significant difference between the incidence of cerebral infarction in stenosis ≥ 50% group (6.1%) and stenosis < 50% group (2.1%) within 7 days after TIA (Table IV).

DISCUSSION

TIA, as a common ischemic cerebrovascular disease, is an independent risk factor of cerebral infarction (2). According to several cohort studies, the incidence of cerebral infarction in TIA patients within 7 days is as high as 8-10.5%, which is a high-risk period of secondary cerebral infarction (3). Emergency clinical evaluation and treatment after TIA can reduce the risk of secondary cerebral infarction thereafter. Therefore, identifying high-risk TIA patients quickly is of great important.

Since 2005, the ABCD score has been fully

Table I. *Comparison of general data*

Items	TIA	Cerebral infarction	P value
Age	60.60±11.81	64.94±10.77	0.01
Attack time (min)	46.94±56.73	31.31±42.46	0.064
Triglyceride (mmol/L)	2.10±2.29	4.66±25.67	0.456
Fasting blood glucose (mmol/L)	5.99±2.56	5.93±2.65	0.879
Low density cholesterol (mmol/L)	3.04±0.87	3.03±1.06	0.912
Homocysteine (mg/L)	13.99±8.76	13.80±8.71	0.934
Hypertension n (%)	38(54.29)	49(67.12)	0.093
Diabetes n (%)	10(15.29)	11(20.19)	0.21
Smoking history n (%)	29(43.85)	32(46.75)	0.99
History of alcoholism n (%)	18(26.23)	25(34.25)	0.364

Table II. *Correlation between ABCD^3 score and incidence of cerebral infarction in patients with transient ischemic attack within 7 days*

Groups	TIA	7-day incidence of cerebral infarction (%)
Low-risk group	62	1 (1.6)
Moderate-risk group	60	4 (16.7)
High-risk group	35	26 (74.3)$^{*,\#}$

** Compared with low-risk group, P<0.05 Compared with low-risk group, P<0.05*

Table III. *Relationship between vascular stenosis and incidence of cerebral infarction within 7 days after TIA attack*

Groups	Number of TIA cases	Infarct incidence (%)
Vascular stenosis≥50%	76	26 (34.2)*
Vascular stenosis <50%	81	5 (6.2)

*Compared with vascular stenosis <50% group, P<0.05

Table IV. *Association of ABCD^3 score with vascular stenosis and incidence of cerebral infarction in TIA patients within 7 days*

Groups	ABCD^{3}score	TIA	7-day incidence of cerebral infarction (%)
Vascular stenosis ≥ 50%	<4	36	2 (6.1)
	≥4	40	24 (60.0)
Vascular stenosis < 50%	<4	47	1 (2.1)
	≥4	34	4 (11.8

verified (6). In a large cohort, the score was modified and validated by parameters easily available to the emergency department, namely, diabetes (7) (ABCD^2) and dual TIA events (8) (ABCD^3). The validated revision improved the ability of scoring to distinguish risks: the ABCD^2 score of diabetes was better than the ABCD score (7), and the ABCD^3 score of double events was better than the ABCD^2 score (9). In clinical work, ABCD^3 score is one of the most commonly used tools to evaluate the risk of TIA secondary cerebral infarction. Our study also demonstrated that ABCD^3 score has predictive value for TIA secondary cerebral infarction. In this study, the results showed that there was a positive correlation between the ABCD^3 score and the incidence of cerebral infarction within 7 days after TIA. Within 7 days after TIA, there was no significant difference in the incidence of cerebral infarction between the moderate-risk group and the low risk group. However, within one week after

TIA, there was significant difference in the incidence of cerebral infarction between the high-risk group and the moderate-risk group or the low-risk group. These results show that the higher the $ABCD^3$ score of TIA patients, the higher the incidence of cerebral infarction in the short term. Therefore, our results further prove that $ABCD^3$ score has an important predictive significance for TIA patients with early secondary cerebral infarction.

In conclusion, $ABCD^3$ combined with vascular stenosis is of great significance in predicting the incidence of cerebral infarction in the near future. Moreover, the accuracy of prediction is obviously improved, therefore this method is worthy of clinical promotion and application.

REFERENCES

1. Kang DW, Han MK, Kim HJ, et al. Silent new ischemic lesions after index stroke and the risk of future clinical recurrent stroke. Neurology 2016; 86:277-85.
2. Brouwer-Goossensen D, Genugten LV, Lingsma H, Dippel D, Koudstaal P, Hertog HD. Determinants of intention to change health-related behavior and actual change in patients with TIA or minor ischemic stroke. Patient education and counseling 2016; 99:644-50.
3. Rothwell PM, Giles MF, Flossmann E, Lovelock CE, Redgrave JN, Warlow CP, Mehta Z. A simple score (ABCD) to identify individuals at high early risk of stroke after transient ischaemic attack. Lancet (London, England) 2005; 366:29-36.
4. Easton JD, Saver JL, Albers GW, et al. Definition and evaluation of transient ischemic attack: a scientific statement for healthcare professionals from the American Heart Association/American Stroke Association Stroke Council; Council on Cardiovascular Surgery and Anesthesia; Council on Cardiovascular Radiology and Intervention; Council on Cardiovascular Nursing; and the Interdisciplinary Council on Peripheral Vascular Disease. The American Academy of Neurology affirms the value of this statement as an educational tool for neurologists. Stroke 2009; 40:2276-93.
5. Chen L, Zhan Q, Ma C, et al. Reproducibility of middle cerebral artery stenosis measurements by DSA: Comparison of the NASCET and WASID Methods. PloS one 2015; 10:e0130991.
6. Giles MF, Rothwell PM. Systematic review and pooled analysis of published and unpublished validations of the ABCD and ABCD2 transient ischemic attack risk scores. Stroke 2010; 41:667-73.
7. Johnston SC, Rothwell PM, Nguyen-Huynh MN, Giles MF, Elkins JS, Bernstein AL,Sidney S. Validation and refinement of scores to predict very early stroke risk after transient ischaemic attack. Lancet (London, England) 2007; 369:283-92.
8. Muller MD, Lyrer P, Brown MM, Bonati LH. Carotid artery stenting versus endarterectomy for treatment of carotid artery stenosis. The Cochrane database of systematic reviews 2020; 2:Cd000515.
9. Vigen T, Thommessen B, Ronning OM. Stroke risk is low after urgently treated transient ischemic attack. J Stroke Cerebrovascular Dis: 2018; 27:291-95.

LETTER TO THE EDITOR

Analysis of risk factors affecting the prognosis of septic shock and clinical intervention

W-W. Jin[1#], D-L. Song[2#], X. Gao[3], H-Y. Zhang[4], Q-X. Ren[5] and Y. Chen[6]

[1]Department of Clinical Laboratory, Yantai Yuhuangding Hospital, Yantai, China; [2]Department of Hepatology, Yantai Qishan Hospital, Yantai, China; [3]Department of Clinical Laboratory, Qingdao Central Hospital, Qingdao University, Qingdao, China; [4]Department of Gastroenterology, People's Hospital of Rizhao, Rizhao, China; [5]Department of Clinical Laboratory, People's Hospital of Rizhao, Rizhao, China: [6]Hospital Infection-Control Department, the People's Hospital of Zhangqiu Area, Jinan, P.R. China

Received November 17, 2020 – Accepted January 27, 2021

[#]These Authors contributed equally to this work

To the Editor,

Septic shock (SS), a common clinical syndrome, occurs in a subset of patients with sepsis and comprises an underlying circulatory and cellular/metabolic abnormality. It is a common complication of patients admitted to intensive care units (ICU). If there is no timely diagnosis and treatment, multiple organ failure can occur in the late stage, with a high mortality rate (1, 2). Great progress has been made on the pathogenesis, diagnosis and treatment of SS in recent years. However, as a complex clinical syndrome, the mortality rate remains at 20-50%, ranking first among patients in ICUs (3-5). The risk factors affecting the prognosis of SS and the formulation of corresponding intervention measures are of great significance to reduce the mortality and improve the prognosis. In this study, univariate and multivariate Logistic regression analysis were carried out on clinical data and test indexes of 119 SS patients, and the risk factors of death were retrospectively analyzed. Corresponding intervention countermeasures were put forward in order to find a better method of diagnosis and treatment, and provide the basis for improving the survival rate and quality of life of patients.

MATERIALS AND METHODS

Clinical materials

One hundred and nineteen patients with SS admitted to the ICU at Yantai Yuhuangding Hospital from June 2012 to December 2018 were included in this study. According to prognosis, the patients were divided into a death group (observation group) of 55 patients, and a non-death group (control group) of 64 patients who were cured and survived for more than 28 days. There were 32 males and 23 females in the observation group, with an average age of (57.36±11.65) years, and 36 males and 28 females, with an average age of (43.27±12.41) years in the control group. The diagnostic criteria of SS refer to the 1992 American College of Thoracic Physicians/Association of severe Medicine (ACCP/SCCM) consensus meeting on the diagnostic criteria of SS (6). Exclusion criteria: patients with shock caused by cardiogenic shock or other non-

Key words: septic shock; risk factors; prognosis; intervention

Corresponding Author:
Dr Yan Chen,
Hospital Infection-Control Department,
the People's Hospital of Zhangqiu Area,
Jinan250200, P.R. China
e-mail: chenyanjnzq@163.com

0393-974X (2021)
Copyright © by BIOLIFE, s.a.s.
This publication and/or article is for individual use only and may not be further reproduced without written permission from the copyright holder.
Unauthorized reproduction may result in financial and other penalties
DISCLOSURE: ALL AUTHORS REPORT NO CONFLICTS OF INTEREST RELEVANT TO THIS ARTICLE.

infectious causes; patients with shock caused by multiple organ dysfunction resulting from a malignant tumor at the end stage; patients with shock caused by acute and chronic organophosphorus pesticide poisoning. This study was approved by the hospital ethics committee, and informed consent was obtained from the patients or their relatives.

The general data of the two groups were collected and recorded, including sex, age, chronic history, time of stay in ICU, history of operation and site of infection. At the same time, the clinical data of systemic inflammatory response syndrome (SIRS), multiple organ dysfunction syndrome (MODS), acute physiology and chronic health system (APACHE II) score, arterial blood pressure and albumin were collected. The inflammatory factor *C-reactive protein* (*CRP*) was determined by ADVIA2400 rate nephelometry with Siemens automatic biochemical analyzer, and the relative reagent was used. IL-6 and CXCL-12 were detected by enzyme-linked immunosorbent assay (ELISA, Virun Sairun Co., Ltd., Germany) and FL-312e automatic enzyme labeling instrument (Bio-Kinetics Co., Ltd., USA). The APACHEII score scale includes three parts: acute physiology score, age score and chronic health score. The theoretical maximum score is 71. The higher the score, the higher the mortality (7).

Table I. *Distribution and constituent ratio of pathogenic bacteria in patients with septic shock*

Pathogenic bacteria	strains	Ratio(%)
Gram-negative bacteria	**160**	**52.98**
Pseudomonas aeruginosa	36	11.92
Klebsiella pneumoniae	30	9.93
Escherichia coli	29	9.61
Acinetobacter baumannii	28	9.27
Acinetobacter Roux	12	3.97
Enterobacter cloacae	10	3.31
Stenotrophomonas maltophilia	7	2.32
Enterobacter aerogenes	7	2.32
Alcaligenes faecalis	1	0.33
Gram-positive bacteria	**86**	**28.48**
Staphylococcus aureus	32	10.60
Streptococcus haemolyticus	27	8.94
Streptococcus pneumoniae	20	6.62
Enterococcus faecium	7	2.32
Fungus	**56**	**18.54**
Total	302	100.00

Statistical analysis

The data were analyzed by SPSS25.00 statistical software and expressed by mean ±standard deviation. Student's *t*-test was used for comparison between groups, and χ^2 test was used to compare all counting data between groups. In multivariate logistic regression analysis, the statistically significant parameters in the prior univariate analysis were used as independent variables, and the mortality of SS was taken as the dependent variable to analyze the independent risk factors of death in SS. The difference was statistically significant when $p < 0.05$.

RESULTS

Distribution and constituent ratio of pathogenic bacteria

As shown in Table I, a total of 302 strains of pathogenic bacteria were detected in 119 patients with SS. Among them, there were 160 strains of gram-negative bacteria (accounting for 52.98%), 86 strains of gram-positive bacteria (accounting for 28.48%) and 56 strains of fungi (accounting for 18.54%).

Univariate analysis of general data and clinical case data of the two groups

APACHE II score, an index to reflect the disorder of physiological parameters in patients with SS, is composed of acute physiological parameters, chronic health status and age, and takes physiological and laboratory data as quantitative indicators. The higher the APACHE II score, the

more serious the patient's condition. APACHE II score can be used for a comprehensive evaluation of the disease severity of patients with SS. Systemic inflammatory response syndrome (SIRS) refers to a variety of pathogenic factors (such as severe infection, trauma) acting on the human body. It causes systemic metabolic abnormalities and overreaction of the body's immune system, resulting in the uncontrolled release of pro-inflammatory factors. Under the influence of these comprehensive factors, patients may have dysfunction or failure of two or more systems or organs at the same time or in a short time, which is called MODS (Multiple organ dysfunction syndrome). There is a close relationship between MODS and the prognosis of SS. Through the regulation of inflammatory response and comprehensive treatment, the mortality of patients with ICU SS can be effectively reduced. The decrease of albumin level indicates that the patient is in a state of consumption, and the decomposition of a large amount of protein can cause dysfunction of many tissues and organs of the human body. Albumin usually reflects the nutritional status of the body, but in patients with SS the plasma albumin reflects the immune status of the body. The results of the current study showed that there were significant differences

Table II. *Univariate analysis of general data and clinical case data of two groups of patients [($\bar{x}$±s),%]*

Variable		Observation group(n=55)	Control group(n=64)	χ^2/t	*p*
Gender	Male	32	36	χ^2=0.045	0.832
	Female	23	28		
Age (years)		57.36±11.65	43.27±12.41	*t*=2.849	0.027
ICU hospitalization time (d)		12.35±6.34	11.27±6.25	*t*=0.601	0.592
Chronic medical history [n (%)]		26(47.27)	25(39.06)	χ^2=0.814	0.376
APACHEII score		25.16±5.25	17.78±3.69	*t*=5.643	0.000
Infection site [n(%)]					
Lower respiratory tract		37(67.27)	34(53.13)	χ^2=2.460	0.117
Abdominal cavity		19(34.55)	20(31.25)	χ^2=0.146	0.703
blood		30(54.55)	21(32.81)	χ^2=5.705	0.017
Other		8(14.55)	7(10.94)	χ^2=0.350	0.554
Surgical history [n(%)]		21(38.18)	22(34.38)	χ^2=0.186	0.666
Arterial pressure (mmHg)		42.32±8.17	58.23±11.34	*t*=-2.782	0.030
Albumin(g/L)		22.97±5.69	28.31±7.52	*t*=-5.425	0.000
SIRS(n)		3.35±0.97	1.32±0.84	*t*=5.712	0.000
MODS(n)		4.06±1.34	1.92±0.96	*t*=6.231	0.000

in age, APACHE II score, blood infection, arterial blood pressure, albumin level, SIRS and MODS number between the observation group and the control group (p=0.027, 0.000, 0.017, 0.030, 0.000, 0.000, 0.000, respectively) (p<0.05) (Table II). Clinicians should make correct judgments on the prognosis of patients with SS based on the results of APACHE II scores, take effective interventions to reduce these scores, thus minimizing the mortality. It also suggested that in clinical treatment of SS, in addition to basic treatment such as maintaining blood pressure, replenishing blood volume, anti-infective therapy and vasoactive drugs, the number of organs in MODS should be closely monitored and active treatment and measures should be given to protect organ function.

Comparison of serum inflammatory factor (CRP, IL-6 and CXCL-12) levels between the two groups

C-reactive protein (CRP) is a positive acute phase protein synthesized by the liver. CRP is positively correlated with the severity of the disease. According to the changes of serum CRP in patients, the degree of tissue injury can be reflected, and it is a commonly used index to evaluate infection. IL-6 is a pro-inflammatory factor produced and released by fibroblasts, monocytes and endothelial cells, and has an important value in the early diagnosis of inflammation and evaluation of the severity of the disease. CXCL-12 is a potential inflammatory chemokine of monocytes, B lymphocytes, T cells and DC cells, which has a certain effect on the immune regulation of patients. The expression level of CXCL-12 in serum of patients with SS is significantly increased, and continues to rise with the aggravation of the disease. Results of current study showed that the levels of serum inflammatory factors (CRP, IL-6 and CXCL-12) in SS patients in the observation group were significantly higher than those in the control group (t=10.564, 9.362, 17.369, p=0.000, 0.000, 0.000, respectively) (Table III).

Multivariate logistic regression analysis of death in SS

Multivariate logistic regression analysis was performed, with the statistically significant parameters in the univariate analysis as independent variables and the mortality of SS as dependent variables. The results showed that APACHE II score, serum albumin, SIRS, MODS and CXCL-12 were independent risk factors for death in SS (p<0.01) (Table IV).

Comparison of the levels of serum inflammatory factors (CRP, IL-6 and CXCL-12) in the control group before and after treatment

The levels of serum inflammatory factors CRP, IL-6 and CXCL-12 in patients in the control group after treatment were significantly lower than those before treatment (t=10.246, 8.324, 19.347, p= 0.000,

Table III. *Comparison of serum levels of inflammatory factors CRP, IL-6 and CXCL-12 between the two groups ($\bar{x}\pm s$)*

Group	n	CRP (mg/L)	IL-6 (ng/L)	CXCL-12 (pg/L)
Observation group	55	175.36±34.23[a]	225.36±45.67[a]	7.89±1.65[a]
Control group	64	104.19±25.75	109.90±29.41	3.26±0.41
t		10.564	9.362	17.369
p		0.000	0.000	0.000

[a]: p<0.01.

Table IV. *Multivariate Logisitic regression analysis of death in patients with septic shock*

Variable	*B*	*S.E*	*Wald*	*p*	*OR*	95%*CI*
Age	0.495	0.432	1.536	0.234	1.653	0.756-3.248
APACHE II Score	1.214	0.729	10.325	0.000	5.674	1.965-5.362
Blood infection	0.503	0.574	3.625	0.062	0.963	0.325-1.897
Arterial pressure	0.976	0.595	2.723	0.126	2.386	0.896-3.267
Albumin	2.796	0.731	7.526	0.003	3.054	1.687-2.115
SIRS	1.096	0.354	11.367	0.000	2.978	1.768-5.509
MODS	2.825	0.512	12.367	0.000	4.326	2.563-4.697
CRP	1.264	0.654	3.707	0.057	3.521	0.985-4.237
IL-6	1.524	0.623	3.718	0.055	3.269	0.992-3.216
CXCL-12	0.967	0.349	13.679	0.000	2.963	1.679-5.637

0.000, 0.000, respectively), and the difference was statistically significant. Comparison of serum levels of CRP before and after treatment is shown in Fig. 1. Comparison of serum levels of IL-6 before and after treatment is shown in Fig. 2. Comparison of serum levels of CXCL-12 before and after treatment is shown in Fig. 3. Through the detection of inflammatory factors, we can intuitively judge and analyze the disease degree of patients with SS, formulate the best nursing and treatment plan, and improve the clinical effect.

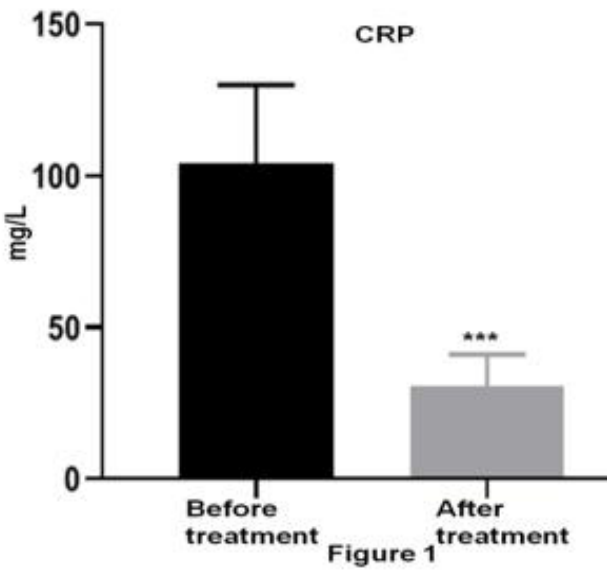

Fig. 1. *Comparison of serum levels of CRP before and after treatment in the control group*

DISCUSSION

In ICUs, SS is a complex clinical syndrome and a common complication with the characteristics of rapid progress and high mortality (8-10). The occurrence and development are multi-step processes involving

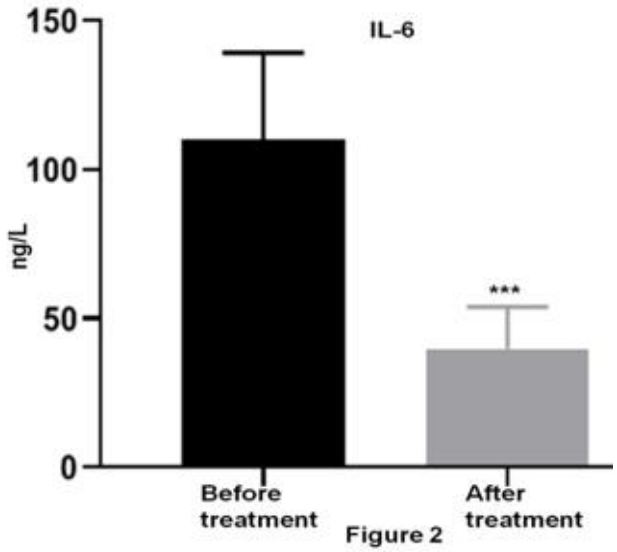

Fig. 2. *Comparison of serum levels of IL-6 before and after treatment in the control group*

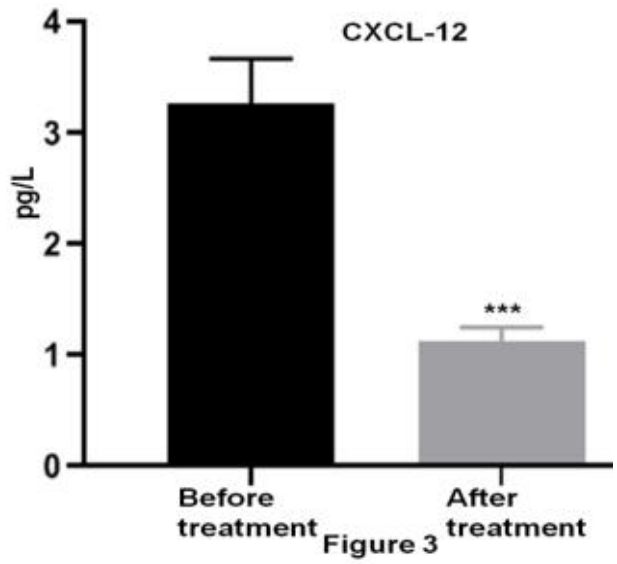

Fig. 3. *Comparison of serum levels of CXCL-12 before and after treatment in the control group *** compared with that before treatment, $p < 0.001$.*

various factors. It is necessary to analyze the risk factors affecting the prognosis, track the progress of patients in time, and formulate corresponding intervention programs to reduce mortality, improve prognosis and patients' quality of life.

APACHE II has become a scoring system widely used in ICUs all over the world, and has been widely recognized by scholars (11). The results of this study showed that the APACHE II score of the observation group was significantly higher than that of the control group, which could be used as an independent risk factor for death in SS, and it had high application value in predicting the prognosis of SS. SIRS and MODS were also indicated as risk factors for death. Hypoalbuminemia was a risk factor for death from SS, so it was beneficial to improve the prognosis of patients with SS by replenishing albumin in time, promoting anabolism and protecting the function of tissues and organs. CXCL-12 was an independent risk factor for death from SS.

In summary, analyzing the risk factors for death in patients with SS, and implementing comprehensive treatment and nursing in a targeted manner can effectively reduce the mortality rate, improve its prognosis and the quality of life of patients. However, the verification of the above risk factors for death in SS patients should be confirmed in a larger cohort.

ACKNOWLEDGEMENTS

This research was supported by the National Foundation of Natural Science of China (31471114, 31500837), China Postdoctoral Science Foundation (2017M622129), Qingdao Postdoctoral Applied Research Project, and Source Innovation Program (Talent Development Special-2019 Youth Special) (19-6-2-43-cg).

REFERENCES

1. Connor EE, Jackson NR, McGoey RR. Pathology image of the month: rapidly progressive hemorrhagic cellulitis of bilateral lower extremities with subsequent septic shock and death. J La State Med Soc 2016; 168:109-12.
2. Peake SL, Delaney A, Bailey M, et al. Goal-directed resuscitation for patients with early septic shock. N Engl J Med 2014; 371:1496-506.
3. Lee R, Lee D, Gowda NB, et al. Increased rates of septic shock, cardiac arrest, and mortality associated with chronic steroid use following anterior cervical discectomy and fusion for cervical stenosis. Int J Spine Surg 2020; 14:649-56.

4. Seymour CW, Rosengart MR. Septic shock: advances in diagnosis and treatment. JAMA 2015; 314:708-17.
5. Camou F, Oger S, Paroissin C, et al. Plasma Neutrophil Gelatinase-Associated Lipocalin (NGAL) predicts acute kidney injury in septic shock at ICU admission. Ann Fr Anesth Reanim 2013; 32:157-64.
6. Muckart DJ, Bhagwanjee S. American College of Chest Physicians/Society of Critical Care Medicine Consensus Conference definitions of the systemic inflammatory response syndrome and allied disorders in relation to critically injured patients. Crit Care Med 1997; 25:1789-95.
7. Tavakolian Ferdousie V, Mohammadi M, Hassanshahi G, et al. Serum CXCL10 and CXCL12 chemokine levels are associated with the severity of coronary artery disease and coronary artery occlusion. Int J Cardiol 2017; 233:23-28.
8. Rusconi AM, Bossi I, Lampard JG, Szava-Kovats M, Bellone A, Lang E. Early goal-directed therapy vs usual care in the treatment of severe sepsis and septic shock: a systematic review and meta-analysis. Intern Emerg Med 2015; 10:731-43.
9. Morgan RW, Fitzgerald JC, Weiss SL, Nadkarni VM, Sutton RM, Berg RA. Sepsis-associated in-hospital cardiac arrest: Epidemiology, pathophysiology, and potential therapies. J Crit Care 2017; 40:128-35.
10. Tang Y, Sorenson J, Lanspa M, Grissom CK, Mathews VJ, Brown SM. Systolic blood pressure variability in patients with early severe sepsis or septic shock: a prospective cohort study. BMC Anesthesiol 2017; 17:82.
11. Chatterjee K, Goyal A, Chada A, Kakkera KS, Corwin HL. National trends (2007-2013) of clostridium difficile infection in patients with septic shock: impact on outcome. J Hosp Med 2017; 12:717-722.

LETTER TO THE EDITOR

Knockdown of Metadherin suppressed the progression of oral squamous cell carcinoma via PI3K/AKT signaling pathway

ZY. Ding[1], G. Dong[2], G. Yin[3], LL. Yu[4], WX. Li[5] and B. Ding[6]

[1]Emergency Department, Weifang People's Hospital, Weifang, China; [2]Department of Stomatology, Qingdao Municipal Hospital, Qingdao, China; [3]Department of Clinical Laboratory, Qingdao Central Hospital, Qingdao University, Qingdao, China; [4]Department of Endoscopic Room, the People's Hospital of Zhangqiu Area, Jinan, China; [5]Department of Clinical Laboratory, Weifang People's Hospital, Weifang, China; [6]Department of Stomatology, Qingdao Central Hospital, Qingdao University, Qingdao, China

Received September 30, 2020 – Accepted January 29, 2021

To the Editor,

Oral squamous cell carcinoma (OSCC) is a common oral carcinoma, which accounts for 90% of oral cancers (1). In spite of recent advancement in chemotherapy, radiotherapy and targeted therapy, the prognosis of OSCC is poor due to aggressive local invasion and metastasis. Hence, it is necessary to reveal the intrinsic mechanism of OSCC and find more effective therapeutic targets. Recent research has shown that epithelial-mesenchymal transformation (EMT) is a critical process for tumor cells to acquire invasive and motility properties, and the modulation of intercellular adhesion components, such as E-cadherin, N-cadherin, and Vimentin, is the main reason for OSCC metastasis (2). Moreover, increasing evidence have indicated that abnormal activation of PI3K/AKT signaling contributed to the EMT initiation and formation of invasive carcinoma (3). PI3K/AKT signaling may therefore play a critical regulatory role in the treatment of metastatic tumors.

Metadherin (MTDH) has been confirmed to have a role in the development and progression of various tumors (4). For instance, Hu et al. identified that MTDH was up-regulated in prostate cancer (5). High expression of MTDH was also found in colorectal cancer and was involved in cell progression (6). Moreover, MTDH was highly expressed in OSCC cells and tissues and was correlated with the prognosis of OSCC patients (7). Furthermore, MTDH is involved in the progression of giant cell tumor of bone by regulating cell proliferation, invasion and metastasis through modulating PI3K/AKT signaling pathways (8). However, it is unclear whether MTDH can be a potential therapeutic target and promising candidate for OSCC.

The aim of this study was to investigate the role and mechanism of MTDH in OSCC. Results showed that MTDH was increased in OSCC tissues and cells. Knockdown of MTDH significantly suppressed the progression of OSCC. Moreover, AKT/PI3K pathway was inhibited by decreasing MTDH, suggesting that MTDH/AKT/PI3K pathway might play an important role in OSCC progression.

Key words: MTDH; oral squamous cell carcinoma; PI3K/AKT

Corresponding Author:
Dr Bo Ding,
Department of Stomatology,
Qingdao Central Hospital, Qingdao University,
127 Siliu South Road, Qingdao 266042,
Shandong Province, China
e-mail: dingbozhui33916@163.com

0393-974X (2021)
Copyright © by BIOLIFE, s.a.s.
This publication and/or article is for individual use only and may not be further reproduced without written permission from the copyright holder.
Unauthorized reproduction may result in financial and other penalties
DISCLOSURE: ALL AUTHORS REPORT NO CONFLICTS OF INTEREST RELEVANT TO THIS ARTICLE.

MATERIALS AND METHODS

Tissue samples

Fifty pairs of OSCC tissues and normal tissues were collected from Qingdao Central Hospital. The patients participated in the study had not received any treatment prior to surgery. All samples were stored at –80°C until RNA isolation. All patients provided written informed consent to participate in the study. This study was approved by the ethics committee of Qingdao Central Hospital.

Cell culture and cell transfection

The OSCC cell lines (SCC15 and CAL27) and normal oral keratinocyte cell line NOK1 were obtained from the American Type Culture Collection (ATCC; Rockville, MD, USA). Normal keratinocyte NOK1 was maintained in KSFM medium (Life Technologies, USA) and the oral cancer cell lines were cultured in RPMI-1640 with 10% fetal bovine serum, penicillin (100U/ml) and streptomycin (100μg/ml), which was incubated at 37°C under 5% CO_2 atmosphere.

The siRNA or over-expression vector of MTDH (si-MTDH or pcDNA-MTDH) was designed by GenePharma (Shanghai, China). The transfection procedures were performed by Lipofectamine 2000™ reagent (Invitrogen) following the manufacturer's instructions and incubated at 37°C under 5% CO2.

RNA isolation and quantitative real-time PCR (qRT-PCR)

TRIzol reagent (Invitrogen) was applied for isolating total RNA from cells or tissues. All-in-One™ miRNA First-Strand cDNA Synthesis Kit was carried out to synthesize cDNA. TaqMan PCR kit was used for performing qRT-PCR. All reactions were performed three times. The $2^{\Delta\Delta Ct}$ method was applied for detecting the mRNA expression. The primers used in this study were as follows: MTDH 5'-AAATAGCCAGCCTA TCAAGACTC-3' (forward), 5'-TTCAGACTTGGTCTGTGAAGGAG-3' (reverse); 5'-CGCTCTCTGCTCCTCCTGTT-3' (forward), 5'-CCATGGTGTCTGAGCGATGT-3' (reverse).

Western blot assay

After transfection for 48 h, total proteins were isolated from OSCC tissues and cells. Electrophoresis separation was performed using 10-12% sodium dodecyl sulfate polyacrylamide gel (SDS-PAGE), then the proteins were transferred to polyvinylidene fluoride (PVDF) membranes. Afterwards, the membrane was blocked with 5% skim milk for 2 h, and incubation was carried out with the following primary antibodies: E-cadherin (Abcam, ab40772, 1:2000), N-cadherin (Abcam, ab98952, 1:1000), Vimentin (Abcam, ab92547, 1:1000), PI3K (CST, #4249, 1:1000), p-PI3K (CST, #4228, 1:1000), AKT (CST, #2920, 1:2000), p-AKT (CST, #13038, 1:1000) at 4°C overnight, and then the second goat anti-rabbit antibody for 2 h. The enhanced chemiluminescence kit (ECL, Millipore) was used to detect the signals. GAPDH served as a loading control.

MTT assay

OSCC cells were added to 96-well plates at density of 5×10^3 cells/well. The cells were incubated for 24, 48, 72 and 96 h; 20 ul MTT medium was then added to each well. After incubating for 4 h at 37°C, 100 ul DMSO was

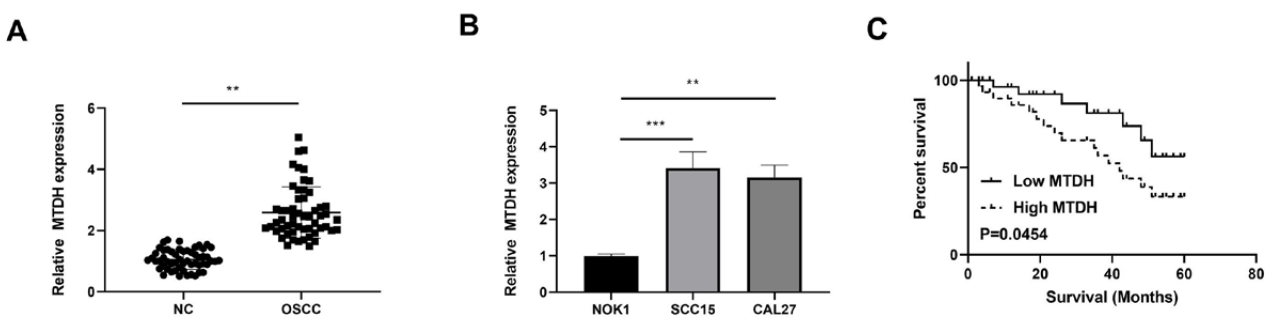

Fig. 1. *MTDH was highly expressed in OSCC.* ***A)*** *MTDH expression detected in OSCC tissues and normal tissues.* ***B)*** *MTDH expression detected in OSCC cell lines and normal cells.* ***C)*** *Overall survival correlation analysis was performed for OSCC patients with different levels of MTDH. **P < 0.01.*

added for additional 10 min. Cell viability was measured by detecting the absorbance at 24, 48, 72, 96 h at a wavelength of 490 nm.

Transwell assays

Cell migration was performed using a Transwell chamber without pre-coating with Matrigel while cell invasion used a Transwell chamber pre-coated with Matrigel. The OSCC cells (1×10^5) were seeded into the top chamber and RPMI-1640 medium containing 20% fetal bovine serum (FBS) was added into the lower chambers. Then the cells were allowed to incubate for 24 h at 37°C. The migratory or invasive cells in the bottom chamber were stained with 0.1% crystal violet. Images of the migration cells or invasion cells were photographed under a microscope.

Statistical analysis

The data were displayed as mean ± SD and SPSS 17.0 statistical software (SPSS, USA) was applied to analyze the data. Student's *t*-test was used to compare the difference between two groups and Tukey's post hoc test after One-way ANOVA was applied to compare the differences between more than two groups. The Kaplan-Meier survival analysis was carried out to analyze the overall survival. P values of <0.05 were considered to have statistical significance.

RESULTS

MTDH was highly expressed in OSCC and closely correlated with the prognosis of OSCC patients

QRT-PCR was first performed to measure MTDH expression in OSCC in order to explore its role in the development of OSCC. As shown in Fig. 1A, MTDH expression level in tumor tissues was increased in comparison with non-tumor tissues. Similarly, MTDH expression was observed to be higher in OSCC cells than in normal NOK1 cells (Fig. 1B). Furthermore, the high expression of MTDH was related to the poor survival rate of OSCC patients (Fig. 1C). The results above indicated that up-regulation of MTDH was correlated with OSCC progression.

Knockdown of MTDH inhibited the tumorigenesis of OSCC

Subsequently, siRNA-MTDH was utilized to decrease the expression of MTDH in SCC15 and CAL27 cells. As expected, MTDH expression was significantly decreased in the cells transfected with si-MTDH compared with the control group (si-NC) (Fig. 2A). The OSCC cell viability was tested by MTT assay and the results showed that the absorbance was significantly reduced by si-MTDH (Fig. 2B). Transwell assay was applied to assess the migration and invasion cells. As shown in Fig. 2 C, D, knockdown of MTDH inhibited the cell migratory and invasive ability of SCC15 and CAL27 cells.

Ove-expression of MTDH enhanced the development of OSCC

Overexpression vector of MTDH was used to increase the expression of MTDH in SCC15 and CAL27 cells. As shown in Fig. 3A, MTDH expression was significantly increased in the cells transfected with pcDNA-MTDH compared with the control group. MTT assay results discovered that the viability of SCC15 and CAL27 cells was significantly elevated by pcDNA-MTDH (Fig. 3B). Transwell analysis showed that the migration and invasion cells were increased by over-expression of MTDH in SCC15 and CAL27 cells (Fig. 3 C, D).

Down-regulation of MTDH inhibited EMT and PI3K/AKT signaling pathway in OSCC

The precise molecular mechanism of MTDH was then investigated in SCC15 cells. Firstly, the effects of si-MTDH or pcDNA-MTDH on the related proteins of EMT and PI3K/AKT signaling pathway were detected, which is important in the tumorigenesis of OSCC. Western blot results showed that N-cadherin and Vimentin expression was declined while E-cadherin expression was facilitated by si-MTDH. However, over-expression of MTDH showed the opposite effect on these proteins (Fig. 4A). Then, the protein levels of PI3K, p-PI3K and AKT, p-AKT in SCC15 cells after treating with si-MTDH were measured to explore the underlying mechanism of MTDH in OSCC development. Western blot results showed that the phosphorylation of PI3K and AKT expression was decreased remarkably by si-MTDH, while increased by pcDNA-MTDH (Fig. 4B). Taken together, these data suggest that MTDH might

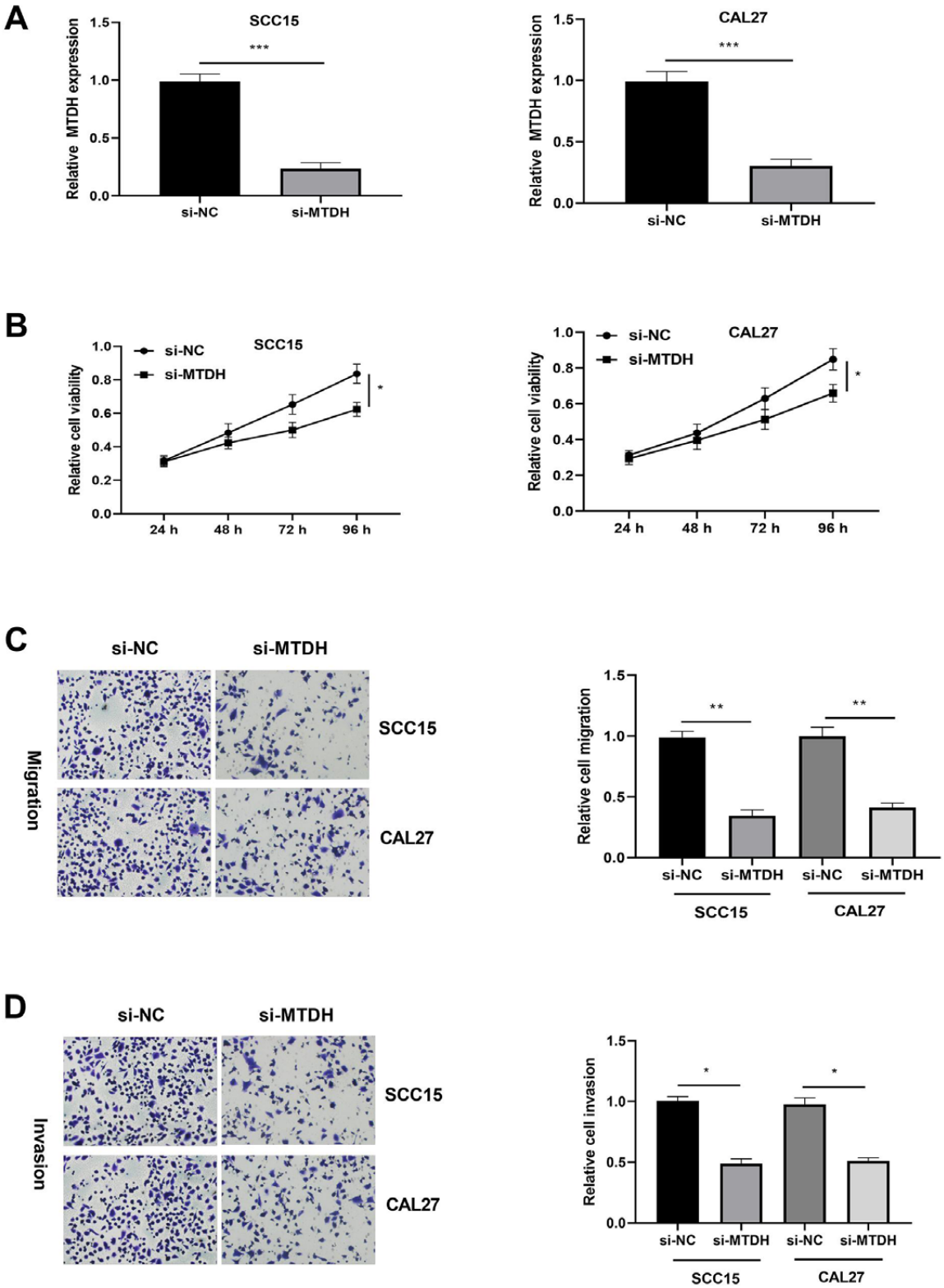

Fig. 2. *Knockdown of MTDH suppressed OSCC cell proliferation, migration and invasion.* ***A****) MTDH expression tested in SCC15 and CAL27 cells transfected with si-MTDH.* ***B****) SCC15 and CAL27 cell viability measured after treating with si-MTDH.* ***C, D****) SCC15 and CAL27 cell migration and invasion rate examined after treating with si-MTDH. * P <0.05, ** P <0.01.*

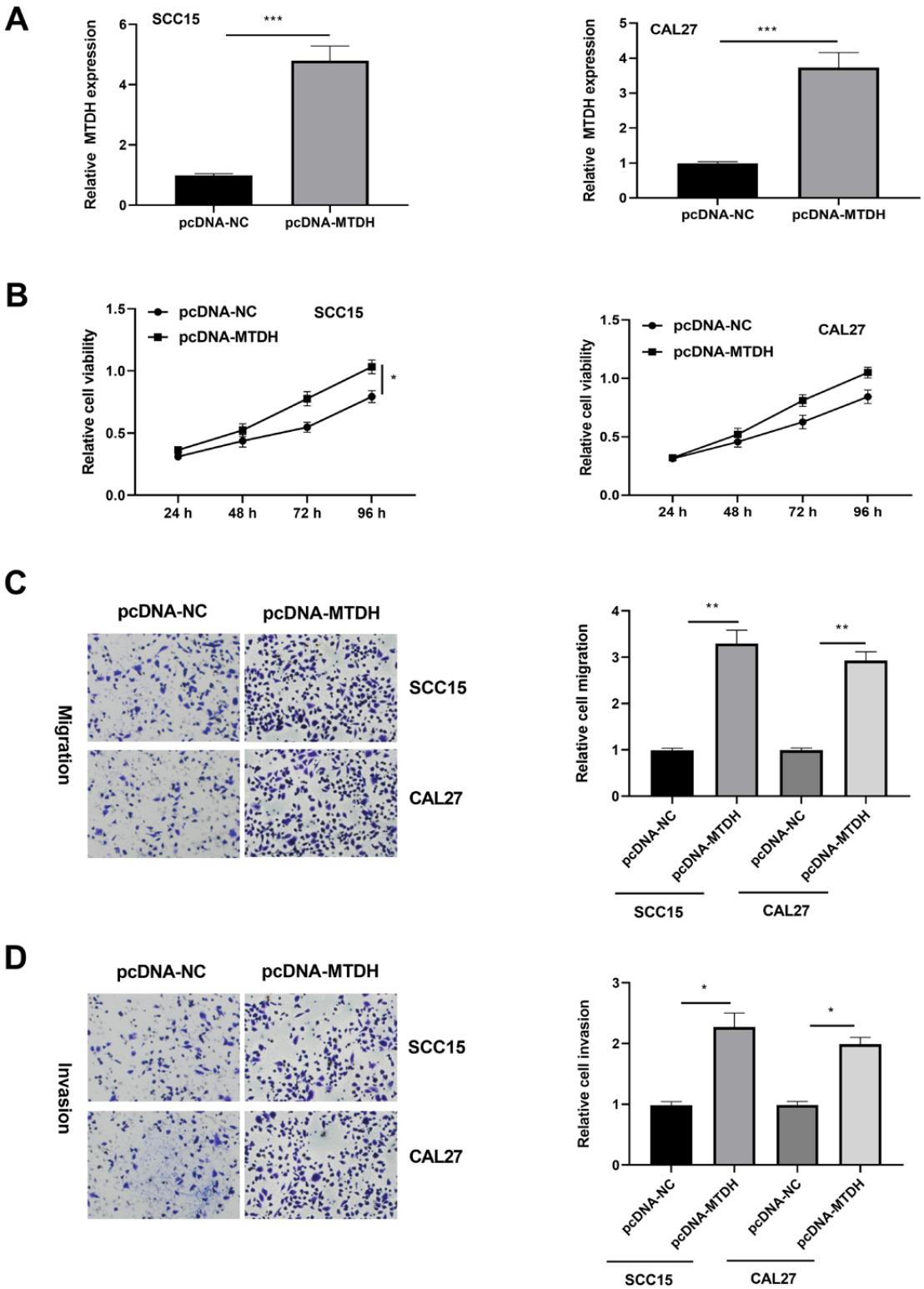

Fig. 3. *Over-expression of MTDH enhanced OSCC cell proliferation, migration and invasion.* ***A****) MTDH expression tested in SCC15 and CAL27 cells transfected with pcDNA-MTDH.* ***B****) SCC15 and CAL27 cell viability measured after treating with pcDNA-MTDH.* ***C, D****) SCC15 and CAL27 cells migration and invasion rate examined after treating with pcDNA-MTDH. * P <0.05, ** P <0.01.*

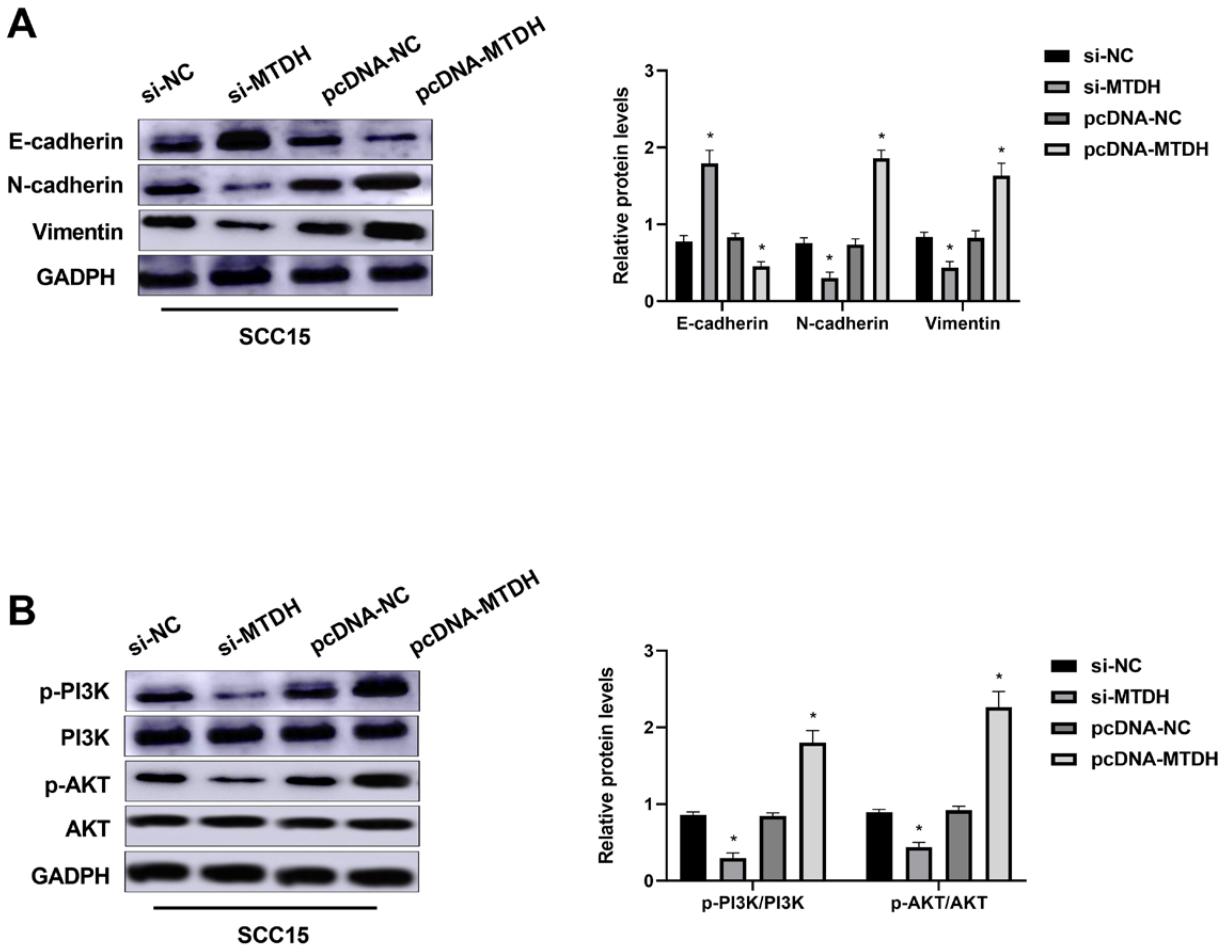

Fig. 4. *Knockdown of MTDH inhibited the activation of EMT and AKT pathway in OSCC cells.* ***A****) Western blot analysis of E-cadherin, N-cadherin and Vimentin levels in SCC15 cells after treating with si-MTDH or pcDNA-MTDH.* ***B****) Western blot analysis of PI3K, p-PI3K, AKT, p-AKT levels in SCC15 cells after treating with si-MTDH or pcDNA-MTDH.*

regulate OSCC progression through EMT and PI3K/AKT signaling pathway.

DISCUSSION

As the incidence of OSCC is rising, more attention has been paid to the study of potential molecular mechanism of OSCC (9). MTDH was reported as an oncogene in multiple cancers. Li et al. showed that MTDH was up-regulated in glioma and inhibit glioma cell viability and invasion (10). Moreover, MTDH was shown with high expression in melanoma and was involved in the development of melanoma (11). The present study demonstrated that MTDH was highly expressed in OSCC tissues and associated with the prognosis of OSCC patients. Knockdown of MTDH suppressed OSCC proliferation, migration and invasion. A previous study reported that MTDH participated in tumor progression through modulating PI3K/AKT signaling pathway (12). Here, we investigated whether PI3K/AKT signaling pathway was involved in the progress of OSCC regulated by MTDH. The results showed that knockdown of MTDH inhibited the activation of PI3K/AKT pathway.

We summarized all results of our studies and drew the conclusion that MTDH was highly expressed in OSCC, and its high expression was closely related to the poor prognosis of OSCC patients. Moreover, knockdown of MTDH inhibited OSCC cell progression through PI3K/AKT pathway, providing a novel idea of the treatment of OSCC.

REFERENCES

1. Jornet PL, Garcia FJ, Berdugo ML, Perez FP, Lopez AP. Mouth self-examination in a population at risk of oral cancer. Aust Dent J 2015; 60:59-64.
2. Liu Y. Cellular and molecular mechanisms of renal fibrosis. Nat Rev Nephrol 2011; 7:684-96.
3. Zhao YY, Jia J, Zhang JJ, et al. Inhibition of histamine receptor H3 suppresses the growth and metastasis of human non-small cell lung cancer cells via inhibiting PI3K/Akt/mTOR and MEK/ERK signaling pathways and blocking EMT. Acta Pharmacol Sin 2020; doi: 10.1038/s41401-020-00548-6.
4. Sarkar D, Fisher PB. Advances in Cancer Research. AEG-1/MTDH/LYRIC implicated in multiple human cancers. Preface. Adv Cancer Res 2013; 120:xi-xiv.
5. Hu K, Mu X, Kolibaba H, Yin Q, Liu C, Liang X, Lu J. Metadherin is an apoptotic modulator in prostate cancer through miR-342-3p regulation. Saudi J Biol Sci 2018; 25:975-81.
6. Li J, Huang C, Li J, et al. Knockdown of metadherin inhibits cell proliferation and migration in colorectal cancer. Oncol Rep 2018; 40:2215-23.
7. Xia X, Du R, Zhao L, Sun W, Wang X. Expression of AEG-1 and microvessel density correlates with metastasis and prognosis of oral squamous cell carcinoma. Hum Pathol 2014; 45:858-65.
8. Chen F, Wang S, Wei Y, et al. Norcantharidin modulates the miR-30a/Metadherin/AKT signaling axis to suppress proliferation and metastasis of stromal tumor cells in giant cell tumor of bone. Biomed Pharmacother 2018; 103:1092-100.
9. Liu C, Wang Z, Wang Y, Gu W. MiR-338 suppresses the growth and metastasis of OSCC cells by targeting NRP1. Mol Cell Biochem 2015; 398:115-22.
10. Li L, Zhang H. MicroRNA-379 inhibits cell proliferation and invasion in glioma via targeting metadherin and regulating PTEN/AKT pathway. Mol Med Rep 2018; 17:4049-56.
11. Liu K, Jin J, Rong K, Zhuo L, Li P. MicroRNA-675 inhibits cell proliferation and invasion in melanoma by directly targeting metadherin. Mol Med Rep 2018; 17:3372-79.
12. Zhu B, Chen H, Zhang X, et al. Serum miR-30d as a novel biomarker for multiple myeloma and its antitumor role in U266 cells through the targeting of the MTDH/PI3K/Akt signaling pathway. Int J Oncol 2018; 53:2131-44.

LETTER TO THE EDITOR

Association of SREBF-2 gene polymorphisms with the risk of developing type 2 diabetes mellitus

Y. Zhang[1], XX. Sun[1], YC. Liu[2] and YD. Wang[1]

[1]Department of Massotherapy, Binzhou Municipal Hospital of Traditional Chinese Medicine, Binzhou, Shandong, China; [2]Department of Hematology, Affiliated Hospital of Weifang Medical University, Weifang, Shandong, China

Received November 25, 2020 – Accepted January 29, 2021

To the Editor,

Type 2 diabetes mellitus (T2DM) is a popular metabolic disorder and accounts for more than 90% of all diabetes cases . Due to the complexity of etiology and the insufficient understanding of T2DM, it is difficult to accurately estimate its incidence and conduct an effective intervention. Thus, it is essential to research the probable mechanisms of diabetes mellitus.

Gene polymorphism is a common cause of many common diseases, including T2DM. Accumulating evidence indicates these polymorphisms are associated with the pathology of T2DM and improve hereditary susceptibility . Sterol regulatory element binding protein transcription factor 2 (SREBF-2) is mainly involved in the accommodation of lipid and carbohydrate metabolism . In non-alcoholic fatty liver disease, the SREBF-2 rs133291 C/T polymorphism influences the lipid metabolism . In patients with coronary artery disease and T2DM, SREBP-2 mRNA expression levels in epicardial adipose tissues are significantly increased, indicating SREBP-2 is associated with the development of T2DM . In an investigation of the Iranian population, the correlation of T2D susceptibility and SREBF-2 polymorphisms rs2267439 and rs2267443C/T was revealed . However, the association between the SNPs of SREBF-2 and the Chinese Han population remains unclear.

Therefore, this investigation aimed to reveal the probable association between rs2267439 and rs2267443 SNPs of SREBF-2 and the risk of T2DM in a sample of Chinese Han.

MATERIALS AND METHODS

Study subjects

A total of 289 subjects, 152 T2DM patients and 137 healthy controls, from the Affiliated Hospital of Weifang Medical University were enrolled in our study. All these participants in our study were from the Chinese Han population and there was no kinship among them. All patients provided written informed consent prior to experiments. The protocols of the study were approved by the Ethics committee of the Affiliated Hospital of Weifang Medical University.

The patients were diagnosed as T2DM according to the American Diabetic Association (ADA) guidelines. The inclusion criteria for T2DM cases were: no family history of diabetes; fasting blood glucose (FBG) ≥126 mg/dl; blood glucose ≥200 mg/dl; or glycosylated hemoglobin level> 6.5% 2 hours after a meal . Some T2DM patients with malignant tumors, pancreatitis, diabetes insipidus, anemia, and chronic liver disease were excluded. The patients included had not taken any hypoglycemic agents, antihypertensive drugs, or antilipemic agents prior to the

Key words: SREBF-2; rs2267439; rs2267443; T2DM; Chinese Han population

Corresponding Author:
Dr. Yanchao Liu,
Department of Hematology, Affiliated Hospital of Weifang Medical University, 2428 Yuhe Road, Kuiwen District, 261000, Weifang, China
Tel./Fax: +86-05363081100
e-mail: liuyanchaowf@163.com

0393-974X (2021)
Copyright © by BIOLIFE, s.a.s.
This publication and/or article is for individual use only and may not be further reproduced without written permission from the copyright holder.
Unauthorized reproduction may result in financial and other penalties
DISCLOSURE: ALL AUTHORS REPORT NO CONFLICTS OF INTEREST RELEVANT TO THIS ARTICLE.

study. The criteria of healthy controls were: i) no diabetes; ii) no family history of diabetes; iii) no hypertension; iv) similar age, and body mass index (BMI) with T2DM patients. All the study subjects underwent detailed clinical examines and the demographical features and diagnostic anthropometric items, including fasting blood glucose, total cholesterol, triglycerides, high-density lipoprotein (HDL), and low-density lipoprotein (LDL), were measured and summarized.

Five ml whole blood specimens were isolated from all study subjects and anticoagulated by adding 5% ethylenediamine tetraacetic acid (EDTA). All these specimens were applied to measure biomedical parameters and extract DNA. DNA was obtained from each venous blood specimen according to the guidelines of the TaKaRa Genome DNA Extraction Kit (TaKaRa Corporation, Beijing, China) and stored at -20°C.

Genotyping

Polymerase chain reaction (PCR) was used to amplify the partial sequence of target gene SREBF-2 using Phanta HS Super-Fidelity DNA Polymerase (Vazyme, Nanjing, China). The primers used to amplify the fragments of rs2267439 and rs2267443 were designed on the software Primer Premier 5.0 and synthesized by Shanghai Sangon Biotech Corporation. Designed primers are shown in Table I. The PCR was as follows: 10 µl 5×SF Buffer, 1 µl dNTP Mix (10 mM each), 2 µl forward primer, 2 µl reverse primer, 5 µl genomic DNA, 1 µl Phanta HS Super-Fidelity DNA Polymerase, and 29 µl deionized distilled water. The PCR reaction procedures included a pre-degeneration at 95°C for 3 min followed by 27 cycles of 95°C for 10 sec, 60°C for 30 sec, 72°C for 30 sec, and a final extension at 72°C for 10 min. The obtained PCR products were purified with Hieff NGS® DNA Selection Beads (Yeasen, Shanghai, China) and sequenced by Applied Biosystems 3730×l automated sequencer (Applied Biosystems, CA, USA). The results were analyzed by Vector NTI software.

Statistical analysis

All results of this study were analyzed by SPSS 21.0 software. The genotype and allele frequency of rs2267439 and rs2267443 were obtained by counting. The Hardy-Weinberg equilibrium (HWE) of each polymorphism was analyzed to assess statistical difference. The *chi*-squared test was used to compare the differences of the genotype and allele distribution between the T2DM group and controls. Logistic regression was used to correct comparisons for age, gender, and BMI. The association between the SREBF-2 polymorphism and T2DM susceptibility was evaluated by odds ratio (OR) and 95% confidence interval (95% CI) results. $P < 0.05$ was considered statistically significant.

RESULTS

Basic features

The demographical features and anthropometric measurements of 152 T2DM patients and 137 healthy controls participating in this study are shown in Table II. No significant differences were found between the age and gender of T2DM patients and those of controls (all $P > 0.05$). The comparison of BMI and some risk factors including fasting blood glucose, total cholesterol, triglycerides, HDL, and LDL between cases and controls were analyzed. The results showed that BMI, fasting blood glucose, total cholesterol, triglycerides, and LDL in T2DM patients

Table I. *Primer sequences of SREBF-2 gene rs2267439 and rs2267443 polymorphisms*

Variations		Primer sequences
rs2267439	For.	5'- ATTCACACCCAGGCCTTTGGCCT -3'
	Rev.	5'- ACACGCCCATGAACAAACTCCAAG -3'
rs2267443	For.	5'- TGCTTTGTGGAAGGTTGGCAGAG -3'
	Rev.	5'- AGCAGCGCTGTTTCATGGTCT -3'

were higher than those in controls (all $P < 0.01$). The HDL of T2DM patients was significantly decreased compared to the control participants ($P < 0.05$).

Gene polymorphisms and T2DM

The genotype and allele distribution of SREBF-2 rs2267439 and rs2267443 of all individuals in our study are presented in Table III. The HWE results proposed that the distributions of each SNP in the control group did not deviate from HWE, suggesting good representativeness of our collection specimens.

The rs2267439 polymorphism between controls and T2DM patients was significantly different, which was demonstrated by CT (60.5% *vs* 51.1%, $P < 0.05$). The risk of individuals carrying CT showed a higher risk of having T2DM (OR=2.081, 95%CI=1.144-3.785). Moreover, the T allele of rs2267439 also was significantly increased in the patients with T2DM compared to the controls (57.9% *vs* 46.7%, $P < 0.01$). The T allele of rs2267439 elevated the risk of T2DM when compared with the C allele (OR=1.568, 95%CI=1.129-2.179). However, the frequency of SREBF-2 gene rs2267443 polymorphism was not significantly different between case and control groups (all $P > 0.05$).

In order to determine the results more

Table II. *Demographics and risk factors in T2DM patients and control subjects*

Variable	Cases (n = 152)	Controls (n = 137)	*P*
Age (years)	52.53±7.38	54.09±7.84	0.348
Female/ Male	67/85	63/74	0.745
BMI (kg/m^2)	24.41±4.38	23.14±3.62	0.002
Fasting blood glucose (mmol/l)	9.27±1.07	5.28±0.42	< 0.001
Total cholesterol (mmol/l)	5.19±0.66	4.49±0.47	< 0.001
Triglycerides (mmol/l)	1.90±0.54	1.42±0.35	< 0.001
HDL (mmol/l)	1.14±0.33	1.45±0.27	0.026
LDL (mmol/l)	2.84±0.35	2.70±0.45	0.007

BMI: body mass index; HDL: high density lipoprotein; LDL: low density lipoprotein

Table III. *Association of SREBF-2 gene rs2267439 and rs2267443 polymorphisms with T2DM susceptibility*

Genotype/Allele	Case n=152 (%)	Control n=137 (%)	*P* value	OR (95%CI)	P^a	OR(95%CI)^a
rs2267439						
CC	24 (15.8)	38 (27.7)	-	-	-	-
CT	92 (60.5)	70 (51.1)	0.015	2.081(1.144-3.785)	0.034	2.225(1.063-4.658)
TT	36(23.7)	29 (21.2)	0.060	1.966(0.969-3.987)	0.715	0.896(0.495-1.620)
C	128 (42.1)	146 (53.3)	-	-	-	-
T	176 (57.9)	128 (46.7)	0.007	1.568(1.129-2.179)	0.038	1.653(1.028 -2.660)
P_{HWE}	-	0.758				
rs2267443						
GG	94(61.84)	86(62.77)	-	-	-	-
GA	46(30.26)	41(29.9)	0.920	1.026(0.615-1.714)	0.842	1.098(0.437-2.747)
AA	12(7.89)	10(7.30)	0.837	1.098(0.451-2.670)	0.914	1.055(0.401-2.799)
G	230(75.7)	214(78.1)	-	-	-	-
A	74(24.3)	60(21.9)	0.487	1.148(0.778-1.692)	0.687	1.122(0.640-1.968)
P_{HWE}	-	0.107				

HWE: Hardy-Weinberg equilibrium; [a]: adjusted for age: gender and BMI

accurately, we used age, gender, and BMI as common confounding factors, and re-analyzed the relationship between genetic polymorphisms and T2DM susceptibility. The adjusted results are shown in Table III showing that the SREBF-2 gene rs2267439 was still significantly related to T2DM susceptibility, and individuals with CT genotype and T allele were at higher risk of T2DM (OR=2.225, 95%CI=1.063-4.658; OR=1.653, 95%CI=1.028 -2.660, respectively).

DISCUSSION

Diabetes mellitus is a fastest-growing body metabolic disease . More than 500 genes have been identified to be highly associated with T2DM during the last decade. Moreover, the gene mutation frequency based on overall T2DM predisposition can indicate individuals with a high future risk of diabetes (9, 10).

In the present study, the frequencies of CT genotype and T allele were significantly elevated in the T2DM group, indicating that the increased CT genotype and T allele may contribute to the onset of T2DM in the Chinese Han population. The re-analyzed results showed that individuals with CT genotype had a 2.225-fold increased risk of developing T2DM when compared with CC carriers, and individuals carrying T allele had a risk 1.653 times higher than subjects with C allele. A previous study confirmed that rs2267439 polymorphism in SREBR-2 showed a significant association with the onset of T2DM in the Iranian population . A publication by Kim et al. showed that the T allele of rs2267439 also significantly increases the susceptibility of avascular necrosis in the Korean population . All these findings are in agreement with the present results, suggesting genotype CT and allele T may elevate the risks of T2DM.

In conclusion, the results of this study proved that the rs2267439 polymorphism of the SREBF-2 gene was closely correlated with the risks of T2DM in the Chinese Han population. No significant association between the rs2267443 polymorphism and T2DM was found. The CT genotype and T allele in rs2267439 elevated the risk factors of T2DM.

REFERENCES

1. Zhuang H, Han J, Cheng L, Liu SL. A positive causal influence of IL-18 levels on the risk of T2DM: A Mendelian randomization study. Front Genet 2019; 10:295.
2. Chen DW, Shi JK, Li Y, Yang Y, Ren SP. Association between ApoE polymorphism and type 2 diabetes: A meta-analysis of 59 studies. Biomed Environ Sci 2019; 32:823-38.
3. Poletti S, Aggio V, Bollettini I, Falini A, Colombo C, Benedetti F. SREBF-2 polymorphism influences white matter microstructure in bipolar disorder. Psychiatry Res Neuroimaging 2016,;257:39-46.
4. Musso G, Cassader M, Bo S, De Michieli F, Gambino R. Sterol regulatory element-binding factor 2 (SREBF-2) predicts 7-year NAFLD incidence and severity of liver disease and lipoprotein and glucose dysmetabolism. Diabetes 2013; 62:1109-20.
5. Pérez-Belmonte LM, Moreno-Santos I, Cabrera-Bueno F, et al. Expression of Sterol Regulatory Element-Binding Proteins in epicardial adipose tissue in patients with coronary artery disease and diabetes mellitus: preliminary study. Int J Med Sci 2017; 14:268-74.
6. Galavi H, Noorzehi N, Saravani R, Sargazi S, Mollashahee-Kohkan F, Shahraki H. Association study of SREBF-2 gene polymorphisms and the risk of type 2 diabetes in a sample of Iranian population. Gene 2018; 660:145-50.
7. Classification and diagnosis of diabetes: standards of medical care in diabetes - 2018. Diabetes Care 2018; 41:S13-s27.
8. Cole JB, Florez JC. Genetics of diabetes mellitus and diabetes complications. Nat Rev Nephrol 2020; 16:377-90.
9. Udler MS, McCarthy MI, Florez JC, Mahajan A. Genetic risk scores for diabetes diagnosis and precision medicine. Endocr Rev 2019; 40:1500-20.
10. Zhao L, Zheng YY, Chen Y, et al. Association of genetic polymorphisms of SelS with Type 2 diabetes in a Chinese population. Biosci Rep 2018; 38.
11. Kim TH, Baek JI, Hong JM, et al. Significant association of SREBP-2 genetic polymorphisms with avascular necrosis in the Korean population. BMC Med Genet 2008; 9:94.

LETTER TO THE EDITOR

Up-regulation of miR-934 serves as an independent prognostic factor for lung cancer and promotes proliferation, migration and invasion of non-small cell lung cancer cells

YB. Zhao[1], XY. Zhao[2], J. Jia[2], J. Liu[3], JL. Xu[4] and N. Li[1]

[1]Department of Oncology, Qingdao Central Hospital, Qingdao City, Shandong Province, China; [2]Department of Oncological Surgery, the Fourth People's Hospital of Zibo City, Zibo City, Shandong Province, China; [3]Department of Hepatology, Qingdao No. 6 People's Hospital, Qingdao City, Shandong Province, China; [4]Department of Cardiothoracic Surgery, Zhucheng People's Hospital, Weifang City, Shandong Province, China

Received December 9, 2020 – Accepted January 29, 2021

To the Editor,

Non-small cell lung cancer (NSCLC) is one of the most common malignant tumors in the world, and is the leading cause of cancer-related deaths. The American Cancer Society estimates that the incidence of NSCLC in 2012 was 125/100,000 men (0.125%) and 50/100,000 women (0.05%) (1). Currently, advanced imaging and cytology-based screening strategies have significantly improved the early diagnosis of NSCLC, and a variety of targeted drugs have been successfully used in clinical treatments, such as Gefitinib (2). The 5-year survival rate of NSCLC increased from 12% in 1975-1977 to 18% in 2005-2011 (1). However, the vast majority of NSCLC cases were diagnosed in the late stage, which is a key factor in the high mortality rate of the disease (3), therefore, it is urgent to find effective methods of NSCLC screening and clinical prognostic markers.

MicroRNAs (miRNAs) are small single-stranded RNA molecules composed of 18-23 nucleotides, which play the role of oncogenes or anti-oncogenes in the process of tumor formation, proliferation, angiogenesis, epithelial mesenchymal transition (EMT), apoptosis, invasion and metastasis. For example, miR-124 inhibits migration and invasion of lung cancer cells by inhibiting EMT (4). In recent years, miRNAs, as a biomarker for the diagnosis and prognosis of solid tumors, have become a hotspot in tumor research. For NSCLC, several reported biomarkers have been reported to predicate the prognosis of patients and regulate tumor progression. For example, miR-133a acts as a valuable independent prognostic biomarker, the high expression level of which indicates the better prognosis of patients (5).

miR-934 was identified as a dysregulated miRNA in NSCLC (6), and its abnormal expression in other cancers has been reported to play roles in the disease development of cancers, including ovarian cancer, pancreatic cancer, and bladder cancer (7-9). The present study aims to evaluate the expression and clinical relevance of miR-934 in NSCLC, and to review the biological regulation of miR-934 on NSCLC cells. The results indicate that miR-934 could be a prognostic biomarker and therapeutic target for NSCLC treatment.

MATERIALS AND METHODS

Clinical samples

The Ethics Research Committee of Zhucheng People's Hospital approved this study. All patients in the study

Key words: miR-934; non-small cell lung cancer; prognosis; progression

Corresponding Author:
Dr Jinlong Xu,
Department of Cardiothoracic Surgery,
Zhucheng People's Hospital, No. 59, Nanhuan Road,
Weifang City, Shandong Province, 262200, China
Tel./Fax: +86 0536 6357127
e-mail: xujl_longcheng@163.com

0393-974X (2021)
Copyright © by BIOLIFE, s.a.s.
This publication and/or article is for individual use only and may not be further reproduced without written permission from the copyright holder.
Unauthorized reproduction may result in financial and other penalties
DISCLOSURE: ALL AUTHORS REPORT NO CONFLICTS OF INTEREST RELEVANT TO THIS ARTICLE.

provided written informed consent. All tissue samples from NSCLC patients were treated and anonymized according to ethical and legal standards.

The inclusion criteria were as follows: a) prior to the study, the patients had not received any treatment procedures; b) the clinical records and histopathological diagnosis were well documented; c) all patients had not been diagnosed with other cancers; d) the histological diagnosis was assessed by two independent pathologists based on WHO classification. According to the inclusion criteria, a total of 144 NSCLC patients were included in this study.

Paired NSCLC and adjacent non-tumor tissue samples were collected at Qingdao Central Hospital from July 2008 to August 2012. All the tissues were frozen immediately after surgery and stored in liquid nitrogen until used. Patients were followed up for a period of 5 years, the end point of which was September 2017. During the follow-up period, the survival status of patients from diagnosis to the last follow-up was recorded, and the overall survival rate was measured. Gender, age, smoking status, tumor location, tumor size, differentiation, LN metastasis, TNM stage clinical data and pathological characteristics are shown in Table I.

Cell lines and transfection

The human NSCLC cell line H1299, NCI-H292, A549, NCI-H1650, and normal human bronchial epithelial cell line NHBE were obtained from the Type Culture Collection of the Chinese Academy of Sciences (Shanghai, China). The cells were cultured in RPMI-1640 (Hyclone, USA) medium containing 10% fetal bovine serum (FBS, Gibco, USA) with 37°C in a humidified atmosphere containing 5% CO_2. For *in vitro* studies, miR-934 mimic (5'-UGUCUACUACUGGAGACACUGG-3'), mimic negative control (NC, 5'-UUCUCCGAACGUGUCACGUU-3'), miR-934 inhibitor (5'-CCAGUGUCUCCAGUAGUAGACA), and inhibitor NC (5'-CAGUACUUUUGUGUAGUACAA-3')

Table I. *Correlation between miR-934 expression levels and clinical features in lung cancer patients*

Parameters	Cases No. (n = 144)	miR-934 expression		*P*
		Low (n = 65)	High (n = 79)	
Age (years)				
≤ 60	75	31	44	0.339
> 60	69	34	35	
Gender				
Female	71	30	41	0.493
Male	73	35	38	
Smoking Status				
Nonsmoker	71	29	42	0.307
Smoker	73	36	37	
Tumor location				
Central	74	30	44	0.254
Peripheral	70	35	35	
Tumor size				
< 3 cm	64	34	30	0.085
≥ 3 cm	80	31	49	
Differentiation				
High-moderate	65	24	41	0.072
Poor	79	41	38	
LN Metastasis				
No	88	48	40	0.004*
Yes	56	17	39	
TNM Stage				
I-II	91	49	42	0.006*
III-IV	53	16	37	

LN: lymph node

were transfected into NSCLC cells with transfection reagent Lipofectamine 2000 (Thermo fisher scientific, USA) to study the effect of miR-934 on the function of NSCLC cells.

RNA extraction and qRT-PCR analysis

Total RNA was extracted using Trizol reagent (Invitrogen Life Technologies, USA) according to the manufacturer's instructions. Reverse transcription kit (Thermo Fisher Scientific, USA) was used to timely reverse the extracted RNA into complementary cDNA, and qRT-PCR expression was performed using SYBR Green I Master Mix kit (Invitrogen, USA) in the ABI 7500 Real-time PCR system. In the qRT-PCR reactions, U6 was used as an internal reference, and the relative expression of RNA was calculated by the method of $2^{-\Delta\Delta Ct}$. Primer sequences used in this study were as follows: miR-934, Forward 5'-GCCTAGAAACATCCTCCCGG-3', Reverse 5'-AGGCCATGTGTCGTGGTCG-3'; U6 Forward 5'-GCTTCGGCAGCACATATACTAAAAT-3', Reverse 5'-CGCTTCAGAATTTGCGTGTCAT-3'. The PCR reaction conditions were: 95°C for 5 min, followed by 40 cycles of 95°C denaturation for 30 s, 50°C annealing for 30 s, and finally 72°C extension for 45 s.

Cell proliferation assay

For the cell proliferation assay, transfected cells were seeded in 96-well plates at a density of 1.5×10^3 cells/well, and their viability was detected at different times (0, 24, 48, and 72 hours). Before each test, 10 μl CCK-8 reagents were added, and then incubated for 2 h in an incubator to detect the change of light absorption value at 450 nm.

Cell migration and invasion assay

Changes in cell migration and invasion ability were verified by Transwell assay. 1×10^5 cells/well. Transfected cells were first added to matrigel-containing or matrigel-free Transwell chambers with medium contacting 1% FBS, and the culture medium containing 10% FBS was added to the lower chamber and placed in an incubator to continue the culture. After 24 hours, the matrigel, uninvaded, and immigrated cells in the upper chamber of Transwell were wiped off with cotton swabs, fixed by paraformaldehyde for 10 min, and stained with crystal violet for 20 min. The number of migrated and invaded cells was randomly selected in 5 fields under a microscope.

Dual-luciferase reporter assay

The CDK6-WT reporter vector was constructed by inserting the 3'UTR of CDK6 containing the binding sites of miR-934 into the dual-luciferase reporter vector pmirGLO (Promega, USA). On the other hand, the CDK6-MUT was also constructed by point mutations in the binding sites between miR-934 and CDK6 3'UTR. The A549 cells were then seeded in a 48-well plate and co-transfected with luciferase plasmids and miR-934 mimic, miR-934 inhibitor, or corresponding NCs. The luciferase activity levels were detected by the Dual-Luciferase Reporter Assay Kit (Promega, USA).

Statistical analysis

All statistical analyses were carried out using SPSS version 22.0 and GraphPad Prism 7.0. The relationship between clinical parameters and the expression of miR-934 were calculated using *chi*-square test. Student's *t*-test was used to evaluate the differences of miR-934 expression in NSCLC and its corresponding non-tumor lung tissues. The differences between multiple groups were evaluated by one-way ANOVA followed by the Tukey post hoc. Kaplan-Meier method was used to calculate the survival rate after tumor resection assessed by the log-rank test, and Cox proportional hazard model was used to analyze the hazard ratios (HRs) and 95% confidence interval (95% CI) of covariates. Results were considered statistically significant when $P < 0.05$.

RESULTS

Expression of miR-934 in NSCLC and its clinical significance

Normalized to U6 small nuclear RNA, the relative expression levels of miR-934 in NSCLC and normal tissues were calculated. As shown in Fig. 1A, the expression level of miR-934 in NSCLC tissues was significantly higher than that in the corresponding non-cancerous tissues ($P < 0.001$). Moreover, we also observed increased miR-934 expression in NSCLC cell lines H1299, NCL-H292, A549 and NCL-H1650 compared with NHBE cell lines ($P < 0.001$, Fig. 1B).

Using the mean value of miR-934 expression in all 144 NSCLC patients as a cutoff (2.265), the patients were divided into high miR-934 expression group (n =

79) including 37 females and 42 males, and low miR-934 expression group (n = 65) including 32 females and 33 males. The relationship between miR-934 expression level and multiple clinicopathological features of lung patients are shown in Table I. The frequent up-regulation of miR-934 in NSCLC tissues was found to be significantly correlated with lymph node metastasis ($P = 0.004$), and TNM state ($P = 0.006$).

To investigate the effect of high expression of miR-934 on the clinical prognosis of patients, the survival rate of patients in the high miR-934 expression group was compared with those in the low miR-934 expression group. From the results of Kaplan-Meier survival analysis, the overall survival of lung patients with high expression of miR-934 were significantly poorer (log rank $P = 0.004$, Fig. 2). In addition, multivariate analysis confirmed that miR-934 expression (HR = 2.715, 95% CI = 1.299-5.674, $P = 0.008$), lymph node metastasis (HR = 2.067, 95% CI = 1.045-4.088, $P = 0.037$), and TNM stage (HR = 2.340, 95% CI = 1.117-4.904, $P = 0.024$) were independent prognostic factors for NSCLC (Table II).

miR-934 regulated cell proliferation, migration, and invasion by targeting CDK6

In addition, to study the clinical significance of miR-934 in NSCLC, *in vitro* functional assays were also performed to further verify whether miR-934 is involved in the progression of NSCLC. A549 and H1299 of four NSCLC cells with the highest miR-934 expression were transfected with miR-934 mimic, mimic NC, miR-934 inhibitor, or inhibitor NC. As shown in Fig. 3A, the expression level of miR-934 in miR-934 mimic-transfected cells was significantly higher than that of controls. On the contrary, the expression level of miR-934 was significantly reduced after the transfection of miR-934 inhibitor ($P < 0.001$).

The results of CCK-8 assay demonstrated that transfection with miR-934 mimic increased the proliferation of A549 and H1299 cells, while the transfection of miR-934 inhibitor reduced the proliferation of these NSCLC cells ($P < 0.01$, $P < 0.001$, Fig. 3B). Furthermore, the Transwell assay verified the effect of miR-934 on the migration and invasion ability of NSCLC cells. As shown in Fig. 3 C and D, the overexpression of miR-934 could promote the ability of cell migration and invasion, whereas the knockdown of miR-934 suppressed the migration and invasion of A549 and H1299 cells, which again verified the correlation between the high expression of miR-934 and LN metastasis ($P < 0.01$, $P < 0.001$). These results indicated that overexpression miR-934 promoted the growth,

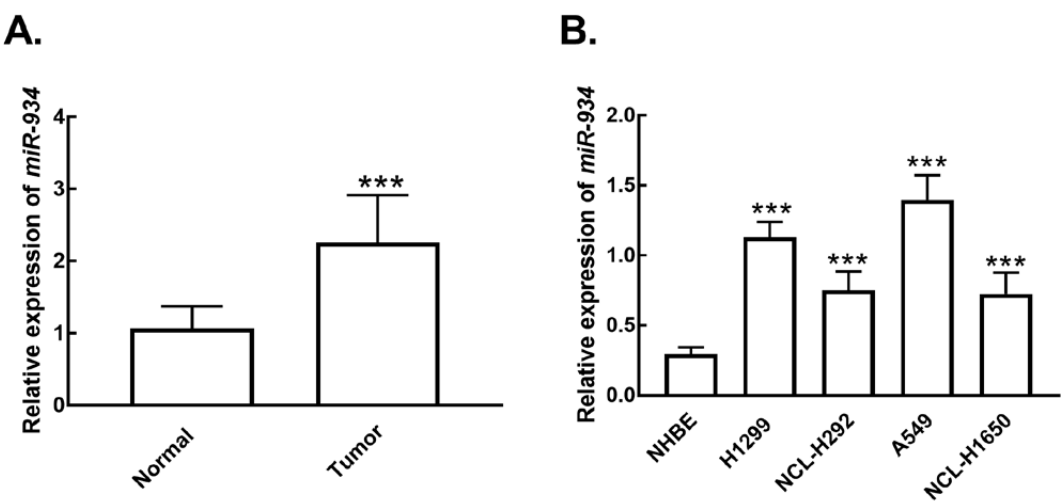

Fig. 1. *The expression of miR-934 was measured in tissues and cell lines by qRT-PCR.* ***A)*** *Compared with normal tissues, miR-934 expression was significantly increased in tumor tissues collected from the patients (***P < 0.001).* ***B)*** *Compared with normal bronchial epithelial cells, the expression level of miR-934 was significantly increased in lung cancer cells (***P < 0.001).*

Table II. *Multivariate Cox analysis of miR-934 and clinical parameters in relation to overall survival*

Characteristics	Multivariate analysis		
	HR	95% CI	*P*
miR-934	2.715	1.299-5.674	0.008
Age	1.283	0.628-2.622	0.494
Gender	1.123	0.580-2.171	0.731
Smoking Status	1.273	0.666-2.433	0.465
Tumor location	1.581	0.759-3.294	0.222
Tumor size	1.192	0.602-2.409	0.615
Differentiation	1.262	0.661-2.409	0.481
LN Metastasis	2.067	1.045-4.088	0.037
TNM Stage	2.340	1.117-4.904	0.024

LN: lymph node

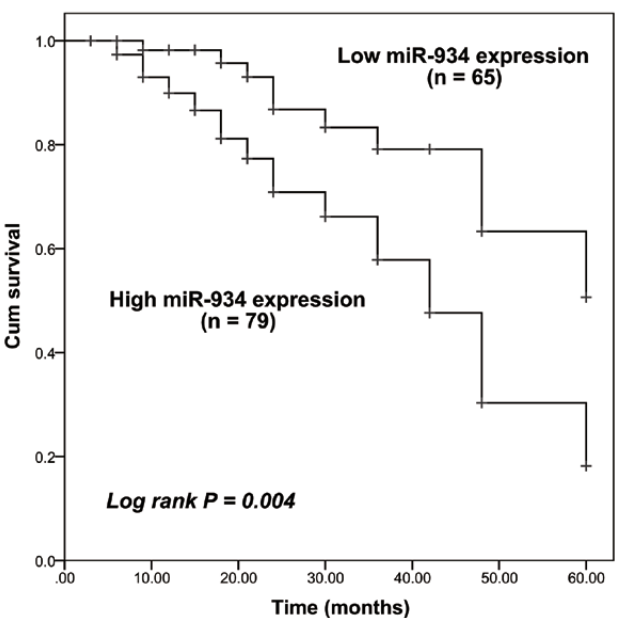

Fig. 2. *Kaplan-Meier survival curves for NSCLC patients based on miR-934 expression. Patients with high expression of miR-934 had poorer overall survival than those with low expression (log rank P = 0.004).*

migration, and invasion of NSCLC *in vitro*. CDK6 was predicted as the potential target of miR-934 with the binding site shown in Fig. 4A. Through the luciferase assay, it was found that the overexpression of miR-934 significantly inhibited the luciferase activity of CDK6 WT, which was enhanced by the knockdown of miR-934 ($P < 0.001$, Fig. 4B). Whereas the luciferase activity of CDK6 MUT was not affected by the changes in miR-934 expression.

DISCUSSION

Although the targeted therapy of NSCLC has made great achievements, the prognosis of NSCLC is still poor, as the occurrence is a complex process that may be affected by the environment and personal factors. Tumor development is a slow multistage process involving a wide range of molecular biological changes. An increasing number of abnormally expressed genes in the tissue and serum

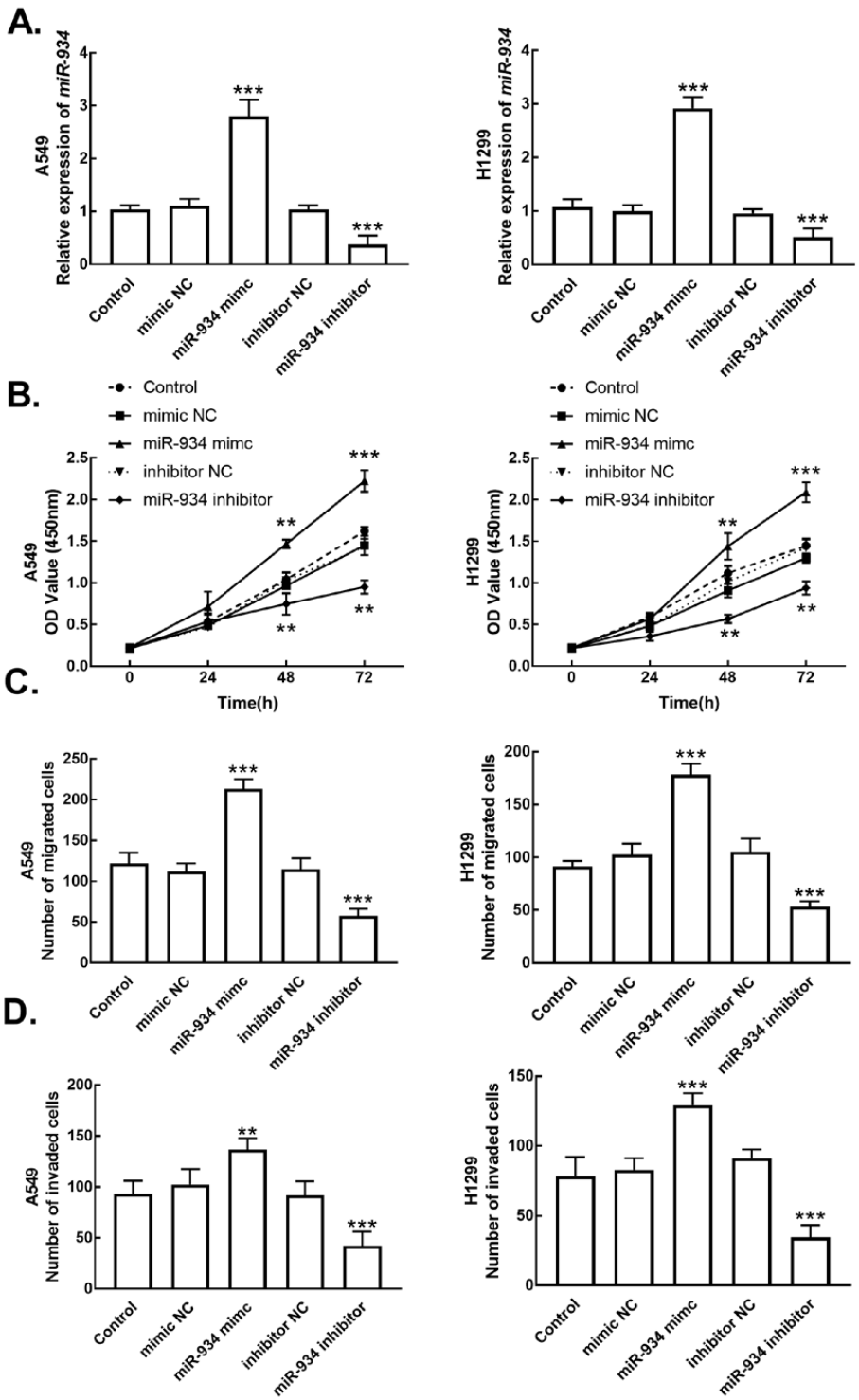

Fig. 3. *Effect of miR-934 on the function of NSCLC cells A549 and H1299.* ***A****) After the transfection of miR-934 mimic and inhibitor, the expression of miR-934 in cells was detected by qRT-PCR (***P < 0.001).* ***B****) NSCLC cell proliferation after transfecting with miR-934 mimic and inhibitor was detected by CCK-8 assay. miR-934 mimic could significantly promote cell proliferation of NSCLC, while miR-934 inhibitor reduced cell proliferation of NSCLC (**P < 0.01, ***P < 0.001).* ***C, D****) The migration and invasion ability of cells transfected with miR-934 mimic or inhibitor were analyzed by Transwell assay. miR-934 mimic significantly increased the ability of cells to migrate and invade, while miR-934 inhibitor weakened the ability of cells to migrate and invade (**P < 0.01, ***P < 0.001).*

of patients have been identified as tumor markers in various cancers.

In the present study, we verified the increased expression level of miR-934 in NSCLC, which is consistent with previous reports that miR-934, as an oncogene, was up-regulated in bladder cancer (9), ovarian cancer (7), and pancreatic cancer (8). It was also found that the high expression of miR-934 was significantly correlated with lymph node metastasis and TNM stage of NSCLC patients. In addition, the overall survival time of patients with high miR-934 expression was shorter than that of patients with low miR-934 expression. The expression levels of miR-934 can be used as an independent prognostic factor for patients with NSCLC. To the best of our knowledge, this is the first analysis of the expression and clinical significance of miR-934 in patients with NSCLC, and further demonstrates that miR-934 can be used as a biomarker for prognosis in patients with NSCLC. *In vitro* cell experiments revealed that the high expression of miR-934 could significantly promote the proliferation, migration, and invasion ability of NSCLC cells, indicating that miR-934 is involved in the progress of NSCLC as an oncogene. Previously, CDK was reported to be dysregulated in NSCLC and it could bind with miR-934 (10, 11). Here, CDK6 was demonstrated to be the direct target of miR-934 during its biological function in the progression of NSCLC.

Through a series of experiments, our study results provide the first convincing evidence that miR-934 expression level is increased in NSCLC tissue

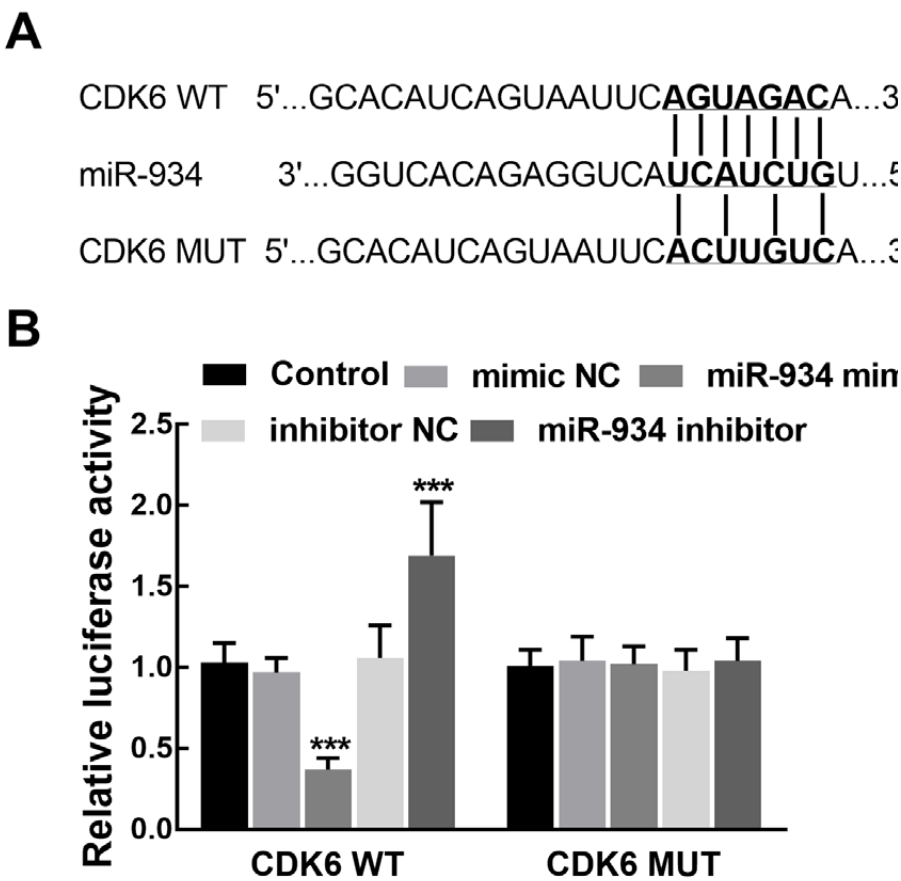

Fig. 4. *CDK6 was identified as the direct target of miR-934 in A549 cells.* ***A****) The binding sites between miR-934 and the 3'UTR of CDK6.* ***B****) The relative luciferase activity of CDK6 WT was inhibited by the overexpression of miR-934 and enhanced by the knockdown of miR- 934. While the luciferase activity of CDK6 MUT was not affected by the dysregulation of miR-934. (***P < 0.001).*

and cells, which has a good prognostic value and promotes the development of NSCLC by targeting CDK6, suggesting that miR-934 may be a useful prognostic marker of NSCLC.

REFERENCES

1. Siegel RL, Miller KD, Jemal A. Cancer statistics, 2016. CA: a cancer journal for clinicians 2016; 66:7-30.
2. Shaw AT, Yasothan U, Kirkpatrick P. Crizotinib. Nature Rev Drug Discovery 2011; 10:897-8.
3. Abu-Duhier FM, Javid J, Sughayer MA, Mir R, Albalawi T, Alauddin MS. Clinical significance of circulatory miRNA-21 as an efficient non-invasive biomarker for the screening of lung cancer patients. APJCP 2018; 19:2607-11.
4. Li Z, Wang X, Li W, Wu L, Chang L, Chen H. miRNA-124 modulates lung carcinoma cell migration and invasion. Int J Clin Pharmacol Ther 2016; 54:603-12.
5. Yang ZQ, Wu CA, Cheng YX. Prognostic value of microRNA-133a expression and its clinicopathologic significance in non-small cell lung cancer: a comprehensive study based on meta-analysis and the TCGA database. Oncol Res Treat 2018; 41:762-8.
6. Sun L, Chen Y, Su Q, Tang X, Liang Y, Che G, Luo F. Increased Plasma miRNA-30a as a Biomarker for Non-Small Cell Lung Cancer. Med Sci Monit 2016; 22:647-55.
7. Hu Y, Zhang Q, Cui J, et al. Oncogene miR-934 promotes ovarian cancer cell proliferation and inhibits cell apoptosis through targeting BRMS1L. Eur Rev Med Pharmacol Sci 2019; 23:5595-602.
8. Jin Y, Weng Y, Wang Y, et al. miR-934 as a prognostic marker facilitates cell proliferation and migration of pancreatic tumor by targeting PROX1. Onco Targets Ther 2020; 13:3389-99.
9. Yan H, Ren S, Lin Q, et al. Inhibition of UBE2N-dependent CDK6 protein degradation by miR-934 promotes human bladder cancer cell growth. FASEB 2019; 33:12112-23.
10. Liu L, Chen Y, Li Q, Duan P. lncRNA HNF1A-AS1 modulates non-small cell lung cancer progression by targeting miR-149-5p/Cdk6. J Cell Biochem 2019; 120:18736-50.
11. Geng B, Liang M, Qin L, Zhao W, Wang H, Wang L, et al. An TRIM59-CDK6 axis regulates growth and metastasis of lung cancer. J Cell Mol Med 2019; 23:1458-69.

LETTER TO THE EDITOR

Long non-coding RNA FGD5-AS1 promotes cell viability and metastasis in osteosarcoma by regulating miR-520c-3p

L-Z. Sun[1], Y-Z. Jiang[2], S-X. Luan[3], Y-L. Shi[1] and Q. Wang[2]

[1]Department of Orthopedics, Weifang People's Hospital, Weifang, Shandong Province, P.R. China;
[2]Department of Orthopedics, Hanting People's Hospital, Weifang, Shandong Province, P.R. China;
[3]Reproductive Medicine Centre, Weifang People's Hospital, Weifang, Shandong Province, P.R. China

Received November 3, 2020 – Accepted February 4, 2021

To the Editor,

Osteosarcoma (OS) is a common malignant bone tumor that usually occurs in children and adolescents. Lung metastasis is one of the characteristics of OS. Cell metastasis usually leads to poor prognosis in OS patients . In recent years, with the advancement of medical technology, the prognosis of OS patients has improved, and 5-year survival rate has reached about 70% . Nevertheless, the patients still have many adverse reactions after receiving treatment. Chemotherapy may cause organ damage, while surgical treatment may cause limb damage . No matter which treatment method is adopted, it will bring inconvenience to the future life of OS patients. It is therefore of great significance to explore new gene therapy methods to relieve the suffering and improve the prognosis.

In the past few years, many studies have shown that long non-coding RNAs (lncRNAs) are RNAs at the length of more than 200 nucleotides. Previous studies have shown that lncRNA FGD5-AS1 plays important roles in malignant tumors. For example, lncRNA FGD5-AS1 promoted the development of glioblastoma by regulating miR-129-5p/HNRNPK axis to activate Wnt/β-catenin signaling . Nevertheless, the regulatory mechanism of lncRNA FGD5-AS1 is still unknown in OS.

It has been shown that lncRNA FGD5-AS1 participates in tumorigenesis through sponging microRNAs (miRNAs). In this study, miR-520c-3p is predicted to have a binding site with lncRNA FGD5-AS1. Therefore, this study aims to explore the molecular mechanisms of FGD5-AS1 and miR-520c-3p in OS. This research will expand our understanding of OS epigenetic regulation.

MATERIALS AND METHODS

Experimental OS specimens and normal specimens were obtained from 102 OS patients who had not undergone preoperative chemotherapy or radiotherapy in Weifang People's Hospital from 2016 to 2019 (55 males and 47 females; mean age 21 years, range from 14 to 36 years; median follow-up time, 28 months). Written informed consents were obtained from the patients or their legal guardians. The patients had undergone surgical resection and were confirmed by postoperative pathological examination. These tissues were frozen in liquid nitrogen and stored at −80 C. This study was approved by the Institutional Ethics Committee of Weifang People's Hospital according to the Declaration of Helsinki.

Cell culture and transfection

Human osteoblasts hFOB1.19 and OS cell line U2OS were purchased from ATCC (Manassas, VA, USA).

Key words: FGD5-AS1; osteosarcoma; miR-520c-3p; cell viability; migration; invasion

Corresponding Author:
Dr Suxian Luan,
Reproductive Medicine Centre, Weifang People's Hospital,
No.151 Guangwen Street, Kuiwen District, Weifang,
261041, Shandong Province, P.R. China
Tel.: +86 0537-963360
e-mail: huafufan4640805@163.com

0393-974X (2021)
Copyright © by BIOLIFE, s.a.s.
This publication and/or article is for individual use only and may not be further reproduced without written permission from the copyright holder.
Unauthorized reproduction may result in financial and other penalties
DISCLOSURE: ALL AUTHORS REPORT NO CONFLICTS OF INTEREST RELEVANT TO THIS ARTICLE.

The growth conditions of U2OS and hFOB1.19 cells were 5% CO_2, 37°C and culture medium (90%RPMI-1640+10%FBS). MiR-520-3p mimic and inhibitor, FGD5-AS1 siRNA and vector (RiboBio, Guangzhou, China) were transfected into U2OS cells, respectively.

RT-qPCR

Total RNA from OS tissues and cells was extracted by TRIzol (Sigma, USA). The purity and concentration of the RNA was evaluated based on the OD at 260 nm and the OD 260/230 and 260/280 ratios using MaestroNano®, a micro-volume spectrophotometer (Maestrogen, Las Vegas, NV, USA). The recommended parameters of RNA quality for cDNA synthesis are OD 260/230 >1.8 and OD 260/280 ratio in the range of 1.8-2.0. The cDNA solution was synthesized using a miScript Reverse Transcription kit (Qiagen, Germany). RT-qPCR assay was performed using the miScript SYBR®Green PCR kit (Qiagen, Germany) according to the manufacturer's instructions. FGD5-AS1 and miR-520c-3p were normalized to U6 or GAPDH internal reference using the $2^{-\ CT}$ method. The primers used were: FGD5-AS1 forward, 5′-GAA GGG CCG AAG AGC TCA AT-3′ and reverse, 5′-GGC TCG CAA AGT GTC TGT TG-3′; miR-520c-3p forward: 5′-GAA GCA CTT TCT GTT GTC TGAA-3′and reverse, 5′-TCA AAC GGT AAC CCT CTA AAA GGA-3′; U6-forward: 5′-GCT TCG GCA GCA CAT ATA CTA AAA T-3′and reverse, 5′-CGC TTC ACG AAT TTG CGT GTC AT-3′; GAPDH forward: 5′-AGA AGG CTG GGG CTC ATT TG-3′, and reverse, 5′-AGG GGC CAT CCA CAG TCT TC-3′.

CCK-8 assay

The transfected U2OS cells were cultured in 96-well plates for 24 h (at 37°C, 5% CO_2). Next, the transfected U2OS (2×10^4/well) cells were incubated for 24, 48, 72 and 96 h, respectively. The transfected U2OS cells were then incubated with CCK-8 solution (Dojindo, Kumamoto, Japan) for 4 h. The absorbance at 450 nm was observed with a spectrophotometer (Molecular Devices).

Transwell assay

Transwell chambers (8 μm pore size; Millipore) were used to evaluate cell migration and invasion in 24-well plates. Transfected U2OS cells (2×10^4 cells/well) without serum were placed on the uncoated membrane of the upper chamber, and the lower chamber was filled with 10% FBS. For invasion assay, the transfected U2OS cells were put in the upper chamber with 100 μl Matrigel (dilution, 1:8 in RPMI-1640 medium). Cells were incubated at 37°C for 24 h. Finally, the cells on the lower surface of the membrane were fixed with 4% paraformaldehyde and stained with 1% crystal violet (Solarbio) for 30 min. The moving cells were examined under a light microscope (Olympus Corporation, Tokyo, Japan).

Luciferase reporter assay

The 3'-UTR of wild-type or mutant FGD5-AS1 was inserted into the pcDNA3.1 plasmid vector (Promega, Madison, USA). Next, the luciferase vector and miR-520c-3p mimics were transfected into U2OS cells and incubated for 20 min at room temperature; 48 h after transfection, the medium was discarded and washed once with PBS. Finally, the luciferase activity was measured using a dual luciferase assay system (Promega, USA).

Statistical analysis

All experiments were repeated in triplicate. The data are expressed as mean ± SD and analyzed by SPSS 18.0 or GraphPad Prism 6. Statistical differences were performed by Student's *t*-test (two groups) or ANOVA followed by Tukey's test (three groups). The Kaplan-Meier method was used to assess the overall survival rate, and the log-rank test was used to compare the difference between the curves. The correlation between miR-520c-3p and FGD5-AS1 expression was examined by Pearson's correlation analysis. $P < 0.05$ was considered a statistically significant difference.

RESULTS

Expression of FGD5-AS1 is increased in OS tissues

The expression of FGD5-AS1 in OS tissues and cells was measured by RT-qPCR. Compared with normal tissues, upregulation of FGD5-AS1 was detected in OS tissues (n=102, $P < 0.01$, Fig. 1A). Similarly, FGD5-AS1 expression in U2OS cells was also upregulated compared with hFOB1.19 cells ($P < 0.01$, Fig. 1B). In addition, the relationship between FGD5-AS1 and the 5-year overall survival rate of OS patients was analyzed. The high expression of FGD5-AS1 was found related to the shorter overall survival ($P = 0.0027$, Fig. 1C). These findings indicate that FGD5-AS1 is involved in the pathogenesis of OS.

FGD5-AS1 promotes cell viability, migration and invasion in OS

FGD5-AS1 siRNA or vector was transfected into U2OS cells to explore the function of FGD5-AS1 in OS. RT-qPCR showed that FGD5-AS1 vector enhanced its expression, while FGD5-AS1 siRNA reduced its expression in U2OS cells (P < 0.01, Fig. 1D). Functionally, it was found that the upregulation of FGD5-AS1 promoted U2OS cell proliferation. Downregulation of FGD5-AS1 inhibited cell proliferation in U2OS cells (P < 0.05 or 0.01, Fig. 1E). Transwell assay showed that overexpression of FGD5-

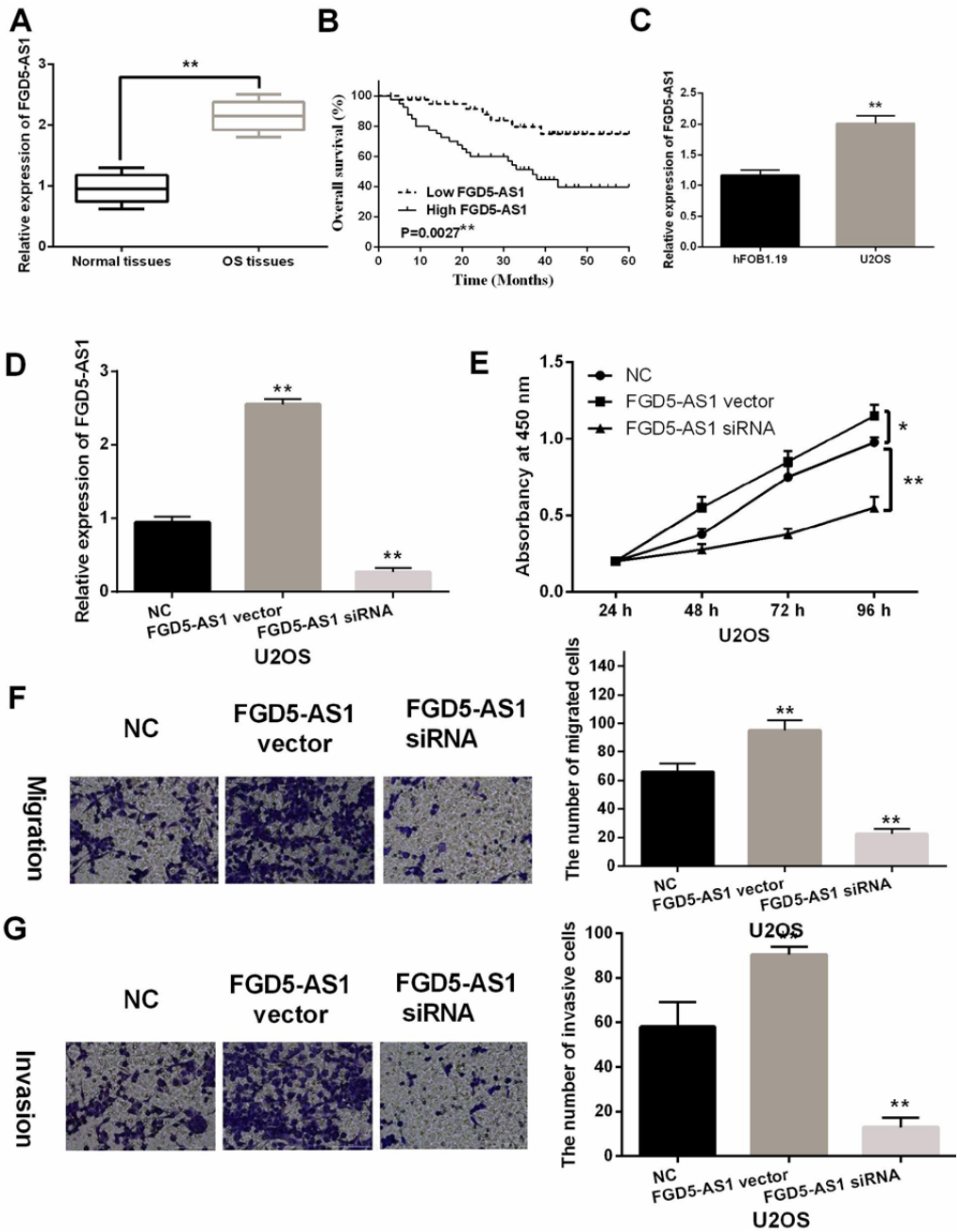

Fig. 1. *Upregulation of FGD5-AS1 promotes cell viability, migration and invasion in OS.* ***A)*** *FGD5-AS1 expressions in OS tissues (n=102).* ***B)*** *FGD5-AS1 expressions in U2OS and hFOB1.19 cells.* ***C)*** *High FGD5-AS1 expression was correlated with shorter overall survival in OS patients.* ***D)*** *FGD5-AS1 expression in U2OS cells with FGD5-AS1 siRNA or vector* ***E-G)*** *Cell proliferation, migration and invasion in U2OS cells with FGD5-AS1 siRNA or vector (200X). * P <0.05, ** P <0.01.*

AS1 promoted cell migration in U2OS cells. In contrast, knockdown of FGD5-AS1 inhibited cell migration ($P < 0.01$, Fig. 1F). In addition, overexpression of FGD5-AS1 promoted cell invasion, while downregulation of FGD5-AS1 inhibited cell invasion in U2OS cells ($P < 0.01$, Fig. 1G). In summary, FGD5-AS1 participates in the development of OS by promoting cell viability, migration and invasion.

FGD5-AS1 directly interacts with miR-520c-3p

StarBase (http://starbase.sysu.edu.cn/index.php) predicts that FGD5-AS1 has a binding site for miR-520c-3p (Fig. 2A). To verify this prediction, we designed a luciferase reporter assay. We found that miR-520c-3p mimics reduced the luciferase activity of wild-type FGD5-AS1, but had no effect on the mutant FGD5-AS1 ($P < 0.01$, Fig. 2B). It was also found that FGD5-AS1 expression was negatively correlated with miR-520c-3p expression in OS tissues ($P < 0.0001$, $R^2=0.6579$, Fig. 2C). In addition, the effect of FGD5-AS1 on the expression of miR-520c-3p in U2OS cells was investigated, and found that miR-520c-3p expression was reduced by upregulation of FGD5-AS1, but increased by the downregulation of FGD5-AS1 ($P < 0.01$, Fig. 2D). At the same time, FGD5-AS1 expression was also reduced by miR-

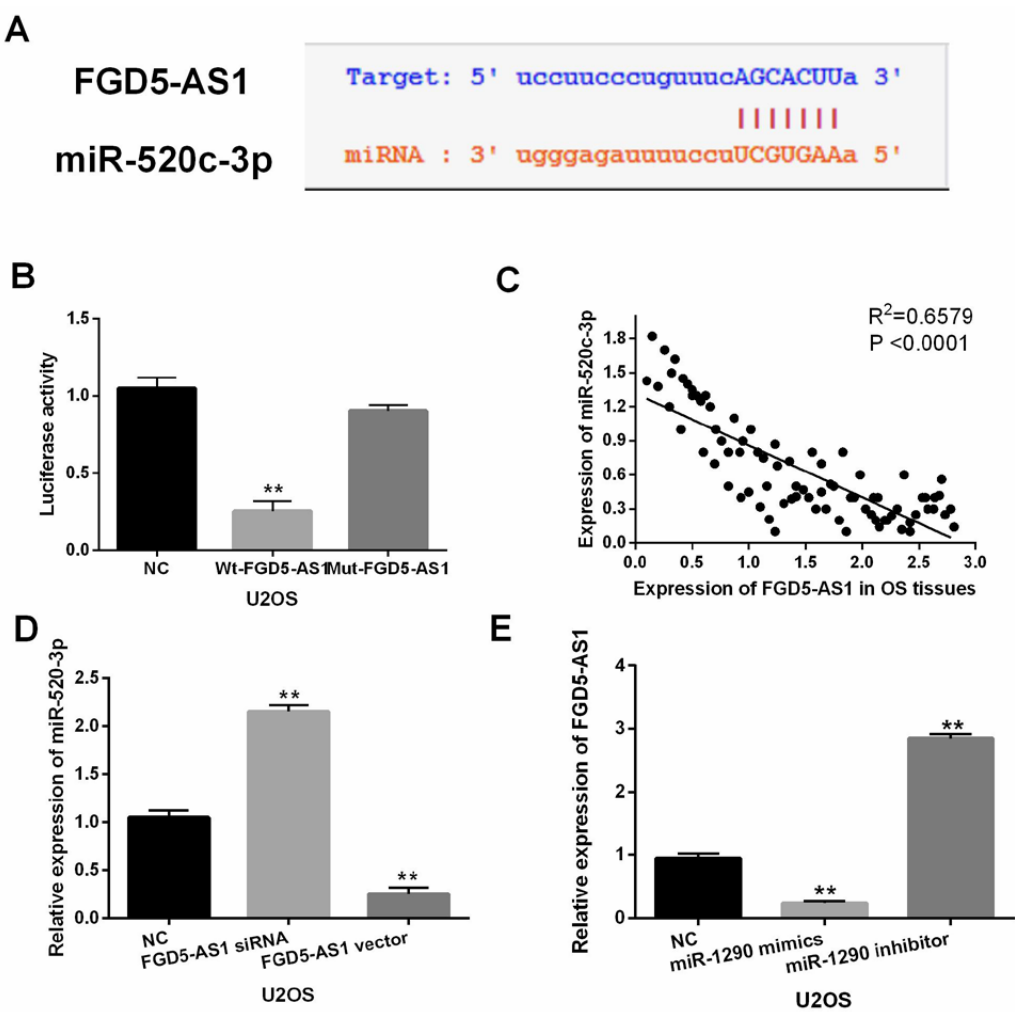

Fig. 2. *FGD5-AS1 directly interacts with miR-520c-3p.* ***A****) The binding sites between FGD5-AS1 and miR-520c-3p.* ***B****) Luciferase reporter assay.* ***C****) A negative correlation between FGD5-AS1 and miR-520c-3p was identified in OS tissues.* ***D****) MiR-520c-3p expression in U2OS cells with FGD5-AS1 siRNA or vector.* ***E****) FGD5-AS1 expression in U2OS cells with miR-520c-3p mimics or inhibitor ** P <0.01*

520c-3p mimics and promoted by miR-520c-3p inhibitor in U2OS cells (P < 0.01, Fig. 2E). The results indicate that FGD5-AS1 directly targets miR-520c-3p and negatively regulates its expression in OS.

Downregulation of miR-520c-3p promotes cell viability, migration and invasion in OS

The expression of miR-520c-3p was measured in OS tissues and cell lines. Downregulation of miR-

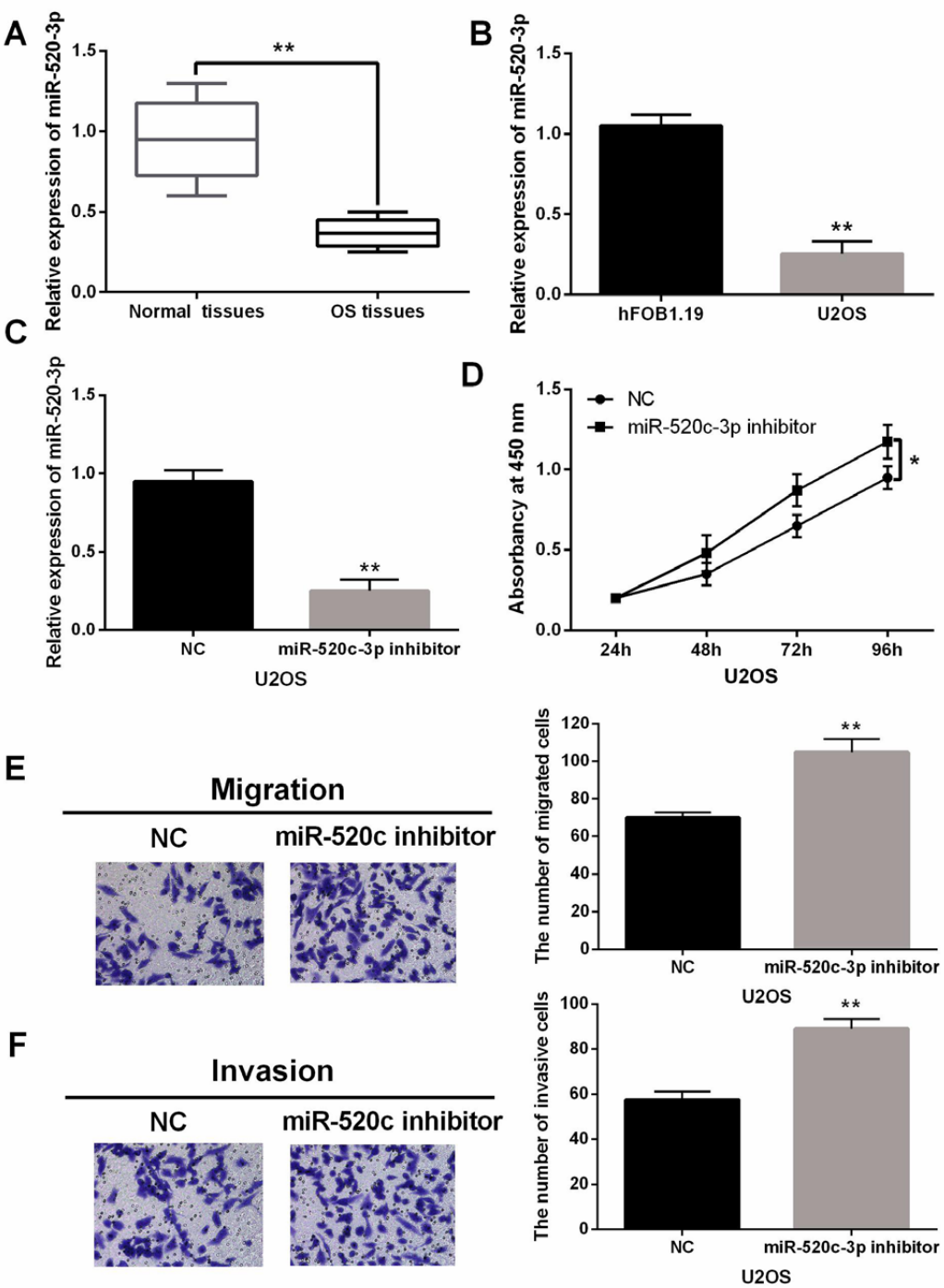

Fig. 3. *Downregulation of miR-520c-3p promotes cell viability, migration and invasion in OS.* ***A****) MiR-520c-3p expressions in OS tissues (n=102) and normal tissues.* ***B****) MiR-520c-3p expressions in U2OS and hFOB1.19 cells.* ***C****) MiR-520c-3p expression in U2OS cells with its inhibitor.* ***D-F****) Cell proliferation, migration and invasion U2OS cells with miR-520c-3p inhibitor (200X). * P <0.05, ** P <0.01*

520c-3p was found in OS tissues and U2OS cells (n=102, P<0.01, Fig. 3 A, B). In order to investigate whether miR-520c-3p is involved in the progression of OS, miR-520c-3p inhibitors were transfected into U2OS cells. RT-qPCR showed that the expression of miR-520c-3p was reduced by its inhibitor (P<0.01, Fig. 3C). In addition, knockdown of miR-520c-3p promoted cell proliferation in U2OS cells (P<0.05, Fig. 3D). Similarly, downregulation of miR-520c-3p promoted U2OS cell migration (P<0.01, Fig. 3E). In addition, miR-520c-3p inhibitor also promoted cell invasion in U2OS cells (P< 0.01, Fig. 3F). Therefore, downregulation of miR-520c-3p promotes cell viability, migration and invasion in OS.

FGD5-AS1 is involved in OS progression through regulating miR-520c-3p

To explore the interaction between FGD5-AS1 and miR-520c-3p, miR-520c-3p mimics were transfected into U2OS cells with FGD5-AS1 vector. It was found that the decreased expression of miR-520c-3p induced by the FGD5-AS1 vector was restored by miR-520c-3p mimics (Fig. 4A). Functionally, overexpression of miR-520c-3p weakened the promoting effect of FGD5-AS1 on cell proliferation in U2OS cells (P < 0.01, Fig. 4B). Consistently, the promotion of cell migration and invasion induced by upregulation of FGD5-AS1 was also impaired by miR-520c-3p overexpression

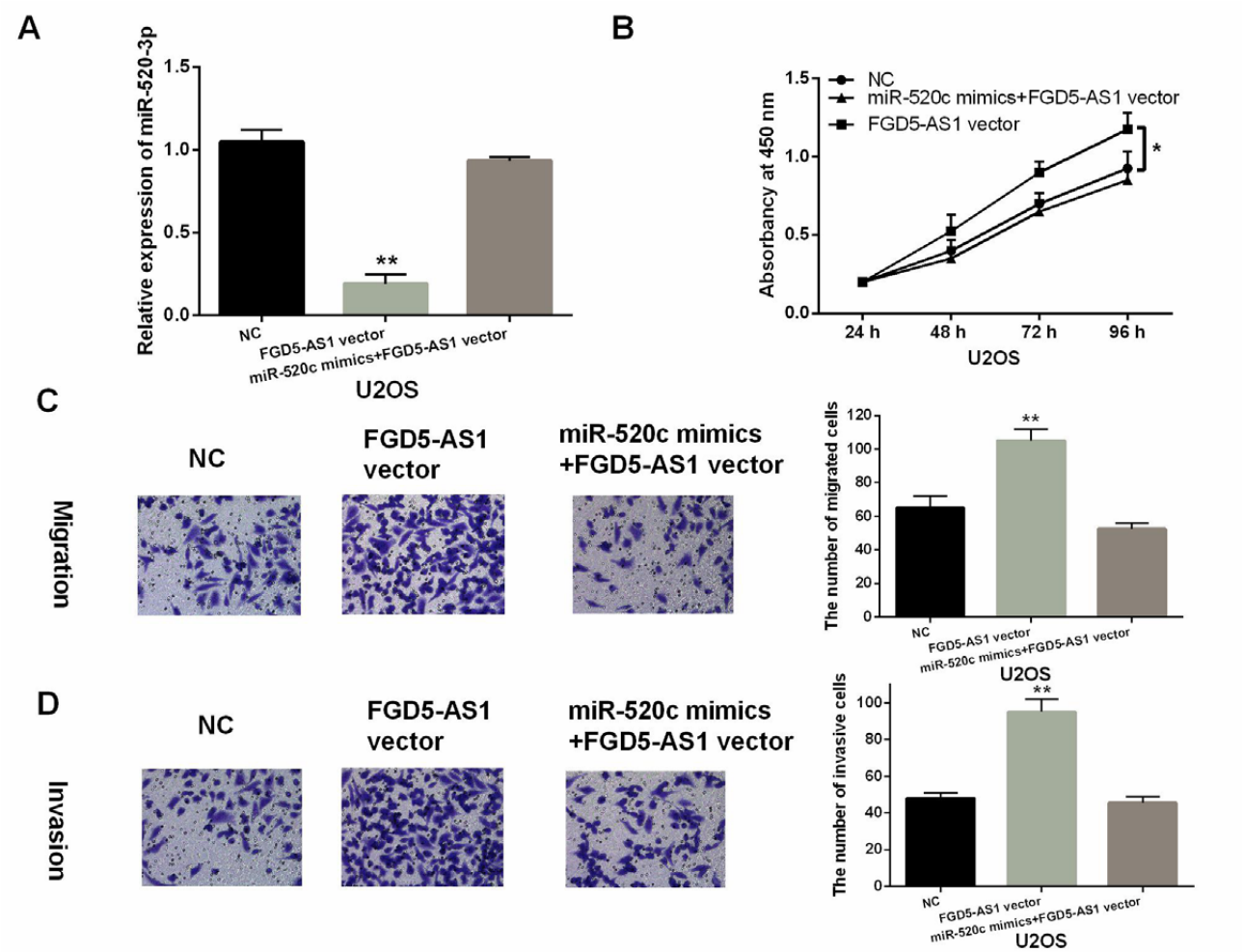

Fig. 4. *FGD5-AS1 is involved in OS progression through regulating miR-520c-3p.* ***A)*** *MiR-520c-3p expression in U2OS cells with FGD5-AS1 vector and miR-520c-3p mimics.* ***B-D)*** *Cell proliferation, migration and invasion in U2OS cells with FGD5-AS1 vector and miR-520c-3p mimics (200X). ** P<0.01*

in U2OS cells (P < 0.01, Fig. 4 C, D). In general, overexpression of miR-520c-3p attenuated the promoting effect of FGD5-AS1 on the proliferation, migration and invasion of OS cells.

DISCUSSION

Recently, the upregulation of FGD5-AS1 has been detected in non-small cell lung cancer and oral cancer . Functionally, lncRNA FGD5-AS1 acted as a competing endogenous RNA on miR-383 to enhance the malignant characteristics of esophageal squamous cell carcinoma by increasing SP1 expression . Here, we found that lncRNA FGD5-AS1 was upregulated in OS tissues and cells. In addition, the high expression of lncRNA FGD5-AS1 was related to the poor prognosis of OS patients. Functionally, upregulation of FGD5-AS1 promoted cell proliferation, migration and invasion in OS. Our results are consistent with previous studies. In addition, we also found that lncRNA FGD5-AS1 plays a carcinogenic effect in OS by regulating miR-520c-3p expression, and miR-520c-3p was downregulated and acted as a tumor suppressor in OS. More importantly, overexpression of miR-520c-3p weakened the carcinogenic effect of lncRNA FGD5-AS1 in the progression of OS.

Similar to this study, the downregulation and anti-tumor effects of miR-520c-3p have been found in acute myeloid leukemia and hepatocellular carcinoma . In particular, lncRNA HOXA-AS2 has been found to promote cell migration and invasion by acting as a ceRNA of miR-520c-3p in OS , indicating that miR-520c-3p inhibits cell migration and invasion in OS. In conclusion, upregulation of FGD5-AS1 promotes cell viability, migration and invasion in OS by downregulating miR-520c-3p. However, this study still has some shortcomings, such as the small number of samples and lack of *in vivo* experiments.

REFERENCES

1. Geller DS, Gorlick R. Osteosarcoma: a review of diagnosis, management, and treatment strategies. Clin Adv Hematol Oncol 2010; 8:705-18.
2. Clark JC, Dass CR, Choong PF. A review of clinical and molecular prognostic factors in osteosarcoma. J Cancer Res Clin Oncol 2008; 134:281-97.
3. Bielack SS, Hecker-Nolting S, Blattmann C, Kager L. Advances in the management of osteosarcoma. F1000Res 2016; 5:2767.
4. Wu L, Zhu X, Song Z, Guo M, Liang J, Yan D. FGD5-AS1 facilitates glioblastoma progression by activation of Wnt/beta-catenin signaling via regulating miR-129-5p/HNRNPK axis. Life Sci 2020; 117998.
5. Fu J, Cai H, Wu Y, Fang S, Wang D. Elevation of FGD5-AS1 contributes to cell progression by improving cisplatin resistance against non-small cell lung cancer cells through regulating miR-140-5p/WEE1 axis. Gene 2020; 755:144886.
6. Liu L, Zhan Y, Huang Y, Huang L. LncRNA FGD5-AS1 can be predicted as therapeutic target in oral cancer. J Oral Pathol Med 2020; 49:243-52.
7. Gao J, Zhang Z, Su H, Zong L, Li Y. Long Noncoding RNA FGD5-AS1 Acts as a competing endogenous RNA on microRNA-383 to enhance the malignant characteristics of esophageal squamous cell carcinoma by increasing SP1 expression. Cancer Manag Res 2020; 12:2265-78.
8. Dong X, Fang Z, Yu M, et al. Knockdown of long noncoding RNA HOXA-AS2 suppresses chemoresistance of acute myeloid leukemia via the miR-520c-3p/S100A4 axis. Cell Physiol Biochem 2018; 51:886-96.
9. Miao HL, Lei CJ, Qiu ZD, Liu ZK, Li R, Bao ST, Li MY. MicroRNA-520c-3p inhibits hepatocellular carcinoma cell proliferation and invasion through induction of cell apoptosis by targeting glypican-3. Hepatol Res 2014; 44:338-48.
10. Wang Y, Zhang R, Cheng G, Xu R, Han X. Long non-coding RNA HOXA-AS2 promotes migration and invasion by acting as a ceRNA of miR-520c-3p in osteosarcoma cells. Cell Cycle 2018; 17:1637-48.

LETTER TO THE EDITOR

Color doppler flow imaging evaluates the influence on subclavian artery steal caused by vertebral artery hypoplasia

Q.Q. Shao[1,2*], T. Zhao[2*], J.H. Ren[2], B. Wang[1] and H.J. Sun[1]

[1]Department of Medical Ultrasound, Shandong Qianfoshan Hospital, Cheeloo College of Medicine, Shandong University, Jinan, Shandong, China; [2]Department of Medical Ultrasound, Linyi People's Hospital, Linyi, Shandong, China

Received November 17, 2020 – Accepted February 4, 2021

[*]These Authors contributed equally to this work

To the Editor,

Posterior circulation ischemia (PCI) is defined as transient ischemic attack (TIA) or ischemic stroke caused by vertebrobasilar artery diseases (1). It has been documented that the incidence and total mortality of ischemic stroke resulting from PCI are estimated to be 14% and 21%, respectively (2). Subclavian artery steal (SAS) caused by subclavian artery (SA) stenosis is a major cause for PCI. SAS refers to the occurrence of morphological changes of vertebral artery (VA) flow spectrum and partial or complete reverse of blood flow direction when SA has a significant stenosis or occlusion at the proximal segment of VA opening that produces blood flow reversal of ipsilateral VA into SA owing to siphoning (3). Early detection of SA stenosis and identification of stenosis severity are crucial for clinical intervention and treatment. Furthermore, Color Doppler Flow Imaging (CDFI) is an important non-invasive technique for screening SA stenosis. However, there is no relevant study to clarify the specific criteria for identifying the severity of SA stenosis. Only Hua et al. (4) proposed the diagnostic criteria for severe SA stenosis. Moreover, it has been reported that the severity of SA stenosis can be indirectly reflected by the morphological changes of VA flow spectrum and the degree of blood flow reversal (5, 6). In addition, prior studies have demonstrated that the degree of steal may be aggravated by the increase of the severity of SA stenosis, accompanied by changes in the type of steal (7, 8). However, the premise of this conclusion is the patency of steal access. In the case of destroyed patency of blood vessels in steal access (e.g., VA stenosis, occlusion), the severity of SA stenosis may be inconsistent with the type of steal (9). In this case, the error of this method shall be taken into consideration when evaluating the severity of SA stenosis according to the degree of SAS. In the present study, with 155 cases of severe stenosis of unilateral SA [including 52 cases with VA dysplasia (VAH)] a retrospective analysis was conducted to analyze the impact of VAH on the degree of SAS.

MATERIALS AND METHODS

Subjects

A total of 5,026 patients who had undergone carotid ultrasound in Linyi People's Hospital of Linyi from January 2016 to August 2019 were retrospectively reviewed. Among these patients, 207 were severe

Key words: color doppler flow imaging; subclavian steal imaging; vertebral artery dysplasia

Corresponding Author:
Hongjun Sun, Ph.D.,
Department of Medical Ultrasound,
Shandong Provincial Qianfoshan Hospital,
Shandong University, No. 16766 Jingshi Road,
Lixia District, Jinan250014, Shandong, China
e-mail: hy8v5l@163.com

0393-974X (2021)
Copyright © by BIOLIFE, s.a.s.
This publication and/or article is for individual use only and may not be further reproduced without written permission from the copyright holder.
Unauthorized reproduction may result in financial and other penalties
DISCLOSURE: ALL AUTHORS REPORT NO CONFLICTS OF INTEREST RELEVANT TO THIS ARTICLE.

unilateral SA stenosis, and were all diagnosed by ultrasound and digital subtraction angiography (DSA). The exclusion criteria were: quality of the image does not accord with the diagnostic criteria (15 cases); patients with severe SA stenosis caused by nonatherosclerotic lesions, such as Takayasu's arteritis, trauma or radiation injury to the neck (6 cases); patients with severe stenosis or occlusion of bilateral subclavian artery (3 cases); patients with VA stenosis diagnosed by ultrasound or DSA (12 cases); patients with severe stenosis in the internal or common carotid artery (16 cases). A total of 155 patients with severe stenosis of unilateral SA were included in the study, including 99 males and 56 females, with the average age of 66.3±10.9 years, ranging from 35-88 years. There were 52 cases of VAH combined with severe stenosis of unilateral SA, including 41 cases and 11 cases of severe stenosis of unilateral SA with ipsilateral and contralateral VAH, respectively. All patients provided signed informed consent voluntarily prior to the study, which was approved by the ethics committee of our hospital.

Digital subtraction angiography

Whole-brain angiography was performed by using Plate angiography system (Siemens Neurostar Plus/ T.O.P, Erlangen, Germany). Imaging was performed from the lateral, posterior-anterior and oblique directions. According to the North American Symptomatic Carotid Endarterectomy Trial method (10), the lumen narrowing rate of SAS = (1- [residual diameter of stenosis segment/ original diameter of the segment distal to stenosis] ×100%) was calculated. In cases with poststenotic dilation, the relative normal diameter distal to the poststenotic dilation was considered to be the original diameter; 70-99% lumen narrowing was defined as severe stenosis. The examination results from DSA and CDFI were double-blinded.

Ultrasonography

Philips IE33 and EPIQ5 color doppler ultrasound diagnostic instruments were used. The combination of 5-12MHz linear array probe and 3-5MHz convex array probe was applied. The patient lay supine on the examination bed with the head tilted back, fully exposing the front of the neck. First, the course of VA and SA, with or without plaque and stenosis of lumen was observed in 2-D mode, and the inner diameter of bilateral VA was measured in V2 segment. The blood flow of bilateral vertebral arteries and the initial SA were shown by CDFI. Pulsed doppler flow imaging was then used to measure the blood flow spectra of bilateral vertebral arteries, the initial stenosis and the distal stenosis of the SA (measuring the blood flow velocity at the end of systole and the end of diastole in both locations). When measuring velocity, the angle between ultrasound beam and blood flow was set at ≤60°.

Evaluation criteria

The severity of stenosis of carotid artery and VA systems was judged according to Guidelines for Vascular Ultrasound Examination of Stroke in China (11).

According to previous reports, the diagnostic criteria for severe SA stenosis were: PSV≥343 cm/s; EDV≥60 cm/s; PSV at the stenotic segment/PSV at the segment distal >4 (12).While the type of steal was determined by the change of blood flow spectrum in V2 segment of VA: Occult steal: normal direction of blood flow, mid-contraction notch; Partial steal: Blood flow reversal in systole with no abnormality in diastole; Complete steal: Blood flow reversal during the whole cardiac cycle

VAH was defined with the diameter of unilateral VA ≤2.5mm or <50% of the contralateral VA (13).

Statistical analysis

SPSS version 23.0 was used for statistical analysis. Ages were compared by using the independent *t*-test, and other general conditions of the patients were compared by χ^2. χ^2 was also used to compare SAS types between the VAH group and non-VAH group, ipsilateral VAH group and contralateral aortic dyplasia groups. A p-value < 0.05 was considered statistically significant.

RESULTS

The general indicators were compared between the VAH group and the non-VAH group in patients with severe unilateral SA stenosis: there was no significant difference in prevalence between male and female. Compared with the VAH group, the incidence of the left side of the non-VAH group was significantly higher than that of the right side. Both the VAH group and the non-VAH group had asymmetrical upper limb blood pressure.

The comparison of clinical symptoms in the VAH

group and the non-VAH group: the VAH group was vulnerable to vertigo compared with the non-VAH group, and the prevalence of upper limb weakness in VAH group was higher than that in non-VAH group (Table I).

The types of SA were compared between the VAH group and the non-VAH group in patients with severe unilateral SA stenosis: in the VAH group, the main manifestations were concealed type (48.1%) and partial type (42.3%), while in the non-VAH group, there was little difference among the the concealed type, partial type and the complete type, moreover, the proportion of partial type (39.8%) was slightly higher.

Table I. *Comparison of clinical symptoms in the VAH group and the non-VAH group [% (case)]*

Group	Dizziness		Upper limb weakness	
	symptomatic	asymptomatic	symptomatic	asymptomatic
VAH severe stenosis	32 (61.5%)	20 (38.5%)	38 (73.1%)	14 (26.9%)
Non-VAH severe stenosis	37 (35.9%)	66 (64.1%)	23 (22.3%)	80 (77.7%)
χ^2 -value	9.180		37.285	
P-value	0.002		0.000	

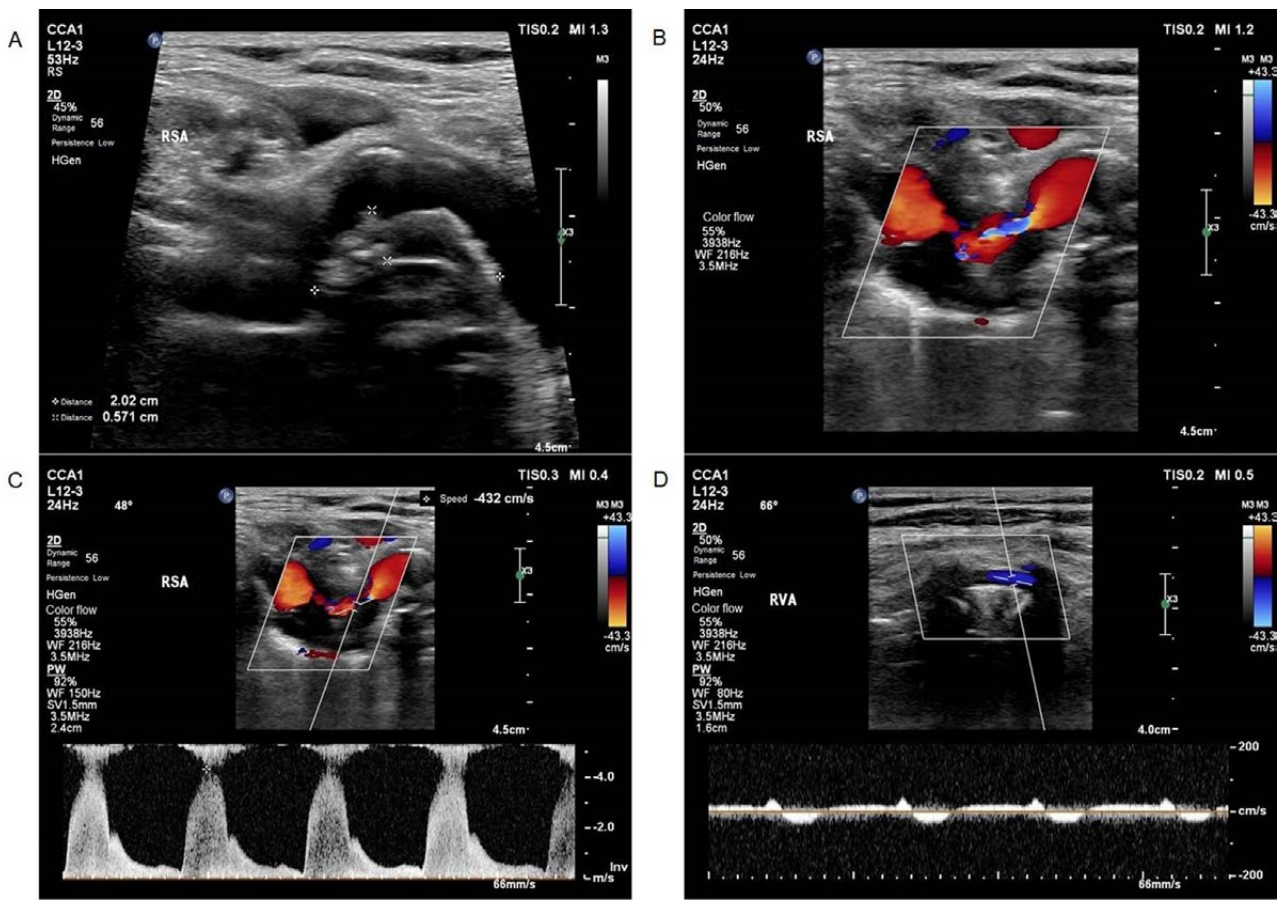

Fig. 1. *A 55-year-old male patient. Both ultrasound and DSA confirmed severe stenosis at the initial segment of the right SA.* ***a)*** *Two-dimensional ultrasonography showed the echo of plaque at the opening of the right SA.* ***b)*** *CDFI showed severe SA stenosis at the opening of the right SA.* ***c)*** *Pulsed doppler flow imaging showed PSV = 432 cm/s at the stenotic site.* ***d)*** *The spectrum of the right vertebral artery (inner diameter 3.0 mm) showed the reverse diastolic flow.*

Table II. *Comparison of SAS types in patients with severe stenosis of unilateral SA in the VAH group and the non-VAH group [% (case)]*

Group	Number	SAS type		
		concealed type	partial type	complete type
VAH severe stenosis	52	25 (48.1%)	22 (42.3%)	5 (9.6%)
Non-VAH severe stenosis	103	31 (30.1%)	41 (39.8%)	31 (30.1%)
χ^2 -value		9.386		
P-value		0.009		

Table III. *Comparison of blood stolen types of SA in ipsilateral group and contralateral group for patients with severe stenosis of unilateral SA [% (case)]*

Group	Number	SAS type		
		concealed type	partial type	complete type
Ipsilateral VAH severe stenosis group	41	19 (46.3%)	18 (43.9%)	4 (9.8%)
Contralateral VAH severe stenosis group	11	6 (54.5%)	4 (36.4%)	1 (9.1%)
χ^2 -value		0.242		
P-value		0.884		

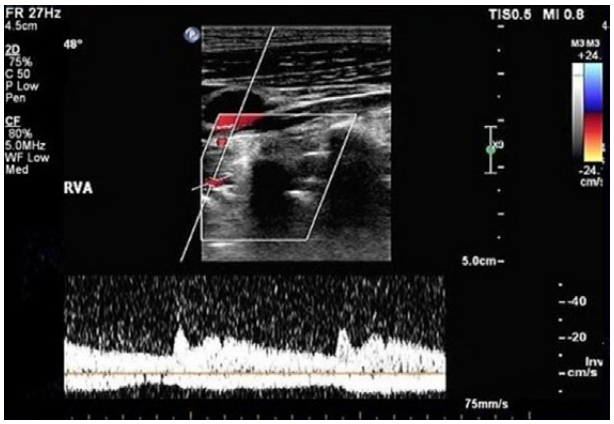

Fig. 2. ***A)*** *A 54-year-old male patient. Right VAH (inner diameter 2.0 mm), right SA initial severe stenosis, ultrasound suggested concealed blood steal.* ***B)*** *Fig. 1 patient, right VAH (inner diameter 2.1 mm), ultrasound suggested partial blood steal.*

There was a statistically significant difference in SAS between the VAH group and the non-VAH group in patients with severe stenosis of unilateral SA (Table II). There was no statistically significant difference in SAS between the ipsilateral VAH group and the contralateral VAH group (Table III).

Figs. 1-4 show CDFI and blood flow spectrum characteristics of SA and VA in patients with severe stenosis of unilateral SA in the VAH group and the non-VAH group. Color flow imaging showed that for patients with severe stenosis of unilateral SA, both in the VAH group and the non-VAH group, the stenosis of SA showed thinning of blood flow beam, and the blood flow spectrum showed widening of high velocity band (Fig. 1). In the VAH group, the main manifestations were concealed type (Fig. 2A)

and partial type (Fig. 2B), however, there was no significant difference among the three types of SAS in the non-VAH group (Fig. 3).

DISCUSSION

VAH is a common anatomical variation of vertebral-basilar artery system. The present study found that in the non-VAH group, there was no significant difference between the three types of SAS. When combined with ipsilateral or contralateral VAH, the main types of SAS were occult (46.3%, 54.5%). The difference between the two groups was statistically significant (p=0.009), and the degree of blood steal was significantly reduced in the VAH group, which was inconsistent with the degree of SA stenosis. Our study showed that VAH alleviates the degree of SAS, therefore the effect of VAH on SAS must be considered when diagnosed with SAS combined with VAH.

SA stenosis or occlusion is one of the important reasons of posterior circulation ischemia, accounting for 14-21% of cerebrovascular diseases (14). When the degree of stenosis is mild, the patient may have no obvious symptoms. When the degree of stenosis increases, the patient may have upper limb muscle pain and weakness as well as posterior circulation ischemia. Therefore, early and accurate diagnosis of SA stenosis has important clinical significance. The study shows that the degree of SAS has important reference value for ultrasonic diagnosis of SA stenosis (15).

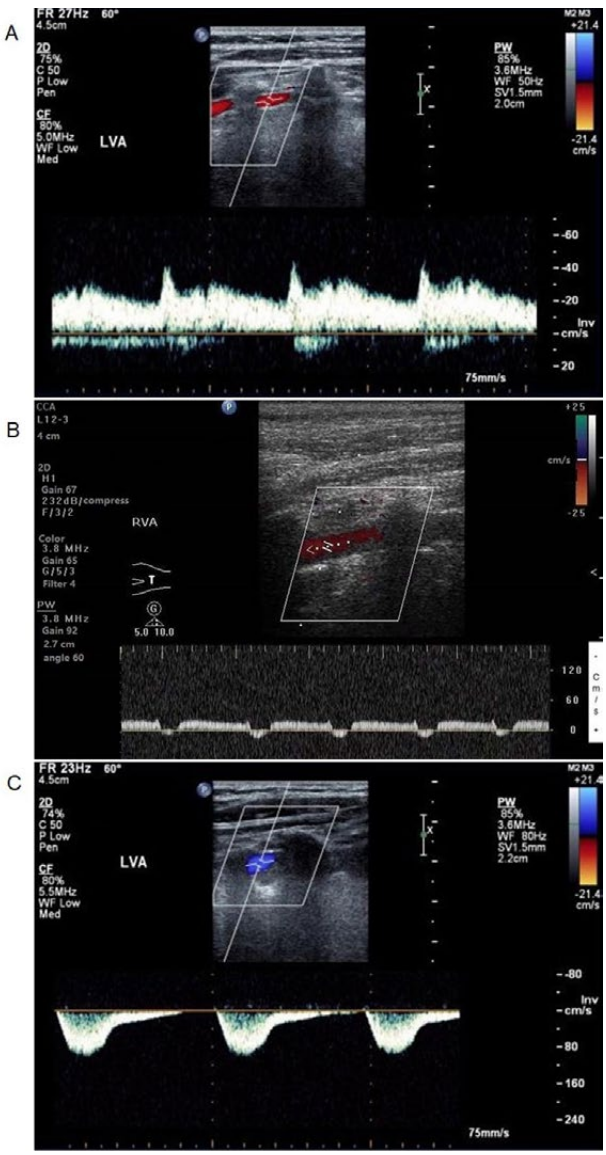

Fig. 3. *VA flow spectrum of three patients in the non-VAH group.* ***a)*** *A 62-year-old male patient with severe left SA stenosis, and ipsilateral VA CDFI indicates concealed blood steal.* ***b)*** *A 65-year-old male with severe right SA stenosis, and Ipsilateral VA CDFI indicates partial blood steal.* ***c)*** *A 55-year-old female patient with severe left SA stenosis, and Ipsilateral VA CDFI indicates complete blood steal.*

REFERENCES

1. Savitz S I, Caplan L R. Vertebrobasilar disease. N Engl J Med 2011; 352:446-84.
2. Qureshi A I, Ziai WC, Yahia AM, et al. Stroke-free survival and its determinants in patients with symptomatic vertebrobasilar stenosis: a multicenter study. Neurosurgery 2003; 52:1033-39.
3. Reivich M, Holling HE, Roberts B, Toole JF. Reversal of blood flow through the vertebral artery and its effect on cerebral circulation. N Engl J Med 1961; 265:878-85.
4. Hua Y, Jia L, Li L, et al. Evaluation of severe subclavian artery stenosis by color Doppler flow imaging. Ultrasound Med Biol 2011; 37:358-63.
5. Branchereau A, Magnan PE, Espinoza H, Bartoli JM. Subclavian artery stenosis: hemodynamic aspects and surgical outcome. J Cardiovasc Surg (Torino) 1991; 32:604-12.
6. Sakima H, Wakugawa Y, Isa K, et al. Correlation between the degree of left subclavian artery stenosis and the left vertebral artery waveform by pulse Doppler ultrasonography. Cerebrovasc Dis 2011;

31:64-67.
7. Yip PK, Liu HM, Hwang BS, Chen RC. Subclavian steal phenomenon: a correlation between duplex sonographic and angiographic findings. Neuroradiology 1992; 34:279-82.
8. Kliewer MA, Hertzberg BS, Kim DH, Bowie JD, Courneya DL, Carroll BA. Vertebral artery Doppler waveform changes indicating subclavian steal physiology. AJR Am J Roentgenol 2000; 174:815-19.
9. Saia A, Manzoni S, Iaia V. Subclavian steal diagnosis: Doppler sonography vs. angiography. Ital J Neurol Sci 1983; 4:439-42.
10. Clinical alert: benefit of carotid endarterectomy for patients with high-grade stenosis of the internal carotid artery. National Institute of Neurological Disorders and Stroke and Trauma Division. North American Symptomatic Carotid Endarterectomy Trial (NASCET) investigators. Stroke 1991; 22:816-17.
11. Hua Y, Hui PJ, Xing YQ. Guidelines for vascular ultrasound examination of stroke in China. Chinese J Med Ultrasound (Electronic Edition) 2015; 23:274-78.
12. Hua Y, Jia L, Li L, Ling C, Miao Z, Jiao L. Evaluation of severe subclavian artery stenosis by color Doppler flow imaging. Ultrasound Med Biol 2011; 37:358-63.
13. Wang LL, Hua Y, Ling C. Detection of vertebral artery dysplasia by color doppler flow imaging. Chinese J of Cerebrovascular Disease 2009; 6:396-99.
14. Kalaria VG, Jacob S, Irwin W, Schainfeld RM. Duplex ultrasonography of vertebral and subclavian arteries. J Am Soc Echocardiogr 2005; 18:1107-11.
15. Qureshi AI, Ziai WC, Yahia AM, et al. Stroke-free survival and its determinants in patients with symptomatic vertebrobasilar stenosis: a multicenter study. Neurosurgery 2003; 52:1033-39.

LETTER TO THE EDITOR

ASCL1 can bind to miR-135a-2 promoter elements to promote miR-135a-2 transcription and stem phenotypes in Huh7 cells

L. Zhang[1*], Z-P. Feng[2*], F-Q. Liu[2], R. Yan[2], L-Y. Yin[2], H. Shen[2] and X-H. Liang[2]

[1]Department of Endoscopy, Affiliated Cancer Hospital & Institute of Guangzhou Medical University, Guangzhou, China; [2]Department of Gastroenterology, Zengcheng District people's Hospital of Guangzhou, Guangzhou, China

Received May 22, 2020 – Accepted February 9, 2021

[*]These authors contributed equally to this work

To the Editor,

In 2018, the statistical data showed that liver cancer is the sixth most commonly diagnosed cancer and the fourth leading cancer-related cause of death, with approximately 841,000 new cases and 782,000 deaths every year (1). Hepatocellular carcinoma (HCC) makes up about 90% of primary liver cancers (2). HCC has extremely unfavorable prognosis and high recurrence risk due to high intrahepatic and extrahepatic metastases (3). However, the detailed mechanisms of HCC metastasis still need to be elucidated.

Cancer stem cells (CSCs) play an indispensable role in cancer metastasis. CSCs are a sub-population of cancer cells that is characteristic of self-renewal, differentiation, and homeostatic control capabilities (4). Even though the potential importance of CSCs in clinical therapy has attracted researchers' attention, CSC regulatory mechanisms remain unclear. Recent studies have established that aberrantly expressed miRNAs in cancers contribute to CSC properties (5).

Our previous research demonstrated that the miR-135a level is markedly increased in HCC. The present study reveals that HCC stem cell markers are significantly increased in miR-135a-overexpressing cells. In addition, miR-135a upregulation can elevate the stemness phenotype of HCC cells. Subsequent assays have shown that the transcription factor ASCL1 can combine with the promoter elements of miR-135a-2 to promote transcription of miR-135a.

MATERIALS AND METHODS

Cell culture and transfection

The human HCC cell line, Huh7, was purchased from Type Culture Collection Cell Bank, Chinese Academy of Science Committee (Shanghai, China). Dulbecco's Modified Eagle's medium (DMEM; Invitrogen) containing 10% fetal bovine serum (FBS; Invitrogen) was used to culture Huh7 cells. Transfection was performed according to the methods described in a previous study (6).

Quantitative PCR (qPCR) and Western blotting assay

The qPCR and Western blotting were carried out according to the methods described in our previous study (6). The primers were as follows: ALDH1: forward, CGGGAAAAGCAATCTGAAGAGGG, reverse, GATGCGGCTATACAACACTGGC; EpCAM: forward, GCCAGTGTACTTCAGTTGGTGC, reverse,

Key words: miR-135a; stem cell; HCC; ASCL1

Corresponding Author:
Dr Xing-hua Liang,
Department of Gastroenterology,
Zengcheng District people's Hospital of Guangzhou,
Guangming East Road,
Guangzhou Zengcheng District,
Guangzhou 511300, Guangdong, China
e-mail: liangxinghua77@163.com

0393-974X (2021)
Copyright © by BIOLIFE, s.a.s.
This publication and/or article is for individual use only and may not be further reproduced without written permission from the copyright holder.
Unauthorized reproduction may result in financial and other penalties
DISCLOSURE: ALL AUTHORS REPORT NO CONFLICTS OF INTEREST RELEVANT TO THIS ARTICLE.

CCCTTCAGGTTTTGCTCTTCTCC; CD133: forward, CACTACCAAGGACAAGGCGTTC, reverse, CAACGCCTCTTTGGTCTCCTTG.

Tumor sphere formation assay

Cells were seeded into 96-well plates and maintained using DMEM/F12 serum-free medium (Invitrogen) containing 2% B-27 (Invitrogen), 20 ng/mL basal fibroblast growth factor (bFGF; PeproTech), 20 ng/mL epidermal growth factor (EGF; PeproTech), 0.4% bovine serum albumin (BSA; Sigma-Aldrich), and 5 μg/mL insulin (Sigma-Aldrich). Serum-free medium was replenished every two days. The culture was finished after seven days.

Side population assay

The cells were harvested and re-suspended in DMEM (Invitrogen) supplemented with 2% FBS and 10 mM HEPES buffer. They were subsequently maintained with 2.5 μg/mL Hoechst 33342 (Invitrogen) for 90 min at 37°C. Then, cold phosphate buffer saline (PBS) was used to wash the cells, after which they were re-suspended in PBS supplemented with 2% FBS and 10 mM HEPES. The ratio of side population (SP) cells was quantified using flow cytometry (Beckman Coulter) according to the methods described previously (7).

Construction of vectors

The full-length sequences encoding ASCL1 were amplified using the Pfu Ultra II Fusion HS DNA Polymerase (Stratagene) and inserted into the pcDNA3.1 plasmid (Invitrogen). The promoter fragments for miR-135a-1/-2 from -2500 to +500 bp upstream of the transcription start site were amplified by PCR using TaKaRa LA Taq (Takara) and subcloned into the pGL3 basic firefly luciferase reporter system. The pGL3 constructs containing mutant miR-135a-2 promoter in the ASCL1 binding sites were created using a QuikChange Site-Directed Mutagenesis kit (Stratagene). The primers were as follows: miR-135a-1, forward, 5'-TTCTTCTCTGATGCATGACTG-3', reverse, 5'-GAATCATTTGAACAGGGGA- 3'; miR-135a-2, forward, 5'-TAATCTAATGCTTCATTTCTTC-3', reverse, 5'-GCAGAGTGCATGTTTTCT-3'.

Luciferase reporter plasmid construction and luciferase assay

The miR-135a-1/2 promoter fragments were amplified and inserted into the pGL3-Basic plasmid (Promega). A total of 2.5 μg of pGL3-Basic plasmid containing miR-135a-1/2 promoter and 0.25 μg of Renilla/luciferase vector (Promega) were co-transfected into Huh7 cells using Lipofectamine 3000 (Invitrogen). Then, 48 h after transfection, luciferase and Renilla signals were evaluated using the Dual Luciferase Reporter Assay Kit (Promega) following the manufacturer's protocol.

Chromatin immunoprecipitation (ChIP) assay

The ChIP assay was implemented using the Immunoprecipitation Assay Kit (Millipore). Subsequently, DNA from ChIP was quantified using qPCR with SYBR Green (Applied Biosystems). The primers for amplification of miR-135a-2 promoter were as follows: forward, 5'-AGGAGAACAAAATATCTGTC-3', reverse, 5'-AGTGACAGCACAGATGATA-3'.

Statistical analysis

All experiments were repeated three times. All statistical analyses were completed using the statistical software SPSS 20.0. Statistical significance between groups was evaluated using the Student's *t*-test. $P<0.05$ indicated a statistically significant difference.

RESULTS

HCC stem cell markers are significantly increased in miR-135a-overexpressing cells

Our previous study found that miR-135a contributes to the motility of Huh7 cells (6). Since CSCs play an indispensable role in cancer metastasis, the influence of miR-135a on HCC cell stem properties was evaluated. Firstly, miR-135a levels were overexpressed and inhibited in HCC cell line Huh7 (Fig. 1A). Subsequently, the mRNA levels of HCC stem cell markers ALDH1, EpCAM (8), and CD133(9) were detected. The qPCR assay demonstrated that overexpression of miR-135a can significantly increase, while inhibition can dramatically suppress their expression (Fig. 1B). Western blotting assays demonstrated a similar trend on a protein level, in accordance with the mRNA expression results (Fig. 1C).

Altogether, the levels of HCC stem cell markers ALDH1, EpCAM, and CD133 were significantly increased in miR-135a-overexpressing cells on both

mRNA and protein levels, suggesting that miR-135a may regulate the stemness characteristics of HCC cells.

miR-135a increases the proportion of CSCs in a population of HCC cells

The influence of miR-135a on self-renewal capabilities of HCC cells was confirmed using a tumor sphere formation assay. Notably, the spheres originated from miR-135a-overexpressing cells were larger than those from the control cells. However, the spheres derived from miR-135a-inhibiting cells were smaller in relation to those formed from the control cells (Fig. 2A).

One of the methods used to detect stem cells is based on the activity of ATP-binding cassette (ABC)

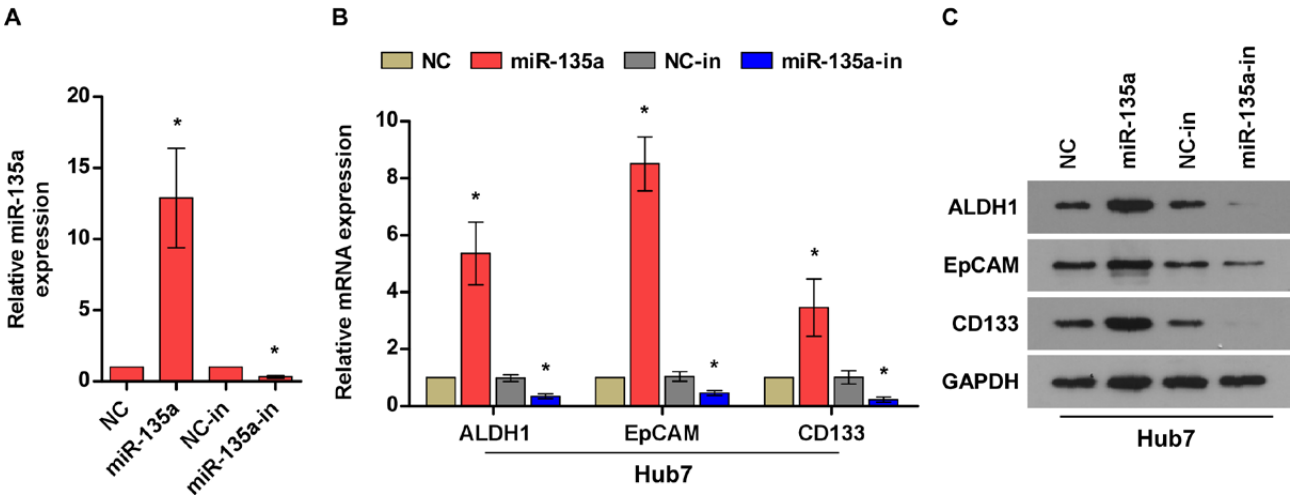

Fig. 1. *HCC stem cell markers are significantly increased in HCC HepG2-overexpressing miR-135a cells.* ***A)*** *qPCR assay results for relative miR-135a mRNA levels in Hub7 cells.* ***B)*** *qPCR assay results for HCC stem cell marker mRNA levels in Huh7 cells.* ***C)*** *Western blotting assay results for HCC stem cell marker protein levels in Huh7 cells. *P<0.05; NC: negative control; NC-in: negative control inhibitor.*

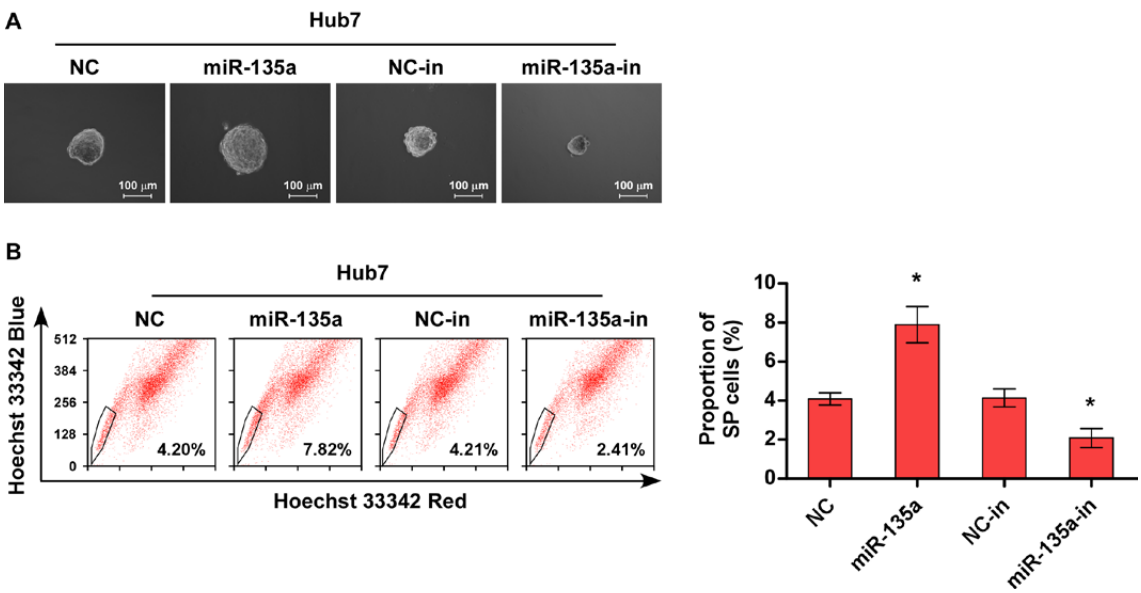

Fig. 2. *miR-135a promotes stem cell phenotypes in HCC Huh7 cells.* ***A)*** *Tumor formation assay shows that miR-135a induces HCC cells to form larger spheres than control. miR-135a-inhibiting cells form smaller spheres relative to NC-in cells.* ***B)*** *Representative (left panel) and qualitative (right panel) Fig.s for SP cells, suggesting that miR-135a increases the proportion of SP cells in population of HCC Huh7 cells. NC: negative control; NC-in: negative control inhibitor.*

transporter, which distinguishes a portion of SP cells stained with less Hoechst 33342 dye from total cells (7). Subsequently, the influence of miR-135a on SP cells was evaluated. Upregulation of miR-135a dramatically elevated the ratio of SP cells. On the contrary, the number of SP cells was dramatically decreased in miR-135a-downregulating cells (Fig. 2B). Taken together, tumor sphere formation and SP assays showed that upregulation of miR-135a promotes CSC-like characteristics of HCC cells (9).

ASCL1 can combine with the miR-135a-2 promoter to facilitate transcription

MiR-135a has two isoforms, which are miR-135a-1 and miR-135a-2. By analyzing the public University of Cingifornia Sisha Cruz (UCSC) dataset (http://genome.ucsc.edu/), it was found that the gene transcribing miR-135a-1 is located in *GLYCTK* genes (Fig. 3A), while miR-135a-2 is located in *RMST* gene (Fig. 3B). Therefore, it was hypothesized that miR-135a-1 and miR-135a-2 share the same promoter with the *GLYCTK* and *RMST* genes, respectively. In addition, the JASPAR dataset (http://jaspar.genereg.net/) showed that ASCL1 might bind with the miR-135a-1 and -2 promoter regions. The regions of miR-135a-1 and -2 promoters (defined as response elements) that ASCL1 can interact with are illustrated in Fig. 4A. In addition, it has been reported that CAGCTG is the sequence recognized by ASCL1 (10). According to this data, only the miR-135a-2 promoter contains the recognized sequences, suggesting that ASCL1 may combine with the miR-135a-2 promoter (Fig. 4B). To confirm this prediction, the promoter for the miR-135a-1 or miR-135a-2 gene from -2500 to +500 bp of the transcription start site was cloned into the pGL3 basic firefly luciferase reporter system. The pGL3 plasmid and plasmid-upregulated ASCL1 were co-transfected into the HCC cell line Huh7. The luciferase reporter assay showed that ASCL1 has no effect on transcription of miR-135a-1 (Fig. 4C). Nevertheless, ASCL1 significantly increased the luciferase activity of cells co-transfected with the construct, including the miR-135a-2 promoter (Fig. 4D). When the ASCL1 recognition sites were mutated, the luciferase reporter assay indicated that the effect of ASCL1 on miR-135a-2 regulation disappears (Fig. 4D). Moreover, the ChIP assay demonstrated that ASCL1 can combine with the miR-135a-2 promoter (Fig. 4E).

Taken together, these findings show that the transcription factor ASCL1 can bind with the promoter elements of miR-135a-2.

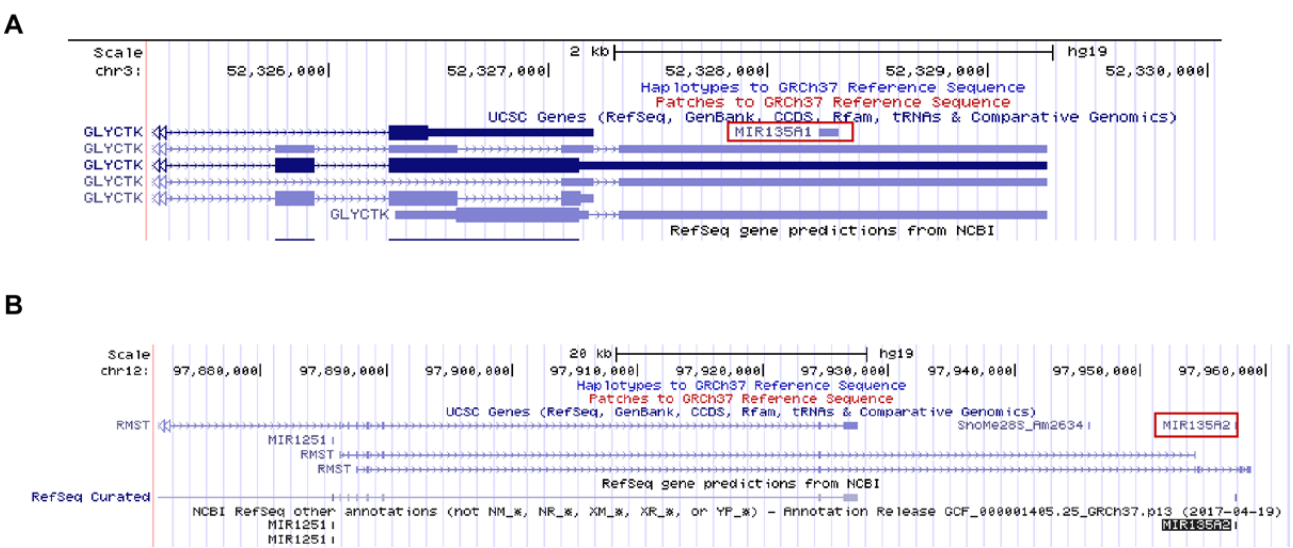

Fig. 3. *Location diagram for miR-135a-1 and promoter regions of miR-135a-1 (**A**) and miR-135a-2 (**B**).*

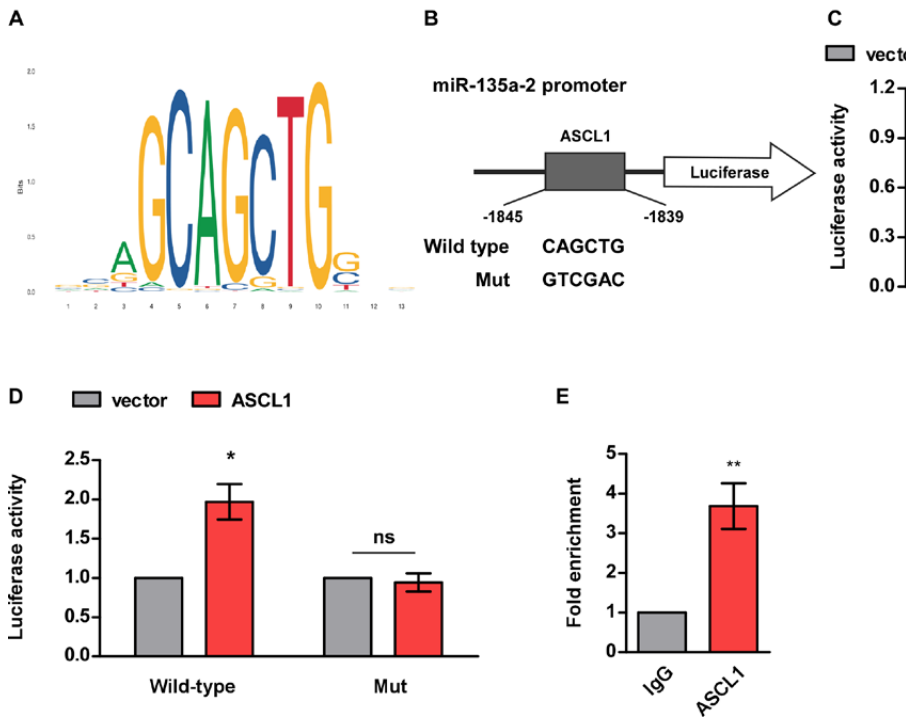

Fig. 4. *ASCL1 can combine with miR-135a-2 promoter elements.* ***A****) Possible miR-135a-1/-2 promoter response elements for interaction with ASCL1.* ***B****) Schematic of miR-135a-2 promoter plasmid is depicted with ASCL1 binding site locations and point mutation sequences.* ***C****) Luciferase reporter assay for HCC cells co-transfected with miR-135a-1 promoter reporter plasmid (wild-type at ASCL1 binding sites) and pcDNA3.1-ASCL1.* ***D****) Luciferase reporter assay for HCC cells co-transfected with miR-135a-2 promoter reporter constructs (wild- and mutant-type at ASCL1 binding sites) and pcDNA3.1-ASCL1.* ***E****) ChIP assay shows that ASCL1 can bind with miR-135a-2 promoter. ns: no significance; *P<0.05; **P<0.001.*

DISCUSSION

The present study demonstrated that upregulation of miR-135a can promote the expression of HCC stem cell markers and increase the proportion of CSCs in a population of HCC cells. Further analysis showed that the ASCL1/miR-135a-2 signal axis has a vital function in progression of HCC. In conclusion, these results suggest that miR-135a functions as an onco-miR in HCC and might represent an important target for clinical intervention in HCC.

Our previous study showed that miR-135a can directly target the 3'-UTR of FOXO1 (6). Accordingly, it has been reported that miR-135a contributes to the maintenance of spermatogonial stem cells by targeting FoxO1 (11). The present findings extend the essential functions of miRNAs in the maintenance of stem cell characteristics in HCC progression.

The function and modulation mechanisms by which miR-135a is involved in cancer have been widely investigated. However, the mechanisms regulating the miR-135a level are poorly understood. Wei et al. have shown that STAT5a can bind to both the miR-135a-1 promoter elements and miR-135a-2 to facilitate their transcription (12). The present research found that ASCL1 can combine with the promoter regions of miR-135a-2 to enhance its transcription.

The present study suggests that miR-135a might be a new therapeutic target for HCC. The therapeutic effects of miR-135a on HCC progression require further investigation using *in vivo* experiments.

ACKNOWLEDGEMENTS

This research was supported by the Science and

Technology Projects Foundation of Guangzhou city (No. 201804010416).

REFERENCES

1. Bray F, Ferlay J, Soerjomataram I, Siegel RL, Torre LA, Jemal A. Global cancer statistics 2018: GLOBOCAN estimates of incidence and mortality worldwide for 36 cancers in 185 countries. CA Cancer J Clin 2018; 68:394-424.
2. Llovet JM, Montal R, Sia D, Finn RS. Molecular therapies and precision medicine for hepatocellular carcinoma. Nat Rev Clin Oncol 2018; 15:599-616.
3. Yuan JH, Yang F, Wang F, et al. A long noncoding RNA activated by TGF-beta promotes the invasion-metastasis cascade in hepatocellular carcinoma. Cancer Cell 2014; 25:666-81.
4. Saygin C, Matei D, Majeti R, Reizes O, Lathia JD. Targeting Cancer Stemness in the Clinic: From Hype to Hope. Cell Stem Cell 2019; 24:25-40.
5. Garofalo M, Croce CM. Role of microRNAs in maintaining cancer stem cells. Adv Drug Deliv Rev 2015; 81:53-61.
6. Zeng YB, Liang XH, Zhang GX, et al. miRNA-135a promotes hepatocellular carcinoma cell migration and invasion by targeting forkhead box O1. Cancer Cell Int 2016; 16:63.
7. Fong D, Yeh A, Naftalovich R, Choi TH, Chan MM. Curcumin inhibits the side population (SP) phenotype of the rat C6 glioma cell line: towards targeting of cancer stem cells with phytochemicals. Cancer Lett 2010; 293:65-72.
8. Xiang X, Deng L, Xiong R, et al. Tex10 is upregulated and promotes cancer stem cell properties and chemoresistance in hepatocellular carcinoma. Cell Cycle 2018; 17:1310-8.
9. Flores-Tellez TN, Villa-Trevino S, Pina-Vazquez C. Road to stemness in hepatocellular carcinoma. World J Gastroenterol 2017; 23:6750-76.
10. Park NI, Guilhamon P, Desai K, et al. ASCL1 Reorganizes Chromatin to Direct Neuronal Fate and Suppress Tumorigenicity of Glioblastoma Stem Cells. Cell Stem Cell 2017; 21:411.
11. Moritoki Y, Hayashi Y, Mizuno K, et al. Expression profiling of microRNA in cryptorchid testes: miR-135a contributes to the maintenance of spermatogonial stem cells by regulating FoxO1. J Urol 2014; 191:1174-80.
12. Wei X, Cheng X, Peng Y, Zheng R, Chai J, Jiang S. STAT5a promotes the transcription of mature mmu-miR-135a in 3T3-L1 cells by binding to both miR-135a-1 and miR-135a-2 promoter elements. Int J Biochem Cell Biol 2016; 77:109-19.

LETTER TO THE EDITOR

Endocrine relation of cardiovascular dysfunction with inflammation in hyperthyroidism

MA. Iqbal[1], Z. Naseem[1], S. Ahmad[2] and N. Roohi[1]

[1]*Institute of Zoology, University of the Punjab, Quaid-i-Azam Campus, Lahore, Pakistan;*
[2]*King Edward Medical College University, Neela Gumbad, Lahore, Pakistan*

Received July 29, 2020 – Accepted February 9, 2021

To the Editor,

Thyroid hormones regulate multiple life functions by controlling the metabolism of carbohydrates, lipids and translation of many proteins in humans (1). The levels of thyroid hormones are precisely tuned and regulated by negative feedback loops in a time- and dose-specific manner through subsequent increases or decreases in type 2 iodothyronine deiodinase (D2) and type 3 iodothyronine deiodinase (D3). Hyperthyroidism is associated with severe cardiovascular effects including sinus tachycardia, systolic hypertension, changes in ventricular systolic and diastolic function, changes in peripheral vascular resistance and predisposition to dysrhythmias (especially atrial fibrillation or AF) (2).

C-reactive protein (CRP) is an acute-phase plasma protein that serves a specific function in the risk of manifesting cardiovascular dysfunction in which inflammation plays a pronounced participatory role (3). Interleukin-6 (IL-6) is a pleiotropic cytokine that is produced by a wide variety of immune and non-immune cells, including fibroblasts, endothelial cells, leukocytes, and many tumor cell lines. IL-6 exerts its biological action by acting on a specific receptor, IL-6R, which is a membrane-bound glycoprotein of 80 kDa (4). Homocysteine (Hcy), on the other hand, is a sulphur-containing amino acid that is produced by methionine metabolism in humans. Deviations in the plasma Hcy concentrations are associated with an increased risk of atherosclerosis and a variety of other pathologies (5). As these inflammatory markers are strong prognosticators of different clinical events, great clinical importance lies in deranged levels of these circulating inflammatory cytokines. The present study was designed to determine the deviations in three inflammatory markers that are primarily influenced by hyperthyroidism i.e., IL-6, CRP and homocysteine. In addition, the responsiveness of the anti-thyroid treatment was also assessed in a follow-up group of this research.

MATERIALS AND METHODS

The study plan was endorsed by the Institutional Ethics Review Committee of the Department of Zoology, University of the Punjab, Lahore, Pakistan. A total of 179 subjects (58 males and 121 females) fulfilling the inclusion and exclusion criteria were recruited for this prospective investigation. Age-matched controls (n=60; 40 females and 20 males), subclinical (n=34; 21 females and 13 males) and overt hyperthyroid (n=50; 35 females and 15 males) were recruited. Attaining euthyroid state, a group (n=35; 25 females and 10 males) of newly diagnosed hyperthyroid subjects on anti-thyroid therapy (average of 30-60 mg of Carbimazole/day) was

Key words: IL-6; CRP; homocysteine; hyperthyroidism; euthyroid

Corresponding Author:
Prof. Nabila Roohi,
Department of Zoology,
University of the Punjab,
Quaid-i-Azam Campus,
Lahore 54590, Pakistan
e-mail: nabilaruhi@gmail.com

0393-974X (2021)
Copyright © by BIOLIFE, s.a.s.
This publication and/or article is for individual use only and may not be further reproduced without written permission from the copyright holder.
Unauthorized reproduction may result in financial and other penalties
DISCLOSURE: ALL AUTHORS REPORT NO CONFLICTS OF INTEREST RELEVANT TO THIS ARTICLE.

also approached, after three months, for follow-up investigation to evaluate the efficacy of the treatment.

Determination of the thyroid profile, Free-T_4 (FT_4), Free-T_3 (FT_3) and thyroid stimulating hormone (TSH), was carried out by Radioimmunoassay (RIA) using commercially available kits (Beckman Coulter, Czech Republic) at the Institute of Nuclear Medicine and Oncology Lahore (INMOL), Pakistan. High sensitivity C-reactive protein (hs-CRP) was measured by using research grade Calbiotech, enzyme-linked immunosorbent assay (ELISA) kit. The levels of IL-6 and Hcy were measured using research grade Glory Biosciences ELISA kits.

A written informed consent was obtained from each of the participants included in the study. A comprehensive proforma was designed to record the demographic variables of the participating subjects. Exclusion criteria for subjects with thyroidal dysfunction were diabetes mellitus, obesity, cardiovascular complications, hypertension and a family positive history of these diseases. Subjects having any previous record of drug addiction and liver dysfunction such as hepatitis were also excluded, as these conditions may impair normal physiology and metabolism. Pregnant women were also excluded from this study. Blood pressure of all enrolled subjects was measured by using commercially available digital blood pressure monitor (CITIZEN, micro HumanTech CH-452). Height (m) and weight (kg) of all subjects were measured for evaluation of body mass index (kg/m^2).

Statistical analysis

Statistical comparisons among Control (C), Subclinical (S), Overt Hyperthyroid (O) and Follow-up (F) groups were carried out by one-way ANOVA. Significant means ($P < 0.05$) were compared by using "Student Newman Keuls" (SNK) test as the treatments had an unequal number of observations.

RESULTS

Table I represents an overall comparison of thyroid profile and inflammatory markers in the groups studied. Patients having FT_4 and FT_3 levels exceeding normal level (11.5–23.5 pmol/L and 2.5–5.8 pmol/L, respectively) and TSH below the normal level (0.3–5 mIU/L) were considered as clinically hyperthyroid patients, whereas subclinical hyperthyroid subjects had normal FT_3 and FT_4 but reduced TSH level (6). Moreover, control subjects had normal thyroid and regulatory hormone status.

FT_4. Highly significant difference ($P \leq 0.001$) of FT_4 was noticed in control *vs* overt hyperthyroid patients indicating 160% elevation in overt state as compared with control. Similarly, highly significant ($P \leq 0.001$) difference was found with 135% elevation of FT_4 in overt state, when compared with subclinical hyperthyroid patients. Overt *vs* follow-up groups indicated highly significant ($P \leq 0.001$) reduction of 68% in follow-up as compared to overt group (Table. I).

Table I. *Overall comparison of thyroid profile and inflammatory markers in Control, Subclinical, Overt and Follow-up groups*

Parameters	Control	Subclinical	Overt	Follow-up	*P*-value
	Mean±SEM				
FT_4 (pmol/L)	17.53±0.36	19.36±0.93	45.65±2.49	14.66±1.08	<0.0001*
FT_3 (pmol/L)	3.91±0.09	4.62±0.20	28.77±1.94	4.96±0.16	<0.0001*
TSH (mIU/L)	1.97±0.15	0.09±0.01	0.04±0.007	0.72±0.21	<0.0001*
CRP (mg/L)	4.46±0.20	5.32±0.64	6.81±0.70	5.30±0.96	0.0125*
IL-6 (ng/L)	12.69±0.55	17.41±0.63	19.02±1.21	15.46±0.94	<0.0001*
Hcy (µmol/L)	11.89±0.76	8.86±0.81	8.01±0.25	10.64±0.65	<0.0001*

*Values are Mean±SEM. *indicates significance at P <0.001*

FT_4: free tetra-iodothyronine; FT_3: free tri-iodothyronine; TSH: thyroid stimulating hormone; CR: C-reactive protein; IL-6: interleukin-6; Hcy: homocysteine

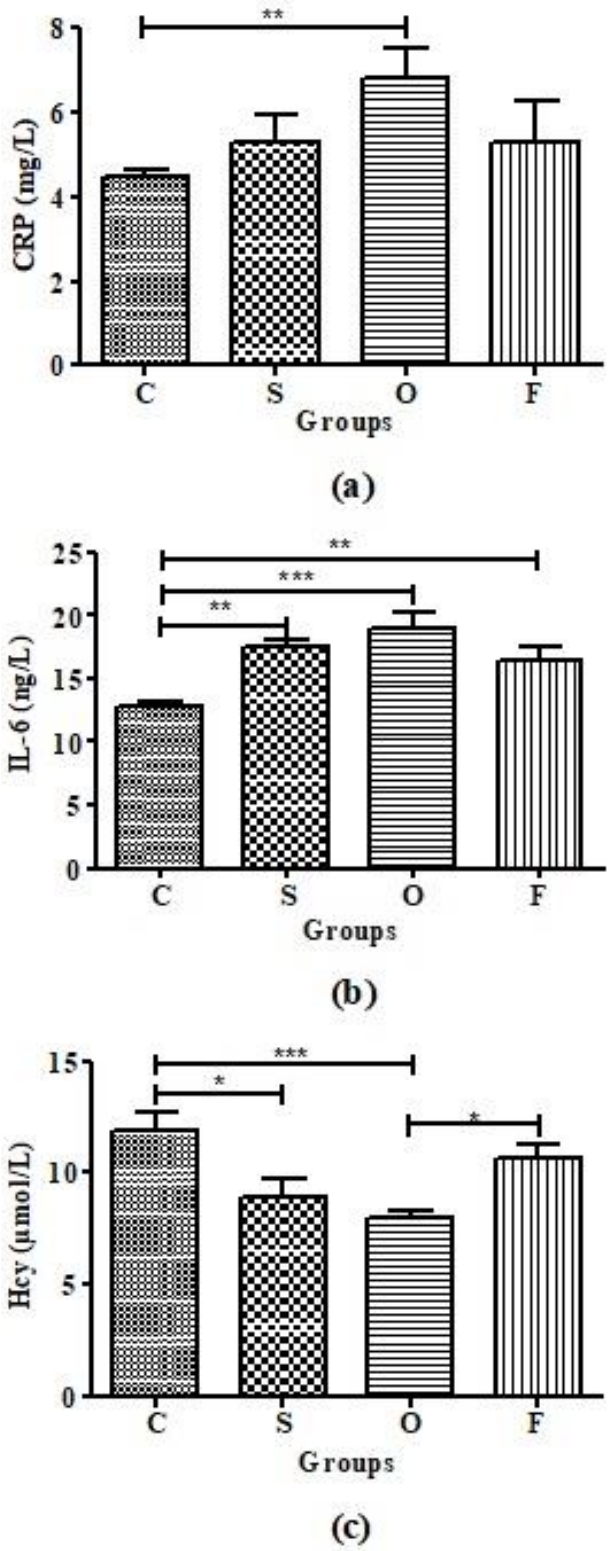

Fig. 1. ***a-c****) Inflammatory markers in comparable groups. Values are Mean±SEM, significant at *P ≤ 0.05, **P ≤ 0.01 and ***P ≤ 0.001*

FT_3: Marked difference ($P \leq 0.001$) of FT_3 was found in overt *vs* control comparison with 635% elevation. Moreover, highly significant difference ($P \leq 0.001$) was observed in subclinical and overt comparison depicting 522% increase in the overt group as compared with subclinical. Lastly, overt *vs* follow-up comparison depicted significant difference ($P \leq 0.001$) with 82% decline of FT_3 in follow-up after anti-thyroid treatment (Table I).

TSH: Highly significant difference ($P \leq 0.001$) of TSH was found in control *vs* subclinical, overt and follow-up comparisons with 95%, 98% and 63% reduction in subclinical, overt and follow-up groups, respectively. Prominent difference ($P \leq 0.05$) with 700% increase of TSH in follow-up group, was found in subclinical *vs* follow-up comparison. In the end, follow-up group demonstrated marked ($P \leq 0.05$) elevation of TSH level with 1700% when it was compared with overt state (Table. I).

CRP: Highly significant difference ($P \leq 0.01$) was evidenced in control *vs* overt group comparison with 53% elevation of CRP in overt as compared to controls. All other group comparisons i.e., control *vs* subclinical and follow-up, subclinical *vs* overt and follow-up and overt *vs* follow-up, demonstrated non-significant differences (Fig. 1a).

IL-6: Highly significant difference ($P \leq 0.001$) was noticed in control *vs* overt with 50% elevation of IL-6 in overt group as compared with healthy controls. Moreover, control *vs* subclinical and follow-up comparison presented pronounced difference ($P \leq 0.01$) with 37% and 30% elevation of IL-6 in subclinical and follow-up group, respectively, as compared to controls. All other group comparisons such as subclinical *vs* overt and follow-up, and overt *vs* follow-up demonstrated non-significant difference (Fig.1b).

Hcy: Significant difference ($P \leq 0.05$) was found in comparison of control *vs* subclinical with 25% decline of Hcy in subclinical group as compared to controls. Controls *vs* overt comparison demonstrated highly significant difference ($P \leq 0.001$) with 33% decrease in overt state as compared to controls. Subclinical *vs* overt and follow-up comparison did not present any significant difference. Lastly, in overt *vs* follow-up contrast, significant ($P \leq 0.05$)

increase of 33% was observed in the follow-up, when compared with overt group (Fig.1c).

DISCUSSION

The increasing trend of CRP level can be explained by the fact that clinically overt hyperthyroidism is characterized by enhanced low-density lipoprotein oxidation. Several metabolic cascades are triggered upon this oxidation in endothelium and vascular zone, which encompass the production and appearance of chemotactic and adhesion molecules and the proliferation of smooth muscle cells. As a result of these metabolic alterations, macrophage cells move inside the sub-endothelial cavity, where these cells transform into foam cells. Interaction of these foam cells with T lymphocytes results in immune response and causes production of acute phase reactant (CRP) and proinflammatory cytokines (IL-6 and IL-b) (3, 7). Mild reduction was observed in the follow-up group upon the restoration of thyroid profile.

Elevated levels of IL-6 in the subclinical as well as clinical hyperthyroid groups were highlighted in our investigation. Mononuclear cells in hyperthyroidic situations have a crucial role in the biosynthesis of IL-6, as these cells have a receptor for the thyroid hormones. IL-6 is primarily involved in the induction of the acute phase response proteins, the activation of T cells, and the transformation of B cells to plasma cells, and may influence the regulation of endocrine glands (8). It can cause cardiac hypertrophy through the IL-6 signal transducing receptor component, glycoprotein 130 (gp130), thus indicating abnormal left ventricular dysfunction (9). In spite of having anti-thyroidal treatment, the subjects in the follow-up did not show a significant decline. This shows that the normalization of IL-6 is quite a slow process, even after having normal thyroid profile. It is noteworthy that increased levels of this cytokine in subclinical hyperthyroid condition anticipates the prognosis of the altered cardiac physiology.

Decreased level of Hcy in both subclinical and clinical hyperthyroid conditions was observed. Clinically hyperthyroid conditions are accompanied by decreased creatinine levels and increased GFR. Moreover, folate levels in hyperthyroid subjects is reportedly higher as compared to control and hypothyroid subjects. It is a well-established fact that folate concentrations have inverse relationship with the Hcy levels in the plasma, hence predicting that folate concentration is a determinant factor of plasma Hcy levels in hyperthyroid subjects (10). Many experimental studies have proved that increased T_4 in hyperthyroid condition affects the enzyme involved in folate metabolism. Methylene tetrahydrofolate reductase is increased in hyperthyroidism and reduced in hypothyroidism. This deviation is relevant to the Hcy status in hyperthyroidism. This enzyme is responsible for the formation of 5-methyltetrahydrofolate which functions as methyl donor during the remethylation of Hcy (11).

Pertinently, in the case of the follow-up group receiving Carbimazole anti-thyroid treatment, improvement in the plasma Hcy concentration was observed after obtaining euthyroid clinical state, suggesting that reduced levels of Hcy are reversible. This study concludes that hyperthyroidism markedly influences the biosynthesis of inflammatory markers. CRP and IL-6 has a positive association with FT_4 and FT_3 levels, whereas Hcy demonstrated a negative relation with thyroid hormones. Elevated CRP and IL-6 in hyperthyroidism prognosticate future cardiovascular risks in these patients.

ACKNOWLEDGEMENTS

The present work is a part and continuation of the Ph.D research entitled “Predictive biomarkers of cardiovascular risks in hyperthyroid patients from Lahore, Pakistan” submitted to Higher Education Commission (HEC), Pakistan. Moreover, the authors gratefully acknowledge the HEC, Pakistan for financing this study vide letter No.112-33289-2BMI-342(50022893).

REFERENCES

1. Akinsete A, Oyenusi E, Odugbemi B, Odugbemi T, Temiye, E. Spectrum of Thyroid Abnormalities among Children Living with HIV in Lagos, Nigeria. J. Thyroid Res 2019; 2019:1-6
2. Chen Q, Yan Y, Zhang L, Cheng K, Liu Y, Zhu W. Effect of hyperthyroidism on the hypercoagulable

state and thromboembolic events in patients with atrial fibrillation. Cardiology 2014; 127(3):176-82.
3. Czarnywojtek A, Owecki M, Zgorzalewicz-Stachowiak M, Woliński K, Szczepanek-Parulska E, Budny B, Sawicka N. The role of serum C-reactive protein measured by high-sensitive method in thyroid disease. Arch Immunol Ther Exp 2014; 62(6):501-9.
4. Kishimoto T, Akira S, Taga T. Interleukin-6 and its receptor: a paradigm for cytokines. Sci 1992; 258:593-97.
5. Cullen CE, Carter GT, Weiss MD, Grant PA, Saperstein, DS. Hypohomocysteinemia: a potentially treatable cause of peripheral neuropathology? Phys Med Rehabil Clin N Am 2012; 23(1):59-65.
6. Surks MI, Ortiz E, Daniels GH, et al. Subclinical thyroid disease: scientific review and guidelines for diagnosis and management. JAMA 2004; 291(2):228-38.
7. Lau DC, Dhillon B, Yan H. Adipokines: molecular links between obesity and atheroslcerosis. Am J Physiol Heart and Circulatory Physiol 2005; 288(5):2031-41.
8. Salvi M, Girasole G, Pedrazzoni MA, et al. Increased serum concentrations of interleukin-6 (IL-6) and soluble IL-6 receptor in patients with Graves' disease. J Clin Endocrinol Metab 1996; 81(8):2976-9.
9. Kanda T, Takahashi T. Interleukin-6 and cardiovascular diseases. Jpn Heart J 2004; 45(2):183-93.
10. Orzechowska-Pawilojc A, Siekierska-Hellmann M, Syrenicz A, Homocysteine, folate, and cobalamin levels in hyperthyroid women before and after treatment. Endokrynologia. Polska 2009; 60(6):443-48.
11. Finklestein JD, Methioinie metabolism in mammals. J. Nutr Biochem 1990; 1(5):228-37.

LETTER TO THE EDITOR

Transient hyperthyroidism in a 6-year-old girl with Epstein-Barr virus infection: a link between infectious mononucleosis and autoimmune thyroid disease

M. Valenzise, U. Cucinotta, T. Aversa, M.F. Messina, M. Wasniewska and G.B. Pajno

Department of Human Pathology of Adulthood and Childhood, University of Messina, Messina, Italy

Received June 16, 2020 – Accepted December 7, 2020

To the Editor,

Epstein-Barr virus (EBV) infection, like other type of herpes virus, has been shown to be involved in several major autoimmune diseases, including systemic lupus erythematosus (SLE), multiple sclerosis (MS) and rheumatoid arthritis (RA) (1). This infection may play a role in both initiating the autoimmune process and exacerbating disease progression. Viral infections, and in particular Hepatitis C Virus (HCV), parvovirus B19, EBV, are also frequently cited as a major environmental factor involved in subacute thyroiditis and autoimmune thyroid disease, and the association between EBV infections and subacute thyroiditis has already been reported in literature (2-3). Antibodies against EBV viral capsid antigen (Ig G-VCA) and antibodies against early antigen (IG G-EA-D/DR) have been more often found in thyroiditis than in controls (4-6).

Case report

A 6 year-old girl was admitted to our Department for a fever of unknown origin, resistant to anti-inflammatory drugs and antibiotics. She presented cervical lymphoadenopathy, throat inflammation, moderate elevation of white blood count (WBC) and markers of inflammation (ESR, CPR), spleen and liver enlargement confirmed by ultrasound and high titer of anti-EBV IG M, previously negative (Table I). The suspicion of EBV infection was confirmed by the clinical picture and by the titers of antibodies against the virus. Because of the persistence of tachycardia in absence of fever, thyroid function was investigated with the following results: suppressed Thyroid Stimulating Hormone (TSH) levels (0.1 µUI/ml range 0.2-4.2) with high levels of free triiodothyronine (FT3) and free thyroxine (FT4) (FT3 8.96 pg/ml range 2-4.40; FT4 pmol/L 38.15 range 12-22) (Table I).

Antiperoxidase and antithyroglobulin antibodies were positive, but anti-TSH receptor antibodies were negative. Ultrasound examination showed a normal echogenicity of the whole gland and a normal blood flow based on power Doppler analysis. Considering these findings and the absence of neck pain, a subacute thyroiditis was excluded and the diagnosis of hyperthyroidism, caused by disruption of EBV-induced thyroid follicles, probably in course of Hashimoto's thyroiditis (HT), was made. The clinical symptoms were remitted in the following weeks after beginning methimazole therapy (7.5 mg/die). After a two-month follow-up period, anti-EBV IgG became positive. After three months, the treatment was progressively interrupted for the remission of clinical symptoms and normal levels

Key words: thyroid; infectious mononucleosis; EBV; Hyperthyroidism; autoantibodies

Corresponding author:
Dr Mariella Valenzise,
Department of Human Pathology of Adulthood and Childhood,
University of Messina, Messina, UOC di Pediatria,
Pad. NI, 3° piano, AOU Policlinico Gaetano Martino,
Via Consolare Valeria, 1, 98126 - Messina, Italy,
e-mail: mariella.valenzise@unime.it

0393-974X (2021)
Copyright © by BIOLIFE, s.a.s.
This publication and/or article is for individual use only and may not be further reproduced without written permission from the copyright holder.
Unauthorized reproduction may result in financial and other penalties
DISCLOSURE: ALL AUTHORS REPORT NO CONFLICTS OF INTEREST RELEVANT TO THIS ARTICLE.

of FT4 and TSH were observed. The antibody titer became normal four months later (Table I). Human Leucocyte Antigen (HLA) studies revealed: HLA DRB1, 1101, 1104, DRB3, DQB1.0301.0303.

DISCUSSION

EBV is one of the most common viral infections all over the world and is the main virus responsible for the clinical syndrome known as infectious mononucleosis (IM). Complications associated with IM are not rare and include hematological, neurological, cardiological, hepatic and splenic involvement, sometimes with lethal outcome. The virus is also considered to be an etiological factor of autoimmune diseases. It remains in the body throughout life, which explains the chronic course of autoimmune diseases that are often accompanied by exacerbations of symptoms. The thyroid gland can be involved, presenting thyroiditis after the invasion by different types of virus. EBV is capable of precipitating autoimmune disease by a variety of possible mechanisms (7). Paradoxically, infections may enhance autoimmune thyroid diseases, but they may also be protective. Indeed, the hygiene hypothesis implies that the immune system is educated by multiple exposures to different infections allowing it to control autoimmune responses better. Therefore, improved living standards are associated with the increasing risk of autoimmune diseases, while the lower socio-economic groups have a reduced prevalence of thyroid autoantibodies.

Specific infections are considered to be a triggering factor of disease initiation as they may free antigens, form altered antigens or cause molecular mimicry, determine cytokine and chemokine secretion, induce aberrant HLA-DR expression and Toll-Like–Receptor (TLR) activation. Autoimmune and inflammatory diseases are associated with TLR3/4 overexpression, which is in favour of environmental pathogens (8).

It is well known that the genetic background of the host plays an important role in enhancing autoimmune disease. HLA alleles, especially DR-DQ haplotypes, might contribute to the molecular pathogenesis of early-onset autoimmune thyroid diseases, as in our patient. Recently, Assaad et al. showed a significant positive correlation between serum EBNA-1 IgG levels and anti-thyroperoxidase (TPO) titer in healthy control subjects, underlining the role of EBV in triggering thyroid autoimmunity early before true development of HT. The authors report that the direct relationship between serum TSH and EBV VCA IgG and the negative relation between serum FT3 and EBNA-1IgG would suggest that EBV status may be associated with the degree of thyroid hormonal dysfunction (9).

Due to the age of our patient thyrotoxicosis factitia

Table I. *Biochemical data at diagnosis of thyroiditis (T1); after two months (T2) and four months (T3)*

BIOCHEMICAL DATA	T1	T2	T3
WHITE BLOOD CELL COUNT	14410 cells/mm^3 (n.v. 6000-12000)	8000 mm^3	6500 mm^3
Lymphocytes	65%	40%	38%
Monocytes	10%	6%	6%
CPR	16 mg/dl (0-0.5)	0.5 mg/dl	0.5
AST	158 U/L (0-42	56	40
ALT	256 U/L (0-50)	50	50
Anti-EBV-IG M	Positive	-	
Anti EBV –IG G	-	Positive	
TSH	0.1 mcUI/ml(n.v.0.2-4.2)	1.5 mcUI/ml	1.2
FT3	8.96 pg/ml (2.0-4.40)	3.58 pg/ml	2.9
FT4	38.15 pmol/L (12-22)	20.50 pmol/L	18
Abs TPO	580 IU/ml (0-34)	480	30
TRAbs	Negative	Negative	Negative

should have been considered, but it was excluded in this case because no drugs containing thyroid hormone were introduced, and high thyroid hormones levels were found after 15 days of admission in the hospital. Graves' disease was excluded because of the absence of anti-TSH receptor antibodies (TRAbs) and the normal ultrasound pattern of the thyroid gland. The resolution of the hyperthyroid phase in our patients underlines how this phenomenon, named hashitoxicosis, is often followed by definitive resolution with no relapses and persistent euthyroidism or hypothyroidism (10). Another study reports that the reactivation of persistent EBV causes secretion of TRAbs, absent in our patient, in EBV-infected B lymphocytes with TRAbs on their surface (11). The absence of significant elevation of inflammatory markers and the absence of thyroid pain, usually present in subacute thyroiditis, allowed to exclude this diagnosis in our patient.

The clinical history, the presence of EBV IG-M, previously negative, the thyroid hormone levels and the discovery of autoantibodies against the thyroid gland allowed to confirm the diagnosis of mild hyperthyroidism, like virus-induced HT in a patient with EBV infection. Our case underlines the possible evidence that EBV infections are involved in the pathogenesis of some cases of HT, mainly in predisposed individuals, and highlights the need to evaluate thyroid function in patients with viral infections and tachycardia without fever, especially in patients without underlying cardiac diseases.

Further studies are needed to clarify the relationship between viruses and thyroid disease, in order to develop new strategies for prevention and/or treatment.

REFERENCES

1. Sorgato CC, Lins-E-Silva M, Leão JC, Richardson Vasconcelos L, Romao TP, Duarte AL, Gueiros LA. EBV and CMV viral load in rheumatoid arthritis and their role in associated Sjogren's syndrome. J Oral Pathol Med 2020; 49(7):693-700.
2. Espino Montoro A, Medina Perez M, Gonzalez Martin MC, Asencio Marchante R, Lopez Chozas JM. Subacute thyroiditis associated with positive antibodies to the Epstein-Barr virus. An Med Interna 2020; 17:546-48.
3. Volta C, Carano N, Street ME, Bernasconi S. Atypical subacute thyroiditis caused by EBV infection in a three-year-old girl. Thyroid 2005; 15:1189-91.
4. Thomas D, Karachaliou F, Kallergi K et al. Herpes virus antibodies seroprevalence in children with autoimmune thyroid disease. Endocrine 2008; 33(2):171-5.
5. R. Desailloud, D Hober. Viruses and thyroidits: an update. Virol J 2009; 6:5.
6. Vrbikova J, Janatkova I, Zamrazil V, Tomiska F, Fucikova T. Epstein-Barr virus serology in patients with autoimmune thyroiditis. Exp Clin Endocrinol Diabetes 1996; 104:89–92
7. Kirino S, Nakatani H, Honma A et al An eight-year-old girl with autoimmune polyglandular syndrome type3A that developed during the course of primary Epstein-Barr virus (EBV) infection: clinical implication of EBV in autoimmune thyroid disease. Immunol Med 2020; 43(1):57-60.
8. H.J Anders, D. Zecher, RP Pawar, P S Patole. Molecular mechanisms of autoimmunity triggered by microbial infection Arthritis Res Ther 2005; 7(5):215-24.
9. Assaad SN, Meheissen MA, Elsayed ET Alnakhal SN, Salem TK. Study of Epstein-Barr virus serological profile in Egyptian patients with Hashimoto's thyroiditis: a case-control study. J Clin Transl Endocrinol 2020; 20:100222 .
10. Wasniewska M, Corrias A, Salerno MC et al. Outcomes of children with hashitoxicosis. Horm Res Paediatr 2012; 77(1):36-40.
11. Nagata K, Nakayama Y , Higaki K et al. Reactivation of persistent Epstein-Barr virus (EBV) causes secretion of thyrotropin receptor antibodies (TRAbs) in EBV-infected B lymphocytes with TRAbs on their surface. Autoimmunity 2015; 48(5):328-35.

LETTER TO THE EDITOR

Interleukin-6 as unfavorable prognostic factor in patients affected by Covid-19 and hip fracture

A. Pantalone[1], D. Bruni[1], P. Pantalone[2] and R. Buda[1]

[1]Orthopaedic and Traumatology Unit, Department of Medicine and Science of Aging, University G. "d'Annunzio" of Chieti-Pescara, Chieti, Italy; [2]Biodiscovery Institute and School of Life Sciences, University of Nottingham, Nottingham, United Kingdom

Received June 29, 2020 – Accepted December 7, 2020

To the Editor,

On April 4th 2020, 15,362 people died in Italy due to COVID-19; in this situation almost 4,000 persons required intensive care hospitalization, exhaustingly burdening the healthcare system of the most targeted regions such as Lombardy. More than 80% of the deceased were ≥70 years old, constituting the most vulnerable portion of the population in this time of emergency and sorrow. Such alarm forced a progressive worldwide action through lockdown measures involving several billions of people in an attempt to contain the emergency below the single national healthcare systems capability threshold. In these conditions, however, the typical risk factors for hip fracture (HF) remained the same, if not increased due to a forced self-isolation in a domestic environment. Ordinarily, 75% incidence of HF has been reported in subjects aged 75 years or over (1). The inflammation mechanism triggered by HF is still a subject of further investigation. Nevertheless, elevated cytokine interleukin 6 (IL-6) is an additional prognosis marker for fractures in osteoporothic patients (2), and its role has been revealed to be crucial in the inflammatory and healing processes (3). In particular, an association between hip fracture and high IL-6 concentrations in post-surgery has been described (4).

With regard to COVID-19 pathophysiology, the infection of COVID-19 of upper and lower respiratory tract triggers a pro-inflammatory cascade release of cytokines causing a mild to highly acute respiratory syndrome, resulting in extensive tissue damage and multiple organ dysfunction. The main cytokine being released in this signalling storm is IL-6 (5). In light of these considerations, patients infected by SARS-CoV-2 may be more susceptible to acute pulmonary infection if a fracture in lower limb occurs, as analogously described for pneumonia cases (6). Consequently, the mortality rate of COVID-19 may increase further in older patients with a hip fracture, as recently reported by Mi et a.l (7) and LeBrun et al. (8), although a larger cohort is required to corroborate this statement to demonstrate a synergic effect of IL-6 produced within the two pathologies.

In conclusion, these reflections suggest that an extra level of surveillance and treatment is crucial for hip fracture patients affected by COVID-19. As such, Il-6 could be exploited as a determinant prognostic factor to monitor the severity of pre- and post-surgery.

Key words: hip fracture; Interleukin-6; COVID-19; SARS-CoV-2

Corresponding Author:
Andrea Pantalone, Ph.D., M.D.
Orthopaedic and Traumatology Unit,
Department of Medicine and Science of Aging,
University G. "d'Annunzio" of Chieti-Pescara, SS. Annunziata Hospital,
Via dei Vestini 35, 66013 Chieti, Italy
Tel.: +39 0871 358359 - Fax: +39 0871 358229
e-mail: andrea.pantalone@unich.it

0393-974X (2021)
Copyright © by BIOLIFE, s.a.s.
This publication and/or article is for individual use only and may not be further reproduced without written permission from the copyright holder.
Unauthorized reproduction may result in financial and other penalties
DISCLOSURE: ALL AUTHORS REPORT NO CONFLICTS OF INTEREST RELEVANT TO THIS ARTICLE.

REFERENCES

1. Vanasse A, Orzanco MG, Dagenais P, et al. Secular trends of hip fractures in Québec, Canada. Osteoporos Int 2012; 23:1665-72. https://doi.org/10.1007/s00198-011-1749-0
2. Cauley JA, Danielson ME, Boudreau RM, et al; Health ABC Study. Inflammatory markers and incident fracture risk in older men and women: the Health Aging and Body Composition Study.J Bone Miner Res 2007; 22(7):1088-95. doi: 10.1359/jbmr.070409.
3. Prystaz K, Kaiser K, Kovtun A, et al. Distinct effects of IL-6 classic and trans-signaling in bone fracture healing. Am J Pathol 2018; 188(2):474-490. doi: 10.1016/j.ajpath.2017.10.011.
4. Saribal D, Hocaoglu-Emre FS, Erdogan S, Bahtiyar N, CaglarOkur S, Mert M. Inflammatory cytokines IL-6 and TNF-α in patients with hip fracture. Osteoporos Int 2019; 30(5):1025-31. doi: 10.1007/s00198-019-04874-2.
5. Conti P, Ronconi G, Caraffa A, Gallenga CE, Ross R, Frydas I, Kritas SK. Induction of pro-inflammatory cytokines (IL-1 and IL-6) and lung inflammation by Coronavirus-19 (COVI-19 or SARS-CoV-2): anti-inflammatory strategies. J Biol Regul Homeost Agents 2020; 14: 34(2). pii: 1. doi: 10.23812/CONTI-E.
6. Chen YC, Lin WC. Risk of long-term infection-related death in clinical osteoporotic vertebral fractures: a hospital-based analysis. PLoS One 2017; 9:12(8):e0182614. doi: 10.1371/journal.pone.0182614.
7. Mi B, Chen L, Xiong Y, Xue H, Zhou W, Liu G. Characteristics and early prognosis of COVID-19 infection in fracture patients. J Bone Joint Surg Am 2020: doi: 10.2106/JBJS.20.00390.
8. LeBrun DG, Konnaris MA, Ghahramani GC, et al. Hip fracture outcomes during the Covid-19 pandemic: Early Results from New York. J Orthop Trauma 2020 May 27:10.1097/BOT.0000000000001849. doi: 10.1097/BOT.0000000000001849.

LETTER TO THE EDITOR

Polynucleotide biogel enhances tissue repair, matrix deposition and organization

M.T. Colangelo[1], P. Govoni[1], S. Belletti[1], F. Squadrito[2], S. Guizzardi[1] and C. Galli[3]

[1]Histology and Embryology Laboratory, Department of Medicine and Surgery, University of Parma, Parma, Italy; [2]Department of Clinical and Experimental Medicine, University of Messina, Messina, Italy; [3]Department of Medicine and Surgery, University of Parma, Parma, Italy

Received May 27, 2020 – Accepted December 11, 2020

To the Editor,

Wound healing is a complex phenomenon that requires the interplay of different signal cascades and cell phenotypes (1), which eventually deposit a provisional matrix that progressively matures to normal healthy tissue (2). New cell progenitors from the neighboring healthy tissues grow into the provisional matrix and create sound tissue; in the relatively common case of skin wounds, these cells are both epithelial cells, which cover the defect and its provisional matrix, thus isolating and protecting it from the outside environment (3), and fibroblasts, which deposit the underlying connective tissue, mostly composed of collagen, in its diverse isoforms, and proteoglycans (4). If the deposition of extracellular matrix is insufficient, the final tissue will not possess adequate mechanical, functional or even esthetical characteristics (5). As fibroblasts are key to wound healing, it is unsurprising that strategies aiming at improving healing in clinical situations where this is impaired often rely on stimulating or improving fibroblast functionality (6). One such strategy is the use of polynucleotides (PN), polymers consisting of a mixture of double stranded deoxyribonucleotides. They have been used since 2004 in different class III medical devices, e.g. as wound healing accelerators, for intra articular supplementation (7), thanks to their lubricating and visco-elastic properties, and as filler to improve skin turgor and hydration, both over the face and other body areas (8), in skin rejuvenation medical devices. The present study investigated the effects of PN in stimulating the viability of human primary fibroblasts *in vitro* and the regulation of some important matrix components. We further used a mouse model of subcutaneous pouch to assess whether PN improved wound healing and how matrix deposition was affected *in vivo* by comparing its effect with hyaluronic acid, the most popular type of dermal filler.

MATERIALS AND METHODS

PN (Mastelli s.r.l., Sanremo, Italy) are a compound that contains a mixture of deoxyribonucleotide polymers of different lengths. PN are obtained from salmon trout gonads through purification and high-temperature sterilization, to ensure a very high percentage of DNA.

Cell culture

Cell assays were performed with human primary fibroblasts obtained from American Type Culture Collection (LGC Standards S.R.L., Milan, Italy). Cells were routinely maintained in complete Dulbecco modified MEM (DMEM, Life Technologies, Carlsbad,

Key words: polynucleotides; collagen; fibroblasts; wound healing; cell viability

Corresponding Author:
Stefano Guizzardi,
University of Parma,
Department of Medicine and Surgery,
Via Volturno 39, 43126 Parma, Italy
Tel.: +39 0521 903912
e-mail: stefano.guizzardi@unipr.it

0393-974X (2021)
Copyright © by BIOLIFE, s.a.s.
This publication and/or article is for individual use only and may not be further reproduced without written permission from the copyright holder.
Unauthorized reproduction may result in financial and other penalties
DISCLOSURE: ALL AUTHORS REPORT NO CONFLICTS OF INTEREST RELEVANT TO THIS ARTICLE.

CA, USA) supplemented with 10% Fetal Bovine Serum (FBS, LifeTechnologies, Carlsbad, CA, USA), 4 mM L-glutamine (Merck KGaA), 100 IU/ml penicillin and 100 µg/ml streptomycin (PenStrep, Merck KGaA) in a humidified atmosphere with 5% CO2 at 37°C. Culture medium was replaced every 3 days. Cells were monitored by Nikon TMS inverted optical microscope (Nikon, Tokyo, Japan) in phase contrast for morphological characterization. The microscope was equipped with Nikon Digital Sight DS-2Mv acquisition system (Nikon) and images were acquired with NIS Elements F software (Nikon). After reaching 80% confluence, cells were washed with Dulbecco's phosphate buffered saline (PBS w/o Ca^{2+}, w/o Mg^{2+}, Euroclone, Pero, MI, Italy), harvested using trypsin-EDTA (Merck KGaA), resuspended in 10 ml of NaCl cold solution to be counted and seeded onto new plates. Two experimental groups were used in this *in vitro* study, a Control group and a PN group. In each experiment, 24 h after seeding, cells were stimulated with either culture medium (Control) or 100 µg/ml PN to evaluate its effects.

Cell count and viability

Cells were seeded in a 24-well plate at a density of $2x10^4$ cells/well to be stimulated 24 h after seeding. The experiment was performed in triplicate. The number of cells was evaluated for the Control group and PN group after 96 h and 1 week of stimulation by detaching and direct counting with a Coulter Counter (Coulter Electronics Limited, England). Briefly, after collecting the supernatant for the ELISA assays, each sample was washed with PBS (Ca^{2+} and Mg^{2+} free), detached with 300 µl of trypsin-EDTA and resuspended in 10 ml of NaCl cold solution for counting.

For cell viability evaluation, cells were seeded in a 96-well plate at a density of $8x10^3$ cells/well in a final volume of 100 µl of culture medium and stimulated 24 h after seeding. The Control group and PN group were evaluated after 96 h and 1 week from stimulation by MTT (Roche Applied Science, Monza, Italy) and Cell Titer-Glo® (Promega, Madison, WI, USA) assays.

The MTT assay was used according to the manufacturer's indications and eight wells were assigned for each experimental condition. Briefly, 10 µl of MTT labeling reagent was added at final concentration 0.5 mg/ml and the plate was placed into a thermostatically controlled incubator for 3 h. Once the incubation was completed, 110 µl of solubilization solution (anhydrous isopropanol containing 0.1 N HCl and 10% Triton X-100) was added, the contents were mixed for 5 min on an orbital shaker and the absorbance was read at 570 nm by a microplate reader (Infinite F200 TECAN, Switzerland).

The bioluminescence assay was performed according to the recommendations of the manufacturer and four wells were assigned for each experimental condition. Briefly, the plate was equilibrated to room temperature for 30 min and a volume of Cell Titer-Glo® Reagent equal to the volume of cell culture medium was then added. The content was mixed for 2 min on an orbital shaker to induce cell lysis and intracellular adenosine 5'-triphosphate (ATP) release into the culture medium and transferred from each well to a new opaque-walled multi-well plate. The plate was incubated at room temperature for 10 min to stabilize luminescence signal and finally the samples were read with a microplate reader (Infinite F200 TECAN, Switzerland). Control wells containing medium without cells were used to obtain a value for background luminescence.

Protein content and ELISA assay

To quantitate the protein content of Control and PN groups, cells were seeded in a 24-well plate at a density of $2x10^4$ cells/well, stimulated after 24 h and evaluated 96 h and 1 week after stimulation. The experiment was performed in triplicate. Briefly, samples were gently rinsed with PBS, left to dry for 2 h to be then solubilized with 200 µL of 5% NaOH DOC (Sigma-Aldrich) and left to stir for 1 h. After adding 2 ml of Lowry Reagent Solution containing $Na_2CuEDTA$, Na_2CO_3 and NaOH, samples were left to stir for 10 min and transferred to a sonicator, 200 µL of Folin & Ciocalteu's Phenol Reagent Working Solution (Sigma-Aldrich) were added and after 2 min the content was mixed for 1 h on an orbital shaker. The amount of proteins was estimated by reading the absorbance at 750 nm by a microplate reader (Infinite F200 TECAN, Switzerland) and the amount of proteins in the given unknown solution was calculated from the standard curve.

Collagen 1 and Collagen 3 expressions were measured by quantitating the protein in the supernatant collected in the Control group and PN group as described above. Cell culture media was centrifuged at 1000 rpm for 20 min

to eliminate cell remnants and all reagents and working standards were prepared following the manufacturer's recommendations. Samples were then assayed using Human Pro-Collagen I alpha 1 SimpleStep ELISA Kit (Abcam, Cambridge, UK) and Human Collagen III Alpha (COL3A1) ELISA Kit (Abbkine, Wuhan, China). The experiments were performed in triplicate.

For Collagen I secretion, supernatants were diluted into Sample Diluent NS and assayed. Fifty µL of all sample and standard were added to appropriate wells. After adding (50 µL) of the Antibody Cocktail to each well, the plate was sealed and incubated for 1 h at room temperature on a plate shaker set to 400 rpm. Each well was then washed with 350 µL 1X Wash Buffer PT for 3 times and, after complete removal of the liquid, 100 µL of TMB Development Solution were added to each well. The plate was incubated for 10 min in the dark on the plate shaker, 100 µL of stop solution were then added to each well, the plate was shaken for 1 min and the optical density (O.D.) recorded at 450 nm by a microplate reader.

For Collagen III secretion, after adding diluted standard (50 µL) to standard well, sample diluent (40 µL) and sample (10 µL) were added to testing sample well. The plate was covered and incubated for 45 min at 37°C and each well was then washed with Wash buffer (250 µL) for 5 times. After removing any remaining Wash buffer, HRP-Conjugated detection antibody (50 µL) was added and the plate was covered and incubated for 30 min at 37°C. The washing process was repeated for five times as described above and then chromogen solution A (50 µL) and chromogen solution B (50 µl) were added to each well. The contents were gently mixed and the plate was incubated for 15 min at 37°C while protecting it from light. (50 µl) stop solution was then added to each well and the O.D. was recorded at 450 nm by a microplate reader.

In vitro scratch assay

To determine the polydeoxyribonucleotide effect on cell spreading and migration capabilities, cells were seeded into a 12-well plate at a density of $20x10^4$ cells/well and grown to full confluence. The assay was performed in triplicate. After aspirating the culture medium from all wells, a linear wound was generated in the monolayer of cells with a 200 µL plastic pipette tip by gliding the tip across cell surface from a 12-o'clock to 6-o'clock location. Any cellular debris was removed by washing with PBS and cells were stimulated by adding culture medium (control group) or PN. After 48 and 96 h of incubation, images of migrated cells were taken using a digital camera connected to an inverted optical microscope in phase contrast to observe the closure of the wound area.

After 96 h, samples were fixed to be stained with Giemsa (Merck KGaA). Briefly, pure methanol was added to each well to then be replaced with 1ml of Giemsa solution. After 2 min, 3 ml of H_2O were added and the components were mixed by shaking the plate for 2 min. After removing the staining solution, the samples were rinsed with tap water and allowed to dry. Samples were observed with a Nikon Eclipse 80i optical microscope (Nikon), equipped with a Nikon Digital Sight DS-2Mv camera and imaged with NIS Elements F control software (Nikon).

In vivo experiment and histology

The test was conducted at the University of Messina after ethics committee approval and in accordance with the National Ethical Guidelines (Italian Ministry of Health; D.L.vo 116, January 27, 1992) and the Guide for the Care and Use of Laboratory Animals (NIH publication no. 85–23, revised 1996). For this protocol 6 female C57BL mice, 14 weeks old, weighting 25-32 g were used. Animals were divided into 3 groups of 2 animals each. The first group was injected with polynucleotide gel (20mg/ml), the second group was injected with hyaluronic acid and the third group (control) was injected with NaCI 0.9% saline solution. The injection technique (microwheals technique) consisted of serial superficial intradermal injections of 0.3 ml of product.

Four injections were performed in sites with 1 cm spacing for each animal. All the animals were observed for 24, 48 and 72 h, 1 week and 2 weeks, to monitor the appearance of any toxic effects. Injection sites were examined for any signs of cutaneous irritation (erythema, edema and eschar). Moreover, the mice were anaesthetized after 2 weeks and received cutaneous punch biopsy (diameter 4 mm) for histological analysis in the treated areas.

The tissues obtained from the sacrificed animals were fixed in 4% neutral formaldehyde diluted in phosphate-buffered saline, were dehydrated in graded ethanol, cleared in xylene and embedded in paraffin after 24 h.

Samples were then sliced with a microtome at a 6 μm thickness and mounted on glass slides. Paraffin was then removed from the slides using xylene and the slides were subsequently dehydrated in alcohol. After washing with demineralized water, in order to morphologically assess tissue composition, some slides were dipped into Harris hematoxylin (Hematoxylin BCS certified-C.I. 75290 by Bio-Optica Milano S.p.A.) for 60 s and rinsed with tap water until clear, dipped in yellowish eosin in 25% solution (Eosin Y BSC certified-C.I. 45380 by Bio-Optica Milano S.p.A.) for 3 min and rinsed again with water. To highlight the presence of collagen in the EMC, other slides were incubated with a 0.1% Sirius Red solution (Sirius Red F3B 200, Mobay Chemical Co., Union, New Jersey, USA), dissolved in aqueous saturated picric acid for 1 h and washed in acidified water (0.5% hydrogen chloride). All samples where then washed with demineralized water, dehydrated in ethanol, cleared in xylene and mounted in a resinous medium (Fisher Chemical Permount Mounting Medium). Microphotographs of experimental H&E and picro-Sirius Red stained tissues were taken using an optical microscope Nikon Eclipse 80i (Nikon Instruments, Italy) equipped with a camera, Nikon Digital Sight DS-2Mv, connected to the control software, NIS-Elements D version 3.06 (Nikon Instruments). The samples stained with picro-Sirius Red were observed also with a polarized light microscope (the same instrument as above with the addition of polarizing filter).

Statistical analysis

Data were analyzed using Prism X (GraphPad, La Jolla, CA, USA). All values were reported as the mean ± Standard Deviation of repeated experiments performed in triplicate. ANOVA test was used to determine the statistical significance of the differences observed between groups. P values < 0.05 were considered significant.

RESULTS

PN improved the cell number in human fibroblasts cultures

We first investigated whether PN improved the cell growth of primary human fibroblasts. To this purpose, fibroblasts were cultured in the absence or in the presence of 100 μg/ml PN. Transmission light microscopy revealed that cells in both groups appeared healthy, elongated and, mostly, spindle shaped, but cells in the PN group were considerably more tightly packed than in control samples (Fig. 1 A-B). We then detached the cells at 96 h and 1 week of culture and counted them: an average of more than $4x10^4$ cells were counted in the treated wells, versus fewer than half that number for the control group at both time points (Fig. 1E, $p<0.001$).

These results were validated, with established viability assays. We decided to first use MTT, a well-established assay based on the reduction of this compound to insoluble and colored Formazan. Once the MTT was added to the wells, blue precipitates formed in the cell cytoplasm, as a consequence of their respiratory activity (Fig. 1 C, D). These precipitates revealed a higher number of cells in the treated wells. We then proceeded to solubilize Formazan and quantitate it by reading its absorbance at 570 nm. Absorbance was slightly but significantly higher in the PN-treated group after 96 h of culture (Fig. 1F, $p<0.01$), suggesting increased cell viability following PN treatment, although no significant difference was detected after 1 week of culture. To confirm these data, cell viability was also assessed by chemiluminescence, using the Cell titer GLO assay. The assay revealed that viability levels for cells cultured in medium enriched with 100 μg/ml PN were significantly higher than in the control group both after 96 h and after 1 week of treatment (Fig. 1G, $p<0.001$).

PN enhanced protein synthesis and the expression of collagen I and III

We measured the amount of proteins in the wells by Lowry's assay, a well-known method for protein quantification. Consistently with the tests above, the amount of proteins in the lysates from PN-stimulated samples was significantly higher than in the control group at both 96 h and 1 week of culture (Fig. 1H, $p<0.01$).

We then proceeded to quantitate the levels of Collagen protein in the supernatants of cell cultures grown in the presence or in the absence of 100 μg/ml PN for 96 h or 1 week. The expression levels of Collagen 1a1 and 3a1 increased over time in both groups, as did cell number, as shown in Figs. 1 and 2.

However, when normalizing the increase in Collagen production by the increase in cell number, it was still possible to observe that Collagen 1a1 and 3a1 production in the PN-stimulated group significantly exceeded that of the control group (Fig. 2 A, B, $p<0.01$), pointing to a specific regulation by PN.

PN enhanced wound healing in vitro and in vivo

We next assessed the reparative potential of PN by performing a scratch assay *in vitro*. After the well surface was scratched with a pipette tip, thus freeing cells from contact inhibition, the cells were followed up as they bridged the gap (Fig. 2 C, D). Although, as expected, cells in both groups started to proliferate and fill the scratched area, by 96 h of culture from stimulation, cells in the PN-treated group had occupied significantly more well surface than the control cells (Fig. 2E), prompting us to further investigate the regenerative potential of PN *in vivo*.

When the *in vivo* experiment was performed, during the period of clinical observation, it was impossible to detect any phenomenon of erythema, edema and eschar in the experimental mice cohorts at any experimental time (24, 48 and 72 h, 1 week and 2 weeks, data not shown).

Histological analysis of the skin samples 2 weeks after the injection procedure revealed that the wounds had healed uneventfully in all groups. However, abundant granulation tissue was observable in the control group (Fig. 3 A, D). The edges of the lesion were still visible and the newly formed tissue was occupied by a large inflammatory infiltrate (Fig. 3D). The healing area was markedly narrower in the hyaluronic acid group (Fig. 3 B, E), especially in the mid-portion, where tissue contraction had reduced granulation tissue to a thin band, constellated by a reduced but visible inflammatory infiltrate (Fig. 3E). Tissue healing was at an even more advanced stage in the PN-treated animals (Fig. 3 C, F), where the wound had almost completely disappeared and the two healing margins were tightly juxtaposed, with scarce inflammatory cells to mark the former

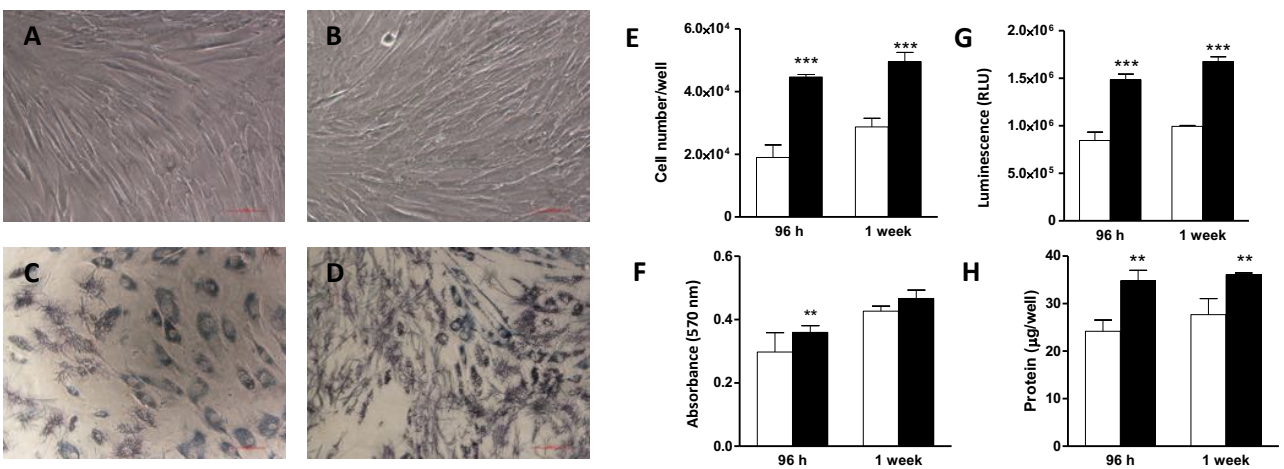

Fig. 1. ***A, B****) Microphotographs of primary human fibroblasts after 1 week of culture in the absence (A) or in the presence (B) of Polynucleotides (PN), observed at phase contrast. Magnification= 10 x.* ***C, D****) Microphotographs of primary human fibroblasts after 1 week of culture in the absence (C) or in the presence (D) of PN, after addition of MTT reagents. MTT creates blue needle-shape precipitates when it gets reduced to Formazan. Cells appeared more numerous in the presence of PN (B, D).* ***E****) Cells were also counted with a Coulter Counter at 96 h and 1 week of culture from stimulation. Cell number was significantly higher in the presence of PN. ***=p<0.001.* ***F****) Formazan deposits were solubilized and quantitated by absorptiometry at 96 h and 1 week of culture from stimulation. Viability levels were significantly higher in the presence of PN at 96 h of culture from stimulation. **=p<0.01.* ***G****) Cell viability was quantitated by Cell Titer GLO assay in the absence or in the presence of PN at 96 h and 1 week of culture from stimulation. Viability levels were significantly higher in the presence of PN at both time-points. ***=p<0.001. H) Protein content was also quantitated by Lowry assay in the absence or in the presence of PN after 96 h and 1 week of culture from stimulation. Protein levels were significantly higher in the presence of PN at 96 h and 1 week of culture from stimulation. **=p<0.01.*

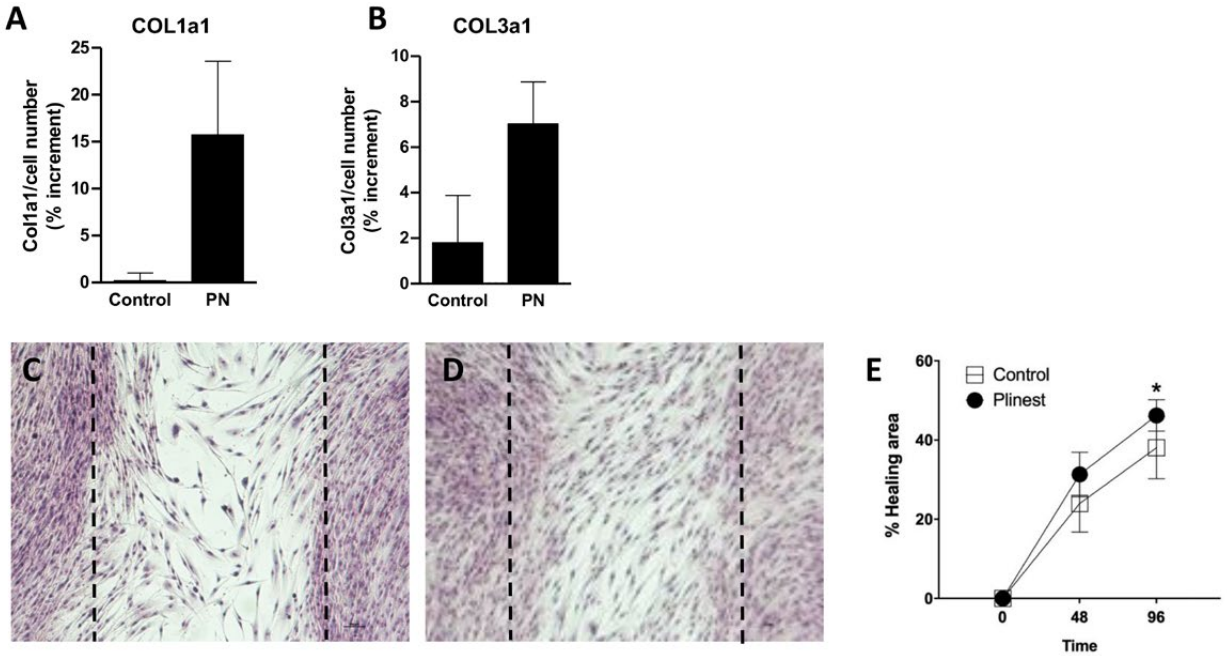

Fig. 2. *Histograms representing the expression of Collagen 1a1 (**A**) and Collagen 3a1 (**B**) in the culture supernatants of primary fibroblasts grown in the absence or in the presence of PN, as the ratio between the percent increase in Collagen production from 96 h to 1 week of culture from stimulation and the percent increase in cell number during the same time span. PN stimulated a higher expression of Collagen 1a1 and Collagen 3a1 compared to cell growth (A, B). **p<0.01. Transmitted light microphotographs of scratch test assay of (**C**) control cells and (**D**) cells stimulated with PN for 96 h of culture, stained with Giemsa protocol (Magnification 10 x). A visibly higher number of cells is bridging the scratch area in the presence of PN, as confirmed by (**E**) quantification of occupied area by a common image processing software at 3 time points.*

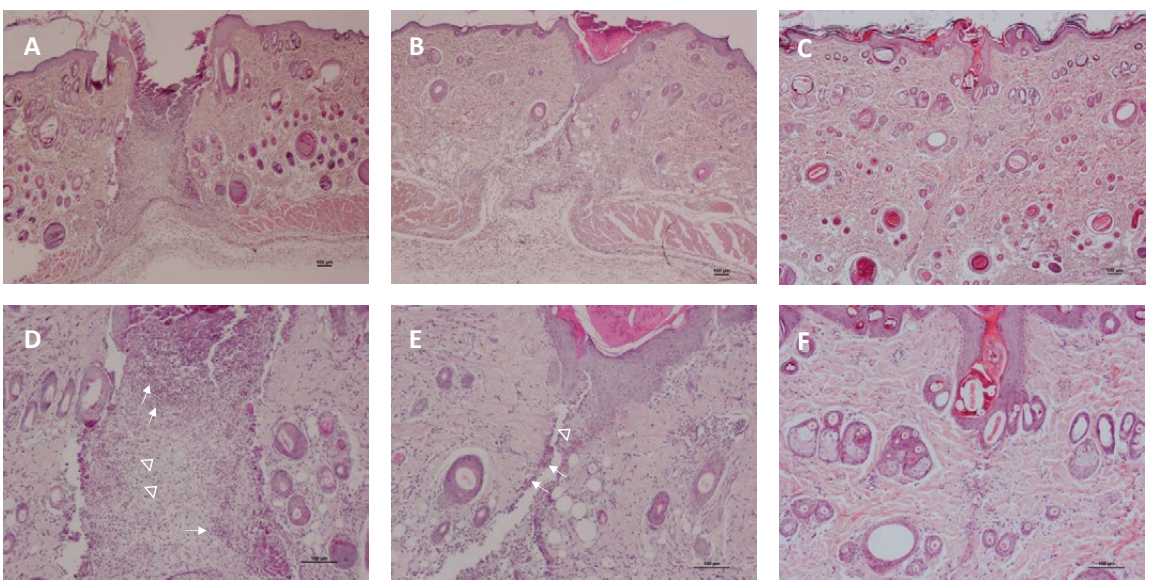

Fig. 3. *Microphotographs of healing wounds in the control (**A, D**), HA (**B, E**), and PN (**C, F**) group after Hematoxylin & Eosin staining. After incision in the dorsal skin of mice, wounds were sutured (control group) or HA or PN were inserted in the wound prior to suturing. The healing area is still visible in the control group, it is strongly reduced in the HA-treated animals and it almost completely disappeared in the PN-treated group 2 weeks after surgery. White arrows indicate the inflammatory infiltrate; white void arrowheads indicate the granulation tissue. Magnification = 4x (A, B, C) or 10 x (D, E, F).*

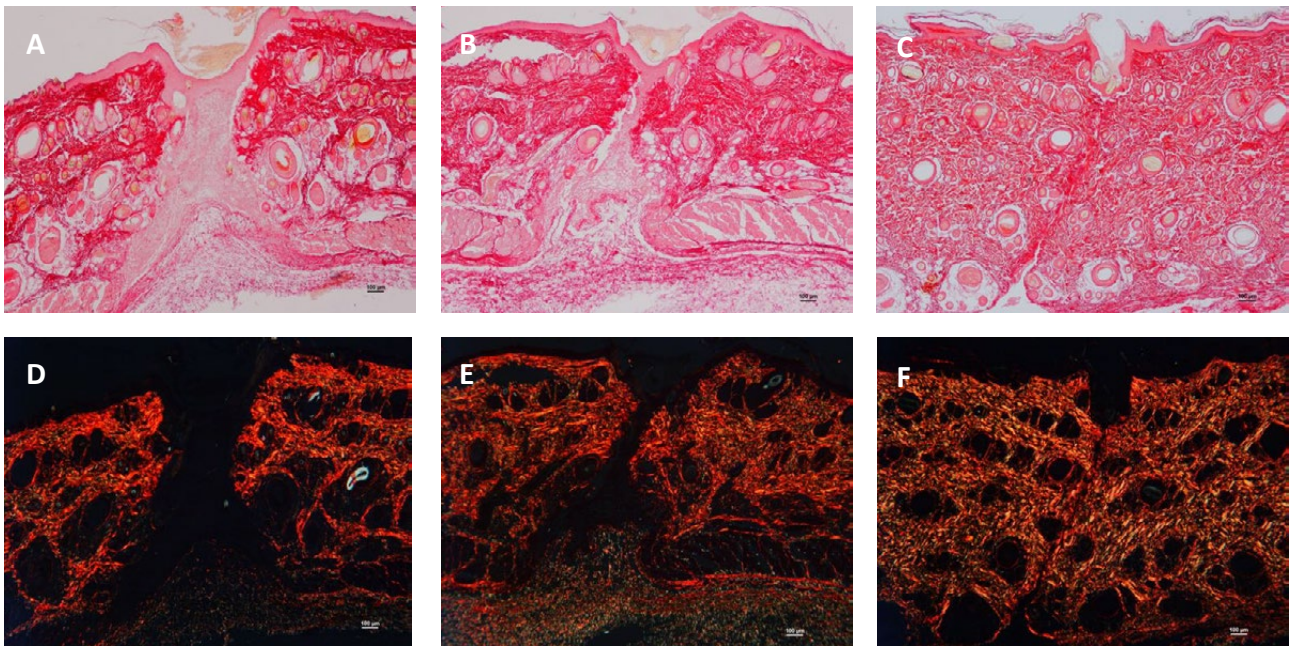

Fig. 4. *Microphotographs of healing wounds in the control (**A, D**), HA (**B, E**), and PN (**C, F**) group after Sirius Red staining for collagen at transmitted (A, B, C) or polarized light (D, E, F). The wounds are almost completely healed in the PN-treated group (C, F), and collagen fibers appear mature and well organized. This stands in stark contrast to the control group (A, D) where the defect is still devoid of collagen fibers or the HA-treated wounds (B, E), where the collagen fibers only partially occupy the healing tissue area. Magnification= 4x*

location of the wound. Histology failed to detect the persistence of polynucleotide gel inside the skin, due to its complete absorption. An abundant fibroblast population of normal appearance was also visible in the wound (Fig. 3F). Sirius Red staining was then used to disclose the deposition of extracellular matrix in and around the wound (Fig. 4). Polarized light observation was used to further enhance the appearance of the woven fibrils of collagen in the tissue (Fig. 4 D-F). No assembled mature fibrils were visible in the control wound tissue (Fig. 4 A, D), which appeared as a black gap separating the wound margins at polarized light (Fig. 3D). Similarly, although a signal reinforcement was observed in the margins of wounds treated with hyaluronic acid, where new matrix was being deposited, and although the gap in this group was significantly narrower than in the control group (Fig. 4E), a collagen-void area was still visible. In contrast, the wound margins appeared in contact in the PN-treated wounds and the continuity of the extracellular matrix was apparently restored. Only a band of signal reinforcement was visible along the wound line (Fig. 4C), and polarized light confirmed the still relative immaturity of the tissue in that area, where fibrils were still only partially organized (Fig. 4F).

DISCUSSION

Polynucleotides (PN) are a medical device gel made up of salified chains of deoxyribonucleic acids. Thanks to the abundance of polar functional groups (9), PN can attract and permanently bind water molecules. Polynucleotides are subject to physiological degradation by specific enzymes (endogenous DNases naturally present in tissues), which thus leads to the slow and progressive release of water molecules *in situ*. This process produces also oligonucleotides and free nucleotides, which are known to be physiologically present in the cell interstitium as degradation products (9). They can therefore be gradually and completely eliminated through a physiological cellular mechanism, which thus ensures the biocompatibility of the product.

Our results show that PN enhance fibroblast growth and viability *in vitro*. We observed a significant increase in cellularity in the treated cultures, using a selection of different methods, and promoted wound healing *in vitro*, as measured by scratch assay. Interestingly, our results also show that PN significantly stimulated the *in vitro* production of Collagen 1a1 and Collagen 3a1, two important isoforms of Collagen. The former, and more abundant form, Collagen 1a1, is the predominant isoform in mature tissues, whereas Collagen 3a1 is highly expressed during wound healing, and is remodeled and replaced by Collagen 1a1 as healing proceeds (10). Though the increase in Collagen production could indicate promotion of natural tissue repair, which could prove clinically important, e.g. to fill contracted or depressed spaces, an important concern with increasing Collagen deposition is the possibility of actually promoting fibrosis, a clinical situation where the physiological tissue structure is subverted by an excess of Collagen, which leads to functional and morphological impairment (11). To address these concerns, we also conducted an *in vivo* experiment by comparing PN effect with that of HA, a dermal filler widely used in aesthetic medicine, in a well-established model of dorsal sub-cutaneous pouch in mice. The effects of PN on Collagen expression are indeed visible at the histological analysis, as the polarized light analysis of Sirius Red-stained samples revealed that PN-treated tissues present a mature matrix, with well-organized Collagen fibers that have almost completely bridged the surgically-created gap, unlike the controls and the hyaluronic acid-treated group. The animal study therefore confirmed that PN not only create an environment that favors collagen deposition, but also indirectly promote its prompt recovery, without showing signs of fibrosis (Fig. 4).

REFERENCES

1. Sorg H, Tilkorn DJ, Hager S, Hauser J, Mirastschijski U. Skin wound healing: an update on the current knowledge and concepts. Eur Surg Res 2017; 58(1-2):81-94.
2. Cañedo-Dorantes L, Cañedo-Ayala M. Skin acute wound healing: a comprehensive review. Int J Inflam 2019; 2019:3706315.
3. Takeo M, Lee W, Ito M. Wound healing and skin regeneration. Cold Spring Harb Perspect Med 2015; 5(1):a023267.
4. Bainbridge P. Wound healing and the role of fibroblasts. J Wound Care 2013; 22(8):407-412.
5. Xue M, Jackson CJ. Extracellular matrix reorganization during wound healing and its impact on abnormal scarring. Adv Wound Care 2015; 4(3):119-36.
6. Nourian Dehkordi A, Mirahmadi Babaheydari F, Chehelgerdi M, Raeisi Dehkordi S. Skin tissue engineering: wound healing based on stem-cell-based therapeutic strategies. Stem Cell Res. Ther. 2019; 10(1).
7. Vanelli R, Costa P, Rossi SMP, Benazzo F. Efficacy of intra-articular polynucleotides in the treatment of knee osteoarthritis: A randomized, double-blind clinical trial. Knee Surgery, Sport Traumatol Arthrosc 2010; 18(7):901-7.
8. Cavallini M, Bartoletti E, Maioli L, et al. Consensus report on the use of PN-HPT™ (polynucleotides highly purified technology) in aesthetic medicine. J Cosmet Dermatol 2020; jocd.13679.
9. Hwang K-H, Kim J-H, Park EY, Cha S-K. An effective range of polydeoxyribonucleotides is critical for wound healing quality. Mol Med Rep 2018; 18(6):516-172.
10. Bainbridge P. Wound healing and the role of biomarkers and biofilms. J Wound Care 2013; 22(8):407-12.
11. Karsdal MA, Nielsen SH, Leeming DJ, et al. The good and the bad collagens of fibrosis – Their role in signaling and organ function. Adv. Drug Deliv. Rev. 2017; 121:43-56.

LETTER TO THE EDITOR

Functional recovery in subjects undergoing nasal surgery: a new therapeutic strategy

L. Maiolino[1], I. La Mantia[1], C. Grillo[1], Ct. Grillo[1] and G. Ciprandi[2]

[1]Clinica Otorinolaringoiatrica, Università degli Studi di Catania, Catania, Italy; [2]Allergy Clinic, Casa di Cura Villa Montallegro, Genoa, Italy

Received October 13, 2020 – Accepted December 16, 2020

To the Editor,

The histological layer covering the nasal cavities entails a series of strata in the craniocaudal sense: epithelial layer, basal membrane, lymphoid layer, glandular layer, and vascular layer (1). The epithelial component is the most sensitive to the traumatic damage induced by surgical interventions on the nasal area. The nasal mucosa is constituted by a pseudostratified richly vascularized, ciliated columnar epithelium, and includes numerous muciparous goblet cells and glands of the lamina propria (2). The nasal mucosa's importance entails the high functional specificity of its constituent elements, including inspired air climatization and filtration, defense against pathogens and pollutants, and olfaction. The different cellular and glandular elements are typically differentiated into i) ciliated columnar cells, arranged in the pseudostratified columnar epithelium, based on the double level stratification of the nuclei, with cilia that arise from the apical membrane, ii) non-ciliated cells, iii) muciparous goblet cells, producing mucus, with a defensive action, and with the well-developed endoplasmic reticulum, characterized by intense secretory activity, iv) basal cells, with modest shape and mitotic activity, and mucous glands. Nasal surgery frequently causes mucosal damage, which may have relevant functional consequences. Moreover, patients experience disturbing symptoms after sinonasal surgery (3). Consequently, the therapeutic strategy should be addressed to relieve symptoms and restore mucosal integrity and nose functions (4, 5). In this regard, a new multi-component medical device (Rinocross®; DMG Italia, Pomezia, Italy), containing D-panthenol, hyaluronic acid (HA), vitamin E, vitamin A, and biotin, has been proposed for the topical treatment of post-surgical complications. The device was tested on patients with atrophic rhinitis. The rationale of its use in patients who underwent sinonasal surgery is based on the multi-functional activities exerted by the different components which exert anti-inflammatory, antioxidant, repairing, hydrating, and lubricating activities. The current study therefore investigated the efficacy and safety of this compound's "eutrophic" property in patients who had undergone sinonasal surgery.

MATERIALS AND METHODS

The study enrolled 40 subjects (22 males and 18 females, aged between 21 and 59 years) subjected to various surgical interventions involving the nasal area. The patients were divided into two groups, A and B, each consisting of 20 people, which differed in the treatment methods following surgery. The study was performed according to the Helsinki Conference's ethical rules, and the internal review board approved the procedure. Each patient signed informed consent.

Key words: sinonasal surgery; treatment; D-panthenol; hyaluronic acid; vitamin A; vitamin E; biotin

Corresponding Author:
Prof. Giorgio Ciprandi,
Allergy Clinic,
Casa di Cura Villa Montallegro,
Genoa, Italy
e-mail: gio.cip@libero.it

0393-974X (2021)
Copyright © by BIOLIFE, s.a.s.
This publication and/or article is for individual use only and may not be further reproduced without written permission from the copyright holder.
Unauthorized reproduction may result in financial and other penalties
DISCLOSURE: ALL AUTHORS REPORT NO CONFLICTS OF INTEREST RELEVANT TO THIS ARTICLE.

Group A included patients subjected to septoplasty surgery (6 patients), turbinate decongestion surgery (8 patients), and nasal polypectomy surgery (6 patients), using functional endoscopic sinus surgery (FESS). Group A was treated with Rinocross® nasal spray, two sprays per nostril, two times a day for one month.

Group B included patients who underwent septoplasty surgery (5 patients), turbinate decongestion surgery (9 patients), and nasal polypectomy surgery, using FESS (6 patients). Group B was treated with saline isotonic solution nasal spray, two sprays per nostril, two times a day for one month.

At baseline (T0), the investigators performed: anamnestic assessment, administration of a specific questionnaire, with subjective evaluation scale by visual analogic scale (VAS) of nasal obstruction, nasal dryness, hyposmia/anosmia, and presence of epistaxis. Investigators performed nasal endoscopy, anterior rhinomanometry, and mucociliary transport time. The score obtained by the VAS was categorized in 5 severity grades: 0= absent; 1-2= mild; 3-5= moderate; 6-8= severe; 9-10= very severe. At the end of the treatment (T1), investigators re-evaluated the patients performing the same procedures.

The statistical analysis was performed using the *chi*-squared test. With a p-value less than 0.05, the differences were selected as significant, and Graphpad analyzed data.

RESULTS

Baseline data (T0)

Endoscopic findings. In Group A, 5 (15%%) patients had mild mucosal hyperemia, 8 (40%) moderate, and 7 (35%) intense hyperemia. One patient (5%) had mild septal deviation, 3 (15%) moderate, and 2 (10%) intense septal deviation. Two patients (10%) had mild turbinate hypertrophy, 3 (15%) moderate, and 3 (15%) intense turbinate hypertrophy. Two patients (10%) had moderate polyposis, and 4 (20%) intense polyposis. In Group B, 3 (25%%) patients had mild mucosal hyperemia, 8 (40%) moderate, and 9 (45%) intense hyperemia. Two patients (10%) had mild septal deviation, 3 (15%) moderate, and 3 (15%) intense septal deviation. Five patients (25%) had mild turbinate hypertrophy, 2 (10%) moderate, and 1 (1%) intense turbinate hypertrophy. Four patients (20%) had moderate polyposis.

Anterior rhinomanometry. In group A, 5 (25%) patients had mild reduction of nasal airflow (700-870 cm^3/sec), 6 (30%) had moderate (500-700 cm^3/sec), and 9 (45%) severe nasal obstruction (300-500 cm^3/sec). After decongestion with an adrenergic agent, 3 patients had moderate, and 9 had severe obstruction. In Group B, 8 (40%) patients had a mild reduction of nasal airflow, 6 (30%) had moderate, and 6 (30%) severe nasal obstruction. After decongestion with an adrenergic agent, 6 patients had moderate and 6 had severe obstruction.

Mucociliary clearance. In Group A, the mucociliary clearance time was mildly reduced (17.1 minutes) in 7 patients, moderately (18.8 min) in 9, and intensely (19.2 min.) reduced in 4 patients.

In Group B, the mucociliary clearance time was mildly reduced (17.6 minutes) in 5 patients, moderately (18.5 min) in 11, and intensely (19.7 min.) reduced in 4 patients.

Symptom perception. In Group A, the nasal obstruction was evaluated as mild by 5 (25%) patients, moderate by 9 (45%), intense by 5 (25%), and severe by 1 (5%) patient. The nasal dryness was considered mild by 2 (10%) patients, moderate by 12 (60%), intense by 3 (15%), and severe by 3 (15%) subjects. The olfaction impairment was evaluated mild by 6 (30%) patients, moderate by 8 (40%), and intense by 6 (30%) patients. Epistaxis was considered mild by 5 (25%) patients and moderate by 1 (5%) patient. In Group B, the nasal obstruction was evaluated as mild by 7 (35%) patients, moderate by 9 (45%), and intense by 4 (20%) patients. The nasal dryness was considered mild by 5 (25%) patients, moderate by 9 (45%), intense by 4 (20%), and severe by 2 (10%) subjects. The olfaction impairment was evaluated mild by 7 (35%) patients, moderate by 10 (50%), and intense by 3 (15%) patients. Epistaxis was considered mild by 3 (15%) patients and moderate by 2 (10%) patients.

End of treatment data (T1)

Endoscopic findings. In Group A, 2 (10%) patients had mild mucosal hyperemia, and 1 (5%) moderate hyperemia. In Group B, 1 (5%%) patient had mild mucosal hyperemia, 3 (15%) moderate, and 1 (5%) intense hyperemia.

Anterior rhinomanometry. In group A, 1 (5%) patients had a mild reduction of nasal airflow, and 1

(5%) patients had a moderate nasal obstruction. In Group B, 2 (10%) patients had a mild reduction of nasal airflow, and 1 6 (5%) had a moderate nasal obstruction.

Mucociliary clearance. In Group A, the mucociliary clearance time was normal (13.9 min) in 16 patients and moderately (18.1 min) reduced in 4 patients. In Group B, the mucociliary clearance time was mildly reduced (17.1 min) in 9 patients, and moderately (18.3 min) in 11 patients.

Symptom perception. In Group A, the nasal obstruction was evaluated as mild by 9 (45%) patients, moderate by 7 (35%), intense by 3 (15%), and severe by 1 (5%) patient. The nasal dryness was considered mild by 2 (10%) patients and moderate by 3 (15%) subjects. The olfaction impairment was evaluated mild by 10 (50%) patients, moderate by 6 (30%), and intense by 4 (20%) patients. No patient reported epistaxis. In Group B, the nasal obstruction was evaluated as mild by 2 (10%) patients and moderate by 3 (15%) patients. The nasal dryness was considered mild by 3 (15%) patients, moderate by 3 (15%), and intense by 1 (5%) subject. The olfaction impairment was evaluated mild by 3 (15%) patients and moderate by 5 (25%) patients. No patient reported epistaxis.

Intergroup comparison. Nasal endoscopy findings improved more significantly ($p=0.009$) in Group A than in Group B, nasal airflow increased ($p=0.008$) in Group A than in Group B, the mucociliary transport time more significantly improved ($p<0.01$) more in Group A than in Group B, nasal obstruction was more significantly reduced ($p<0.0001$) in Group A than in Group B, nasal dryness was more significantly improved ($p=0.008$) in Group A than in Group B, and olfaction more significantly improved ($p<0.0001$) in Group A than in Group B.

All treatments were well-tolerated by all patients, and no clinically relevant adverse events were reported.

DISCUSSION

Surgical trauma can induce clinical consequence attributable to the mucosa's structural "fragility" and the impaired nasal functions associated with surgical wounds. The symptom severity and functional impairment are related to the surgery abrasiveness; in fact, FESS is scarcely demolitive, thus safeguarding the nose's structural and functional structures also in children (6).

In the post-surgical period, treatment aims to restore the structural and functional integrity of the nasal mucosa. Various types of treatment have been proposed over time, using the compounds available at that time. A revolution in the field of epithelial eutrophism has been offered by HA, the main constituents of the extracellular matrix, endowed with numerous hygroscopic, rheological, and viscoelastic properties (7). HA modulates the cascade of inflammatory events, provides antioxidant activity and dampens cytokine overload (8). HA also exerts an intense tissue repair activity, achieved by cellular migration and proliferation. HA limits collagen's conversion from soluble to an insoluble form, representing a lubricating factor capable of promoting the fibrous component's sliding. The tested medical device contains other components able to repair and restore the damaged mucosa, namely D-panthenol (9), vitamin E (10), vitamin A (11), and biotin (12).

The current study showed that the new multi-component medical device significantly improved the macroscopic features, nasal airflow, mucociliary transport time, and symptom perception in patients who underwent sinonasal surgery. Moreover, Rinocross® nasal spray was significantly more effective than a comparative compound. The efficacy was also associated with optimal safety as the new medical device was well-tolerated by all patients, and no clinically relevant adverse events occurred during the intranasal administration period. On the other hand, this study has some limitations, including the open design, the lack of biomarker assessment, and the limited number of enrolled patients, therefore, the outcomes should be considered as preliminary. Consequently, further studies should be performed to bridge these gaps. In conclusion, the new multi-component medical device could be a promising treatment for patients after sinonasal surgery as it provided rapid symptom relief, mucosal repairing, and functional restoring.

REFERENCES

1. Moon KC, Han SK. Surgical anatomy of the

Asian nose. Facial Plast Surg Clin North Am 2018; 26(3):259-68.
2. Lund VJ, Stammberger H, Fokkens WJ, et al. European position paper on the anatomical terminology of the internal nose and paranasal sinuses. Rhinol Suppl 2014; 24:1-34.
3. Bruggers S, Sindwani R. Evolving trends in powered endoscopic sinus surgery. Otolaryngol Clin North Am 2009; 42:789-98.
4. Talmadge J, Nayak JV, Yao W, Citardi MJ. Management of postsurgical empty nose syndrome. Facial Plast Surg Clin North Am 2019; 27(4):465-75.
5. Bergmark RW, Gray ST. Surgical management of turbinate hypertrophy. Otolaryngol Clin North Am 2018; 51(5):919-28.
6. Shay SG, Valika T, Chun R, Rastatter J. Innovations in endonasal sinus surgery in children. Otolaryngol Clin North Am 2019; 52(5):875-90.
7. Gelardi M, Taliente S, Fiorella ML, et al. Ancillary therapy of intranasal T-LysYal for patients with allergic, non-allergic, and mixed rhinitis. J Biol Reg Homeost Ag 2016;30:99-106.
8. Krasinski R. Hyaluronan-mediated regulation of inflammation Postepy Hig Med Dosw 2009; 19:61:683-9.
9. Proksch E, de bony R, Trapp S, Boudon S. Topical use of dexpanthenol: a 70th-anniversary article. J Dermatol Treat 2017; 28:766-73.
10. Khadangi F, Azzi A. Vitamin E - the next 100 years. IUBMB Life 2019;71(4):411-15.
11. Polcz ME, Barbul A. The Role of Vitamin A in Wound Healing. Nutr Clin Pract 2019; 34(5):695-700.
12. Mock DM. Biotin: From nutrition to therapeutics. J Nutr 2017; 147(8):1487-92.

JOURNAL OF BIOLOGICAL REGULATORS & HOMEOSTATIC AGENTS Vol. 35, no. 1, 367-370 (2021)

LETTER TO THE EDITOR

Sagittal spine alignment and postural balance in pre-puberty age: a multidisciplinary and multi-professional rehabilitative point of view

T. Paolucci[1], F. Agostini[2], M. Mangone[2], A. Bernetti[2], B. Cordiani[3], R.G. Bellomo[4], R. Saggini[1] and C. Villani[2]

[1]Department of Medical Science and Oral Biotechnology, G. D'Annunzio University of Chieti-Pescara, Italy; [2]Department of Anatomical and Histological Sciences, Legal Medicine and Orthopedics, Sapienza University of Rome, Italy; [3]Department of Ophthalmology and Ocular Surgery, Britannico Hospital, Rome, Italy; [4]Physical Medicine and Rehabilitation, Carlo Bò University of Urbino, Urbino, Italy

Received October 27, 2020 – Accepted January 11, 2021

To the Editor,

What is the correct alignment of the spine functional to postural control in healthy children? Can we say that it exists? Lee CS et al. suggested that there is a significant variability in sagittal profile of the cervical spine in asymptomatic children, and cervical kyphosis was found in approximately 40% of their study cohort (1). Moreover, predicating "abnormal" to lordosis and kyphosis values alone, without considering overall sagittal balance, is incorrect, considering that there is a slight tendency for thoracic kyphosis (TK) and lumbar lordosis (LL) to increase with age (2). TK and LL are also in balance with each other in normal standing posture so that the minimal amount of energy is used for maintaining posture (3). The differences between normal and pathologic curvatures of the spine are less clear in the sagittal plane than in the coronal plane, especially in children (4-6). Postural control is also a very complex matter that involves multiple control channels. Postural stability and adjustments are thought to be associated not only with age, but also by sensory maturation. Within typical (asymptomatic) sensory development, sensory maturation occurs first within the visual system, followed by the proprioceptive system, and then finally, the vestibular system, reaching functional maturity between nine and twelve years of age, when the ability to perform anterior-posterior adjustments becomes evident (7, 8). In the literature, some studies emphasize the importance of dental malocclusion alterations and their correlation in postural imbalance, both on the sagittal and frontal surfaces of the spine. The hypothesis supports that dental vertical occlusal alteration could influence stress distribution in the cervical columns, including a malfunction of the temporomandibular joint (TMJ). Other studies suggest prudence regarding this hypothesis as it could not conclusively associate dental occlusion to an instantaneous impact on the postural body changes. It is also known that latent strabismus can affect both postural control and postural alignment (7). Considering these premises, the relationship between balance and sagittal spine alignment, in particular, have been poorly investigated in pre-puberty age considering a global postural approach point of view. Thus, the aim of this research was to investigate how important the sagittal spine alignment in postural control is in pre-puberty age (primary outcome) and the interference

Key words: pediatric; posture; vision; rehabilitation; lordosis

Corresponding Author:
Teresa Paolucci MD,
Department of Medical Science and Oral Biotechnology,
G. D'Annunzio University of Chieti-Pescara,
via dei Vestini, 32, 66013 Chieti, Italy
Tel.: +39 3404751090
e-mail: francescoagostini.ff@gmail.com

0393-974X (2021)
Copyright © by BIOLIFE, s.a.s.
This publication and/or article is for individual use only and may not be further reproduced without written permission from the copyright holder.
Unauthorized reproduction may result in financial and other penalties
DISCLOSURE: ALL AUTHORS REPORT NO CONFLICTS OF INTEREST RELEVANT TO THIS ARTICLE.

with other postural control systems such as vision and TMJ (secondary outcome).

MATERIALS AND METHODS

An observational cross-sectional studies study was carried out in accordance with the STROBE guidelines: healthy children between the ages of 8 and 12 years were enrolled in the study from June 2016 to June 2017 at the Physical and Rehabilitative Medicine inpatients clinic of the Umberto I University Hospital in Rome. The children were recruited after a physiatrist examination of the child's posture, sent by the pediatrician for the annual postural screening. The inclusion criteria were: age from 8 to 12 years, pre-puberty age (menarche in females and age less than 12 in males). The exclusion criteria were: connective or ligament laxity, scoliosis, acute or chronic spine pain, other postural disorders, menarche in females, vestibular disorders, and use of orthotics correction for flat foot, cognitive or neurological disorders. The children were divided into two groups based on the presence or absence of lumbar hyperlordosis; the postural examination and the presence of hyperlordosis was clinically performed by a physician-physiatrist experienced in disorders of the spine. All participants and parents signed informed consent forms after receiving detailed information about the aims of the study. The study respected the procedures per the Declaration of Helsinki and the rights of human subjects involved in the study were protected. The protocol study was approved by the Ethics Committee of Umberto I University Hospital in Rome.

Measurements

Age, height, weight, and Body Mass Index (BMI) were measured by the physiatrist upon entry into the study. A clinical examination was performed to exclude scoliosis or other postural disorders. After enrolment in the study, the participants underwent vision examination, stomatognathic evaluation, clinical postural evaluation and a stabilometric test to assess balance control in quiet stance.

Visual test

The ophthalmologist observed any possible presence of latent strabismus and measured the visual acuity. The cover test was used to define the presence and amount of ocular deviation as latent strabismus. The children enrolled in the study had no corrections with lenses already in use.

Temporomandibular joint evaluation

The temporomandibular joint (TMJ) evaluation included the measurement of the maximal opening of the mouth (vertical incisal edge difference) in cm. Values were classified according to the classification of Helkimo for impaired vertical mobility: 30–39 mm slightly impaired movement, ≤ 29 mm severely impaired movement, ≥ 40 mm normal range of movement.

Stabilometry test

Stabilometry measures the average result of body oscillations expressed as Center of Pressure (CoP) displacement. Data were collected using a baropodometric platform (software Milletrix System-Pedissence) to perform the CoP oscillations, sway area, length, and velocities of CoP for open eyes (OE) and closed eyes (CE) conditions. The stabilometry test was performed collecting the position of CoP during quiet standing and the measurement lasted for 51.2 seconds (Fig. 1). After being informed about the test procedure, participants were instructed to stand erect but not at attention, with arms along the trunk and feet at an angle of about 30 degrees open to the front and the heals approximately 3 cm apart. In the OE condition, subjects fixated on a mark on the wall at a distance of 1.5 m at eye level. The test order, OE/CE, was randomized. In order to minimize any external disturbances or cues for the test subjects, the environment was brightly lit naturally and very quiet. The test was performed by the physiatrist. No relevant adverse event occurred during test detection (9-11).

Postural evaluation of alignment on the sagittal plane of the spine

The measurement of the arrows on the sagittal plane is obtained by measuring the linear distance in millimetres between the thoracic apical vertebra of C7, T12 and L3 and the lead wire tangent to the apex of the physiological dorsal kyphosis (Fig. 1). Children were asked to stay in a natural straight standing position and palpation identification of spinous processes in the spine were made by the physician. It was decided to adopt a simple measurement test, easily reproducible and safe, according

to Stagnara, the values at C7 and L3 levels should be between 25 and 40 mm (6). A clinical diagnosis of lumbar hyperlordosis was then made by a doctor with expertise in spine disorders, also referring to the measurement of the arrows on the sagittal plane. No X-rays of the column were repeated for the current study. If the parents already had previous X-rays of the spine, they were visualised by the doctor.

Statistical analysis

Data were reported in terms of mean and standard deviation. Demographical and clinical continuous parameters were compared using two-tailed unpaired Student's *t*-test. Pearson coefficient was used to test the correlation between stabilometric parameters and anthropometric measures. The same coefficient was also used to test the correlation between ages, stature and stabilometric parameters. Differences among cover classes, these classes being an ordinal value, were tested using nonparametric Kruskall Wallis analysis: considering *orthophore* = 0 (Cover test =0, no strabism) while *exophoria* or *esophoria* (Cover test 1= esophoria, Cover test 2= exophoria) for presence of ocular latent deviation. For all the tests, the alpha level of significance was set at 0.05 (12).

RESULTS

Twenty-five children (15 males, 10 females) without lumbar hyperlordosi and 25 children (16 males, 9 females) with lumbar hyperlordosis were enrolled in this study. Tables I and II show demographical and clinical data for the two groups of children. Significant correlations were found between anthropometric measures and stability. Specifically, mandibular mobility, compared to the measurement of the maximum vertical mouth opening, was found significantly correlated in OE condition with the length of CoP (R= -0.372, p=0.008) and with mean velocity of CoP oscillation (R=-0.384, p=0.006). No significant results were found in CE condition, leading to significant correlations and with the Romberg Index (RI) of these two parameters (R=0.286,

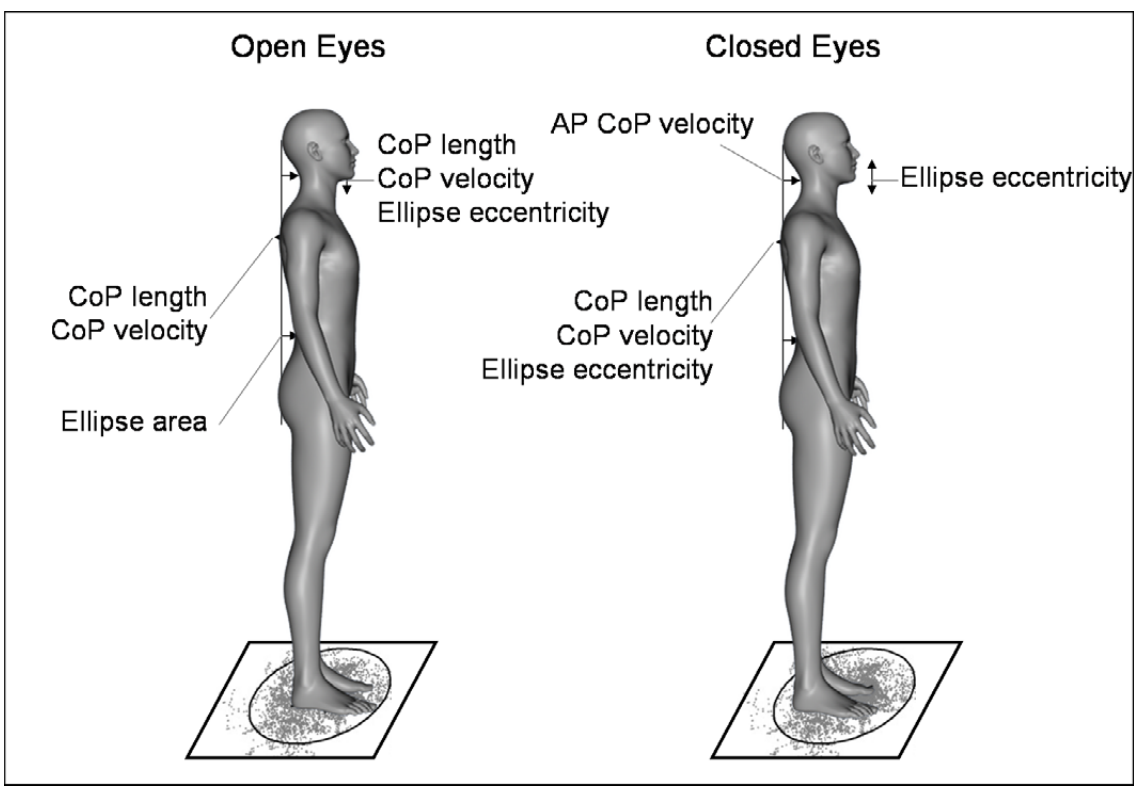

Fig. 1. *Stabilometric parameters and anthropometric measures. Significant correlations were found between anthropometric measures and postural stability.*

p=0.044 and R=0.319, p=0.024, respectively). The maximal opening of the mouth was also found significantly correlated in both conditions with the eccentricity of the ellipse (R=0.336, p=0.017 in OE condition and R=0.468, p=0.0007 in CE condition). Considering the measurements of the spine arrows on the sagittal plane, the dorsal arrow was found significantly correlated with length of CoP both in OE and CE (R=-0.336, p=0.017 and R=-0.295, p=0.037, respectively). Similar results were found for the correlation with the mean velocity of oscillation (R=-0.350, p=0.013 and R=-0.360, p=0.010, respectively). The dorsal arrow was also found significantly correlated with the eccentricity in OE (R=0.414, p=0.003). The lumbar arrow resulted significantly correlated with the area of ellipse in OE (R=0.319, p=0.024) (Fig. 2). The cervical arrow resulted significantly correlated with the mean velocity of CoP only along antero-posterior axis in CE condition (R=-0.304, p=0.032). Regarding vision results, the area of ellipse resulted significantly different among the three Cover classes in CE condition (p=0.028), resulting also in a significant effect of Covert class on the RI of area (p=0.018). No gender differences were detected among the stabilometric parameters. Conversely, significant correlations for age were found with mean velocity of CoP in CE condition (R=0.292, p=0.039) and with eccentricity index in OE condition (R=-0.281, p=0.048). BMI was found significantly related with eccentricity index in both conditions (OE: R=0.317, p=0.0249; CE: R=0.347, p=0.0147) and with the mean velocity of CoP oscillation in OE condition (R=-0.337, p=0.0166).

DISCUSSION

The aim of this research was to investigate whether and how an early asymptomatic alteration of the sagittal profile of the spine in pre-puberty age, can influence postural control in a quiet state, and the results showed an interesting correlation between anthropometric measures and postural stability. The proprioceptive system in maintaining spinal alignment and balance has a central role in preventing juvenile idiopathic scoliosis, and dorsal kyphosis is often a compensation of lumbar hyperlordosis. As the present results suggest, this compensation is not purely biomechanical but also proprioceptive. The results suggest that an initial increase likely leads to compensations in the upper portions of the spine, such as increased dorsal kyphosis, with greater energy expenditure in postural control (increase the CoP area of ellipse and velocity

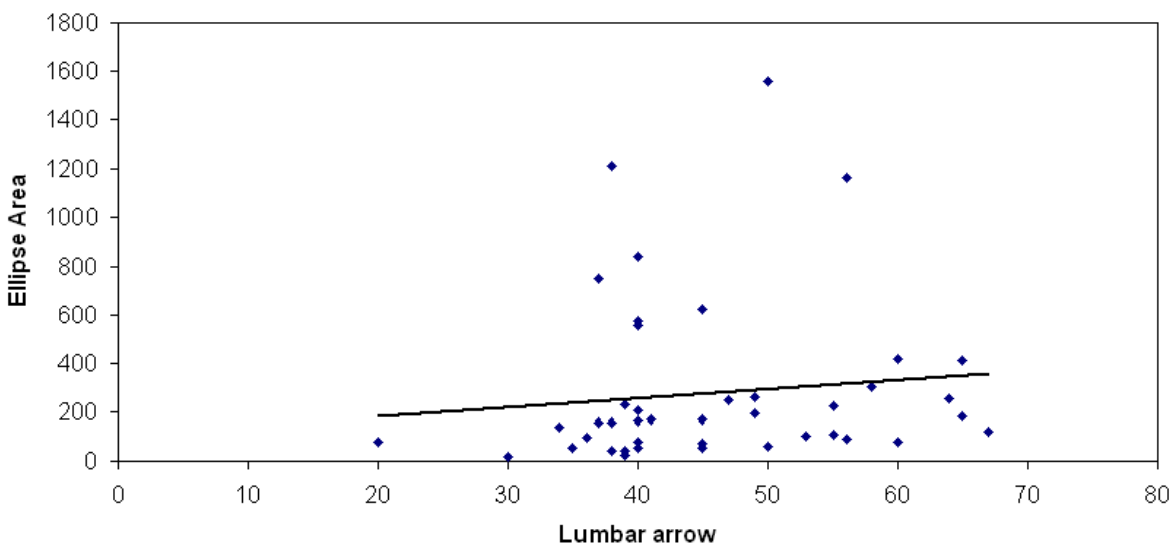

Fig. 2. *Correlation between lumbar arrow and area of ellipse in open eyes (OE) condition.*

of oscillation). It is therefore important to observe, in advance, the correct harmony of the curves of the spine on the sagittal plane in order to prevent future postural disorders Moreover, the non-invasive postural clinical examination, according to the measurement of the sagittal spine arrows, could be a good screening method in this age group (8-12 years) to detect alterations of the column alignment early. When the lumbar arrow is greater than the criteria indicated by Stagnara (> 40 mm), the postural system would seem to become more unstable by increasing the CoP surface and the velocity of the oscillations. This complex interaction derived by sensory input and adapted motor output needS future investigation in quiet stance and in dynamic conditions in pre-puberty age. This result focused attention on the fact that in children an unstructured postural disorder may be related to other subsystems that interact with

Table I. *Mean and standard deviations for the children without lumbar hyperlordosis (15 females and 10 males), and those with lumbar hyperlordosis (16 females and 9 males).*

Parameters	**Children without lumbar hyperlordosis**	**Children with lumbar hyperlordosis**	p-value
Age (years)	10.04±1.02	10.00±0.76	0.876
Males / females	15/10	16/9	-
Stature (m)	1.44±0.06	1.46±0.05	0.229
Weight (kg)	35.6±4.4	37.0±5.4	0.307
Body mass Index (kg/m^2)	17.1±1.8	17.3±2.2	0.804
Lumbar Arrow (mm)	37.4±4.4	53.0±8.0	**<0.001**
Dorsal Arrow (mm)	36.4±9.5	48.4±9.7	**<0.001**
Cervical Arrow (mm)	33.1±6.9	38.0±6.0	**0.010**
Vertical opening mouth (cm)	4.7±0.6	4.5±0.5	0.272

The last columns report the p-value of two-tailed unpaired t-test performed between the two groups (in bold if statistically significant); (C7 and L3 levels should be between 25 and 40 mm).

Table II. *Stabilometry parameters: mean and standard deviation.*

Stabilometry Data		Children without lumbar hyperlordosis		Children with lumbar hyperlordosis		p*
		Mean	±SD	Mean	±SD	
Sway area (mm^2)	OE	253.15	±119.51	294.41	±153.91	ns
	CE	177.89	±114.30	185.79	±114.99	ns
Length of the path (mm)	OE	875.90	±280.43	1038.24	±306.89	ns
	CE	828.91	±353.78	994.73	±485.09	ns
Velocities (m/sec)	OE	18.65	±13.93	19.85	±16.35	ns
(CoP)	CE	19.01	±14.43	19.49	±15.41	ns
Romberg Index		112.31	±152.60	118.49	±110.91	ns

p>0.05: No statistically significant difference between the two groups for unpaired Student's t-test; open eyes (OE) and closed eyes (EC).

posture control.. Results from the present study could be used as an aid for planning appropriate therapy in pre-puberty growth phase with spinal malalignment in order to restore a relatively healthy posture (3, 5, 7). A limitation of our work is that lateral deviation and protrusion were not considered because there were no cross bites.

ACKNOWLEDGEMENTS

The Authors thank Dr. Marco Iosa and Dr. Giovanni Morone, from Fondazione Santa Lucia IRCCS (Rome, Italy) for their contribution.

REFERENCES

1. Lee CS, Noh H, Lee DH, Hwang CJ, Kim H, Cho SK. Analysis of sagittal spinal alignment in 181 asymptomatic children. J Spinal Disord Tech 2012; 25(8):E259-63.
2. Lippi L, de Sire A, Desilvestri M, Baricich A, et al. Can scoliosis lead to spinal cord ischaemia? Early diagnosis and rehabilitation: A paradigmatic case report and literature review. J Back Musculoskelet Rehabil 2020; DOI: 10.3233/bmr-200070
3. Scaturro D, de Sire A, Terrana P, et al. Adolescent idiopathic scoliosis screening: Could a school-based assessment protocol be useful for an early diagnosis? J Back Musculoskelet Rehabil 2020 DOI: 10.3233/bmr-200215
4. Bellomo RG, Pezzi L, Paolucci T, Porreca A, Saggini R. Primary school screening of flatfoot in 6-year-old children: a descriptive study to plan a rehabilitative approach. J Biol Regul Homeost Agents 2020; 34(1):297-303.
5. Paolucci T, Pezzi L, Mannocci A, La Torre G, Bellomo RG, Saggini R. Flat foot and postural harmony in 6-year-old Caucasians: What is their relationship? Ann Rehabil Med 2020; 44(4):320-26.
6. Mangone M, Paoloni M, Procopio S, et al. Sagittal spinal alignment in patients with ankylosing spondylitis by rasterstereographic back shape analysis: an observational retrospective study. Eur J Phys Rehabil Med 2020; 56(2):191-96.
7. Paolucci T, Piccinini G, Iosa M, Piermattei C, De Angelis S, Zangrando F, Saraceni VM. The importance of trunk perception during brace treatment in moderate juvenile idiopathic scoliosis: What is the impact on self-image? J Back Musculoskelet Rehabil 2017; 30(2):203-10.
8. Murgia M, Bernetti A, Delicata M, et al. Inter- and intra-interviewer reliability of Italian version of Pediatric Evaluation of Disability Inventory (I-PEDI). Ann Ig 2018; 30(2):153-61.
9. Mangone M, Bernetti A, Agostini F, et al. Changes in spine alignment and postural balance after breast cancer surgery: a rehabilitative point of view. Biores Open Access 2019; 8(1):121-28.
10. Damiani C, Mangone M, Paoloni M, et al. Trade-Offs with Rehabilitation Effectiveness (REs) and Efficiency (REy) in a sample of Italian disabled persons in a in post-acuity rehabilitation unit. Ann Ig 2020; 32(4):327-35.
11. Seccia R, Boresta M, Fusco F, et al. Data of patients undergoing rehabilitation programs. Data Brief 2020; 30:105419.
12. Paolucci T, Bernetti A, Sbardella S, et al. Straighten your back! Self-correction posture and postural balance in "non rehabilitative instructed" multiple sclerosis patients. Neuro Rehabilitation. 2020; 46(3):333-41.

LETTER TO THE EDITOR

A new concept radiofrequency device for the treatment of cellulite

P. Amori[1], G. Vitiello[1], A. Cancelli[2], R. Sadoughifar[3,4], M. Tirant[5], N. Van Thuong[5], K.M. Lomonosov[6] and T. Lotti[1,6]

[1]Department of Dermatology, University of Rome G. Marconi, Rome, Italy; [2]LET'S – ISTC- CNR, Rome Italy; [3]Institute of Dermatologic and Regenerative Sciences, Florence, Italy; [4]Bidar Skin Center, Teheran, Iran; [5]Hanoi Medical University, Department of Dermatology, Hanoi, Vietnam; [6]Department of Dermatology and Venereology, I.M. Sechenov First Moscow State Medical University, Moscow, Russia

Received August 3, 2020 – Accepted January 14, 2021

To the Editor,

As known, the so-called "cellulite" affects a great percentage of women worldwide. To treat this condition, which in itself is bound to worsen over the years, there are many current treatments, in addition to the common recommendations such as lifestyle changes, appropriate diet, exercise and weight control. The different therapeutic approaches available can be classified into topical (for example products containing methylxanthines, retinol, and botanical derivatives), massage (performed manually or by means of devices, to promote lymphatic drainage and improve the microcirculation of the subcutaneous tissue), pharmacological (oral treatment), non-invasive (acoustic waves, radiofrequency, infrared light and intense pulsed light, ultrasound, cryolipolysis) and minimally invasive (carboxytherapy, mesotherapy, subcision) (1-3). Among these, there is a technology based on the application of radiofrequency energy (RF). Moreover, this technology is also normally used to treat abdominal laxity and any fat local accumulation, having a positive action on the adipocyte metabolism and stimulating production of new collagen.

A new device, based on the application of radiofrequency energy, which seems innovative and very promising, has just been made available on the market. This device, unlike other RF-based technology delivering only a single signal, is able to simultaneously deliver 4 different RF signals, optimizing the deepness level and massively increasing the efficacy of the energy interacting in 4 different ways with different tissues. The four signals have frequencies of 0.4 MHz; 0.9 MHz; 1.3MHz; 2.4 MHz, respectively, and they are managed by the algorithm of the technology crosslinking the signals in function of the purpose. With this technology, it is therefore possible that the applied energy reaches four different depths simultaneously, which is not possible with other devices.

The purpose of this study, intended as a preliminary study, is to clinically evaluate whether this equipment allows to obtain appreciable results.

MATERIALS AND METHODS

Twenty cellulite patients aged between 30 and 60 years were enrolled in the study. Exclusion criteria were those commonly adopted as contraindications to skin treatments with RF (pacemaker wearers, skin infections, etc.). All patients were recommended, for the entire duration of the study, not to change their own usual lifestyle. Before recruitment, each patient signed informed consent.

Firstly, a clinical assessment of each patient's cellulite

Key words: cellulite; radiofrequency; tetra-wave; multi-wave; medical aesthetics; regenerative medicine

Corresponding Author:
Dr Roxanna Sadoughifar,
Bidar Skin Center,
Apt 9.29. Bidar street,
Fereshteh Ave, Tehran
Tel.: +98 22049547
e-mail: bidarskincenter@gmail.com

0393-974X (2021)
Copyright © by BIOLIFE, s.a.s.
This publication and/or article is for individual use only and may not be further reproduced without written permission from the copyright holder.
Unauthorized reproduction may result in financial and other penalties
DISCLOSURE: ALL AUTHORS REPORT NO CONFLICTS OF INTEREST RELEVANT TO THIS ARTICLE.

grade was performed, according to the Nürnberger-Müller grading scale. This assessment showed 3 patients in grade I, 9 in grade II and 8 in grade III. Each patient also underwent an ultrasound assessment (Hitachi Aloka Medical ProSound F75, Olympus Corporation, Tokyo, Japan) of the legs, performed on the thigh, knee and ankle area, using a 15 MHz probe. The same evaluation was repeated, for each patient and in the same way, at the end of the treatment. As is known, this allows the effectiveness of the treatment to be objectively assessed, by measuring the thickness of the subcutaneous tissue (4). Before treatment, the leg circumference was bilaterally measured. In fact, the measurement of leg circumference has long been used to evaluate any improvements in cellulite therapy (3, 5). In addition, photographs of each patient were taken in standard projections. Finally, a questionnaire was submitted to each patient, before and after the treatment, to evaluate the perception of the appearance of the area affected by cellulite, and of the presence of feelings of heaviness or tenderness in the legs. The feeling of heaviness is certainly a subjective fact, but it represents one of the symptoms that push patients to consult a healthcare professional. Therefore, the persistence, reduction or disappearance of this sensation is in any case an indicator, albeit subjective, of the degree of satisfaction of the treatment by the patients.

Each patient underwent 10 sessions of application of radiofrequency energy, by an Italian device named Thuzzle® (GMV, Rome, Italy). The energy was supplied by a handpiece identified as TetraWave handpiece, since it is able to deliver 4 electromagnetic waves simultaneously, each one different from the other in power, frequency, duration, and electrode geometry (multi-wave technology). These parameters, in fact, are the ones influencing the deepness reached by the energy during the treatment, plus the conductivity of the specific tissue the energy is passing through (dermis, fat, muscle, bones, etc). Therefore, the Tetrawave handpiece, differently from any other RF-based technology delivering only a single signal, is able to deliver 4 different RF signals, optimizing the deepness level and massively increasing the efficacy of the energy interacting in 4 different ways with different tissues. The four signals have respectively frequencies of 0.4 MHz; 0.9 MHz; 1.3MHz; 2.4 MHz, and they are managed by the algorithm of the technology crosslinking the signals in function of the purpose.

For this study, the cellulite protocol embedded in the device was used, maximizing the signal with lowest frequency, and delivered by the most distant electrodes placed on the handpiece, to generate a deeper electromagnetic field. The power and the duration of every single signal is regulated by the algorithm, while the total power (maximum 200 W) can be adjusted by the operator in function of the skin temperature shown on the handpiece and on the screen of the device (the target temperature was 42°C at the dermis level) and the sensitivity of the patient.

There are no standard protocols for RF treatment time in the literature and the number of sessions varies from 1 to 24 (5). It was therefore decided to follow the instructions provided by the manufacturer of the device. Each session lasted 40 min, 20 min per leg. A cycle was 10 sessions, one week apart. No anesthesia was administered before, during, or after the treatment. Each leg was treated from knee to hip. The haunch was divided into 4 quadrants, each of which was dealt with for about 5 min. Firstly, the upper quadrant was treated; an inert conductive gel was applied on the skin, then, by placing the handpiece flat, and making sure to always keep the entire surface of the handpiece in contact with the skin, a continuous slow rotary movement was performed, moving the handpiece backward and forward. The other quadrants were treated in the same way. At the end of the cycle, the clinical assessment of each patient was repeated according to the Nürnberger-Müller grading scale; ultrasound evaluation and leg measurement, of the same previous areas, were again performed for each patient, as well as photographing in standard projections.

RESULTS

Two patients gave up before the end; one because she had mild vascular disease and another because she started a laser hair removal treatment. The first of these had suffered from postpartum vasculopathy which she had not reported in the medical history before treatment. Vasculopathy is actually a contraindication to the use of radiofrequency. The second, however, despite advice, wanted to start another different treatment, and two simultaneous treatments do not allow us to correctly evaluate the effectiveness. In both cases, it was obviously decided

to stop the treatment of cellulite. All the remaining 18 patients showed an improvement in cellulite. A reduction was recorded in the leg diameters, a diminished thickness of the subcutaneous tissue by ultrasound imaging, and an improvement in the appearance of the skin. The clinical assessment of each patient's cellulite grade according to the Nürnberger-Müller grading scale, showed 9 patients in grade I, 9 in grade II, and none in grade III (Figs.1-4). After each session a redness was observed on the treated areas, as well as an increase in local temperature, however, both phenomena had a short duration. No other *sequelae* or complications were observed after treatment in any of the patients; in fact, radiofrequency cosmetic treatments are generally well-tolerated and do not involve particular side effects or complications (5).

DISCUSSION

In the international scientific community, there is a lack of unanimous agreement on recognizing

Fig. 1. ***A)*** *Patient A, before and after, front section.* ***B)*** *Patient A, before and after, right side section.* ***C)*** *Patient A, before and after, left side section.* ***D)*** *Patient A, before and after, rear section*

the nosological identity of cellulite and on the pathophysiological mechanisms that underlie it (3). According to some, cellulite would originate from alterations of the lymphatic system at the level of adipose deposits (6). In the initial phase of cellulite, there would thus be an accumulation of fluids and other substances in the interstitial space, which would give rise to a local reaction which, in turn, would worsen the condition (6). At the origin, there would be the action of female sex hormones on fat deposits and on vessels (6). The most widespread opinion today is that cellulite results essentially from an excessive accumulation of fat in the subcutaneous adipose tissue, which exerts considerable pressure on the surrounding skin tissue, creating an irregular dimpled appearance (7). The disorders of the extracellular matrix and of the lymphatic system, with regional lymphostasis, may in turn represent the pathophysiological mechanism leading to cellulite (7).

The application of radiofrequency energy to treat cellulite is based on internal thermogenesis induced by applied energy (8). The increase in internal temperature then determines vasodilation and increases microcirculation, new collagen formation, and contraction of existing collagen fibers (9-11). Monopolar, bipolar or multipolar radiofrequency, however, acts only at a single depth; notably, monopolar radiofrequency acts deeply, whereas bipolar acts superficially, as known. The multipolar radiofrequency, instead, acts always at the same depth, depending on the distance between the electrodes at the surface of the handpiece. The equipment we used (Thuzzle®), instead, employing the same handpiece and simultaneously 4 waves different for power, frequency, duration, and electrode geometry, reaches 4 different depths at the same time (simultaneously controlled electromagnetic multi-energy, or concentrated controlled multi-wave). Thus, it acts on 4 different tissues: adipose tissue, lymphatic vessels, blood vessels, and skin collagen. In other words, Thuzzle® acts on the causes of cellulite, in the same session and simultaneously, allowing better and faster results. The shape of the handpiece, furthermore, permits an easy and wide contact with the skin surface. The device allows, moreover, to check, in real time, as mentioned before, 3 parameters: dermis temperature, power density absorbed by the tissue, and quality contact (i.e., the correct positioning of the handpiece on skin surface). This enhances the safety and the quality of the treatment. In fact, a single cycle of treatment allowed to obtain good results, as shown by leg measurement and ultrasound imaging, photographs, and clinical assessment according to the Nürnberger-Müller grading scale.

Despite the exiguous number of patients enrolled

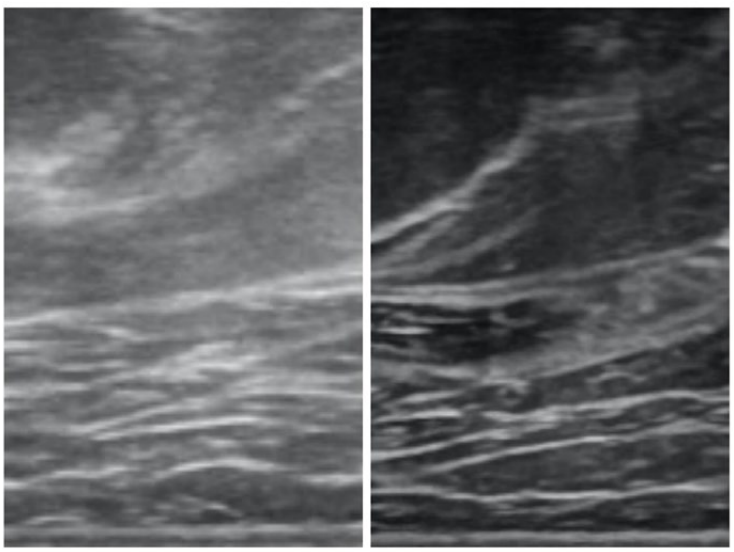

Fig. 2. *Patient A: ultrasound scan, before and after.*

Fig. 3. ***A)*** *Patient F, before and after, front section.* ***B)*** *Patient F, before and after, right side section.* ***C)*** *Patient F, before and after, left side section.* ***D)*** *Patient F, before and after, rear section.*

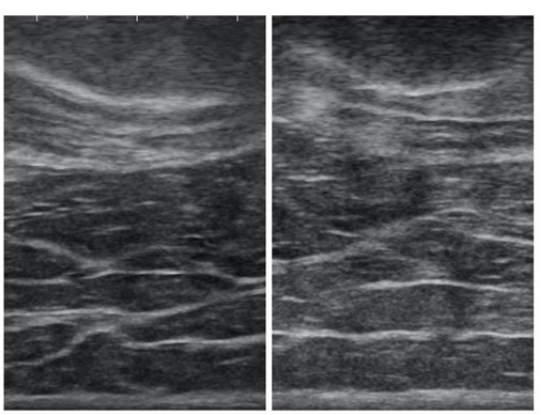

Fig. 4. *Patient F: ultrasound scan, before and after.*

in this study, the obtained results show the high effectiveness of the performed treatment. In fact, all patients who finished the cycle of treatment showed an improvement in skin appearance, a reduction in the diameters of the legs, and a reduction in the thickness of the subcutaneous tissue, as confirmed by the final clinical assessment of each patient's cellulite grade, according to the Nürnberger-Müller grading scale. Further studies are needed to confirm our initial observations.

REFERENCES

1. Bussoletti C, Mastropietro F, Tolaini MV, Celleno L. Assessment of tolerability and efficacy of an anti-cellulite food supplement. J Appl Cosmetol 2012; 30:61-77.
2. Ruiz MA, Morales ME, Clares B, Lopez-Viota M, Cuevas C, Gallardo V. Technological study of anticellulite formulations. J Appl Cosmetol 2010; 28:51-61.
3. Friedmann DP, Vick GL, Mishra V. Cellulite: a review with a focus on subcision. Clin Cosmet Investig Dermatol 2017; 10:17-23.
4. Ramalho Pianez L, Silva Custódio F, Michelini Guidi R, Nunes de Freitas J, Sant'Ana E: Effectiveness of carboxytherapy in the treatment of cellulite in healthy women: a pilot study. Clin Cosmet and Investig Dermatol 2016; 9:183-90.
5. Alizadeh Z, Halabchi F, Mazaheri R, Abolhasani M, Tabesh M. Review of the mechanisms and effects of noninvasive body contouring devices on cellulite and subcutaneous fat. Int J Endocrinol Metab 2016; 14(4):e36727.
6. De Godoy JM, Groggia MY, Ferro Laks L, De Godoy MFG. Intensive treatment of cellulite based on physiopathological principles. Dermatol Res Pract 2012; 2012:834280.
7. De Godoy JMP, De Godoy ACP, De Godoy MFG. Considering the hypothesis of the pathophysiology of cellulite in its treatment. Dermatol Reports 2017; 9:7352.
8. Belenky I, Margulis A, Elman M, Bar-Yosef U, Paun SD. Exploring channeling optimized radiofrequency energy: a review of radiofrequency history and applications in esthetic fields. Adv Ther 2012; 29:249-66.
9. Yokoyama Y, Akita H, Hasegawa S, Negishi K, Akamatsu H, Matsunaga K. Histologic study of collagen and stem cells after radiofrequency treatment for aging skin. Dermatol Surg 2014; 40:390-97.
10. Meyer PF, De Oliveira P, Silva FKBA, et al. Radiofrequency treatment induces fibroblast growth factor 2 expression and subsequently promotes neocollagenesis and neoangiogenesis in the skin tissue. Lasers Med Sci 2017; 32:1727-36.
11. Fritz K, Bernardy J, Tiplica GS, Machovcova A. Efficacy of monopolar radiofrequency on skin collagen remodeling: a veterinary study. Dermatol Ther 2015; 28:122-25.

LETTER TO THE EDITOR

How to classify the covid-19 phenotype: a response from *"the first soldier in the first trench"* in Lombardy, north-western Italy

C E. Gallenga[1,4], C. Contini[2], M. Tana[3], D. D'Eliseo[4], A.L. Giuliani[1], F. Di Virgilio[1] and S. Paglia[5]

[1]Experimental Medicine, Department of Medical Sciences, University of Ferrara, Italy; [2]Infectious Diseases, Department of Medical Sciences, University of Ferrara, Italy; [3]Department of Medicine and Aging Science, G. D'Annunzio University, Chieti-Pescara, Italy; [4]UOC Ophthalmology, Santa Maria delle Croci Hospital, Ravenna, Italy; [5]Department of Emergency, ASST Lodi and Codogno Hospitals, Lombardy, Italy

Received September 29, 2020 – Accepted January 15, 2021

To the Editor,

This short note is dedicated to Dr Lin Wenliang, a young ophthalmologist working at the Central Hospital in Wuhan, China, who first warned of this new disease and died of the contagion, to all the doctors and medical and voluntary staff who have disappeared due to the pandemic, and provides an opportunity to offer the perspective of *"soldiers in the first trench"* to the general public.

The single-stranded RNA β-coronavirus SARS-CoV-2 causes airborne respiratory infection through droplet inhalation or mucosal contact. The oral-nasal- eye-settings have been evidenced as the main gateway (1), spreading in the population at a rate of 0.8-3% more than normal flu and affecting mainly men, since immune genes are more expressed on the X chromosome (2). The four structural proteins – S (spike) protein, membrane protein, envelope protein, nucleocapsid protein – work to infect the epithelial target cell via a class I trimeric glycoprotein fusion protein, cleaved by the host furin protease into two polypeptides, S1 and S2: the former binds the host receptor, the latter mediates fusion of the viral envelope with the cell membrane (3). The binding of CoV-19 to ACE2 and to the Toll-Like Receptor (TLR) causes release of pro-IL-1β and IL-6. IL1β is cleaved by caspase 1, followed by inflammasome activation and production of active mature IL-1β, mediator of lung inflammation, fever and fibrosis (4).

ACE2 is the main receptor for SARS-CoV2 (5), diffusely expressed in human eye epithelial cells, retina, conjunctiva, adnexal gland, goblet cells, heart, kidney, gut and endothelium, participating in the renin-angiotensin system (RAS), driving the physiological activity on water and salt metabolism, regulation of cardiovascular, urinary and reproductive system (3), and interfering on pathophysiological processes such as inflammatory response (4).

The N-terminal peptidase domain of ACE2 has two protrusions, forming a peptide substrate binding site between them. The extended SARS-CoV-2 receptor-binding domain (RBD) is combined with the bottom side of the ACE2 small bump (3), whilst the N-terminal helix of ACE2 accommodates in the recess of the outer surface of the receptor-binding motif (RBM). The expression in the cell membranes is weaker than the cytoplasm.

By inducing pro-inflammatory cytokines and lung inflammation (6), anecdotal evidence suggests that IL-6 blockade is beneficial (7); anti-inflammatory

Key words: SARS COV-2; COVID-19; staging tool; Lombardy cluster; home therapy; ACE2 and P2X7 receptors; Cytokines IL-1/IL-6; Dr Li Wenliang

Corresponding Author:
Carla Enrica Gallenga, MD,
Ophthalmologist, FEBO, PhD course Molecular Medicine,
Dept. Of Medical Sciences, University of Ferrara,
via Aldo Moro 8, 44124 Cona, Ferrara, Italy
Tel.: +39 3288767725
e-mail: gllcln@unife.it

0393-974X (2021)
Copyright © by BIOLIFE, s.a.s.
This publication and/or article is for individual use only and may not be further reproduced without written permission from the copyright holder.
Unauthorized reproduction may result in financial and other penalties
DISCLOSURE: ALL AUTHORS REPORT NO CONFLICTS OF INTEREST RELEVANT TO THIS ARTICLE.

strategies have been suggested and more than 30 research protocols have been approved to date by the Italian Drug Agency AIFA. A new proposal based on an antiretroviral drug has been published (1). Although it is debated whether hyperinflammation in COVID-19 should be considered a macrophage

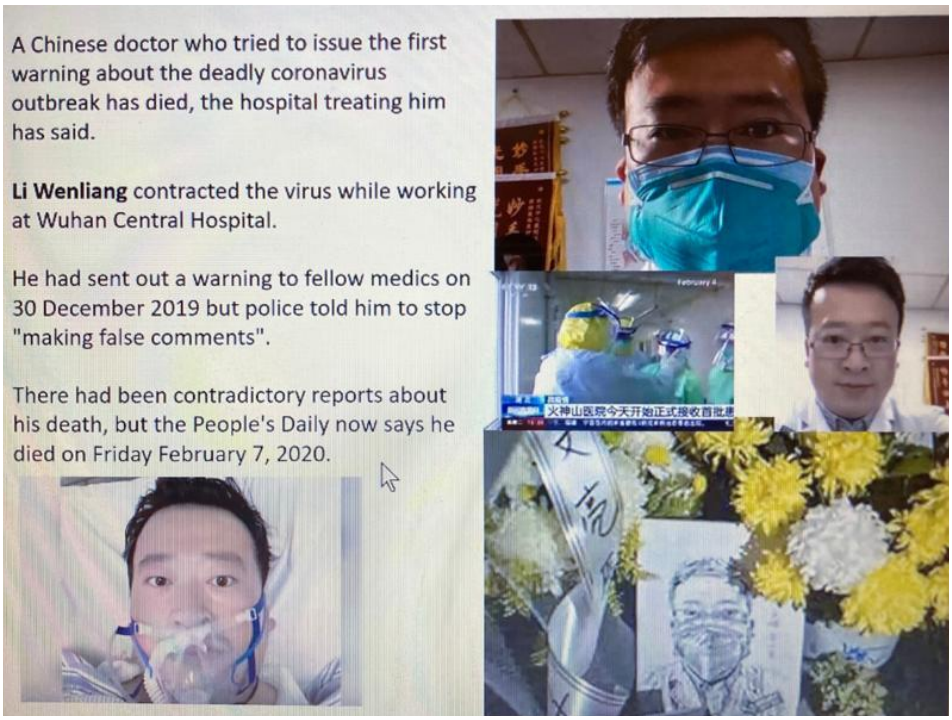

Fig. 1. *Dr Li Wenliang, Ophthalmologist. Source: Webinar COVID-19: Lombard Ophthalmological Society, June 2020.*

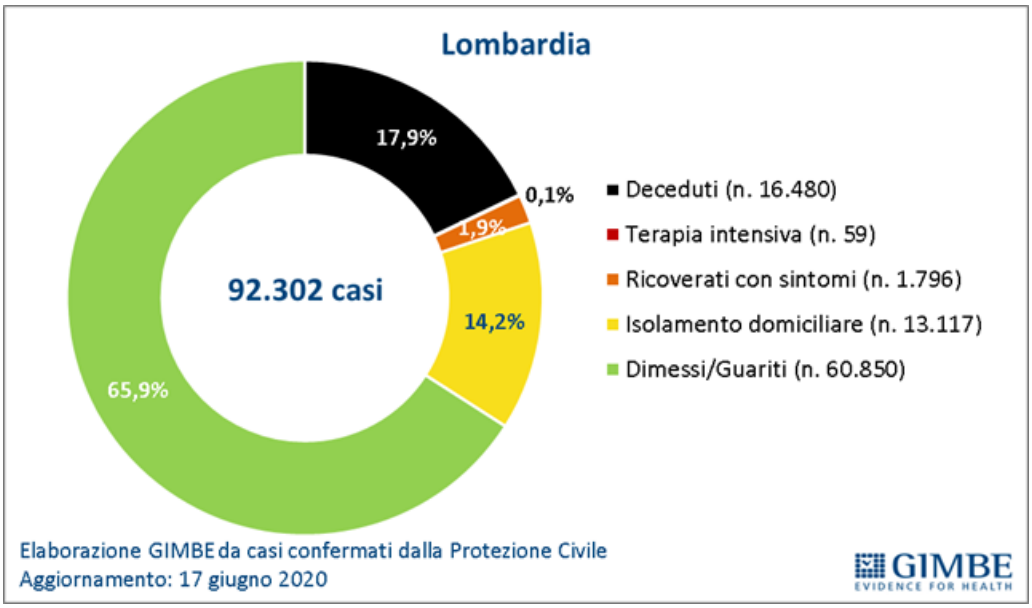

Fig. 2. *Original figure. Data released by The GIMBE Foundation about the pandemic in Lombardy region (February-June 2020). A total of 238,011 infectious cases have been registered all over Italy up to now (June 17th), of which 28,924 health workers. Black: deceased; pink & brown: ICU + symptomatic hospitalized patients; yellow: quarantined at home; green: recovered. GIMBE Foundation processing from cases confirmed by the Civil Protection (figure courtesy of GIMBE Foundation). Updated 17 June 2020.*

activation syndrome (MAS) *sensu strictu* (8), also macrophage inhibition is likely to be a crucial step in preventing the viral extensive lung injury leading to the hyper inflammation and cytokine storm (9). It has also been suggested that a new promising target receptor to down-modulate macrophage responses might be the P2X7 receptor (P2X7R) (10), that would pave the way for a new class of therapeutical agents.

Rationale

The 2020 pandemic supported by the new Coronavirus β-gene SARS-CoV-2 and spread all over the world, possibly from a cluster in Wuhan, Hubei province, China, in the wintertime 2019-2020, found globally national health systems unprepared to face an airborne viral infection, as well as the great pandemics of the twentieth century by the HN flu viruses. The world scientific literature has received tens of thousands of contributions, developing basic and clinical knowledge, therapeutic hypotheses, experimental protocols, autonomous or authorized and promoted by national regulatory authorities.

Although traces of the viral genome have only recently been found in the wastewater of northern Italian cities, stored in November/December 2020 and only now re-evaluated ad hoc, as well as in the wastewater of Paris in March/April 2020, the origin of the pandemic is still not defined, although a rationale for the spillover between mammals, from bats to humans, has been published (11).

The first identification of a suspected new viral syndrome is linked to a young ophthalmologist at Wuhan Central Hospital who first reported the event, was infected and died of COVID-19. This letter is dedicated to the memory of Dr Li Wenliang (Fig. 1) and, based on what has been reported to date, two other ophthalmologists from Wuhan Central Hospital, Mei Zhongming and Zhu Heping who also died from this virus.

An epidemic cluster developed in the region of Lombardy, in the north-west of Italy, in February 2020, leading to preventive medical measures and a blocking health policy, identifying some municipalities with disease clusters as 'red zones'; however, 92,302 infected persons and more than 16,000 deaths have been recorded in Lombardy to date (Fig.2).

In March 2020, Prof. Zhiyong Peng Director of ICU Wuhan University South Central Hospital met Prof. Enrico Storti Director of the Emergency Department UOC Anaesthesia & Resuscitation ASST Lodi, Lombardy province, Italy and Dr. Stefano Paglia Head of Emergency Department ASST Lodi and Codogno, Italy, through a web conference aimed at identifying the standard of care and to share knowledge on the symptoms and clinical presentation of the disease, and the use of ultrasound and walking test for risk stratification, in order to plan the response of hospital management and health policy to the pandemic.

MATERIALS AND METHODS

On March 15, 2020, during a medical grand-round, a summary of symptom identification and classification in 5 phenotypes was presented by Dr Stefano Paglia, head of the Hospital Emergency Department, Lodi and Codogno Hospitals, Lombardy, where the first Italian patient was diagnosed, hospitalized and recovered. It is necessary to underline that at that time the autoptic knowledge was limited to the three autoptic reports carried out in Wuhan. This report seems useful for both noting the classification and the coherent rational treatment approach, while still remaining a sustainable and feasible medical hypothesis. Consequently, a treatment paper has been published with these phenotypes (1) and we report here the table of phenotypes actually revised.

The five different COVID-19 phenotypes, which correspond to a possible different therapeutic management

Phenotype I: patient with fever who does not necessarily present respiratory symptoms, there is no hypoxia in arterial blood gas analysis and chest X-ray is negative or with minimal alterations. In this patient the swab is carried out only if a previous contact is considered at risk. This patient is safely discharged with quarantine indication if he/she does not show any significant alteration when performing a specific respiratory activity test (quick walking test with an oximeter on the finger, generally of 6 minutes). At the "follow-up" no return to ER was observed with a favorable outcome. In these patients, ultrasound of the chest is not recommended, because it will probably be positive and, in any case, will

not indicate hospitalization. This category is believed to represent the majority of patients. Quarantine at home under a safety protocol, use of mask, alert to relatives to follow rules against risk of contagion, general practitioner/ family doctor control, monitoring saturation with an oximeter and telemedicine follow-up. In this setting, the supportive strategy* suggested by Contini and coll. (1) could be effective.

Phenotype II: patient with fever plus pulmonary thickening on chest X-ray or in the presence of arterial blood gas hypoxia. The patient must be hospitalized in the medical area and must be observed, as in the following hours he/she can either undergo rapid deterioration or turn towards a significant improvement. The patient cannot be discharged. These patients are approximately 20 times more frequent than those who end up in resuscitation.

Phenotype III: hypoxia frank to arterial EGA, fever and multiple thickenings on chest X-ray. The patient responds to oxygen therapy set at 15 l/min (i.e. with SpO2> 90 mmHg with O2), and needs hospitalization in a sub-intensive area.

Phenotype IV: pre-respiratory distress syndrome picture that requires C-PAP (continuous ventilation at positive pressure) to obtain acceptable levels of pressure/ flow (ratio between oxygen pressure and oxygen flow with normal values above 350).

Phenotype V: full-blown respiratory distress syndrome, typical of males between 35 and 70 years of age (or older) arriving with oxygen pressure values of up to 35-40 mmHg, apparently in less serious conditions than the data show. In this case, pulmonary ultrasound can make a difference, distinguishing patients with “wet” interstitial syndrome, i.e. only B lines and a conserved sliding, from “dry” patients with an interstitial syndrome composed of multiple pleural sub consolidation and reduced sliding. In the first case, an attempt with C-PAP continuous ventilation at positive pressure is desirable, while in the second, early intubation is mandatory.

A cmmon feature of COVID-19 positive patients is leukopenia, associated with respiratory alkalosis on arterial blood gas analysis, with multiple lung consolidations on chest X-ray. CT is not essential and is risky as it requires continuous transport of patients to other departments.

A common feature observed in the hospitals most involved is that there is a pre-epidemic phase of about a week with some daily/sporadic cases followed by the real epidemic phase in which patients arrive in two waves, one around midday and one around 8 pm.

*Experience so far suggests immediately starting home therapy with NSAIDs or steroids (but not paracetamol, which reduces systemic glutathione), and antibiotics in case of bacterial superinfection (in the sputum), starting with 1 mw heparin from days 3-5. Adding hydroxychloroquine or ivermectin is a personal option of the family doctor who, with mandatory PPE, has to visit the patient at home. Until vaccination, the real match against the COVID-19 pandemic must be played at home.

DISCUSSION

Staying at home, using a mask and gloves, no hand contact, physical distancing, cleaning hands and surfaces and air pollution from droplets, temperature control, symptoms - including conjunctivitis in 'asymptomatic' individuals - quarantine and swabs, RT-PCR serology and research into neutralizing antibodies, and the use of personal protective equipment have now become part of popular common sense. The new media are providing a great deal of support in combating the pandemic thanks to their extensive daily coverage and bringing the safety measures imposed by health policy into every home.

This type of classification might apparently be in conflict with some of the scientific rules of the triage societies: but it had been suggested before the scientific community (academic or real-world) opened its eyes to the global depth of the pandemic. Here the parameters for triage are not based on age or multi-disabilities; rather the phenotypic classification directs the choice towards clinical appropriateness. This is also the mood to be found at the same time in the statement of the Ethics Committee of the Republic of San Marino (12).

From the point of view of the doctor involved in triage and in the dedicated COVID-19 Hospital Department, the classification of phenotypes simplifies the relationship with the therapeutic project, the insertion of the patient in a possible trial (always in compliance with the Helsinki declaration), the control of therapy, the indication to the nursing staff; and, last but not least, the interview

with the caregiver and relatives who, after entering the infirmary, no longer have any chance to meet the sick relative during hospitalization. Unfortunately, the last greeting was often only from afar, in the closed coffin, while the patient was taken to be cremated.

From the point of view of the general practitioner and the family doctor, the classification of Paglia has been and is an important diagnostic support for the therapeutic decision and health information to the patient, family and community. From the researcher's point of view, it is a useful springboard to classify the stages of disease and frame the results offered to the scientific community. Conclusively, this phenotype classification appears as a useful tool for triage, family doctors, general practitioners and for the entire knowledge of the disease itself and merits more investigations and comments.

ACKNOWLEDGEMENTS

The Authors thank Nino Cartabellotta, Gimbe Foundation, Bologna President, Italy, Enrico Storti, Director UOC Anesthesia & Resuscitation, ASST Lodi, Italy, and Zhiyong Peng, Director ICU Wuhan University South-Central Hospital, China. The study was supported by FAR University of Ferrara, Italy, and FAR G. D'Annunzio University, Chieti-Pescara, Italy.

REFERENCES

1. Contini C, Gallenga CE, Neri G, Maritati M, Conti P. A new pharmacological approach based on remdesivir aerosolized administration on SARS-CoV-2 pulmonary inflammation: a possible and rationale therapeutic application. Medical Hypotheses 2020; 144:109876. doi: 10.1016/jmehy.2020.109876. E-pub 24 May 2020, 109876.
2. Schurz H, Salie M, Tromp G, et al. The X chromosome and sex-specific effects in infectious disease susceptibility. Hum Genomics 2019; 13:2. doi: 10.1186/s40246-018-0185-z.
3. Yin X, Zang J. Advances in the research of ocular surface β gene coronavirus receptor. Chin J Exper Ophthalmol 2020; 38:254-56. doi:10.3760/cma.j.cn115989-20200223-00098.
4. Tay MT, Poh CM, Rénia L, et al. The trinity of COVID-19:immunity, inflammation and intervention. Nat Rev Immunol 2020: 20(6):363-74. doi: 10.1038/s41577-020-0311-8.
5. Lan J, Ge J, Yu J, et al. Crystal structure of the 2019-n-CoV spike receptor-binding domain bound with the ACE2 receptor. BioRxiv 2020.02.19. doi: 10.1101/2020.02.19.956235.
6. Stawicki SP, Jeanmonod R, Miller AC, et al. The 2019-2020 novel coronavirus (severe acute respiratory syndrome coronavirus 2) pandemic: a joint American College of Academic International Medicine-World Academic Council of Emergency Medicine Multidisciplinary COVID-19 working group Consensus paper. J Glob Infect Dis 2020; 12(2):47-93. doi: 10.4103/jgid.jgid_86_20.
7. Mehta P, McAuley DF, Brown M, Sanchez E, Tattersall RS, Manson JJ. COVID-19: consider cytokine storm syndromes and immunosuppression. Lancet 2020; 395:1033-34. doi: 10.16/S0140-6736(20)30628-0.
8. Henderson LA, Canna SW, Schulert GS, et al. On the alert for cytokine storm: Immunopathology in COVID-19. Arthritis Rheumatol 2020; 72(7):1059-1063 doi: 10.1002/art.41285.
9. Wang J, Jiang M, Chen X, Montaner LJ. Cytokine storm and leukocyte changes in mild versus severe SARS-CoV-2 infection: review of 3939 COVID-19 patients in China and emerging pathogenesis and therapy concepts. J Leukoc Biol 2020 108(1):17-41. doi: 10.1002/JLB.3COVR0520-272R.
10. Di Virgilio F, Tang Y, Sarti AC, Rossato M. A rationale for targeting the P2X7 receptor in Coronavirus disease 19 (COVID-19). Br J Pharmacol, 2020: 177(21):4990-94.01111/bph.15138. doi: 10.1111/bph 15138.
11. Contini C, Di Nuzzo M, Barp N, et al. The novel zoonotic covid-19 pandemic: An expected global health concern. J Infect Dev Ctries 2020; 14:254-64. doi: 10.3855/jidc.12671.
12. Repubblica di San Marino - Comitato Sammarinese di Bioetica. Legge 29 gennaio 2010 n. 34. Risposta alla richiesta di parere urgente su aspetti etici legati all'uso della ventilazione assistita in pazienti di ogni età con gravi disabilità in relazione alla pandemia da Covid-19. Approvato 16 Marzo 2020. http://www.superando.it/files/2020/03/2116003PARERECSB_COVID_.pdf

LETTER TO THE EDITOR

Role of blood cell counts in the treatment of plantar fasciitis with shockwave therapy

A. Notarnicola[1,2], G. Maccagnano[3], G. Farì[1,2], F.P. Bianchi[4], I. Covelli[1,2], G. Solarino[1,2] and B. Moretti[1,2]

[1]Orthopedics Section, Department of Medical Sciences of Basis, Neurosciences and Organs of Sense, Faculty of Medicine and Surgery, University of Study of Bari, General Hospital, Bari, Italy; [2]Course of Motor and Sports Sciences, Department of Medical Sciences of Basis, Neurosciences and Organs of Sense, Faculty of Medicine and Surgery, University of Study of Bari, Bari, Italy; [3]Clinical and Experimental Medicine Department, Faculty of Medicine and Surgery, University of Study of Foggia, Riuniti Hospital, Foggia, Italy; [4]Department of Biomedical Sciences and Human Oncology, Faculty of Medicine and Surgery, University of Study of Bari, General Hospital, Bari, Italy

Received June 26. 2020 – Accepted January 18, 2021

To the Editor,

ESWT (Extracorporeal Shockwave Therapy) is a biostimulation technique which, through the physical "cavitation" effect, is able to reach biological effects. Due to revascularization, cell proliferation, modulation of inflammation and pain, ESWT is applied for the treatment of musculoskeletal disorders (1). The spread of acoustic waves on tissues is able to stimulate the healing of the target structure. Although the mechanisms of ESWT are not yet completely known, shock waves (SWs) are able to produce an interstitial and extracellular response leading to tissue regeneration and repair (2). According to literature, SWs are responsible for cellular responses and modelling growth factor release, including vascular endothelial growth factor, insulin-like growth factor, transforming growth factor, bone morphogenetic proteins, and other signaling molecules such as nitric oxide (3).

ESWT is indicated for the treatment of tendinopathy and plantar fasciitis, with a success rate up to 88% (4). There is contradictory information regarding the epidemiological and clinical features of the patient which may influence the therapeutic response to ESWT. In fact, there is a lack of relevant literature consisting of the prognostic effects of ESWT on the pathological model of tendinopathy and fasciopathy. In a previous study, it was verified that the involvement of the non-dominant limb and repeated cycles of SWs represent negative prognostic parameters, whilst the male gender and high Body mass index (BMI) are potential success factors (5). No differences were found in relation to age, diet, blood-type, work or physical activity, co-morbidity, drug intake, location of the pathology, Energy Density Flux (EDF) administered or other concomitant physiotherapy treatments. According to recent literature on the treatment of plantar fasciitis, the Authors identified the high visual analog scale (VAS), early onset symptoms and the presence of spur as important prognostic factors for the success of ESWT (6).

In order to correctly identify the adequate patient for SW treatment, it is recommended to

Key words: shock waves; fascitiis; tendinopathy; blood count; platelet; hematoma

Corresponding Author:
Angela Notarnicola, M.D. Ph.D.,
Orthopedics Section, Department of Medical Sciences of Basis,
Neurosciences and Organs of Sense, Faculty of Medicine and Surgery,
University of Study of Bari, General Hospital, Bari,
Piazza Giulio Cesare n.11, 70124, Bari, Italy
Tel./fax.: +39 0805592938
email: angelanotarnicola@yahoo.it

0393-974X (2021)
Copyright © by BIOLIFE, s.a.s.
This publication and/or article is for individual use only and may not be further reproduced without written permission from the copyright holder.
Unauthorized reproduction may result in financial and other penalties
DISCLOSURE: ALL AUTHORS REPORT NO CONFLICTS OF INTEREST RELEVANT TO THIS ARTICLE.

monitor the patient's chemical blood values. In fact, severe coagulopathy and thrombocytopenia were considered as a contra-indications to SW treatment, due to the risk of bleeding and haematomas caused by the therapy. However, no attention has been paid to the role of Complete Blood Count (CBC) in the response to ESWT. The aim of this study is to verify whether, in the treatment of plantar fasciitis with SW, the response to the therapy can be influenced by the concentrations of different blood cell lines.

MATERIALS AND METHODS

This is an observational prospective study. For one year, the patients affected by plantar fasciitis (PF), who had undergone ESWT were enrolled. The study was approved by the local Ethics Committee and written consent was obtained from each patient. The clinical diagnosis of PF was confirmed by the criterion of tenderness extended along the plantar fascia, which increased after stretching of the plantar fascia due to passive toe dorsiflexion. The following were used as inclusion criteria: patients aged 18-85 years; plantar fasciitis confirmed by ultrasound exam; persistent pain for at least three months before shock waves; patients undergoing SW treatment for plantar fasciitis. Exclusion criteria were: patients taking medications that could affect the clotting mechanism and haemostasis; traumatic events in the area that had occurred in the previous six months; secondary causes of heel pain due to a chronic inflammatory disorder. Each patient was evaluated at the beginning of treatment (T0) and after three months (T1).

To calculate the sample size, a mean value of VAS at T0 was assumed equal to 7.0, with an average value at T1 of 5.5; for both means valued a standard deviation of 3.3 was hypothesized. The Student's *t*-test was used to evaluate the results; a significance level (alpha) of 0.01 and the test power to 99% was set. Stata MP15 software (StataCorp LLC, 4905 Lakeway Drive College Station, Texas 77845-4512 USA) was used to calculate the sample size.

Functional scales

The VAS scale quantified pain (score of increasing pain intensity from 0 to 10). Disability functional outcomes included the Lower Extremity Functional Scale (LEFS) (this scale runs from 0 to 80 points, with higher scores indicating greater levels of function), the Foot Functional Index (FFI) (this score ranges from 0% to 100% of disability) and American Orthopaedic Foot and Ankle-Hindfoot Scale (AHS) (this score rates from 0 to 100 points or percent of functional ability). Only at T1 Roles and Maudsley (RM) scores were used to quantify perception of improvement by the patient (from 1 for excellent to 4 for poor).

SW therapy

The ESWT was delivered using a focalized shock wave device (Minilith, Storz, Switzerland) with ultrasound tracking. The protocol included three sessions, one per week, giving 2000 impulses per session at an energy flux density (EDF) between 0.17 and 0.25 mJ/mm2; this treatment was combined with a self-administered plantar fascia-specific stretching program for eight-weeks.

For each patient, the demographic data (age, gender), anthropometric data (weight, height, BMI), clinical data (smoking habit, right or left foot localization of the disease, presence, and localization of calcaneous spur, EDF, previous treatments) and scales scores (VAS, Ankle-Hindfoot Scale, Lower Extremity Functional scale, Foot function Index at T0 and T1, Roles and Maudley Score at T1) were recorded. Furthermore, the hematochemical parameters of examination [Erythrocytes (*106/IU), leukocytes (*103/IU), hemoglobin (g/dL), hematocrit (%), neutrophils (%), eosinophils (%), basophils (%), lymphocytes (%), monocytes (%), platelets (*103/IU)] were reported. The compiled forms were put into a database built with Office Excel software and analyzed using Stata MP15 Software (StataCorp LLC, 4905 Lakeway Drive College Station, Texas 77845-4512 USA). Continuous variables were expressed in mean ± standard deviation (SD) and range; the categorical variables were expressed as proportions. The Skewness and Kurtosis test was used to evaluate the distribution of continuous variables, whilst it was not possible to build a normalization model for those variables which were not normally distributed. In order to compare the continuous variables that cannot be normalized between times, the Wilcoxon signed rank test (no parametric) was used. Univariate linear regression was used to study the association between each of the outcomes (score difference between T1 and T0 for each evaluation scale) and the determinants (values of the blood exams); correlation coefficients were calculated, indicating a 95% confidence interval (95%CI) and the Student's *t*-test. The multivariate

Table I. *The sample features were expressed in mean ±SD (range)*

Variable	Value
EDF (mJ/mm2)	0.09 ± 0.07 (0.17 – 0.25)
Erythrocytes (*10^6/IU)	4.6±0.4 (3.5-5.7)
Leukocytes (*10^3/IU)	6.7±2.1 (3.5-15.7)
Hemoglobin (g/dL)	13.5±1.4 (9.5-16.5)
Hematocrit (%)	39.6±4.0 (30.1-49.0)
Neutrophils (%)	57.4±9.0 (39.0-79.3)
Eosinophils (%)	3.2±2.7 (0.0-19.2)
Basophiles (%)	0.5±0.2 (0.2-1.4)
Lymphocytes (%)	32.2±8.3 (14.2-49.0)
Monocyte (%)	6.7±1.5 (3.9-11.0)
Platelets (*10^3/IU)	239.7±59.3 (118.0-408.0)

linear regression was used to evaluate the association between each outcome (score difference between T1 and T0 for each functional scale) and the variables of hemato-chemical tests, the epidemiological, anthropometric, and clinical data; the correlation coefficients were calculated, indicating a 95% CI and the Student's *t*-test. A value $p<0.05$ was considered significant for all tests.

RESULTS

The study sample was made up of 140 subjects, 89 females (63.6%). The mean age of the group was 58.9±11.2 years (32-81 years) height 1.66±0.09 m (range:1.48-1.85 m), weight 79.1±13.0 kg (range: 50-110 kg), BMI (kg/cm2) 28.8±4.3 (range: 17.9-40.1). Nineteen subjects were smokers (13.6%). Seventy-one subjects received treatment on the left foot (50.7%), 69 subjects received treatment on the right foot (49.3%); ninety-one had subcalcaneal spur (65.0%), and 51 had retrocalcaneal spur (36.4%). Clinical features at baseline time are described in Table I.

After SW treatment, a statistically significant improvement, confirmed by all functional scales (outcome variables described in Table II) emerged with the comparison of the pre-treatment. At T1 the average value of the Roles and Maudley Score was 2.3±1.1 (range: 1-4). The univariate analysis showed statistically significant relationship between the different VAS value in T1 and T0 and platelet count at T0 (coef. =0.01; 95%CI=0.00-0.01; p=0.038), while no differences were found between the VAS value and the erythrocytes (coef.= -0.45; 95%CI= -1.23-0.34; p=0.267) and the leukocytes (coef.=0.01; 95%CI=-0.16-0.18; p=0.902). There were not any statistically associations between the outcomes and the determinants analyzed (p>0.05). The multivariate analysis showed a statistically significant relationship between the VAS value at T1 and T0 and the platelet count at T0 (coef.=0.01; 95%CI=0.00-0.02; p=0.027; table 3), while there were no further associations between the outcomes and the remaining determinants in analysis (p>0.05). No associations were found between platelet count and the difference between T1 and T0 of FFI (coef.=0.00; 95%CI=-0.01-0.01; p=0.094), AHS (coef.=0.06; 95%CI=-0.01-0.13: p=0.108) and LEFS (coef.=-0.02; 95%CI=-0.06-0.03; p=0.460).

Table II. *The VAS value, Ankle-Hindfoot Scale, Lower Extremity Functional scale and Foot function Index at different follow-ups were expressed in mean ±SD (range).*

Variable	T0	T1	difference T1-T0	p-value
VAS	7.6±1.5 (3-10)	4.8±2.8 (0-10)	-2.8±2.1 (-9-0)	0.000
AHS	42.4±26.9 (16-85)	71.0±27.0 (16-100)	28.6±25.2 (0-82)	0.000
LEFS	30.0±16.7 (0-60)	46.9±20.7 (0-80)	18.7±14.5 (0-60)	0.000
FFI	67.5±12.5 (42-88)	46.8±24.1 (0-88)	-20.7±18.3 (-74-0)	0.000

Table III. *Analysis of the determinants of the VAS value between T1 and T0 in a multivariate linear regression model.*

Variable	coef.	95%CI	p-value
Erythrocytes (*10^6/IU)	-0.7	-1.5-0.2	0.141
Leukocytes (*10^3/IU)	-0.1	-0.3-0.1	0.325
Platelets (*10^3/IU)	0.01	0.00-0.02	0.027
gender (male/female)	0.2	-0.6-1.1	0.592
age (years)	-0.02	-0.05-0.02	0.341
BMI (kg/cm2)	-0.01	-0.09-0.08	0.855
Previous therapies (yes/no)	0.3	-0.6-1.1	0.513
EDF (mJ/mm2)	-5.2	-16.4-5.9	0.357

DISCUSSION

According to the literature, this study is the first on this specific issue. The purpose of the study is to define the potential role of blood cell count in response to SW treatment. Our results indicate that there was a positive relationship between VAS change and platelet count at T0. Applying the effect of mechanical stimulation, SW treatment causes bleeding and triggers an inflammatory response, followed by a proliferative and angiogenetic response. Platelets may play a key role during the primary hemostasis phase (platelet cap formation) after ESWT. The exact mechanism of platelet activation by SW has not been discussed in the literature. Knowledge of the physical phenomenon of the acoustic wave allows us to hypothesize that the rapid increase and following decrease of pressure can induce a mechanical-biological modulation of platelets, inducing their activation, without causing their rupture. The reason for this hypothesis lies in the fact that ESWT in vitro is not able to reduce the mesenchymal stem cell activity (7), but at the same time it is able to induce a slight change in cellular morphology (8). Moreover, in the event of platelet break due to shock waves, it is reasonable to expect a higher release of growth factors compared to that found in platelet lysate products (9). In previous works, the Authors observed how stimulation of PRP (subsequently added to an osteoblast culture) through SW, was able to produce an increase in expression of a series of growth factors (10). This study has some limitations. Firstly, at the end of SW treatment and at follow-up there was no new examination of the hematocrit in order to verify possible effects on each cell line (changes in cell count or their mutual relationship). Secondly, there was no control group of patients treated with alternative methods or placebo, and this reduces the level of evidence of the study. Lastly, the follow-up period was short. As this issue is innovative, it is necessary to study in depth this aspect by further in vitro and in vivo studies analyzing other pathological models treated by SW therapy (fracture consolidation delays, shoulder tendinopathy, etc.).

In conclusion, after SW treatment, a statistically significant improvement, confirmed by all functional scales, resulted compared to pre-treatment. The study did not reveal a clear role of platelets in outcomes due to the low sample size but showed a potential relationship between the different VAS values at T1 and T0 and platelet count at T0.

Knowing the effects of SW in relation to the platelet count, this aspect may be of particular importance in the treatment of fracture consolidation delays, in which the haematoma is a relevant element for healing. Further investigations are needed to define a model that may consider the results of physical examination, imaging studies and laboratory tests, and is able to identify the proper patients enrolment, timing of application and the optimal parameters of ESWT protocol.

ACKNOWLEDGEMENT

The authors thank Brian John Molloy B.A. for language revision.

REFERENCES

1. D'Agostino MC, Frairia R, Romeo P, et al.

Extracorporeal shockwaves as regenerative therapy in orthopedic traumatology: a narrative review from basic research to clinical practice. J Biol Regul Homeost Agents. 2016; 30(2):323-32.

2. Wang CJ. Extracorporeal shockwave therapy in musculoskeletal disorders. J Orthop Surg Res 2012; 7:11.
3. Chamberlain GA, Colborne GR. A review of the cellular and molecular effects of extracorporeal shockwave therapy. Vet Comp Orthop Traumatol 2016; 29(2):99–107.
4. Aqil A, Siddiqui MR, Solan M, Redfern DJ, Gulati V, Cobb JP. Extracorporeal shock wave therapy is effective in treating chronic plantar fasciitis: a meta-analysis of RCTs. Clin Orthop Relat Res 2013; 471:3645-52.
5. Notarnicola A, Maccagnano G, Tafuri S, et al. Prognostic factors of extracorporeal shock wave therapy for tendinopathies. Musculoskelet Surg 2016; 100(1):53-61.
6. Yin M, Ma J, Xu J, et al. Use of artificial neural networks to identify the predictive factors of extracorporeal shock wave therapy treating patients with chronic plantar fasciitis. Sci Rep 2019; 9(1):4207.
7. Sun D, Junger WG, Yuan C, et al. Shockwaves induce osteogenic differentiation of human mesenchymal stem cells through ATP release and activation of P2X7 receptors. Stem Cells 2013; 31(6):1170–80.
8. Raabe O, Shell K, Goessl A, et al. Effect of extracorporeal shock wave on proliferation and differentiation of equine adipose tissue-derived mesenchymal stem cells in vitro. Am J Stem Cells 2013; 2(1):62–73.
9. Ionita CR, Troillet AR, Vahlenkamp TW, Winter K, Brehm W, Ionita JC. Comparison of humoral insulin-like growth factor-1, platelet-derived growth factor-BB, transforming growth factor-beta1, and interleukin-1 receptor antagonist concentrations among equine autologous blood-derived preparations. Am J Vet Res 2016; 77(8):898-905.
10. Notarnicola A, Tamma R, Moretti L, et al. Effect of shock wave treatment on platelet-rich plasma added to osteoblast cultures. Ultrasound Med Biol 2011; 37(1):160-8.

JOURNAL OF BIOLOGICAL REGULATORS & HOMEOSTATIC AGENTS Vol. 35, no. 1, 391-395 (2021)

LETTER TO THE EDITOR

Peripheral longitudinal acute meniscal lesion: conservative treatment based on medium molecular weight hyaluronic acid

N. Setaro, S. Amico and A. Gigante

Department of Clinical and Molecular Science, School of Medicine, Università Politecnica delle Marche, Ancona, Italy

Received November 6, 2020 – Accepted January 20, 2021

To the Editor,

Historically, the menisci were considered to be a functionless vestigial structure, one that should be entirely removed once damaged. Since King reported "the function of the semilunar cartilages" in 1936, the importance of meniscal functions in the knee joint has been gradually recognized. In 1948, Fairbank reported joint degenerative changes were observed after meniscectomy, suggesting such changes were due to loss of the weight-bearing function of the meniscus. In the 1980s, several biomechanical studies addressed the importance of the meniscus as a joint stabilizer and shock absorber in the knee joint (1), and meniscal preservation has been recognized to be essential to retention of normal knee biomechanics. However, meniscectomy to remove the damaged, unstable portion of the meniscus has still been for many years the gold standard of surgical treatment for meniscal lesions since there have been no effective therapeutic methods able to preserve this important anatomical structure. Indeed, due to the unique vascular anatomy of the meniscus, with only the outer third of the tissue having a ready blood supply, treatment outcomes of these injuries can vary, based on the individual lesion pattern. In detail, the meniscal lesions in the vascular zone of the peripheral area, such as vertical longitudinal lesions, have good indications for effective meniscal repair (2). However, even the most promising studies on meniscal sutures in the literature report a failure rate close to 20% (3). This failure rate rises further in studies with a follow-up of more than 2 years. Tuckman et al. reported a failure rate of 36% of the meniscal sutures after 2 years of follow-up. To reduce the rate of these failures, biological therapies have been combined with meniscal sutures (4). However, although there are studies in the literature on the efficacy of hyaluronic acid (HA) treatment of degenerative meniscal lesions, to our knowledge no study in the literature has evaluated the regenerative properties that hyaluronic acid could have in the treatment of traumatic meniscal lesions of the red-red and white-red area. The primary purpose of the present study was to evaluate the efficacy and safety of intra-articular hyaluronic acid injection in acute peripheral longitudinal meniscal lesions. Secondly, we aimed to assess the progression of osteoarthritis in the treated knee versus the contralateral knee.

MATERIALS AND METHODS

Patients

Patients aged 18 to 50 years with peripheral longitudinal

Key words: knee; meniscal; acute lesions; peripheral injury; hyaluronic acid; orthopedic; conservative treatment; molecular weight; cartilage; injection

Corresponding Author:
Nicola Setaro, MD
Department of Clinical and Molecular Sciences,
Università Politecnica delle Marche
Via Tronto 10/ 60126, Ancona, Italy
Tel.: +39 071 5963346 - Fax: +39 071 5963341
e-mail: nicola.setaro@libero.it

0393-974X (2021)
Copyright © by BIOLIFE, s.a.s.
This publication and/or article is for individual use only and may not be further reproduced without written permission from the copyright holder.
Unauthorized reproduction may result in financial and other penalties
DISCLOSURE: ALL AUTHORS REPORT NO CONFLICTS OF INTEREST RELEVANT TO THIS ARTICLE.

acute internal or external meniscus lesions were recruited. Each patient who participated in the study read and signed an informed consent. Confirmation of the lesion, its classification and its position in the meniscal context were assessed by high field Magnetic Resonance Imaging (hf-MRI). In addition, a bilateral X-ray of the knees under load (Rosemberg projections) was performed to assess the initial state of osteoarthritis. The inclusion criteria were: patients suffering from acute meniscal injury, longitudinal lesion positioned in the peripheral third of the meniscus and age between 18 and 50 years. The exclusion criteria were: patients with primary or secondary OA assessed with AP and LL grade 2, 3 and 4 radiography according to the Kellgren-Lawrence criteria; patients with previous knee injuries; patients who had already undergone knee or meniscus surgery; patients under the age of 18 or over 50. Between March 2017 and April 2019, 40 patients (16 males and 24 females) were recruited. Fifteen patients showed a peripheral longitudinal lesion of the external meniscus (EM), while twenty-five patients showed a peripheral longitudinal lesion of the internal meniscus (IM). Each patient underwent an infiltrative cycle of three intra-articular injections (one every 7 days) of Condronil® Ialdue (Geopharma s.r.l.). This is a sterile, injectable, biodegradable and isotonic gel, for intra-articular use. Chondronil® Ialdue consists of a medium molecular weight hyaluronic acid (1000-1500 kDalton), produced by streptococcus equi bacteria, formulated at a concentration of 20mg/ml in a physiological buffer. The choice of using a medium molecular weight hyaluronic acid was based on several studies in the literature which have shown that this formulation of hyaluronic acid is the most effective one to increase the number of synovial fibroblastic-like cells and the synthesis of chondrocytes (5). After each injection, patients were advised to apply ice on the knee for two days. They were also advised to avoid excessive functional loads on the knee for one month after treatment. Patients were also advised to lose weight and perform muscle strengthening exercises without loading the knee (leg extension or swimming) for 2 months. Swimming was recommended 3 times a week, while leg extension exercises were performed every day for 20 minutes a day.

Infiltrative technique

Intra-articular injections were performed without anesthesia, on a sterile field, with a 21G needle. Before the injection, the presence of intra-articular effusion was evaluated (when it was present it was aspirated before injecting hyaluronic acid). The needle was introduced into the joint through an anterolateral access. The procedure thus performed usually allows the patient to get up and leave a few minutes after the treatment with the advice to apply ice 2-3 times over the same day and the next day.

Follow-up

Each patient underwent a clinical evaluation before treatment, then 3, 6, 12 and 24 months after the infiltrative cycle. The clinical evaluation consisted of the subjective global pain assessed by VAS (Visual Analogue Scale) pain score. The intensity of pain, symptoms, daily activity, sport activity, and quality of life were assessed by the KOOS (Knee injury and Osteoarthritis Outcome Score). Throughout the study, the occurrence of adverse events was checked both at the time of injection and in the following days. In particular, skin redness in the area around the injection, excess pain and systemic adverse events were checked. Furthermore, at one year and two years of follow-up, patients underwent weight-bearing radiographic evaluation of both knees (Rosemberg projections) to assess whether there was a difference in osteoarthritis progression between the treated knee and the healthy knee.

Statistical analysis

Values±Standard Deviation (SD) are given as mean±SD. The differences between the continuous variables were assessed using an unpaired Student's *t*-test or Mann–Whitney test according to the characteristics of the data distribution. A Student's *t*-test was used to test pre- and post-operative values±SD of continuous variables. The differences for categorical variables were tested with the *Chi*-squared test. A value of p value <0.05 was considered significant.

RESULTS

Of the 40 patients who participated in the study, 24 were female and 16 were male. The characteristics of the patients (age, side affected and body mass index) are shown in Table I. The results of the VAS score, pre-treatment and after 3, 6, 12 and 24 months from the treatment are shown in Table II. The KOOS

results divided into the various items, pretreatment, after 3, 6, 12 and 24 months from the treatment are reported in Table III. Three months after treatment, a statistically significant improvement was observed in both the VAS score and the KOOS score in all patients. However, four patients (three women and one man) still complained of slight residual pain while carrying out some daily activities. All four of these patients had a body mass index greater than 30. These patients underwent a second infiltrative cycle with Condronil® Ialdue three months after the first cycle. In detail the pretreatment average values ±SD of the VAS scale were 7.5±1.4; after 3 months from the treatment these values ±SD were

Table I. *Comparison by age, side affected and body mass index between the male and female patients.*

	Mean age	Dominant limb	Body mass index
Male	40.5±5.4	63%	24.8±1.5
Female	39.4±5.7	58%	22.4±1.9

Table II. *Clinical outcomes measured by the VAS score; pretreatment and after 3, 6, 12 and 24 months of follow-up.*

	Pretreatment	**3 months**	**6 months**	**12 months**	**24 months**
VAS	7.5±1.4	1.5±1.9	2.4±1.4	1.1±1.5	1.2±0.8

Table III. *Clinical outcomes measured by the KOOS score; pretreatment and after 3, 6, 12 and 24 months of follow-up.*

	KOOS pain	**KOOS Symptoms**	**KOOS Daily activity**	**KOOS Sport**	**KOOS Quality of Life**
Pretreatment	25.00	17.86	25.00	10.00	18.75
3 months	86.11	92.86	86.76	65.00	87.50
6 months	77.78	89.29	79.41	40.00	50.00
12 months	91.67	92.86	92.65	75.00	87.50
24 months	86.76	89.29	92.65	75.00	87.50

1.5±1.9. The difference between the two values ±SD had statistical significance ($p < 0.05$). Likewise, the KOOS evaluation showed statistically better average results in all items after three months of treatment compared to pretreatment. Six months after treatment, 25 patients no longer had symptoms, either in terms of pain or in terms of functional limitation. Eight patients reported mild pain only during intense knee activities (among these were the four patients who had needed the second infiltrative cycle after three months). The remaining 7 patients reported significant improvement in the 5 months after treatment, but they have reported the reappearance of some symptoms in the past few weeks. The mean VAS score at six months (2.4±1.4) showed an increase in pain in the patient group compared to the score reported three months after treatment. However, the results remained statistically better when compared with those before treatment. The KOOS evaluation also showed a worsening of the results in all items when compared with those registered during the evaluation made after 3 months from the treatment, but also in this case the results remained statistically better than the pretreatment. No other treatment was administered to the 25 patients who no longer exhibited symptoms. In contrast, the remaining 15 patients underwent an additional infiltrative cycle (three Condronil® Ialdue injections, one every 7 days). In the follow-up one year after the first infiltrative cycle, clinically 36 patients reported that they had no more pain and no functional limitations; 15 reported that they returned to physical activity at the pretreatment level without limitations; 14 had never done physical activity and continued not to do so; 7 reported having stopped sporting activity, but for reasons unrelated to the meniscal injury. Two patients reported onset of pain rarely, only during knee load activity, but they were still satisfied with the results of the treatment. Otherwise, 2 other patients were not fully satisfied and decided to undergo surgical treatment. The VAS scale showed the lowest pain score (1.1±1.5) of the whole study. The KOOS scores were the best of the whole study both in terms of pain reduction, both in terms of improvement of symptoms, and return to daily and sports activities as well as in terms of quality of life. At the follow-up two years from the start of the study, the 2 patients who had chosen to undergo surgery were excluded from the study; 2 others did not respond to the contact details we had for them. Of the remaining 36 patients, 31 no longer needed further infiltration cycles and were carrying out their daily and sports activities normally. Instead, the remaining 5 requested to undergo a new infiltrative cycle due to the sporadic reappearance of pain. However, these 5 patients also said they were satisfied with the treatment and to have avoided surgical treatment. The VAS scale (1.2±0.8) confirmed the results obtained in the 12-month follow-up. The KOOS scores were only slightly worse in terms of pain and symptoms when compared with the 12-month follow-up, however there was no worsening in terms of daily activities and sports activities, nor in quality of life. Furthermore, no adverse events (either local or systemic) were recorded during the study, or immediately after the injection, or in the following days. In addition, bilateral radiographs of the knees under weight (Rosemberg projections) performed at one year and two years of follow-up showed no significant differences in the progression of osteoarthritis between the treated and the contralateral knee according to the Kellgren-Lawrence classification.

DISCUSSION

Although, to date, no substance has been found to induce predictable, spontaneous meniscal healing, a recent *in vitro* study conducted on human synovial cells stimulated with HA showed that treatment with HA (0.1 mg/mL) increases the expression of tGF-β1 and VEGF (6). Two preclinical studies have been performed on rabbits with meniscal lesions. In both studies, weekly intra-articular injections of HA were compared with intra-articular injections of saline. After six weeks, administration of HA resulted in lesion filling and a change in cell population from fibroblast-like to chondrocyte-like cells faster and in greater quantities than control (8). These two studies confirm that hyaluronic acid injections in animals increase the speed of meniscal healing, which is evident only a few weeks after treatment. In humans, the healing potential

of a meniscal injury has been shown to depend on the injury site, its length and stability (9). However, to our knowledge, no clinical study is present in the literature on the real efficacy of hyaluronic acid in the treatment of acute meniscal lesions. This study focused on the biological characteristics of meniscal lesions and the intrinsic repair capacity of peripheral longitudinal lesions of the meniscus. The aim was to evaluate the efficacy of the intra-articular injection of Condronil® Ialdue combined with a specific rehabilitative protocol in the treatment of acute peripheral longitudinal meniscal lesions both in terms of pain reduction and functional recovery of the knee. Analysis of the results showed that 3 injections (one per week) of Condronil® Ialdue significantly reduced pain in patients with acute peripheral meniscal injury, as demonstrated by VAS scores and KOOS pain and KOOS symptoms. It also showed a return to daily and sporting activities comparable to pre-injury levels. At one year of follow-up, 90% of patients confirmed the results without the need for any other infiltrative treatment. At two years of follow-up, 77.5% of patients confirmed the results without the need for any other infiltrative treatment. The long-term benefit cannot be due only to the momentary viscoupling activity of the HA or to the temporary restoration of the composition of the synovial fluid. Longer-term effects are much more likely to be related to the biological stimulus produced by HA used to promote repair of meniscal lesions (10). No adverse events were observed during treatment in any patient, demonstrating the safety of infiltrative treatment with hyaluronic acid. Obviously, not all meniscal lesions have the same response potential to biological stimulation with intra-articular injections of HA. However, promising clinical results should lead to the consideration of conservative treatment also for acute meniscal injuries.

REFERENCES

1. Baratz ME, Fu FH, Mengato R. Meniscal tears: the effect of meniscectomy and of repair on intraarticular contact areas and stress in the human knee. A preliminary report. Am J Sports Med 1986; 14(4):270-75.
2. Fillingham YA, Riboh JC, Erickson BJ, Bach BR, Yanke AB. Inside-out versus all-inside repair of isolated meniscal tears: an updated systematic review. Am J Sports Med 2017; 45(1):234-42.
3. Majeed H, Karuppiah S, Sigamoney KV, Geutjens G, Straw RG. All-inside meniscal repair surgery: factors affecting the outcome. J Orthop Traumatol Off J Ital Soc Orthop Traumatol 2015; 16(3):245-9.
4. Moran CJ, Busilacchi A, Lee CA, Athanasiou KA, Verdonk PC. Biological augmentation and tissue engineering approaches in meniscus surgery. Arthrosc J Arthrosc Relat Surg Off Publ Arthrosc Assoc N Am Int Arthrosc Assoc 2015; 31(5):944-55.
5. Gupta RC, Lall R, Srivastava A, Sinha A. Hyaluronic acid: molecular mechanisms and therapeutic trajectory. Front Vet Sci [Internet] 2019 [cited 2020 Oct 30];6. Available from: https://www.ncbi.nlm.nih.gov/pmc/articles/PMC6603175/
6. Tetik O, Kocabey Y, Johnson DL. Synovial abrasion for isolated, partial thickness, undersurface, medial meniscus tears. Orthopedics 2002; 25(6):675-8.
7. Duchman KR, Westermann RW, Spindler KP, et al. The fate of meniscus tears left in situ at the time of anterior cruciate ligament reconstruction: a 6-year follow-up study from the MOON Cohort. Am J Sports Med 2015; 43(11):2688-95.
8. Suzuki Y, Takeuchi N, Sagehashi Y, Yamaguchi T, Itoh H, Iwata H. Effects of hyaluronic acid on meniscal injury in rabbits. Arch Orthop Trauma Surg 1998; 117(6–7):303-6.
9. Weiss CB, Lundberg M, Hamberg P, DeHaven KE, Gillquist J. Non-operative treatment of meniscal tears. J Bone Joint Surg Am 1989; 71(6):811-22.
10. Migliore A, Granata M. Intra-articular use of hyaluronic acid in the treatment of osteoarthritis. Clin Interv Aging 2008; 3(2):365-9.

LETTER TO THE EDITOR

Bone health, vitamin D status and oral hygiene screening in breast cancer women before starting osteoporosis treatment: a cross-sectional study

A. de Sire[1,2*], M. Ferrillo[3*], A. Gennari[4], C. Cisari[1,5], S. Pasqua[5], P.L. Foglio Bonda[6], M. Invernizzi[1,5#] and M. Migliario[6#]

[1]Physical and Rehabilitation Medicine, Department of Health Sciences, University of Eastern Piedmont "A. Avogadro", Novara, Italy; [2]Rehabilitation Unit, "Mons. L. Novarese" Hospital, Moncrivello, Vercelli, Italy; [3]Dental School, Department of Surgical Sciences, University of Turin, Turin, Italy; [4]Division of Oncology, Department of Translational Medicine, University of Eastern Piedmont, Novara, Italy; [5]Physical Medicine and Rehabilitation Unit, University Hospital "Maggiore della Carità", Novara, Italy; [6]Dental Clinic, Department of Translational Medicine, University of Eastern Piedmont "A. Avogadro", Novara, Italy

Received November 23, 2020 – Accepted January 21, 2021

[*]*Contributed equally to this work as first authors*
[#]*Contributed equally to this work as senior authors*

To the Editor,

Breast cancer (BC) is the most common malignancy and cause of mortality in women, presenting also with several treatment-related disabling complications (e.g. breast cancer-related lymphedema, BC-related fatigue, axillary web syndrome, physiological disorders) (1-4). In this scenario, an increased survival rate of women affected by BC with estrogen receptor-positive (ER) tumors has been observed after the introduction of adjuvant therapies, such as tamoxifen and aromatase inhibitors (AIs), aimed at reducing the proliferative effects of estrogens on breast tissue in ER-positive BC patients (5). However, these anti-hormonal pharmacological interventions, promoting bone resorption through aromatase blockade at bone tissue level might lower bone mineral density (BMD) with a resulting pathological condition, defined as cancer treatment-induced bone loss (CTIBL) (5-6).

Moreover, BC women undergoing cancer treatments and anti-osteoporotic drugs might experience osteonecrosis of the jaw and periodontal tissue diseases, including gingivitis, and infections (7). Nevertheless, chronic oral diseases are still frequently neglected in BC patients, and detailed indications about oral health screening, evaluation and treatment before CTIBL treatment initiation are missing.

In this cross-sectional study we therefore assessed bone health and oral hygiene status in BC women before CTIBL treatment initiation. The aim is twofold: to provide new data on oral health status in BC survivors undergoing CTIBL treatment, and to propose a feasible clinical pathway in order to better define a patient-oriented multidisciplinary management of these women.

Key words: oral health; bone health; osteoporosis; vitamin D deficiency; breast cancer

Corresponding Author:
Alessandro de Sire, MD
Physical and Rehabilitative Medicine,
Department of Health Sciences,
University of Eastern Piedmont "A. Avogadro"
Viale Piazza D'Armi, 1 - 28100 Novara, Italy
Tel.: +39 03213734800
e-mail: alessandro.desire@gmail.com

0393-974X (2021)
Copyright © by BIOLIFE, s.a.s.
This publication and/or article is for individual use only and may not be further reproduced without written permission from the copyright holder.
Unauthorized reproduction may result in financial and other penalties
DISCLOSURE: ALL AUTHORS REPORT NO CONFLICTS OF INTEREST RELEVANT TO THIS ARTICLE.

MATERIALS AND METHODS

Participants

In this observational cross-sectional study, we recruited women referred to the Outpatient Service for Oncological Rehabilitation of the Physical Medicine and Rehabilitation Unit of the University Hospital "Maggiore della Carità", Novara, Italy. Patients were recruited over a 6-month period, from January to June, 2020.

The inclusion criteria were the following: women with a diagnosis of invasive BC surgery performed at least 12 months earlier; tamoxifen or AI adjuvant hormone therapy; post-menopausal status. Exclusion criteria were the following: psychiatric or neurological diseases; evidence of major concurrent diseases; patients undergoing treatment with corticosteroids, immunoglobulin, or immunosuppressive drugs; fully edentulous patients; patients suffering or having suffered in the past from major oral infections; dental elements less than 10; patients unable to understand the informed consent.

The study was approved by the Local Ethics Committee (CE 61/10, prot.392 CE). All the participants were asked to carefully read and sign an informed consent, and the researchers provided to protect the privacy and the study procedures according to the Declaration of Helsinki, with pertinent National and International regulatory requirements. Moreover, the study was performed in accordance with the "Strengthening the Reporting of Observational Studies in Epidemiology" (STROBE) Guidelines (https://www.equator-network.org/wp-content/uploads/2015/10/STROBE_checklist_v4_cross-sectional.pdf).

All the included patients underwent a bone and functional screening and were then referred to the Dental Clinic of the University Hospital 'Maggiore della Carità' of Novara to undergo a clinical assessment of their oral health status before initiating anti-osteoporotic treatment (Fig. 1). The following demographic and anamnestic data were collected: sex, age, Body Mass Index (BMI), smoking habit, BC situs (right/left), BC type (lobular/ductal), histological type (in situ/infiltrative), type of breast surgery (conservative/mastectomy), sentinel lymph node biopsy (SLNB), axillary lymph node dissection (ALND), adjuvant hormone therapy (tamoxifen or aromatase inhibitors). The following data regarding bone health were also collected: previous femur fragility fractures, previous vertebral fragility fractures, lumbar spine (LS) bone mineral density (BMD), LS Tscore, LS Zscore, femoral neck (FN) BMD, FN Tscore, FN Zscore, osteoporosis, osteopenia, Fracture Risk Assessment tool (FRAX®) major osteoporotic fractures, FRAX® hip fractures, serum 25-hydroxy-vitamin D (25(OH)vit. D) (ng/ml), serum 25(OH)vit. D ≥30 ng/ml, serum 25(OH)vit. D ≥20 and <30 ng/ml, serum 25(OH)vit. D <20 ng/ml, serum calcium (mg/dl), serum parathyroid hormone (PTH) (pg/ml), serum alkaline phosphatase (ALP) (U/l).

Furthermore, all the participants underwent a specialistic oral health evaluation, including the following outcome measures: the Decayed, Missing and Filled Permanent Teeth Index (DMFT), to assess dental caries prevalence as well as dental treatment needs; the Oral Hygiene Index (OHI), for the presence of debris/stain and calculus on the dental elements; the Plaque Control and Record Index (PCR), to assess the presence of plaque on the dental elements; Gingival Bleeding Index (GBI), to evaluate gingival inflammation; the Periodontal Screening and Recording Index (PSR), to assess periodontal status; the Winkel Tongue Coating Index (WTCI), to evaluate the amount of tongue coating.

Statistical analysis

Data management and analyses were conducted according to a pre-specified statistical analytical plan. Statistical analysis was performed using STATA v. 12 (StataCorp LP, College Station, TX). The continuous variables are presented as means ± standard deviations, or median and interquartile range. The Shapiro–Wilk test was performed to assess the distribution of all continuous data; as the data did not follow a normal distribution, Wilcoxon rank sum test was used to compare continuous variables between the two groups; Fisher exact test was performed to compare categorical variables between the two groups. Pearson correlation coefficients and regression analyses assessed associations and correlations among oral health status of study participants, analyzing a correlation with clinical and demographic features. A p-value of 0.05 was considered statistically significant.

RESULTS

Of 128 subjects recruited, 6 did not match the inclusion/exclusion criteria and were excluded, thus, 122 postmenopausal BC women (mean aged

55.6±10.4 years) were included in the final analysis. Demographic and clinical characteristics of the patients enrolled are summarized in Table I.

Regarding bone health assessment, the mean LS BMD was 1.049±0.147g/cm2, whereas the mean FN BMD was 0.747±0.109 g/cm2; 23% of BC women had osteoporosis and 52.5% had osteopenia. The FRAX® major osteoporotic fractures score was 7.7±4.4% and the FRAX® hip fractures score was 1.7±2.0%, testifying a mild risk of fractures in the subsequent 10 years. Furthermore, the mean serum level of 25(OH) vit. D was 23.9±16. ng/ml, and 89 patients (72.9%) reported hypovitaminosis D ([25(OH)vit. D] <30 ng/ml). Lastly, mean serum calcium level was 9.2±0.5 mg/dl. Further details on bone health status in our sample of BC women are depicted by Table II.

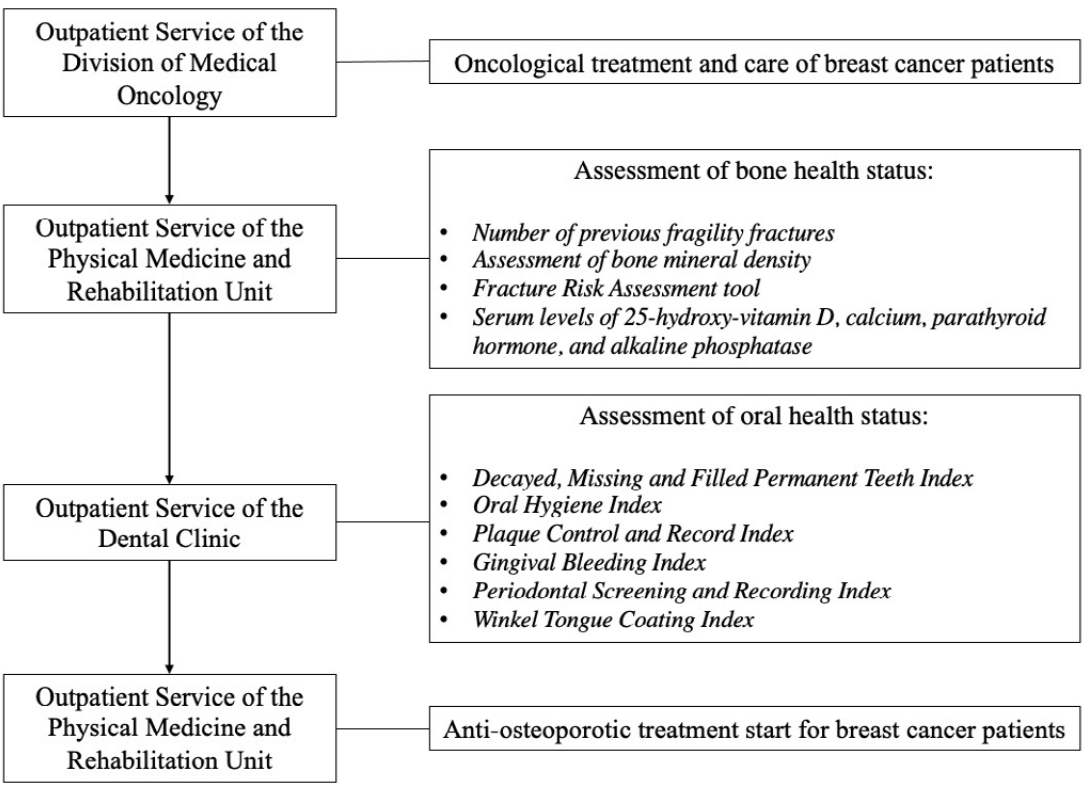

Fig. 1. *Flow chart of a feasible multidisciplinary bone and oral health management of breast cancer patients.*

Table I. *Anamnestic characteristics of breast cancer women included in the study (n=122).*

Age (years)	55.6±10.4
BMI (kg/m^2)	23.9±5.4
Smokers	22 (18.0%)
Laterality (right/left)	52/70
Type of breast cancer (lobular/ductal)	38/84
Histological type (in situ/infiltrative)	60/62
Type of breast surgery (conservative/mastectomy)	36/86
SLNB	104 (85.2%)
ALND	18 (14.8%)
Tamoxifen	48 (39.3%)
Aromatase inhibitors	74 (60.7%)

Continuous variables are expressed as means ± standard deviations; categorical variables are expressed as counts (percentages); ratios are expressed as x/y. Abbreviations: BMI: body mass index; SLNB: sentinel lymph node biopsy; ALND: axillary lymph node dissection.

DMFT index had a high average value of 16.07±7.05 and similarly, OHI showed that only 11.5% (n=14) had good oral hygiene while 35.3% had a sufficient oral health and 53.2% (n=65) had an insufficient status. PCR index showed that in 33.6% (n=41) the plaque was present from 50% and 75% of the sites investigated and in 18.0% (n=22) of BC women in more than 75%. From PSR index assessment, it emerges that only 2.5% (n=3) had good oral health while 18.9% (n=23) had gingivitis, 63.1% (n=77) had a moderate periodontitis and 15.6% (n=19) had serious periodontitis. Further details on the results obtained are reported in Table III. There were no statically significant correlations (p>0.05) among oral health indexes and BMD or vitamin D status.

DISCUSSION

This cross-sectional study aimed to assess bone health status and oral hygiene in a wide cohort (n=122) of BC patients, thus showing a possible correlation between bone health, vitamin D status, and oral health in BC women undergoing tamoxifen or AI treatment. These findings might provide more information to the body of knowledge surrounding the correlation between osteoporosis, BC, and oro-dental diseases (e.g. periodontitis, poor oral health, jaw osteonecrosis).

A recent metanalysis, performed by Hadji et al. (8), investigated the potential effect of endocrine therapies on bone metabolism in postmenopausal women, confirming that the use of AIs is associated with an average bone loss of 2.6% after 12 months of treatment and of 3.5% after 24 months.

Osteoporosis is a systemic condition that might also affect the jawbones, the structure of which may be also impaired by periodontitis, a chronic infection-mediated condition resulting in a loss of clinical attack level of the soft tissue to teeth and resorption of alveolar bone (9). The association between

Table II. *Bone health in breast cancer women included in the study (n=122).*

Previous femur fragility fractures	4 (3.3%)
Previous vertebral fragility fractures	5 (4.1%)
LS BMD (g/cm^2)	1.049 ± 0.147
LS Tscore	-1.0 ± 1.2
LS Zscore	0.0 ± 1.0
FN BMD (g/cm^2)	0.747 ± 0.109
FN Tscore	-1.5 ± 1.0
FN Zscore	-0.3 ± 0.6
Osteoporosis	28 (23.0%)
Osteopenia	64 (52.5%)
FRAX® major osteoporotic fractures (%)	7.7 ± 4.4
FRAX® hip fractures (%)	1.7 ± 2.0
Serum 25(OH)vit. D (ng/ml)	23.9 ± 16.2
Serum 25(OH)vit. D ≥30 ng/ml	33 (27.1%)
Serum 25(OH)vit. D ≥20 and <30 ng/ml	48 (39.3%)
Serum 25(OH)vit. D <20 ng/ml	41 (33.6%)
Serum calcium (mg/dl)	9.2 ± 0.5
Serum PTH (pg/ml)	21.8 ± 7.9
Serum ALP (U/l)	134.3 ± 73.1

Continuous variables are expressed as means ± standard deviations; categorical variables are expressed as counts (percentages). Abbreviations: LS: lumbar spine; BMD: bone mineral density; FN: femoral neck; FRAX®: Fracture Risk Assessment tool; 25(OH)vit. D: 25-hydroxy-vitamin D; PTH: parathyroid hormone; ALP: alkaline phosphatase.

Table III. *Oral hygiene status in breast cancer women included in the study (n=122).*

DMFT	16.07±7.05
OHI	
Optimal	*0 (0.0%)*
Good	*14 (11.5%)*
Sufficient	*43 (35.3%)*
Insufficient	*65 (53.2%)*
PCR	
From 0% to 25%	*13 (10.7%)*
>25% and ≤50%	*46 (37.7%)*
>50% and ≤75%	*41 (33.6%)*
>75%	*22 (18.0%)*
GBI	
From 0% to 25%	*114 (93.44%)*
>25% and ≤50%	*8 (6.56%)*
>50% and ≤75%	*0 (0.0%)*
>75%	*0 (0.0%)*
PSR	
Normal periodontal health status	*3 (2.5%)*
Gingivitis	*23 (18.9%)*
Mild/moderate periodontitis	*77 (63.1%)*
Severe periodontitis	*19 (15.6%)*
WTCI	
Grade 0	*10 (7.8%)*
Grade 1	*81 (63.3%)*
Grade 2	*37 (28.9%)*

Continuous variables are expressed as means ± standard deviations; categorical data are expressed as counts (%). Abbreviations: DMFT: Decayed, Missing and Filled Permanent Teeth; OHI: Oral Hygiene Index; PCR: Plaque Control and Record; GBI: Gingival Bleeding Index; PSR: Periodontal Screening and Recording; WTCI: Winkel Tongue Coating Index.

periodontitis and osteoporosis has been investigated by Lin et al. (10) in a large-scale population-based cohort study (1,878,401 individuals) showing a significant correlation in women.

Oral hygiene assessment might be considered as crucial in BC women and could be implemented and screened in the clinical practice even in other disabling conditions, as shown by our group in recent observational studies performed on right stroke survivors (11) and on subjects with amyotrophic lateral sclerosis (12). In this context, rehabilitation and oral health interventions could be included within the quality-of-life interventions for an adequate management of BC survivors (4).

The main limitation of this study the cross-sectional design that hinders any potential causality relationship and long-term follow-up evaluation. However, this is the first study that assessed oral health status with several specific oral hygiene indexes, and the largest case history evaluating a possible correlation between oral health and bone health in BC women undergoing tamoxifen or AIs treatment.

Taken together, our findings showed that BC women had high prevalence of osteopenia/osteoporosis, hypovitaminosis D, and a very high prevalence of mild/moderate periodontitis and low oro-dental care. This study might be a starting point for future works investigating the correlation between BC, osteoporosis and oral health to define a patient-oriented multidisciplinary management.

REFERENCES

1. Invernizzi M, Runza L, De Sire A, Lippi L, Blundo C, Gambini D, Boldorini R, Ferrero S, Fusco N. Integrating augmented reality tools in breast cancer related lymphedema prognostication and diagnosis. J Vis Exp 2020; (156). doi: 10.3791/60093.
2. de Sire A, Losco L, Cigna E, et al. Three-dimensional laser scanning as a reliable and reproducible diagnostic tool in breast cancer related lymphedema rehabilitation: a proof-of-principle study. Eur Rev Med Pharmacol Sci 2020; 24:4476-85.
3. de Sire A, Invernizzi M, Lippi L, Cisari C, Özçakar L, Franchignoni F. Blurred lines between axillary web syndrome and Mondor's disease after breast cancer surgery: A case report. Ann Phys Rehabil Med 2020; 63(4):365-67.
4. Paolucci T, Bernetti A, Paoloni M, et al. Therapeutic alliance in a single versus group rehabilitative setting after breast cancer surgery: psychological profile and performance rehabilitation. Biores Open Access 2019; 8(1):101-10. doi: 10.1089/biores.2019.0011.
5. Rizzoli R, Body JJ, DeCensi A, Reginster JY, Piscitelli P, Brandi ML. Guidance for the prevention of bone loss and fractures in postmenopausal women treated with aromatase inhibitors for breast cancer: an ESCEO position paper. European Society for Clinical and Economical aspects of Osteoporosis and Osteoarthritis (ESCEO). Osteoporos Int 2012; 23(11):2567-76.
6. Migliaccio S, de Sire A, Marocci C, et al. Approach in aromatase inhibitors - induced osteoporosis: results from an Italian multicenter observational study. Clin Cases Miner Bone Metab 2018; 15(3):334-39.
7. Taichman LS, Van Poznak CH, Inglehart MR. Self-reported oral health and quality of life of postmenopausal breast cancer survivors on aromatase inhibitors and women without cancer diagnoses: a longitudinal analysis. Support Care Cancer 2016; 24(11):4815-24.
8. Hadji P, Asmar L, Van Nes JG et al. The effect of exemestane and tamoxifen on bone health within the tamoxifen exemestane adjuvant multinational (TEAM) trial: a meta-analysis of the US, German, Netherlands and Belgium sub-studies. J Cancer Res Clin Oncol 2011; 137(6):1015-25.
9. Guiglia R, Di Fede O, Lo Russo L, Sprini D, Rini GB, Campisi G. Osteoporosis, jawbones and periodontal disease. Med Oral Patol Oral Cir Bucal. 2013; 1;18(1):e93-9
10. Lin TH, Lung CC, Su HP, et al. Association between periodontal disease and osteoporosis by gender: a nationwide population-based cohort study. Medicine (Baltimore) 2015; 94(7):e553.
11. de Sire A, Baricich A, Ferrillo M, Migliario M, Cisari C, Invernizzi M. Buccal hemineglect: is it useful to evaluate the differences between the two halves of the oral cavity for the multidisciplinary rehabilitative management of right brain stroke survivors? A cross-sectional study. Top Stroke Rehabil 2020; 27(3):208-14.
12. de Sire A, Invernizzi M, Ferrillo M, et al. Functional status and oral health in patients with amyotrophic lateral sclerosis: A cross-sectional study. NeuroRehabilitation. 2020; 31. doi: 10.3233/NRE-201537.

LETTER TO THE EDITOR

Bad oral habits: a review of the literature

L. Giannini[1,2], G. Galbiati[1,2], P. Cressoni[1,2] and L. Esposito[1,2]

[1]Department of Biomedical, Surgical and Dental Sciences, School of Dentistry, University of Milan, Milan, Italy; [2]Fondazione IRCCS Cà Granda, Ospedale Maggiore Policlinico, Milan, Italy

Received September 29, 2020 – Accepted February 5, 2021

To the Editor,

Bone and dental growth are closely related to oral functions. Bad oral habits extended over a long period could cause damage to the dento-skeletal development. The most common are sucking the thumb (or another finger), lips or objects, as well as atypical swallowing and oral breathing.

Sucking habits cause a combination of the direct pressure on teeth by the thumb or objects, with an alteration of the pressure of the resting cheeks and lips. Usually the thumb or another finger, is put between the teeth at an angle which pushes the mandibular incisor lingually and the upper incisor buccally. The displacement degree of the teeth is related to the time of sucking during the day more than the pressure that it creates. For children, whose suction is strenuous but not constant, a significant incisor dislocation may not occur, but then a continuous non-nutritive sucking habit causes an anterior open bite. By the geometry of the jaws, 1 mm of posterior teeth eruption creates a 2 mm open bite anteriorly. The pressure of the cheeks is bigger at the corners of the mouth, explaining, probably, why the upper jaw tends to assume a V shape with a constriction at the level of the canines (1).

Tongue thrust is another bad oral habit where the interposition of the tongue between the dental arches can be observed. At the same time, a low activity of the elevator muscles of the mandible in contrast to a high activity of the perioral muscles, in particular of the mental muscle, can be observed.

The diagnosis should be made as soon as possible as, if not treated early, severe malocclusions can result.

The aim of this study is to analyze the literature in order to identify the effects of bad oral habit on the development of malocclusions.

MATERIALS AND METHODS

The aim of this manuscript consists in analyzing the Literature, to evaluate the effects caused by bad oral habits on the development of malocclusions. The research was made using the database of the US National Library of Medicine through PubMed, (http://www.ncbi.nlm.nih.gov/si- tes/entrez/query.fcgi), then manually extended by the evaluation of bibliographic sources (Fig. 1). The key words used were “oral habits and malocclusion”. The research was limited to the years of publication between 1990 and 2021. One hundred and thirty-eight articles were found. Titles and abstracts of each article were read and evaluated by two independent operators. The articles in which the purpose and results were not pertinent and articles without an abstract were omitted. By this screening only 13 articles were related to the research and the full text was considered.

Key words: bad oral habits; atypical swallowing; growth development; onychophagy; crossbite

Corresponding Author:
Dr Lucia Giannini,
Ospedale Maggiore Policlinico,
Via Francesco Sforza 35,
20122 Milano (Mi). Italy
Tel.: +39 0255032520 - Fax: +39 0255032520
e-mail: luciamariachiaragiannini@gmail.com

0393-974X (2021)
Copyright © by BIOLIFE, s.a.s.
This publication and/or article is for individual use only and may not be further reproduced without written permission from the copyright holder.
Unauthorized reproduction may result in financial and other penalties
DISCLOSURE: ALL AUTHORS REPORT NO CONFLICTS OF INTEREST RELEVANT TO THIS ARTICLE.

RESULTS

The most recurring bad oral habits are sucking the thumb or another finger and the use of a pacifier. Just one article was found regarding onychophagy, which appeared later in age than the other two bad habits. Mistry and Moles in their study in 2010 compared two groups of children between 7 and 13 years of age, divided by the presence or not of sucking (2, 3). For each patient, the impressions were taken, and the plaster models were used to measure the occlusal differences between the two groups. The results demonstrate that there is a significant difference in the values of open bite and overjet in the two groups studied (4-6). In fact, the authors stated that sucking could lead to a significant increase of the risk of open bite. Other authors studied the influence of sucking in children with posterior crossbite. The results showed that children with crossbite had less occlusal strength and were positive with sucking in the medical history. The authors concluded that non-nutritive sucking plays a key role in the etiology of posterior crossbite.

Researchers obtained, for each model, the measures of length, width, arch depth, overjet, overbite and posterior crossbite. The values were compared by dividing the subjects by the duration of the bad habit. The results indicated that if the habits continued over 4 years, the negative effects on the occlusion were major compared to the ones who ended the habit earlier. The prevalence of anterior open bite, posterior crossbite and increased overjet are directly proportional to the length of time of the habits (7-10). The authors also investigated the effects of the habits on the occlusion in mixed dentition subjects. For this study, 630 children were selected. By the analysis of the plaster models, it resulted that the presence of anterior open bite and posterior crossbite could be prevented by interrupting the bad habits (11). The results demonstrated that the use of a pacifier increases the risk of posterior cross bite, and that the longer this habit lasts, the major is the risk of malocclusion. Bishara highlights the importance of early treatment. He claims that the pre-contact of the deciduous canine can be an important diagnostic index of the degree of the development of the crossbite in children with this habit (12).

Onychophagy is as common in adults as in children, and is generally linked to a psycho-emotional state of anxiety. Children biting their

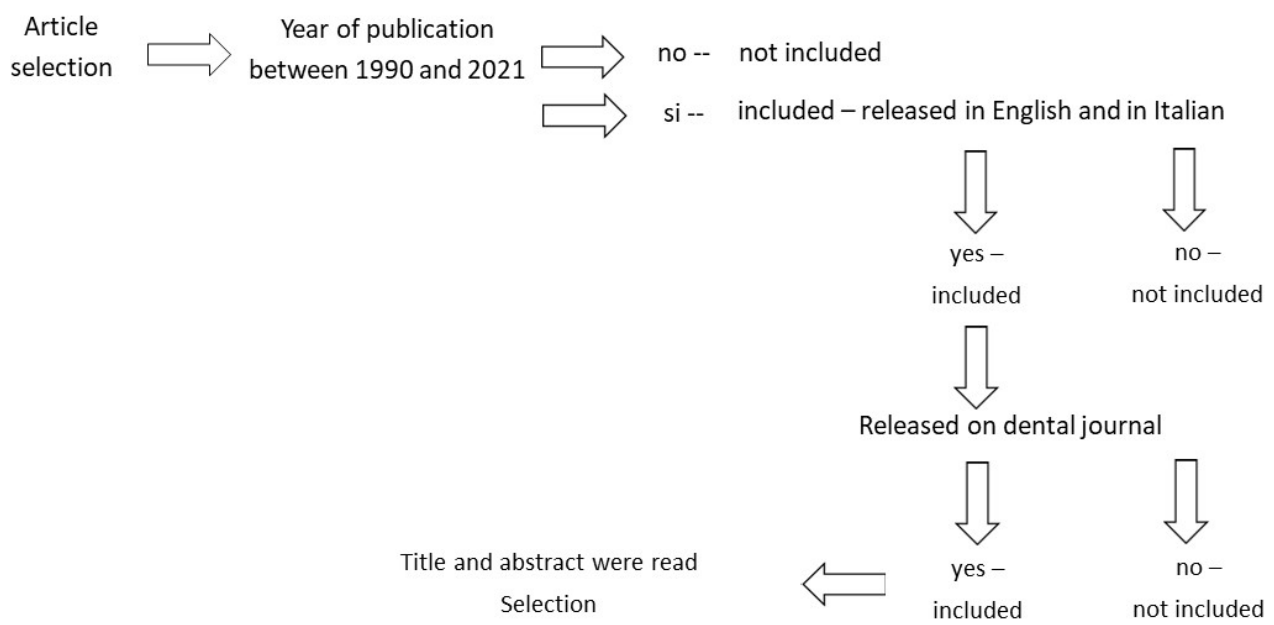

Fig. 1. *Literature review of bad oral habits.*

nails show an evolutional disturbance connected to the oral phase of psychological development. The incidence occurs in children from 4 to 6 years of age, settles around the age of 7-10, increases in teenagers and reduces around 16 years of age. The cause is hard to determine, however, it is generally related to a state of anxiety and usually disappears when there is no anxiety. If linked to other disturbances, it can become a complex problem to rectify.

Children with this habit have a bigger risk of developing problems at the level of the incisors, including the radicular resorption and dental malposition. The apical radicular resorption is one of the most common and undesirable effects of orthodontic treatment, in particular of the upper incisors. Unphysiological strengths imprinting their action on teeth, such as onychophagy, can accelerate this resorption or even cause it. Clinical exams demonstrated that in these patients it is easy to observe dental crowding, teeth rotations, abrasions on the incisal surface of the mandibular incisors and protrusion of the maxillary incisors. Despite all of that, onychophagy is not associated to any type of specific malocclusion since the information is vague and there is no relevant statistical evidence.

DISCUSSION

Bad oral habits can be associated to the development of malocclusions. The two principal habits involved in their development are thumb sucking and the use of a pacifier. The most frequent repercussions of the dental-skeletal development are anterior open bite and posterior crossbite (8, 9).

Sucking can lead to a dislocation of the upper incisor sectors, retroinclination of the lower incisors and an increased overjet.

Two studies particularly investigated the role of pressure on the development of the malocclusion. There is a directly proportional correlation between the pressure values developing in the oral cavity during sucking, and the severity of the malocclusion (6, 7). Also the duration of the sucking is extremely important in terms of hours a day and years before the interruption of the bad oral habit. More specifically, if the sucking lasts beyond 3 years of age, there is an increased risk of developing malocclusions. This is why the timing of action on children prone to this bad oral habit is essential.

Bad oral habits are highly correlated to the development of malocclusions, such as anterior open bite and posterior crossbite, highlighting the importance of an early treatment, even considering that these are parts of a physiological evolution in the first years of life (13).

REFERENCES

1. Warren JJ, Slayton RL, Bishara SE, Levy SM, Yonezu T, Kanellis MJ. Effects of nonnutritive sucking habits on occlusal characteristics in the mixed dentition. Pediatr Dent 2005; 27(6):445-50.
2. Mistry P, Moles DR, O'Neill J, Noar J. The occlusal effects of digit sucking habits amongst school children in Northamptonshire (UK). J Orthod 2010; 37(2):87-92.
3. Ling HTB, Sum FHKMH, Zhang L, Yeung CPW, Li KY, Wong HM, Yang Y. The association between nutritive, non-nutritive sucking habits and primary dental occlusion. BMC Oral Health 2018; 18(1):145
5. Maspero C, Farronato M, Bellincioni F, Annibale A, Machetti J, Abate, A, Cavagnetto D. Three-dimensional evaluation of maxillary sinus changes in growing subjects: a retrospective cross-sectional study. Materials 2020; 13:1007.
6. Pisani L, Bonaccorso L, Fastuca R, Spena R, Lombardo L, Caprioglio A. Systematic review for orthodontic and orthopedic treatments for anterior open bite in the mixed dentition. Prog Orthod. 2016; 17(1):28.
7. Farronato G, Maspero C, Esposito L, Briguglio E, Farronato D, Giannini L. Rapid maxillary expansion in growing patients. Hyrax versus transverse sagittal maxillary expander: a cephalometric investigation. Eur J Orthod 2011; 33:185-9.
8. Maspero C, Farronato M, Bellincioni F, et al. Assessing mandibular body changes in growing subjects: a comparison of CBCT and reconstructed lateral cephalogram measurements. Sci Rep 2020; 10:117-22.
9. Farronato G, Giannini L, Galbiati G, Maspero C. Modified Hyrax expander for the correction of upper midline deviation: a case report. Minerva Stomatol

2011; 60:195-204.
10. Farronato G, Maspero C, Giannini L, Farronato D. Occlusal splint guides for presurgical orthodontic treatment. J Clin Orthod 2008; 42:508-12.
11. Maspero C, Prevedello C, Giannini L, Galbiati G, Farronato G. Atypical swallowing: a review. Minerva Stomatol 2014; 63:217-27.
12. Bishara SE, Warren JJ, Broffitt B, Levy SM. Changes in the prevalence of nonnutritive sucking patterns in the first 8 years of life. Am J Orthod Dentofacial Orthop 2006; 130(1):31-6.
13. Maspero C, Cavagnetto D, Abate A, Cressoni P, Farronato M. Effects on the facial growth of rapid palatal expansion in growing patients affected by juvenile idiopathic arthritis with monolateral involvement of the temporomandibular joints: a case-control study on posteroanterior and lateral cephalograms. J Clin Med 2020; 9:1159

LETTER TO THE EDITOR

Airborne contamination during a full-mouth disinfection session: Pilot study before COVID-19 pandemic

F. Esposito[1,2], M. Boccuzzi[1], A. Riad[3], C. Preda[1,2], A. Chiesa[1,2], G. Oldoini[1] and A.M. Genovesi[1,4]

[1]Tuscan Stomatologic Institute, Versilia General Hospital, Lido di Camaiore, Italy; [2]Study Center for Multidisciplinary Regenerative Research, Guglielmo Marconi University, Rome, Italy; [3]Department of Public Health, Faculty of Medicine, Masaryk University, Brno, Czech Republic; [4]Unicamillus International Medical University, Department of Dentistry, Rome, Italy

Received October 28, 2020 – Accepted February 8, 2021

To the Editor,

The World Health Organization (WHO) released guidelines for the use of special Personal Protective Equipment (PPE) and avoiding and minimising use of aerosols during the COVID-19 pandemic (1). Professional dental hygiene is the most aerosol-producing chair-side activity in dentistry. A small fraction of contaminated droplets usually goes back into the air during almost all dental procedures, and virus, bacteria, and fungi could contaminate each surface in the dental office for days (2).

The One-Stage Full-Mouth Disinfection (FMD) introduced by Quirynen and co-workers in 1995 is the most used approach in professional oral hygiene (3). It consists of treating the patient's mouth all in one session, thus reducing the overall treatment time and site-to-site cross-infection risk. The standard procedure includes the use of chlorhexidine mouthwashes before the debridement (4). Different studies have reported the benefits of combining full-mouth debridement with the use of mouth rinses with antiseptic agents before or during the session (5). A recent review by James P. et al. confirmed the benefits of pre-operative Chlorhexidine oral rinses in terms of better clinical outcome and reduced bacterial contamination (6). Different alternatives to Chlorhexidine have been suggested to overcome Chlorhexidine side effects and explore the potential new adjunctive effect of other products such as ozonised water that is effective against different micro-organisms such as bacteria, virus, and fungi (7).

The aim of the present pilot study was to evaluate the antimicrobial efficacy of pre-operative rinses using ozonised water and Chlorhexidine before FMD in terms of airborne contamination prevention.

MATERIALS AND METHODS

To assess the bacterial load on the surfaces near dental chairs in a dental clinic (due to the contamination of aerosol during these treatment procedures), a slide was positioned 35 cm in front of the patient's oral cavity. The present clinical study was conducted in accordance with the 2008 Declaration of Helsinki. Each patient had to sign an informed written consent and answer a specific anamnestic questionnaire about their general and oral health. According to the inclusion and exclusion criteria, all consecutive patients needing a professional oral hygiene section were enrolled in the study (after the screening) between January and December, 2019.

The inclusion criteria were: patients aged between 25 and 60 years and with moderate gingivitis; patients with good compliance with their oral hygienist (both

Key words: aerosol; airborne contamination; bacteria; chlorhexidine; COVID-19; decontamination; disinfection; droplets

Corresponding Author:
Dr Francesca Esposito,
P.O. Tuscan Stomatologic Institute,
via padre Ignazio da Carrara, 39
Forte dei Marmi, 55042 (LU)
Tel.: +39 3480805381 - Fax: +39 0584618414
e-mail: doc.fraesposito@gmail.com

0393-974X (2021)
Copyright © by BIOLIFE, s.a.s.
This publication and/or article is for individual use only and may not be further reproduced without written permission from the copyright holder.
Unauthorized reproduction may result in financial and other penalties
DISCLOSURE: ALL AUTHORS REPORT NO CONFLICTS OF INTEREST RELEVANT TO THIS ARTICLE.

for home and professional treatments); and patients with good general health.

The exclusion criteria were: pregnancy; systemic conditions impairing oral health; professional hygiene or antibiotic therapy within the previous four months; mental disorders or physical disabilities affecting patient compliance; abscess, or other relevant inflammatory phenomena in the oral cavity; smoking more than ten cigarettes per day.

Study protocol

At least 40 patients were required for the study. The treatment procedure consisted of a periodontal examination (probing with a standard periodontal North-Caroline probe), after which the patients were randomly allocated to one of the two groups of treatment. At baseline (T0) patients were simply motivated to carry out a better home oral hygiene by using a chlorhexidine mouthwash and a sonic or electric toothbrush to reduce oral inflammation and plaque, according to the principle of modified full-mouth disinfection (MFMD) introduced by Genovesi and co-workers (7).

At T1 (after ten days), a full-mouth disinfection session was performed to patients according to the treatment group. Control (C) group (Control-group, n=30): All patients rinsed their mouths for 1.5 min with physiological water, then ultrasonic debridement, scaling and deplaquing were performed. The session concluded with air-polishing and again a 1.5-min rinse with physiological water. In the test (T) group (Ozone-group, n=30), all patients rinsed their mouths for 1 min and 30 s with ozoned water (1:3) and then 1 min with digluconate chlorhexidine 0.20% (Plakout Active - Polifarma Benessere Srl), for decontamination purposes. Then, ultrasonic debridement, scaling and deplaquing were performed. The session concluded with air-polishing and, again, 1-min rinse with digluconate chlorhexidine 0.20. Three patients (of the same group) were treated consecutively with the same microbiological test plate positioned at a 35-cm distance from them.

Microbiological analysis

The Mikrocount® (supplied by De Marco S.r.l. Via F. Tajani, 9 - 20133 Milan, produced by Schülke, Germany) is a simple microbiological test that uses small dip slides of 12.5cm². Mikrocount® dip slides are a tool to systematically monitor environmental hygiene in a dental or medical clinic. These types of slides are used for sterilisation and disinfection control of surfaces and airborne disinfection, and their protocol has been validated in different studies. As reported in the literature, this test is very rapid, convenient, safe, and uncomplicated (8). One dip slide is sufficient to determine the total plate count within the scope of microbiological monitoring. It contains nutrients for the growth of the most common bacteria, enterobacteria, yeasts and fungi; specific characteristics are as follow:

- Presentation: 4.5 ml medium each side
- Agar surface: 12.5 cm²
- Shelf-life: 9 months
- Storage: 10–25°C.

One slide of Mikrocount® TPC test was unscrewed and extracted from the cylindrical container without touching the culture media surfaces. The surface was positioned at a 90° angle from the patient's head. After

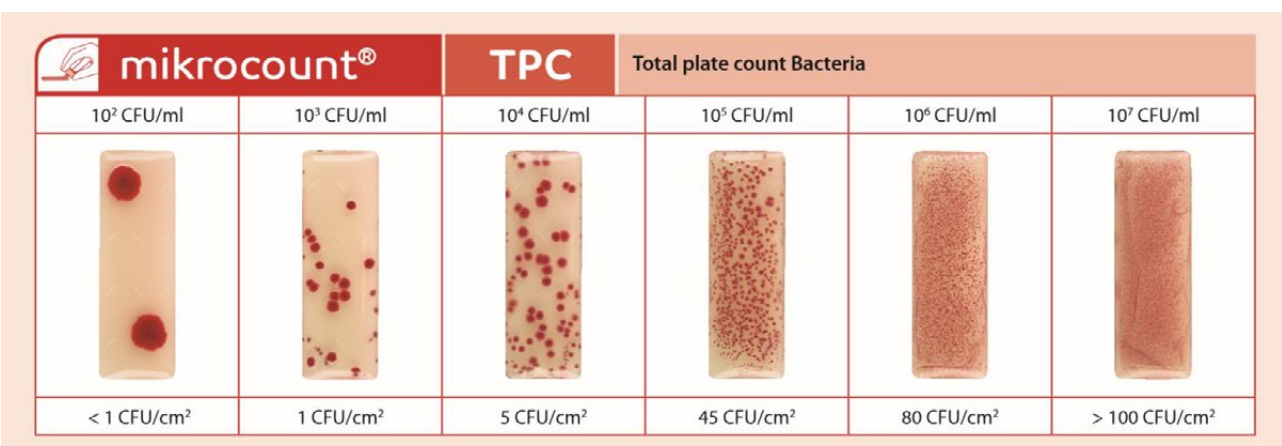

Fig. 1. *The estimated bacterial concentration using the mean distribution in the slide (1 CFU/Site= 1/1.25 x 104 CFU/10 M2).*

three consecutive patients, the slide was inserted in the container and incubated at 30±1°C for 24–48 h as indications of the producer. After incubation, the bacterial growth on media (plate count agar with triphenyl tetrazolium chloride and neutralising) was examined, and the bacterial concentration was estimated using the visual scheme shown in Fig. 1 (1 CFU/Site= 1/1.25 x 104 CFU/10 M2), classifying the slide in VI classes. One slide was used for three consecutive patients of the same groups, i.e. 10 times for each group of treatment.

Statistical analysis

Data were expressed as a mean ± standard deviation (SD) of values assigned for each patient; 1 point for class I, 2 points for class II, 3 points for class III, 4 points for class IV, 5 points for class V, 6 points for class VI. The *t*-test for independent samples was used to evaluate the statistical difference between the control group and test groups. A value of $P \leq 0.01$ was taken as being statistically significant. A Microsoft Excel spreadsheet (Microsoft Windows 2019) was used to display the statistics.

RESULTS

Sixty patients were considered eligible and enrolled in the study. The anamnestic data are resumed in Table I, and no significant differences were registered between the control group (C-group) and test group (T-group) ($p<0.05$).

In the C-group, no slides were associated with class I, class V or class VI while one slide was classified as class II, (3 patients); six slides were in class III and three slides in class IV. In the T-group, one slide was associated with class I, six slides with class II, three slides with class III and 0 slide with class VI. These data are shown in Table II.

A score was assigned to each patient corresponding to the slide class. The mean (± SD) score in the C group was 3.2±0.63, in the T group 2.2±0.63. A high score represents a high microbe contamination of the slides. The score in the T group was statistically significantly less than the C-group with p-value ≤ 0.01.

Table I. *Anamnestic data: sample size, age, gender, smoking. Only patients who smoked less than 10 cigarettes per day were admitted to the study.*

	C group	**T group**
Sample size	30	30
Age	39.38±5.08	41.0 ±7.14
Gender F/M	16/14	15/15
Smoking habits* (less Y/N)	7/23	9/21

Table II. *Class attribution for each slide. One slide corresponds to 3 patients.*

Classes	**I**	**II**	**III**	**IV**	**V**	**VI**
C-group (slide/patients)	0/0	1/3	6/18	3/9	0/0	0/0
T-group (slide/patients)	1/3	6/18	3/9	0/0	0/0	0/0

DISCUSSION

The aim of the present pilot trial was to evaluate the bacterial contamination of a surface 35 cm distant from the oral cavity of patients treated by non-surgical periodontal therapy. As reported in the results, in the T group, a water-ozone rinse was used immediately before the FMD, showing effectiveness in preventing airborne contamination. The Mikrocount® TPC test revealed significantly fewer bacteria, yeasts, and fungi in patients who received the pre-operative rinse by ozonised water than patients who received a physiological water rinse. In other fields of medicine, pre-operative oral decontamination by an antimicrobic rinse has also been recommended by recent systematic reviews (9). The classic cross-over study of Sekino and co-workers reported that a Chlorhexidine mouthwash used before and after dental treatments reduces plaque formation significantly (as well as decreasing the bacteria count) (10). Nevertheless, other studies have reported that prolonged use of Chlorhexidine has several side effects, and that the personal microbiota of patients will return in the same pattern as before the use of the antimicrobic substance (11). However, more worrying, is that even in healthy individuals, a major shift in their saliva will lead to more acidic conditions and a lower nitrite availability (12).

Ozone is a triatomic molecule with three atoms of oxygen that could be used as a carrier for airborne disinfection, using its antimicrobial property against bacteria, viruses, fungi, and protozoa, and its anti-inflammatory and analgesic properties for stimulating healing, blood circulation, and the modulation of the immune system.

A limitation of the present study may be related to the microbiological test used. It is an efficient and validated test, but it is limited only to bacteria and fungi, not viruses. Furthermore, it would be interesting to compare several antimicrobic pre-operative protocols, such as including a larger sample and a stratification of patients according to plaque index (considering that some patients may have more plaque and tartar, therefore contributing to more airborne contamination). The present pilot study reports that a rinse with watered ozone, immediately before a session of FMD, has positive effects in preventing airborne contamination after an oral hygiene session, which is significantly greater than a rinse with physiological water.

ACKNOWLEDGEMENTS

The authors would like to acknowledge the director of Istituto Stomatologico Toscano, Prof. Ugo Covani who allowed this pilot study and Dr. Simone Marconcini who helped authors during the elaboration of this clinical study for the thesis of master's degree. The work of A.R. was supported by the grant projects of Masaryk University no. MUNI/IGA/1543/2020 and MUNI/A/1608/2020.

REFERENCES

1. Spagnuolo G, De Vito D, Rengo S, Tatullo M. COVID-19 outbreak: an overview on dentistry. Int J Environ Res Public Health 2020; 17:2094.
2. Kohn WG, Harte JA, Malvitz DM, Collins AS, Cleveland JL, Eklund KJ. Centers for Disease Control and Prevention. Guidelines for infection control in dental health care settings--2003. J Am Dent Assoc 2004; 135:33-47.
3. Quirynen M, Bollen CM, Vandekerckhove BN, Dekeyser C, Papaioannou W, Eyssen H. Full- vs. partial-mouth disinfection in the treatment of periodontal infections: short-term clinical and microbiological observations. J Dent Res 1995; 74:1459-67.
4. Quirynen M, Mongardini C, de Soete M, et al. The rôle of Chlorhexidine in the one-stage full-mouth disinfection treatment of patients with advanced adult periodontitis. Long-term clinical and microbiological observations. J Clin Periodontol 2000; 27:578–589.
5. Young MP, Korachi M, Carter DH, Worthington HV, McCord JF, Drucker DB. The effects of an immediately pre-surgical chlorhexidine oral rinse on the bacterial contaminants of bone debris collected during dental implant surgery. Clin Oral Implants Res 2002; 13:20-9.
6. James P, Worthington HV, Parnell C, et al. Chlorhexidine mouthrinse as an adjunctive treatment for gingival health. Cochrane Database Syst Rev

2017; 3:CD008676.
7. Cosola S, Giammarinaro E, Genovesi AM, et al. A short-term study of the effects of ozone irrigation in an orthodontic population with fixed appliances. Eur J Paediatr Dent 2019; 20:15-18.
8. Salo S, Alanko T, Sjöberg AM, Wirtanen G. Validation of the Hygicult E dipslides method in surface hygiene control: a Nordic collaborative study. J AOAC Int 2002; 85:388-94.
9. Butera A, Maiorani C, Natoli V, et al. Bio-inspired systems in nonsurgical periodontal therapy to reduce contaminated aerosol during COVID-19: A comprehensive and bibliometric review. J Clin Med 2020; 9:3914.
10. Sekino S, Ramberg P, Guzin Uzel N, Socransky S, Lindhe J. The effect of a chlorhexidine regimen on de novo plaque formation. J Clin Periodontol 2004; 31:609614.
11. Flötra L, Gjermo P, Rölla G, Waerhaug J. Side effects of chlorhexidine mouth washes. Scand J Dent Res 1971; 79:119-25.
12. Bescos R, Ashworth A, Cutler C, et al. Effects of Chlorhexidine mouthwash on the oral microbiome. Sci Rep 2020; 10:5254.

ERRATA CORRIGE

Due to a printing error, in the article "Montelukast sodium combined with budesonide for cough variant asthma in children" published in Volume 34 No. 6 the tables were not included, therefore we are publishing the article again with the relevant tables.

LETTER TO THE EDITOR

Montelukast sodium combined with budesonide for cough variant asthma in children

AH. Li[1], YH. Gao[2], YM. Liu[3], YQ. Hu[4], H. Wei[5] and SQ. Lv[1]

[1]Department of Pharmacy, Weifang People's Hospital, Weifang, China; [2]Department of Pediatrics, Jiyang People's Hospital, Jinan, China; [3]Department of Cardiac function, Qingdao Central Hospital, Qingdao University, Qingdao, China; [4]Department of Endocrinology, The People's Hospital of Zhangqiu Area, Jinan, China; [5]Department of Ward, The People's Hospital of Zhangqiu Area, Jinan, China

Received May 22, 2020 - Accepted November 18, 2020

To the Editor,

Cough variant asthma (CVA), also known as occult asthma and allergic cough, is a common respiratory disease in children and belongs to a special type of asthma (1). The clinical symptoms mainly include long-term repeated dry cough. It is characterized as a persistent disease, with high recurrence rate and low cure rate, leading to a risk of asthma (2). Generally, the average physical functions of children are weaker than adults, and the delay of treatment may cause life-threatening complications (3). Therefore, timely and accurate diagnosis is of particular importance for therapy in the early stage.

Montelukast is a potent and selective leukotriene receptor antagonist non-steroidal anti-inflammatory drug (4), which can selectively inhibit the activity of leukotriene polypeptide in airway smooth muscle, as well as effectively prevent and inhibit the increase of vascular permeability caused by leukotriene, airway eosinophil (EOS) infiltration and bronchospasm. It specifically reduces airway cellular and non-cellular inflammatory substances caused by allergen stimulation as well as inhibiting airway hyperresponsiveness induced by allergens. Montelukast sodium employs its high affinity for the cysteyl leukotriene-1 receptor to selectively suppress the binding of cysteyl leukotriene to the cysteyl leukotriene-1 receptor to mediate airway hyperresponsiveness and lung function (5).

MATERIALS AND METHODS

Eighty children diagnosed with CVA were selected for the study and randomly divided into a combined treatment group and a control group, with 40 patients in each group. There were 23 males and 17 females in the control group, with an average age of (4.65±1.29) years. In the combined treatment group, there were 22 males and 18 females, with an average age of (5.18±1.35) years. The study was reviewed and approved by the hospital committee and all parents or guardians of the patients signed the informed consent.

Diagnostic criteria

According to the Guidelines for the Diagnosis and Treatment of Chronic Cough in Chinese Children revised by the Respiratory Group Chronic Cough Group of the Pediatrics Branch of the Chinese Medical Association in 2013, CVA is profiled as continuous cough more than 4 weeks, symptoms of dry cough, night or early morning attacks, worsened cold cough, clinically no infection symptoms or antibacterial drugs for a long time ineffective.

Key words: montelukast sodium; budesonide; CVA in children

Corresponding Author:
Dr Suqin Lv,
Department of Pharmacy,
Weifang People's Hospital,
151 Guangwen Street,
Weifang 261041,China
e-mail: mtp9bh@163.com

0393-974X (2021)
Copyright © by BIOLIFE, s.a.s.
This publication and/or article is for individual use only and may not be further reproduced without written permission from the copyright holder.
Unauthorized reproduction may result in financial and other penalties
DISCLOSURE: ALL AUTHORS REPORT NO CONFLICTS OF INTEREST RELEVANT TO THIS ARTICLE.

The treatment with bronchodilators was adopted to relieve cough symptoms. The lung ventilation function was normal, and the bronchial provocation test was airway hyperresponsiveness. An allergic disease or positive family history can be diagnosed using an allergen test. Chronic cough symptoms from other conditions were excluded.

Treatment

All children were given conventional treatments, such as anti-asthma, anti-cough, anti-infection, and phlegm elimination. In the control group, patients were treated with budesonide aerosol inhalation, 1 m/time, 2 times/d, 6-8 hours apart, 1 month/course, for a total of 4 courses. In the combined treatment group, the therapy adopted in the control group was combined with montelukast sodium. Under 5 years old, the dosage was 4 mg/time, while for the patients 5 years old and above, the dosage was 5 mg/time, for a total of 4 courses of treatment.

Lung function indicators were measured before and after treatment in the two groups, including forced vital capacity (FVC), forced expiratory volume in the first second (FEV1), and the ratio of the two (FEV1/FVC), and the peak night and day expiratory flow (PEF). Significant effect: the cough and other symptoms of the child basically disappeared within 14 days of receiving treatment, and lungs showed no obvious positive signs after examination, and there were no signs of recurrence after 6 months of follow-up. Effective: cough and other symptoms disappeared within 1 month after treatment, and lungs did not show obvious positive signs after examination, and there was no sign of recurrence after 6 months of follow-up. Ineffective: cough symptoms and other symptoms did not disappear within 1 month after receiving treatment, and lungs showed obvious positive signs after examination.

Statistical analysis

The data obtained in this study were analyzed using statistical software SPSS17.0. Counting data were expressed as percentages and *Chi*-squared test was used. The data were expressed as mean ± standard deviation of three independent biological experiments. Comparison between groups was performed using independent sample *t*-test. In the group comparison, paired sample *t*-test was used, and P <0.05 indicated that the difference was statistically significant.

RESULTS

The time of cough relief and disappearance in the combined treatment group was significantly shorter than that of the control group (P <0.05) (Table I). The total effective rate of the combined treatment group was 92.86%, which was significantly elevated compared with the control group of 69.05% (P <0.05) (Table II).

There was no significant difference in pulmonary function indexes between the two groups before treatment (P> 0.05). After treatment, the pulmonary function indexes of the two groups increased significantly (P <0.05), and the lung function in the patients from the combined treatment group was significantly improved compared to that in control group (P> 0.05) (Table III).

DISCUSSION

CVA is a clinically specific bronchial asthma with a high incidence in children (6, 7). CVA presents

Table I. *Comparison of cough relief and disappearance time*

Groups	Numbers	Cough relief	Cough disappears
Control groups	40	7.53	12.46
Combined treatment groups	40	9.47	17.12
χ^2		6.413	5.352
P		0.012	0.025

Table II. *Efficacy comparison between the combined treatment group and the control group*

Groups	Numbers	Significant effect	effective	ineffective	Total effective rate
Control group	40	18	10	12	28(70%)
Combined treatment groups	40	24	13	3	37(92.5)
χ^2					5.752
P					0.018

Table III. *Comparison of lung function indicators between the two groups*

Groups	Numbers	FVC(L)		FEV1(L)		FEV1/ FVC	
		Before treatment	After treatment	Before treatment	After treatment	Before treatment	After treatment
Control group	40	2.92	3.54	1.63	2.45	55.82	69.21
Combined treatment groups	40	2.86	4.02	1.62	2.96	56.64	73.63
t		0.91	6.85	0.282	4.66	0.249	6.365
P		0.361	0.000	0.785	0.000	0.813	0.000

the characteristics of high response and chronic airway inflammation, suggesting that the clinical treatment should target the control of chronic airway inflammation, and it is particularly critical to reduce airway hyperresponsiveness (8). Therefore, early and effective treatment is of great significance for improving the prognosis of such patients.

Montelukast sodium combined with budesonide in the treatment of CVA can effectively improve lung function of patients, improve clinical effectiveness, and facilitate timely recovery (9). In this study, the combined treatment significantly shortened the time of cough relief and disappearance. The total effective rate of treatment was also higher than that of the control group, indicating a favorable clinical effectiveness in the treatment of CVA. The lung function of patients who received therapy of montelukast sodium combined with budesonide was markedly improved after evaluating indexes such as FEVl and FVC, compared to patients who received single budesonide nebulized inhalation therapy.

In summary, the combined clinical effect of montelukast sodium and budesonide in the treatment of CVA is comparatively favorable to single use of budesonide, which provides new insights for the future treatment against CVA in clinical practice.

REFERENCES

1. Wang Y, Pengyu Z, Jiejun T, Zhiwei L, Wanying Q, Lujia L, Zhijun L. Therapeutic effects of Kangzhi syrup in a guinea pig model of ovalbumin-induced CVA. Evid Based Complement and Alternat Med 2018:1-11.
2. Nakajima T, Nishimura Y, Nishiuma T, Kotani Y, Funada Y, Nakata H, Yokoyama M. Characteristics of patients with chronic cough who developed classic asthma during the course of CVA: a longitudinal

study. Respiration 2005; 72:606-11.

3. Zhou J, Zhao X, Zhang X, et al. Values of fractional exhaled nitric oxide for cough-variant asthma in children with chronic cough. J Thorac Dis 2018; 10:6616-23.
4. Ozkan E, Akyuz C, Sehirli AO, Topaloglu U, Ercan F, Sener G. Montelukast, a selective cysteinyl leukotriene receptor 1 antagonist, reduces cerulein-induced pancreatic injury in rats. Pancreas 2010; 39:1041-46.
5. Peng J, Zhou H, Kuang G, Xie L, Tian T, Liu R. The selective cysteinyl leukotriene receptor 1 (CysLT1R) antagonist montelukast regulates extracellular matrix remodeling. Biochem Biophys Res Commun 2017; 484:474-79.
6. Fujimura M, Ogawa H, Nishizawa Y, Nishi K. Comparison of atopic cough with CVA: is atopic cough a precursor of asthma? Thorax 2003; 58:14-18.
7. Li W, Ban C, Zhang J, Hu Y, Han B, Han B. Correlation study of CVA and mycoplasma pneumonia infection in children. Pak J Pharm Sci 2017; 30:1099-102.
8 Corrao WM. Pearls and pitfalls in the diagnosis of CVA. Allergy Asthma Proc 2018; 39:466-67.
9 Shin J, Oh SJ, Petigara T, et al. Comparative effectiveness of budesonide inhalation suspension and montelukast in children with mild asthma in Korea. J Asthma 2019; 1-11.